Structural studies of doped ruthenium oxides

Neil Gavin Parkinson

Structural Studies of Doped Ruthenium Oxides

Neil Gavin Parkinson

Thesis submitted in part fulfilment of the requirements for the degree of

Doctor of Philosophy
at the
University of Durham

Departments of Chemistry and Physics

September 2003

Structural Studies of Doped Ruthenium Oxides

Submitted for the degree of Doctor of Philosophy, September 2003
by Neil Gavin Parkinson, Chemistry and Physics Departments, University of Durham

Abstract

The mixed ruthenium-copper oxide $Sr_2YRu_{1-x}Cu_xO_6$, is superconducting for low copper doping levels (x = 0.05 to 0.15), without the presence of cuprate planes, which are present in most high-temperature superconductors. Intriguingly the superconducting transition temperature and the Néel temperature are both ~ 30 K in this double perovskite, and thus below this temperature superconductivity and long-range magnetic order coexist. In order to better understand the materials, both the crystal and magnetic structures need to be determined and this thesis concerns itself with this task through the utilisation of neutron and X-ray diffraction.

This thesis begins with an introduction to the ruthenate double perovskites and examines particularly the necessary requirements for long-range magnetic order to establish itself in the material. An ordered crystal structure and an absence of competing magnetic interactions are prerequisites for magnetic ordering. This leads on to the copper doped ruthenates and the characterisation of the materials as superconductors.

Initially the $A_2YRu_{1-x}Cu_xO_6$ family, where A = Sr or Ba, is examined by neutron powder diffraction as yttrium is non-magnetic. This allowed the influence of the crystal structure on the magnetic structure of the ruthenium sublattice to be determined and its interactions revealed. The replacement of yttrium by a rare-earth element (e.g. Ho, Tb, Pr) has a profound effect on the magnetic interactions present in the material. Variable temperature neutron diffraction was vital, both for determining the magnetic structure and the interplay of these interactions in the material.

The position of copper within this framework was examined, particularly by anomalous X-ray diffraction, and its important influence on the materials is discussed.

Declaration

The work described in this thesis was carried out in the Departments of Chemistry and Physics at the University of Durham between October 1999 and September 2002, under the supervision of Prof. Judith A.K. Howard and Prof. P.D. Hatton. All the work is my own, unless otherwise stated, and has not been previously submitted for a degree at this or any other university.

Neil Parkinson

Dedication

For mum and dad
who have moved heaven and earth
to get me here

Acknowledgements

This thesis could not have produced without the help and support of people that I now wish to express my gratitude. Firstly, I must thank Professor Judith Howard who has shown an unbelievable amount of faith in me, and my ability to get the thesis completed on time. Professor Peter Hatton has shared also this belief in my talents over the years and is also rewarded with the completion of this thesis. For both, this must have been the most important aspect of the tuition, particularly when the end seemed so very far away, and I will now carry this confidence on in future life.

There could be no experiments without the samples, and for this I am grateful to the ceaseless Professor Maw-Kuen Wu and his dedicated laboratory, including Boon-How Mok and the late Din-Yeuan Chen, who taught me many things. The majority of the experiments have been conducted at large scale facilities and many instrument scientists and support staff have given their time and experience. Clemens Ritter has been a most professional instrument scientist and offered valuable advice for all the experiments at the ILL, while Philip Pattison has been absolutely indispensable at the ESRF. Ken Andersen introduced me to neutron diffraction at OSIRIS and Richard Ibberson furthered this at HRPD. Likewise, the Chiu Tang welcomed me to the SRS, and Robert Bewley was always most helpful at HET. Many thanks to all the guys who helped with the experiments. Additionally, I express my gratitude to the beamtime panels and facilities (ILL, ISIS, ESRF (CRG) and SRS) for their wisdom, and EPSRC for giving me the opportunity to do a PhD.

I have been blessed with two departments and groups of people, who have given me much encouragement over the years. In crystallography, I was first guided into GSAS by Ivana, who helped me out at crucial times when I was lost. For the first few days, the computers were an absolute jungle for me and I was fortunately Mike (I) was on hand to direct me out. With his job transfer, Mike (II) has more than taken up this task and provided much humour over the last few months in particular. This was complemented by the photographic skills of Horst, and Luc, who reassured me that MSBlast would not destroy everything. Amber spent some considerable time helping me fix this and has offered good advice throughout my time in the office, while Philip insured that I don't take things too seriously as most problems can be solved with refreshment. While at the ILL, John was keen that I should sample the local

hospitality and Andres always kept me amused. I greatly enjoyed my time playing football with Dima and appreciate the patience Olga must have shown while he was running me home in the car afterwards. During the writing up of the thesis I have been accompanied throughout by Andrei and Raju, who have both kept up my spirits with their stories, and for this opportunity I am grateful to Charlie for her kind donations. Victoria and Elinor have been particularly encouraging of me 'to get it done' and tolerated my antics with good humour. And finally a big thank you to Irene for helping out on so many occasions and for making lab lunches great.

I have had many a good time with my friends in Room 12, and I certainly must thank Ian Terry and Dan Read for getting me into the PhD, and Brian Tanner for his calmness. Also I am grateful to Andrea Li Bassi for teaching me a repertoire of Italian, likewise Persian from Mohammad, and Tom Hase for helping me out on so many occasions, on such a diverse range of topics. Of the current students, James, Sean, Kath, Amir and Phil have been particularly helpful when I've wanted to worm my way out of something. A great time on the HERCULES course was had with Stuart, and his computer skills have been replaced by Tom Beale's seamless running of the network. Finally, a word for John Dobson, the man who provides an education which no university possibly could, and probably should, but a great guy.

I have been a member of St. Aidan's College for the last eight years and have been made to feel very welcome at my Durham home, and appreciate very much the scholarships. To all the students and staff, and you know who you are, I thank you, and hope that we meet again some time soon, preferably in the bar.

In the wider Durham community I must thank the staff of Dryburn Hospital, especially all the consultants, doctors, nurses and physiotherapists (!) who helped restore me back to health. While for bringing hope I owe Martin O'Shea a great deal.

Back home, I have appeared intermittently over the past four years, though have always been warmly received by 'my mates back home.' To Nathan, Ross, Adam and Charlie thanks for the many 'first night back' and 'last night back' evenings we have enjoyed.

Finally, none of this would have been possible without the love and unconditional support of my mum and dad, my brothers and sisters, Michelle, John, Craig and Emma. Together, with the help of all the in-laws and countless nieces, nephews, aunts, uncles, cousins and grandad home is a nice place to be.

Table of Contents

1 Introduction to the Ruthenates

1.1 Perovskites

The perovskites have been extensively studied over time owing to the many important materials at the forefront of solid-state research which adopt this structure. From the early 1950's, the work of Jonker and van Santen on the intriguing electrical and magnetic properties of $La_{1-x}Sr_xMnO_3$ [1] has paved the way to the current research on colossal magnetoresistive materials [2]. The discovery of superconductivity in ceramic copper oxides by Müller and Bednorz in 1986 [3] accelerated research in doped perovskites.

The ideal perovskite structure, ABX_3, where X is typically oxygen, consists of B ions at the centre of oxygen octahedra, which usually form a corner sharing arrangement. The A ions reside in the centre of the remaining space and usually have less direct influence on the properties of the perovskite than the $[BO_6]$ octahedra, which are shown in Figure 1.1 with the unit cell of size a_p.

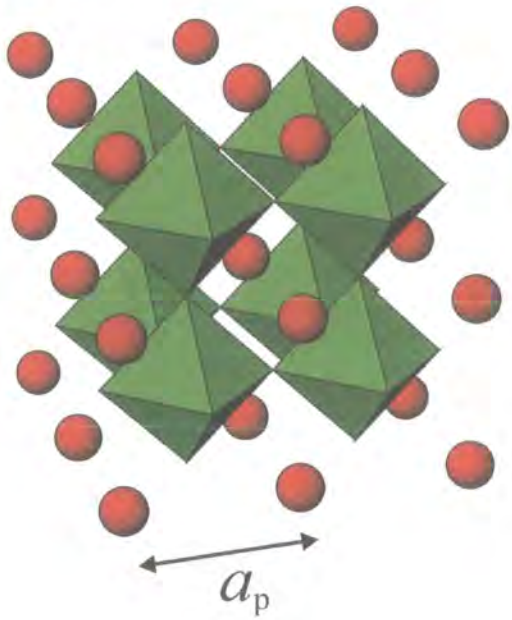

Figure 1.1 Crystal structure of the simple cubic perovskite ABO_3 in relation to the unit cell of dimension a_p. The A ions are shown as red circles with one B ion at the centre of each octahedra, the corners of which denote the oxygen positions.

1.2 Double Perovskites

The double perovskite structure has been studied for almost as long as the perovskite structure, since the early 1950's [4-6]. The general formula of a double perovskite is $A'A''B'B''O_6$, where two different species are allowed for both the A and B cations as

denoted by the primes. In the case of $A'=A''$ and $B'=B''$ the system reduces to the simple perovskite as previously described. Typically only one species is chosen for the A cations based on size, usually a large species such as Sr^{2+}, Ba^{2+} or La^{3+}. Greater variation of the properties of the double perovskites can be observed by varying the B cations and studies of virtually every transition metal and 4*f* element have been performed. Hence, in double perovskite systems it is usually only the B cations that are chosen to have two or more different species, as this is where the interesting physics and chemistry manifests itself.

The B cations are six-coordinate and are located in the centre of the octahedra. There are three possible arrangements of B cations in the double perovskites and these are shown in Figure 1.2. The first is a random arrangement of B' and B'' cations amongst the octahedra. The second is an alternating arrangement of B' and B'' cations at the centre of the oxygen octahedra and is known as the rock salt or 1:1 ordered structure. The third possible arrangement is a layered structure which has alternate layers of only B', then only B'' at the centre of the octahedra. The last type is extremely rare and was first synthesised in 1990 in La_2CuSnO_6 [7], followed by Sr doped $La_{2-x}Sr_xCuSnO_6$ [8] and finally Ln_2CuMO_6 (Ln = La, Pr, Nd, and Sm; M = Sn and Zr) [9], only six compounds in 50 years of double perovskite study.

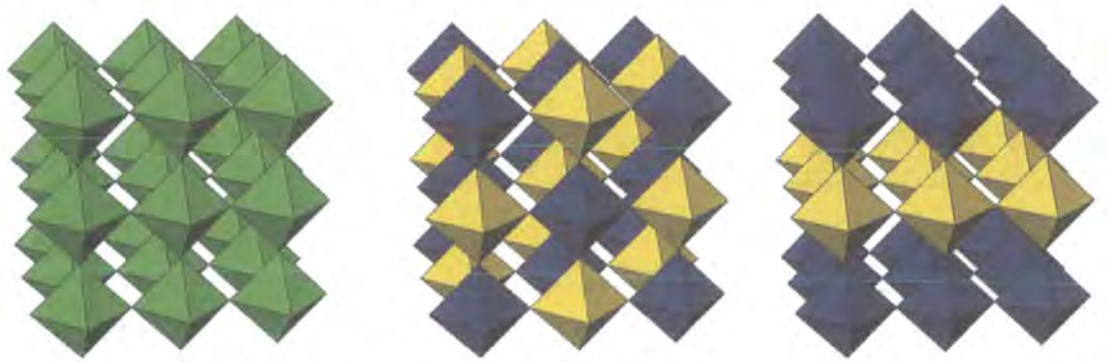

(a) (b) (c)

Figure 1.2 The three types of *B* cation ordering possible in the double perovskite system, (a) random, (b) rock salt and (c) layered. (The *A* cations are omitted for clarity.) The [*B*'O_6] octahedra are shown in blue, the [*B*"O_6] octahedra in yellow and an equal probability of either in green.

Following the successful synthesis of the layered compound Anderson *et al.* compiled all of the data on over 300 double perovskites studied since the 1950's [10] to suggest the likely structure that would be adopted by a new compound. They reported that the most important factor in determining the B cation arrangement was the charge difference, followed by the difference in ionic radii between the two B cations. As the

difference in the valence state of the two *B* cations was increased, then the 1:1 ordered (rock salt) arrangement would be favoured. Also, that as the difference in ionic radii of the two *B* cations was increased this would also favour the 1:1 ordering. (This can be viewed simply that as the *B* cations become more similar it matters less on which site they are located, hence tending towards a random arrangement). In fact, for charge differences greater than 2, the rock salt arrangement is preferred, whereas if this is less than 2, the random arrangement is more common. For charge differences of 2 the rock salt arrangement is preferred for ionic radii differences greater than 0.2 Å, whereas for less than 0.2 Å the random arrangement becomes prevalent. The layered structure appears to be energetically favoured at the fine boundary between the two other arrangements.

The *B* cations are the most important ions in the material in terms of both structure and properties. Once the *B* cations have been chosen, the *A* cation is selected largely based on its size and hence ability to stabilise the perovskite structure. From simple geometrical arguments Goldschmidt [11] defined a parameter '*t*' used to indicate the likely stability of a compound in perovskite form. In Equation 1.1 it has been slightly modified for the double perovskite form,

$$t = \frac{\frac{r_{A'} + r_{A''}}{2} + r_O}{\sqrt{2}\left(\frac{r_{B'} + r_{B''}}{2} + r_O\right)} \qquad \textbf{Equation 1.1}$$

where $r_{A'}$, $r_{A''}$, $r_{B'}$, $r_{B''}$ and r_O are the ionic radii of the ions. When *t* is unity, the double perovskite is cubic, however as *t* is reduced from 1 the more distorted the structure becomes. In particular the *A*-O bonds are placed under tension and the *B*-O bonds become compressed, which causes the tilting of the [BO_6] octahedra so these strains can be partially relieved. From this equation it becomes clear why large species are chosen for the *A* cations, in order to reduce strain and allow the [BO_6] to fit into a double perovskite structure comfortably. As the model is a simple one and takes no account of the properties of any individual ion, there is no fixed lower bound for *t* allowed by the perovskite structure. However, typically a value for *t* below 0.9 [12] indicates that a structure other than the perovskite one is probably more favourable.

Apart from their size, the *A* cations are also selected because they can influence the valence state of the *B* cations, which can have a large impact on the properties of the material. This is why there have been many studies in which the La^{3+} *A* cation has

been replaced by the similarly sized Sr^{2+} ion owing to their difference in valence state, which causes a compensating change in valence state of the *B* cations. In an undistorted cubic double perovskite ($t = 1$) the *A* cations are twelve-coordinated, with the four oxygen anions in the same layer, four in the layer above and four in the layer below. The effect of the tilting and distortion of the octahedra reduces the coordination number of *A* cation from 12 to typically 8-10. The tilting and distortion of the octahedra was classified by Glazer [13] along with the displacements of the *A* or *B* cations [14].

1.3 Ruthenates

The ruthenium double perovskites of general formula $A'A''B'Ru O_6$ have been studied extensively due to the interesting electrical and magnetic properties of the Ru^{5+}:$4d^3$ ion. Ruthenium is usually pentavalent in the double perovskites as determined from a variety of Mössbauer studies [15-17]. Principally two groups have performed the remainder of the work on the ruthenium double perovskites, Battle's research team [18-29] through the 80's and 90's, and latterly Doi, Hinatsu and co-workers [30-38].

1.3.1 One magnetic *B* cation, Ru^{5+}

It was only during the 1980's with the increasing availability of reliable powder neutron diffraction instruments that the magnetic structures of the ruthenates could be determined for the first time. Initially Battle chose double perovskites in which ruthenium was the only magnetic species which could order. It was determined that *B* cation ordering of some nature was an essential prerequisite for long-range magnetic order to develop and hence be observed in a neutron diffraction pattern as magnetic peaks.

For instance in Sr_2YRuO_6 [20], Sr_2LuRuO_6 [23], Ba_2YRuO_6 [23] and Ba_2LuRuO_6 [23] the Ru^{5+} ions order in a 1:1 arrangement over the two *B* sites with diamagnetic Y^{3+} or Lu^{3+}. Similarly Ca_2YRuO_6 [21], Ca_2LaRuO_6 [18, 19] and Ca_2NdRuO_6 [25] all adopt a 1:1 ordering with Ru on the *B* sites. However as the intended *A* cation was the relatively small Ca^{2+} ion, this often lead to a similarly sized ion taking its place (either partially or completely) and thus the above formulae can be better written as $Ca_{1.43}Y_{0.57}[(Ca_{0.57}Y_{0.43})Ru]O_6$, $CaLa[CaRu]O_6$ and $CaNd[CaRu]O_6$. In the case of Ca_2NdRuO_6 the interaction between Ru^{5+} and Nd^{3+} is weakened to such an extent due to its position on the *A* site that the Nd^{3+} cannot order magnetically, hence its

inclusion in the discussion here. Nevertheless they all adopt a 1:1 ordering of Ru with the other *B* cation(s) as would be expected from the simple charge and size difference analysis of Anderson *et al* [10].

A schematic of the 1:1 ordered arrangement in the double perovskite A_2MRuO_6 (*M* non-magnetic) is shown in Figure 1.3, which allows the pathways between the magnetic Ru^{5+} ions to be seen clearly. With a rock salt arrangement and only one magnetic ion, each Ru^{5+} ion is in the same environment and thus the potential for magnetic frustration is reduced. Magnetic interactions weaken with distance and usually only nearest-neighbour (NN) and next-nearest-neighbour (NNN) interactions need be considered. With the rock salt arrangement the closest *B* cation to Ru is always *M*, but there is no magnetic Ru-O-*M* interaction as *M* is not magnetic. Hence the strongest interaction is via nearest-neighbours (NN) along the pathway Ru-O-O-Ru and separated by $\sim\sqrt{2}a_p$ (where a_p is the unit cell parameter of the simple cubic perovskite ABO_3). When this interaction dominates, as is the case for the listed compounds above, a Type I structure results as shown in Figure 1.4, in which 8 of the 12 nearest-neighbour Ru ions are coupled antiferromagnetically. This is consistent with magnetic susceptibility measurements which determined the interactions to be predominantly antiferromagnetic in all the materials. The Néel temperatures are 26 – 35 K [20, 23] for the Sr and Ba compounds, but typically lower for the Ca series 12 – 16 K [15].

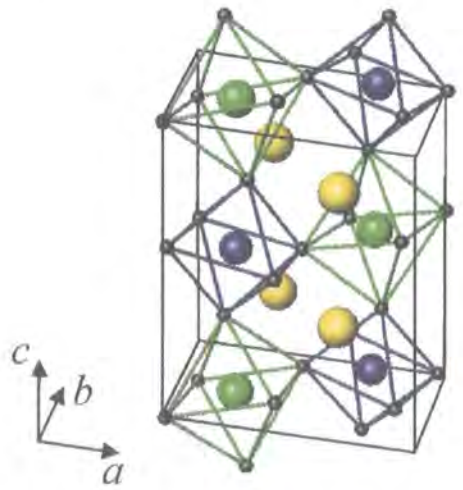

Figure 1.3 The crystal structure of a double perovskite which allows the pathways between each ion to be seen clearly. The *A* cations are shown in yellow, the Ru^{5+} ions in blue, the *B"* ions in green and the oxygens in black at the corners of the octahedra.

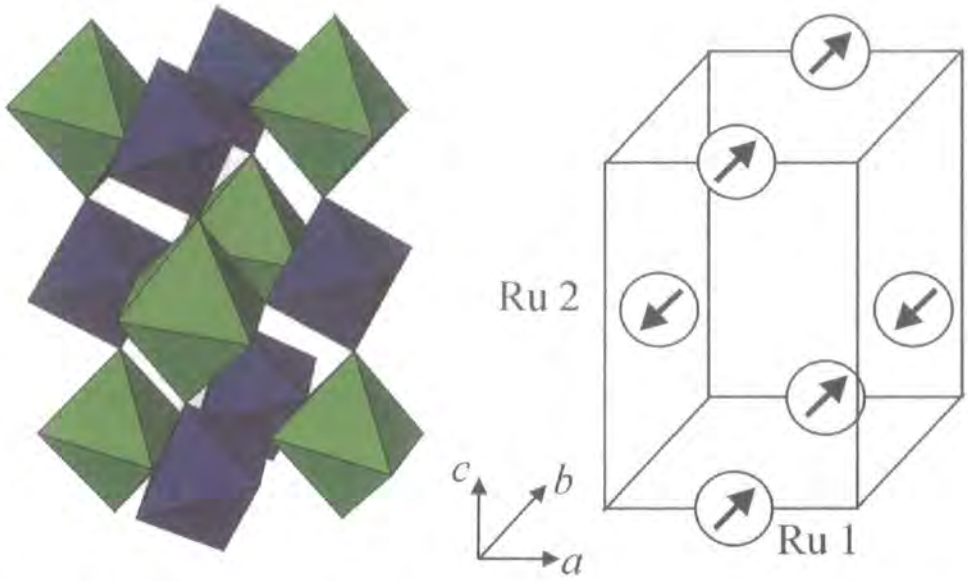

Figure 1.4 The crystal structure (omitting Sr atoms) is shown alongside the magnetic unit cell of dimensions $\sim\sqrt{2}a_p \times \sim\sqrt{2}a_p \times \sim 2a_p$, which displays only Ru ions for clarity. In the Type I antiferromagnetic structure, the two independent Ru ions (labelled Ru 1 and Ru 2) in the magnetic unit cell couple antiferromagnetically. The direction of the arrow indicates the direction of the magnetic moment and its length indicates the magnitude. Alternatively the structure may be envisaged with the magnetic moments parallel in the (002) plane, but anti-parallel in adjacent (002) planes.

One would expect the NN interaction to dominate as the NNN interaction is via the Ru-O-*M*-O-Ru pathway. In the above examples $M = Y^{3+}$, Lu^{3+} or Ca^{2+}, ions not noted for magnetic behaviour and fully ionised, so it would be surprising if any of these interactions were particularly strong. Thus the only magnetic interaction of significance is the Ru-O-O-Ru interaction which leads to a moment of 1.85 – 2.10 μ_B at 4.2 K for the crystallographically similar structures listed above [20, 23, 25]. The Ca compounds Ca_2YRuO_6 [15] and Ca_2NdRuO_6 [25], with noticeably more distorted structures have smaller moments of 1.2(1) and 1.5(2) μ_B, presumably for this reason.

Only in one material, that of Ba_2LaRuO_6 [18, 19] is the NNN interaction of significance compared to the strong NN interaction. This compound also has the 1:1 ordered arrangement of Ru and La ions, and thus the NNN pathway is along Ru-O-La-O-Ru. It is believed that due to the large unit cell size (as a result of A = Ba, B' = La) the NN interaction strength decreases more rapidly than the NNN interaction. This allows the NNN interaction to become significant enough to modify the magnetic structure to Type IIIa (illustrated in Figure 1.5) without appreciably changing the ordered moment (1.96(10) μ_B) or transition temperature (29.5 K) [19].

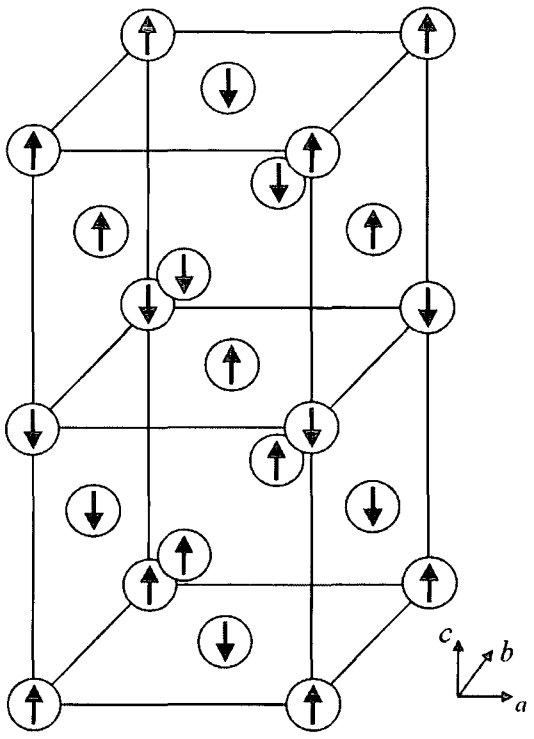

Figure 1.5 The Type IIIa magnetic structure of Ba_2LaRuO_6 where only Ru ions are shown.

In all the materials discussed thus far, there has had to be *B* cation ordering of the ions in order for a long-range magnetic structure to develop in the material. However there was one study on $BaLaZnRuO_6$ [24] in which the Zn and Ru ions were disordered and a magnetic structure developed, but this serves only to emphasize the more general behaviour.

With disorder over the *B* sites the nearest-neighbour to a Ru ion could be a Ru or Zn ion. As Ru^{5+} is the only magnetic ion, the nearest-neighbour distance is reduced to $\sim a_p$ along the pathway Ru-O-Ru. The NNN interaction is therefore via Ru-O-O-Ru at a distance of $\sim\sqrt{2}a_p$ and both these interactions are predicted to be antiferromagnetic. It is expected that the Ru-O-Ru interaction would be the strongest and hence dominate the ordering, leading to a Type G antiferromagnetic structure as shown in Figure 1.6(a) where all 6 antiferromagnetic Ru-O-Ru interactions are satisfied, but no Ru-O-O-Ru antiferromagnetic interactions are satisfied. In fact a Type A magnetic structure is adopted (Figure 1.6(b)), where only 2 out of 6 Ru-O-Ru interactions are satisfied, but now 8 out of 12 Ru-O-O-Ru interactions are satisfied. This indicates that the Ru-O-O-Ru interactions are very much stronger than expected or that there are more Ru-O-O-Ru connections than expected from a completely disordered structure. The authors reasoned that there were more Ru-O-O-Ru interactions than expected,

implying a short-range ordering of the *B* cations (too short to be observed in a neutron powder pattern), making the Type A magnetic structure favoured over Type G. (From the charge difference of Zn^{2+} and Ru^{5+} the ions were expected to be ordered, so short-range ordering of the ions is not unreasonable on these grounds.) Without this short-range ordering it would not be clear whether the Type G structure would be adopted, or whether the competing NNN interactions could lead to a frustrated magnetic structure or a spin glass. It is clear however that the disorder in the system leads to a slightly lower Néel temperature of ~20 K [16] and a magnetic moment of 1.5(1) μ_B [24].

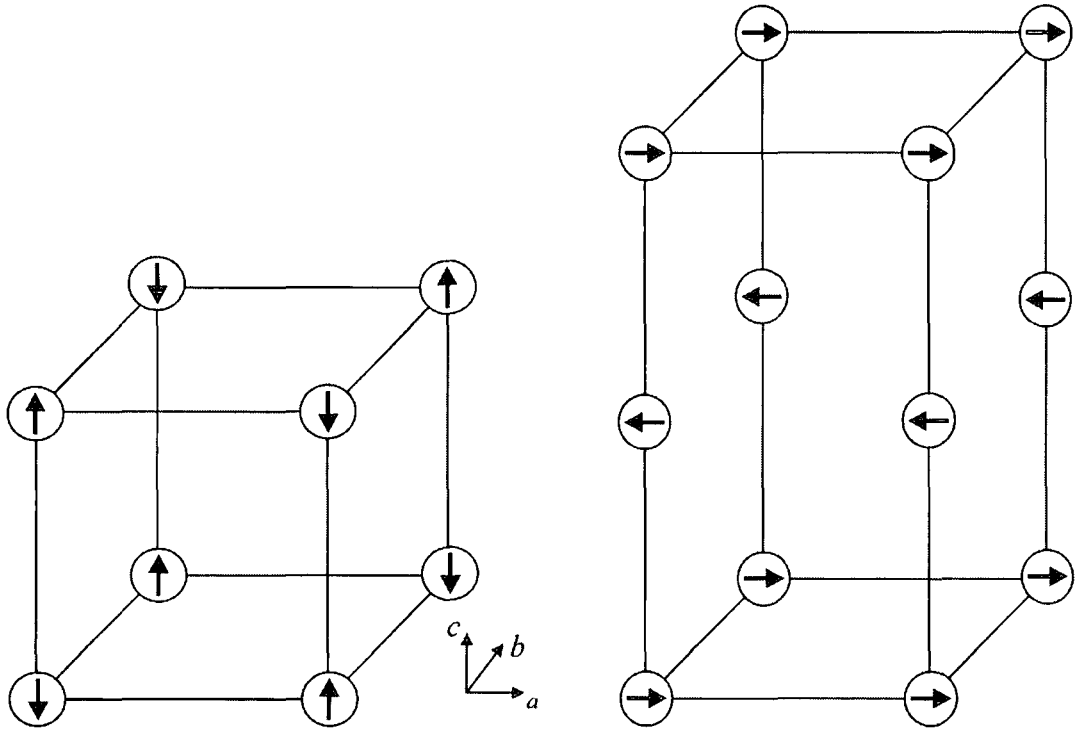

(a) (b)

Figure 1.6 The potential magnetic structures of $BaLaZnRuO_6$ are (a) Type G and (b) Type A. All *B* sites are shown with a magnetic ion, as any of them may have a Ru ion resident in a disordered arrangement.

Hence in all the materials thus examined *B* cation ordering, albeit possibly short-ranged, has been a requirement for long-range magnetic ordering to be observed, in order to minimise the potential for competing interactions.

1.3.2 Two magnetic *B* cations

Throughout the 1990's much research was focussed on the ruthenate double perovskite system, which was providing a glimpse of the possible magnetic interactions between 3*d* and 4*d* transition metal ions. Studies were undertaken on

$Sr_{1+x}La_xCuRuO_6$ [26, 27], La_2MnRuO_6 [30], Sr_2FeRuO_6 [24], *A'A''*$CoRuO_6$ [28] (where *A'*=Sr or Ba and *A''*=Sr, La or Ba), La_2NiRuO_6 [22] and $BaLaNiRuO_6$ [24]. Despite the many magnetic 3*d* transition partners for ruthenium on the *B* sites none was able to couple to form a long-range magnetic structure. Instead very complex magnetic behaviour was observed in magnetic susceptibility measurements, which was interpreted as the development of a spin glass phase or spin clusters.

There are two primary reasons for the lack of an ordered magnetic structure to develop in the material. The first is that none of the aforementioned compounds has a fully ordered arrangement of *B* cations. Both $SrLaCoRuO_6$ and $BaLaCoRuO_6$ [28] which were expected to have a rock salt arrangement of Co^{2+} and Ru^{5+} ions have ~10 % disorder on these sites, but all the rest are completely disordered. Thus in a material of A_2MRuO_6 (*M* = magnetic ion) there are a plethora of magnetic interactions, for example Ru-O-Ru, Ru-O-*M*, *M*-O-*M*, Ru-O-O-Ru, Ru-O-O-*M* and *M*-O-O-*M* as the NN and NNN interactions. Owing to the random positions of the *B* cations, each ion will be in a different environment, experiencing different interactions from different directions. Hence a long-range magnetic structure although still possible, is less likely to be adopted.

The second point concerns the nature of the interactions which will be present in the system. Magnetic interactions are critically dependant on ion type, bond angles and interatomic distances. Illustrating this is the case of Sr_2FeRuO_6, the Ru-O-Ru and Fe-O-Fe interactions are expected to be antiferromagnetic, whereas Ru-O-Fe interactions are ferromagnetic. Thus considering only the NN interactions, there can be competition between the different interactions, which leads to magnetic frustration and the development of a spin-glass [24]. In the highly (~90 %) ordered systems (e.g. $BaLaCoRuO_6$ [28]) there is essentially only one NN interaction, the Ru-O-Co ferromagnetic interaction. It is the NNN antiferromagnetic interactions (Ru-O-O-Ru and Co-O-O-Co) which compete with Ru-O-Co to create magnetic frustration and which highlight the similar interaction strengths of the Ru and Co ions.

Additionally the nature of the magnetic interaction, ferromagnetic or antiferromagnetic, is not always clear in the material, particularly as it depends on the bond angle. For the majority of the ruthenates the [BO_6] octahedra are fairly regular if tilted. Also the majority of the pathways of the type *B*-O-*B* are close to linear and thus of predictable nature. The nature of the interaction becomes less clear when the bond angle is reduced from 180° to 160-170° [27, 28]. As the X-ray or neutron powder

diffraction pattern only measures the average structure, even were this bond angle ~175°, there may be local distortions which reduce this and thus the interaction may also change throughout the material. Clearly, even in a material with *B* cation ordering, magnetic frustration and spin clusters are likely to result from variety in the nature of the interactions through the sample dependant on local distortions.

In summary, none of the materials developed a long-range magnetic structure due to competing interactions in the material. This could be brought about by the type of ions generating conflicting interactions (even were the structure ordered) or disorder of the *B* cations causing different environments for each ion. Very often a combination of the two was responsible.

Recent studies have focussed on the magnetic interactions of Ru^{5+} with 4*f* systems and this has proved less complicated than the 3*d* transition metals. Most of the 4*f* ions were examined in Doi and Hinatsu's systematic study [31] on Sr_2LnRuO_6 (*Ln* = Eu-Lu). The magnetic susceptibility measurements in all these compounds showed clear magnetic transitions at 30 – 46 K. Above the magnetic transition temperature the paramagnetic behaviour is dominated by the Ln^{3+} rather than Ru^{5+} ion. However below the magnetic transition the Ru^{5+} ion dominates and the magnetic interactions are predominantly antiferromagnetic.

The X-ray data indicated that all the materials adopt a rock salt arrangement of *B* cations, Ru^{5+} and Ln^{3+}. This was to be expected for a charge separation of 2 and a difference in ionic radius [39] between 0.33 – 0.49 Å. Hence the study of the 4*f* systems is simpler than that of the transition metals in this respect, as each ion of its type has the same environment. Thus, we need only consider the NN interactions Ru-O-*Ln* and the NNN interactions Ru-O-O-Ru and *Ln*-O-O-*Ln*.

Owing to the similarity of the transition temperatures in the materials it is believed that the Ru-O-O-Ru interactions dominate the ordering, rather than Ru-O-*Ln* which would vary from compound to compound [31]. The interaction between the rare-earths is not expected to be strong as typically they order at very low temperatures. The precise magnetic structure would require low temperature neutron powder diffraction data to be measured.

The first system to be examined by this technique was Sr_2ErRuO_6 [25] and both the Ru^{5+} and Er^{3+} ions form a magnetically ordered structure. Figure 1.7(a) shows the magnetic structure of the system to be composed of Ru^{5+} ions in a Type I structure, as is the case for many of the ruthenates previously described, where Ru^{5+} is the only

magnetic ion on the *B* site. The Er^{3+} also adopts a Type I structure which interpenetrates in such a way that the Er^{3+} moments in the (002) plane are anti-parallel to the Ru^{5+} moments. This increases the number of antiferromagnetic interactions between nearest-neighbours Ru^{5+} and Er^{3+} to 4 out of 6, rather than 2 out of 6 were they parallel, whilst maintaining 8 out of 12 next-nearest-neighbours anti-parallel.

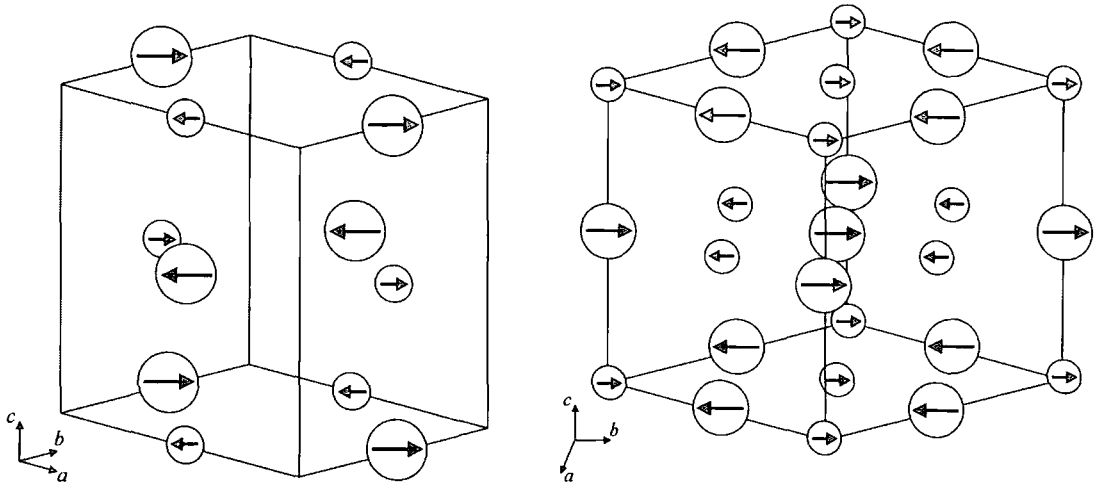

Figure 1.7 The magnetic structure of Sr_2ErRuO_6 can be envisaged in two ways. (a) Both the Ru^{5+} (small circles) and Er^{3+} ions (large circles) each adopt a Type I antiferromagnetic structure which interpenetrate each other. The lengths of the arrows denote the relative magnitudes of the magnetic moments. In the (002) planes atoms of a different type are aligned anti-parallel. (b) Imagining the ions all to be of one type the magnetic structure is Type C.

As some next-nearest-neighbours rather than all the nearest-neighbours are antiferromagnetically coupled, this suggests that the Ru-O-O-Ru interaction (or Er-O-O-Er) can be stronger than the Ru-O-Er interaction. This agrees with Doi and Hinatsu's findings described above [31], that the interaction Ru-O-O-Ru was stronger than Ru-O-*Ln* due to the similarity in ordering temperature of all compounds Sr_2LnRuO_6 (*Ln* = Eu-Lu). For this study on Sr_2ErRuO_6 [25] the authors reasoned that the Er-O-O-Er interaction would be negligible in comparison, as the stronger Er-O-Er interaction in Er_2O_3 leads to the very low ordering temperature of 3.4 K [40]. Thus, the interactions were placed in order of strength Ru-O-O-Ru > Ru-O-Er > Er-O-O-Er and hence the Er^{3+} sublattice orders not due to self-interaction, but because of the magnetic interaction with the ordered Ru^{5+} sublattice. This explains why it may be better to regard the magnetic structure as Type C (Figure 1.7(b)), as the two sublattices although composed of different ion types are far from independent.

Neutron diffraction patterns collected at different temperatures were able to determine the development of the ordered moment with temperature. At the lowest temperature (4.2 K) the Ru^{5+} and Er^{3+} magnetic moments are 1.74(6) μ_B and 4.59(3) μ_B respectively. With increasing temperature the Er^{3+} moment was found to decrease faster than the Ru^{5+} moment, which added supporting evidence for the order of the strengths of interaction.

Further neutron diffraction experiments have been undertaken on Sr_2HoRuO_6 [32, 36], Sr_2TbRuO_6 [33, 36], Ba_2ErRuO_6 [37], A_2LnRuO_6 (A = Sr, Ba; Ln = Tm, Yb) [38], Ba_2NdRuO_6 [34] and Ba_2PrRuO_6 [35] in this series. The choice of Ba for the A cation was necessary for the Pr and Nd compounds due to their larger size. The use of smaller Ca^{2+} had served as a warning in Ca_2NdRuO_6 and Ca_2HoRuO_6 [25] as the partial inclusion of Ca^{2+} on the B sites had prevented long-range ordering of the rare earth metal atoms. The Sr analogues could not even be synthesized [31]. For all the materials prepared, the magnetic measurements revealed principally antiferromagnetic interactions with transition temperatures of 36-58 K, though Ba_2PrRuO_6 was much higher with T_N = 117 K. The neutron studies showed the ordering of the B cations and the interpenetration of the Type I sublattices as with Sr_2ErRuO_6 [25]. However whereas Sr_2ErRuO_6 has ferrimagnetic ordering of the two ions types in each (002) plane, Sr_2YbRuO_6, Ba_2YbRuO_6, Ba_2NdRuO_6 and Ba_2PrRuO_6 have ferromagnetic ordering in this respect.

In summary, the ruthenate perovskites allow a wonderful opportunity to study the interactions of many magnetic species and their magnetic structures. When the Ru^{5+} is the only magnetic ion present, competition between interactions is minimised by reducing their number if the B cations adopt an ordered arrangement. With the introduction of a second magnetic ion B cation order is still important. This was evidenced by the ease that the 4*f* systems have for crystal and magnetic ordering of the B sites, whereas the 3*d* systems do not. In this case of the 4*f* systems the situation is further helped by the interactions between rare-earths being weak. For the 3*d* transition metals, the similarity of their size with the Ru^{5+} ion means the B cations order (if at all) to a lesser degree, thus leading to an increased number of interactions through the crystal in a non-regular way. This coupled with the greater strength of the magnetic interactions of the 3*d* elements, inevitably leads to magnetic frustration of these systems.

1.3.3 Magnetic Exchange Interactions

In order for long-range magnetic order to develop in a material there must be magnetic exchange interactions between the magnetic species. The nature of these interactions for the transition metals can be predicted by correct application of the Goodenough-Kanamori-Anderson rules [41], named after three of the pioneers in this field. The full treatment is quite complicated, but the three most important rules according to Khomskii [42] are listed below, from which the correct behaviour can most often be predicted.

Rule 1: The 180° exchange between half-filled orbitals is relatively strong and antiferromagnetic.

Rule 2: The 90° exchange between half-filled orbitals is ferromagnetic and relatively weak.

Rule 3: When the exchange is due to an overlap between an occupied and an empty orbital, the resulting exchange is ferromagnetic and relatively weak.

The double perovskites are ideally suited to the study of these magnetic interactions as the crystal structure has *B'*-O-*B''* bonds which are 180° in a cubic system, though this angle is reduced by any octahedral tilting distortions. From application of the first rule, the majority of interactions are antiferromagnetic in nature. For a transition metal ion at the centre of the oxygen octahedra, the degeneracy of the 5 orbitals is lifted and those orbitals with the electron density along the *B*-O axes ($d_{x^2-y^2}$ and d_{z^2}) have their energies raised, while those that have the electron density between the axes (d_{xy}, d_{xz} and d_{yz}) are at lower energies. For the Ru^{5+} ion with the $4d^3$ outer electron configuration, the three *d* electrons are able to occupy these three lowest energy states and still maximise the spin as according to Hund's rules. As a d^3 ion the nature of the magnetic exchange interactions are given simply by Goodenough-Kanamori-Anderson rules [41].

The nature of the magnetic exchange interactions between transition metals and rare-earths has been less well studied, though many of the lessons still apply. In particular, the majority of the interactions will be antiferromagnetic. Typically the rare-earths have very low magnetic ordering temperatures, illustrated by Tb_2O_3 with a Néel temperature of 2.4 K [43, 44], and Ho_2O_3, which does not order and remains

paramagnetic [45]. This is due to the poor spatial overlap of the 4*f* orbitals with the oxygen anion, which gets worse as the 4*f* series is traversed from left to right and the orbitals become progressively contracted. This overlap is also reduced in the perovskites (A_2RuLnO_6) when the Ru-O-*Ln* bond angle deviates from 180°, which occurs due to octahedral tilting distortions of the crystal structure, and so weakens the magnetic exchange interaction.

1.4 Copper Doped Ruthenates

There have been two principal groups of researchers working on the mixed ruthenium-copper oxides and the work of each team is reviewed separately.

1.4.1 The work of Wu *et al.*

The discovery in 1986 by Bednorz and Müller of high-temperature superconductivity in a ceramic oxide [3] prompted much research in this field. Early work focussed on increasing T_C, the temperature at which the material loses electrical resistance, above 77 K, the boiling point of nitrogen. This was first achieved with Wu's synthesis of $YBa_2Cu_3O_{7-\delta}$ (YBCO) [46]. Substitution of barium by other divalent elements proved difficult, until $YSr_2Cu_3O_{7-\delta}$ was produced by Wu [47], albeit multiphase. Single-phase samples were not synthesised until copper was partially replaced by another element, such as Al, Pb, Fe or Co [48].

Encouraged by these successes, Wu began to investigate the effect of doping with other elements, notably ruthenium, due to its interesting electrical and magnetic properties. It was during these attempts to synthesise $YSr_2Cu_{3-y}Ru_yO_7$ that $Sr_2YRu_{1-x}Cu_xO_6$ [49] was discovered, and its remarkable properties subsequently investigated.

The $Sr_2YRu_{1-x}Cu_xO_6$ system was examined for copper doping levels between $x = 0$ and 0.5 [49]. The parent compound, Sr_2YRuO_6, is an antiferromagnetic insulator, as determined by Battle *et al.* [20]. However, Wu's study showed that for samples with $x > 0.04$ superconductivity was induced. X-ray powder diffraction measurements confirmed the crystal structures of the materials to be distorted double perovskites with the 2116 stoichiometry. These measurements also showed that for samples with $x > 0.2$ sizeable impurity phases developed (~ 2 %), and for $x = 0.50$ the fraction of $YSr_2Cu_3O_{7-\delta}$ had reached 15 %. However, for $x < 0.2$ the copper was soluble and included in the lattice, as evidenced by the increased lattice parameters with doping

level x, due to the larger copper replacing the smaller ruthenium in the main phase. As the level of copper doping, x, is so low when superconductivity is induced, there are no CuO_2 planes present in the material, which are normally required in high-temperature superconductors.

Electrical measurements showed that the zero resistance temperature was ~ 30 K in the materials, as shown in Figure 1.8. To confirm the superconducting status of the materials, magnetic susceptibility measurements were also collected and are shown in Figure 1.9. As required, there is a diamagnetic response in the zero field cooled (ZFC) data, albeit weak. The field cooled (FC) measurements show an increase in the magnetic susceptibility at ~ 30 K, and a peak at 26 K. These features were interpreted as indicating ferromagnetism and antiferromagnetism respectively. From the difference in the maximum of the FC curve and the minimum of the ZFC curve, the superconducting volume was estimated to be at least 8 % of the sample volume, indicating a bulk phenomenon.

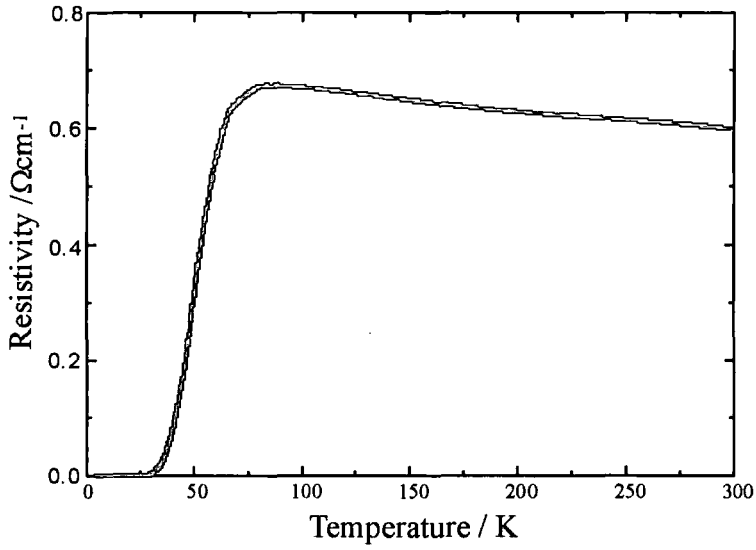

Figure 1.8 The electrical resistivity of $Sr_2YRu_{0.90}Cu_{0.10}O_6$, as measured on sintered bars of 3 ×4 ×1 mm^3 [50].

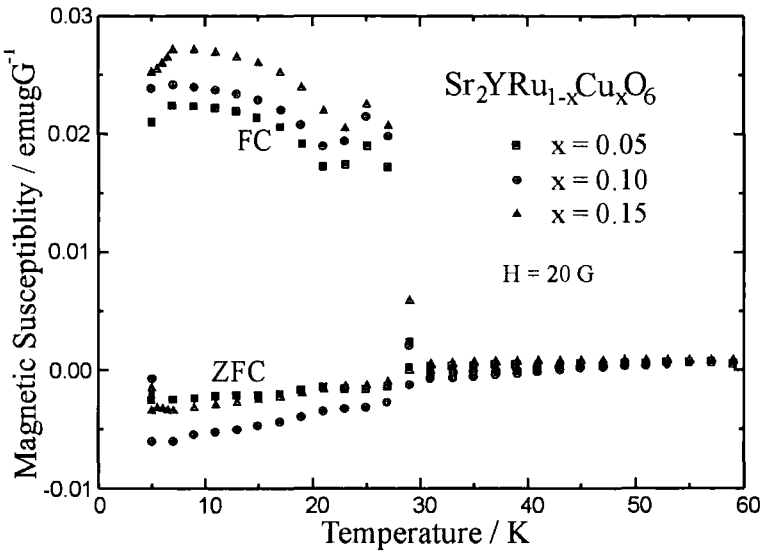

Figure 1.9 The magnetic susceptibility data for the $Sr_2YRu_{1-x}Cu_xO_6$ series [50].

The combination of the electrical and magnetic data suggested that there is a coexistence of the superconductivity and magnetism in the $Sr_2YRu_{1-x}Cu_xO_6$ system below ~ 30 K. The proximity of the two transition temperatures, T_C and T_M, suggested that there might be a link between them. The magnetic susceptibility data estimated the moment to be ~ 4 μ_B, consistent with the spin-only value of the Ru^{5+} ion. This confirms the antiferromagnetic nature in the doped samples of $Sr_2YRu_{1-x}Cu_xO_6$ has the same origin as in Sr_2YRuO_6 [20], namely superexchange between the Ru^{5+} ions. The doping of the copper, probably as the Cu^{3+} species, was thought to introduce holes into the material and allow formation of Ru^{6+}. Wu reasoned that via the process of double exchange [51, 52] these holes would be mobile and move through the Ru^{5+} framework, accounting for the ferromagnetic nature of the material. The notion was put forward tentatively that this could explain the similarity of the transition temperatures in the materials.

The family of mixed ruthenium-copper oxides was expanded with the $Ba_2YRu_{1-x}Cu_xO_6$ series [53]. Electrical measurements, similar to those in Figure 1.10 were performed and show the onset of superconductivity at ~ 90 K, while the zero resistance temperature is ~ 30 K.

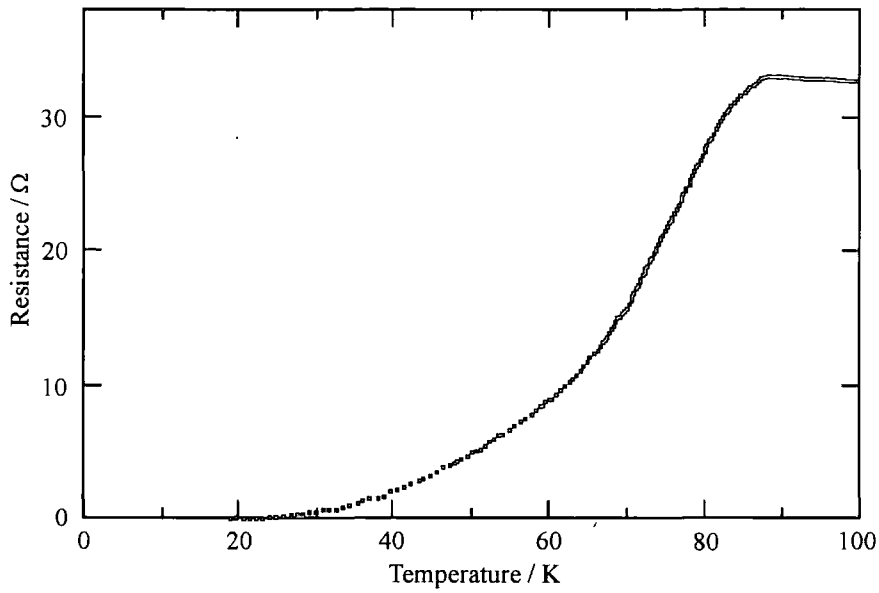

Figure 1.10 Resistance of the $Ba_2YRu_{0.90}Cu_{0.10}O_6$ sample as measured using the four probe technique on a sample with dimensions of 3 ×4 ×1 mm^3 [50].

The magnetic susceptibility measurements shown in Figure 1.11 display a diamagnetic response, giving credence to the superconducting nature of the samples. The superconducting transitions are broad in the $Ba_2YRu_{1-x}Cu_xO_6$ and $Sr_2YRu_{1-x}Cu_xO_6$ series, and this could be due to the suppression of the superconductivity by magnetic scattering or imperfections in the samples [49].

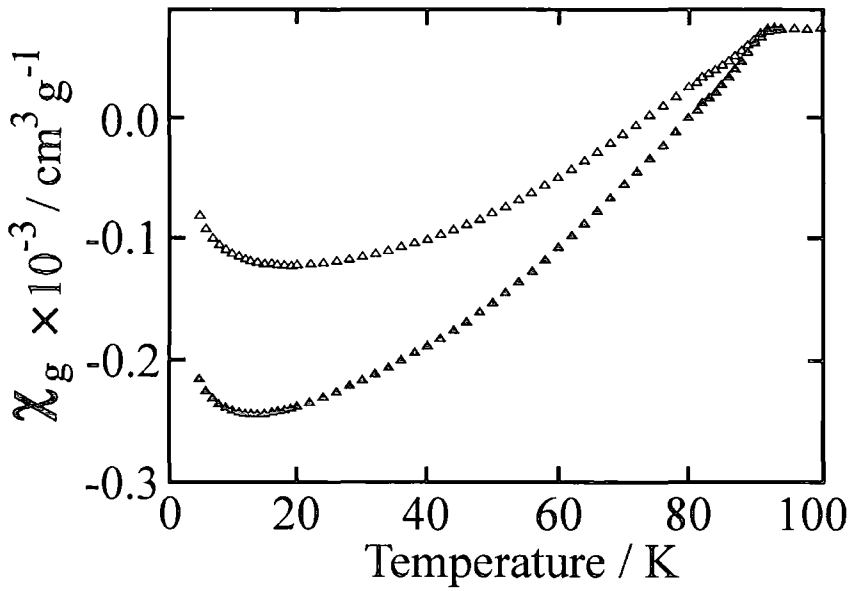

Figure 1.11 Magnetic susceptibility measurements of $Ba_2YRu_{0.90}Cu_{0.10}O_6$. The open triangles represent the FC data, the closed triangles the ZFC data, with a 1000 G field [50].

The problem in ascribing superconductivity in these mixed ruthenium-copper oxide materials, $Sr_2YRu_{1-x}Cu_xO_6$ and $Ba_2YRu_{1-x}Cu_xO_6$, stems from the possibility of 123

related superconductors, such as $YSr_2Cu_3O_{7-\delta}$ and $YBa_2Cu_3O_{7-\delta}$, forming from the same constituent elements. This was evidenced by a report from Motohashi *et al.* [54], in which an attempt to synthesise $Sr_2YRu_{1-x}Cu_xO_6$ with $x = 0.80$ failed, and large quantities of $YSr_2Cu_3O_{7-\delta}$ were produced. However, it was pointed out in the initial study of Wu [49] that for high copper doping levels ($x > 0.2$), impurities do form. Thus, the work of Motohashi does not discredit the work of Wu for low copper doping levels.

In order to dispel notions that a 123 type superconductor, such as $YSr_2Cu_3O_{7-\delta}$ or $YBa_2Cu_3O_{7-\delta}$, is responsible for the superconductivity observed in these mixed ruthenium-copper systems, specific heat measurements were performed [55]. Two peaks appear in the specific heat at T_C and T_M, which were attributed to these transitions, and agreed with Wu's Monte Carlo calculations. The calculations suggested also a canted magnetic order at low temperatures, for $T < T_1$, with either antiferromagnetic or ferromagnetic order observed at higher temperatures, for $T_1 < T < T_M$.

Clearly, the magnetic ordering is very important, so to expand the knowledge of the materials, rare-earth elements such as holmium were substituted for yttrium. The inclusion of holmium was expected to markedly affect the superconducting properties of the materials, due to the large moment of the Ho^{3+} ion. However, the $Sr_2HoRu_{1-x}Cu_xO_6$ system [56] behaves very similarly to the $Sr_2YRu_{1-x}Cu_xO_6$ series, and superconducts with a T_C only a few Kelvin below the yttrium analogue.

The impurity concerns would be addressed by the synthesis of a superconducting 2116 material, formed from elements which only produce a non-superconducting 123 partner. $PrBa_2Cu_3O_{7-\delta}$ was one of the few 123 materials which was believed to be non-superconducting [57]. Recently, it has been shown that with diligent preparation conditions superconducting $PrBa_2Cu_3O_{7-\delta}$ can be grown, albeit with difficulty [58], though the result has not been universally accepted. So, if superconducting $Ba_2PrRu_{1-x}Cu_xO_6$ were produced, then there would be virtually no possibility of an impurity phase containing a 123 material being responsible for the superconductivity. Preliminary results of the $Ba_2PrRu_{1-x}Cu_xO_6$ system were published [59] in which a diamagnetic response was observed at ~ 10 K, suggestative, but not confirming, a superconducting transition at this temperature.

Wu recognised at an early stage that the superconducting properties of the materials are difficult to establish from powder samples alone. Continued efforts have been

made to synthesise single crystals of these mixed ruthenium-copper oxides and just recently this has been achieved [60]. To date, the single crystals of $Sr_2YRu_{1-x}Cu_xO_6$ and $Ba_2YRu_{1-x}Cu_xO_6$ series are small, growing as octahedra with a 1-3 mm body diagonal, or as hexagonal plates of up to 6 mm respectively. However, work is continuing to improve the solution growth technique and hopefully yield single crystals which will be large enough for electrical, magnetic and neutron diffraction measurements.

1.4.2 The work of Blackstead, Dow and Harshman

A second group, led by Blackstead, Dow and Harshman have been interested in these mixed ruthenium-copper oxides, and have published many papers over the past 3 - 4 years [61-78]. However, despite this volume of publications, over 95 % of the data, details and analysis appears in just two papers [62, 70]. Initially the group were supplied samples from Wu's laboratory, in order to conduct experiments requiring highly specialised equipment, such as Mössbauer spectroscopy and neutron diffraction. Since June 2001, they have been producing superconducting samples of $Sr_2YRu_{1-x}Cu_xO_6$, although these are of lower quality admittedly [68]. However, all the results discussed here were performed using Wu's higher quality samples.

Mössbauer experiments were conducted on $Sr_2YRu_{0.95}Cu_{0.05}O_6$ at 4, 23, 30 and 40 K using a ^{99}Rh source [67]. The transmission Mössbauer effect spectrum measured at 4 K is split into 18 different lines, which indicates that ruthenium is present as the Ru^{5+} ion, from comparison with other spectra of ruthenate materials. At 23 K the lines are less distinct, and there is only one broad line at 30 K, while at 40 K the line narrows to the instrumental resolution. These results suggest that a magnetic transition is likely between 23 and 30 K.

This Mössbauer study is largely repeated in [62], albeit in lower detail, but the majority of the paper concerns itself with the electrical and magnetic properties of $Sr_2YRu_{1-x}Cu_xO_6$. They interpret their data as showing the onset of superconductivity at ~ 45 K and the zero resistance temperature as ~ 30 K. A diamagnetic response at 30 K is present, while a slight bump at 23 K is interpreted as the magnetic ordering temperature of ruthenium.

In the later magnetisation study [70], the authors also claimed to see a departure from Curie-Weiss behaviour that they had not noted before, interpreted as indicating ordering of copper at 65 K in the $Sr_2YRu_{0.85}Cu_{0.15}O_6$ sample. This is complimented by

neutron powder diffraction data measured on this sample at 9 and 40 K. At other temperatures, only 20° segments of diffraction patterns were collected at 14 irregular temperature intervals up to 100 K, with different measuring times. As such, the one crystal peak in these 20° segments was assumed to be constant and the magnetic moment estimated from the one or two peaks in the pattern, which extend to 29-35 K in the data. However, even without magnetic peaks, a magnetic moment was refined, calculating magnetic intensity within the background noise for temperatures up to 85 K. In order to have accord with their ruthenium magnetic ordering temperature of 23 K, for temperatures higher than this, the magnetic intensity was calculated from a magnetic moment only attributed to the 15 % copper. The disparity between their copper ordering temperatures passed without comment. The author of this thesis disagrees with these findings, and this is discussed further in Chapter 3 and in print [50].

Muon spin resonance studies were conducted on $Sr_2YRu_{0.90}Cu_{0.10}O_6$, [62, 77]. Initially, it was claimed [62] that there were two muon sites within $Sr_2YRu_{1-x}Cu_xO_6$, one in the $YRu_{1-x}Cu_xO_4$ layer, another in the SrO layer. They attributed 90 % of the muon signal to the $YRu_{1-x}Cu_xO_4$ layer and 10 % to the SrO layer, based on the local magnetic fields determined from the neutron data. It was reasoned that as muons carry positive charge, the smaller signal implies that this is the layer that is doped with holes, so that the supercurrent is carried through the SrO layer.

The fitted parameters, the precession frequency, which determines the local magnetic field, and the relaxation rate, which determines the fluctuations of the spins, varied with temperature. The results from the two muon signals were interpreted as a demonstrating a weak diamagnetic response and ruthenium magnetically ordering, both at 30 K. Owing to the contrasting nature of this 30 K ruthenium ordering temperature with the 23 K value reported from later neutron measurements, the authors assumed a spin-glass state between these two temperatures [77], despite correlations between the fitted parameters.

Microwave surface resistance measurements were performed [62] and from the similarity of the results with the magnetic field applied parallel and perpendicular to the field, the superconductivity was assumed to be in a crystallographic layer. The authors believe that this is the SrO layer, largely based on the interpretation of the muon data, and the fact that the magnetic field in this plane should be approximately zero. The authors extend their idea to the vast majority of high-temperature

superconductors, both with and without cuprate planes, and suggest that the SrO or BaO layers are responsible for the superconductivity [72, 74-76, 78]. The idea has met scepticism within the superconductor community.

In order to further promote their superconducting SrO or BaO theory, the $Ba_2GdRu_{1-x}Cu_xO_6$ system has been synthesised and studied [70]. The series is reported to be non-superconducting, while from magnetic measurements and surface resistance measurements they claim to observe copper ordering at 86 K, ruthenium ordering at 50 K, and gadolinium ordering at 12 K, distinct ordering temperatures for each ion. However, due to the extremely high absorption of naturally occurring Gd, neutron diffraction experiments, which would unambiguously determine this, were not performed.

According to their "charge reservoir" theory of superconductivity, the Gd^{3+} ion with $L = 0$ is not crystal field split, so the ion has ability to recoil and break the Cooper pairs. However, ions with $L \neq 0$ are crystal field split and so do not have the ability to recoil and break the Cooper pairs, allowing a supercurrent. This explains why $Sr_2YRu_{1-x}Cu_xO_6$ superconducts and $Ba_2GdRu_{1-x}Cu_xO_6$ does not. (Presumably the Y^{3+} ion does not qualify as although $L = 0$, $J = 0$ also.)

The location of the Gd^{3+} ion appears to be crucial, with the fact that it is next to the SrO layer means that it is close enough to break the Cooper pairs there. However, the Gd^{3+} ion is in the $GdRu_{1-x}Cu_xO_4$ plane, and so the pair breaking properties of the ion would surely prevent supercurrents in this plane also. So, it is hard to see how the $Ba_2GdRu_{1-x}Cu_xO_6$ series can discriminate in favour of the SrO layer theory proposed by Blackstead, Dow and Harshman, and the ruthenium-copper layer theory of Wu.

1.5 Other Ruthenate Superconductors

This section will detail briefly some other superconductors in which ruthenium plays a prominent role in the properties of the materials.

1.5.1 Sr_2RuO_4

Since the discovery of the high-temperature superconductors in the cuprates, there have been many attempts to reproduce the planar structure with elements other than copper. Despite an enormous scientific effort, this has only been achieved with ruthenium in Sr_2RuO_4. Superconducting Sr_2RuO_4 was first reported by Maeno *et al.* [79] in 1994, but since then the system has been extensively studied with over 500

papers published on the material. These were comprehensively reviewed by Mackenzie and Maeno [80], though only the most salient points will be compared and contrasted with the mixed ruthenium-copper systems here.

In both systems, Sr_2RuO_4 and $Sr_2YRu_{1-x}Cu_xO_6$, the superconductivity is believed to reside in the ruthenate layer, RuO_2 or $YRu_{1-x}Cu_xO_6$ respectively. Though in Sr_2RuO_4 the ruthenium is present as Ru^{4+} ($4d^4$), whereas in the mixed ruthenium-copper oxides it is as Ru^{5+} ($4d^3$) ions. The impurities have to be kept to an absolute minimum as the superconductivity in Sr_2RuO_4 is *p*-wave, which is unconventional and easily destroyed, and even in the purest samples T_C is only 1.5 K. This is in direct contrast to the superconductivity present in $Sr_2YRu_{1-x}Cu_xO_6$, which is probably conventional *s*-wave, and is robust against impurities and temperature, with $T_C \sim 30$ K.

1.5.2 Rutheno-cuprates

There is a further class of superconductors in which ruthenium and copper are both present and play a key role in the properties of the materials. These are the rutheno-cuprates, where there are distinct CuO_2 and RuO_2 planes, the former responsible for the superconductivity and the later for the magnetism. The superconducting and magnetic transition temperatures are widely spaced and this is in stark contrast to the mixed ruthenium-copper oxides of Wu.

The most widely studied rutheno-cuprate material, $RuSr_2GdCu_2O_8$, has $T_C \sim 36$ K [81] and $T_M \sim 133$ K [82], and so there is a coexistence of superconductivity and magnetism at low temperatures. Neutron diffraction data determined that the ruthenium moments are $\sim 1\ \mu_B$ and anti-parallel in all three crystallographic directions in a Type G magnetic structure, with a slight canting of no more than $0.1\ \mu_B$ away from the *c*-axis. This small ferromagnetic component was observed from hysteresis loops, while the limit of $0.1\ \mu_B$ was determined from a polarised neutron diffraction study [83], and is lower than the limit of $0.3\ \mu_B$ set by the unpolarised study [82]. Therefore, the magnetic structure of the ruthenium is a canted antiferromagnetic (i.e. weak ferromagnet).

The $RuSr_2GdCu_2O_8$ is classed as a 1212 compound in keeping with its stoichiometry, but there is also the similar 1222 class of compounds, such as $RuSr_2Gd_{1+x}Ce_{1-x}Cu_2O_{10}$, which are less well studied. For $x = 0.4$ [84] $T_C \sim 42$ K and $T_M \sim 180$ K and so there appears to be little difference between the two sets of rutheno-cuprates.

1.6 References

1 G.H. Jonker and J.H. Van Santen, *Physica* **16,** 337 (1950).

2 S. Jin, M. McCormack, T.H. Tiefel and R. Ramesh, *Journal of Applied Physics* **76,** 6929 (1994).

3 J.G. Bednorz and K.A. Muller, *Zeitschrift Fur Physik B* **64,** 189 (1986).

4 E.G. Steward and H.P. Rooksby, *Acta Crystallographica* **4,** 503 (1951).

5 F. Galasso, L. Katz and R. Ward, *Journal of American Chemical Society* **81,** 820 (1959).

6 E.J. Fresia, L. Katz and R. Ward, *Journal of American Chemical Society* **81,** 4783 (1959).

7 M.T. Anderson and K.R. Poeppelmeier, *Chemistry of Materials* **3,** 476 (1991).

8 M.T. Anderson, K.R. Poeppelmeier, S.A. Gramsch and J.K. Burdett, *Journal of Solid State Chemistry* **102,** 164 (1993).

9 M. Azuma, S. Kaimori and M. Takano, *Chemistry of Materials* **10,** 3124 (1998).

10 M.T. Anderson, K.B. Greenwood, G.A. Taylor and K.R. Poeppelmeier, *Progress in Solid State Chemistry* **22,** 197 (1993).

11 V.M. Goldschmidt, *Str. Nor. Videnskakad* **1,** 1 (1926).

12 O. Scmitz-Dumont and H.Z. Kasper, *Z. Anorg. Allg. Chem.* **341,** 252 (1965).

13 A.M. Glazer, *Acta Crystallographica* **B,** 3384 (1972).

14 A.M. Glazer, *Acta Crystallographica* **A,** 756 (1975).

15 R. Greatrex, N.N. Greenwood, M. Lal and I. Fernandez, *Journal of Solid State Chemistry* **30,** 137 (1979).

16 I. Fernandez, R. Greatrex and N.N. Greenwood, *Journal of Solid State Chemistry* **32,** 97 (1980).

17 N.N. Greenwood and A. Earnshaw, eds. *Chemistry of the Elements*, Pergamon Press: Oxford. 1257 (1984).

18 P.D. Battle, *Materials Research Bulletin* **16,** 397 (1981).

19 P.D. Battle, J.B. Goodenough and R. Price, *Journal of Solid State Chemistry* **46,** 234 (1983).

20 P.D. Battle and W.J. Macklin, *Journal of Solid State Chemistry* **52,** 138 (1984).

21 P.D. Battle and W.J. Macklin, *Journal of Solid State Chemistry* **54,** 245 (1984).

22 P.D. Battle and C.W. Jones, *Materials Research Bulletin* **22,** 1623 (1987).

23 P.D. Battle and C.W. Jones, *Journal of Solid State Chemistry* **78,** 108 (1989).

24 P.D. Battle, T.C. Gibb, C.W. Jones and F. Studer, *Journal of Solid State Chemistry* **78,** 281 (1989).

25 P.D. Battle, C.W. Jones and F. Studer, *Journal of Solid State Chemistry* **90,** 302 (1991).

26 M.P. Attfield, P.D. Battle, S.K. Bollen, S.H. Kim, A.V. Powell and M. Workman, *Journal of Solid State Chemistry* **96,** 344 (1992).

27 S.H. Kim and P.D. Battle, *Journal of Magnetism and Magnetic Materials* **123,** 273 (1993).

28 S.H. Kim and P.D. Battle, *Journal of Solid State Chemistry* **114,** 174 (1995).

29 P.D. Battle, J.R. Frost and S.H. Kim, *Journal of Materials Chemistry* **5,** 1003 (1995).

30 N. Kamegashira, T. Mori, A. Imamura and Y. Hinatsu, *Journal of Alloys and Compounds* **302,** L6 (2000).

31 Y. Doi and Y. Hinatsu, *Journal of Physics-Condensed Matter* **11,** 4813 (1999).

32 Y. Doi, Y. Hinatsu, K. Oikawa, Y. Shimojo and Y. Morii, *Journal of Materials Chemistry* **10,** 797 (2000).

33 Y. Doi, Y. Hinatsu, K. Oikawa, Y. Shimojo and Y. Morii, *Journal of Materials Chemistry* **10,** 1731 (2000).

34 Y. Izumiyama, Y. Doi, M. Wakeshima, Y. Hinatsu, K. Oikawa, Y. Shimojo and Y. Morii, *Journal of Materials Chemistry* **10,** 2364 (2000).

35 Y. Izumiyama, Y. Doi, M. Wakeshima, Y. Hinatsu, Y. Shimojo and Y. Morii, *Journal of Physics-Condensed Matter* **13,** 1303 (2001).

36 Y. Doi, Y. Hinatsu, K. Oikawa, Y. Shimojo and Y. Morii, *Journal of Alloys and Compounds* **323,** 455 (2001).

37 Y. Izumiyama, Y. Doi, M. Wakeshima, Y. Hinatsu, A. Nakamura and Y. Ishii, *Journal of Solid State Chemistry* **169,** 125 (2002).

38 Y. Doi, Y. Hinatsu, A. Nakamura, Y. Ishii and Y. Morii, *Journal of Materials Chemistry* **13,** 1758 (2003).

39 http://barns.ill.fr/dif/icsd/elementr.html

40 K.A. Gschneider and E. Le Roy, eds. *Handbook on the Physics and Chemistry of the Rare Earths*, Vol. III, North Holland (1979).

41 J.B. Goodenough, *Magnetism and the Chemical Bond*, John Wiley and Sons, New York, 393 (1963).

42 M. Ziese and J. Thornton, eds. *Spin Electronics*, Lecture Notes in Physics 569, Springer-Verlag, Berlin, 493 (2001).

43 B.C. Gerstein, F.J. Jelinek and F.H. Spedding, *Physical Review Letters* **8,** 425 (1962).

44 R.W. Hill, *Journal of Physics C-Solid State Physics* **19,** 673 (1986).

45 J.P. Schille, P. Sainctavit, C. Cartier, D. Lefebvre, C. Brouder, J.P. Kappler and G. Krill, *Solid State Communications* **85,** 787 (1993).

46 M.K. Wu, J.R. Ashburn, C.J. Torng, P.H. Hor, R.L. Meng, L. Gao, Z.J. Huang, Y.Q. Wang and C.W. Chu, *Physical Review Letters* **58,** 908 (1987).

47 M.K. Wu, J.R. Ashburn, C.A. Higgins, B.H. Loo, D.H. Burn, A. Ibrahim, T.D. Rolin, F.Z. Chien and C.Y. Huang, *Physical Review B* **37,** 9765 (1988).

48 S.A. Sunshine, L.F. Schneemeyer, T. Siegrist, D.C. Douglass, J.V. Waszczak, R.J. Cava, E.M. Gyorgy and D.W. Murphy, *Chemistry of Materials* **1,** 331 (1989).

49 M.K. Wu, D.Y. Chen, F.Z. Chien, S.R. Sheen, D.C. Ling, C.Y. Tai, G.Y. Tseng, D.H. Chen and F.C. Zhang, *Zeitschrift Fur Physik B-Condensed Matter* **102,** 37 (1997).

50 N.G. Parkinson, P.D. Hatton, J.A.K. Howard, C. Ritter, F.Z. Chien and M.K. Wu, *Journal of Materials Chemistry* **13,** 1468 (2003).

51 C. Zener, *Physical Review* **82,** 403 (1951).

52 P.W. Anderson and H. Hasegawa, *Physical Review* **100,** 675 (1955).

53 D.Y. Chen, F.Z. Chien, D.C. Ling, J.L. Tseng, S.R. Sheen, M.J. Wang and M.K. Wu, *Physica C* **282,** 73 (1997).

54 T. Motohashi, A. Yoshikawa, J. Shimoyama and K. Kishio, *Physica C* **282,** 515 (1997).

55 M.K. Wu, D.Y. Chen, F.Z. Chien, D.C. Ling, Y.Y. Chen and H.C. Ren, *International Journal of Modern Physics B* **13,** 3585 (1999).

56 M.K. Wu, D.Y. Chen, D.C. Ling and F.Z. Chien, *Physica B* **284,** 477 (2000).

57 C.H. Booth, F. Bridges, J.B. Boyce, T. Claeson, Z.X. Zhao and P. Cervantes, *Physical Review B* **49,** 3432 (1994).

58 M. Luszczek, W. Sadowski, T. Klimczuk, J. Olchowik, B. Susla and R. Czajka, *Physica C* **322,** 57 (1999).

59 M.K. Wu, B.H. Mok, M.J. Wang, D.C. Yuan, S.M. Rao, P.D. Hatton and N.G. Parkinson, *Journal of Low Temperature Physics* **131,** 1053 (2003).

60 S.M. Rao, J.K. Srivastava, H.Y. Tang, D.C. Ling, C.C. Chung, J.L. Yang, S.R. Sheen and M.K. Wu, *Journal of Crystal Growth* **235,** 271 (2002).

61 D.R. Harshman, H.A. Blackstead, W.J. Kossler, A.J. Greer, C.E. Stronach, E. Koster, B. Hitti, M.K. Wu, D.Y. Chen, F.Z. Chien and J.D. Dow, *International Journal of Modern Physics B* **13,** 3670 (1999).

62 H.A. Blackstead, J.D. Dow, D.R. Harshman, M.J. DeMarco, M.K. Wu, D.Y. Chen, F.Z. Chieng, D.B. Pulling, W.J. Kossler, A.J. Greer, C.E. Stronach, E. Koster, B. Hitti, M. Haka and S. Toorongian, *European Physical Journal B* **15,** 649 (2000).

63 D.R. Harshman, W.J. Kossler, A.J. Greer, C.E. Stronach, E. Koster, B. Hitti, M.K. Wu, D.Y. Chen, F.Z. Chien, H.A. Blackstead and J.D. Dow, *Physica B* **289,** 360 (2000).

64 H.A. Blackstead, J.D. Dow, D.R. Harshman, D.B. Pulling, W.J. Kossler, A.J. Greer, C.E. Stronach, E. Koster, B. Hitti, M.K. Wu, D.Y. Chen and F.Z. Chien, *Physica C* **341,** 163 (2000).

65 M. Lehmann, J.D. Dow and H.A. Blackstead, *Physica C* **341,** 309 (2000).

66 H.A. Blackstead, J.D. Dow, D.R. Harshman, D.B. Pulling, M.K. Wu, D.Y. Chen and F.Z. Chien, *Physica C* **341,** 571 (2000).

67 M. DeMarco, H.A. Blackstead, J.D. Dow, M.K. Wu, D.Y. Chen, F.Z. Chien, M. Haka, S. Toorongian and J. Fridmann, *Physical Review B* **62,** 14301 (2000).

68 H.A. Blackstead, J.D. Dow, P.J. McGinn and D.B. Pulling, *Journal of Superconductivity* **13,** 977 (2000).

69 H.A. Blackstead, J.D. Dow and D.R. Harshman, *Journal of Superconductivity* **13,** 981 (2000).

70 H.A. Blackstead, J.D. Dow, D.R. Harshman, W.B. Yelon, M.X. Chen, M.K. Wu, D.Y. Chen, F.Z. Chien and D.B. Pulling, *Physical Review B* **63,** 214412 (2001).

71 H.A. Blackstead, J.D. Dow, D.R. Harshman, D.B. Pulling, M.K. Wu, D.Y. Chen and F.Z. Chien, *Solid State Communications* **118,** 355 (2001).

72 J.D. Dow, H.A. Blackstead and D.R. Harshman, *Physica C* **364,** 74 (2001).

73 D.R. Harshman, W.J. Kossler, A.J. Greer, C.E. Stronach, D.R. Noakes, E. Koster, M.K. Wu, F.Z. Chien, H.A. Blackstead, D.B. Pulling and J.D. Dow, *Physica C* **364,** 392 (2001).

74 J.D. Dow and D.R. Harshman, *Physica B* **312,** 53 (2002).

75 J.D. Dow and D.R. Harshman, *Philosophical Magazine B-Physics of Condensed Matter Statistical Mechanics Electronic Optical and Magnetic Properties* **82,** 1055 (2002).

76 J.D. Dow and D.R. Harshman, *Journal of Physics and Chemistry of Solids* **63,** 2309 (2002).

77 D.R. Harshman, W.J. Kossler, A.J. Greer, D.R. Noakes, C.E. Stronach, E. Koster, M.K. Wu, F.Z. Chien, J.P. Franck, I. Isaac and J.D. Dow, *Physical Review B* **67,** 054509 (2003).

78 J.D. Dow and D.R. Harshman, *Physica C-Superconductivity and Its Applications* **388,** 447 (2003).

79 Y. Maeno, H. Hashimoto, K. Yoshida, S. Nishi Zaki, T. Fujita, J.G. Bednorz and F. Lichtenberg, *Nature* **372,** 532 (1994).

80 A.P. Mackenzie and Y. Maeno, *Reviews of Modern Physics* **75,** 657 (2003).

81 A.C. McLaughlin and J.P. Attfield, *Physical Review B-Condensed Matter* **60,** 14605 (1999).

82 J.D. Jorgensen, O. Chmaissem, H. Shaked, S. Short, P.W. Klamut, B. Dabrowski and J.L. Tallon, *Physical Review B* **63,** 054440 (2001).

83 J.W. Lynn, B. Keimer, C. Ulrich, C. Bernhard and J.L. Tallon, *Physical Review B* **61,** R14964 (2000).

84 I. Felner, U. Asaf, Y. Levi and O. Millo, *Physical Review B* **55,** R3374 (1997).

2 Experimental Discussion

This thesis is concerned with the determination of the crystal and magnetic structures of mixed ruthenium-copper oxides in order to understand the materials' properties. To facilitate this task powder diffraction patterns have been collected and model structures refined using the Rietveld refinement method. It is not the aim of this thesis to give a full treatise on data collection or refinement strategies; for these the interested reader is referred to the excellent text of Young [1]. From the X-ray powder diffraction pattern, the crystal structure can be refined. However, neutron diffraction also allows the possibility of determining the magnetic structure, though this is by no means trivial, as will be seen later. During the course of this study both techniques were applied, though owing to the magnetic nature of the materials, the weight of the thesis lies with neutron diffraction.

2.1 Neutron Diffraction Facilities

The neutron powder diffraction experiments have been conducted at two dedicated neutron facilities, which are among the best in the world. The Institut Laue Langevin (ILL) is a 60 MW research nuclear reactor, situated in Grenoble, France. The ILL provides a constant source of neutrons for over 40 instruments, which cater for a wide variety of scientific research. The second facility is the ISIS spallation source, which is located in the Oxfordshire countryside, close to Didcot. This pulsed neutron source has 25 neutron and muon instruments, and is also available to users in the academic community. Full details concerning the sources and their respective suites of instruments can be found on their web pages [2, 3] and only those features specific to the instruments used during this study will be discussed here.

2.2 Neutron Diffraction Instruments

These neutron powder diffraction instruments fell broadly into two classes, irrespective of their source, those of high resolution with low neutron flux, or high-flux, but with generally low resolution. All the instruments can accommodate a variety of apparatus to enable the study of the materials under non-ambient conditions. As the materials are magnetic with typical transition temperatures of ~ 30 K, cryostats capable of temperatures from 2 K to 300 K were employed at each instrument.

2.2.1 High-resolution studies at D1A

D1A is a high-resolution powder diffractometer at the ILL, with 25 detectors spread over an angular range of 150°. Utilising a constant wavelength of 1.904 Å, this allows data to be collected routinely to $(\sin\theta)/\lambda \sim 0.5$ Å^{-1}, which is equivalent to ~ 1 Å. The high take off angle of 122° ensures high-resolution at large scattering angles, where the peak density is often at its greatest. The high-resolution is achieved by employing a small step size of 0.1° for the detector bank, while the counting statistics can be improved by repeating the scans. Owing to the high-resolution of D1A, it is ideal for studying crystal structures. However, its flux is approximately a factor of 200 lower than D1B (Section 2.2.4), so only a few temperature points can be examined during any experimental run.

2.2.2 High-resolution studies at D2B

A second high-resolution diffractometer at the ILL was used for studying the materials, namely D2B. The instrument D2B has 64 detectors spaced every 2.5° and by employing a small step size of 0.05° a large angular range of data from 0° to 160° can be collected with great precision. Using the constant wavelength of 1.594 Å allows the diffraction pattern up to $(\sin\theta)/\lambda \sim 0.62$ Å^{-1}, or equivalently *d*-spacings down to ~ 0.81 Å, to be measured. When this optimum wavelength of 1.594 Å is used there are two modes of operation of D2B, either high-flux or high-resolution, depending on the collimation used, 20' or 5' respectively. The high-flux mode gives a beam with 10^7 neutrons per second at the sample, whereas the high-resolution mode has an order of magnitude less, but is essential when extremely high-resolution is required.

2.2.3 High-resolution studies at HRPD

In contrast to the previously described constant wavelength powder diffractometers, HRPD (High-Resolution Powder Diffractometer) is an important part of the ISIS facility and so is a time-of-flight diffractometer. The resolution in terms of *d*-spacing between peaks, is not determined by the angular resolution, as at a constant wavelength diffractometer, but by the time resolution. The time taken for the neutron to travel from the source to the detector in an elastic scattering allows one to determine its wavelength. The more accurately this wavelength is known, then the

better the resolution of the diffraction pattern. By increasing the flight path, the neutrons of different wavelengths will be spread out more temporally at the detector, thereby increasing the resolution in the diffraction pattern. Also, the longer the flight path the smaller the error in *d*-spacing originating from the finite size of the moderator where the neutron is "born." HRPD has a flight path of almost 100 m and attains a resolution of $\Delta d / d \sim 4 \times 10^{-4}$. The 100 K methane moderator produces a Maxwellian distribution of neutrons which peaks at ~ 2 Å, at a much shorter wavelength than OSIRIS (Section 2.2.5), due to the higher temperature of the moderator. Owing to this, HRPD is ideally suited to measuring low *d*-spacing peaks, usually where there is overlap of peaks in the diffraction pattern, as the high-resolution will also alleviate this problem. As ever, the disadvantage of high-resolution is reduction in the flux, because in order for the different pulses of neutrons not to overlap in time at the instrument, only 20 % the pulses are let through the choppers.

2.2.4 High-flux studies at D1B

In order to fully determine the temperature dependence of the crystal and magnetic structures of the materials, the constant wavelength diffractometer D1B at the ILL was used. The high-flux diffractometer D1B has 400 detectors spaced every 0.2° to create a detector bank 80° wide. In these experiments the detector bank was stationary, typically between 5° and 85°, as this is where the magnetic peaks appeared at low temperature, when the constant wavelength is 2.524 Å. This allowed the temperature to be increased continuously at a rate of 0.2 - 0.3 K per minute, from 2 K to 50 K and a diffraction pattern collected every 10 minutes, for a typical experiment. This strategy, rather than using a sequence of fixed temperature steps, ensured the maximal use of beam-time without significant loss of accuracy of temperature. However by utilising the wavelength of 2.524 Å, only peaks up to $(\sin\theta)/\lambda \sim 0.27$ Å^{-1} are measured and coupled with the low resolution (0.2°) the atomic coordinates and thermal parameters have to be set at the values obtained from analysis of the high-resolution data. No accuracy is lost by adopting this approach, provided that the high-resolution data indicates that the crystal structure does not vary greatly with temperature. Owing to the high-flux available at D1B, each diffraction pattern has sufficient counting statistics to allow accurate refinement of the lattice parameters with temperature, and the development of the magnetic moment to be measured in

detail. Hence a large temperature region could be explored rapidly using this diffractometer, which was capable of accessing temperatures between 2 and 300 K.

2.2.5 High-flux studies at OSIRIS

OSIRIS is at the ISIS facility and as such is a time-of-flight instrument, but differs from HRPD in a number of respects. Firstly, the liquid H_2 moderator is kept at 22 K and therefore yields less energetic neutrons than are used at HRPD, with a Maxwellian distribution of wavelengths around 6 Å. This is ideal for studying magnetic structures as they often have peaks at very large *d*-spacings, which require a comparatively long wavelength in order to be measured. The resolution is not as impressive as HRPD as the flight path is not as long, though it is still good with $\Delta d/d \sim 5 \times 10^{-3}$. The flux at the sample is approximately an order of magnitude larger than D1B, as it uses a range of wavelengths, rather than discarding most of the intensity to obtain a monochromatic beam. Owing to the combination of high-flux and good resolution, the diffraction patterns measured at OSIRIS were expected to be good enough to confirm the crystal structure and determine the magnetic structure. In order to measure a full diffraction pattern from 1 Å to 9 Å the data had to be collected in 7 overlapping 1.5 Å slices. In certain circumstances this can prove beneficial as the entire flux could be focussed on a small region of the diffraction pattern in order to highlight a particular detail of the structure. Each full diffraction pattern was measured over ~ 3.5 hours, with longer time spent at high *d*-spacing, to compensate for the reduced flux at longer wavelengths.

2.3 X-ray Synchrotron Diffraction Facilities

Two X-ray synchrotron facilities have been used to complete the studies of the materials. The European Synchrotron Radiation Facility (ESRF) is a third generation synchrotron, with almost 50 beamlines, and is on the same site in Grenoble as the ILL. The Synchrotron Radiation Source (SRS), situated near Daresbury (U.K.), is a second generation synchrotron and retains almost 40 beamlines. The choice of a synchrotron, rather than laboratory source, was necessitated because both a high-flux and tunable wavelength were required for the measurements, as will be discussed further in Chapter 6. The complete details of the synchrotrons can be found on their respective websites [4, 5] and the following section will only give the most relevant points.

2.4 X-ray Synchrotron Diffraction Instruments

The experiments were performed at the CRG beamline BM1B of the ESRF and the Station 2.3 at the SRS. This was necessary as each beamline has a different range of wavelengths for experimentation and allowed anomalous diffraction patterns to be collected around different absorption edges of the constituent elements.

2.4.1 Powder diffraction studies at BM1B

Situated on a bending magnet at the ERSF, BM1B can be used as a high-resolution and high intensity powder diffractometer. The available wavelength range is 0.4 Å to 1.2 Å, and so energies only as low as 10 keV are reached. Owing to this energy range, studies at the Ru *K*-edge (22117 eV) are possible, whereas those at the Cu *K*-edge (8979 eV) and Tb L_{III}-edge (7514 eV) are below the limit of practical usage. The diffractometer is equipped with 6 detectors, spaced 1.1° apart, which allow rapid data collection. Typically a small step size, such as 0.004°, is employed and the high-resolution is maintained by analyser crystals in front of each detector. With the use of a wavelength of ~ 0.5 Å and data measured between from 2.524° to 75.484° in 2θ, information which extends up to $\sin\theta/\lambda \sim 1.22$ Å^{-1}, or to *d*-spacings as low as ~ 0.41 Å is collected.

2.4.2 Powder diffraction studies at Station 2.3

Station 2.3 at the SRS can be used for powder diffraction studies with a broad wavelength range of 0.5 - 3 Å. This enables the lower energy, longer wavelength Cu *K*-edge (8979 eV) and Tb L_{III}-edge (7514 eV) to be reached, and indeed this is the optimum energy region to study on Station 2.3. Typically, diffraction patterns are measured with a step size of 0.01° for scattering angles of 2θ in the range 10° to 100°. High resolution is maintained by accuracy of the incident wavelength, with $\Delta\lambda/\lambda \sim 1.7 \times 10^{-4}$.

2.5 Sample Preparation

All the powder samples have been well prepared in the laboratory of Prof. Maw-Kuen Wu, by Dr. Din-Yeuan Chen and Dr. Boon-How Mok. The details of the preparation of the mixed ruthenium-copper oxides have been published [6, 7] and those details most pertinent for their synthesis are presented here.

All the samples were prepared by a solid-state reaction method with the oxides of the constituent elements thoroughly mixed in stoichiometric amounts. Each mixture was calcined at 1000°C for several days in an Al_2O_3 crucible and the resultant product pressed into a pellet. Depending on the particular series being synthesised, the sintering and annealing conditions varied as indicated in Table 2.1. The annealing stage, which is crucial for the production of superconducting samples, was often repeated 2 or 3 times. X-ray diffraction patterns were collected in between each anneal to ensure that the correct phase had developed and the impurities were at a minimum. Further characterisation measurements performed on the samples have been described in Chapter 1.

Material	Sintering Conditions	Annealing Conditions
$Sr_2YRu_{1-x}Cu_xO_6$	1390°C for 12 hours in O_2	1330-1400°C for 12 hours in O_2
$Ba_2YRu_{1-x}Cu_xO_6$	1460°C for 12 hours in O_2 (70%) & Ar(30%)	1400°C for 12 hours in O_2 (70%) & Ar(30%)
$Sr_2HoRu_{1-x}Cu_xO_6$	1375°C for 12 hours in O_2 (70%) & Ar(30%)	1300°C for 12 hours in O_2 (70%) & Ar(30%)
$Ba_2PrRu_{1-x}Cu_xO_6$	1300°C for 12 hours in O_2	1300°C for 12 hours in O_2

Table 2.1 The synthesis conditions of the ruthenium-copper oxides, where the copper doping level of x is 0.05 to 0.15.

From the synthesis procedure it would be hoped that single phase material developed with the least amount of impurity possible. From the later diffraction experiments described in Chapter 3 through to Chapter 6, the stoichiometry of the materials has been largely assumed. The use of high intensity and resolution synchrotron X-rays (Chapter 6) enabled the identification of small amounts of crystalline impurities and the deviation from stoichiometry is discussed briefly. However, if amorphous impurity phases were present in the samples then this would cause a departure from the sample stoichiometry in a manner which has not been measured. Furthermore, any volatility of the starting reagents could also result in non-stoichiometric samples as not all of the material would end up in the final product. Likewise, there is always the possibility of contamination from the Al_2O_3 crucible adding to the resultant sample or sample coating the crucible, though no evidence was found of aluminium inclusion in either the intended phase or a crystalline impurity in any diffraction pattern.

2.6 References

1 R.A. Young, ed. *The Rietveld Method*, Oxford University Press: Oxford (1993).

2 http://www.ill.fr/

3 http://www.isis.rl.ac.uk/

4 http://www.esrf.fr/

5 http://www.srs.ac.uk/srs/

6 D.Y. Chen, F.Z. Chien, D.C. Ling, J.L. Tseng, S.R. Sheen, M.J. Wang and M.K. Wu, *Physica C* **282,** 73 (1997).

7 M.K. Wu, B.H. Mok, M.J. Wang, D.C. Yuan, S.M. Rao, P.D. Hatton and N.G. Parkinson, *Journal of Low Temperature Physics* **131,** 1053 (2003).

3 Neutron Diffraction Studies of $Sr_2YRu_{1-x}Cu_xO_6$ and $Ba_2YRu_{1-x}Cu_xO_6$

3.1 Introduction

The two title series were studied using neutron powder diffraction in order to determine both the crystal and magnetic structures. Neutron diffraction has two major advantages over X-ray diffraction for determining the crystal structures of metal oxides. Unlike in X-ray diffraction patterns, there is no reduction of intensity at high angles due to atomic form factors, which allows access to large $(\sin\theta)/\lambda$ where much of the structural information can be gleaned. An additional advantage of neutron diffraction is that the scattering lengths do not vary in the same manner as the X-ray scattering factors. Thus, the relative scattering power of oxygen is enhanced with neutrons compared to X-rays and so allows the positions of the oxygen atoms that lie on non-special positions, to be determined more precisely. Neutron diffraction is the tool of choice for magnetic structure determination as the spin of neutron is sensitive to the magnetic moments of the ions, whereas X-ray diffraction is relatively insensitive to the magnetic structure.

The neutron diffraction experiments were performed at the Institut Laue-Langevin (ILL) and the ISIS facility. The high-resolution powder diffraction instrument D2B was used to determine the crystal structures accurately. With the crystal structures already determined, the use of high flux instruments such as D1B and OSIRIS would allow the intimate study of the magnetic structure development with temperature. This chapter will discuss the experiments performed on $Sr_2YRu_{1-x}Cu_xO_6$ and $Ba_2YRu_{1-x}Cu_xO_6$, where only one magnetic ion, Ru^{5+}, is considered.

3.2 Magnetic Form Factor of Ru^{5+}

In a neutron diffraction experiment the neutron scatters off the nucleus and due to its small size in comparison to the wavelength there is no appreciable deviation of the form factor from 1. Hence intensity can be measured in the diffraction pattern to high $(\sin\theta)/\lambda$ values readily. However, the magnetic intensity in a neutron diffraction pattern results from the interaction of the incident neutron with the electrons in the ion responsible for the magnetic properties. Clearly, this results in a magnetic form factor

for the magnetic intensity of similar magnitude to the atomic form factor for X-ray diffraction, and so will have a significant effect of the diffraction pattern.

The magnetic form factors are listed in *The International Tables of Crystallography* [1] for all recorded values. The only magnetic species in these systems are the Ru^{5+} ions, however there is no recorded magnetic form factor for this ion, the only ruthenium species listed are the neutral Ru atom and the Ru^{+} ion. The closest X-ray atomic form factor known is for Ru^{4+} and was only recently determined [2]. However, the atomic form factor for X-rays and the magnetic form factor for neutrons will not be identical as the electrons responsible for magnetic properties are those in unfilled shells and thus on average will be nearer the extremities of the ion. This results in the magnetic form factor having a more marked decrease on the intensity of the magnetic peaks than does the atomic form factor for X-rays, and so would not be the most exact substitute.

The absence of the Ru^{5+} magnetic form factor has not prevented powder neutron diffraction determining magnetic structures as evidenced by the vast body of literature covered in Chapter 1 [3-12]. The earliest studies on ruthenate double perovskites [3-7] used only the lowest angle magnetic peak at $(\sin\theta)/\lambda \sim 0.06$ Å^{-1} and assumed a magnetic form factor of unity. With improvements in Rietveld analysis of magnetic structures, later studies [8-12] used the Zr^{+} magnetic form factor listed in *The International Tables for Crystallography* [1] as this is isoelectronic with Ru^{5+}.

To determine the magnetic form factor accurately Equation 3.1 must be considered where $\langle j_0 \rangle$ is the primary contribution to the magnetic form factor of the transition elements and $s = (\sin\theta)/\lambda$. The coefficients A, a, B, b, C, c and D are the values which are quoted and a study of the magnetic form factors of the transition elements in every ionic state listed in *The International Tables for Crystallography* was undertaken. Comparison of the known magnetic form factors for isoelectronic species showed them to be quite different as the magnetic form factor results from the spatial extent of the electrons which contribute to the magnetic properties. In this case the spatial extent of the Ru^{5+} is far less than Zr^{+} due to the extra four units of nuclear charge, and so the Zr^{+} magnetic form factor will not be the best substitute. In fact, a better comparison is between adjacent element species Z^{n+} and $(Z+1)^{(n-1)+}$ as the reduced size of the element is compensated by the reduced ionic state.

$$\langle j_0 \rangle = A\, exp(-as^2) + B\, exp(-bs^2) + C\, exp(-cs^2) + D \qquad 3.1$$

Furthermore it was found that the magnetic form factor of one species could be mapped onto an adjacent species (either the next element or the next ionic state) by application of a common scaling factor in the exponent of each exponential term. The scaling factor would depend upon the specific transposition. Scaling factors vary regularly across the transition series and depend whether we are considering Z^{n+} to $Z^{(n+1)+}$ or Z^{n+} to $(Z+1)^{n+}$. An advantage of the scaling factors in the exponents is that they can be applied successively, and as such, the magnetic form factor for Ru^{5+} was estimated from Ru^{+} using a scaling factor of 0.63184. The Ru^{5+} magnetic form factor used was A = 0.441, a = 21.046 (33.309), B = 1.4775, b = 6.0360 (9.553), C = -0.9361, c = 4.2473 (6.722) and D = 0.0176 where the Ru^{+} value, if different, is shown in brackets. The magnetic form factors of Ru^{+}, Zr^{+} and the calculated Ru^{5+} are shown in Figure 3.1 and illustrates that the use of Zr^{+} form factor is actually worse than simply using Ru^{+} as the Zr^{+} ion is even less point-like. Comparison with the Ru^{4+} X-ray atomic form factor (the closest available to Ru^{5+}) confirms that the magnetic form factor decreases faster for the reason described earlier and shows that the calculated Ru^{5+} magnetic form factor lies within an acceptable upper bound.

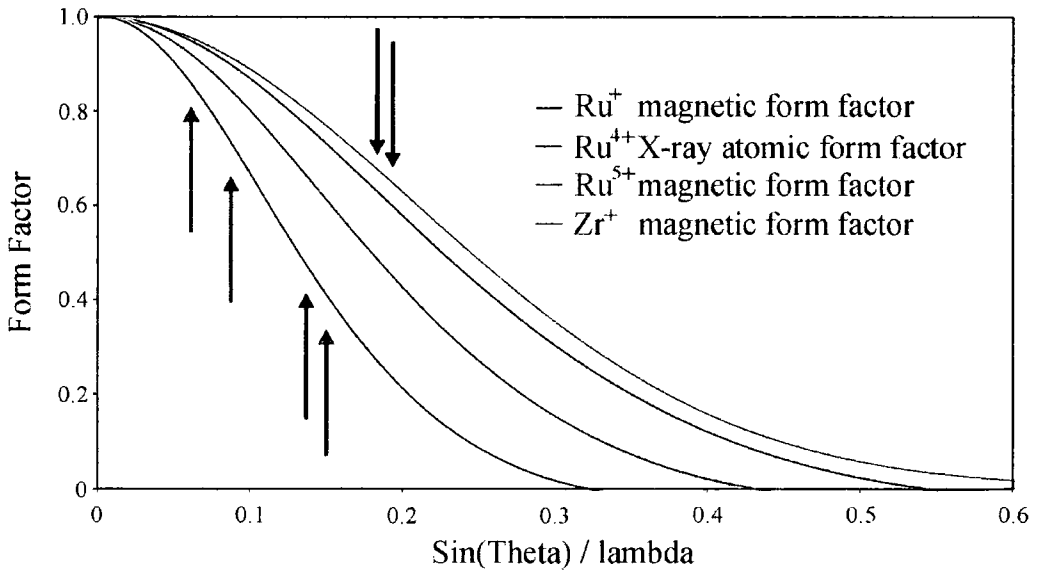

Figure 3.1 The magnetic form factors of Zr^{+}, Ru^{+} and Ru^{5+} are compared over the region of $(\sin\theta)/\lambda$ of interest with the positions of the first six magnetic peaks are indicated by arrows. Also shown is the X-ray atomic form factor of Ru^{4+} in order to show the X-ray form factor has a less severe effect on the intensities in a diffraction pattern than the calculated Ru^{5+} magnetic form factor.

All subsequent magnetic refinements used this calculated Ru^{5+} magnetic form factor as it is the best workable estimate of the magnetic form factor for Ru^{5+}, that is until an accurate single crystal study of a Ru^{5+} compound can be made. Refinements using alternative magnetic form factors such as Ru^{+} and Zr^{+}, yielded results which were 0.15 μ_B and 0.25 μ_B higher respectively, as the sharper drop off requires a larger moment to replicate the diffraction pattern. Hence, imprecise knowledge of the magnetic form factor does not impede a reasonably accurate magnetic moment determination, though suggests some studies may have systematically underestimated, or overestimated, the Ru^{5+} moment. The actual magnetic form factor of the Ru^{5+} ion is likely to be closer to the calculated Ru^{5+} values used here and this sets an error of ~ 0.10 μ_B on the magnetic moment from this source.

3.3 Neutron Diffraction Experiments on $Sr_2YRu_{1-x}Cu_xO_6$

Three members of the $Sr_2YRu_{1-x}Cu_xO_6$ series, x = 0.05, 0.10 and 0.15, were examined by powder neutron diffraction in order to determine the trends in crystal or magnetic structure with temperature and increased copper doping. The parent compound, Sr_2YRuO_6 had been studied previously by Battle *et al* [4] and so was not re-studied here. Experiments were undertaken at D2B to determine the crystal structure accurately, then at D1B to determine the temperature dependence of the magnetic structure. Finally confirmatory experiments at the high intensity and medium-resolution diffractometer OSIRIS were performed to search for any copper ordering in the materials. For all the diffraction measurements typically 3 – 4 g of material were contained in 12-16 mm diameter vanadium cans and details of the absorption correction appear in Appendix B.7.

3.3.1 Crystal Structure of $Sr_2YRu_{1-x}Cu_xO_6$

Diffraction patterns were measured for $Sr_2YRu_{1-x}Cu_xO_6$ with x = 0.05, 0.10 and 0.15 at 2, 21, 26, 28 and 42 K on diffractometer D2B in the high-flux mode. This allowed a diffraction pattern to be collected in 4 hours with sufficient statistics to determine the crystal and magnetic structures accurately through the magnetic ordering temperatures. All the $Sr_2YRu_{1-x}Cu_xO_6$ series were refined using GSAS [13] as distorted double perovskites in the monoclinic space group $P2_1/n$ with a unit cell of $\sqrt{2}a_p \times \sqrt{2}a_p \times 2a_p$ (where a_p is the unit cell parameter of a simple cubic perovskite) as this gave much the best fit to the data. The space group $P2_1/n$ allows an 1:1 ordered

arrangement of the *B* cations, namely Y, Ru and Cu, over the two possible sites, 2*c* at (0, ½, 0) and 2*d* at (½, 0, 0). The X-ray study (Chapter 6) was unable to determine precisely the ordering level in $Sr_2YRu_{0.85}Cu_{0.15}O_6$ due to a small impurity presence, though the material was ordered to a high degree. Owing to the similarity in neutron scattering lengths of the three elements (Y, Ru, Cu) the calculated neutron diffraction patterns would be unaffected by the *B* cation ordering level, so a 1:1 ordering of Ru(Cu):Y could be assumed. Even were the disorder of the *B* cations to be due to partial Cu exchange with Y, the initial suggestion from the X-ray data, the magnetic intensity of the calculated patterns would not change as neither ion is magnetic.

The neutron diffraction pattern of $Sr_2YRu_{0.85}Cu_{0.15}O_6$ measured at 42 K is shown in Figure 3.2. Unlike the X-ray diffraction patterns there is no atomic form factor fall off for the crystal structure peaks and this allowed meaningful data collection to high angles. The peaks in the pattern were indexed by a single phase confirming that this is above the magnetic ordering temperature. Refinements of the oxygen occupancies showed the sites to be fully occupied. Thus partial substitution of Ru^{5+} by Cu^{3+} is believed to lead to doping of holes into the structure as suggested previously [14], rather than significant oxygen vacancies. There are no major discrepancies between the model profile and the experimental data, indicating that the refined model structure is acceptable. Table 3.1 shows the refined crystal structures from analysis of both the 42 K and 2 K data and it can be seen that the crystal structure does not change appreciably over this temperature range. The temperature factors are given in terms of B_{iso}, where $B_{iso} = 8\pi^2 U_{iso}$.

From the crystal structure information in Table 3.1 the principal bond lengths and angles could be calculated and are shown in Table 3.2. These results are similar to the previous published study on the parent compound, Sr_2YRuO_6. The deviation of the Ru-O-Y bond angles from 180° to ~ 157° can be evidenced clearly by the tilted [BO_6] octahedra in Figure 3.3 which shows the refined crystal structure of $Sr_2YRu_{0.85}Cu_{0.15}O_6$.

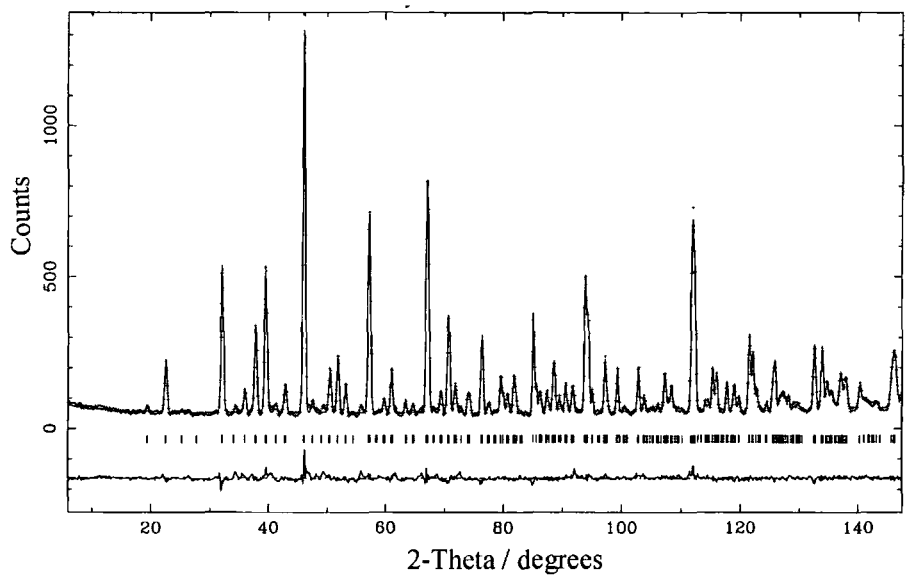

Figure 3.2 The diffraction pattern of $Sr_2YRu_{0.85}Cu_{0.15}O_6$ measured at 42 K using the neutron powder diffractometer D2B. The data points are crosses and the lines are the calculated profile and difference curve. The tick marks indicate the positions of the allowed reflections in space group $P2_1/n$.

$Sr_2YRu_{0.85}Cu_{0.15}O_6$		$P2_1/n$			42 K & **2 K**		
a / Å		b / Å	c / Å	β / °	Volume / Å^3		
5.75972(2)		5.77881(2)	8.14873(6)	90.323(1)	271.220(3)		
5.75961(2)		**5.77870(2)**	**8.14843(6)**	**90.325(1)**	**271.200(4)**		
Atom	Site	x	y	z	Occ	B_{iso}/Å^2	μ/μ_B
Sr	4*e*	0.0079(6)	0.0304(3)	0.7494(4)	1.000	0.24(2)	
		0.0077(6)	**0.0302(3)**	**0.7493(5)**		**0.24(3)**	
Y	2*c*	0	½	0	1.000	0.41(5)	
						0.43(5)	
Ru	2*d*	½	0	0	0.850	0.10(5)	
						0.05(5)	**2.54(10)**
Cu	2*d*	½	0	0	0.150	0.10(5)	
						0.05(5)	
O1	4*e*	0.3013(5)	0.2705(5)	0.9620(4)	1.000	0.33(5)	
		0.3020(5)	**0.2709(5)**	**0.9620(4)**		**0.35(5)**	
O2	4*e*	0.2669(5)	0.2985(5)	0.5367(4)	1.000	0.49(6)	
		0.2662(5)	**0.2983(5)**	**0.5371(4)**		**0.40(5)**	
O3	4*e*	0.9306(5)	0.4845(4)	0.7345(3)	1.000	0.37(4)	
		0.9309(5)	**0.4843(5)**	**0.7344(3)**		**0.36(4)**	

R_p = 5.43 %, R_{wp} = 7.26 %, R_{exp} = 9.83 %, R_{F^2} = 5.75 %
R_p = 5.56 %, R_{wp} = 7.46 %, R_{exp} = 9.83 %, R_{F^2} = 6.39 %

Table 3.1 The lattice parameters and atomic coordinates of $Sr_2YRu_{0.85}Cu_{0.15}O_6$ at 42 K and 2 K (shown in bold) as determined from analysis of the diffraction data obtained at D2B at the ILL.

$Sr_2YRu_{0.85}Cu_{0.15}O_6$		$P2_1/n$		D2B		42 K	
Y-O1	2.207(3)	Ru-O1	1.961(3)	O1-Y-O2	91.7(1)	O1-Ru-O2	90.4(2)
Y-O2	2.207(3)	Ru-O2	1.950(3)	O1-Y-O3	91.4(1)	O1-Ru-O3	90.3(1)
Y-O3	2.199(3)	Ru-O3	1.957(3)	O2-Y-O3	90.3(1)	O2-Ru-O3	90.7(2)
Ru-O1-Y	156.3(1)			Ru-O2-Y	157.7 (1)	Ru-O3-Y	157.2(1)
Sr-O1	2.783(4)	Sr-O1	2.540(5)	Sr-O1	3.341(5)	Sr-O1	2.862(5)
Sr-O2	2.767(4)	Sr-O2	2.548(5)	Sr-O2	3.392(4)	Sr-O2	2.902(5)
Sr-O3	3.188(3)	Sr-O3	2.664(3)	Sr-O3	2.543(4)	Sr-O3	3.247(4)
$Sr_2YRu_{0.85}Cu_{0.15}O_6$		$P2_1/n$		D2B		2 K	
Y-O1	2.209(3)	Ru-O1	1.960(3)	O1-Y-O2	91.9(1)	O1-Ru-O2	90.2(2)
Y-O2	2.209(3)	Ru-O2	1.948(3)	O1-Y-O3	91.4(1)	O1-Ru-O3	90.2(1)
Y-O3	2.199(3)	Ru-O3	1.956(3)	O2-Y-O3	90.3(1)	O2-Ru-O3	90.9(2)
Ru-O1-Y	156.1(1)			Ru-O2-Y	157.7(1)	Ru-O3-Y	157.3(1)
Sr-O1	2.789(4)	Sr-O1	2.536(5)	Sr-O1	3.434(5)	Sr-O1	2.859(5)
Sr-O2	2.763(4)	Sr-O2	2.548(5)	Sr-O2	3.390(4)	Sr-O2	2.907(5)
Sr-O3	3.187(3)	Sr-O3	2.664(3)	Sr-O3	2.544(4)	Sr-O3	3.246(4)

Table 3.2 The principal bond lengths (Å) and bond angles (°) of $Sr_2YRu_{0.85}Cu_{0.15}O_6$ at 2 K and 42 K.

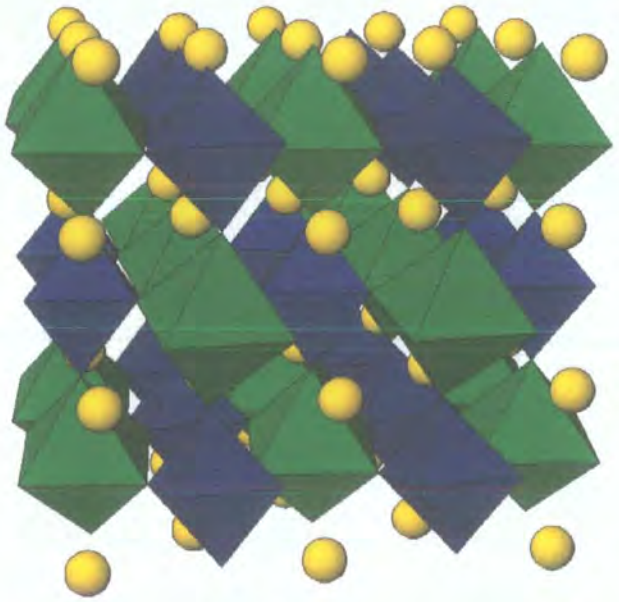

Figure 3.3 The refined crystal structure of $Sr_2YRu_{0.85}Cu_{0.15}O_6$ is a distorted double perovskite. The RuO_6 octahedra (blue) and the YO_6 octahedra (green) are shared at the corners. (The CuO_6 octahedra share the same sites as the RuO_6 and are not shown for clarity.) The Sr atoms are shown as circles (yellow) and are essentially space filling.

The refinements for all the other temperatures and members in the $Sr_2YRu_{1-x}Cu_xO_6$ series yield results which are very similar and full details can be found in the Appendix B.1.1. There are no significant trends in the crystal structure with increased copper doping, except for the expansion of the unit cell volume consistent with the greater size of the Cu^{3+} ion compared to Ru^{5+} ion. This is illustrated in Figure 3.4 which also displays a small increase in unit cell volume with temperature for the series. The majority of the increase is between 28 and 42 K, the region in which magnetic ordering is lost. The expansion is anisotropic with the *c*-axis expanding at approximately twice the normalised rate of the *a* and *b* axes (i.e. $2 \times \Delta a/a \approx 2 \times \Delta b/b \approx \Delta c/c$) for both temperature and copper doping. Unfortunately the changes in the lattice parameters are only ~ 0.0001 Å, for both changes in temperature from 2 K to 42 K, or increasing *x* by 0.05. As such, this anisotropic increase could not be attributed to any particular bond length listed in Table 3.2 as the error in these lengths is over an order of magnitude larger.

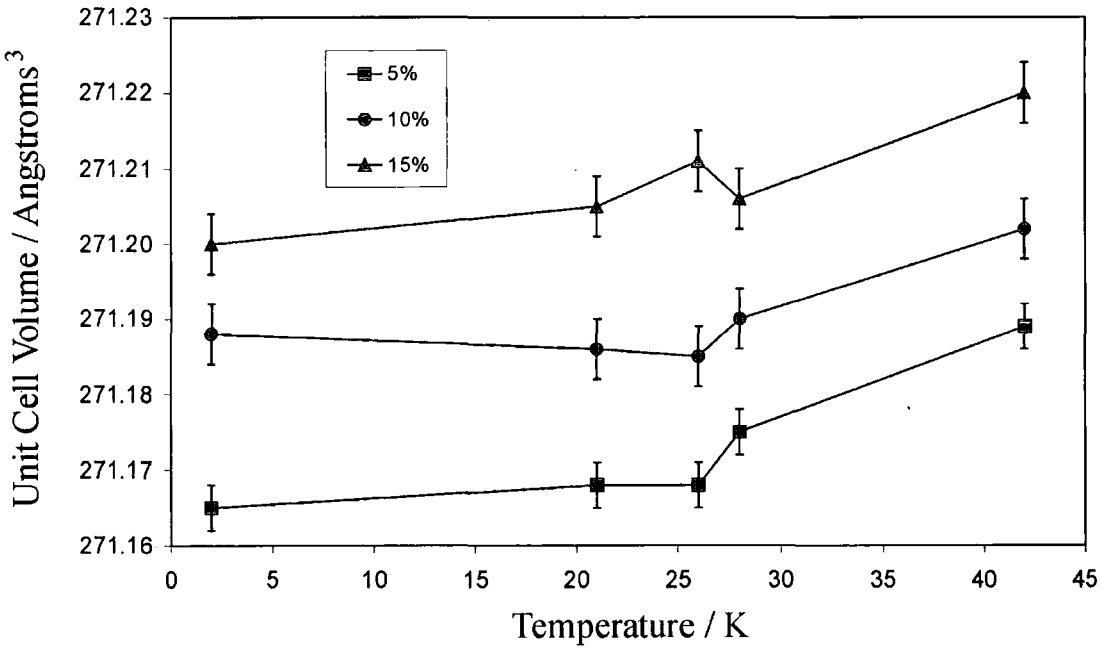

Figure 3.4 The unit cell volume of $Sr_2YRu_{1-x}Cu_xO_6$ with temperature for the different copper doping levels. The individual axes show the same form of increase with temperature and copper doping, only the expansivity is twice as great for the *c*–axis in both cases.

Table 3.1 indicates that the crystal structure of $Sr_2YRu_{0.85}Cu_{0.15}O_6$ does not vary with temperature. Hence the crystal structure obtained from the D2B data could be used to analyse the lower resolution D1B data. Variable temperature diffraction patterns were

collected between 2 K and 150 K using D1B, approximately every 2 K from 2-50 K and every 8 K from 50-150 K. The 42 K diffraction pattern measured at D1B is shown in Figure 3.5 and was refined with R_p = 3.70 %, R_{wp} = 4.78 % and R_{exp} = 1.27 %. These R-factors are typical of all the D1B refinements and full details can be found in the Appendix B.1.3.

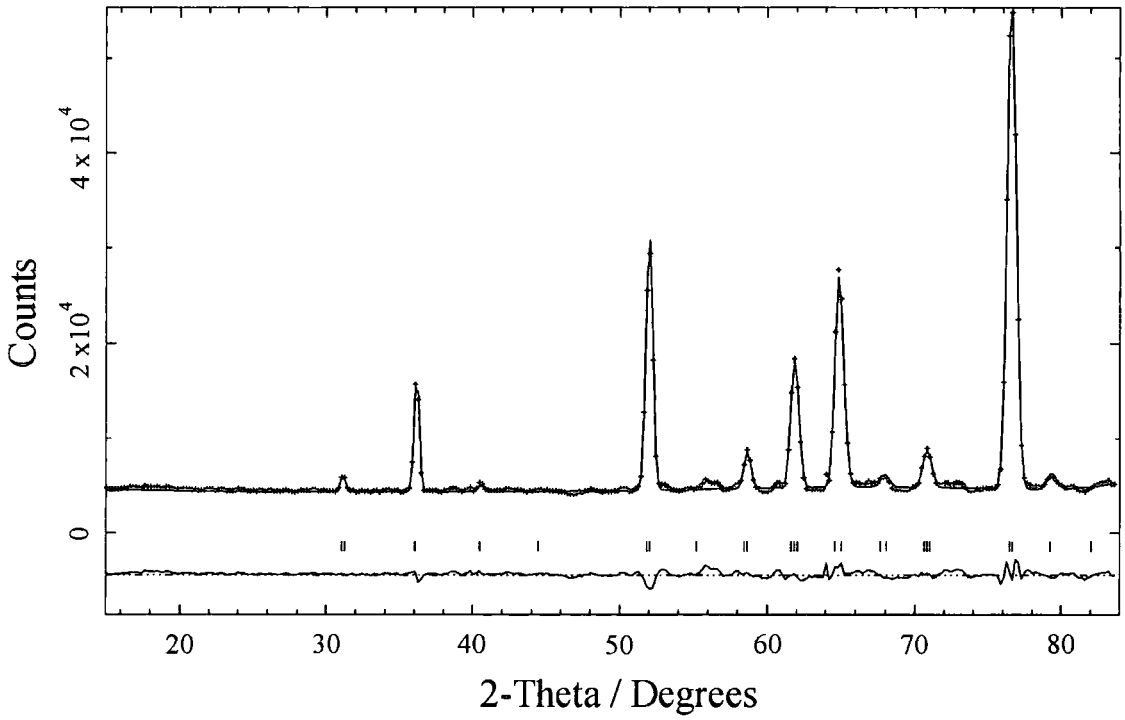

Figure 3.5 The diffraction pattern of $Sr_2YRu_{0.85}Cu_{0.15}O_6$ at 42 K measured at D1B. The data points are given by the crosses and the lines are the calculated profile and difference curve. The tick marks indicate the allowed Bragg reflections. Some broad features in the pattern are not calculated in the model, as these were believed to have an instrumental or impurity origin.

The Rietveld analysis of the 42 K D1B data yielded lattice parameters of a = 5.75948(12) Å, b = 5.77856(12) Å, c = 8.14803(33) Å, β = 90.327(2)° and a volume of 271.174(22) Å^3 which agree well with the D2B values in Table 3.1. These values are all within 3σ, which is taken to be the normal standard when comparing refined lattice parameters from two different instruments, with the difference in errors reflecting well the relative difference in resolution. The refined unit cell volume between 2 K and 150 K is shown in Figure 3.6 (and Appendix B.1.3) and agrees with the results of the D2B refinement. Owing to the poorer resolution of the D1B data, the small increase in unit cell volume could not be measured between 2 and 42 K. However, above ~ 40 K the cell volume increases with an expansivity coefficient $\alpha = 1.1(3) \times 10^{-5}$ K^{-1}. The exact temperature at which the cell volume increases is not

perfectly clear due to the slight discrepancy between the two separate data runs between 2-50 K and 50-150 K. Again the expansion between 50-150 K was anisotropic with the *c*-axis showing double the expansivity of the other 2 axes. As this anisotropy is observed over the full temperature range (2-150 K) it is less likely to be a significant factor in the onset of superconductivity at a specific temperature.

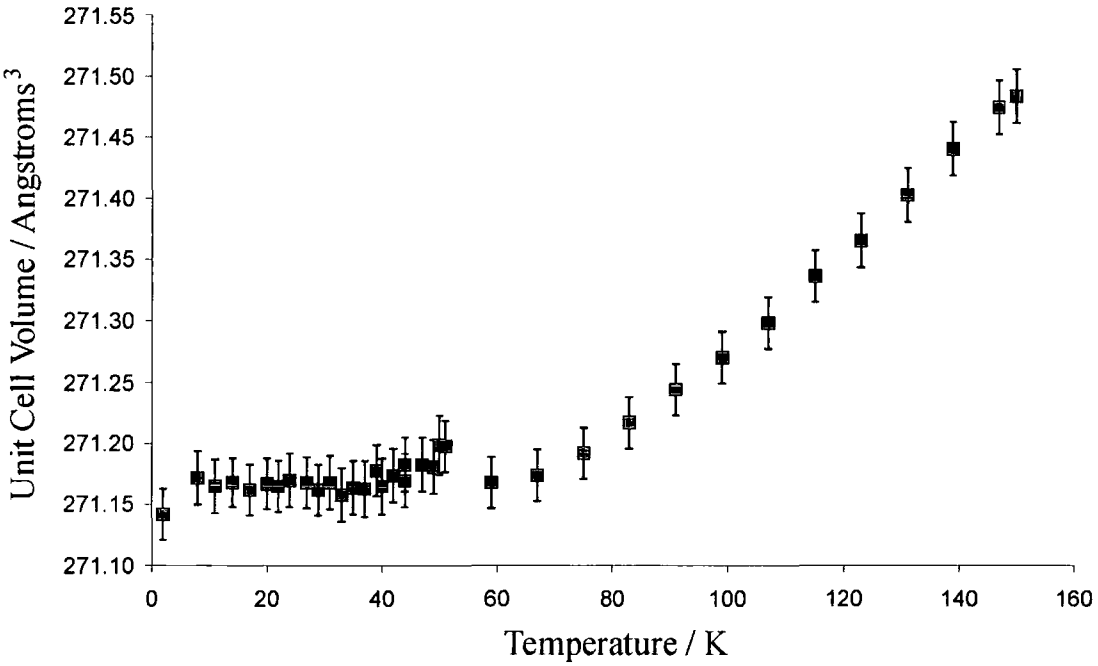

Figure 3.6 The unit cell volume with temperature of $Sr_2YRu_{0.85}Cu_{0.15}O_6$ as determined from analysis of the D1B data between 2 K and 150 K.

The high neutron flux of the D1B diffractometer indicated a small second phase (~ 2 % level) was present in the samples. These features can be seen clearly in the difference curve of the 42 K D1B data (Figure 3.5) at $2\theta \sim 42°$, 50°, 56°, 61° and 72°. The largest of these features, extending between 71-73°, was present in every neutron diffraction pattern measured at D1B, even non-perovskites and samples which had been shown to be impurity-free from synchrotron data. The 71-73° feature maintained the same size relative to the rest of the diffraction pattern irrespective of the measuring time, but decreased in relative size the greater the amount of sample used. Although this feature was attributed to the instrument, probably originating from the cryostat, it is still possible that it obscures impurity peaks itself. Low-resolution neutron diffraction is not really suitable for examining these small impurity phases and this task was left to high-resolution X-ray synchrotron experiments, which will be detailed in Chapter 6.

3.3.2 Magnetic Structure of $Sr_2YRu_{1-x}Cu_xO_6$

The variable temperature neutron powder diffraction patterns collected at D1B for $Sr_2YRu_{0.85}Cu_{0.15}O_6$ are shown in Figure 3.7 between 2 and 50 K. At temperatures below ~ 33 K extra peaks appear in the neutron diffraction patterns, indicative of the formation of long-range magnetic ordering. These are indicated for $Sr_2YRu_{0.85}Cu_{0.15}O_6$ in Figure 3.8 (2 K refinement) as the upper series of tick marks. The lower set denote the crystal structure peaks and judging by their similarity to the patterns above the magnetic ordering temperature, the crystal structure does not change through the magnetic transition.

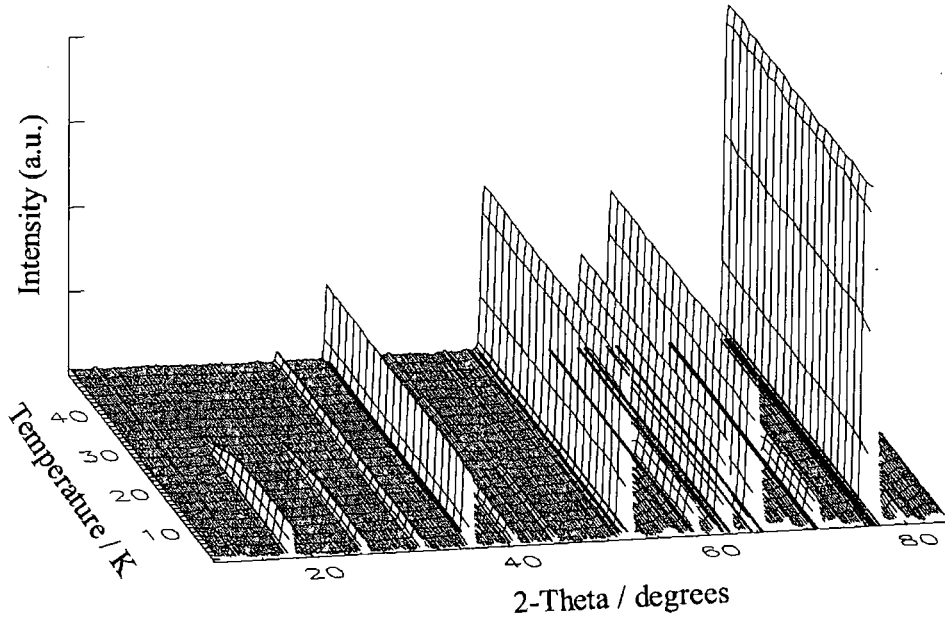

Figure 3.7 The variable temperature neutron diffraction patterns obtained at D1B showing just the 2-50 K region with the angular range 10-85° for $Sr_2YRu_{0.85}Cu_{0.15}O_6$. The magnetic peaks appear below 33 K, whereas the crystal structure intensity remains unchanged.

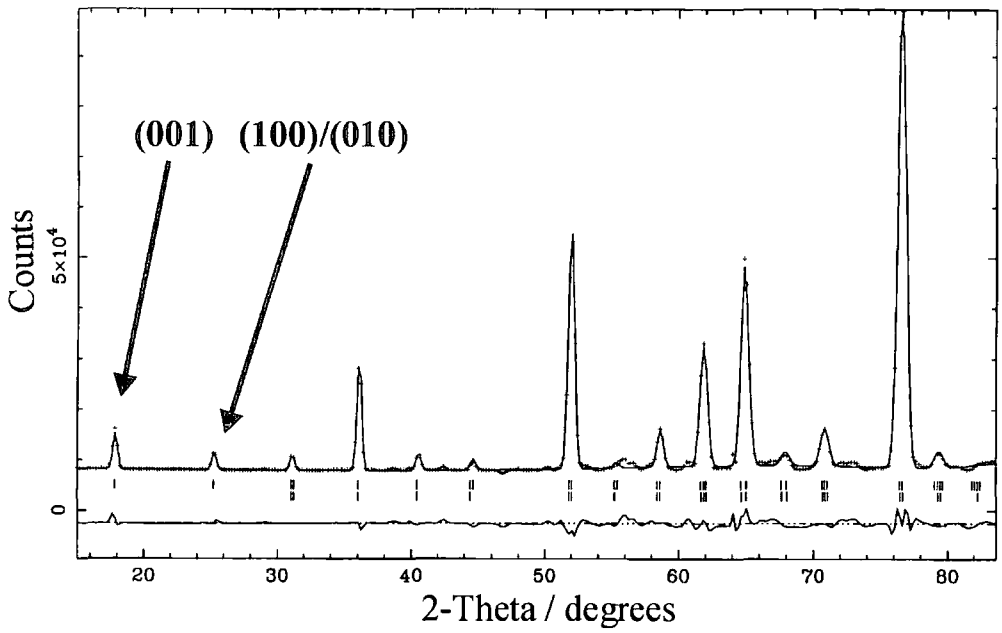

Figure 3.8 The neutron powder diffraction pattern collected at 2 K with calculated and difference curves for $Sr_2YRu_{0.85}Cu_{0.15}O_6$. The upper set of tick marks denote magnetic structure reflections, the lower set indicate the crystal structure reflections. Indexed explicitly are some of the principal magnetic peaks. The refined magnetic moment is 2.43(10) μ_B with R_p = 3.23 %, R_{wp} = 4.48 % and R_{exp} = 0.95 % calculated for this longer 40 minute data collection.

As the extra peaks of magnetic origin do not all coincide with the existing crystal structure peaks it is likely that $Sr_2YRu_{0.85}Cu_{0.15}O_6$ adopts an antiferromagnetic structure. The magnetic unit cell required to index these peaks is the same size as the crystal structure unit cell in this case, though a greater degree of freedom of the magnetic moment is allowed by magnetic structure adopting the space group P-1, with appropriate constraints on the lattice parameters. (The magnetic refinements could proceed with the magnetic structure in the space group $P2_1/n$. However, this places the unnecessary restrictions on the moment couplings as antiferromagnetic in the x and z directions and ferromagnetic in the y direction – or alternatively the opposite of this). In this P-1 magnetic unit cell there are two distinct sites for the Ru^{5+} ions at (½, 0, 0) and (0, ½, ½), which shall be labelled site 1 and site 2 respectively.

As the magnetic peaks obey the relation (h + k + l) = odd, this means the magnetic structure is antiferromagnetic (see Appendix A.3). There was no additional intensity in the pattern for (h + k + l) = even, and thus there was no ferromagnetic component (above ~0.8 μ_B sensitivity) in the magnetic structure. This rules out the possibility of a canted magnetic structure proposed by Wu [14-17] in order to explain the properties

of the materials, if the required ferromagnetic moment is greater than 0.8 μ_B. However, there is believed to be a canted ruthenium magnetic moment in the superconductor $RuSr_2GdCu_2O_8$ with a magnitude no larger than 0.1 μ_B [18, 19], so this may indicate a typical size and that there is scope for the requisite canting.

All the magnetic peaks can be indexed by a Type I magnetic structure, in which the Ru^{5+} ions on the two sites are coupled antiferromagnetically to each other. In this magnetic structure the magnetic moments are parallel in the (002) plane, but in adjacent (002) planes they are anti-parallel as illustrated in Figure 3.9. For $Sr_2YRu_{0.85}Cu_{0.15}O_6$ the (001) and the unresolved combination of the (100) and (010) peaks are indexed in Figure 3.8 explicitly. The presence of a magnetic peak indicates that a component of the magnetic moment is perpendicular to the direction to this scattering vector. Therefore the (001) peak indicates a component of the magnetic moment in the *ab* plane. However as the (100) and (010) were not be resolved, the precise direction of the magnetic moment in the *ab* plane cannot be determined. From refinements of the Ru^{5+} magnetic moment the component in the *ab* plane was sufficient to model all of the magnetic intensity in the diffraction pattern for the Sr series.

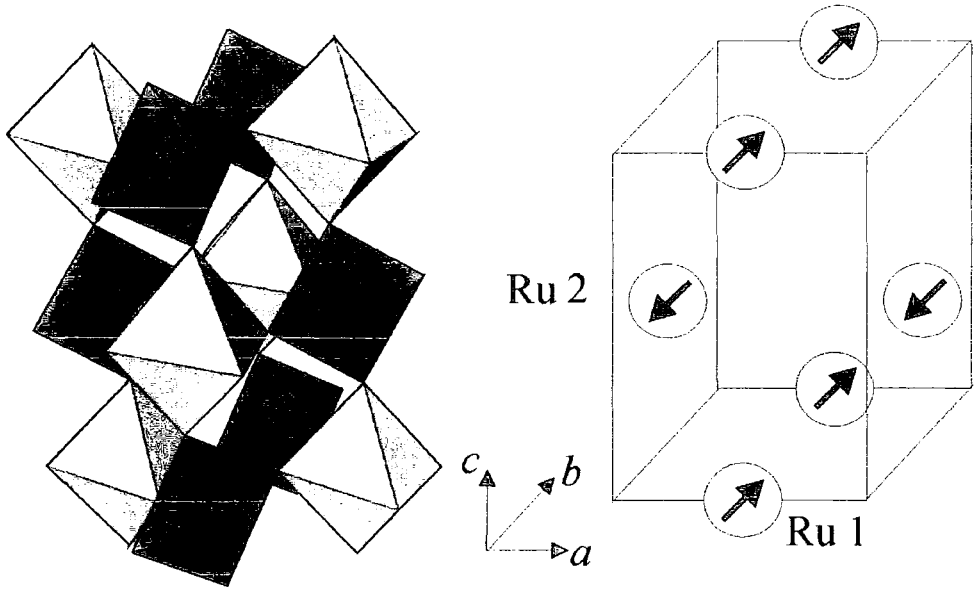

Figure 3.9 The magnetic structure of $Sr_2YRu_{0.85}Cu_{0.15}O_6$ is a Type I antiferromagnet, in which the magnetic moment is orientated in the opposite direction on the two distinct sites in the magnetic cell. The moment direction in the *ab* plane is shown arbitrarily. Here it is shown how the magnetic cell relates to the $Sr_2YRu_{0.85}Cu_{0.15}O_6$ crystal structure. The Ru ions are at the centre of the [RuO_6] (blue) with the [YO_6] (green) sharing oxygens at the corners. The Sr atoms are not shown for clarity.

All the D1B diffraction patterns shown in Figure 3.7 were also used to refine the magnetic structure of $Sr_2YRu_{0.85}Cu_{0.15}O_6$, in addition to the lattice parameters mentioned earlier. The results of the refinements are shown in Figure 3.10 (and Appendix B1.3.) and typically yielded R-factors of $R_p \sim 3.5$ %, $R_{wp} \sim 4.7$ % and $R_{exp} \sim 1.3$ %. The results clearly confirm the magnetic ordering temperature of 33 K, and that within 10 K of this the Ru^{5+} magnetic moment is saturated, as it is close to its 2 K value of 2.43(10) μ_B. This is significantly below its spin-only value of 3.87 μ_B, probably due to covalency effects.

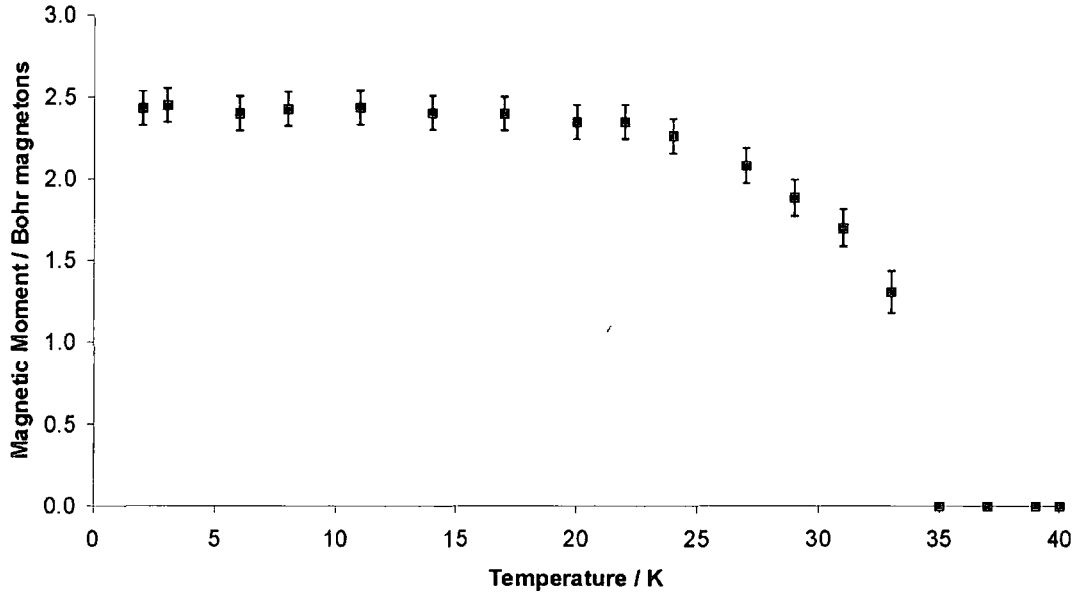

Figure 3.10 The magnetic moment of Ru^{5+} in $Sr_2YRu_{0.85}Cu_{0.15}O_6$ as refined from D1B data.

Our value for T_N of 33 K for $Sr_2YRu_{0.85}Cu_{0.15}O_6$ is considerably higher than the 23 K found previously by others using neutron powder diffraction [20]. They proposed a short-range ordering of the Ru^{5+} ions between 23 K and 30 K to explain the discrepancy between their neutron and magnetic measurements. However this could manifest itself in a broadening of the magnetic peaks, which was not observed in either their study or ours. We believe our results are due to the higher neutron flux of D1B allowing the observation of weak magnetic peaks, as small as ~ 0.8 μ_B for a fully occupied site, to higher temperatures. This sensitivity limit was estimated from the calculated magnetic moment required to raise the magnetic intensity further above the background level than the full width of the background level itself. As such, this sensitivity will vary slightly with sample and amount, but also from diffractometer to

diffractometer. From our neutron diffraction patterns no significant intensity was observed above the ordering temperature of 33 K at the magnetic peak positions. Thus copper ordering existing at higher temperatures could not be confirmed from our neutron diffraction results, though this would have required a magnetic moment of ~ 5 μ_B to detect. The other neutron powder diffraction study of $Sr_2YRu_{0.85}Cu_{0.15}O_6$ [20] claimed magnetic moments of ~ 0.9 μ_B up to 80 K were detected in a sample with 15 % copper (i.e. equivalent to a moment on a fully occupied site of 0.15 μ_B!) As the authors could not observe the magnetic moment of the 85 % ruthenium of ~ 2 μ_B between 23 and 33 K this is a remarkable claim. Further inspection showed that they had simply modelled magnetic intensity within the background noise, and hence their conclusions are of questionable validity.

The magnetic moment was also refined using the neutron diffraction patterns collected at D2B for each member of the series $Sr_2YRu_{1-x}Cu_xO_6$ with x = 0.05, 0.10 and 0.15 at 2, 21, 26, 28 and 42 K (, see Appendix B.1.1). In each compound there was no magnetic intensity at 42 K, but below this temperature the Type I magnetic structure, as previously described, was observed. The results of these magnetic refinements are displayed in Figure 3.11 and show that the magnetic ordering temperature is between 28 K and 42 K in all of the compounds. This is in agreement with the magnetic susceptibility results which indicate an ordering temperature of ~ 30 K for all three compounds in the series and the neutron result of 33 K for $Sr_2YRu_{0.85}Cu_{0.15}O_6$ [21]. The previous studies [14, 15, 17, 22, 23] had determined the coexistence of superconductivity and magnetism. This work confirms the long-range magnetic order below 28 K in all the compounds studied.

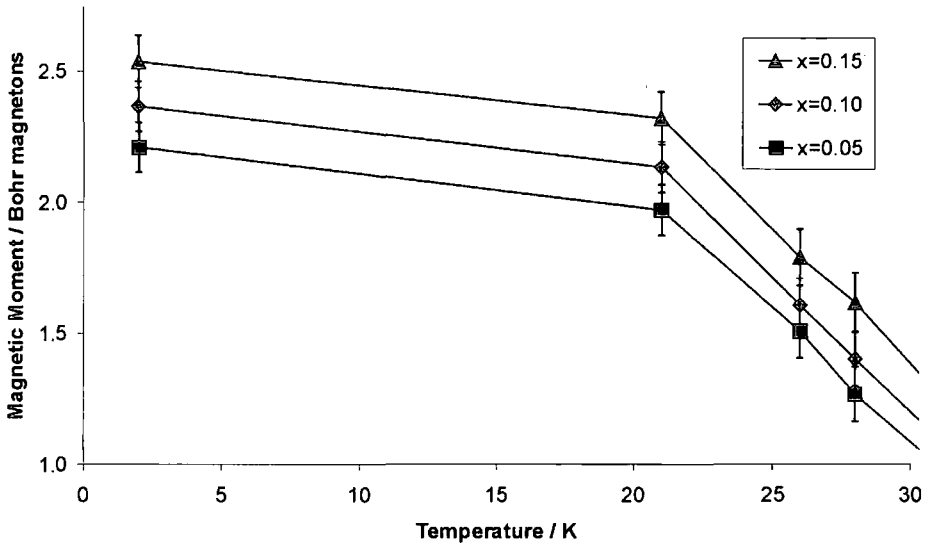

Figure 3.11 The magnetic moment versus temperature for the different copper doping levels (x = 0.05, 0.10, 0.15) for the $Sr_2YRu_{1-x}Cu_xO_6$ series as refined from D2B data. There was no magnetic intensity, hence no magnetic moment, measured at 42 K in any of the samples.

The refined magnetic moments of Ru^{5+} in $Sr_2YRu_{0.85}Cu_{0.15}O_6$ as determined from D1B and D2B data are 2.43(10) μ_B and 2.54(10) μ_B respectively, indicating reasonable agreement of the two diffractometers. Additionally, the magnetic moment of the Ru^{5+} ion at 2 K increases with successive copper doping from 2.21(10) μ_B for x = 0.05, to 2.37(10) μ_B for x = 0.10 and finally to 2.54(10) μ_B for x = 0.15. Extrapolating the trend for a copper concentration of x = 0 yields a moment for the parent compound, Sr_2YRuO_6 of 2.04(10) μ_B. The previous published study of Sr_2YRuO_6 [4] obtained a moment of 1.85(10) μ_B at 4.2 K which is appreciably lower. However in this earlier study on Sr_2YRuO_6 only the lowest angle magnetic peak (at $(\sin\theta)/\lambda \sim 0.06$ Å^{-1}) was used and a magnetic form factor of unity assumed, whereas our calculated value is 0.950. If this factor had been applied then the result would have been 1.95(10) μ_B and within experimental error of our extrapolated value.

When the refined magnetic moment is determined solely from the peak at $(\sin\theta)/\lambda \sim 0.06$ Å^{-1}, as this is the (001) magnetic reflection, then the component of the moment in the c-direction is not measured. Thus, the process of using the (001) peak will underestimate the magnetic moment if there is a c-component. However, for the $Sr_2YRu_{1-x}Cu_xO_6$ system the magnetic moment was refined as lying in the ab plane, so for Sr_2YRuO_6 at least, the moment was not underestimated from this source.

3.3.3 High-flux studies at OSIRIS

Neutron diffraction patterns were collected at OSIRIS on $Sr_2YRu_{0.90}Cu_{0.10}O_6$ at 60 K and 2 K in order to confirm the crystal and magnetic structures. The background subtracted diffraction pattern in Figure 3.12 shows the refinement of $Sr_2YRu_{0.90}Cu_{0.10}O_6$ at 2 K. While the crystal structure refinement (Table 3.3) is reasonable, as evidenced by the difference curve and the expansion of the low *d*-spacing section in Figure 3.13, the magnetic structure is not. As can be seen from Figure 3.12 (inset), the location of the (001) peak is not acceptable and has resulted in the low refined moment of 2.12(10) μ_B, which is much below the value obtained from D2B of 2.37(10) μ_B. The reduced magnetic intensity of the calculated (001) peak minimises the amount of misfit, though this is checked by the need to retain magnetic intensity for the unresolved (100)/(010) peak at ~ 5.78 Å. This peak was not resolved by the D2B data either and so the moment in the *ab* plane could not be determined. But its width here may indicate that the moment does not lie simply along one of the axes, *a* or *b*, but has approximately equal components.

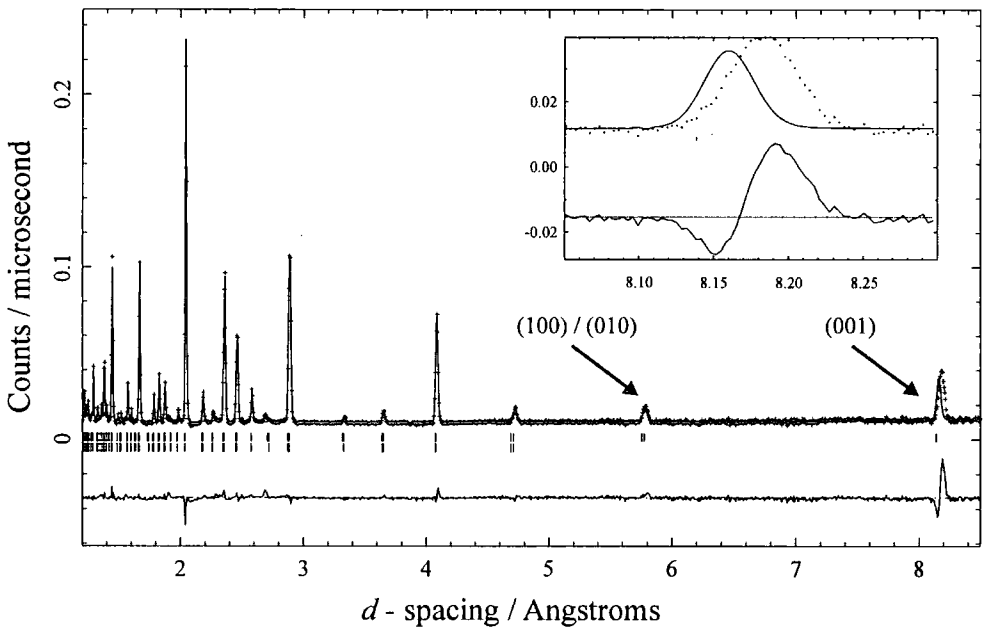

Figure 3.12 The neutron diffraction pattern measured at OSIRIS on $Sr_2YRu_{0.90}Cu_{0.10}O_6$ at 2 K. The data points are indicated by crosses and the calculated profile and difference curve by lines. The lower set of tick marks denote crystal structure reflections and the upper set the magnetic reflections. The magnetic (001) peak at ~ 8.19 Å (inset) is not correctly located and is displaced ~ 0.025 Å, highlighting the increasing error with *d*-spacing at time-of-flight instruments. This calculated peak also lacks the observed intensity.

$Sr_2YRu_{0.90}Cu_{0.10}O_6$		$P2_1/n$			2 K		
a / Å		b / Å	c / Å	β / °	Volume / Å^3		
5.75954(16)		5.77863(16)	8.14824(16)	90.326(2)	271.188(4)		
5.75954(16)		**5.77863(16)**	**8.14824(16)**	**90.326(2)**	**271.188(4)**		
Atom	Site	x	y	z	Occ	B_{iso}/Å^2	μ/μ_B
Sr	4*e*	0.0102(7)	0.0281(4)	0.7436(6)	1.000	0.08	
		0.0102(7)	**0.0279(4)**	**0.7437(5)**		**0.08**	
Y	2*c*	0	½	0	1.000	0.22	
						0.22	
Ru	2*d*	½	0	0	0.900	0.07	2.12(10)
						0.07	**2.34(10)**
Cu	2*d*	½	0	0	0.100	0.07	
						0.07	
O1	4*e*	0.3111(8)	0.2717(9)	0.9573(4)	1.000	0.22	
		0.3111(7)	**0.2719(9)**	**0.9575(4)**		**0.22**	
O2	4*e*	0.2676(7)	0.2927(7)	0.5325(6)	1.000	0.33	
		0.2673(7)	**0.2923(7)**	**0.5329(6)**		**0.33**	
O3	4*e*	0.9304(6)	0.4904(9)	0.7324(4)	1.000	0.23	
		0.9305(6)	**0.4902(8)**	**0.7324(4)**		**0.23**	
ZERO = -2.80(1.75)		DIFC = 17450.97(1.62)		DIFA = -10.24(0.37)			
ZERO = -1.59(1.67)		**DIFC = 17449.79(1.55)**		**DIFA = -9.94(0.36)**		**Crystal**	
ZERO = -1.59(1.67)		**DIFC = 17449.79(1.55)**		**DIFA = -4.44(0.44)**		**Magnetic**	
R_p = 6.76 %, R_{wp} = 6.58 %, R_{exp} = 2.13 %, R_{F^2} = 14.57 %							
R_p = 5.93 %, R_{wp} = 6.20 %, R_{exp} = 2.13 %, R_{F^2} = 14.55 %							

Table 3.3 The lattice parameters and atomic coordinates of $Sr_2YRu_{0.90}Cu_{0.10}O_6$ as refined from the 2 K data collected at OSIRIS. The lattice and thermal parameters were set at the D2B values. The refined values, including instrument parameters are shown for the initial refinement and when additionally DIFA is refined for the magnetic phase (in bold).

As the lattice parameters were initially fixed to the refined lattice parameters from the D2B data, the problem is likely to have its origin in the instrument parameters used. For time-of-flight data, the time measured which directly relates to the *d*-spacing in the diffraction pattern is given by Equation 3.2, where T is the time taken for the neutron to travel from the source to the detector, DIFA, DIFC and ZERO being instrumental constants [13].

$$d \propto T = \text{DIFA}\, d^2 + \text{DIFC}\, d + \text{ZERO} \qquad (3.2)$$

By subtle refinement of the DIFA parameter for just the magnetic phase, the position of the (001) peak and as a direct result the magnetic intensity, are corrected as shown

in Figure 3.14. The refined crystal structure (also shown in Table 3.3) remains virtually unchanged and the magnetic moment becomes 2.34(10) μ_B, much closer to the D2B value of 2.37(10) μ_B.

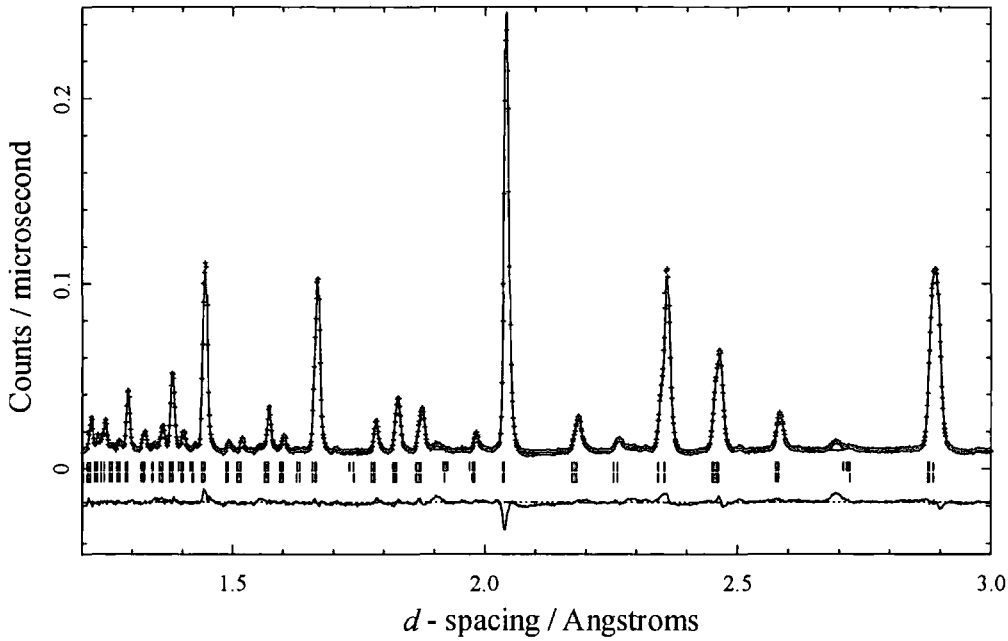

Figure 3.13 The low *d*-spacing section of the diffraction pattern of $Sr_2YRu_{0.90}Cu_{0.10}O_6$ at 2 K. This section of the diffraction pattern, which shows primarily crystal structure intensity, is reasonably replicated by the calculated diffraction profile.

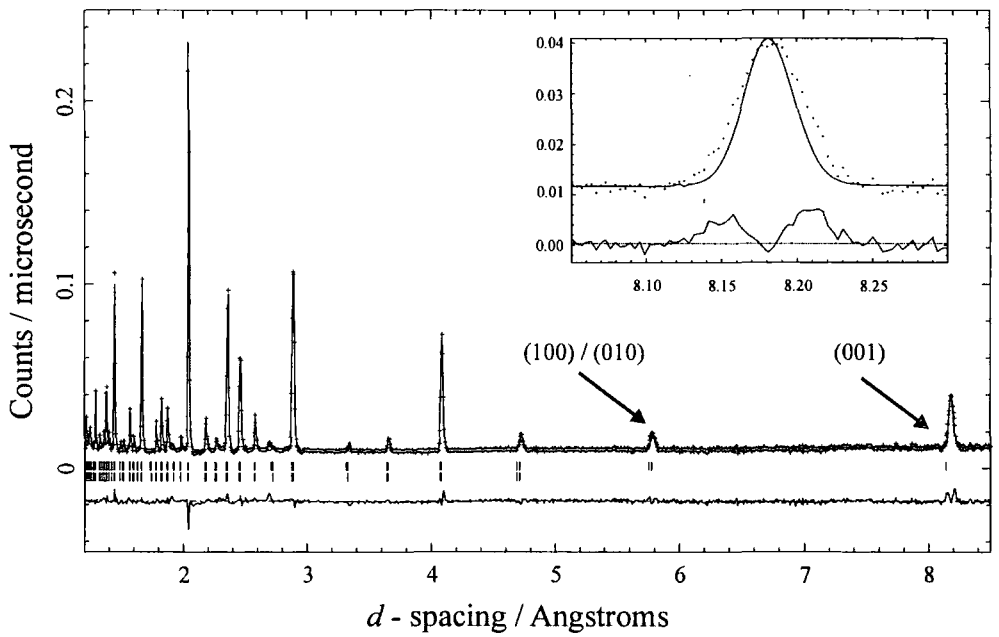

Figure 3.14 The neutron diffraction pattern measured at OSIRIS on $Sr_2YRu_{0.90}Cu_{0.10}O_6$ at 2 K with DIFA refined for the magnetic phase. The calculated magnetic (001) peak at ~ 8.19 Å (inset) is now correctly located and has an intensity comparable with the observed data.

This approach yields a well-calculated diffraction pattern, as firstly none of the crystal structure peaks will be affected as only DIFA in the magnetic phase was refined. The change modifies the d^2 term and so the low d-spacing peaks will be less affected, but these have low intensity anyway owing to the magnetic form factor. Hence, the only peaks which are affected are the high-intensity, high d-spacing magnetic peaks which are precisely the peaks that needed correction.

The beneficial effect of adding this extra refinement parameter is clear to see, however beyond this it is hard to justify. The DIFA parameter depends on absorption, and so is both sample and wavelength dependent. For peaks with large d-spacings, principally the magnetic peaks, the wavelength used to measure them is also comparably long. Refinement of the DIFA parameter in these cases could be accounting for deviations from the $1/v$ absorption model for neutrons travelling with speed v at the long wavelength end of the spectrum. No obvious cause for the failure to index the peaks properly at large d-spacings has been confirmed, though multiple scattering events in the moderator leading to delayed neutrons is one possibility. To date there has been no publication of OSIRIS data with a peak successfully indexed beyond the ~ 5 Å reported for $LuBaCuFeO_{5+\delta}$ [24]. The only other paper which shows refined data greater than this d-spacing is for a polymer and it clearly has problems beyond 8 Å [25].

The crystal structures refined from the D2B and OSIRIS data are compared in Table 3.4 and the bond lengths and angles in Table 3.5, which are not too dissimilar. However, it is noted that the errors are larger for the OSIRIS refinement and that the values for bond length and angles are more scattered. The crystal structure as determined from the OSIRIS data produces a noticeably worse calculated profile when used in the D2B diffraction pattern. However, the crystal structure determined from the D2B data can be used to replicate the OSIRIS data well. Clearly, this confirms that the diffractometer D2B is better for determining crystal structures.

$Sr_2YRu_{0.90}Cu_{0.10}O_6$		$P2_1/n$			2 K		
a / Å		b / Å	c / Å	β / °	Volume / Å^3		
5.75954(2)		5.77863(2)	8.14824(5)	90.326(1)	271.188(3)		
5.75954(16)		**5.77863(16)**	**8.14824(16)**	**90.326(2)**	**271.188(4)**		
Atom	Site	x	y	z	Occ	B_{iso}/Å^2	μ/μ_B
Sr	4*e*	0.0081(5)	0.0307(2)	0.7491(4)	1.000	0.08(2)	
		0.0102(7)	**0.0279(4)**	**0.7437(5)**		**0.08**	
Y	2*c*	0	½	0	1.000	0.22(4)	
						0.22	
Ru	2*d*	½	0	0	0.900	0.07(4)	2.37(10)
						0.07	**2.34(10)**
Cu	2*d*	½	0	0	0.100	0.07(4)	
						0.07	
O1	4*e*	0.3025(4)	0.2706(4)	0.9619(3)	1.000	0.22(4)	
		0.3111(7)	**0.2719(9)**	**0.9575(4)**		**0.22**	
O2	4*e*	0.2670(4)	0.2982(5)	0.5358(4)	1.000	0.33(5)	
		0.2673(7)	**0.2923(7)**	**0.5329(6)**		**0.33**	
O3	4*e*	0.9302(4)	0.4842(4)	0.7339(3)	1.000	0.23(4)	
		0.9305(6)	**0.4902(8)**	**0.7324(4)**		**0.23**	
ZERO = -1.59(1.67)		**DIFC = 17449.79(1.55)**			**DIFA = -9.94(0.36)**		**Crystal**
ZERO = -1.59(1.67)		**DIFC = 17449.79(1.55)**			**DIFA = -4.44(0.44)**		**Magnetic**
R_p = 4.64 %, R_{wp} = 6.37 %, R_{exp} = 9.94 %, R_{F^2} = 4.88 %							
R_p = 5.93 %, R_{wp} = 6.20 %, R_{exp} = 2.13 %, R_{F^2} = 14.55 %							

Table 3.4 The lattice parameters and atomic coordinates of $Sr_2YRu_{0.90}Cu_{0.10}O_6$ at 2 K as determined from refinement of D2B data and OSIRIS data (in bold).

$Sr_2YRu_{0.90}Cu_{0.10}O_6$			$P2_1/n$		D2B		2 K
Y-O1	2.211(2)	Ru-O1	1.957(2)	O1-Y-O2	91.6(1)	O1-Ru-O2	90.3(1)
Y-O2	2.206(2)	Ru-O2	1.950(2)	O1-Y-O3	91.3(1)	O1-Ru-O3	90.4(1)
Y-O3	2.204(2)	Ru-O3	1.952(2)	O2-Y-O3	91.5(1)	O2-Ru-O3	90.6(1)
Ru-O1-Y	156.1(1)		Ru-O2-Y	158.0 (1)		Ru-O3-Y	157.0(1)
Sr-O1	2.787(4)	Sr-O1	2.535(5)	Sr-O1	3.438(5)	Sr-O1	2.857(5)
Sr-O2	2.768(4)	Sr-O2	2.555(5)	Sr-O2	3.387(4)	Sr-O2	2.899(5)
Sr-O3	3.192(3)	Sr-O3	2.661(3)	Sr-O3	2.543(4)	Sr-O3	3.248(4)
$Sr_2YRu_{0.90}Cu_{0.10}O_6$			$P2_1/n$		OSIRIS		2 K
Y-O1	2.253(5)	Ru-O1	1.941(5)	O1-Y-O2	93.2(2)	O1-Ru-O2	91.8(3)
Y-O2	2.174(4)	Ru-O2	1.969(4)	O1-Y-O3	91.5(1)	O1-Ru-O3	91.8(2)
Y-O3	2.216(3)	Ru-O3	1.938(3)	O2-Y-O3	90.4(2)	O2-Ru-O3	90.9(2)
Ru-O1-Y	153.1(2)		Ru-O2-Y	159.9 (3)		Ru-O3-Y	157.4(2)
Sr-O1	2.827(7)	Sr-O1	2.440(6)	Sr-O1	3.521(7)	Sr-O1	2.839(7)
Sr-O2	2.739(5)	Sr-O2	2.604(6)	Sr-O2	3.319(7)	Sr-O2	2.938(5)
Sr-O3	3.142(5)	Sr-O3	2.712(5)	Sr-O3	2.556(5)	Sr-O3	3.233(6)

Table 3.5 The principal bond lengths (Å) and angles (°) of $Sr_2YRu_{0.90}Cu_{0.10}O_6$ at 2 K as determined from refinement of D2B data and OSIRIS data.

The high-flux of OSIRIS does reduce the statistical error on the magnetic moment by a factor of 2 when compared with D1B, however the error is still dominated in both cases by that originating from the magnetic form factor of ~ 0.10 μ_B. The values of the magnetic moment compare favourably with each other provided that the addition of the extra DIFA parameter is valid.

In summary, D2B is excellent for determining crystal structures and although it can be used for magnetic structure determination, the higher flux of D1B is more appropriate, though it is unable to determine crystal structures alone. However, the instrument OSIRIS is able to achieve both tasks adequately provided the diffraction profile at large *d*-spacings can be believed.

The crystal structure from the 60 K data was also refined and was virtually unchanged from 2 K, full details are given in the Appendix B.1.2.1.

Neutron diffraction patterns were also collected on $Sr_2YRu_{0.85}Cu_{0.15}O_6$ at 2 K and 35 K, as we wished to examine whether any copper ordering would be observable and this sample contained the largest proportion of copper in any available sample. Long-range magnetic ordering in $Sr_2YRu_{0.85}Cu_{0.15}O_6$ was not observed for any species above 33 K in the D1B data. It was hoped that by studying the material at the higher

flux OSIRIS diffractometer just above this temperature, any copper ordering if present, would be revealed.

Unfortunately there were technical problems with the computers on OSIRIS. This may have resulted in the various 1.5 Å sections not being combined in the proper way for the 2 K pattern shown in Figure 3.15. This is manifested in the diffraction profile as steps and ridges where the two slices overlap and join (see inset for one example of this) and prevented sensible refinement of the data. The "raw" data only is shown, as the background subtracted file also suffered from truncation at zero, although this could have been rectified. Displaying the "raw" file in Figure 3.15 does serve to illustrate one reason for using the background subtraction for time-of-flight data, as the very high background otherwise yields low *R*-factors irrespective of the model used. Although it has not been refined properly, from its similarity to Figure 3.12, it is clear that there is about the same magnetic intensity in the two patterns.

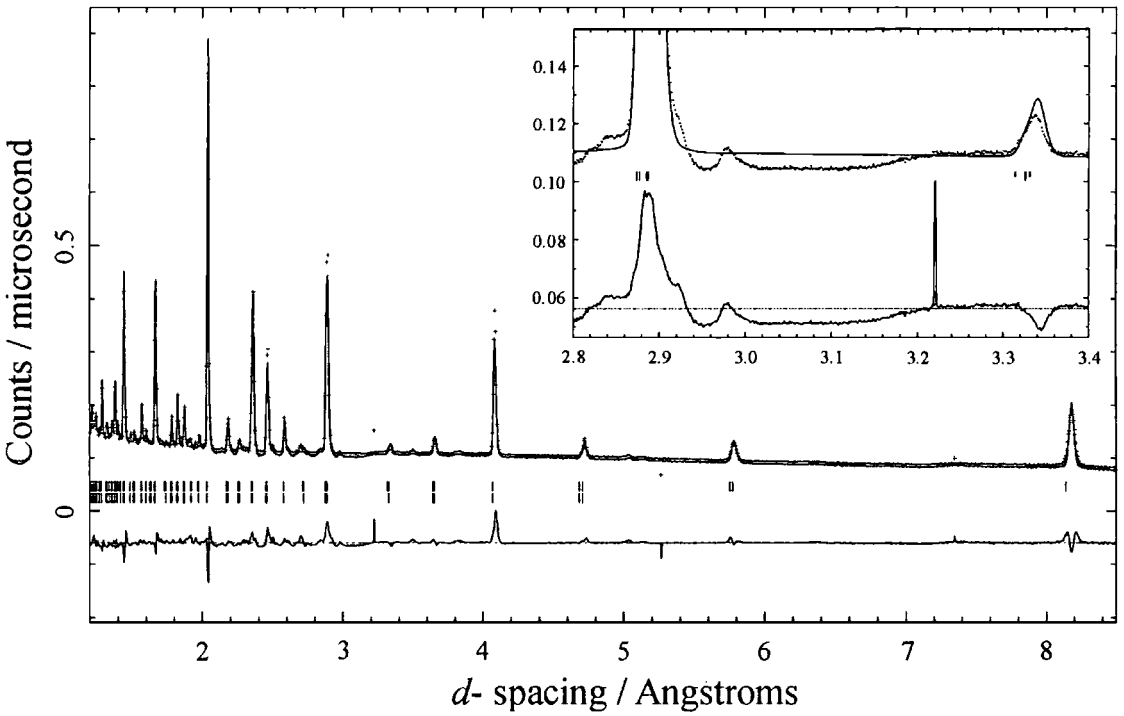

Figure 3.15 The diffraction pattern of $Sr_2YRu_{0.85}Cu_{0.15}O_6$ at 2 K which has not been refined properly due to the incorrect combination of the 1.5 Å sections of the data. This results in steps and ridges (inset) and unreliable relative intensities.

There were no such problems with the 35 K data collection which is shown in Figure 3.16. The thermal parameters and lattice parameters were set at the values interpolation of the 28 K and 42 K values suggested, and the refined parameters are given in Table 3.6. This structure is very similar to the $Sr_2YRu_{0.90}Cu_{0.10}O_6$ structure

refined using OSIRIS data (Table 3.3) and is otherwise unremarkable. However it is very clear from the diffraction pattern (Figure 3.16 insets) that there is *no* magnetic intensity. With the higher flux on OSIRIS it had been hoped that the sensitivity would have been increased and that smaller magnetic moments would have been detectable, particularly as the small *d*-range where the magnetic peaks appear could be focussed on.

Unfortunately, the very high-flux of neutrons was compensated for by the large background and the sensitivity remained at ~ 0.7 μ_B, about the same as D1B, and so would have required an unphysically large moment of ~ 4.5 μ_B on the 15 % copper to be observed as a peak. (The spin-only value for the magnetic moment of copper is 1.73 μ_B for Cu^{2+} and 2.83 μ_B for Cu^{3+}, so clearly it is impossible to measure with the degree of sensitivity at OSIRIS). However, unlike the D1B data where there are only 3-5 points measured across a magnetic peak and when the intensity is low maybe just 1-2, with the OSIRIS data there are 30-40 data points measured across the peak. Hence, a small magnetic moment can be measured more reliably with OSIRIS as it is not so heavily dependent on statistical variations of just one or two detectors.

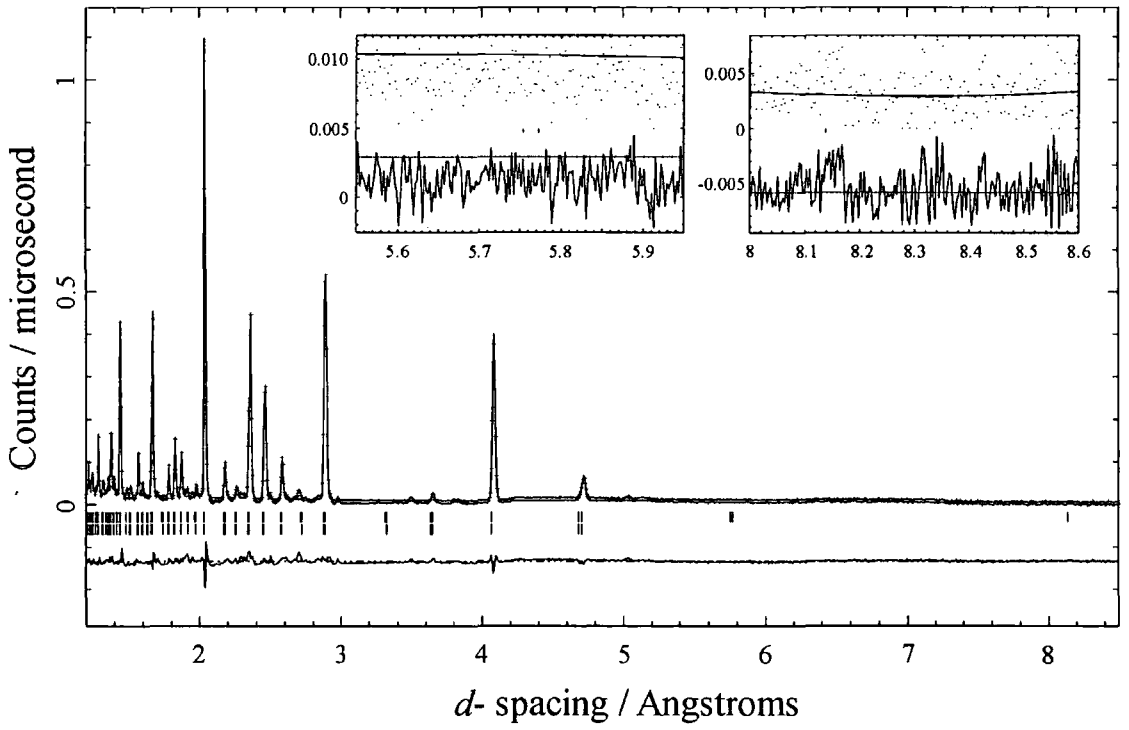

Figure 3.16 Neutron diffraction pattern of $Sr_2YRu_{0.85}Cu_{0.15}O_6$ at 35 K which is just above the magnetic ordering temperature of the Ru^{5+} ions. The insets show the regions where magnetic intensity would be expected to be located, but there is none.

$Sr_2YRu_{0.85}Cu_{0.15}O_6$		$P2_1/n$			35 K	
a / Å		b / Å	c / Å	β / °	Volume / Å^3	
5.75968(16)		5.77878(16)	8.14865(16)	90.324(2)	271.203(4)	
Atom	Site	x	y	z	Occ	B_{iso}/Å^2
Sr	4*e*	0.0102(8)	0.0280(5)	0.7453(6)	1.000	0.08
Y	2*c*	0	½	0	1.000	0.22
Ru	2*d*	½	0	0	0.850	0.07
Cu	2*d*	½	0	0	0.150	0.07
O1	4*e*	0.3100(9)	0.2709(10)	0.9594(5)	1.000	0.25
O2	4*e*	0.2663(8)	0.2963(8)	0.5321(7)	1.000	0.26
O3	4*e*	0.9264(7)	0.4887(9)	0.7341(4)	1.000	0.22

R_p = 14.45 %, R_{wp} = 10.06 %, R_{exp} = 1.18 %, R_{F^2} = 15.00 %

Table 3.6 Lattice parameters and atomic coordinates of $Sr_2YRu_{0.85}Cu_{0.15}O_6$ as refined using OSIRIS data at 35 K.

The earlier finding that there is no magnetic intensity above the Ru^{5+} ordering temperature of 33 K in $Sr_2YRu_{0.85}Cu_{0.15}O_6$ has been confirmed by this experiment. These results obtained at both the high intensity ILL and ISIS sources cast further doubt on the over-interpretation of results measured earlier [20] at the 10 MW MURR reactor.

3.4 Neutron Diffraction Experiments on $Ba_2YRu_{1-x}Cu_xO_6$

Only one composition of the series, namely $Ba_2YRu_{0.90}Cu_{0.10}O_6$, was supplied and examined by powder neutron diffraction. The parent compound, Ba_2YRuO_6 had been studied in the early 1980's by Battle [6] and was determined to be cubic. With the developments in both resolution and intensity of neutron sources during the intervening years, this could be checked with the copper doped sample of $Ba_2YRu_{0.90}Cu_{0.10}O_6$ at D2B. Once the crystal and magnetic structures had been verified, variable temperature diffraction patterns at D1B would explore their temperature dependence.

3.4.1 Crystal Structure of $Ba_2YRu_{0.90}Cu_{0.10}O_6$

The powdered sample of $Ba_2YRu_{0.90}Cu_{0.10}O_6$ was measured at D2B and diffraction patterns were collected at 200 K and 2 K, well above and well below any magnetic ordering temperature. The high-resolution mode was selected to allow the crystal

structure to be determined with the greatest possible accuracy and any deviations from cubic symmetry to be noted. Each diffraction pattern was collected over 8 hours in order to compensate for the reduced flux available in the highest resolution mode of the diffractometer and for any deviations in symmetry to become clear. Unfortunately some of the 200 K data were spoiled and could not be included, thereby reducing the effective measuring time to 4 hours.

The diffraction pattern of $Ba_2YRu_{0.90}Cu_{0.10}O_6$ shown in Figure 3.17 was measured at 200 K and shows very few peaks and so is immediately indicative of a high symmetry structure. The crystal structure was successfully refined in the cubic space group *Fm*3*m* (with a $2a_p \times 2a_p \times 2a_p$ unit cell) as this was able to index all the peaks in the pattern, which showed no sign of distortion. The adoption of the space group *Fm*3*m* means that $Ba_2YRu_{0.90}Cu_{0.10}O_6$ is the first crystallographically characterised high temperature superconductor of cubic symmetry.

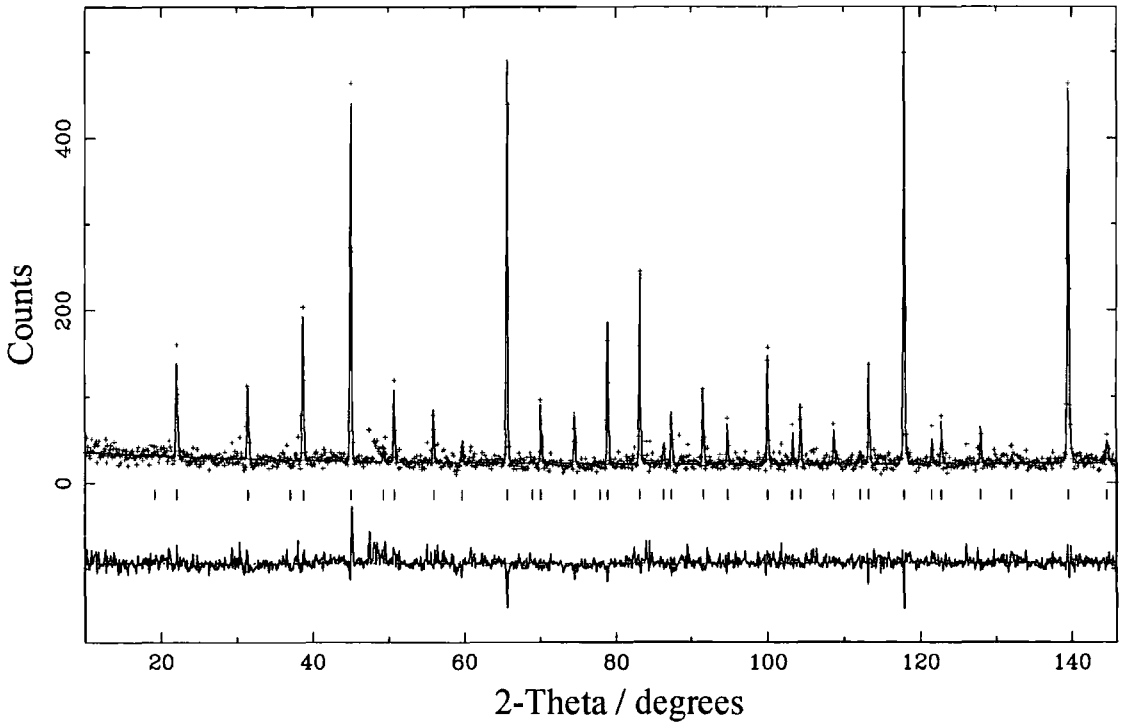

Figure 3.17 The diffraction pattern of $Ba_2YRu_{0.90}Cu_{0.10}O_6$ at 200 K measured on D2B. The data points are marked as crosses and the refined profile is the line, with the difference curve at the bottom of the plot. The allowed reflections are shown as tick marks.

The results of the refinements of both the 2 K and 200 K crystal structures are shown in Table 3.7 and the principal bond lengths and angles in Table 3.8. These results are similar to those of a previous study on the parent compound, Ba_2YRuO_6 [6]. The *R*-values are high, for the example the 200 K refinement has R_p = 16.04 %,

R_{wp} = 20.99 % and R_{exp} = 17.61 %, though this is often the case for metal oxides with a wide spread of intensities, but is also due to the reduced count time and low background for this 200 K data set. As can be seen from the proximity of the fractional atomic coordinates, the crystal structure does not change appreciably over the temperature range measured, although the lattice parameter does change.

$Ba_2YRu_{0.90}Cu_{0.10}O_6$	*Fm*3*m*	200 K and **2 K**
a / Å	Volume / Å^3	
8.32365(6)	576.689(13)	
8.31696(4)	**575.298(8)**	

Atom	Site	*x*	*y*	*z*	Occ	B_{iso}/Å^2	μ/μ_B
Ba	8*c*	¼	¼	¼	1.000	0.18(10)	
						0.14(6)	
Y	4*c*	0	0	0	1.000	0.04(15)	
						0.13(5)	
Ru	4*b*	½	0	0	0.900	0.13(16)	
						0.13(5)	**2.43(19)**
Cu	4*b*	½	0	0	0.100	0.13(16)	
						0.13(5)	
O	24*e*	0.2654(4)	0	0	1.000	0.11(7)	
		0.2653(3)				**0.17(4)**	

R_p = 16.04 %, R_{wp} = 20.99 %, R_{exp} = 17.61 %, R_{F^2} = 7.98 %
R_p = 11.57 %, R_{wp} = 14.60 %, R_{exp} = 11.18 %, R_{F^2} = 32.21 %

Table 3.7 The lattice parameters and atomic coordinates of $Ba_2YRu_{0.90}Cu_{0.10}O_6$ at 200 K and 2 K (in bold) as determined by refinements of the high-resolution D2B data.

$Ba_2YRu_{0.90}Cu_{0.10}O_6$	*Fm*3*m*		200 K and **2 K**		
Y-O	Ru-O	Ba-O	O-Y-O	O-Ru-O	Ru-O-Y
2.209(4)	1.953(4)	2.946(4)	90.00(0)	90.00(0)	180.00(0)
2.206(2)	**1.952(2)**	**2.943(2)**	**90.00(0)**	**90.00(0)**	**180.00(0)**

Table 3.8 The principal bond lengths (Å) and bond angles (°) of the crystal structure refined in space group $Ba_2YRu_{0.90}Cu_{0.10}O_6$ at both 200 K and 2 K (in bold).

The crystal structure of $Ba_2YRu_{0.90}Cu_{0.10}O_6$ derived from the tabulated values is displayed in Figure 3.18. The crystal symmetry imposes restrictions on the [BO_6] octahedra and in the Ba compound the octahedra are regular with O-Ru-O and O-Y-O bond angles all 90°, while the Ru-O-Y bond angle is 180° as shown in Figure 3.18.

The higher symmetry of the octahedra in the Ba system is presumably because of the extra space due to the greater size of Ba^{2+} compared to Sr^{2+}, a fact which is also reflected in the increased lattice parameter. As with the Sr analogue the oxygen sites were fully occupied in $Ba_2YRu_{0.90}Cu_{0.10}O_6$.

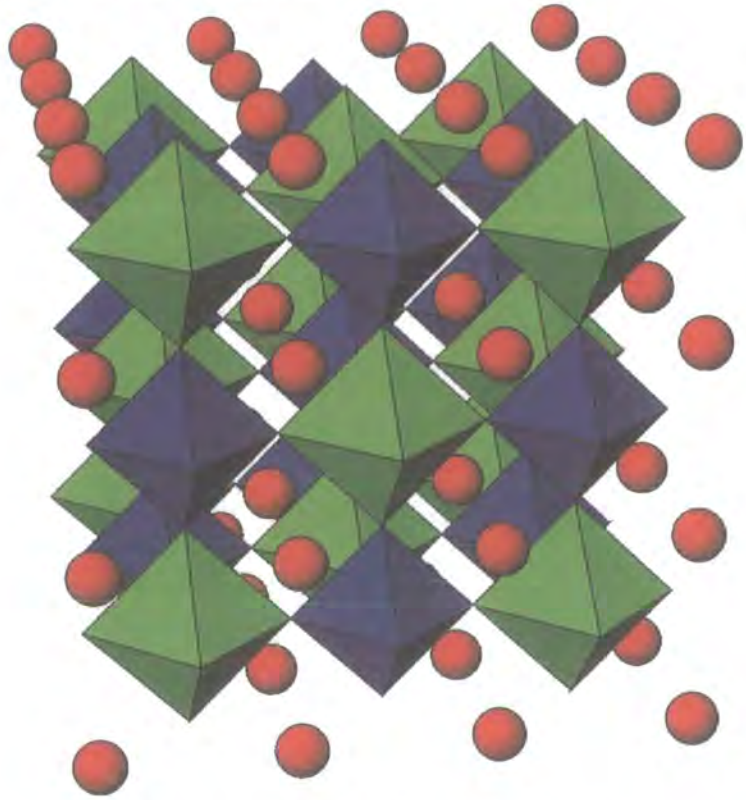

Figure 3.18 The crystal structure of $Ba_2YRu_{0.90}Cu_{0.10}O_6$ as determined from the D2B data. The RuO_6 octahedra (blue) and the YO_6 octahedra (green) are shared at the corners. (The CuO_6 octahedra are set to be on the same site as the RuO_6 octahedra.) The Ba atoms are shown as red circles in the spaces between the octahedra.

3.4.2 Magnetic Structure of $Ba_2YRu_{0.90}Cu_{0.10}O_6$

The neutron diffraction pattern measured at 2 K is shown in Figure 3.19 and the results of the refined crystal structure are shown previously in Table 3.7 and Table 3.8. The magnetic structure was indexed in the Type I antiferromagnetic structure, just as in the Sr based analogues, again with no ferromagnetic component observed. This was achieved using a magnetic cell with the same dimensions as the crystal unit cell (i.e. $2a_p \times 2a_p \times 2a_p$), but with space group P-1, not $Fm3m$ which prohibits a non-zero magnetic moment on Ru^{5+}. In the P-1 setting the independent Ru sites are at (½, 0, 0), (0, ½, 0), (0, 0, ½) and (½, ½, ½) and their relation to the Type I antiferromagnetic structure can be seen in Figure 3.20. Refinements of the magnetic

structure gave a profile which matched the measured profile well, as was reflected in the R-values of R_p = 11.57 %, R_{wp} = 14.60 % and R_{exp} = 11.18 %, which are lower than the 200 K refinement, due to the longer count time.

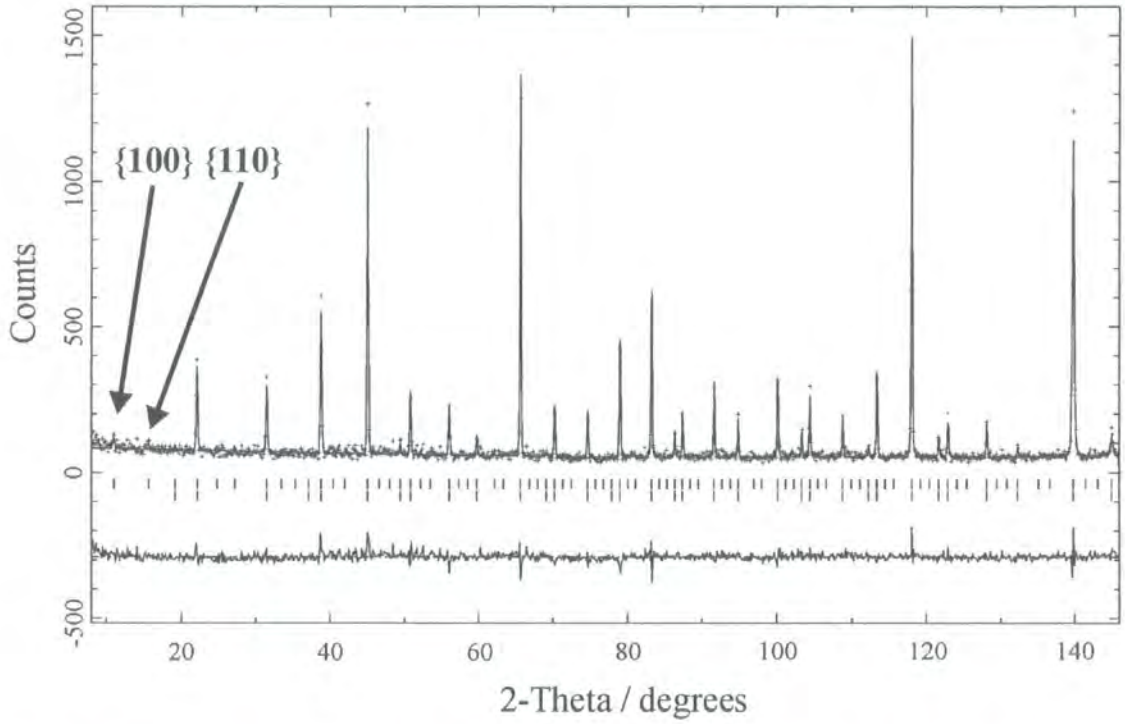

Figure 3.19 Neutron diffraction pattern of $Ba_2YRu_{0.90}Cu_{0.10}O_6$ at 2 K using the high-resolution diffractometer D2B. The lower series of tick marks denote crystal structure peaks while the upper set denote magnetic peaks.

As the crystal structure is cubic this means that a set of reflections, for example {100}, all overlap and thus the direction of the moment cannot be obtained. The magnetic moment of the Ru^{5+} ion was refined to be 2.43(19) μ_B at 2 K in $Ba_2YRu_{0.90}Cu_{0.10}O_6$, which is similar to the 2.37(10) μ_B for Ru^{5+} observed in $Sr_2YRu_{0.90}Cu_{0.10}O_6$. The two values were expected to be close because as both Ru^{5+} sublattices adopt the same magnetic structure within the same 1:1 ordered crystal structure of $[YO_6]$ octahedra.

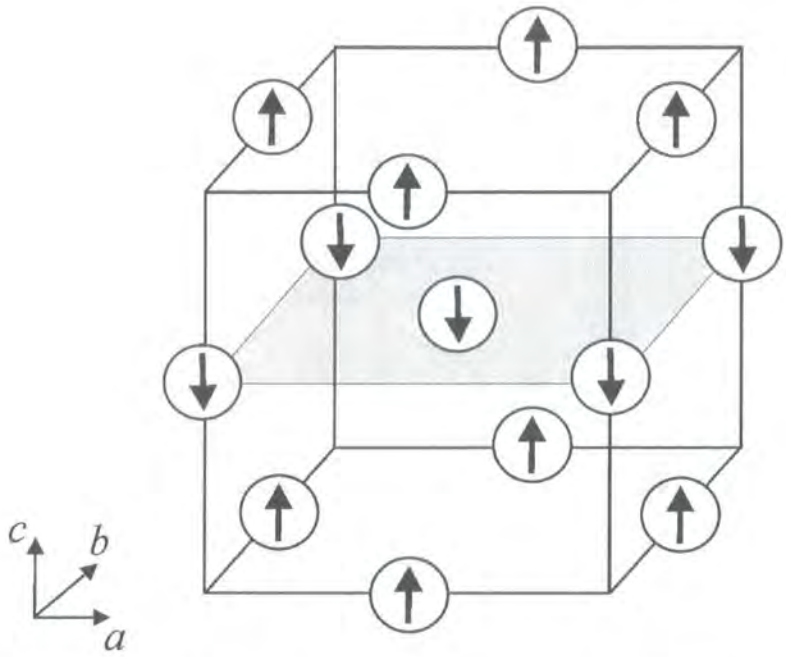

Figure 3.20 The Type I antiferromagnetic structure as viewed on the enlarged $2a_p \times 2a_p \times 2a_p$ unit cell (both crystal and magnetic) of $Ba_2YRu_{0.90}Cu_{0.10}O_6$. The magnetic moments are parallel in any (002) plane and anti-parallel in adjacent (002) planes in the Type I magnetic structure. The moment direction is arbitrarily shown as it cannot be determined for a cubic structure.

3.4.3 Temperature Dependence of the Lattice Parameter and Magnetic Moment of $Ba_2YRu_{0.90}Cu_{0.10}O_6$

Variable temperature neutron powder diffraction data were collected at D1B on $Ba_2YRu_{0.90}Cu_{0.10}O_6$ and grouped into diffraction patterns approximately every ~ 3 K. These are shown in Figure 3.21 and at temperatures below 39 K extra peaks appear in the neutron diffraction patterns, indicative of the formation of long-range magnetic order. The crystal peaks remain unchanged throughout the temperature region and thus indicate that the crystal structure does not undergo any dramatic change as the magnetic structure develops, visually confirming the findings from the D2B refinements. Hence, the atomic coordinates and thermal parameters could be set at the values obtained from analysis of the D2B data shown in Table 3.7, with no loss of accuracy, for the D1B refinements.

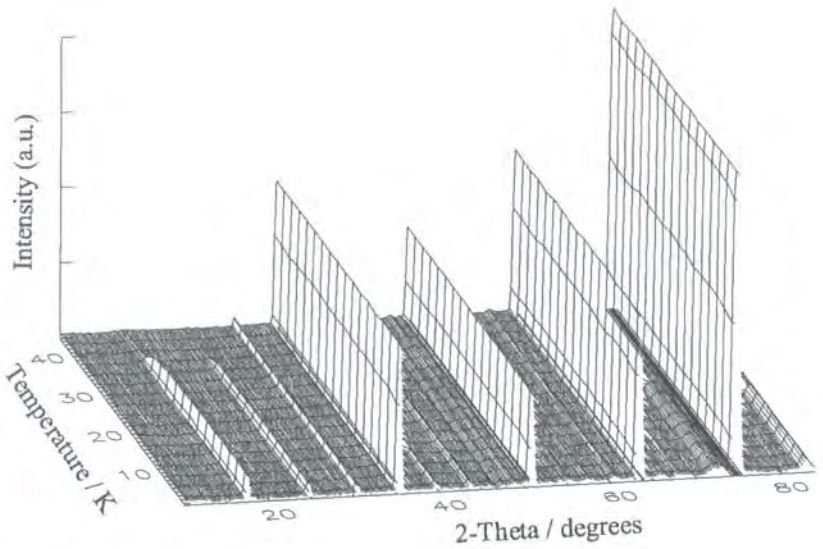

Figure 3.21 Variable temperature neutron powder diffraction patterns measured at D1B on $Ba_2YRu_{0.90}Cu_{0.10}O_6$ between 2 K and 50 K within the angular range of 5° to 85°. The magnetic peaks begin to appear at 39 K.

A longer data collection was taken at 2 K, 40 minutes rather than 10 minutes, to determine the profile well and ensure that the no minute detail of the magnetic structure would be missed. This diffraction pattern is shown in Figure 3.22 and both the lattice parameter *a*, and magnetic moment of the Ru^{5+} ion were refined using the crystal structure derived from the D2B data (Table 3.7) as a model. The profile calculated from the model structure replicates the experimental data well, indicating that neither instrument has biased the refinements.

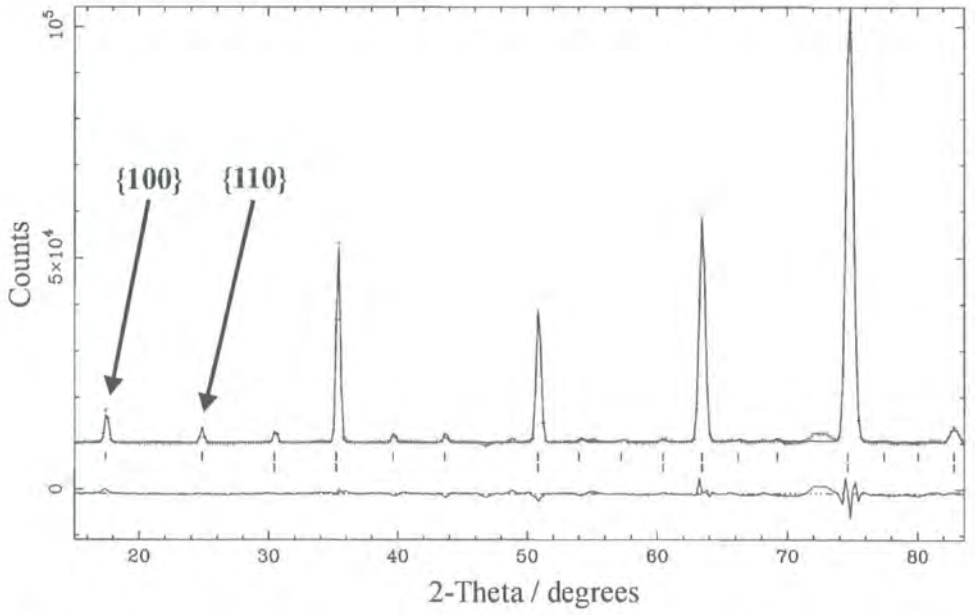

Figure 3.22 Diffraction pattern of $Ba_2YRu_{0.90}Cu_{0.10}O_6$ collected at 2 K and measured using diffractometer D1B. The lower series of tick marks denote the crystal structure reflections and the upper set mark the magnetic reflections.

The refined lattice parameter at 2 K from the D1B data is 8.31750(17) Å which compares well with the refined value of 8.31696(4) Å obtained from the D2B measurements as these were within 3σ. The refined moments of the Ru^{5+} ions at 2 K also compare well with 2.41(10) μ_B and 2.43(19) μ_B calculated from the D1B and D2B data respectively. The *R*-values were also respectable R_p = 3.23 %, R_{wp} = 4.49 % and R_{exp} = 0.95 % and demonstrate the high neutron flux of D1B.

The diffraction patterns at every temperature were also used to refine the lattice parameter and magnetic moment of the Ru^{5+} ion of the model structure with details in the Appendix B.2.2.1. The refinements gave *R*-factors all close to the typical values of $R_p \sim 3.40$ %, $R_{wp} \sim 4.60$ % and $R_{exp} \sim 1.3$ % indicating the quality of the refinements were similar throughout the series. Figure 3.23 displays the variation of lattice parameter *a* with temperature and the steady increase in lattice parameter from 2 K is broken by a sudden decrease of $6.7(8) \times 10^{-4}$ Å between 37 and 39 K. This is precisely the temperature (T_N = 39 K) at which long-range magnetic order develops in the material. Hence the onset of magnetic order is thought to lead to an increase in the size of the lattice. There is no significant expansion of the lattice below T_N, but between 39 K and 100 K the volume expansivity $\alpha = 1.0(1) \times 10^{-5}$ K^{-1}, similar to that of the $Sr_2YRu_{0.85}Cu_{0.15}O_6$ with $\alpha = 1.1(3) \times 10^{-5}$ K^{-1}.

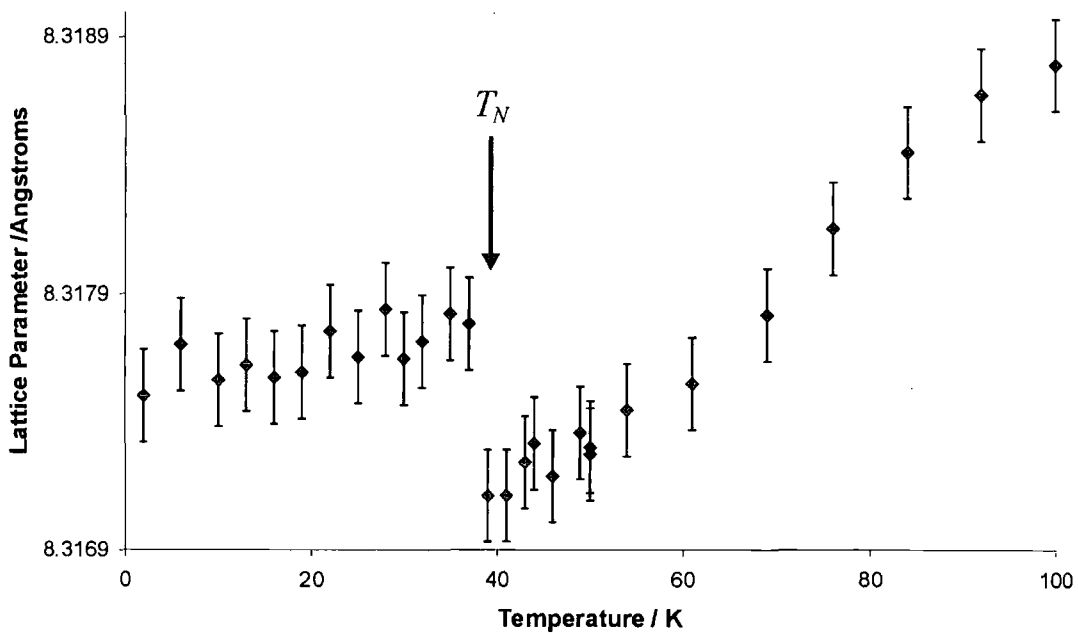

Figure 3.23 Lattice parameter of $Ba_2YRu_{0.90}Cu_{0.10}O_6$ with temperature.

At all temperatures below 39 K there was no deviation from the Type I antiferromagnetic structure. The refined magnetic moment of the Ru^{5+} ion is shown in Figure 3.24 and it is seen that the magnetic moment rapidly saturates at ~ 2.4 μ_B, only a few Kelvin below the long-range magnetic ordering temperature of 39 K. Above 39 K there was no magnetic intensity and so no copper ordering to high temperatures was observed in the Ba compounds also.

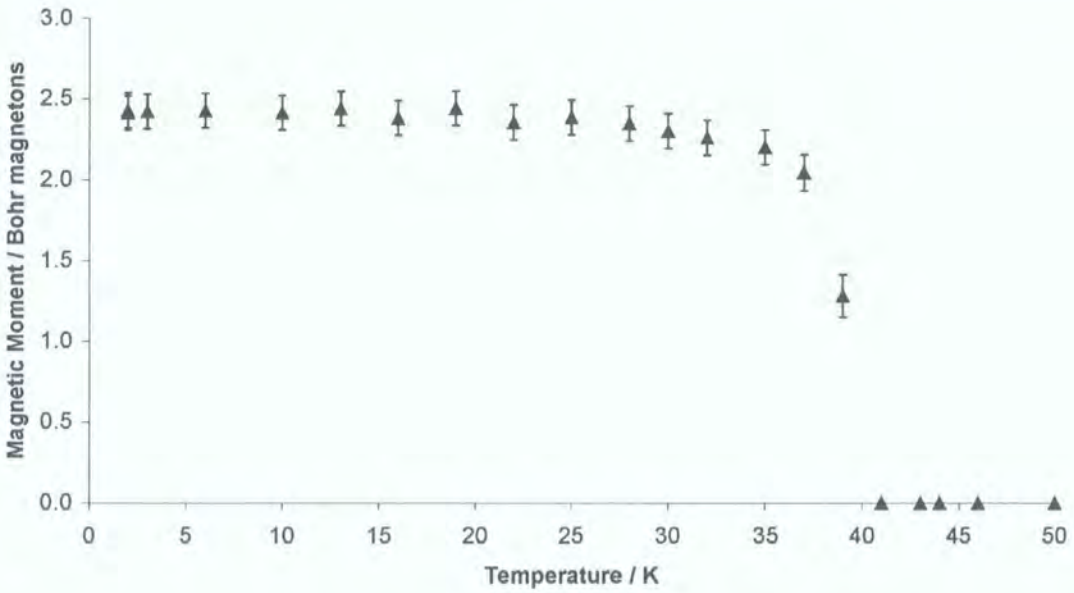

Figure 3.24 The refined magnetic moment of the Ru^{5+} ion in $Ba_2YRu_{0.90}Cu_{0.10}O_6$.

The size of the magnetic moment at 2 K of 2.41(10) μ_B cannot be compared directly with the previous study on the parent compound [6] of 2.11(6) μ_B at 4.2 K, which is significantly lower. Given that the $Sr_2YRu_{1-x}Cu_xO_6$ series displayed an increase in magnetic moment with increased copper doping, it is likely that the Ba series would behave similarly, given that it is similar in all other respects. Additionally the study on Ba_2YRuO_6 used only the lowest angle magnetic ordering peak while assuming a magnetic form factor of unity and so this too would lead to a lower value of the magnetic moment. With these two factors taken into account, the two values are much more likely to be in close agreement. For Sr_2YRuO_6 there had been the possibility of missing the *c*-component of the magnetic moment with Battle's technique, but this does not exist for a cubic system, such as Ba_2YRuO_6, as the directions are equivalent.

The high-flux data also highlighted features unaccounted for by the main phase (Figure 3.22) at 2θ ~ 49°, 55° and 72°. The largest was the instrumental feature at ~72°, although this could obscure impurity peaks itself. These peaks could be indexed

to starting reagents CuO, $BaCO_3$ and likely oxide by-products such as BaO_2, $Ba_3Y_4O_9$ or a related double perovskite. The maximum CuO content is 2 %, which would lead to a sample composition of $Ba_2YRu_{0.92}Cu_{0.08}O_6$. However as the impurity peaks are so broad and with a relatively low intensity it is impossible to rule out the presence of a small $YBa_2Cu_3O_{7-\delta}$ impurity.

3.5 Magnetic Ordering in the One Magnetic Ion Systems

The observation of long-range magnetic order, particularly Type I, in $Sr_2YRu_{1-x}Cu_xO_6$ and $Ba_2YRu_{1-x}Cu_xO_6$ strongly suggests that the *B* cations are 1:1 ordered in the materials. The two systems, $Sr_2YRu_{1-x}Cu_xO_6$ and $Ba_2YRu_{1-x}Cu_xO_6$ are quite similar and this is reflected in the only significant difference between the curves in Figure 3.25, is in the ordering temperature of the Ba and Sr materials, of 39 K and 33 K respectively. These ordering temperatures can be related to the crystal structures of the Ba and Sr materials, where the Y^{3+} ion is unlikely to be involved in the magnetic properties, as it is fully ionised. Thus any magnetic interaction pathway is likely to be along Ru-O-O-Ru bonds, rather than Ru-O-Y-O-Ru bonds. In the Ba compounds the Ru-O-Y bond angles are 180° whereas in the Sr compounds they deviate from 180° as indicated in Table 3.2. It is this deviation which reduces the bond overlap and thus weakens the magnetic interaction between neighbouring Ru^{5+} ions, resulting in the lower ordering temperature in the Sr analogue. This viewpoint is supported by both compounds adopting the Type I antiferromagnetic structure, where the nearest-neighbour interaction (i.e. Ru-O-O-Ru) is far stronger than the next-nearest-neighbour interaction (i.e. Ru-O-Y-O-Ru).

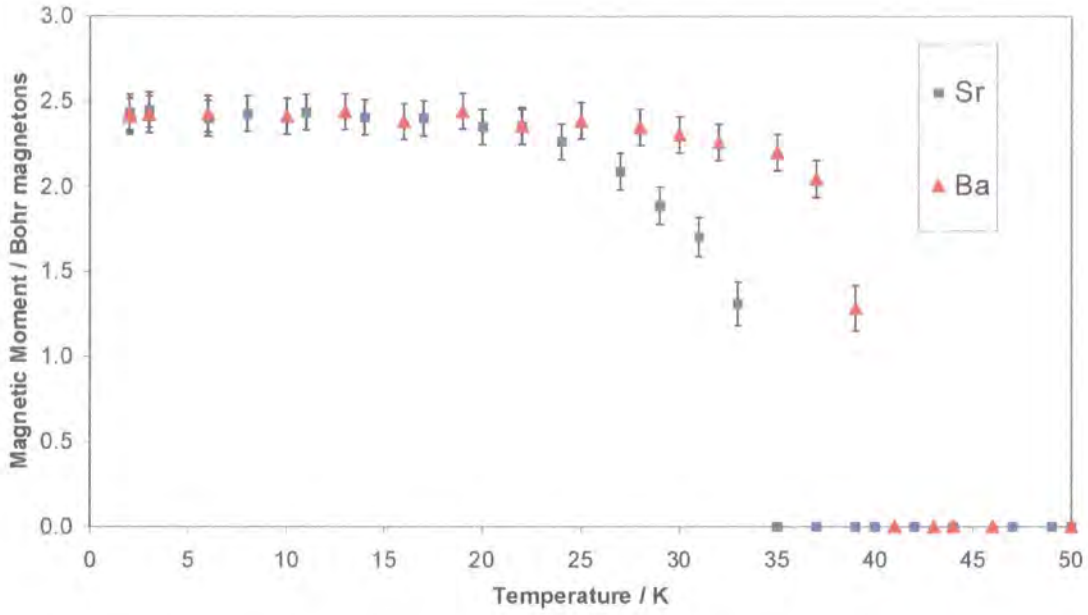

Figure 3.25 Variation of the magnetic moment with temperature for $Sr_2YRu_{0.85}Cu_{0.15}O_6$ and $Ba_2YRu_{0.90}Cu_{0.10}O_6$ as determined from refinements of the D1B data.

The saturated magnetic moment values for the Sr and Ba series are in the range 2.21-2.54(10) μ_B dependant on copper concentration. Other diffraction studies of ruthenates, where Ru^{5+} is the only magnetic ion in a fully ordered 1:1 crystal structure, have determined lower moment values. For example 1.85(10) μ_B for Sr_2YRuO_6 [4], 2.11(6) μ_B for Ba_2YRuO_6 [6], 2.10(8) μ_B for Sr_2LuRuO_6 [6], 2.06(6) μ_B for Ba_2LuRuO_6 [6], 1.92(10) μ_B for Ca_2LaRuO_6 [3] and 1.96(10) μ_B for Ba_2LaRuO_6 [3] which were all reported by Battle *et al.* However, all these results were analysed assuming (and stating) a magnetic form factor of unity, and so would be expected to be lower as discussed already in the case of Sr_2YRuO_6. For the disordered $BaLaZnRuO_6$ [7] the refined magnetic moment of Ru^{5+} is even lower at ~ 1.5 μ_B and is further evidence that the initial assumption of 1:1 ordering in this study is correct. Conversely, the double perovskites with two magnetic ions have larger magnetic moments as evidenced by the 2.74(9) μ_B for Sr_2HoRuO_6 [8, 11] and 2.99(11) μ_B for Sr_2TbRuO_6 [9, 11]. This is due to Doi *et al.*'s use of the Zr^+ magnetic form factor, which over-estimates the Ru^{5+} moment by ~ 0.25 μ_B. Hence, there is no discrepancy between the values reported here and the current body of literature. This work also indicates that the differences between the reported magnetic moment of Ru^{5+} in the one and two magnetic ion systems, is largely due to the differing refinement approaches of the two groups, and not a physical one.

3.6 Conclusions

The $Sr_2YRu_{1-x}Cu_xO_6$ series (with x = 0.05, 0.10 and 0.15) was examined by powder neutron diffraction and each member was refined as a distorted double perovskite in monoclinic space group $P2_1/n$. Copper, which is thought to dope holes into the structure, is included in the lattice, as evidenced by its expansion with increased doping. The expansion of the lattice is anisotropic with the c-axis expanding at twice the normalised rate of the other two axes, for both increased temperature and increased copper doping. Owing to the larger size of Ba compared to Sr, the $Ba_2YRu_{0.90}Cu_{0.10}O_6$ compound can adopt the cubic $Fm3m$ space group and have a more regular network of oxygen octahedra as a result. The lattice increases discontinuously with the onset of long-range magnetic order at 39 K.

Long-range magnetic order is observed in both series of compounds below $T_N \sim 30$ - 40 K. The higher ordering temperature measured in the Ba analogue is attributed to its higher symmetry crystal structure, in particular the oxygen octahedra that are believed to be responsible for the magnetic interaction pathway. An antiferromagnetic Type I magnetic structure, that indicates the strongest interaction is via the Ru-O-O-Ru superexchange pathway, is adopted by all the compounds, with a saturated moment at 2 K of ~ 2.4(1) μ_B for the Ru^{5+} ions. This moment has been shown to lie in the ab plane for the $Sr_2YRu_{1-x}Cu_xO_6$ series and also increase with copper doping. However no long-range copper ordering at higher temperatures was observed in any of these compounds despite the use of the most intense neutron sources in the world. The canted magnetic moment required by Wu's double-exchange explanation of the materials can be no larger than 0.8 μ_B as it was not detected in these experiments.

3.7 References

1 A.J.C. Wilson, ed. *International Tables for Crystallography, Volume C, Mathematical, Physical and Chemical Tables*, Vol. C, Kluwer Academic Press: London. 883 (1992).

2 L. Capogna, E.M. Forgan, G.J. McIntyre, N. Burton, P.G. Kealey, R.S. Perry, L.M. Galvin, A.P. Mackenzie, S. Ikeda and Y. Maeno, *Applied Physics A-Materials Science & Processing* **74**, S926 (2002).

3 P.D. Battle, J.B. Goodenough and R. Price, *Journal of Solid State Chemistry* **46,** 234 (1983).

4 P.D. Battle and W.J. Macklin, *Journal of Solid State Chemistry* **52,** 138 (1984).

5 P.D. Battle and W.J. Macklin, *Journal of Solid State Chemistry* **54,** 245 (1984).

6 P.D. Battle and C.W. Jones, *Journal of Solid State Chemistry* **78,** 108 (1989).

7 P.D. Battle, T.C. Gibb, C.W. Jones and F. Studer, *Journal of Solid State Chemistry* **78,** 281 (1989).

8 Y. Doi, Y. Hinatsu, K. Oikawa, Y. Shimojo and Y. Morii, *Journal of Materials Chemistry* **10,** 797 (2000).

9 Y. Doi, Y. Hinatsu, K. Oikawa, Y. Shimojo and Y. Morii, *Journal of Materials Chemistry* **10,** 1731 (2000).

10 Y. Izumiyama, Y. Doi, M. Wakeshima, Y. Hinatsu, K. Oikawa, Y. Shimojo and Y. Morii, *Journal of Materials Chemistry* **10,** 2364 (2000).

11 Y. Doi, Y. Hinatsu, K. Oikawa, Y. Shimojo and Y. Morii, *Journal of Alloys and Compounds* **323,** 455 (2001).

12 Y. Izumiyama, Y. Doi, M. Wakeshima, Y. Hinatsu, Y. Shimojo and Y. Morii, *Journal of Physics-Condensed Matter* **13,** 1303 (2001).

13 A.C. Larson and R.B. Von Dreele, Los Alamos National Laboratory Report **LAUR 86-748,** 1 (1990).

14 M.K. Wu, D.Y. Chen, F.Z. Chien, S.R. Sheen, D.C. Ling, C.Y. Tai, G.Y. Tseng, D.H. Chen and F.C. Zhang, *Zeitschrift Fur Physik B-Condensed Matter* **102,** 37 (1997).

15 M.K. Wu, D.Y. Chen, F.Z. Chien, D.C. Ling, Y.Y. Chen and H.C. Ren, *International Journal of Modern Physics B* **13,** 3585 (1999).

16 H.C. Ren and M.K. Wu, *Physical Review B* **58,** 15440 (1998).

17 D.Y. Chen, F.Z. Chien, D.C. Ling, J.L. Tseng, S.R. Sheen, M.J. Wang and M.K. Wu, *Physica C* **282,** 73 (1997).

18 J.D. Jorgensen, O. Chmaissem, H. Shaked, S. Short, P.W. Klamut, B. Dabrowski and J.L. Tallon, *Physical Review B* **63,** 054440 (2001).

19 J.W. Lynn, B. Keimer, C. Ulrich, C. Bernhard and J.L. Tallon, *Physical Review B* **61,** R14964 (2000).

20 H.A. Blackstead, J.D. Dow, D.R. Harshman, W.B. Yelon, M.X. Chen, M.K. Wu, D.Y. Chen, F.Z. Chien and D.B. Pulling, *Physical Review B* **63,** 214412 (2001).

21 N.G. Parkinson, P.D. Hatton, J.A.K. Howard, C. Ritter, F.Z. Chien and M.K. Wu, *Journal of Materials Chemistry* **13,** 1468 (2003).

22 H.A. Blackstead, J.D. Dow, D.R. Harshman, M.J. DeMarco, M.K. Wu, D.Y. Chen, F.Z. Chieng, D.B. Pulling, W.J. Kossler, A.J. Greer, C.E. Stronach, E. Koster, B. Hitti, M. Haka and S. Toorongian, *European Physical Journal B* **15,** 649 (2000).

23 D.R. Harshman, H.A. Blackstead, W.J. Kossler, A.J. Greer, C.E. Stronach, E. Koster, B. Hitti, M.K. Wu, D.Y. Chen, F.Z. Chien and J.D. Dow, *International Journal of Modern Physics B* **13,** 3670 (1999).

24 A.W. Mombru, A.E. Goeta, H. Pardo, P.N. Lisboa, L. Suescun, R.A. Mariezcurrena, O.N. Ventura, R. Behak, K.H. Andersen and F.M. Araujo-Moreira, *Journal of Solid State Chemistry* **166,** 251 (2002).

25 Z. Gadjourova, D.M. Marero, K.H. Andersen, Y.G. Andreev and P.G. Bruce, *Chemistry of Materials* **13,** 1282 (2001).

4 Neutron Diffraction Studies of $Sr_2HoRu_{1-x}Cu_xO_6$ and $Sr_2TbRu_{1-x}Cu_xO_6$

4.1 Introduction

Both $Sr_2HoRu_{1-x}Cu_xO_6$ and $Sr_2TbRu_{1-x}Cu_xO_6$ have been studied using neutron powder diffraction in order to elucidate the crystal and magnetic structures. The choice of the 4*f* ions of Ho^{3+} and Tb^{3+} was astute, as both ions have large magnetic moments, potentially ~ 10 μ_B, and do not absorb neutrons overly. From their large size, the Ho^{3+} and Tb^{3+} ions would be expected to order crystallographically with the smaller Ru^{5+} ions [1]. As discussed in Chapter 1, this means that a magnetic structure is much more likely to be developed.

The introduction of a second magnetic ion into the materials was expected to have a large impact on the properties of the materials, especially their superconducting nature. However, $Sr_2HoRu_{1-x}Cu_xO_6$ was reported [2] to be superconducting, despite the large moment of the Ho^{3+}. Determining the magnetic structure could give clues as to why the reported superconductivity is so robust to such a large magnetic moment, and help shape an overall theory for the superconductivity in the mixed ruthenium-copper systems.

The superconducting status of $Sr_2TbRu_{1-x}Cu_xO_6$ is not precisely known, so the Tb system was examined as a comparative study with the Ho series. Those characteristics which are similar or dissimilar, could be drawn upon to determine why $Sr_2HoRu_{1-x}Cu_xO_6$ (and possibly $Sr_2TbRu_{1-x}Cu_xO_6$) superconduct, depending on the resolution of the potential superconducting nature of $Sr_2TbRu_{1-x}Cu_xO_6$. In addition, the materials are interesting in their own right, and would help explain the variety of interactions between rare-earths, Ln^{3+}, and the Ru^{5+} ion.

As an addition to the study of these two systems, the mixed system, $Sr_2Ho_yTb_{1-y}Ru_{1-x}Cu_xO_6$, was studied which would help clarify the roles of each ion in the magnetic ordering scheme.

The crystal structures were determined using HRPD (High-Resolution Powder Diffractometer) at the ISIS facility where possible due to its unparalleled diffraction pattern quality at low *d*-spacings. The high-flux diffractometer D1B was used to examine the magnetic structures of all the materials, in order to determine the magnetic structure development with temperature. Owing to the combination of good

resolution and high-flux at large *d*-spacings, a short study was performed at OSIRIS, to try to elucidate the magnetic structure further.

4.2 Neutron Diffraction Experiments on $Sr_2HoRu_{1-x}Cu_xO_6$

The samples of Sr_2HoRuO_6 and $Sr_2HoRu_{0.95}Cu_{0.05}O_6$ were studied using HRPD in order to determine the trends in crystal structure of a rare-earth ruthenate, and the effect of copper doping. Diffraction patterns were collected at 2, 20 and 50 K for 7 hours each, to investigate the structures through the transition temperatures of the materials. Further experiments were undertaken at D1B on the whole series of $Sr_2HoRu_{1-x}Cu_xO_6$ (x = 0, 0.05, 0.10, 0.15), as these extra samples became available. These experiments were to examine the temperature dependence of the magnetic structures of the materials, to study the ordered moment size of the two ions, Ru^{5+} and Ho^{3+}, and the interaction between them. Further data on $Sr_2HoRu_{0.95}Cu_{0.05}O_6$ was collected at OSIRIS due to its combination of intensity and resolution at high *d*-spacings, which was expected to highlight fine details of the magnetic structure. Typically 3 - 4 grams of material were contained in 12-16 mm diameter vanadium cans and details of the absorption correction appear in Appendix B.7.

4.2.1 Crystal Structure of $Sr_2HoRu_{1-x}Cu_xO_6$

The diffraction pattern of $Sr_2HoRu_{0.95}Cu_{0.15}O_6$ shown in Figure 4.1 and Figure 4.2 was measured at 50 K, above the magnetic ordering temperature, and so provides information on only the crystal structure. The refinements were performed in space group $P2_1/n$ assuming a 1:1 ordering of the Ru(Cu):Ho ions, as would be expected from ions of this charge and size. The diffraction pattern has been shown in two sections, simply to emphasise both the high quality and resolution of the data measured at HRPD, even at these low *d*-spacings, and also, the comparable standard of the crystal model used to calculate the diffraction profile. There is no significant mismatch between the observed intensity and the calculated profile, which is generated from the model crystal structure listed in Table 4.1.

Using the results of the refinements listed in Table 4.1, the principal bond lengths and angles were calculated for $Sr_2HoRu_{0.95}Cu_{0.05}O_6$, as listed in Table 4.2, and compared with the Y counterpart, $Sr_2YRu_{0.95}Cu_{0.05}O_6$. The bond lengths and angles are all fairly similar, as the Y^{3+} has been replaced by the similarly sized Ho^{3+} ion. The crystal

structure is shown in Figure 4.3 and allows the tilts of the oxygen octahedra to be seen, which highlight the deviation of the Ru-O-Ho bond angle to ~ 155-158°.

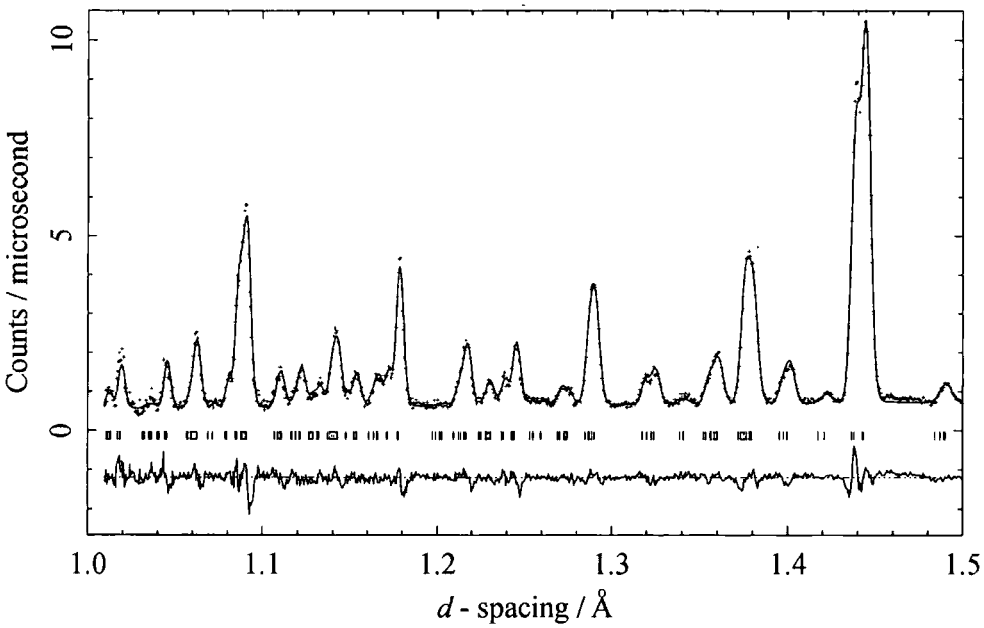

Figure 4.1 The low *d*-spacing segment of the diffraction pattern between 1 Å and 1.5 Å of $Sr_2HoRu_{0.95}Cu_{0.05}O_6$, measured at 50 K on HRPD at ISIS. The observed data points are shown as crosses, the calculated profile and difference curve as lines. The tick marks, which denote allowed crystal structure reflections are shown as short vertical lines.

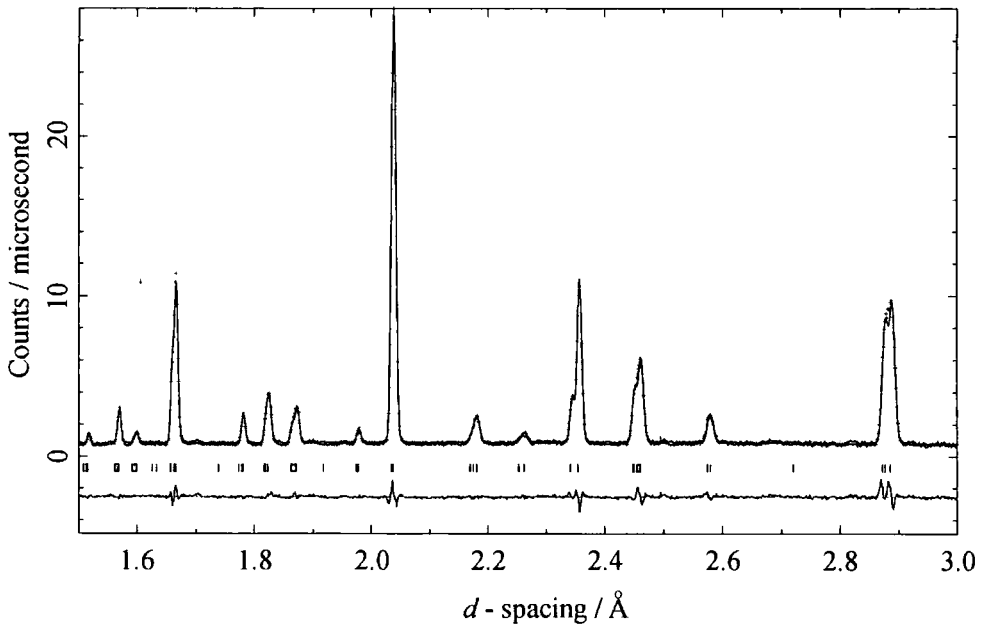

Figure 4.2 The 1.5 Å to 3 Å *d*-spacing region of the diffraction pattern of $Sr_2HoRu_{0.95}Cu_{0.05}O_6$ measured at 50 K. The region of the pattern emphasises the high-resolution of HRPD and the quality of the model structure used to calculate the diffraction profile.

$Sr_2HoRu_{0.95}Cu_{0.05}O_6$		$P2_1/n$			50 K	
a / Å		b / Å	c / Å	β / °	Volume / Å^3	
5.75784(3)		5.77689(3)	8.14340(7)	90.350(1)	270.864(5)	
Atom	Site	x	y	z	Occ	B_{iso}/Å^2	μ/μ_B
Sr	4*e*	0.0067(8)	0.0313(4)	0.7507(6)	1.000	0.30(3)	
Ho	2*c*	0	½	0	1.000	0.20(9)	
Ru	2*d*	½	0	0	0.950	0.38(10)	
Cu	2*d*	½	0	0	0.050	0.38(10)	
O1	4*e*	0.3013(8)	0.2732(8)	0.9620(5)	1.000	0.42(10)	
O2	4*e*	0.2676(7)	0.2969(8)	0.5357(6)	1.000	0.27(12)	
O3	4*e*	0.9258(8)	0.4814(7)	0.7311(5)	1.000	0.38(7)	

R_p = 5.86 %, R_{wp} = 7.12 %, R_{exp} = 4.60 %, R_{F^2} = 5.01 %

Table 4.1 The refined lattice parameters and atomic coordinates of $Sr_2HoRu_{0.95}Cu_{0.05}O_6$ from data measured on HRPD at 50 K.

$Sr_2HoRu_{0.95}Cu_{0.05}O_6$		$P2_1/n$		HRPD	50 K	
Ho-O1	2.198(4)	Ru-O1	1.973(4)	O1-Ho-O2	92.0(2)	O1-Ru-O2	90.1(3)
Ho-O2	2.196(4)	Ru-O2	1.957(4)	O1-Ho-O3	91.2(2)	O1-Ru-O3	91.3(2)
Ho-O3	2.231(4)	Ru-O3	1.936(4)	O2-Ho-O3	91.2(2)	O2-Ru-O3	90.1(2)
Ru-O1-Ho	155.9(2)		Ru-O2-Ho	158.2 (3)		Ru-O3-Ho	155.5(2)
Sr-O1	2.785(6)	Sr-O1	2.543(6)	Sr-O1	3.430(6)	Sr-O1	2.858(6)
Sr-O2	2.777(6)	Sr-O2	2.554(7)	Sr-O2	3.388(6)	Sr-O2	2.882(6)
Sr-O3	3.214(4)	Sr-O3	2.647(4)	Sr-O3	2.512(6)	Sr-O3	3.283(7)
$Sr_2YRu_{0.95}Cu_{0.05}O_6$		$P2_1/n$		D2B	42 K	
Y-O1	2.210(3)	Ru-O1	1.956(3)	O1-Y-O2	91.6(1)	O1-Ru-O2	90.4(2)
Y-O2	2.205(3)	Ru-O2	1.951(3)	O1-Y-O3	91.2(1)	O1-Ru-O3	90.4(1)
Y-O3	2.202(3)	Ru-O3	1.954(3)	O2-Y-O3	90.5(1)	O2-Ru-O3	90.4(2)
Ru-O1-Y	156.5(1)		Ru-O2-Y	158.0 (1)		Ru-O3-Y	157.1(1)
Sr-O1	2.788(4)	Sr-O1	2.546(5)	Sr-O1	3.428(5)	Sr-O1	2.855(5)
Sr-O2	2.772(4)	Sr-O2	2.555(5)	Sr-O2	3.388(4)	Sr-O2	2.894(5)
Sr-O3	3.190(3)	Sr-O3	2.662(3)	Sr-O3	2.540(4)	Sr-O3	3.251(4)

Table 4.2 The refined bond lengths (Å) and bond angles (°) in $Sr_2HoRu_{0.95}Cu_{0.05}O_6$ as determined using HRPD data. They are compared with the results of a previous refinement of $Sr_2YRu_{0.95}Cu_{0.05}O_6$ using D2B data, as discussed in Chapter 3.

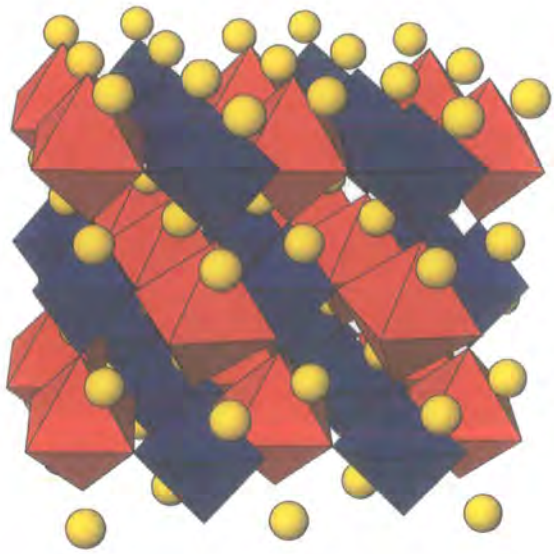

Figure 4.3 Crystal structure of $Sr_2HoRu_{0.95}Cu_{0.15}O_6$, which illustrates the large tilting of the oxygen octahedra. The RuO_6 octahedra are shown in blue, the HoO_6 octahedra in red, and the space filling Sr atoms are the yellow spheres.

The refined crystal structures for $Sr_2HoRu_{0.95}Cu_{0.05}O_6$ at 2 K and 20 K did not vary greatly from this 50 K structure, nor did the refinements from Sr_2HoRuO_6 data, the details of which are in Appendix B.3.1. The unit cell volumes for both members of the $Sr_2HoRu_{1-x}Cu_xO_6$ series are shown in Figure 4.4, and despite the small number of data points, it is quite informative. Once again, there is an expansion of the unit cell with the increased copper doping as one would expect, but also their appears to be a slight increase of 0.07-0.08 $Å^3$ below 20 K in both materials. In $Ba_2YRu_{0.90}Cu_{0.10}O_6$ there was a sudden expansion of the lattice at the magnetic ordering temperature, and this may be similar. However, with so few data points it is difficult to be sure of the expansion, particularly any onset temperature, and so the lattice parameters' variation was also studied using the high-flux diffractometer D1B.

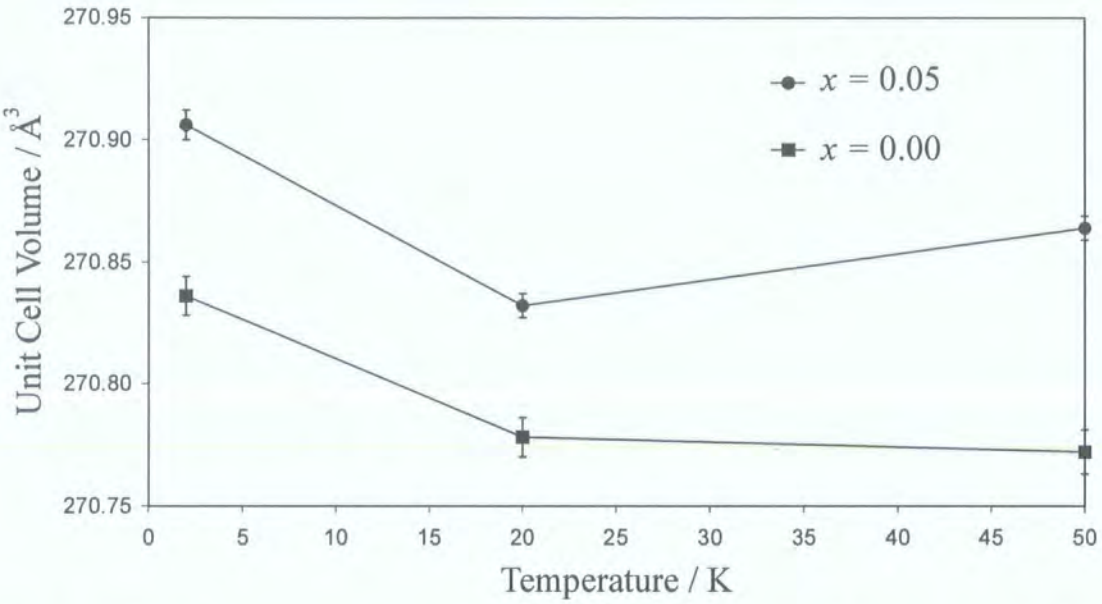

Figure 4.4 The unit cell volume with temperature for the materials, $Sr_2HoRu_{1-x}Cu_xO_6$ for $x = 0$ and 0.05. Although there are very few data points on the plot, the results are still informative.

Data were measured using D1B at the ILL for the entire $Sr_2HoRu_{1-x}Cu_xO_6$ series with $x = 0$, 0.05, 0.10 and 0.15. The temperature of the sample was increased from 2 K to 50 K at a rate of ~ 0.2 K per minute and a diffraction pattern collected every 10 minutes. The diffraction pattern for $Sr_2HoRu_{0.95}Cu_{0.05}O_6$ at 50 K is shown in Figure 4.5 and the lattice parameters were refined using the crystal structure as determined from HRPD. The two sets of lattice parameters agree well, within σ, and there is no significant mismatch between the observed data and calculated profile from the main phase. The feature at 72° is an instrumental peak as mentioned in Chapter 3, and the remaining unindexed impurity peaks will be discussed at length in Chapter 6 from X-ray synchrotron measurements.

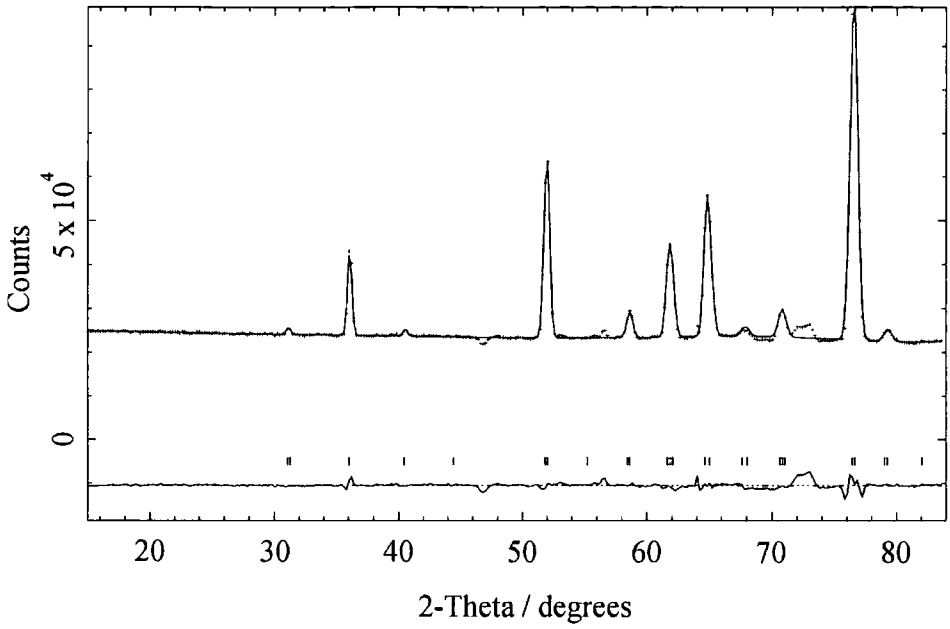

Figure 4.5 Diffraction pattern of $Sr_2HoRu_{0.95}Cu_{0.05}O_6$ at 50 K measured with D1B of the ILL. The data points are shown as crosses and the calculated profile and difference curve as lines. The calculated profile has *R*-factors of R_p = 1.31 %, R_{wp} = 2.32 % and R_{exp} = 0.61 %.

As can be seen from Figure 4.5 the diffraction pattern will not allow precise refinements of the crystal structure details. However, as the crystal structure of the $Sr_2HoRu_{1-x}Cu_xO_6$ did not change markedly with temperature between 2 and 50 K, or with copper doping, the atomic coordinates and thermal parameters were fixed at the values refined using HRPD data. In practice, the 20 K structure of Sr_2HoRuO_6 was used to refine all the D1B data on Sr_2HoRuO_6, while the 20 K structure of $Sr_2HoRu_{0.95}Cu_{0.05}O_6$ was used for the other members of the series. This made no difference to the quality of the refinements using D1B data as the calculated profile, *R*-factors and the refined parameters were the same, irrespective of the slight differences that HRPD was able to measure in the atomic coordinates.

The refinements of the lattice parameters using the D1B data for all members of the series and at all temperatures can be summarised by the unit cell volume, as the individual lattice parameters all showed the same behaviour with temperature. These results are listed in Appendix B.3.2. Figure 4.6 shows that the unit cell volume increases with increasing copper doping, suggesting the inclusion of copper into the main phase in the place of the smaller ruthenium. There is a slight anomaly at the lowest temperatures for $Sr_2HoRu_{0.95}Cu_{0.05}O_6$ which hasn't been explained, nor has the larger increase in unit cell volume for the $x = 0.15$ sample.

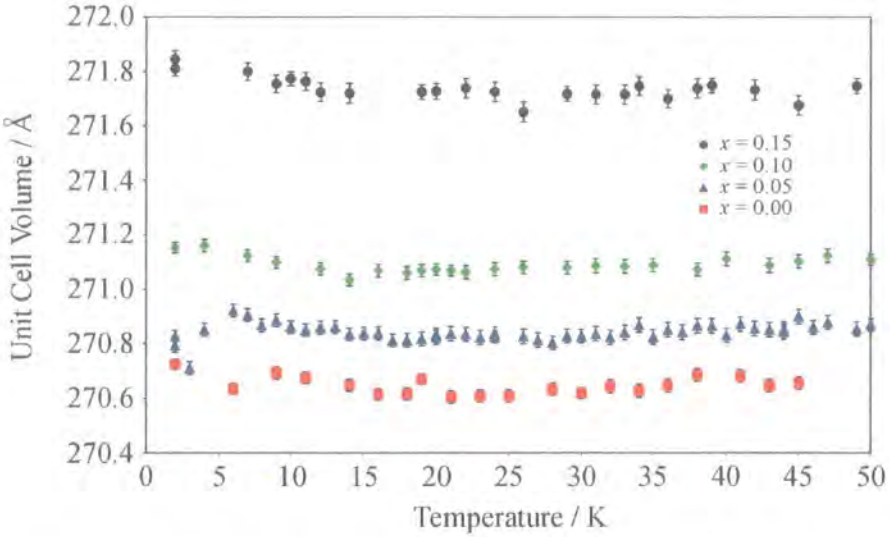

Figure 4.6 Unit cell volume with temperature for the $Sr_2HoRu_{1-x}Cu_xO_6$ series with x = 0, 0.05, 0.10 and 0.15. The unit cell volume increases with successive copper doping.

The unit cell volume appears to be fairly constant for each series over the majority of the temperature range measured, however below 15-20 K, as the material is cooled, the unit cell volume does increase by ~ 0.08 $Å^3$, in agreement with the HRPD data. This is shown more clearly in Figure 4.7 and suggests that the increase starts at ~ 17 K in all the materials, and although not very dramatic, this observation using two different diffractometers and four different samples does increase confidence in the observation. The expansion is once again anisotropic, with the expansivity in the *c*-direction approximately twice that of the *a* and *b* directions.

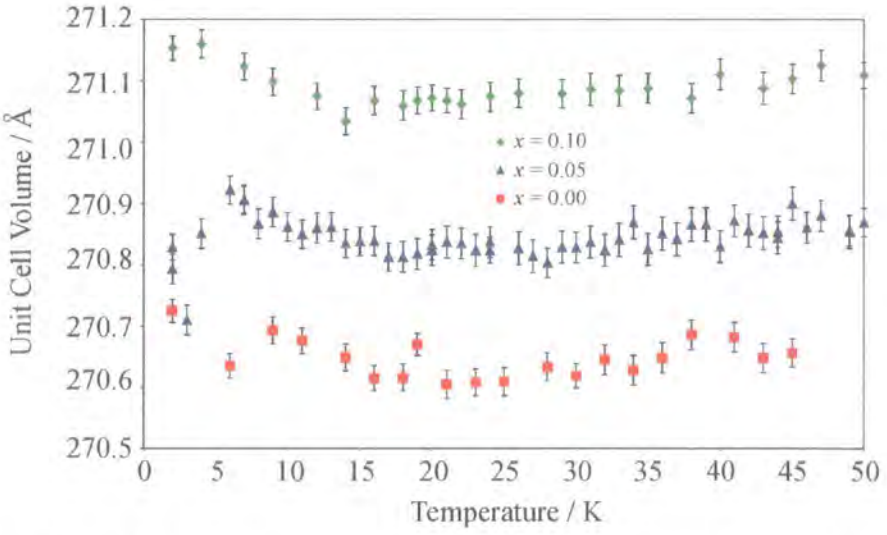

Figure 4.7 Unit cell volume with temperature for $Sr_2HoRu_{1-x}Cu_xO_6$ (x = 0, 0.05, 0.10) at low temperatures. The results for the x = 0.15 are not shown, in order to show the detail of the scale, but these results are similar.

4.2.2 Magnetic Structure of $Sr_2HoRu_{1-x}Cu_xO_6$

The variable temperature neutron powder diffraction patterns measured between 2 and 50 K are shown in Figure 4.8 for Sr_2HoRuO_6, which are typical for the series. Extra peaks appear in the diffraction pattern below 34 K and their intensity increases as the temperature continues to be lowered. These observations indicate the onset of long-range magnetic order at 34 K, and that the magnetic moments become increasingly ordered as the temperature is lowered. Both the profile of the magnetic peaks with temperature (e.g. the unresolved combination of the (100) and (010) at $2\theta \sim 25°$), and the much greater magnetic intensity when compared to $Sr_2YRu_{1-x}Cu_xO_6$ patterns, indicate that the difference between the two is likely to be the large magnetic moment of Ho^{3+}, progressively ordering as the temperature is lowered. The purely crystal structure peaks appear unchanged through the magnetic ordering temperature, confirming visually the finding from the HRPD refinements. The crystal structure, in particular, the assumed 1:1 order of the *B* cations, is supported by the observation of long-range magnetic order.

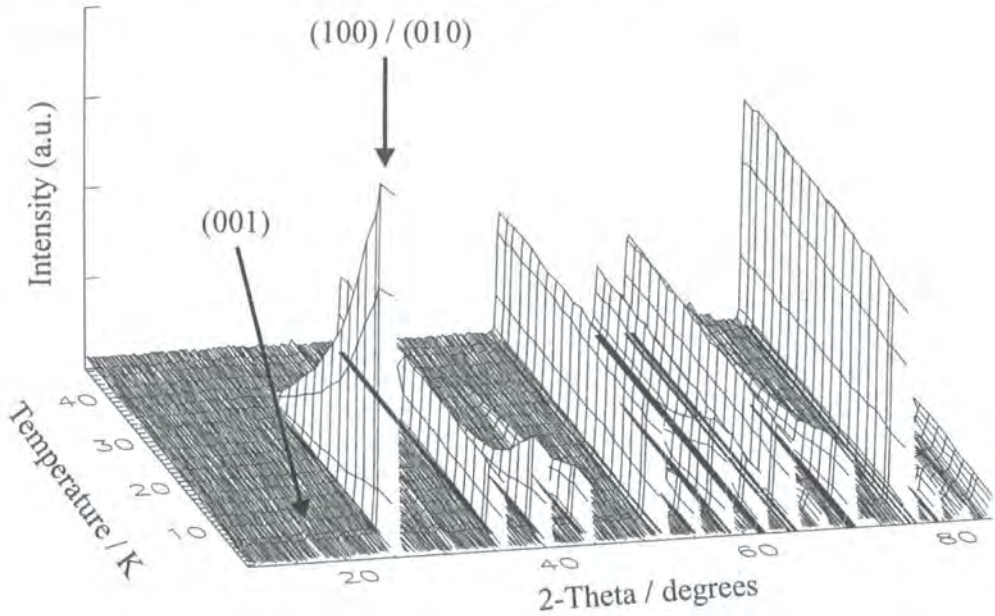

Figure 4.8 Variable temperature neutron powder diffraction patterns collected at D1B on the Sr_2HoRuO_6 sample, which are typical of the series. The magnetic peaks, for instance, the unresolved combination of the (100) and (010) reflections begin to appear at 34 K. The (001) magnetic peak is not detectable until the much lower temperature of 9 K.

The powder diffraction pattern for Sr_2HoRuO_6 measured at 2 K is shown in Figure 4.9, with some of the principal magnetic peaks explicitly indexed. In common with the discussion of the magnetic structure of $Sr_2YRu_{1-x}Cu_xO_6$, a magnetic peak

indicates that a component of the magnetic moment is perpendicular to the scattering vector. Hence, the observation of the (001) indicates that there is a component of the magnetic moment in the *ab* plane, while the unresolved (100)/(010) peak indicates a component in the *c*-direction. This suggests that the component of the magnetic moment in the *ab* plane is only measurable below 9 K.

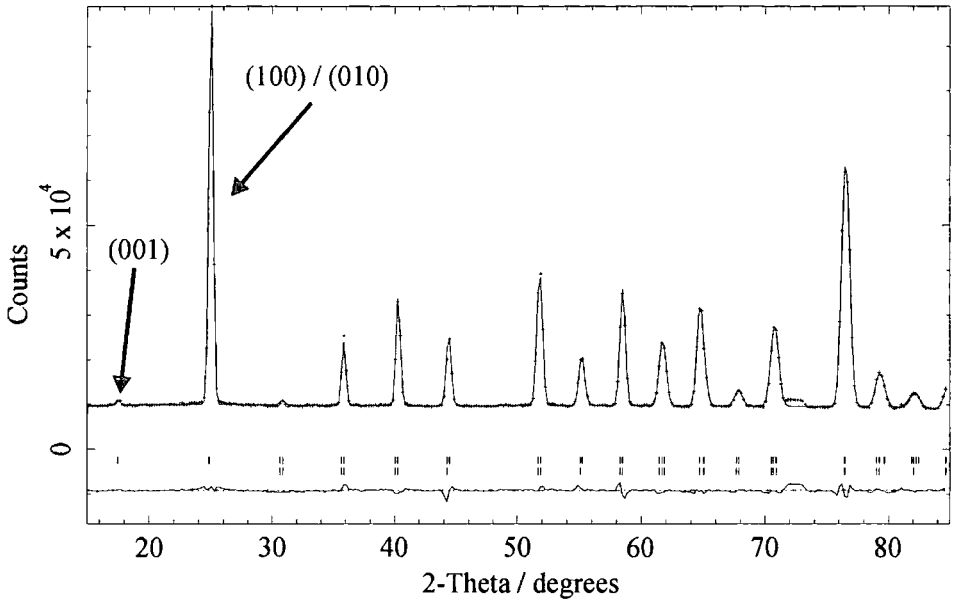

Figure 4.9 Neutron powder diffraction pattern of Sr_2HoRuO_6 measured at 2 K using D1B. The (001) and unresolved combination of the (100) and (010) magnetic peaks are explicitly indexed.

In contrast to $Sr_2YRu_{1-x}Cu_xO_6$, the situation is more complicated in the case of Sr_2HoRuO_6 because of the addition of the extra magnetic ion, Ho^{3+}. As both the Ru^{5+} and Ho^{3+} magnetic ions are on *B* sites ($A_2B'B''O_6$), they will contribute to the same reflections and so the separation of the two magnetic contributions will be more difficult. An outline of this process will be given here, but the derivations of these results are in Appendix A.4. As the location of the magnetic intensity in the diffraction pattern is not primarily coincident with existing crystal structure peaks, this indicates that *both* the Ru^{5+} and Ho^{3+} ions form antiferromagnetic structures. With the magnetic unit cell the same size as the crystal unit cell ($\sim \sqrt{2}a_p \times \sqrt{2}a_p \times 2a_p$), all the magnetic peaks were indexed with $h + k + l$ odd, confirming the antiferromagnetic nature. The magnetic peaks appear in approximately the same places in the diffraction pattern of Sr_2HoRuO_6 as $Sr_2YRu_{1-x}Cu_xO_6$, but with different intensities, indicative that the magnetic structure is similar, but that the moment size is not, most likely due to the Ho^{3+} ion. Thus, the magnetic structure used has the Ru^{5+} and Ho^{3+} ions each ordering in Type I arrangements which interpenetrate, as shown in Figure 4.10.

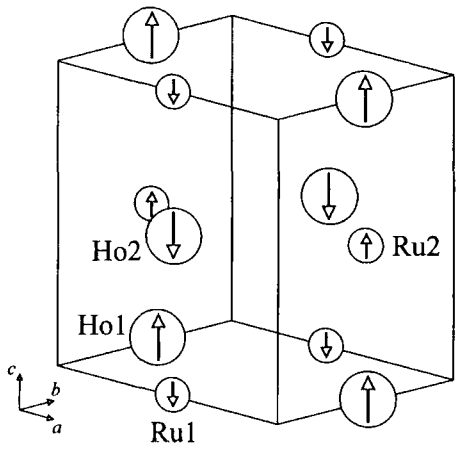

Figure 4.10 The magnetic structure of Sr_2HoRuO_6 where the Ru^{5+} ions at (½, 0, 0) and (0, ½, ½) couple antiferromagnetically in a Type I structure. The Ho^{3+} ions at (0, ½, 0) and (½, 0, ½) also couple antiferromagnetically to form a second Type I magnetic structure, which interpenetrates the first. The magnetic moments are shown arbitrarily in the *c*-direction. The magnitude of the magnetic moment is indicated by the size of the arrow, so in this case the Ho^{3+} moment is larger than the Ru^{5+} moment.

The reflection conditions when both ions adopt this antiferromagnetic structure are derived in Appendix A.4.2, and there can only be magnetic intensity when $h + k + l$ is odd. Restricting the discussion to collinear magnetic structures, there are two possible relative orientations of the two magnetic sublattices. These are the ferromagnetic case, where the moments in the two sublattices are parallel to each other, and ferrimagnetic case, where the moments are anti-parallel to each other. Both magnetic structures are shown in Figure 4.11, and the intra-species interaction is most easily seen from noting the relative directions of the moments in the *ab* plane.

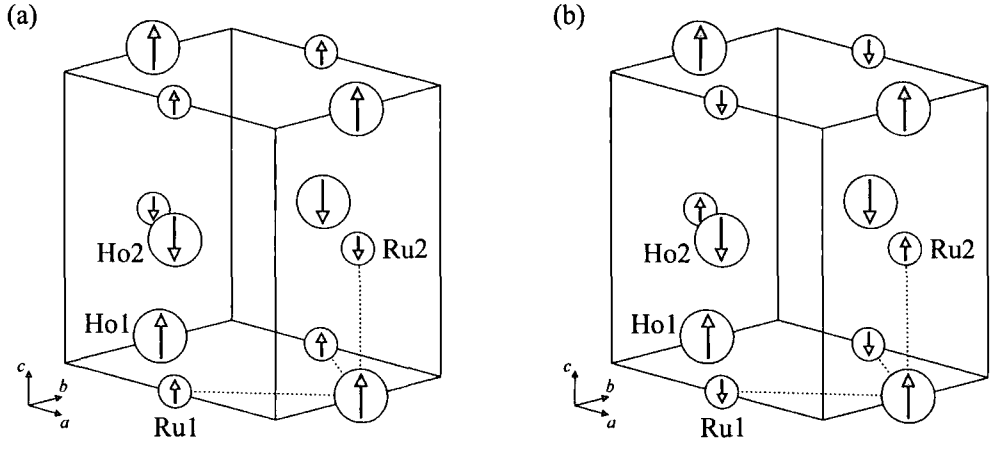

Figure 4.11 The Ru^{5+} and Ho^{3+} ions each form Type I magnetic sublattices. The two sublattices couple (a) ferromagnetically and (b) ferrimagnetically. The nature of this intra-species interaction is most easily seen by the relative direction of the moments of the ions in the *ab* plane, which are parallel and anti-parallel respectively.

The intra-species interaction does not generate any extra magnetic peaks, but it does influence the intensity of the existing magnetic peaks. This information, which is derived in Appendix A.4.2 explicitly, is summarised in Table 4.3. In order to have a magnetic reflection, $h + k + l$ is odd, but whether the magnetic peak is a sum peak, formed from the sum of the magnetic moments of Ru^{5+} and Ho^{3+}, or a difference peak, formed from the difference of the magnetic moments of Ru^{5+} and Ho^{3+}, depends on the relative orientations of the two sublattices.

Type of Reflection	Lattices Parallel Ferromagnetic		Lattices Anti-Parallel Ferrimagnetic	
	$(h + k)$	l	$(h + k)$	l
Sum	even	odd	odd	even
Difference	odd	even	even	odd

Table 4.3 The magnitude of the reflections is governed by the intra-species coupling, as indicated from the sum and difference peaks.

From the diffraction pattern, it will be clear which reflections form sum peaks and which form difference peaks, from the relative intensities. This information is sufficient to indicate whether the magnetic structure is best described by the ferromagnetic interpenetrating Type I structure as in Figure 4.11(a), or the ferrimagnetic interpenetrating Type I structure as in Figure 4.11(b). Knowing the intensities of these peaks, which are formed from the sum and difference of the magnetic moments of the Ru^{5+} and Ho^{3+} ions, allows these moments to be determined. The diffraction pattern of Sr_2HoRuO_6 is reshown in Figure 4.12, with the peaks composed of only reflections where $h + k + l$ is odd indicated by arrows. These are the magnetic peaks, but some also receive an independent contribution from the crystal structure. Those magnetic peaks which are formed only from reflections where l is even (and $h + k$ odd) are shown as red arrows, and where l is odd (and $h + k$ even) as blue arrows. Generally, the magnetic peaks denoted by red arrows (l even) are larger than those indicated by blue arrows (l odd), and so consultation of Table 4.3 suggests that the two sublattices are anti-parallel to each other, in the ferrimagnetic arrangement. When determining which set of peaks is the largest, it is important to realise that some of the arrowed peaks do have a contribution from the crystal structure, the size of which can be seen in higher temperature diffraction patterns, while the magnetic form factor reduces the intensity of magnetic peaks at high angles.

The number of contributing reflections and the direction of the magnetic moment relative to the scattering vector also modify the magnetic intensity. Taking these factors into account does not change the conclusion that the two sublattices are anti-parallel to each other.

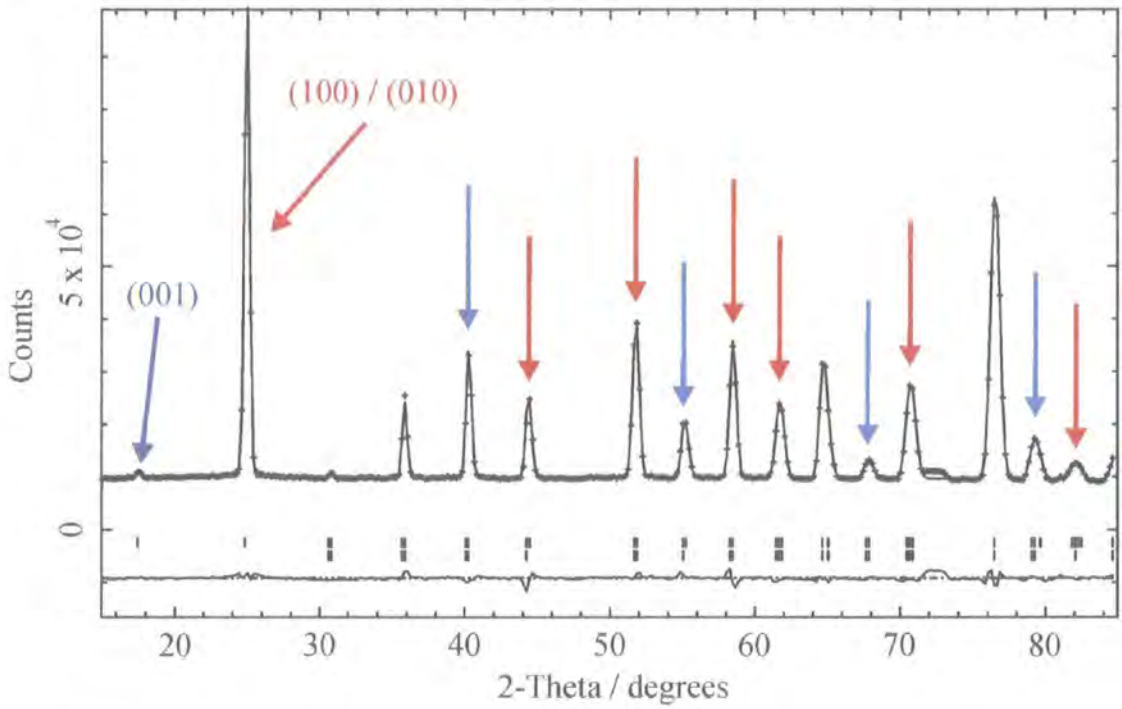

Figure 4.12 The diffraction pattern of Sr_2HoRuO_6, with those peaks composed of reflections where $h + k + l$ is odd, indicated by arrows. The red arrows denote peaks where $(h + k)$ is odd and l is even, whereas the blue peaks those where $(h + k)$ is even and l is odd. In general, those peaks indicated by a red arrow are larger than those peaks indicated by a blue arrow. The data points are shown as crosses, while the calculated profile and difference curve are drawn as lines. The lower series of tick marks indicate crystal structure reflections. The upper series of tick marks denote possible magnetic reflections when the magnetic space group is *P*-1, and explains why more magnetic tick marks are present than indicated by the arrows, as these only indicate the antiferromagnetic possibilities.

As the (001) peak at $2\theta \sim 18°$ is very small, this indicates that there is only a small magnetic moment in the *ab* plane. This fact, coupled with the very large unresolved combination of the (100) and (010) reflections, insist that the magnetic moment lies almost exclusively along the *c*-direction. As both the summation and difference magnetic peaks are all large, the magnetic moment of the Ho^{3+} was expected to be much larger than the Ru^{5+} moment. From this initial work, an appropriate starting magnetic model was deduced and was subsequently refined using GSAS [3].

The refined model is detailed in Table 4.4 and the calculated profile is shown in Figure 4.12, which quite accurately replicates the diffraction pattern. As there is a

very large amount of magnetic diffraction intensity in the pattern, particularly the peak at $2\theta \sim 25°$, this indicates that the refined magnetic structure is reliable. Certainly, for this amount of diffraction intensity to be unaccounted for originally by a crystal structure, requiring the input of vector parameters, the proximity of the observed and calculated profile should be regarded as a great success.

Sr_2HoRuO_6		$P2_1/n$			2 K		
a / Å		b / Å	c / Å	β / °	Volume / Å^3		
5.75715(10)		5.77619(10)	8.14118(29)	90.352(1)	270.725(19)		
Atom	Site	x	y	z	Occ	B_{iso}/Å^2	μ/μ_B
Sr	4*e*	0.0044	0.0311	0.7537	1.000	0.29	
Ho	2*c*	0	½	0	1.000	0.20	7.93(4)
Ru	2*d*	½	0	0	1.000	0.41	1.79(9)
O1	4*e*	0.2980	0.2789	0.9624	1.000	0.38	
O2	4*e*	0.2646	0.2968	0.5400	1.000	0.45	
O3	4*e*	0.9317	0.4792	0.7304	1.000	0.25	

$R_p = 2.06$ %, $R_{wp} = 3.06$ %, $R_{exp} = 0.87$ %, $R_{F^2} = 3.75$ %

Table 4.4 The lattice parameters and magnetic moments of Sr_2HoRuO_6 at 2 K, refined using the D1B data. The atomic coordinates were fixed from the HRPD refinements.

Assignment of the magnetic moments in the *z*-direction is obvious, as the 7.9 μ_B is for the Ho^{3+} ion and the 1.8 μ_B is for Ru^{5+} ion. However, the small component in the *ab* plane is less obvious to assign, as it is only ~ 1.0 μ_B. The refinements with this magnetic component on either ion proceed equally well, and determine the same size of moment in the *ab* plane. None the less, this problem was resolved reasonably from consideration of the temperature dependence of the peaks, as detailed below.

Each powder diffraction pattern shown in Figure 4.8 was used to refine the lattice parameters (discussed earlier in Section 4.2.1) and the magnetic moment of the Ru^{5+} and Ho^{3+} ions. The results of the refinements are detailed in Appendix B.3.2 and typical *R*-factors are $R_p \sim 2.2$ %, $R_{wp} \sim 3.1$ % and $R_{exp} \sim 1.8$ %. The results of the refinements for the magnitude of the magnetic moment in the *z*-direction are shown in Figure 4.13. The Ru^{5+} ordered magnetic moment is approximately constant until 20 K, then decreases and rapidly so above 30 K, until $T_N \sim 34$ K. This behaviour of the Ru^{5+} magnetic moment in Sr_2HoRuO_6 is startlingly similar to the previous findings on $A_2YRu_{1-x}Cu_xO_6$, where *A* = Sr or Ba, despite the presence of the very large ordered

Ho^{3+} moment. Although the Ho^{3+} ions herein also begin to order at 34 K, the rate of ordering of the Ho sublattice is more gradual and constant, but does appear to saturate finally below 5 K.

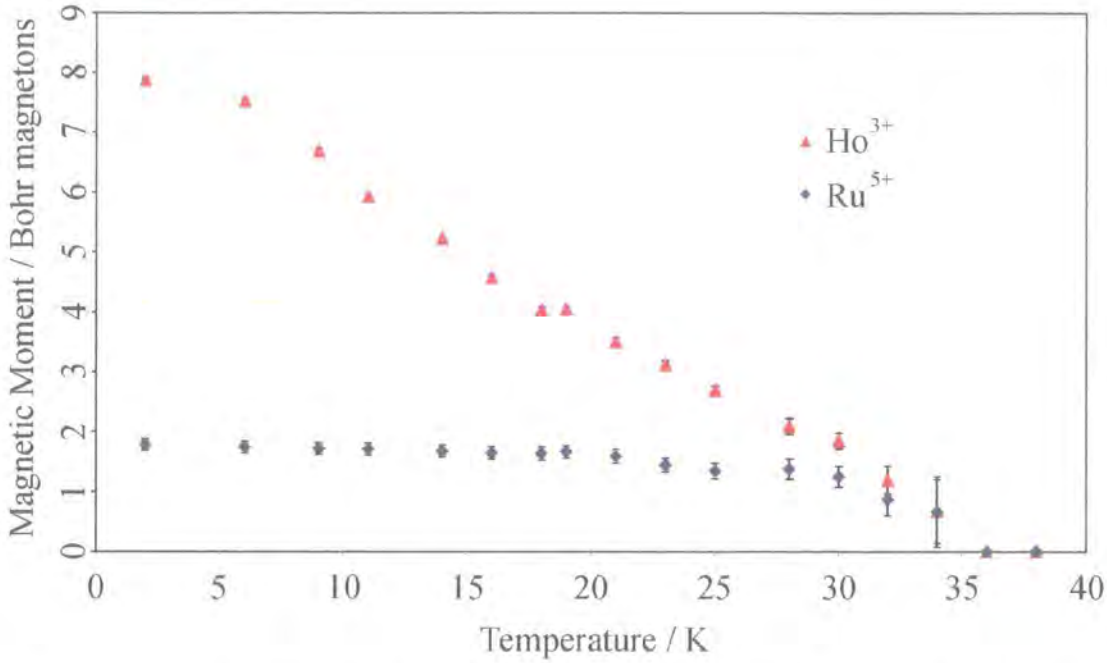

Figure 4.13 Magnitude of the magnetic moment of Ru^{5+} and Ho^{3+} in the *z*-direction. For Sr_2HoRuO_6, the two sublattices are anti-parallel to each other.

The refinement of the moment in the *ab* plane (Figure 4.14) shows that it is no longer measurable above 9 K, as the sensitivity of D1B is ~ 0.8 μ_B. Although the loss of this peak could indicate a spin reorientation with the magnetic moments above 9 K being aligned purely along the *z*-direction, it is also possible that there is still a small magnetic moment present in the *ab* direction, though this is now too small to be measured. If the magnetic moment in the *ab* plane has a similar temperature dependence as the *z*-direction, it is likely that the *ab* moment is predominantly due to the Ho^{3+} ion, and so this is the reason it was assigned this way in Table 4.4. The *ab* component required on the Ru^{5+} ion, to maintain collinearity is sufficiently small to be neglected. As the magnetic moment in the *ab* plane is small compared to the moments in the *z*-direction, Figure 4.13 effectively shows the total magnetic moments in Sr_2HoRuO_6.

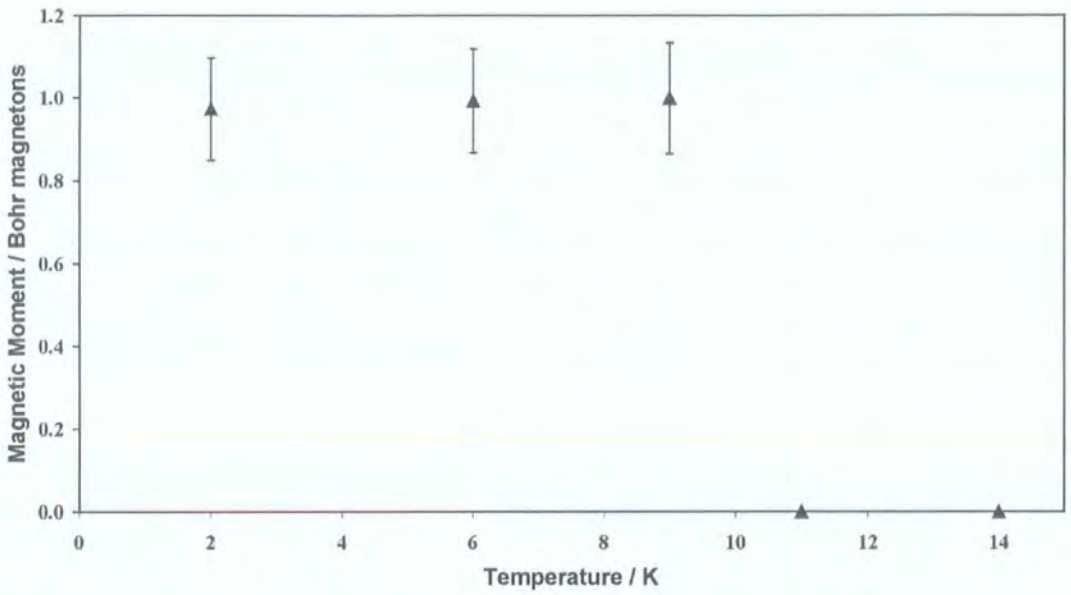

Figure 4.14 The refined magnetic moment in the *ab* plane for Sr_2HoRuO_6.

The magnetic structure of Sr_2HoRuO_6 is given in Figure 4.15 and the effect of the small *ab* component is to incline the magnetic moments at 8 ± 1° from the *c*-axis. The Ho^{3+} and Ru^{5+} ions each form Type I antiferromagnetic structures, which interpenetrate one another.

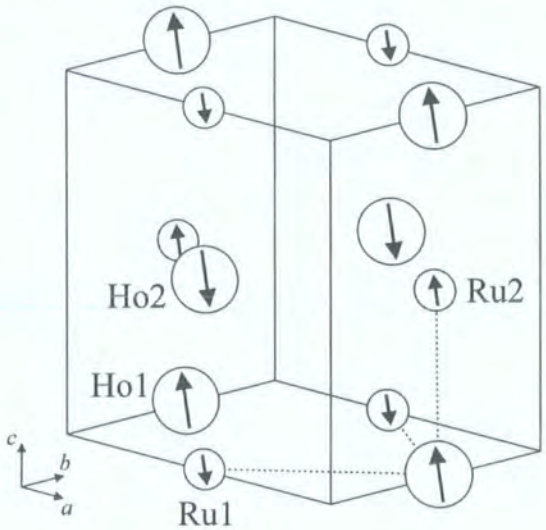

Figure 4.15 The magnetic structure of Sr_2HoRuO_6 with the Ho^{3+} moments denoted by the large arrows, and the Ru^{5+} indicated by the smaller arrows, as the magnetic moment of Ho^{3+} is the larger. The direction of the arrow indicates the direction of the moment. The small *ab* component of the magnetic moment inclines the moments at 8° from the *c*-axis, however this can only be measured below 9 K explicitly.

There has been another published study of Sr_2HoRuO_6 [4], where neutron powder diffraction experiments at 10 K, 25 K, and room temperature were undertaken. Although the results are broadly similar, the measurements reported in this thesis go much further. The crystal structures compare favourably, while the magnetic structures are also the same. However, as the lowest temperature measured was 10 K with a lower flux instrument (although higher-resolution), the (001) peak was not observed. Thus, they omit the component of the moment in the *ab* plane, and the refinements of the *z*-component of the magnetic moment are compared in Table 4.5

Temperature / K	Magnetic Moment in *z*-direction / μ_B	
	These Refinements	Doi and Hinatsu
10	6.68(5) & 1.72(10)	6.66(8) & 2.74(9)
25	2.69(9) & 1.35(13)	3.02(7) & 2.19(10)

Table 4.5 Comparison of the magnetic moments in Sr_2HoRuO_6 as refined in this study, and that of Doi *et al.* [4]. The Ho^{3+} magnetic moment and then the Ru^{5+} magnetic moment are listed.

Considering the rate at which the Ho^{3+} magnetic moment decreases as the temperature is raised, these values are in reasonable agreement. However, the Ru^{5+} moments are consistently over-estimated in the study [4], and this can be attributed to the use of the Zr^+ magnetic form factor, rather than the calculated Ru^{5+} magnetic form factor used here. The use of the Zr^+ magnetic form factor increased the refined magnetic moment of Ru^{5+} by ~ 0.25 μ_B in $Sr_2YRu_{1-x}Cu_xO_6$, where the magnetic intensity was dominated by the (001) peak at the $(\sin\theta)/\lambda \sim 0.06$ Å^{-1}. For Sr_2HoRuO_6, there is much more magnetic intensity at high angles compared with $Sr_2YRu_{1-x}Cu_xO_6$, so the effect of the magnetic form factor is more significant. Reviewing Figure 3.1, it is clear that as the Zr^+ magnetic form factor decreases much more rapidly than Ru^{5+} with increasing $(\sin\theta)/\lambda$, and so using Zr^+ will require successively larger magnetic moments to replicate the magnetic intensity when more magnetic peaks appear at high angles. Hence, the discrepancy between the two values is expected to be larger in Sr_2HoRuO_6, and by only considering the (100) and (010) peaks at $(\sin\theta)/\lambda \sim 0.087$ Å^{-1}, this is ~ 0.50 μ_B for the 10 K refinements, which will increase further as magnetic peaks at higher angles are considered. Therefore, the large difference between the two refined

magnetic moments of Ru^{5+} in Sr_2HoRuO_6 is largely a result of the different magnetic form factors used for this ion.

The main advantage of the measurements undertaken at D1B is that they show the temperature variation of the magnetic moments very well, which provides insight into the magnetic interactions between the magnetic species in Sr_2HoRuO_6. The magnetic structure, ordering temperature, magnetic moment profile with temperature, and saturated magnetic moment size are the same for the Ru^{5+} ions in Sr_2HoRuO_6 and $Sr_2YRu_{1-x}Cu_xO_6$. This indicates that even in Sr_2HoRuO_6, the Ru-O-O-Ru antiferromagnetic interaction controls the ordering of the Ru^{5+} sublattice, and it is the same strength in both the Y and Ho materials.

If the Ho-O-O-Ho interaction were stronger than the Ru-O-O-Ru interaction, the magnetic ordering temperature of the Ho^{3+} ions would be higher than the 34 K observed for the Ru^{5+} sublattice. Therefore the Ho-O-O-Ho interaction is weaker, and as Ho_2O_3 is paramagnetic [5], this suggests that the Ho-O-O-Ho interaction can be ignored altogether. This means that for the Ho sublattice to order, there must be an intra-species interaction between the Ru^{5+} and Ho^{3+} ions. This Ru-O-Ho interaction will only result in ordering of the Ho sublattice, once the Ru sublattice is itself ordered. This explains why the ordering temperature of both the Ru^{5+} and Ho^{3+} ions is coincident at 34 K, as first shown by these new measurements.

The Ru^{5+} ions have two interactions, which are mutually supportive, that try to impose magnetic ordering of the ruthenium sublattice. The Ho^{3+} magnetic sublattice is only supported by one interaction (Ru-O-Ho), which also supports the Ru sublattice. This asymmetry in the beneficiaries of the interactions means that the Ho^{3+} ions cannot order at a higher temperature than the Ru sublattice, irrespective of the order of strengths of the Ru-O-O-Ru and Ru-O-Ho interactions.

However, even the relative strengths of the Ru-O-O-Ru and Ru-O-Ho interactions can be determined from close consideration of Figure 4.13, which shows the development of the Ru^{5+} and Ho^{3+} magnetic moments with temperature. The Ru^{5+} magnetic moment saturates only a few Kelvin below the ordering temperature, whereas the Ho^{3+} ions only gradually order as the temperature is lowered. This indicates that the Ru-O-Ho interaction is much weaker than the Ru-O-O-Ru interaction, especially as the Ho^{3+} magnetic moment only appears to be saturated below 5 K.

So, the magnetic structure of Sr_2HoRuO_6 and its dependence with temperature can be completely explained with the two interactions, Ru-O-O-Ru and Ru-O-Ho. Above

34 K the magnetic moments of both species are disordered. As the temperature is lowered, the Ru^{5+} ions begin to order at 34 K. Comparison of the $Sr_2YRu_{1-x}Cu_xO_6$ and $Ba_2YRu_{1-x}Cu_xO_6$ systems, where essentially the Ru-O-O-Ru is the only interaction, indicated that the ordering temperature of the Ru sublattice was influenced by tilting of the oxygen octahedra. As the Ho system has approximately the same degree of distortion as the Y system in terms of Ru-O-*B'* bond angle, as shown in Table 4.2, which is due to the similar size of these ions, it will have a similar ordering temperature. As the Ru-O-Ho interaction is much weaker than the Ru-O-O-Ru interaction, the Ru sublattice will receive little support from the Ru-O-Ho-O-Ru interaction, and so the ordering temperature will not be raised (from 34 K) by this effect, in the case of Sr_2HoRuO_6. As the Ru sublattice begins to order, the Ru-O-Ho interaction begins to order the Ho sublattice. This ordering of the Ho sublattice is limited by the ordering level of the Ru sublattice, due to the asymmetry of the interactions, but for Sr_2HoRuO_6, this gradual ordering is mainly due to the weakness of the Ru-O-Ho interaction. As the temperature is lowered below 20 K, the Ru sublattice is fully ordered and the Ru-O-Ho interaction is now the controlling factor determining the ordering of the Ho sublattice. As the competing thermal motion decreases, the Ru-O-Ho interaction progressively orders the Ho sublattice, until below 5 K, when it too becomes fully ordered. In this case, where the Ru-O-O-Ru interaction is much stronger (so the Ru sublattice is fully ordered) than the Ru-O-Ho interaction, the ratio of the interactions strengths is given by the ratio of the temperatures at which the sublattices fully order. For Sr_2HoRuO_6, with saturation temperatures of ~ 20 K and ~ 4 K, the Ru-O-O-Ru interaction is approximately 5 times stronger than the Ru-O-Ho interaction.

The magnetic structures of the other members in the $Sr_2HoRu_{1-x}Cu_xO_6$ series were refined similarly using D1B data. The full details of the refinement results can be found in Appendix B.3.2 and the moment in the *ab* plane is shown in Figure 4.16. As this magnetic feature was on the limits of the sensitivity of D1B, the potential increase of magnetic moment size and highest observed temperature with copper doping, could not be confirmed, as they are within the bounds of error for constant values across the series ($x = 0$ to 0.15).

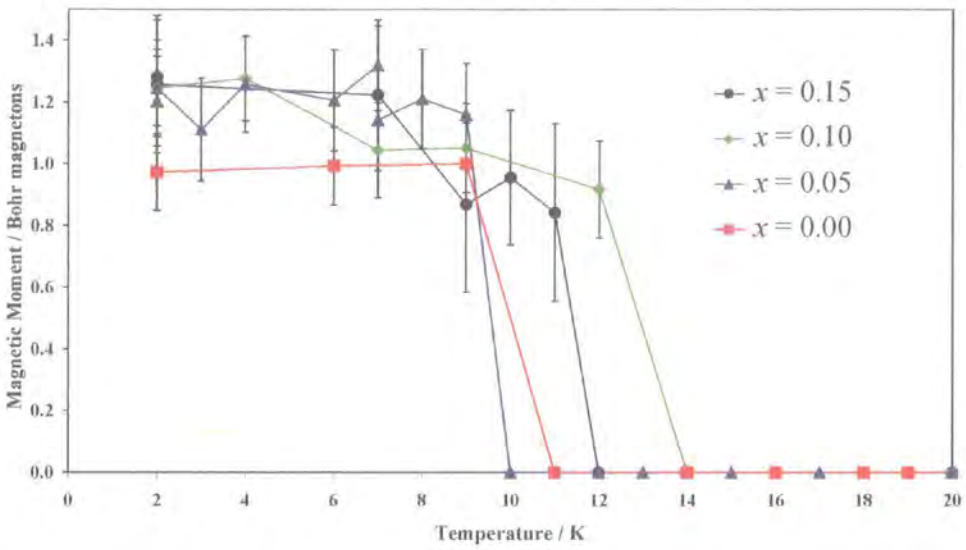

Figure 4.16 The magnetic moment in the *ab* plane for the $Sr_2HoRu_{1-x}Cu_xO_6$ series as determined from Rietveld analysis of D1B data.

The magnetic moment in the *z*-direction was more informative and these refinement results are shown in Figure 4.17 and Figure 4.18. The refinement results for the four members of the series are all broadly similar, for both the Ho^{3+} and Ru^{5+} moment. The magnetic moment of Ho^{3+} for $Sr_2HoRu_{0.95}Cu_{0.05}O_6$ appears to be parallel to the other results, but displaced by 5 K. Owing to sample availability, this sample was measured on a different visit to D1B and it is probable that this is a discrepancy in the recorded sample temperatures, rather than a physical phenomenon of the material itself.

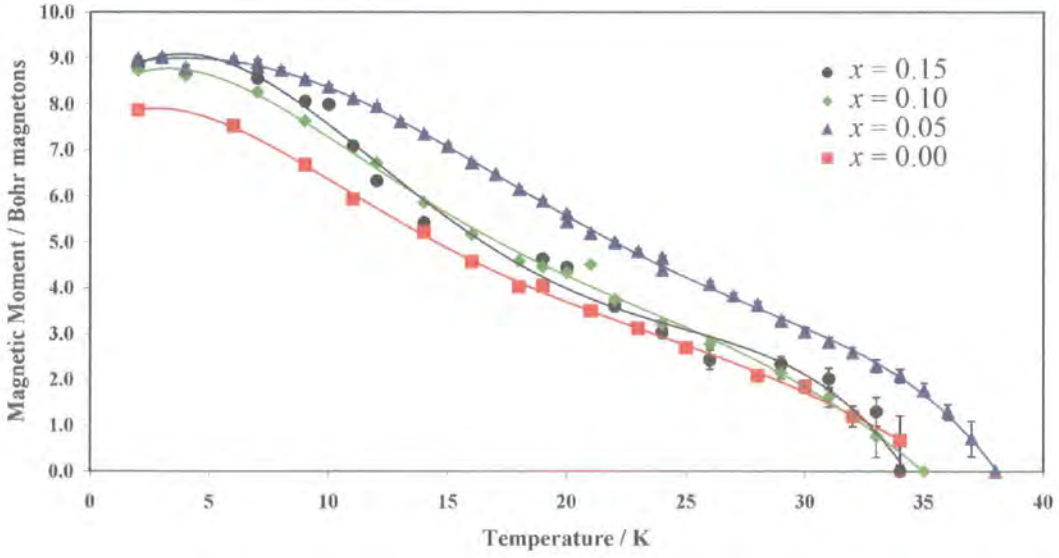

Figure 4.17 The refined magnetic moment of Ho^{3+} in the *z*-direction for the $Sr_2HoRu_{1-x}Cu_xO_6$ series.

The z-component of the magnetic moment on the Ru^{5+} ions is shown in Figure 4.18 and the clear increase in can be seen with increased copper doping. The ordering temperature remains the same however, 34 ± 1 K, as expected, since the octahedral tilting distortions are approximately the same in all the materials, and the crystal structure did not change appreciably with copper doping. This trend with copper doping in the Ho moment is similar, though less clear, but the ordering temperature is the same as the Ru sublattice. The expansion of the unit cell volume below ~ 20 K that was observed in all the materials, is possibly related to the increasingly large magnetic moment of Ho^{3+} ion as the samples were cooled, once the Ru sublattice was fully ordered.

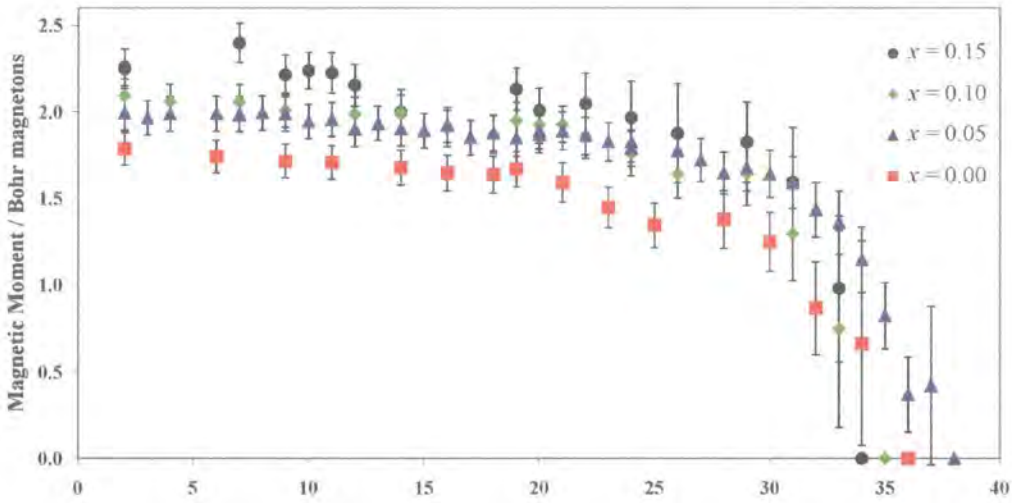

Figure 4.18 The refined magnetic moment in the z-direction for Ru^{5+} in the $Sr_2HoRu_{1-x}Cu_xO_6$ series.

The direction of the moment in the *ab* plane could not be determined from the D1B measurements as the (100) and (010) reflections could not be resolved. However a further study at OSIRIS was undertaken, and it was hoped that the combination of high-flux and resolution at this large d-spacing would allow solution of this problem. The diffraction pattern of $Sr_2HoRu_{0.95}Cu_{0.05}O_6$ at 2 K was measured from 1 to 9 Å over 8 hours, with 5 hours of this time spent measuring the d-spacing slice from 5.1-6.8 Å, in order to get the best possible counting statistics for the (100) and (010) reflections. The raw data are shown in Figure 4.19 and the (100) and (010) are clearly resolved in the inset, as we reported [6]. The data has not been used to refine a model

structure, as HRPD is better for crystal structures and the same problems faced the magnetic refinement that were detailed for $Sr_2YRu_{1-x}Cu_xO_6$ in Chapter 3.

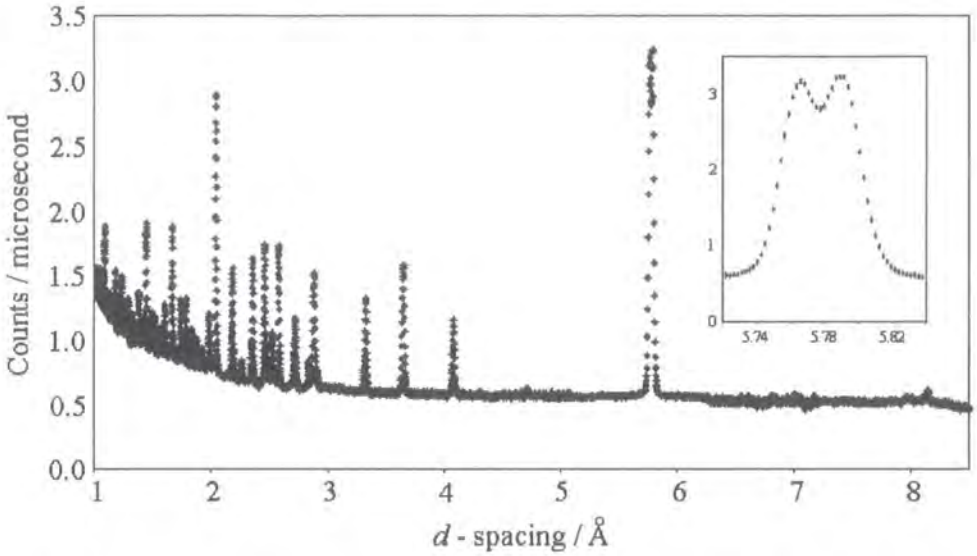

Figure 4.19 The raw data measured at OSIRIS on $Sr_2HoRu_{0.95}Cu_{0.05}O_6$ at 2 K. The inset shows that the (100) and (010) magnetic reflections can be resolved.

The counting errors are smaller than the data points and the two peaks are of virtually identical size. However, even with resolution of the (100) and (010) reflections, the moment direction cannot be determined. This is because the sum of the moments in the *c*-direction is ~ 10 μ_B, whereas the *ab* component is ~ 1 μ_B. A magnetic reflection indicates that a magnetic moment is perpendicular to the scattering vector. So the difference in intensities of the (100) and (010) would be only 1 % if the moment in the *ab* plane was directed along either of the two axis, *a* or *b*. Therefore as a consequence of the large magnetic moment in the *c*-direction, irrespective of whether the (100) and (010) reflections can be spatially resolved, the moment direction in the *ab* plane can not be determined with certainty, even by measuring with a high-flux diffractometer for a long time. Thus, there is no disadvantage from the inability of D1B to resolve the two magnetic reflections, (100) and (010), when the magnetic moments are large in these systems.

4.3 Neutron Diffraction Experiments on $Sr_2TbRu_{1-x}Cu_xO_6$

Neutron diffraction experiments were performed on both Sr_2TbRuO_6 and $Sr_2TbRu_{0.90}Cu_{0.10}O_6$ to determine the magnetic structure with temperature. Using the diffractometer D1B, the temperature dependence between 2 K and 50 K of the Ru^{5+} and Tb^{3+} magnetic ions was examined. This allowed the different magnetic interactions present in this material to be studied, compared and contrasted with $Sr_2HoRu_{1-x}Cu_xO_6$, and lead to a better understanding of the interactions of the Ru^{5+} ion.

4.3.1 Crystal Structure of $Sr_2TbRu_{1-x}Cu_xO_6$

The crystal structures of $Sr_2TbRu_{1-x}Cu_xO_6$, where x = 0 and 0.10 were determined from synchrotron measurements, both at the ESRF and the SRS, and are detailed in Chapter 6. From the low temperature neutron studies on Sr_2HoRuO_6 [4] and Sr_2TbRuO_6 [7], it is known that the two crystal structures are very similar. Owing to the lack of low temperature and high-resolution neutron diffraction studies on $Sr_2TbRu_{1-x}Cu_xO_6$ here, the corresponding $Sr_2HoRu_{1-x}Cu_xO_6$ crystal structures as refined from HRPD data were used as a basis. These structures were closer to the crystal structure reported in Sr_2TbRuO_6 [7] than the results from the synchrotron data, and it was felt that the crystal structure refined from corresponding low temperature neutron diffraction (HPRD) would be a better basis than that of the high temperature X-ray synchrotron data. In any case, the refinements of the lattice parameter and magnetic moment using the D1B data were not markedly different whichever of these crystal structures was chosen. Full details of the crystal structure used are given in Appendix B.3.1.

The diffraction pattern of Sr_2TbRuO_6 at 50 K measured at D1B is shown in Figure 4.20, where it can be seen that the chosen crystal model does lead to a reasonable calculated diffraction profile. As with all measurements on D1B there was the instrumental feature at 72°, probably due to the cryostat. There were no other unindexed peaks visible in the diffraction pattern, indicating that there was no observable impurity content in the Tb material.

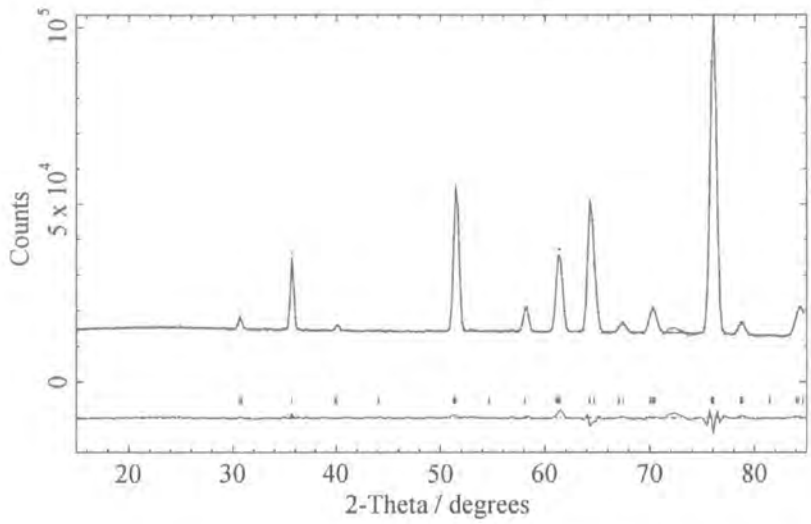

Figure 4.20 The powder neutron diffraction pattern of Sr_2TbRuO_6 measured at 50 K using D1B. The data points are shown as crosses and the calculated profile and difference curve are shown as lines. The tick marks indicate the allowed crystal structure reflections.

Diffraction patterns were also measured at D1B on both compounds, Sr_2TbRuO_6 and $Sr_2TbRu_{0.90}Cu_{0.10}O_6$ from 2 K to 50 K, and the refinement details are given in Appendix B.4.1. The unit cell volume with temperature is shown in Figure 4.21 and shows that this decreases as the copper concentration has increased. The absence of impurities suggests that vacancies are less likely to be the cause, and X-ray synchrotron measurements presented in Chapter 6 also cast doubt on this. A possibility is that the copper doping is successfully doping holes into the structure and this is causing the reduction in unit cell volume. However, for a given doping level, the unit cell volume remains reasonably constant over the temperature range measured.

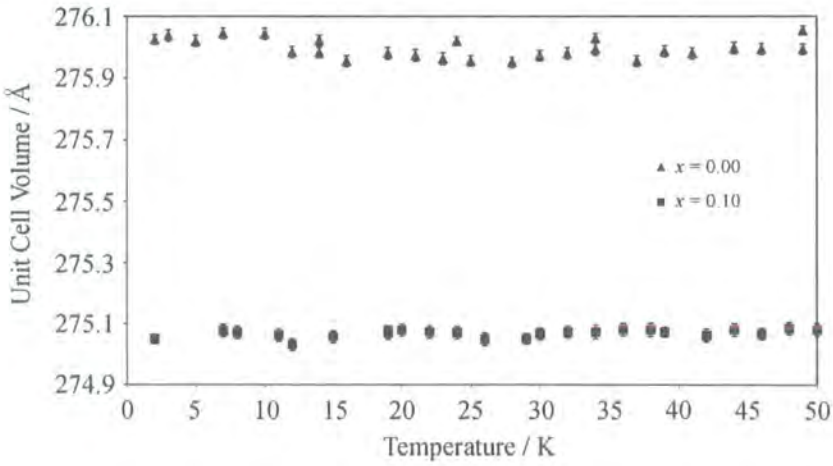

Figure 4.21 Unit cell volume with temperature for $Sr_2TbRu_{1-x}Cu_xO_6$, for x = 0 and 0.10, as refined using D1B data.

4.3.2 Magnetic Structure of $Sr_2TbRu_{1-x}Cu_xO_6$

The magnetic structure of the title series was determined by refinement using data obtained on D1B at the ILL. The variable temperature neutron powder diffraction patterns collected between 2 K and 50 K at D1B on the sample of Sr_2TbRuO_6 are shown in Figure 4.22. Again, extra peaks appear in the diffraction pattern at temperatures below 39 K, indicative of long-range magnetic ordering. The diffraction patterns look similar to those of the $Sr_2HoRu_{1-x}Cu_xO_6$, except the magnetic peaks are not quite so large, indicating a smaller Tb^{3+} moment, and their profile with temperature is different, suggesting different interaction strengths. The crystal structure peaks do not change noticeably, so there are no structural phase transitions and hence, there can be confidence in the crystal structure used at all temperatures.

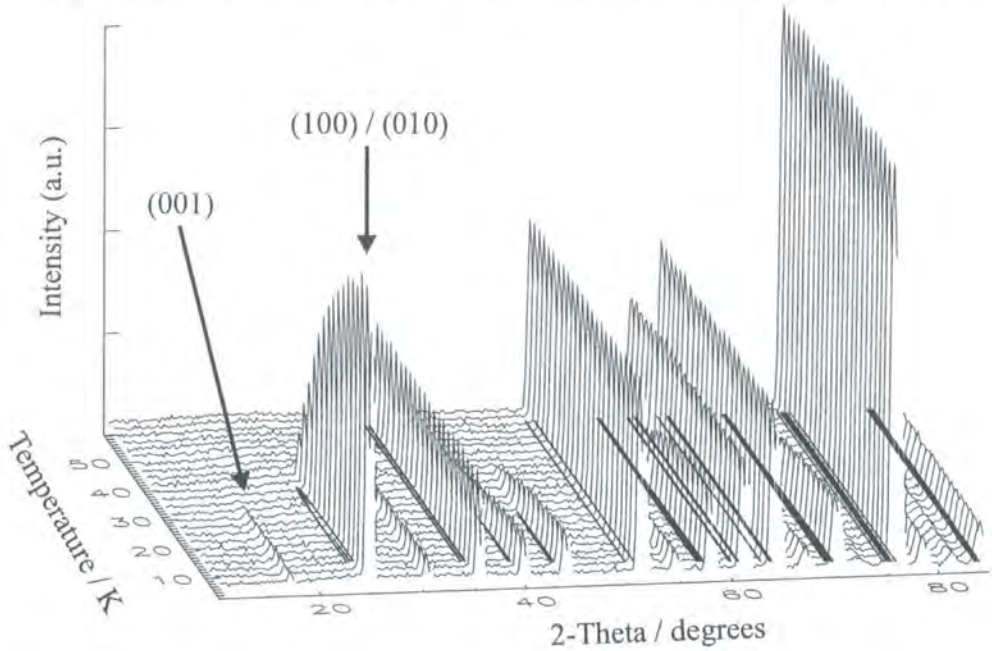

Figure 4.22 The variable temperature neutron powder diffraction patterns measured on Sr_2TbRuO_6 between 2 - 50 K, and 15 ° to 85 ° in 2θ.

The diffraction pattern of Sr_2TbRuO_6 measured at 2 K is shown in Figure 4.23, which explicitly indexes the magnetic peaks using a magnetic unit cell ($\sim \sqrt{2}a_p \times \sqrt{2}a_p \times 2a_p$) that is the same size as the crystal unit cell. As the magnetic peaks can be indexed by reflections where $h + k + l$ is odd, then both the Ru^{5+} and Tb^{3+} ions form antiferromagnetic structures, much like the case of $Sr_2HoRu_{1-x}Cu_xO_6$. With the double perovskite structure, both the Ru^{5+} and Tb^{3+} ion each adopt a Type I magnetic structure. As the set of magnetic peaks with $(h + k)$ being odd, and l being even, are

larger than the remaining magnetic peaks, the two magnetic sublattices couple ferrimagnetically to each other.

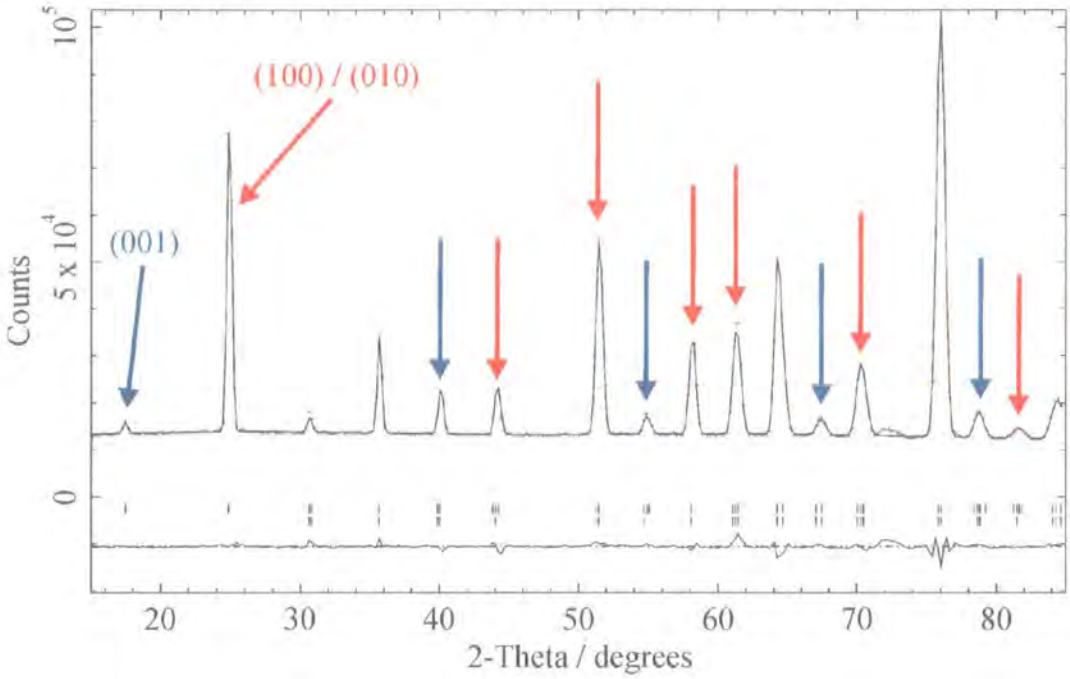

Figure 4.23 The 2 K neutron powder diffraction pattern of Sr_2TbRuO_6. The lower series of tick marks indicate crystal reflections, while the upper series of tick marks denote all possible magnetic reflections. The arrows highlight the antiferromagnetic peaks, which index with $h + k + l$ as odd. Additionally, of these reflections, those with l even are indicated with red arrows, and those with l odd with blue arrows. Explicitly indexed are the (001) and the unresolved combination of the (100) and (010), which aid greatly in determining a starting model for refinement.

The magnetic moment directions were determined from observation of the intensities of the principal magnetic peaks, indexed in Figure 4.23. The small (001) peak indicates a small *ab* component of the magnetic moment. As the unresolved combination of the (100) and (010) are large, while the (001) is not, suggests that the majority of the magnetic moment lies in the *c*-direction. Owing to the smaller size of the magnetic peaks compared to Sr_2HoRuO_6, particularly those involving the sum of the magnetic moments of the two species, the Tb^{3+} moment is expected to be smaller than Ho^{3+}, and this information was used to form a starting model ready for refinement. The calculated profile is shown also in Figure 4.23, and from its proximity to the observed data the model structure listed in Table 4.6 gives a good degree of confidence.

Sr_2TbRuO_6		$P2_1/n$			2 K		
a / Å		b / Å	c / Å	β / °	Volume / Å^3		
5.78874(8)		5.81485(9)	8.20043(24)	90.403(1)	276.025(16)		
Atom	Site	x	y	z	Occ	B_{iso}/Å^2	μ/μ_B
Sr	4*e*	0.0044	0.0311	0.7537	1.000	0.29	
Tb	2*c*	0	½	0	1.000	0.20	4.68(4)
Ru	2*d*	½	0	0	1.000	0.41	1.91(10)
O1	4*e*	0.2980	0.2789	0.9624	1.000	0.38	
O2	4*e*	0.2646	0.2968	0.5400	1.000	0.45	
O3	4*e*	0.9317	0.4792	0.7304	1.000	0.25	

$R_p = 1.86$ %, $R_{wp} = 2.63$ %, $R_{exp} = 0.76$ %, $R_{F^2} = 4.28$ %

Table 4.6 The crystal and magnetic structure of Sr_2TbRuO_6. The fractional coordinates were taken from the refinement of HRPD data of Sr_2HoRuO_6, but the lattice parameters and magnetic moment were refined using the D1B data.

All the neutron diffraction patterns shown in Figure 4.23 were used for refinements of the magnetic structure, so the magnetic moment in the *z*-direction was determined as Figure 4.24 shows. The ordering temperature of both the ruthenium and terbium sublattice is 39 K, but the Ru^{5+} ions saturate at ~ 25 K, whereas the Tb^{3+} at ~ 14 K. The profiles of the two magnetic moments are also similar to each other, with the Ru^{5+} sublattice only increasing its ordering at a slightly quicker rate than the Tb^{3+} sublattice.

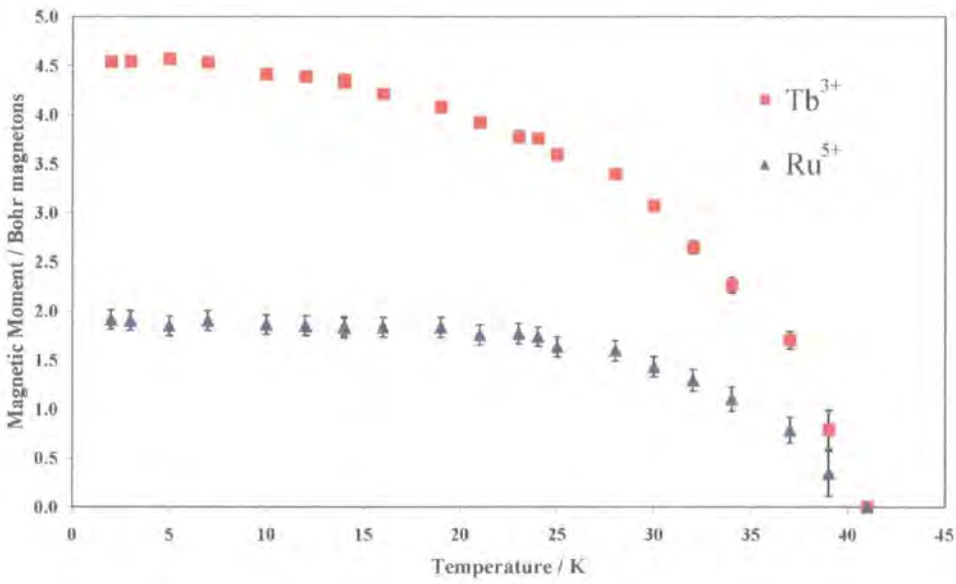

Figure 4.24 The magnetic moment in the *z*-direction for Sr_2TbRuO_6 for the Tb^{3+} and Ru^{5+} ions.

As the (001) peak is observed up to higher temperatures than in Sr_2HoRuO_6, the refined magnetic moment in the *ab* plane is ~ 1 μ_B and persists until 25 K, before disappearing below the background level, as displayed in Figure 4.23. Owing to its temperature dependence, this *ab* component of the magnetic moment is most likely to originate from the Tb^{3+} ion, though a contribution from the Ru^{5+} certainly cannot be ruled out. For simplicity, the *ab* component was attributed solely to the Tb^{3+} ion, and the amount which is needed to maintain collinearity of the magnetic moments on the Ru^{5+} is small enough to be ignored.

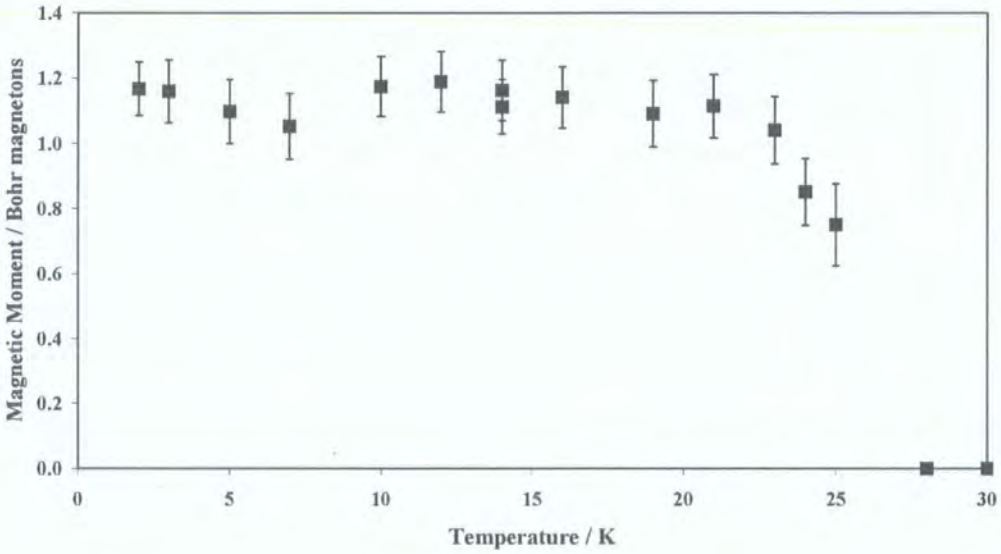

Figure 4.25 The magnetic moment in the *ab* plane of Sr_2TbRuO_6 as determined from refinements using D1B data.

As the *z*-component of the magnetic moment of Tb^{3+} is smaller than the Ho^{3+}, the angle of inclination away from the *z*-axis is 14 ± 1°, rather than 8 ± 1°, the *ab* components being of similar size. Therefore, the magnetic structure of Sr_2TbRuO_6 is as shown in Figure 4.26, with the two interpenetrating Type I antiferromagnetic arrangements coupled ferrimagnetically to each other.

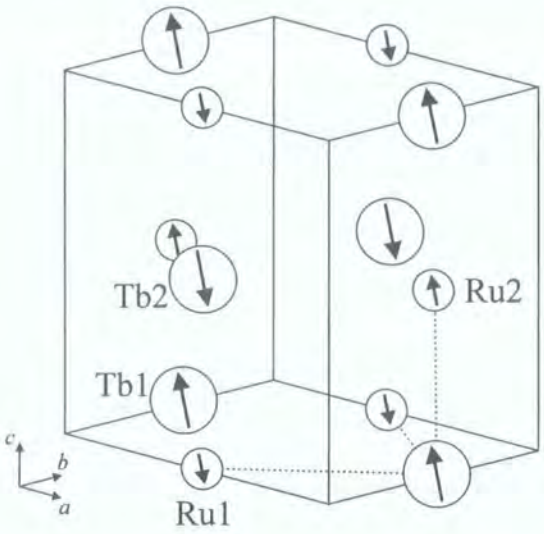

Figure 4.26 The magnetic structure of Sr_2TbRuO_6 where the Ru^{5+} and Tb^{3+} ions each adopt a Type I arrangement, which interpenetrate as shown. The magnetic moments are inclined by 14 ± 1° from the *c*-axis and the two sublattices are coupled ferrimagnetically. The ferrimagnetic arrangement is most easily seen from the relative moment directions on the Ru^{5+} and Tb^{3+} magnetic ions in the *ab* plane. The arrows, representing the moments, are shown larger for Tb^{3+} ions, as this magnetic moment is the largest of the two.

The magnetic structure of Sr_2TbRuO_6 reported by Doi *et al.* [7] also consisted of an interpenetrating Type I arrangement, in agreement with the findings here. As the (001) peak persists to higher temperatures in Sr_2TbRuO_6 compared with Sr_2HoRuO_6, their study did note this peak at 10 K, the temperature which shall be used for comparison between the two studies. The magnetic moments were also directed close to the *c*-axis, with the angle of inclination ~ 20° which is same order as the 14° observed in this study, the difference is probably due to discrepancies between the measured moments. Whereas the Tb^{3+} moments are 4.98(12) μ_B and 4.56(4) μ_B in their study and ours respectively, the Ru^{5+} moments are at even greater variance, with 2.99(11) μ_B and 1.86(10) μ_B as the refined values. The magnetic moment of Tb^{3+} is saturated at 10 K, so the slight difference cannot be due to temperature discrepancies, but probably owes more to the combination of the two magnetic moments, Ru^{5+} and Tb^{3+}, being calculated differently. The greater disparity of Ru^{5+} cannot be explained solely by their use of the Zr^+ magnetic form factor, as changing to the Ru^{5+} magnetic form factor only reduces the calculated moment from 2.99 μ_B to 2.45 μ_B. Attributing the *ab* component entirely to the Ru^{5+} ion, the moment increases from 1.86 μ_B to 2.20 μ_B, though then the gap between the Tb^{3+} moments is widened by ~ 0.1 μ_B. The reported value of the 2.99 μ_B in the other study [7] is the highest reported magnetic

moment of the Ru^{5+} ion in any ruthenate double perovskite known [4, 7-26]. Although ~ 0.55 μ_B of this overestimation is due to the use of the Zr^+ magnetic form factor, the rest has not been explained by any mechanism, while the 1.86 μ_B reported here is far more in keeping with the literature, and more likely to be correct.

A small anomaly was observed in the magnetic measurements [7] at 31 K and tentatively explained by a spin reorientation. However, no spin reorientation was observed from our variable temperature measurements. Additionally, the magnetic moment of Tb^{3+} is found to saturate at 14 K with ~ 4.5 μ_B. Thus, we believe that the measurement of Doi and Hinatsu at 10 K does measure the saturated moment of the Tb^{3+} ion also, and that further ordering of the moment at lower temperatures does not take place. Therefore the discrepancy between the ordered value here of ~ 4.5 μ_B and the theoretical value of 9.72 μ_B is genuine and large.

The temperature dependence of Sr_2TbRuO_6 is very revealing of the magnetic interactions present in the material, as will now be detailed. The Tb-O-O-Tb interaction is thought to be very weak, owing to the very low Néel temperature of Tb_2O_3 of 2.4 K [27, 28], and so will be neglected from further discussion. Therefore, there are only two interactions remaining of importance, the Ru-O-O-Ru and the Ru-O-Tb interaction. As a consequence of the asymmetry of the interactions, the Tb^{3+} sublattice cannot order at a higher temperature than the Ru^{5+} sublattice, irrespective of the relative interaction strengths. However, as soon as the ruthenium sublattice orders, the Ru-O-Tb interaction allows the terbium sublattice to order too, and thus the ordering temperature of the Ru^{5+} and Tb^{3+} ions is the same in Sr_2TbRuO_6.

The ordering temperature of Sr_2TbRuO_6, T_N = 39 K, is elevated only slightly from that observed for Sr_2HoRuO_6, with T_N = 34 K. From the study of $Sr_2YRu_{1x}Cu_xO_6$ and $Ba_2YRu_{1-x}Cu_xO_6$ in Chapter 3, it is known that tilting of the oxygen octahedra, which form an integral part of the interaction pathways, affects the ordering temperature. However, as the ordering temperature only rose from 33 K to 39 K as the Sr was replaced Ba, which allows a cubic structure, the difference in distortion between the Ho and Tb analogues, reflected in the Ru-O-*Ln* bond angle, is unlikely to be the cause. This suggests that the Ru-O-Tb interactions aid the magnetic ordering in Sr_2TbRuO_6 via the Ru-O-Tb-O-Ru pathway, so leading to a higher ordering temperature than if the Ru-O-O-Ru interaction acted alone. Thus, although the Ru-O-O-Ru interaction is about the same strength in Sr_2TbRuO_6 as Sr_2HoRuO_6, the ordering temperature provides the first clue that the Ru-O-Tb interaction is much

stronger than its Ho analogue. The profiles of the Ru^{5+} and Tb^{3+} magnetic moments with temperature are similar to each other, but very different to those observed in Sr_2HoRuO_6 (Figure 4.17), which also indicates that the sublattices order due to a different combination of interaction strengths.

In Sr_2TbRuO_6, the Ru sublattice begins to order at 39 K and saturates at ~ 25 K, which is higher than the values for Sr_2HoRuO_6 of 34 K and ~ 20 K, due to the support the Ru-O-O-Ru interaction receives from the Ru-O-Tb interaction, which the Ru-O-Ho interaction hardly provided. However, the most direct evidence for the much stronger Ru-O-Tb interaction is the magnetic moment of the Tb^{3+} itself. The Tb^{3+} magnetic moment saturates at ~ 14 K, which is much higher than the ~ 4 K of Sr_2HoRuO_6. Also the shape of the Tb^{3+} moment curve is similar to that of Ru^{5+}, which suggests that the ordering of the terbium sublattice by the Ru-O-Tb interaction is partially limited by the level of ordering of the ruthenium sublattice. (The Sr_2HoRuO_6 result gives the perfect example of the magnetic moment of Ho^{3+} not being hindered by the ruthenium sublattice, but by the weakness of the Ru-O-Ho interaction.) Also, the saturation temperatures for the two ions in Sr_2TbRuO_6 are closer, also indicating that this was a factor in the development of the Tb^{3+} moment.

For the same reason that the Tb^{3+} ions cannot begin order at a higher temperature than the Ru^{5+} ions, they cannot saturate at a higher temperature also, even if the Ru-O-Tb interaction is much stronger than the Ru-O-O-Ru interaction. In the limit where the Ru-O-Tb interaction is much stronger than Ru-O-O-Ru interaction, provided the same magnetic structure is adopted, the Ru^{5+} and Tb^{3+} ions would order and saturate at the same temperature. So, even in scenarios when the Ru-O-Tb interaction is stronger, the Tb sublattice can saturate at a lower temperature than the Ru sublattice. Therefore, in the case of Sr_2TbRuO_6, the ratio of the saturation temperatures will not give an accurate idea of the relative strengths of the two interactions, Ru-O-O-Ru and Ru-O-Tb.

For Sr_2HoRuO_6 and $Sr_2YRu_{1-x}Cu_xO_6$ the saturation temperature of the Ru^{5+} ions is ~ 20 K, where the Ru-O-O-Ru interaction is essentially the only one ordering the ruthenium ions. This temperature provides a better value for the basis for the ratio of interaction strengths, as the Ru-O-Tb interaction raises the saturation temperature of the ruthenium sublattice to 25 K. Taking the terbium sublattice to be saturated at ~ 14 K, this provides a ratio of strengths for the Ru-O-Tb and Ru-O-O-Ru interactions to be 0.7:1. So, in the Sr_2TbRuO_6 system the interaction strengths of the

Ru-O-Tb and Ru-O-O-Ru interactions are of about the same order of magnitude. Thus, we have witnessed, in just these two systems studied, a great variation in the strengths of the Ru-O-*Ln* interaction (where *Ln* is a rare-earth element). This large variation in magnetic interaction strengths does not necessarily manifest itself in a large variation of the Néel temperature, but in the temperature dependence of the magnetic moments of each ion. This explains why the Néel temperatures of the Sr_2LnRuO_6 (*Ln* = Eu-Lu) compounds are all similar [21], as determined from magnetic susceptibility measurements, but which were unable to determine the interaction strengths. However, the relative magnitudes of the Ru-O-*Ln* and Ru-O-O-Ru interactions can be determined successfully from variable temperature neutron powder diffraction. This result also illustrates the power of a properly conducted experiment on the high-flux diffractometer D1B. The magnitude of the Ru-O-O-Ru interaction is reasonably constant, though dependent on octahedral tilting distortions, while the Ru-O-*Ln* interaction may vary tremendously, highlighting the interesting and intriguing behaviour of the Ru^{5+} ion with its neighbours. Clearly, the interesting variation in the interaction strengths of Ru-O-*Ln* needs to be explored, so as to determine its maximum influence.

The other member of the series which was measured at D1B, $Sr_2TbRu_{0.90}Cu_{010}O_6$, was refined and the results can be compared with those for Sr_2TbRuO_6. As can be seen from Figure 4.27, the Ru^{5+} magnetic moment is relatively unchanged by the copper doping, however a reduction in the refined moment of Tb^{3+} is observed. The ordering temperature of the Ru^{5+} and Tb^{3+} magnetic moments is lowered from 39 K to 36 K, while the Tb^{3+} saturates at 8 K rather than 14 K as 10 % copper is introduced. All these observations suggest that the introduction of the copper particularly weakens the intra-species interactions between the two sublattices.

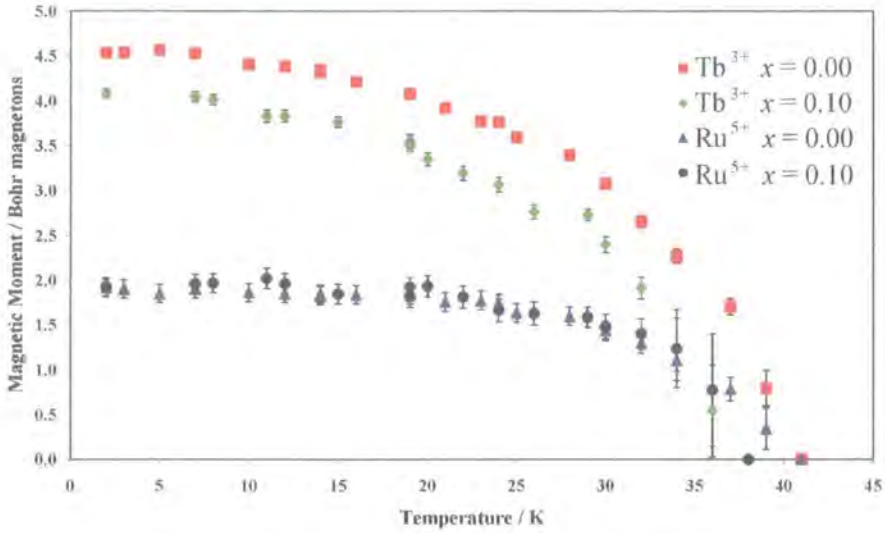

Figure 4.27 The magnetic moments of the Ru^{5+} and Tb^{3+} ions in $Sr_2TbRu_{1-x}Cu_xO_6$ in the *z*-direction as determined from Rietveld analysis using D1B data.

The magnetic moment in the *ab* direction can also be compared for the two members of the $Sr_2TbRu_{1-x}Cu_xO_6$ series, as in Figure 4.28. Again the measurement is on the limit of the sensitivity of D1B, however, the *ab* component of the moment decreases with copper doping. As a result of its smaller magnitude, it fades into the background level at a slightly lower temperature. The dependence of this magnetic moment component on both temperature and copper doping level suggests that the *ab* component is mainly due to the Tb^{3+} and it is not really a spin reorientation, it is just that the *ab* component is too small to be measured.

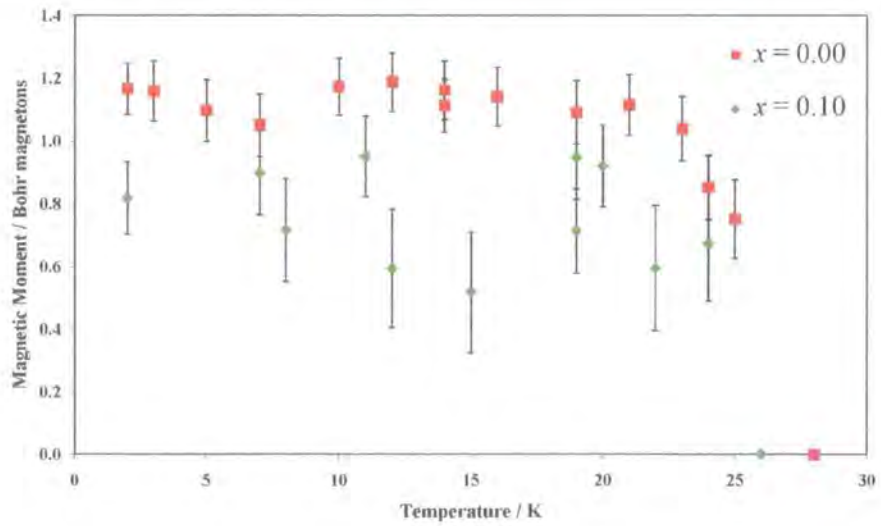

Figure 4.28 The *ab* component of the magnetic moment of $Sr_2TbRu_{1-x}Cu_xO_6$ with $x = 0$ and $x = 0.10$.

4.4 Neutron Diffraction Experiments on $Sr_2Ho_{1-y}Tb_yRu_{1-x}Cu_xO_6$

In order to investigate the nature of the ordering mechanism of the rare-earth species in the ruthenates, mixed Ho/Tb samples were prepared and examined. It is very common with mixed systems for the local cocktail of magnetic interactions to lead to the development of a spin-glass, as no long-range magnetic structure can emerge. Thus, the mixed system would provide a test for some elements of the models proposed for $Sr_2HoRu_{1-x}Cu_xO_6$ and $Sr_2TbRu_{1-x}Cu_xO_6$.

In addition to the two end members, $Sr_2HoRu_{0.90}Cu_{0.10}O_6$ and $Sr_2TbRu_{0.90}Cu_{0.10}O_6$, which were already studied, the mixed systems of $Sr_2Ho_{0.80}Tb_{0.20}Ru_{0.90}Cu_{0.10}O_6$ and $Sr_2Ho_{0.20}Tb_{0.80}Ru_{0.90}Cu_{0.10}O_6$ were measured at D1B in a similar manner.

4.4.1 Crystal Structure of $Sr_2Ho_{1-y}Tb_yRu_{1-x}Cu_xO_6$

In the absence of low temperature high-resolution neutron powder diffraction studies on the mixed samples themselves, the same procedure was adopted as for $Sr_2TbRu_{1-x}Cu_xO_6$. In the case of these mixed systems, the approximation is even more valid as the samples have holmium content. As with the previous studies, variable temperature neutron powder diffraction patterns (Figure 4.30) were measured from 2K to 50 K using diffractometer D1B.

The trend in the lattice parameters is succinctly summarised in the unit cell volume, which shows the same dependencies. The unit cell volume is constant for each member of the series with temperature, except for the small increase observed in $Sr_2HoRu_{0.90}Cu_{0.10}O_6$ below 20 K as discussed in Section 4.2.1, which is not visible here simply due to the scale. The other point of note is the relatively smooth increase in the unit cell volume as the larger Tb^{3+} ions replace the smaller Ho^{3+} ions. As the Tb^{3+} and Ho^{3+} ions have the same charge and are the largest species in $Sr_2TbRu_{0.90}Cu_{0.10}O_6$ and $Sr_2HoRu_{0.90}Cu_{0.10}O_6$, it is not surprising that that replacement of one by the other, leads directly to this change in unit cell volume.

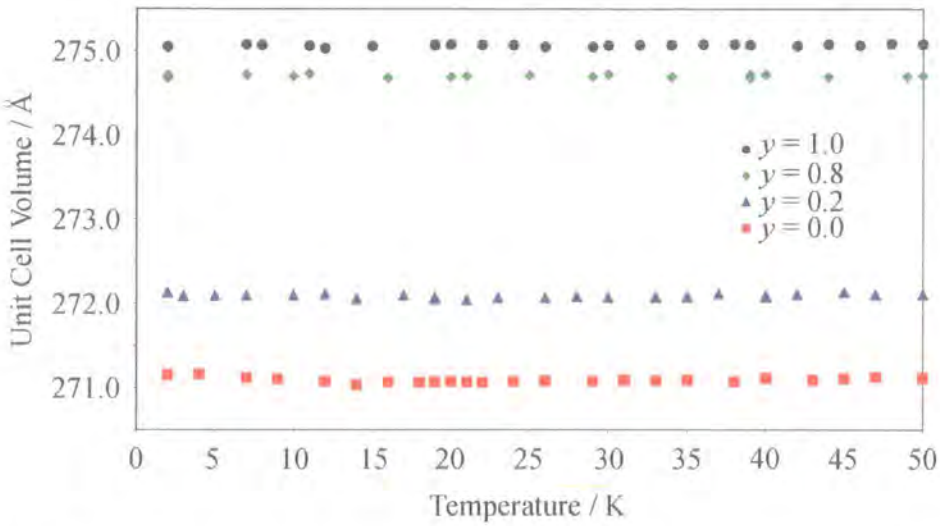

Figure 4.29 The variation in the unit cell volume with temperature for the series $Sr_2Ho_{1-y}Tb_yRu_{0.90}Cu_{0.10}O_6$, which increases as the larger Tb^{3+} ions replace the smaller Ho^{3+} ions.

4.4.2 Magnetic Structure of $Sr_2Ho_{1-y}Tb_yRu_{1-x}Cu_xO_6$

Variable temperature neutron diffraction patterns measured from 2K to 50 K are shown in Figure 4.30 for the $Sr_2Ho_{0.80}Tb_{0.20}Ru_{0.90}Cu_{0.10}O_6$ sample. Extra peaks appear in the diffraction pattern below 35 K, indicative that a long-range magnetic order of some description has formed, rather than a spin-glass. In this case the (001) reflection is absent, but the remaining magnetic peaks are present in the usual places. So preliminary analysis indicates the same magnetic structure as reported for the other compounds in this chapter, except now the moment direction is entirely in the *c*-direction.

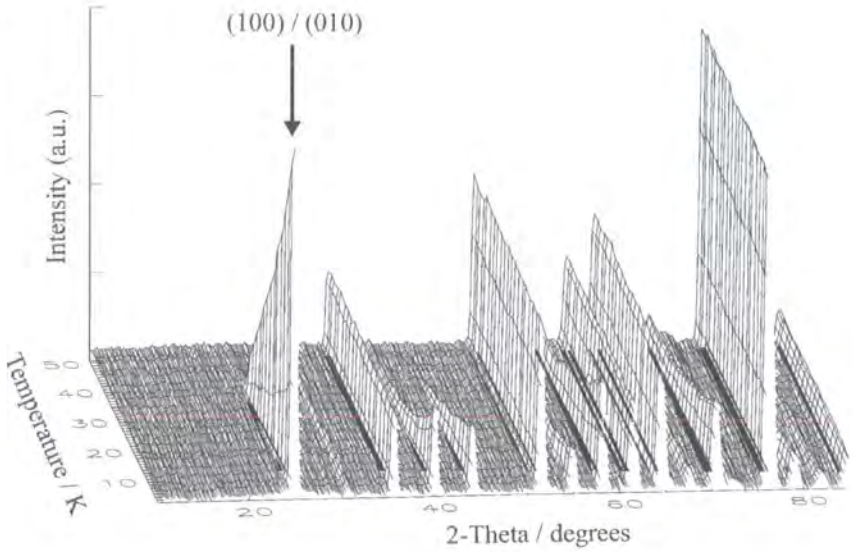

Figure 4.30 Variable temperature neutron powder diffraction patterns of $Sr_2Ho_{0.80}Tb_{0.20}Ru_{0.90}Cu_{0.10}O_6$ measured between 2 K and 50 K using D1B.

The diffraction pattern at 2 K is shown in Figure 4.31 and it can be seen that there is agreement between the observed data and calculated profile, which uses the model of Table 4.7. The magnetic structure is the same interpenetrating Type I structure as reported for the Ho and Tb series. As the Ho^{3+} and Tb^{3+} ions share the same site, there is no way to apportion the magnetic intensity between the two unambiguously, and so the average magnetic moment for the two is recorded. Approximate values can be estimated using the refined magnetic moments for $Sr_2HoRu_{0.90}Cu_{0.10}O_6$ and $Sr_2TbRu_{0.90}Cu_{0.10}O_6$, if desired.

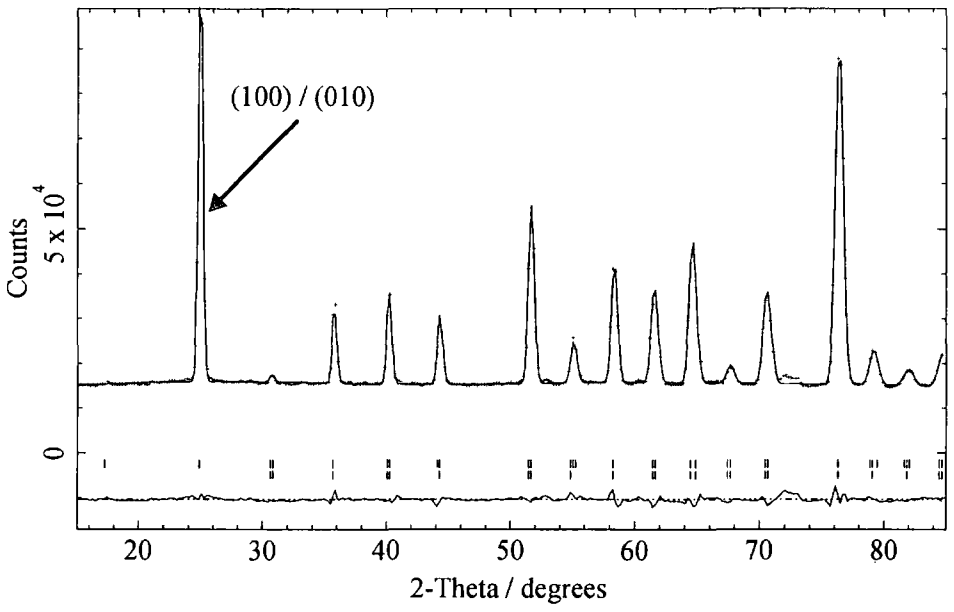

Figure 4.31 The diffraction pattern of $Sr_2Ho_{0.80}Tb_{0.20}Ru_{0.90}Cu_{0.10}O_6$ measured at 2 K with the calculated curve and difference curve also shown. The lower series of tick marks denote crystal structure reflections, while the upper set denote magnetic reflections.

$Sr_2Ho_{0.80}Tb_{0.20}Ru_{0.90}Cu_{0.10}O_6$		$P2_1/n$		2 K		
a / Å		b / Å	c / Å	β / °	Volume / Å^3	
5.75451(10)		5.78368(10)	8.16237(27)	90.256(1)	272.131(18)	
Atom	Site	x	y	z	Occ	B_{iso}/Å^2	μ/μ_B
Sr	4*e*	0.0051	0.0326	0.7510	1.000	0.29	
Ho	2*c*	0	½	0	0.800	0.20	6.73(4)
Tb	2*c*	0	½	0	0.200	0.20	6.73(4)
Ru	2*d*	½	0	0	0.900	0.41	2.03(10)
Cu	2*d*	½	0	0	0.100	0.41	
O1	4*e*	0.2989	0.2752	0.9625	1.000	0.38	
O2	4*e*	0.2666	0.2968	0.5365	1.000	0.45	
O3	4*e*	0.9258	0.4789	0.7300	1.000	0.25	

R_p = 1.86 %, R_{wp} = 2.55 %, R_{exp} = 0.71 %, R_{F^2} = 3.62 %

Table 4.7 The lattice parameters, atomic coordinates, temperature factors and magnetic moments of $Sr_2Ho_{0.80}Tb_{0.20}Ru_{0.90}Cu_{0.10}O_6$. Only the lattice parameters and magnetic moments were refined from the D1B data. The magnetic moments are entirely in the *z*-direction.

The refinement of the $Sr_2Ho_{0.80}Tb_{0.20}Ru_{0.90}Cu_{0.10}O_6$ structures proceeded equally well, and details of all these results for the mixed series samples can be found in Appendix B.5. Comparison of the *z*-component of the magnetic moment of all the holmium and terbium members of the 10 % copper doped samples is shown in Figure 4.32. There is very little difference between any of the curves for the Ru^{5+} magnetic moment, while the rare-earth moment increases and resembles the $Sr_2HoRu_{0.90}Cu_{0.10}O_6$ results more with increasing Ho^{3+} content. Thus, the magnetic properties of the $Sr_2Ho_{1-y}Tb_yRu_{0.90}Cu_{0.10}O_6$ appear to simply be a mix of the two end members, $Sr_2HoRu_{0.90}Cu_{0.10}O_6$ and $Sr_2TbRu_{0.90}Cu_{0.10}O_6$.

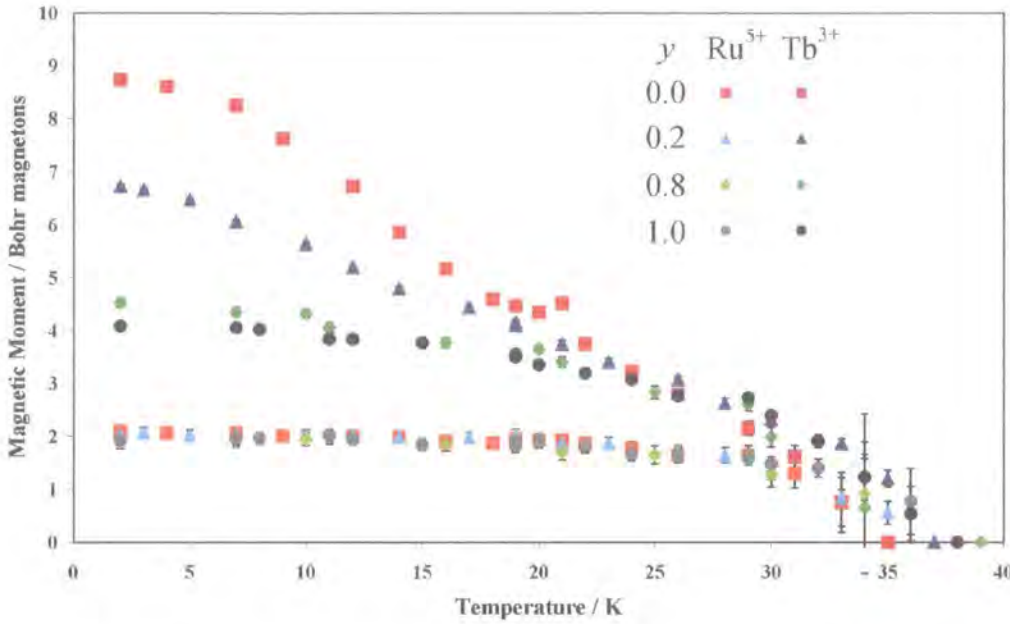

Figure 4.32 The refined magnetic moment in the *z*-direction of the $Sr_2Ho_{1-y}Tb_yRu_{0.90}Cu_{0.10}O_6$ series, where $y = 0$, 0.2, 0.8 and 1.0.

The important information derived from the *ab* component is summarised in Table 4.8. The values derived for the end members have been explained in the earlier sections, however the mixed members initially appear erratic. For $Sr_2HoRu_{0.90}Cu_{0.10}O_6$, the *ab* component was only visible at the lowest temperatures as the Ho^{3+} magnetic moment falls off quickly with temperature. With 20 % of the Ho^{3+} replaced by Tb^{3+}, the magnetic moment per rare-earth of $Sr_2Ho_{0.80}Tb_{0.20}Ru_{0.90}Cu_{0.10}O_6$ is reduced to below the 0.8 μ_B sensitivity, and so it is not observed at any temperature, and hence its value in Table 4.8. For $Sr_2Ho_{0.20}Tb_{0.80}Ru_{0.90}Cu_{0.10}O_6$, the weakness of the Ru-O-Ho interaction compared to the Ru-O-Tb interaction results in the (001) peak not being visible at higher temperatures. Essentially, the tabulated results can be explained as consequence of measuring on the limits of the sensitivity of D1B. However, a truly physical reason cannot be discounted, as the differing interactions between Ru and Ho/Tb could be directly responsible for real changes in temperature and angle that are unknown, due to the uncertainty of the moment direction in the *ab* plane and the insensitivity of the measurement below ~ 0.8 μ_B.

Sample	Highest Temperature Observed / K	Angle of Inclination / °
$Sr_2HoRu_{0.90}Cu_{0.10}O_6$	12	8
$Sr_2Ho_{0.80}Tb_{0.20}Ru_{0.90}Cu_{0.10}O_6$	0	0
$Sr_2Ho_{0.20}Tb_{0.80}Ru_{0.90}Cu_{0.10}O_6$	10	10
$Sr_2TbRu_{0.90}Cu_{0.10}O_6$	24	12

Table 4.8 Comparison of the important information derived from the *ab* magnetic moment, the angle of inclination from the *c*-axis, and the highest temperature at which the component was measured.

The same interpenetrating Type I magnetic structure was adopted for the mixed rare-earth compounds as for the end members (with $y = 0$ and 1, $Sr_2HoRu_{0.90}Cu_{0.10}O_6$ and $Sr_2TbRu_{0.90}Cu_{0.10}O_6$ respectively), rather than a spin-glass. This is the most important observation to be made from these mixed systems, because it indicates that there is not a plethora of significant magnetic interactions present in the material. For Sr_2HoRuO_6 and Sr_2TbRuO_6, the Ho-O-O-Ho and Tb-O-O-Tb interactions are neglected as they are expected to be negligible. The fact that in these mixed systems that Ho-O-O-Tb interactions also exist, but the magnetic structure is the same as the parent compounds, suggests a weakness of this too. It also adds further weight that the Ru-O-Ho and Ru-O-Tb interactions are the cause of the ordering of the rare-earth sublattice, and that this interaction is antiferromagnetic in both cases.

4.5 Magnetic Ordering of the Two Magnetic Ion Systems

The systems studied in this chapter have provided the most illuminating study to date on the interactions of the Ru^{5+} ion with 4*f* ions. The fact that long-range magnetic ordering is observed in these materials means that the number of significant interactions in the materials are few, mutually cooperative, and that the crystal structure is reasonably well ordered, so that the magnetic ions are in similar, rather than locally varying environments.

The ruthenium sublattice is relatively unaffected by the introduction of the rare-earth, *Ln*, into the double perovskite structure. This suggests that the Ru-O-O-Ru interaction, which orders the Ru^{5+} ions in $Sr_2YRu_{1-x}Cu_xO_6$ and $Ba_2YRu_{1-x}Cu_xO_6$, is also responsible for the ordered ruthenium sublattices in $Sr_2LnRu_{1-x}Cu_xO_6$, and is

approximately the same strength. As the ordering interaction is the same, the ruthenium sublattice in the $Sr_2LnRu_{1-x}Cu_xO_6$ adopts the same Type I antiferromagnetic structure. Also, as the ruthenium sublattice has not been greatly affected by the introduction of the rare-earth this also suggests that the *Ln*-O-O-*Ln* interaction is weak, otherwise the Ru-O-*Ln* interaction might have changed the Ru sublattice ordering type.

Although the Ho^{3+} and Tb^{3+} ions have large ordered moments, the interactions between them via the *Ln*-O-O-*Ln* interaction are so weak, as to be negligible. The ordering in the rare-earth sublattice is been entirely due to the Ru-O-*Ln* interaction, which is reliant upon the ordering of the ruthenium sublattice. This explains the coincident ordering temperatures of the Ru^{5+} and Ln^{3+} ions within a sample, irrespective of the order of the interaction strengths of Ru-O-O-Ru and Ru-O-*Ln*.

When the Ru-O-*Ln* interaction is negligible, as for Ru-O-Y, the situation as discussed in Chapter 3 arises. However, when the strength of the Ru-O-*Ln* interaction is significant, but much weaker than the Ru-O-O-Ru interaction, the *Ln* sublattice orders gradually as the temperature is lowered. The only significant limiting factor is the weakness of the Ru-O-*Ln* interaction, and the ratio of the saturation temperatures of the two sublattices predicts the ratio of their interaction strengths. This situation is evidenced in the Ho analogues.

As the strength of the Ru-O-*Ln* interaction increases, the Ru-O-*Ln*-O-Ru interaction adds increasing support to the ordering of the ruthenium sublattice, leading to a slightly higher ordering temperature of both the magnetic ions. The Tb system provides a good example of a system where the Ru-O-O-Ru and Ru-O-*Ln* interactions are about the same strength, and the increase in ordering temperature was from 34 K to 39 K. This small increase, typically less than 10 K, has been noted for the entire 4*f* series by Doi and Hintasu from magnetic susceptibility measurements [21].

Also, as the strength of the Ru-O-*Ln* interaction increases and becomes more comparable to the Ru-O-O-Ru interaction, the ordering of the *Ln* sublattice is more complete at higher temperatures. However, the asymmetry of the interactions still leads to the Ru sublattice ordering to a greater degree at each temperature than the *Ln* sublattice, irrespective of the relative strengths of the Ru-O-O-Ru and Ru-O-*Ln* interactions. This partially limits the ordering of the *Ln* sublattice, though as the Ru-O-*Ln* interaction becomes relatively stronger, the gap closes and the saturation temperature difference of the two sublattices narrows. As the Ru-O-*Ln* interaction

adds support to the ordering of the ruthenium sublattice, the ratio of the ordering temperatures no longer provides the relative strengths of the Ru-O-O-Ru and Ru-O-*Ln* interactions. Instead, the saturation temperature of the ruthenium sublattice is best provided by an equally distorted system, with *Ln* chosen so that the Ru-O-*Ln* interaction is weak (or zero) and these bond angles are equal.

From the variable temperature studies presented here, important discoveries regarding the magnetic interactions of the Ru^{5+} ion have been made. For the Sr_2HoRuO_6 and Sr_2TbRuO_6 samples, the refined magnetic moments at 10 K of Ho^{3+} is 6.76(4) μ_B and Tb^{3+} is 4.56(4) μ_B, values which are in reasonable agreement with the literature of 6.66(8) μ_B and 4.98(12) μ_B respectively [4, 7]. However, the refined Ru^{5+} magnetic moments of 1.72(10) μ_B and 1.86(10) μ_B are in disagreement with those refined by Doi and Hinatsu [4, 7] of 2.74(9) μ_B and 2.99(12) μ_B, although they are in agreement with the rest of the literature [8-19]. Of these, Battle's sole study of a 4*f* ruthenate, Sr_2ErRuO_6 [15], where both ions magnetically ordered, also refined a magnetic moment of Ru^{5+} as 1.74(6) μ_B. Thus, it appears that Doi and Hinatsu's use of the Zr^+ magnetic form factor overestimates the Ru^{5+} magnetic moment, and that it is the same whether the Ln^{3+} ion is magnetic or not. The model developed here to explain the temperature dependence of the magnetic moments also predicts the same magnetic moment of the Ru^{5+} ion, irrespective of the magnetic nature of the Ln^{3+} ion.

Doi and Hinatsu's recent study [26] compiled the 4*f* ruthenates and listed the moment directions, but provided no reason for the differences. Battle's early studies of Sr_2YRuO_6 [10], Ba_2YRuO_6 [13], Sr_2LuRuO_6 [13] and Ba_2LuRuO_6 [13], only considered the (001) magnetic peak in order to determine the moment value, so the direction of the moment was not considered. Our studies of $Sr_2YRu_{1-x}Cu_xO_6$ and $Ba_2YRu_{1-x}Cu_xO_6$ indicate that the magnetic moments do lie in the *ab* plane. As these diffraction patterns are similar to those of the above compounds, it is likely that the moment is always in the *ab* plane when the *B'* cation ($A_2B'RuO_6$) is diamagnetic, and the Ru-O-O-Ru interaction is the only one of significance. The introduction of the second magnetic ion introduces the Ru-O-*Ln* interaction, which may lead to a different direction of the magnetic moments being preferred. Usually this is close to the *c*-axis, though the moments were reported in the *ab* plane for Ba_2NdRuO_6 [22] and Sr_2ErRuO_6 [15]. Although, one of the causes is likely to be the Ru-O-*Ln* interaction, the differences in moment direction reported in Sr_2YbRuO_6 [26] and

Ba_2YbRuO_6 [26], with 23° and 0° of inclination from the *c*-axis respectively, indicate that crystallographic changes may also have an influence.

In two systems studied here, Sr_2HoRuO_6 and Sr_2TbRuO_6, the two sublattices are anti-parallel to each other, which indicate an antiferromagnetic Ru-O-*Ln* interaction. As the sublattices are also anti-parallel in Ba_2HoRuO_6 [26], Sr_2ErRuO_6 [15], Ba_2ErRuO_6 [25], Sr_2TmRuO_6 [26] and Ba_2TmRuO_6 [26], these are also ferrimagnetic Ru-O-*Ln* interactions. However, for Ba_2PrRuO_6 [23], Ba_2NdRuO_6 [22], Sr_2YbRuO_6 [26] and Ba_2YbRuO_6 [26] the sublattices are parallel, indicating a ferromagnetic Ru-O-*Ln* interaction. Therefore, not only can the magnitude of the Ru-O-*Ln* interaction vary, as demonstrated with the Y, Ho and Tb samples, but the sign can vary too. Clearly, the magnetic interactions of the Ru^{5+} ion are as varied as they are interesting.

4.6 Conclusions

The crystal structures of the Sr_2HoRuO_6 and $Sr_2HoRu_{0.95}Cu_{0.05}O_6$ were examined by high-resolution neutron powder diffraction and determined to be disordered double perovskites ($A_2B'B''O_6$), adopting space group $P2_1/n$, which allows the 1:1 ordering of the *B* cations. The crystal structure was shown not to vary appreciably with temperature or copper doping. These crystal structures were used as models to successfully calculate the crystal structure intensity for all the materials studied in this chapter. For the $Sr_2HoRu_{1-x}Cu_xO_6$ series the unit cell volume increased with copper doping, and below 20 K there was a small increase in volume probably due to the magnetic moment of the Ho^{3+} ion becoming very large. For the $Sr_2TbRu_{1-x}Cu_xO_6$ series the unit cell volume decreased with increased copper doping, whereas for the $Sr_2Ho_{1-y}Tb_yRu_{0.90}Cu_{0.10}O_6$ series, there was a reasonably smooth increase in unit cell volume as the larger Tb^{3+} ions replace the smaller Ho^{3+} ions. The only significant change in unit cell volume with temperature, between 2 K and 50 K, was for the $Sr_2HoRu_{1-x}Cu_xO_6$ series and this again showed an anisotropy, with the *c*-axis increase displaying double the expansivity of the other two axes.

The magnetic structures of all the $Sr_2Ho_{1-y}Tb_yRu_{1-x}Cu_xO_6$ members are described by two Type I antiferromagnetic structures which interpenetrate. The Ru(Cu) sublattice forms one of the Type I structures, while the Ho(Tb) sublattice forms the second Type I arrangement. In the cases examined here, the two sublattices couple ferrimagnetically, while the direction of the moments is believed to result from a

combination of the Ru-O-*Ln* interaction and the crystal structure. The inability of D1B to resolve the (100) and (010) peaks was not responsible for the failure of the direction of the moment in the *ab* plane to be found. However, the high-flux of D1B allowed variable temperature measurements to be performed, which allowed the development of the magnetic moments to be determined and provided information on the interactions between the ions.

A theory has been developed in order to explain successfully the temperature dependence of the magnetic moments, including the ordering temperatures. The *Ln*-O-O-*Ln* interaction is believed to be weak, and further evidence for this was found in the existence of long-range magnetic ordering in the mixed rare-earth system, $Sr_2Ho_{1-y}Tb_yRu_{0.90}Cu_{0.10}O_6$. The theory also allows the relative strengths of the interactions to be calculated from the sublattice saturation temperatures. In the cases examined here, the order of the interaction strengths is believed to be Ru-O-O-Ru > Ru-O-*Ln* > *Ln*-O-O-*Ln*, agreeing with previous work [15]. However, from the study of Sr_2HoRuO_6 and Sr_2TbRuO_6 alone, the Ru-O-*Ln* has been found to vary significantly, and that the above order of interactions strengths may not be true in general.

The magnitude of the refined magnetic moment of Ru^{5+} is very similar in the Sr_2LnRuO_6 systems, irrespective of the ordering of the Ln^{3+} ion. Previous studies, which refined large magnetic moments for the Ru^{5+} ions, are largely a consequence of the choice of Zr^+ as the substitute form factor for Ru^{5+}. The Ho^{3+} magnetic moment was found to saturate close to its maximum value allowed by Hund's rules, whereas the Tb^{3+} saturated around half this value. With increasing copper doping, the refined magnetic moment of the Ru^{5+} ion increases in the $Sr_2HoRu_{1-x}Cu_xO_6$ series, whereas the refined Tb^{3+} magnetic moment decreases in the $Sr_2TbRu_{1-x}Cu_xO_6$ members.

The most important findings concern the interactions strengths in the materials. In summary, the magnitude of the Ru-O-O-Ru interaction is reasonably constant, albeit dependent on octahedral tilting distortions, while the Ru-O-*Ln* interaction may vary significantly, highlighting the interesting and intriguing behaviour of the Ru^{5+} ion with its neighbours. Clearly, the interesting variation in the interaction strengths of Ru-O-*Ln* needs to be explored, so as to determine its maximum influence.

4.7 References

1 M.T. Anderson, K.B. Greenwood, G.A. Taylor and K.R. Poeppelmeier, *Progress in Solid State Chemistry* **22,** 197 (1993).

2 M.K. Wu, D.Y. Chen, D.C. Ling and F.Z. Chien, *Physica B* **284,** 477 (2000).

3 A.C. Larson and R.B. Von Dreele, *Los Alamos National Laboratory Report* **LAUR 86-748,** 1 (1990).

4 Y. Doi, Y. Hinatsu, K. Oikawa, Y. Shimojo and Y. Morii, *Journal of Materials Chemistry* **10,** 797 (2000).

5 J.P. Schille, P. Sainctavit, C. Cartier, D. Lefebvre, C. Brouder, J.P. Kappler and G. Krill, *Solid State Communications* **85,** 787 (1993).

6 N.G. Parkinson, P.D. Hatton, M.K. Wu and K.H. Andersen, *The Rutherford Appleton Laboratory ISIS Facility Annual Report 1999-2000 (Science Highlight)* 54 (2000).

7 Y. Doi, Y. Hinatsu, K. Oikawa, Y. Shimojo and Y. Morii, *Journal of Materials Chemistry* **10,** 1731 (2000).

8 P.D. Battle, *Materials Research Bulletin* **16,** 397 (1981).

9 P.D. Battle, J.B. Goodenough and R. Price, *Journal of Solid State Chemistry* **46,** 234 (1983).

10 P.D. Battle and W.J. Macklin, *Journal of Solid State Chemistry* **52,** 138 (1984).

11 P.D. Battle and W.J. Macklin, *Journal of Solid State Chemistry* **54,** 245 (1984).

12 P.D. Battle and C.W. Jones, *Materials Research Bulletin* **22,** 1623 (1987).

13 P.D. Battle and C.W. Jones, *Journal of Solid State Chemistry* **78,** 108 (1989).

14 P.D. Battle, T.C. Gibb, C.W. Jones and F. Studer, *Journal of Solid State Chemistry* **78,** 281 (1989).

15 P.D. Battle, C.W. Jones and F. Studer, *Journal of Solid State Chemistry* **90,** 302 (1991).

16 M.P. Attfield, P.D. Battle, S.K. Bollen, S.H. Kim, A.V. Powell and M. Workman, *Journal of Solid State Chemistry* **96,** 344 (1992).

17 S.H. Kim and P.D. Battle, *Journal of Magnetism and Magnetic Materials* **123,** 273 (1993).

18 S.H. Kim and P.D. Battle, *Journal of Solid State Chemistry* **114,** 174 (1995).

19 P.D. Battle, J.R. Frost and S.H. Kim, *Journal of Materials Chemistry* **5,** 1003 (1995).

20 N. Kamegashira, T. Mori, A. Imamura and Y. Hinatsu, *Journal of Alloys and Compounds* **302,** L6 (2000).

21 Y. Doi and Y. Hinatsu, *Journal of Physics-Condensed Matter* **11,** 4813 (1999).

22 Y. Izumiyama, Y. Doi, M. Wakeshima, Y. Hinatsu, K. Oikawa, Y. Shimojo and Y. Morii, *Journal of Materials Chemistry* **10,** 2364 (2000).

23 Y. Izumiyama, Y. Doi, M. Wakeshima, Y. Hinatsu, Y. Shimojo and Y. Morii, *Journal of Physics-Condensed Matter* **13,** 1303 (2001).

24 Y. Doi, Y. Hinatsu, K. Oikawa, Y. Shimojo and Y. Morii, *Journal of Alloys and Compounds* **323,** 455 (2001).

25 Y. Izumiyama, Y. Doi, M. Wakeshima, Y. Hinatsu, A. Nakamura and Y. Ishii, *Journal of Solid State Chemistry* **169,** 125 (2002).

26 Y. Doi, Y. Hinatsu, A. Nakamura, Y. Ishii and Y. Morii, *Journal of Materials Chemistry* **13,** 1758 (2003).

27 B.C. Gerstein, F.J. Jelinek and F.H. Spedding, *Physical Review Letters* **8,** 425 (1962).

28 R.W. Hill, *Journal of Physics C-Solid State Physics* **19,** 673 (1986).

5 Neutron Diffraction Studies of $Ba_2PrRu_{1-x}Cu_xO_6$

5.1 Introduction

The observations of superconductivity in the 2116 systems, such as $Sr_2YRu_{1-x}Cu_xO_6$ and $Ba_2YRu_{1-x}Cu_xO_6$, are controversial because the materials contain all the necessary ingredients for the formation of 123-type superconductors, namely $YSr_2Cu_3O_{7-\delta}$ (YSCO) and $YBa_2Cu_3O_{7-\delta}$ (YBCO). The diffraction experiments undertaken in this study can determine only bulk phases and any filamentary impurities, which could support a supercurrent, are not detectable. Thus, even if a diffraction experiment shows a material to have no bulk impurities, superconductivity cannot be attributed unambiguously to a ruthenate 2116 phase from this information alone.

$PrBa_2Cu_3O_{7-\delta}$ is unusual within the 123 family, since for many years it was thought not to be a superconductor [1]. Recently it has been shown that with extremely diligent preparation conditions superconducting $PrBa_2Cu_3O_{7-\delta}$ can be grown albeit with difficulty [2], though the result has not been totally accepted. During the attempted preparation of $Ba_2PrRu_{1-x}Cu_xO_6$ it is extremely unlikely that the exact conditions for pure superconducting $PrBa_2Cu_3O_{7-\delta}$ will be present, if it were to form as an impurity phase. If any $PrBa_2Cu_3O_{7-\delta}$ does form, it would be non-superconducting and thus any superconductivity in $Ba_2PrRu_{1-x}Cu_xO_6$ samples would be attributable solely and unambiguously to this 2116 phase.

Samples of $Ba_2PrRu_{1-x}Cu_xO_6$, were synthesised and are claimed to be superconducting when copper is doped into the material [3], though most of the results are thus far unpublished. Powder neutron diffraction experiments were performed on Ba_2PrRuO_6 and $Ba_2PrRu_{0.90}Cu_{0.10}O_6$ in order to show that the materials have the 2116 structure. They would determine also the magnetic structure, which is important as Ru^{5+} and Pr^{3+} ions are magnetic. Should the superconductivity and the 2116 structure be confirmed, then there would be greater confidence in the observed superconductivity in other 2116 ruthenate phases.

5.2 Neutron Diffraction Experiments on $Ba_2PrRu_{1-x}Cu_xO_6$

The crystal and magnetic structures of Ba_2PrRuO_6 and $Ba_2PrRu_{0.90}Cu_{0.10}O_6$ were studied using the high-resolution powder diffractometer D1A. Measurements on both samples were recorded at ~ 5 K and 150 K, which are below and above the magnetic

ordering transition temperature. The diffraction patterns were collected over 7 hours each and an extra diffraction pattern was measured for each sample at 50 K, which is above the magnetic ordering temperature of all the other ruthenate samples studied. High-flux measurements were undertaken on $Ba_2PrRu_{0.90}Cu_{0.10}O_6$ using D1B to determine the temperature dependence of the magnetic structure between 2 K and 130 K. Approximately 3 – 4 grams of material were contained in 12 mm diameter vanadium cans and the absorption correction applied is detailed in Appendix B.7.

5.2.1 Crystal Structure of $Ba_2PrRu_{1-x}Cu_xO_6$

The diffraction pattern of $Ba_2PrRu_{0.90}Cu_{0.10}O_6$ was measured at 150 K using the high-resolution diffractometer D1A as shown in Figure 5.1. The calculated profile using GSAS [4] is obtained from the model crystal structure of Table 5.1. In common with the other ruthenate series, a 1:1 ordering of the Ru(Cu):Pr cations was assumed, as befits the charge and size of the ions. The refinement proceeded well in space group $P2_1/n$ and also as there are no unindexed peaks there is no observable impurity phase $Ba_2PrRu_{0.90}Cu_{0.10}O_6$. In fact, there is no significant unaccounted intensity and the R-factors are R_p = 5.33 %, R_{wp} = 7.26 % and R_{exp} = 7.21 %, which suggest a good quality model and diffraction pattern.

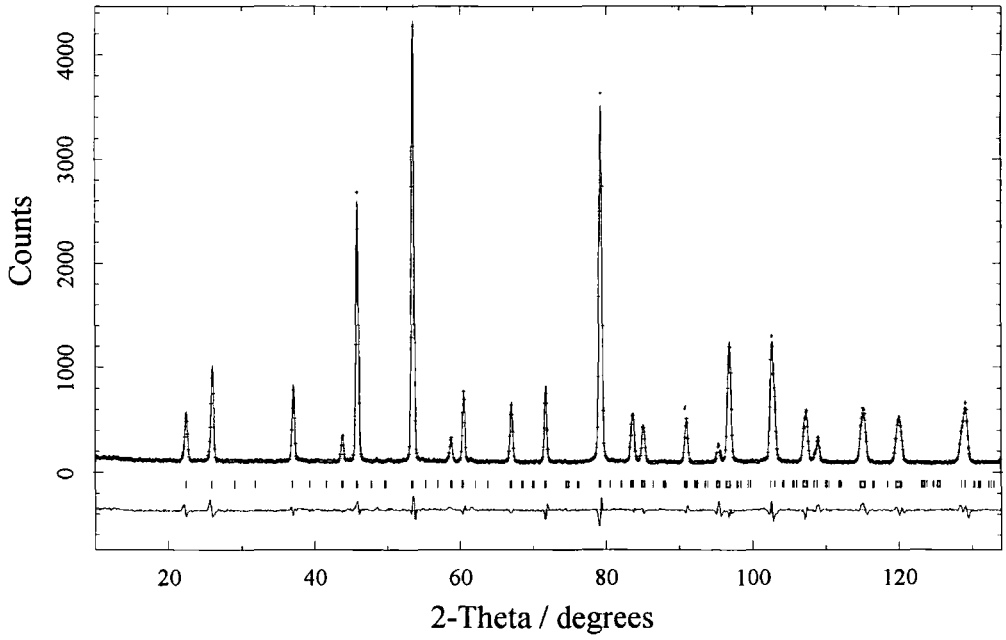

Figure 5.1 Neutron powder diffraction pattern of $Ba_2PrRu_{0.90}Cu_{0.10}O_6$ measured at 150 K using D1A at the ILL. The reflection positions are denoted by the tick marks. The calculated profile is represented by the line, while the crosses denote the data points, and the difference curve between the two is shown at the bottom.

The Ba_2PrRuO_6 sample was also measured at D1A, though the temperature was 125 K, rather than 150 K, owing to a slight cryostat problem. This refined diffraction pattern is shown in Figure 5.2, and it is noted that the peaks have tails which were not observed in the $Ba_2PrRu_{0.90}Cu_{0.10}O_6$ data. This indicates that the feature is due to a sample, rather than instrumental effect. The tails may indicate that the material is slightly strained and that the synthesis conditions, most probably the reaction temperature, were not ideal for the formation of the Ba_2PrRuO_6. Nevertheless, other than the tails the diffraction patterns of Ba_2PrRuO_6 and $Ba_2PrRu_{0.90}Cu_{0.10}O_6$ are very similar, giving confidence that the parent compound is still of sufficient quality. There are also two broad unindexed peaks at ~ 50° and 72° and these relate to BaO. The crystal structure of Ba_2PrRuO_6 was refined similarly to that of $Ba_2PrRu_{0.90}Cu_{0.10}O_6$ and the results are compared in Table 5.1. As the calculated profile still is able to reflect the observed data and the *R*-factors are R_p = 5.32 %, R_{wp} = 7.11 % and R_{exp} = 7.42 %, then the sample and patterns are of a sufficiently high standard for comparison with the copper doped material.

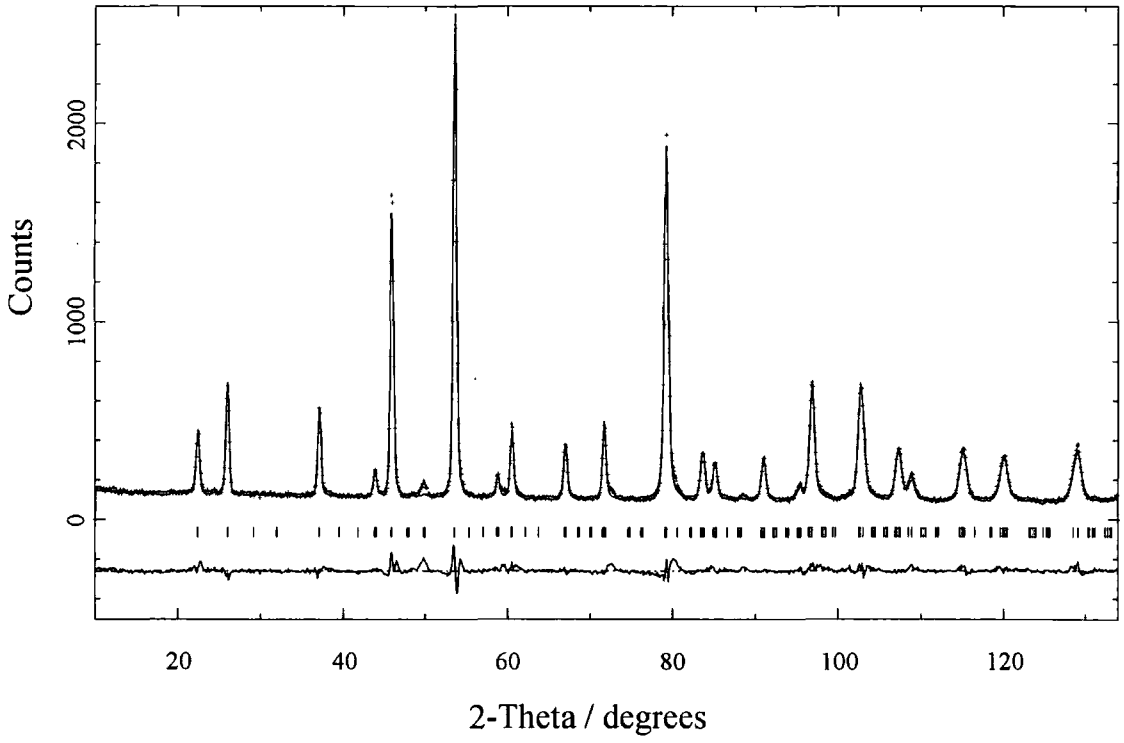

Figure 5.2 Neutron diffraction pattern of Ba_2PrRuO_6 with data shown as crosses, calculated profile and difference curves as lines, with reflections denoted by tick marks. Data were collected using D1A at the ILL.

Ba_2PrRuO_6		$P2_1/n$			150 K	
$Ba_2PrRu_{0.90}Cu_{0.10}O_6$		***$P2_1/n$***			**125 K**	
a / Å		*b* / Å	*c* / Å	*β* / °	Volume / Å^3	
5.96248(7)		5.96746(7)	8.45401(20)	89.781(1)	300.799(15)	
5.96237(4)		**5.96744(4)**	**8.45395(11)**	**89.782(1)**	**300.791(9)**	
Atom	Site	*x*	*y*	*z*	Occ	B_{iso}/Å^2
Ba	4*e*	0.0037(28)	0.0065(48)	0.7524(26)	1.000	0.62(9)
		0.0031(14)	**0.0012(40)**	**0.7562(10)**		**0.60(5)**
Pr	2*c*	0	½	0	1.000	0.52(7)
						0.51(5)
Ru	2*d*	½	0	0	1.000	0.52(7)
					0.900	**0.51(5)**
Cu	2*d*	½	0	0	0.000	0.52(5)
					0.100	**0.51(5)**
O1	4*e*	0.2412(42)	0.2899(23)	0.5178(21)	1.000	0.74(5)
		0.2423(22)	**0.2856(15)**	**0.5176(13)**		**0.80(4)**
O2	4*e*	0.2427(57)	-0.2704(24)	0.5089(25)	1.000	0.74(5)
		0.2481(25)	**-0.2745(15)**	**0.5101(14)**		**0.80(4)**
O3	4*e*	-0.0308(23)	0.5031(44)	0.7303(12)	1.000	0.74(5)
		-0.0348(12)	**0.5016(35)**	**0.7344(7)**		**0.80(4)**

R_p = 5.32 %, R_{wp} = 7.11 %, R_{exp} = 7.42 %, R_{F^2} = 4.54 %
R_p = 5.33 %, R_{wp} = 7.26 %, R_{exp} = 7.21 %, R_{F^2} = 4.97 %

Table 5.1 The crystal structures of Ba_2PrRuO_6 and $Ba_2PrRu_{0.90}Cu_{0.10}O_6$ as determined from refinement of high temperature data measured at D1A.

From the crystal structures listed in Table 5.1, the bond lengths and angles were calculated (Table 5.2), and these show that most of the distortion manifests in one bond angle in each of the octahedra, whether Pr, Ru or Cu. Both crystal structures are quite similar to each other, clearly reflected in the values in Table 5.2, and so copper doping does not greatly affect the crystal structure. A previous study on Ba_2PrRuO_6 [5] determined similar bond lengths, though this did not detect the same level of distortion of the bond angles. The most important feature of the $Ba_2PrRu_{1-x}Cu_xO_6$ crystal structure is the fact that it is a 2116 double perovskite and that it is similar to the other ruthenates studied in this thesis. The crystal structure of Ba_2PrRuO_6 is shown in Figure 5.3, which allows the tilting of the octahedra to be seen clearly.

Ba_2PrRuO_6			$P2_1/n$		D1A		150 K
Pr-O1	2.322(18)	Ru-O1	1.914(19)	O1-Pr-O2	94.6(7)	O1-Ru-O2	95.7(8)
Pr-O2	2.227(21)	Ru-O2	1.994(22)	O1-Pr-O3	90.8(7)	O1-Ru-O3	90.3(9)
Pr-O3	2.288(11)	Ru-O3	1.954(10)	O2-Pr-O3	91.7(8)	O2-Ru-O3	91.2(10)
Ru-O1-Pr	169.0(9)		Ru-O2-Pr	174.9 (11)		Ru-O3-Pr	170.0(7)
Ba-O1	2.963(30)	Ba-O1	2.788(27)	Ba-O1	3.243(26)	Ba-O1	2.989(30)
Ba-O2	2.996(35)	Ba-O2	2.855(30)	Ba-O2	3.090(30)	Ba-O2	3.010(40)
Ba-O3	3.020(50)	Ba-O3	2.980(50)	Ba-O3	2.824(24)	Ba-O3	3.146(23)
$Ba_2PrRu_{0.90}Cu_{0.10}O_6$			$P2_1/n$		D1A		125 K
Pr-O1	2.229(8)	Ru-O1	1.935(9)	O1-Pr-O2	95.3(3)	O1-Ru-O2	96.4(3)
Pr-O2	2.223(10)	Ru-O2	2.001(10)	O1-Pr-O3	90.2(5)	O1-Ru-O3	90.1(6)
Pr-O3	2.255(6)	Ru-O3	1.992(6)	O2-Pr-O3	91.7(5)	O2-Ru-O3	91.6(6)
Ru-O1-Pr	169.7(6)		Ru-O2-Pr	172.9 (7)		Ru-O3-Pr	168.8(4)
Ba-O1	2.995(21)	Ba-O1	2.763(18)	Ba-O1	3.234(18)	Ba-O1	2.980(19)
Ba-O2	3.026(21)	Ba-O2	2.810(19)	Ba-O2	3.165(19)	Ba-O2	2.952(19)
Ba-O3	3.000(40)	Ba-O3	3.000(40)	Ba-O3	2.794(12)	Ba-O3	3.170(12)

Table 5.2 The important bond angles (Å) and bond lengths (°) present in Ba_2PrRuO_6 and $Ba_2PrRu_{0.90}Cu_{0.10}O_6$, as determined from refinement of the high temperature data.

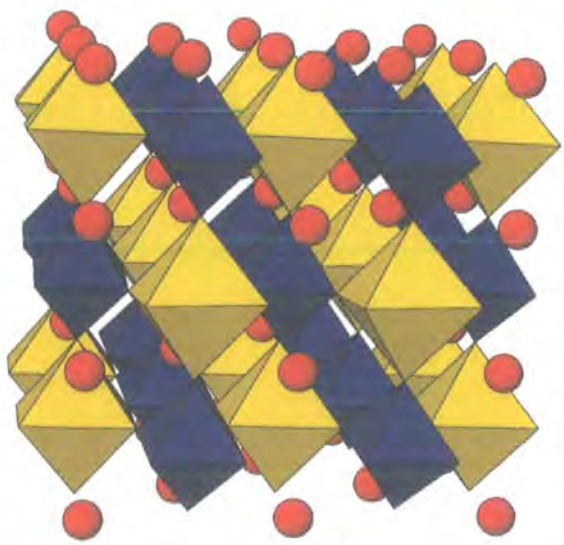

Figure 5.3 The crystal structure of Ba_2PrRuO_6 as determined from refinement. The RuO_6 octahedra (blue) and the PrO_6 octahedra (yellow) are shown with the Ba (red).

The crystal structures of Ba_2PrRuO_6 and $Ba_2PrRu_{0.90}Cu_{0.10}O_6$ were refined from the data collected at 60 K and 5 K for the $x = 0$ sample, and 50 K and 5 K for the copper doped material. These refined crystal structures are listed in Appendix B.6.1 and the bond lengths and angles for Ba_2PrRuO_6 are given in Table 5.3, which shows that there is not much variation of the crystal structure with temperature.

Ba_2PrRuO_6		$P2_1/n$		D1A		60 K	
Pr-O1	2.319(22)	Ru-O1	1.919(24)	O1-Pr-O2	96.0(6)	O1-Ru-O2	97.5(7)
Pr-O2	2.238(26)	Ru-O2	1.979(28)	O1-Pr-O3	91.7(7)	O1-Ru-O3	91.2(8)
Pr-O3	2.261(11)	Ru-O3	1.983(10)	O2-Pr-O3	91.0(7)	O2-Ru-O3	90.3(9)
Ru-O1-Pr	166.8(9)		Ru-O2-Pr	173.4 (10)		Ru-O3-Pr	171.0(7)
Ba-O1	2.947(29)	Ba-O1	2.730(26)	Ba-O1	3.309(24)	Ba-O1	2.996(31)
Ba-O2	2.988(34)	Ba-O2	2.796(28)	Ba-O2	3.130(28)	Ba-O2	3.040(40)
Ba-O3	3.030(50)	Ba-O3	2.960(50)	Ba-O3	2.880(27)	Ba-O3	3.079(27)
Ba_2PrRuO_6		$P2_1/n$		D1A		5 K	
Pr-O1	2.323(19)	Ru-O1	1.914(21)	O1-Pr-O2	96.0(6)	O1-Ru-O2	97.4(7)
Pr-O2	2.233(24)	Ru-O2	1.984(25)	O1-Pr-O3	91.7(7)	O1-Ru-O3	90.8(7)
Pr-O3	2.263(11)	Ru-O3	1.982(10)	O2-Pr-O3	91.4(7)	O2-Ru-O3	90.5(10)
Ru-O1-Pr	167.0(9)		Ru-O2-Pr	173.5 (11)		Ru-O3-Pr	170.4(7)
Ba-O1	2.941(29)	Ba-O1	2.736(27)	Ba-O1	3.303(24)	Ba-O1	3.002(30)
Ba-O2	2.990(40)	Ba-O2	2.800(30)	Ba-O2	3.124(28)	Ba-O2	3.040(40)
Ba-O3	3.020(50)	Ba-O3	2.970(50)	Ba-O3	2.872(26)	Ba-O3	3.087(26)

Table 5.3 The bond lengths (Å) and angles (°) of Ba_2PrRuO_6 as determined by Rietveld analysis of D1A diffraction data measured at 60 K and 5 K.

The $Ba_2PrRu_{1-x}Cu_xO_6$ series has the largest lattice parameters of any of the ruthenates (A_2BRuO_6) in this thesis as barium and praseodymium are the largest A and B cations studied here. The unit cell volume is shown in Figure 5.4 and shows that the $x = 0.10$ volume is larger than the $x = 0$ volume, due to the larger size of copper compared to ruthenium. The unit cell volume is approximately constant below 50 K and increases above this temperature in both materials. The guideline for $Ba_2PrRu_{0.90}Cu_{0.10}O_6$ fairly reflects the variation of unit cell volume with temperature, as Rietveld analysis of the variable temperature data measured on D1B confirmed.

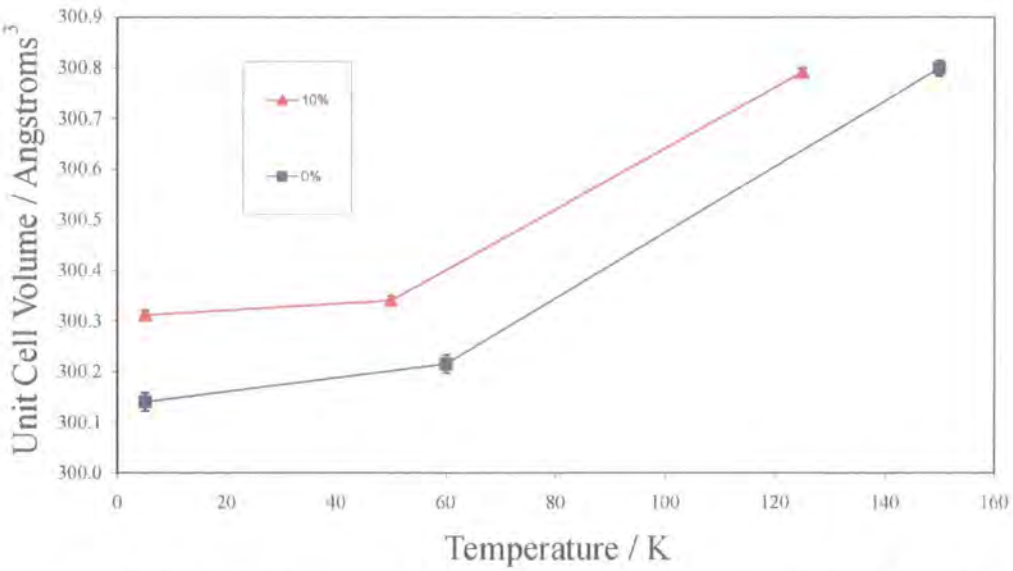

Figure 5.4 The unit cell volume with temperature of the $Ba_2PrRu_{1-x}Cu_xO_6$ series for the $x = 0$ and $x = 0.10$ members.

5.2.2 Magnetic Structure of $Ba_2PrRu_{1-x}Cu_xO_6$

The diffraction pattern of Ba_2PrRuO_6 measured at 5 K is shown in Figure 5.5 and it is immediately apparent that there is very little extra intensity attributable to the magnetic structure, certainly when compared to the other rare-earth ruthenate compounds of Sr_2HoRuO_6 and Sr_2TbRuO_6. For these materials the (001), (100) and (010) magnetic peaks formed an integral part of the magnetic structure determination, but all are absent in the diffraction pattern of Ba_2PrRuO_6. However, the magnetic peaks can still be indexed by a magnetic unit cell which is the same size as the crystal unit cell, just like the other compounds studied. All the magnetic peaks which are present clearly in the diffraction pattern can be indexed with $h + k + l$ being odd, so again indicate an antiferromagnetic nature, which is confirmed from the magnetic measurements presented in Section 5.2.3. This reflection condition means that both the ruthenium and praseodymium sublattices will order as if the intra-species interactions are both antiferromagnetic and results in an interpenetrating Type I magnetic structure.

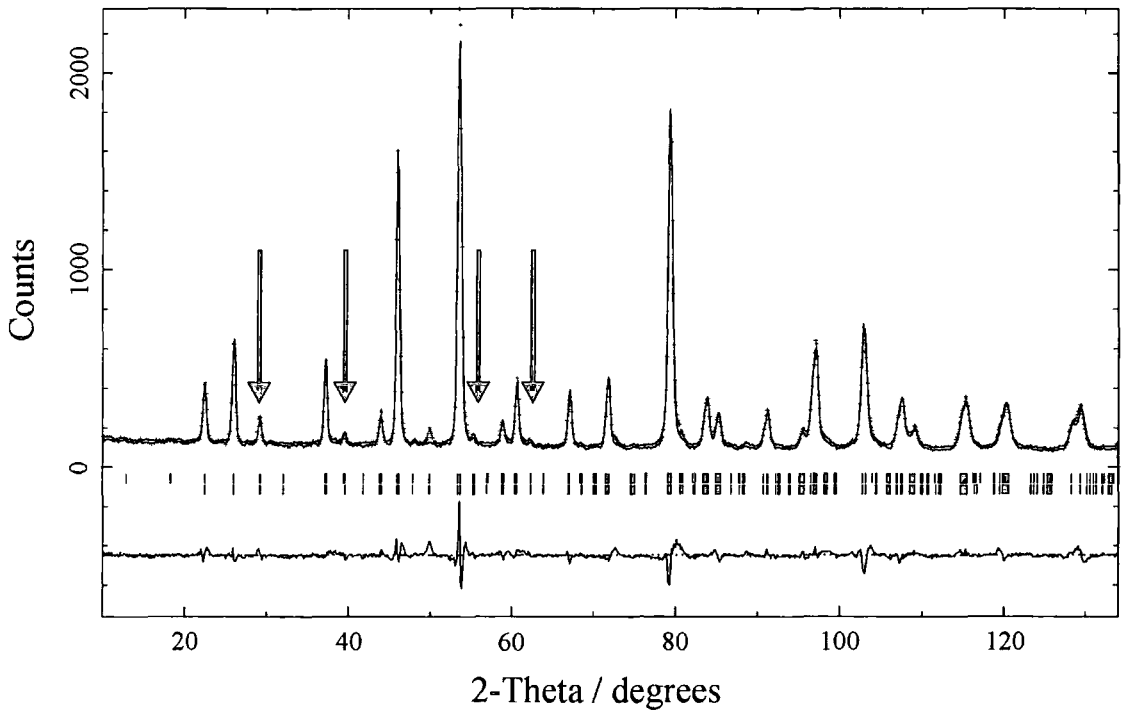

Figure 5.5 The neutron diffraction pattern of Ba_2PrRuO_6 measured at 5 K using D1A. The data points are indicated as crosses, whereas the calculated profile and difference curve are shown as lines. The upper series of tick marks show the reflection positions for magnetic cell, whereas the lower set are the crystal structure reflections as before. The prominent magnetic peaks are indicated by arrows.

Those magnetic peaks which have relatively strong intensities, at $2\theta \sim 29°$, 39°, 55° and 62° all have l odd, in addition to the antiferromagnetic condition that the sum of $h + k + l$ must be odd. In fact, no magnetic intensity is observed for reflections with l even. Reviewing the summary for magnetic intensity when the intra-species interactions are antiferromagnetic in Table 5.4, this suggests that the Ru^{5+} magnetic sublattice is parallel to the Pr^{3+} sublattice. As the antiferromagnetic peaks composed of reflections where l is even are too small to be observed, this indicates that the magnetic moments on the Ru^{5+} and Pr^{3+} are about the same size, so that the difference peaks have approximately zero intensity. As the two sublattices are parallel to each other in Ba_2PrRuO_6, in contrast to the cases in Sr_2HoRuO_6 and Sr_2TbRuO_6, this indicates that the inter-species interaction, Ru-O-Pr is ferromagnetic in nature.

Type of Reflection	Lattices Parallel Ferromagnetic		Lattices Anti-Parallel Ferrimagnetic	
	$(h + k)$	l	$(h + k)$	l
Sum	even	odd	odd	even
Difference	odd	even	even	odd

Table 5.4 Summary of the reflection conditions when the intra-species interactions are antiferromagnetic.

For the previously studied magnetic structures, the (001), (100) and (010) magnetic peaks have proved vital for determining the moment direction, however these peaks are absent in Ba_2PrRuO_6. The moment direction can be obtained still in this system, as zero intensity for these magnetic peaks still provides plenty of information on the moment direction and even on its magnitude. As the magnetic peaks with $h + k + l$ being odd with l odd are formed from the summation of the scattering from the magnetic moments of the Ru^{5+} and Pr^{3+} ions, then the (001) magnetic intensity should be large. However, if the magnetic moment lies in the *c*-direction, then the component of the magnetic moment perpendicular to the (001) scattering vector is zero, and so the magnetic intensity of the (001) would be zero, as is observed. With the magnetic moment in the *c*-direction, the (100) and (010) magnetic peaks would normally be large, however as l is even in both cases, the magnetic intensity results from the difference of the two magnetic moments. If the magnetic moments of the Ru^{5+} and Pr^{3+} ions are equal, then the (100) and (010) magnetic reflections will also have zero magnetic intensity. This is further confirmed by the fact that none of the magnetic peaks with l being even are observed with significant intensity, as mentioned previously. Thus, the absence of these magnetic peaks has not hindered unduly the magnetic structure classification, or the magnetic moment direction determination. The expected magnetic structure consists of two Type I sublattices of Ru^{5+} and Pr^{3+}, which are coupled ferromagnetically to each other, with the moments in the *c*-direction and of similar size for both ions. From previous work on the ruthenates, the magnetic moment size of the Ru^{5+} ion is expected to be $\sim 2\ \mu_B$, as this was found to be largely independent of its magnetic partner. This magnetic structure is illustrated in Figure 5.6.

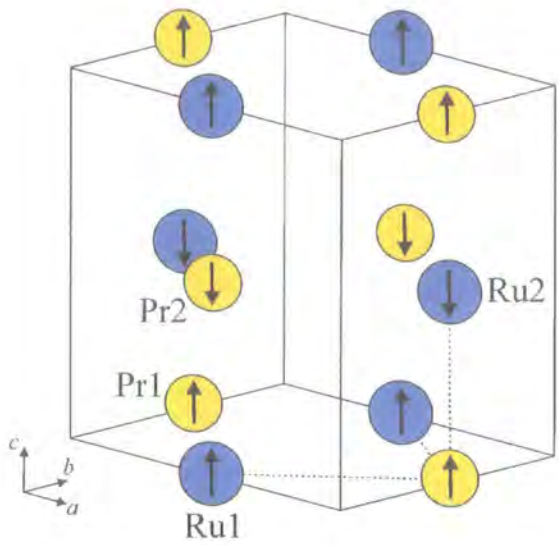

Figure 5.6 The magnetic structure of Ba_2PrRuO_6 in which the Ru^{5+} and Pr^{3+} magnetic ions each order in Type I antiferromagnetic structures which interpenetrate. The inter-species interaction is ferromagnetic and is most easily seen from observing the relative moment directions of the Ru^{5+} and Pr^{3+} ions in the *ab* plane. The moments lie along the *c*-direction and are a similar size for both the Ru^{5+} and Pr^{3+} magnetic ions. To assist the clarity of the diagram the Ru^{5+} ions are shown in blue, the Pr^{3+} ions in yellow, with the former moment size fractionally larger.

This magnetic structure was used as the initial starting model from which the refinements were allowed to proceed to the final calculated profile shown in Figure 5.5 (above). The Pr^{3+} magnetic form factor is known [6] and the calculated magnetic form factor was used again for Ru^{5+}. As can be seen the calculated profile replicates accurately both the crystal and magnetic intensity in the diffraction pattern and yields *R*-factors of R_p = 6.24 %, R_{wp} = 8.19 % and R_{exp} = 7.45 %, which are reasonable. The crystal structure was discussed in Section 5.2.1 and is detailed in Appendix B.6.1.1. The magnetic moments in the *z*-direction were refined as 1.82(15) μ_B for Ru^{5+} and 1.14(11) μ_B for Pr^{3+} at 5 K, with the magnetic structure as shown in Figure 5.6. The magnetic moments of the Ru^{5+} and Pr^{3+} ions are not equal, however, this is not necessary, as the relative magnitudes are determined by the difference magnetic peaks (where *l* is even,) and thus limited by the sensitivity, not the resolution of the magnetic moments. For D1A the sensitivity is ~ 0.8 μ_B at the position of the (100)/(010) peak. Thus, as the moments on the two ions are within this sensitivity limit of ~ 0.8 μ_B of each other, then the difference magnetic peaks will be zero as is observed. Potentially, the sizes of the magnetic moments could have been attributed the other way around, with 1.14(11) μ_B for Ru^{5+} and 1.82(15) μ_B for Pr^{3+}.

However, the previously noted independence of the magnetic moment size of the Ru^{5+} ion with rare-earths strongly supports the case for 1.82(15) μ_B for Ru^{5+} and 1.14(11) μ_B for Pr^{3+}.

The diffraction pattern measured at 50 K on the Ba_2PrRuO_6 sample is displayed in Figure 5.7 and the most startling feature is the presence of the magnetic peaks at this temperature. The diffraction pattern is very reminiscent of the 5 K data shown in Figure 5.5 and both the crystal and magnetic structures refined similarly. The refined magnetic moments of Ru^{5+} and Pr^{3+} are 1.66(16) μ_B and 1.08(12) μ_B respectively. The magnetic ordering temperatures of the other ruthenates studied in this thesis are 30-40 K, and so the existence of the magnetic structure in Ba_2PrRuO_6 at 50 K is an early indication that the interactions are different in this material.

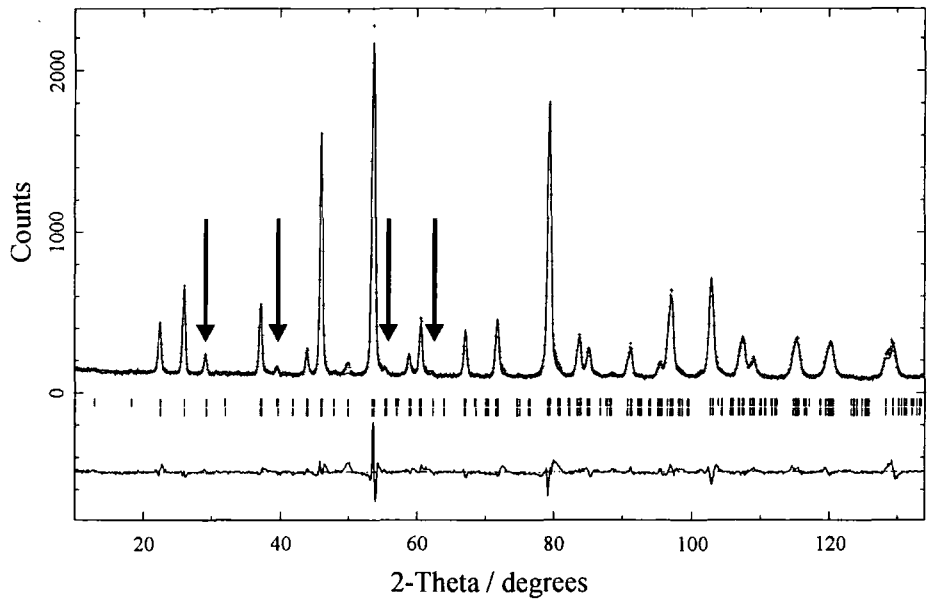

Figure 5.7 Neutron diffraction pattern of Ba_2PrRuO_6 measured at 60 K using diffractometer D1A. The data points are shown as crosses while the calculated profile and difference curve are lines. The upper series of tick marks denote magnetic structure reflections, while the lower set indicate crystal structure reflections.

As the magnetic intensity appears at low angles where peak overlap is less of a problem, especially for antiferromagnetic structures, the neutron flux of an instrument is more important than resolution for determination of the magnetic structure. This is particularly true for $Ba_2PrRu_{1-x}Cu_xO_6$ because the magnetic structure and moment sizes manifest as only a small amount of magnetic intensity. Hence, the $Ba_2PrRu_{0.90}Cu_{0.10}O_6$ magnetic structure will be discussed using the D1B data, though

the results of refinements of the D1A data are in complete agreement, and can be found in Appendix B.6.

Based on magnetic measurements supplied with the samples variable temperature neutron diffraction patterns were collected from 2 to 50 K on $Ba_2PrRu_{0.90}Cu_{0.10}O_6$. As the Pr^{3+} magnetic moment is quite small, each diffraction pattern was measured over 30 minutes with the temperature raised at 0.1 K per minute, so effectively giving a collection every 1.5 K. The angular segment measured was between 15° and 95° as no peaks would be observed below 15°, a fact confirmed by the D1A data. These diffraction results are shown in Figure 5.8 with the magnetic peaks appearing at $2\theta \sim 17°$, 24°, 39° and 53° and persisting relatively unchanged up to 50 K. Thus, the magnetic ordering temperature is higher than 50 K, which is higher than any of the ruthenates previously studied in this thesis.

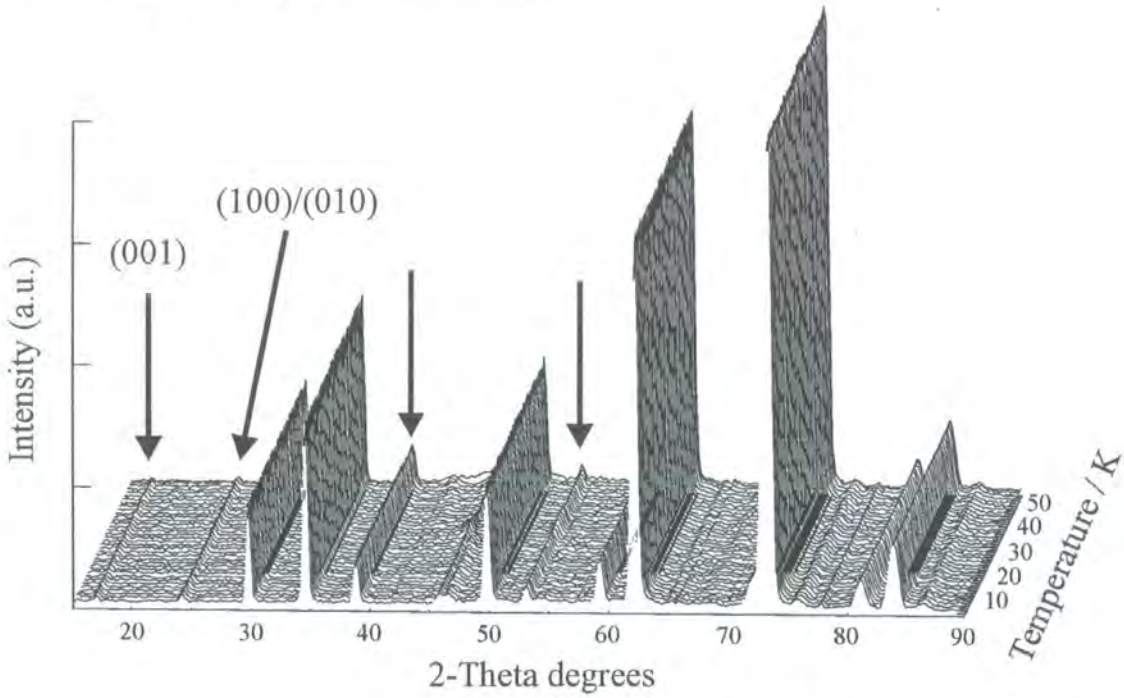

Figure 5.8 Variable temperature neutron diffraction patterns measured every 1.5 K between 2 K and 50 K, 15° and 95°, on $Ba_2PrRu_{0.90}Cu_{0.10}O_6$.

Fortunately the remaining beam-time allowed measurements at higher temperatures to be collected, albeit at the faster rate of ~ 0.8 K per minute and 5 minutes per pattern. This was sufficiently long to allow accurate analysis of the data due to the high-flux of D1B, though the diffraction patterns collected were spaced every 6 K. These data are displayed in Figure 5.9 and show the magnetic peaks at 39° and 53° disappearing above ~ 104 K. The 17° and 24° peak are much weaker, and not clearly visible, but

this is due to the reduced counting time, rather than a spin reorientation in the $Ba_2PrRu_{0.90}Cu_{0.10}O_6$ material.

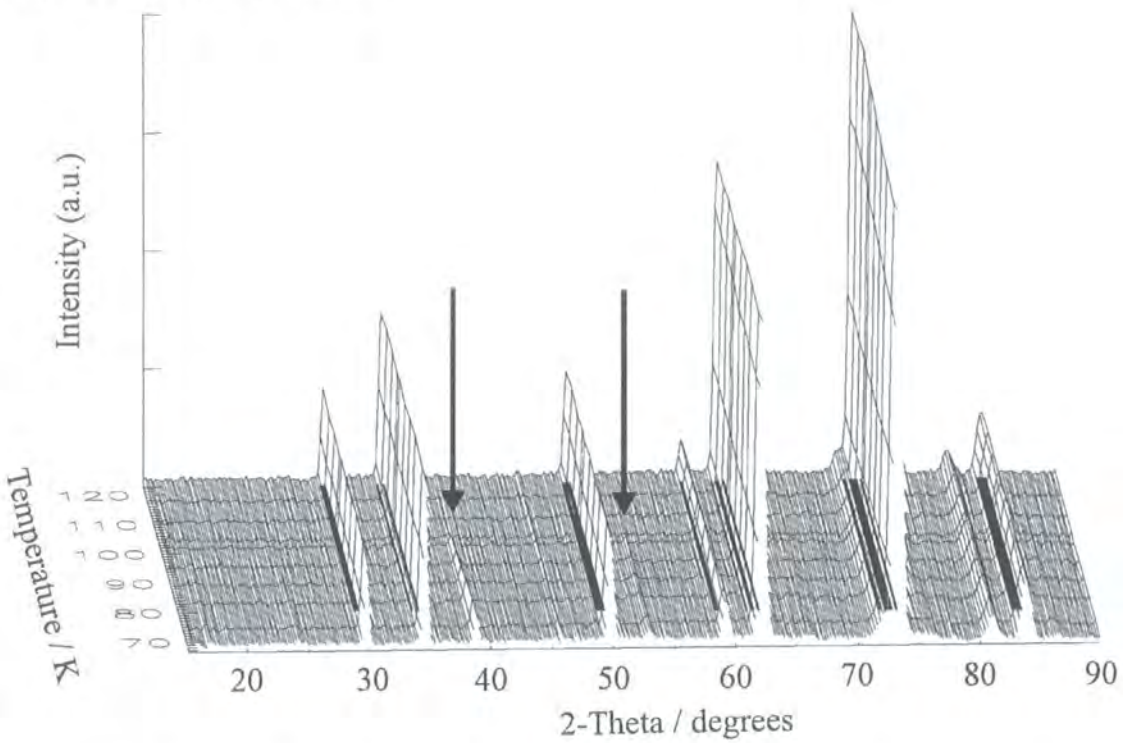

Figure 5.9 Variable temperature neutron diffraction patterns measured every 6 K between 60 K and 130 K, 15° and 95°, on $Ba_2PrRu_{0.90}Cu_{0.10}O_6$.

The refined diffraction pattern measured at 5 K on $Ba_2PrRu_{0.90}Cu_{0.10}O_6$ is shown in Figure 5.10, with the observed magnetic peaks indicated by arrows. The residual intensity at 46° and 72° is not present in the D1A patterns of this material, though would be sufficiently large to be observed if it was due to the material. It is therefore attributed to an instrument or cryostat effect of D1B. The magnetic peaks at 39° and 53° correspond to the magnetic peaks observed in the D1A diffraction patterns at 29° and 39° respectively. From their similar form, the expected magnetic structure of $Ba_2PrRu_{0.90}Cu_{0.10}O_6$ will be broadly similar to Ba_2PrRuO_6. However, small magnetic peaks are clearly visible in the D1B data at 17° and 24°, which are indexed as the (001) and unresolved combination of (100) and (010) reflections. These peaks were observed also in the D1A data measured on $Ba_2PrRu_{0.90}Cu_{0.10}O_6$, but not in the Ba_2PrRuO_6 patterns, and so indicates a genuine difference in the magnetic intensity and structures.

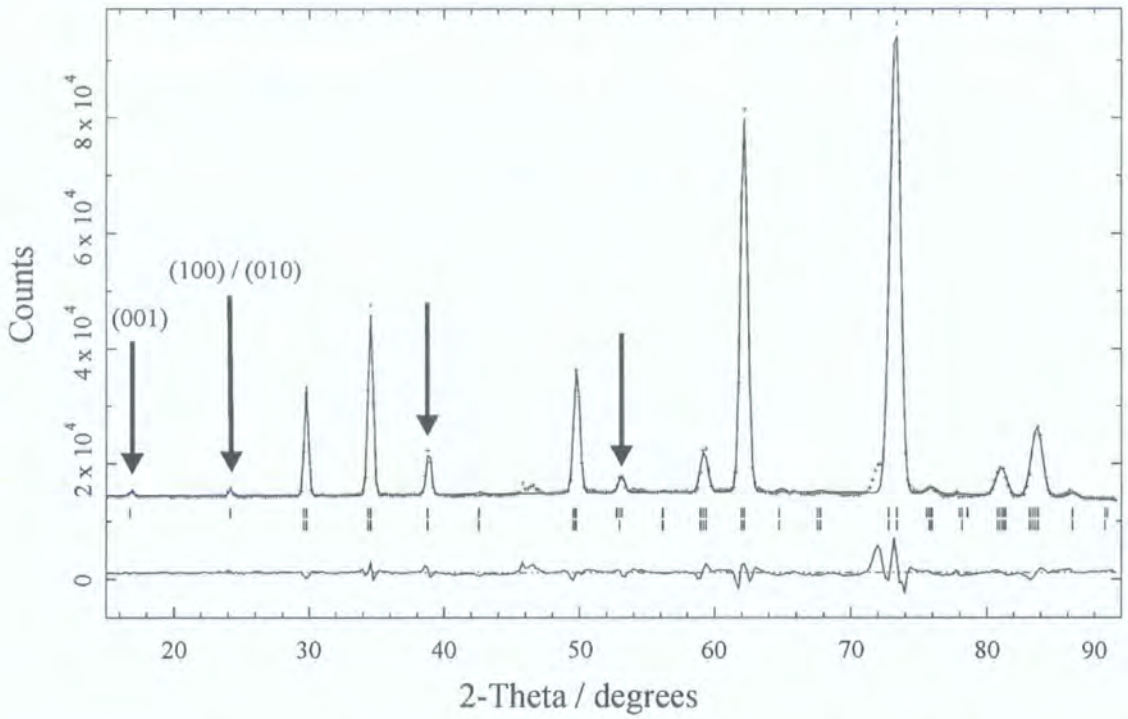

Figure 5.10 The refined diffraction pattern of $Ba_2PrRu_{0.90}Cu_{0.10}O_6$ measured at 5 K using the neutron powder diffractometer D1B. The data points are marked as crosses, whereas the calculated profile and difference curve are shown as lines. The magnetic peaks are indicated by arrows and the magnetic reflection positions denoted by the upper set of tick marks, leaving the crystal structure reflections to the lower set.

The presence of the (001) magnetic peak indicates that there is a component of the magnetic moment in the *ab* plane in the $Ba_2PrRu_{0.90}Cu_{0.10}O_6$ sample. But, as the peak is weak, despite the reflection having *l* odd and being at low angle, this component will be much smaller than the component in the *c*-direction. Just as for the $Sr_2HoRu_{1-x}Cu_xO_6$ and $Sr_2TbRu_{1-x}Cu_xO_6$ series, this small *ab* component cannot be unambiguously apportioned between the two ions Ru^{5+} and Pr^{3+}, but simply for consistency, was allocated to the rare-earth ion, Pr^{3+}. The presence of the faint peak at 24° is the unresolved combination of the (100) and (010) reflections. It is formed from the combination of the *ab* component and the difference between the two *z*-components of the magnetic moments on Ru^{5+} and Pr^{3+}. In Ba_2PrRuO_6 there was no *ab* component and the difference between the two *z*-components was below the sensitivity, so the peak was not observed. As there is an *ab* component in $Ba_2PrRu_{0.90}Cu_{0.10}O_6$, this increases the intensity of the (100)/(010) peak, and so this is observed in both the D1A and D1B patterns of this compound.

Having established the trial magnetic structure and using the crystal structure as determined from analysis of the D1A data at 50 K (Appendix B.6.1.2), the lattice parameters and magnetic structure were refined. The refined crystal structures from the D1A data measured at 5 K and 125 K also gave refined parameters within the experimental error of the results quoted here. This is due to the insensitivity of the D1B patterns and refinements to crystal structure changes, which were small, even when measured on D1A. The crystal structure at 50 K was chosen as ultimately all of the diffraction patterns measured using D1B from 2 K to 130 K were refined. As can be seen from Figure 5.10 the calculated profile is a good representation of the observed data, with *R*-factors of R_p = 2.32 %, R_{wp} = 3.68 % and R_{exp} = 0.80 %. The refined lattice parameters from the D1B 5 K data are a = 5.95405(14) Å, b = 5.95906(14) Å, c = 8.46670 (41) Å, β = 89.797(2)° and unit cell volume is 300.404(29) Å^3. These compare well with the D1A 5 K values of a = 5.95396(5) Å, b = 5.95892(5) Å, c = 8.46448(14) Å, β = 89.817(1)° and unit cell volume of 300.311(29) Å^3. The refined components of the magnetic moments in the *z*-direction are 1.98(18) μ_B for Ru^{5+} and 1.16(12) μ_B for Pr^{3+}, while the *ab* component was fixed at 0.65 μ_B on the rare-earth. These refined values compare very well with the D1A values of 1.98(13) μ_B for Ru^{5+} and 1.14(8) μ_B for Pr^{3+} for the magnetic moments in the *z*-direction.

All the diffraction patterns between 2 K and 130 K were refined similarly and all the results are detailed in Appendix B.6.2, with similar *R*-factors to the 5 K result. The refinement of the lattice parameters gives a unit cell volume for $Ba_2PrRu_{0.90}Cu_{0.10}O_6$ which overlays the D1A guidelines shown earlier in Figure 5.4. The refined *z*-components of the magnetic moments are of great interest and shown in Figure 5.11 for the Ru^{5+} and Pr^{3+} ions in $Ba_2PrRu_{0.90}Cu_{0.10}O_6$. Of immediate note is the high magnetic ordering temperature of *both* the Ru^{5+} and Pr^{3+} magnetic ions, which is ~ 104 K. Although the temperature resolution is not as good at the higher temperature range, it is clear that the saturation temperature is 70-80 K, and it is about the same for both the Ru^{5+} and Pr^{3+} magnetic ions. Thus, in $Ba_2PrRu_{0.90}Cu_{0.10}O_6$ the magnetic moments order over a much more extended temperature range of 25-35 K when compared to the ruthenates studied in Chapters 3 and 4. The saturated *z*-components of the magnetic moments are ~ 1.95(17) μ_B for Ru^{5+}, which is a typical value for ruthenium in this study, and 1.15(10) μ_B for Pr^{3+}, which is much below its spin-only value of 3.58 μ_B.

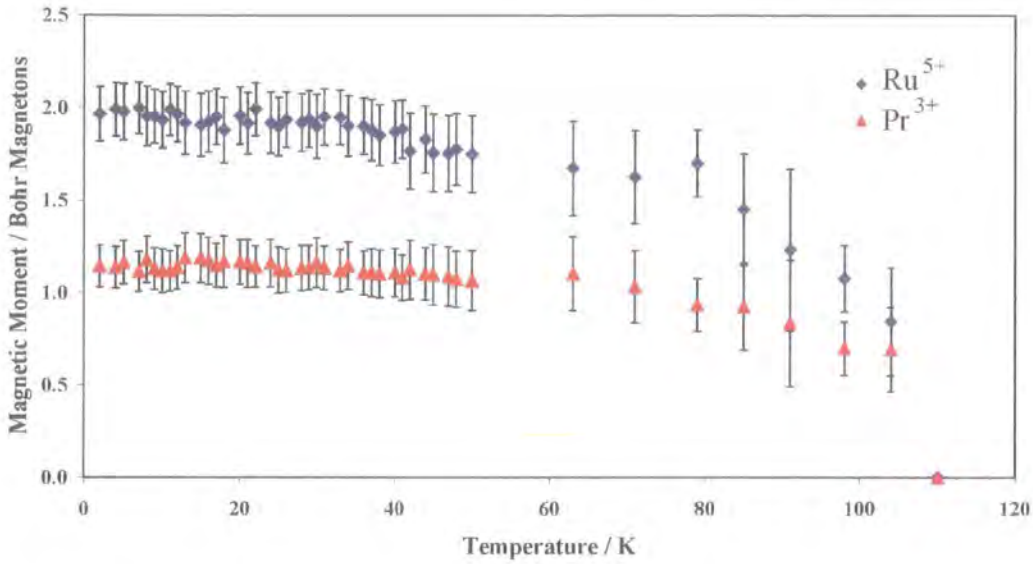

Figure 5.11 The variation with temperature of the refined magnetic moments in the *z*-direction of the Ru^{5+} and Pr^{3+} ions present in the $Ba_2PrRu_{0.90}Cu_{0.10}O_6$ material.

The results of the magnetic refinements are presented in Table 5.5, where only the *z*-component of the magnetic moment is shown. The *ab* component which was fixed at 0.6 μ_B (D1A) or 0.65 μ_B (D1B), could be distributed across the two ions in any way and so is not included in Table 5.5. Although the introduction of the copper is the cause of the *ab* component, the precise mechanism is unclear. Both the Ru^{5+} and Pr^{3+} magnetic moments remain fairly constant over the 5 K to 50 K temperature region. The refined values using the two sets of data measured using D1A and D1B are in good agreement with each other, though the D1B experiment was performed much more quickly. The errors are larger than for the other ruthenates series studied as the magnetic intensity was lower and the moment values are reasonably close to one another. There is some evidence for the magnetic moment size increasing with copper doping concentration, especially for the 5 K results. It is less clear for the 50 K measurements, though with the *ab* component only present in the $x = 0.10$ sample, it is clear that the magnetic moment per ion has to be higher in this sample.

Temperature / K	Magnetic Moment in z-direction / μ_B		
	$x = 0$ (D1A)	$x = 0.10$ (D1A)	$x = 0.10$ (D1B)
5	1.82(15) & 1.14(11)	1.98(13) & 1.14(7)	1.98(18) & 1.16(12)
50	1.66(16) & 1.08(12)	1.71(29) & 1.14(21)	1.75(23) & 1.06(16)

Table 5.5 The refined z-component of the magnetic moments of the ions, Ru^{5+} andPr^{3+}, in the $Ba_2PrRu_{1-x}Cu_xO_6$ series. The values compare the different compositions at the temperatures measured on each diffractometer. The first value listed is the Ru^{5+} magnetic moment, the second is for the Pr^{3+} ion. The *ab* component present in the $x = 0.10$ sample is not included in these values.

The magnetic structure of Ba_2PrRuO_6 has also been refined by the group of Doi and Hinatsu [5]. Their study determined the magnetic structure to be the same interpenetrating Type I magnetic structure with the moments in the z-direction. However, once again the refined moments were larger in their study at 7 K. The Ru^{5+} magnetic moment is 2.0(2) μ_B and Pr^{3+} is 2.2(2) μ_B. Although the Ru^{5+} magnetic moments are comparable, the Pr^{3+} magnetic moments are not, and to determine why, both the magnetic form factor and diffraction pattern have to be considered.

The antiferromagnetic peaks ($h + k + l$ being odd) present in the pattern all have l odd, hence the magnetic peaks only really give the sum of the moments of the Ru^{5+} and Pr^{3+} ions. The difference between these two moments must be zero within the sensitivity of the instrument, as magnetic peaks for l even are not observed. Therefore, the refinements only calculate the sum of the two moments within the constraint that the difference must be sufficiently small to be unobserved in the diffraction pattern.

As the (001), (100) and (010) magnetic peaks are not present in the diffraction pattern, the magnetic intensity is observed from the much larger angle scattering angle where $(\sin\theta)/\lambda \sim 0.132$ Å^{-1}, which are the (111), (1–11), (1-1-1) and (11-1) reflections. Therefore the required magnetic moment needed to replicate the diffraction intensity has to increase by a greater amount than before, as the Zr^+ magnetic form factor has deviated even further from the calculated Ru^{5+} magnetic form factor. At $(\sin\theta)/\lambda \sim 0.132$ Å^{-1} the Zr^+ magnetic form factor is 0.500, whereas the Ru^{5+} magnetic form factor is 0.784. If the 1.82 μ_B refined here (Table 5.5) used the Zr^+, rather than the calculated Ru^{5+} magnetic form factor, this value would scale to 2.85 μ_B. The total magnetic moment, which is what is really refined, would be 3.99 μ_B, very close to Doi's total of 4.2 μ_B. Of course, there would have to be some redistribution of the

magnetic moments to ensure that the difference between the magnetic moments on the Ru^{5+} and Pr^{3+} was not large enough to manifest as peaks in the pattern. But it is clear that the discrepancy between the refinements is due largely to the erroneous use of the Zr^+ magnetic form factor.

There are two supplementary reasons for favouring the refined values in Table 5.5 rather than those given in Doi's study [5]. Firstly, the magnetic moment of the Ru^{5+} ion is constant in all the ruthenates studied so far, as expected. Secondly, the results of the $x = 0.10$ sample support the allocation of magnetic moment between the Ru^{5+} and Pr^{3+} ions as 1.82(15) μ_B and 1.14(11) μ_B for Ba_2PrRuO_6. This is because the new measurements on $Ba_2PrRu_{0.90}Cu_{0.10}O_6$ indicate that there is an *ab* component, which is **determined** from the intensity of the (001) peak unambiguously. The (100)/(010) magnetic peak receives contributions from the difference of the *z*-components of the two magnetic moments, and the *ab* component. However, the **known** *ab* component on its own would fall below the detection level and so requires support from the difference in the *z*-components. The refinements using the $Ba_2PrRu_{0.90}Cu_{0.10}O_6$ data suggest that this extra support can be provided by a moment difference of 0.65 μ_B. As the magnetic moments of the Ru^{5+} and Pr^{3+} magnetic ions will not be too dissimilar in Ba_2PrRuO_6, this supports the case for moments of 1.82(15) μ_B and 1.14(11) μ_B respectively.

5.2.3 Magnetic Measurements on $Ba_2PrRu_{1-x}Cu_xO_6$

As there were no variable temperature neutron diffraction measurements undertaken on Ba_2PrRuO_6 using D1B, the precise ordering temperature was unknown, though from D1A measurements it falls in the range 50-150 K. The D1B studies on $Ba_2PrRu_{0.90}Cu_{0.10}O_6$ suggest a Néel temperature of 104 ± 6 K, and it is likely that the magnetic ordering temperature of Ba_2PrRuO_6 is similar. In order to clarify the magnetic ordering temperatures of the materials, magnetisation measurements were performed using a Vibrating Sample Magnetometer (VSM) with the help of Dr. Ian Terry and Mr. Sean Giblin. For both Ba_2PrRuO_6 and $Ba_2PrRu_{0.90}Cu_{0.10}O_6$ ~ 1.2 grams of powdered material were studied between 80 K and 300 K, with magnetic fields of 0.4 Tesla and 0.2 Tesla respectively.

Figure 5.12 shows the results obtained with the $Ba_2PrRu_{0.90}Cu_{0.10}O_6$ sample, and although the magnitude of the magnetisation is uncalibrated, the magnetic ordering temperature is clearly 103 ± 3 K. This is in close agreement with the 104 K

determined from neutron powder diffraction and shows that the measurements are consistently determining the ordering temperature. The Weiss constant is –181(40) K, where the negative value indicates a predominantly antiferromagnetic nature of the material, whereas the large error reflects the uncertainty due to the noisiness of the data and the small temperature range measured.

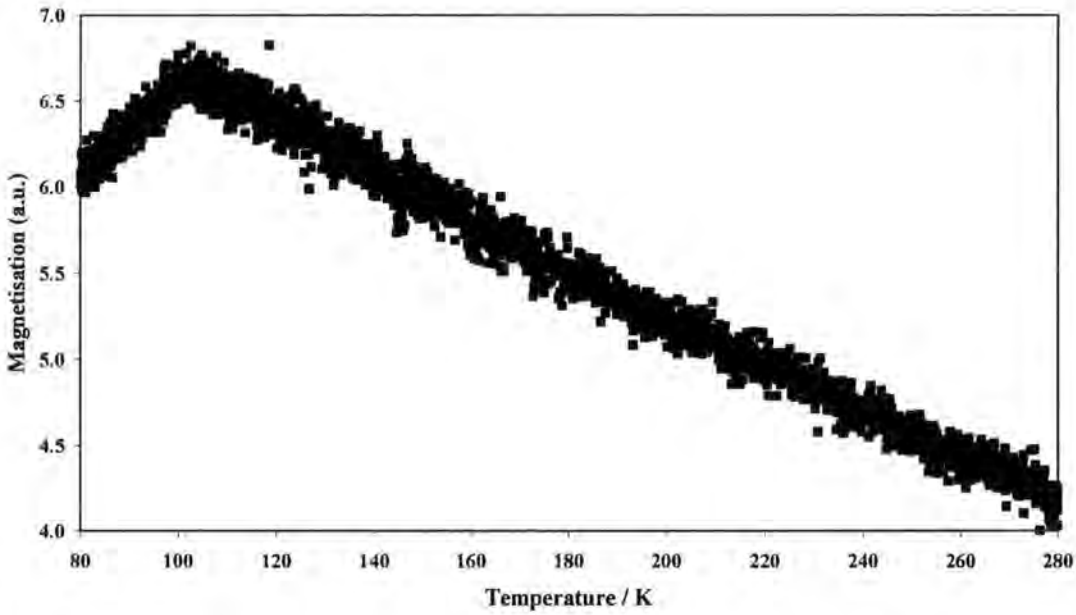

Figure 5.12 The uncalibrated magnetisation of $Ba_2PrRu_{0.90}Cu_{0.10}O_6$ measured between 80 K and 300 K.

The results for the Ba_2PrRuO_6 sample are similar and displayed in Figure 5.13, where the magnetic ordering temperature is 107 ± 5 K. The Weiss constant is again large and negative, -234(40) K, indicative of antiferromagnetism, and it is in agreement with the refined magnetic structure. These results broadly agree with the magnetic susceptibility measurements on Ba_2PrRuO_6 which determined the Néel temperature to be 117 K [5].

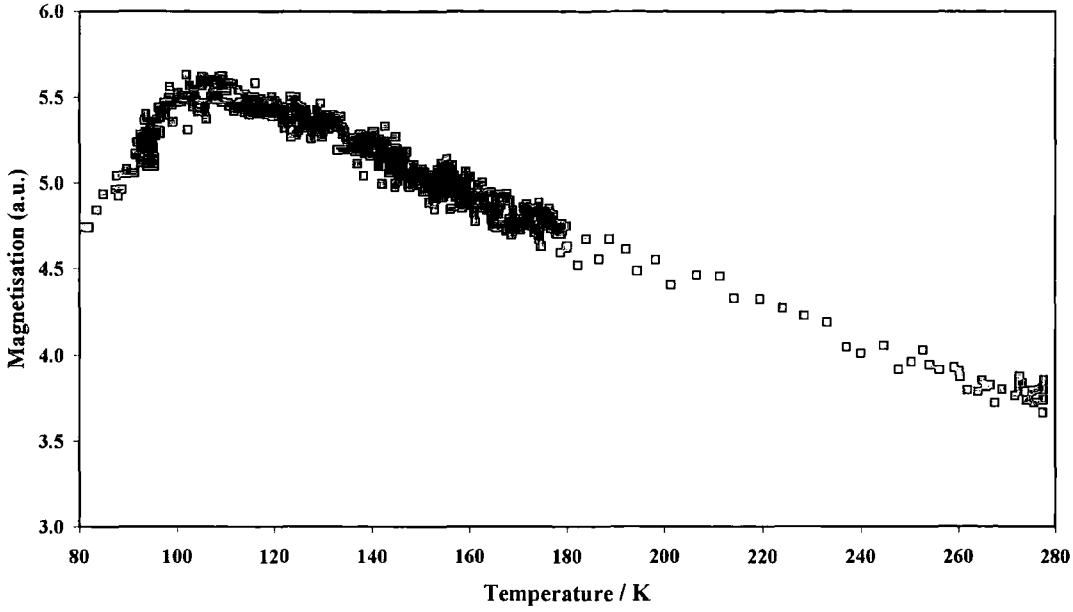

Figure 5.13 The uncalibrated magnetisation of Ba_2PrRuO_6 measured between 80 K and 300 K.

Thus, the Néel temperatures of Ba_2PrRuO_6 and $Ba_2PrRu_{0.90}Cu_{0.10}O_6$ are similar to each other, as one would expect. And although the data are not of the highest quality, they do show the salient points, that the materials are antiferromagnetic with Néel temperatures of ~ 105 K. Of all the ruthenate double perovskites studied [5, 7-23], this is by far the highest magnetic ordering temperature. The next highest is 58 K for Ba_2NdRuO_6 [18], though typically they are 30-50 K, as determined from magnetic susceptibility measurements.

5.3 Magnetic Ordering of the Two Magnetic Ion Systems

The magnetic ordering in the $Ba_2PrRu_{1-x}Cu_xO_6$ system is very interesting because of its initially dissimilar diffraction patterns and temperature dependence compared to the other ruthenates. The high Néel temperature of the materials must be reconciled with the continued adoption of the interpenetrating Type I magnetic structure, and the constancy of the saturated Ru^{5+} magnetic moment. Not only will the explanation have to serve the Ba_2PrRuO_6 series, it will have to fit in with the ideas and discussion of the ruthenates series $Sr_2YRu_{1-x}Cu_xO_6$, $Ba_2YRu_{1-x}Cu_xO_6$, $Sr_2HoRu_{1-x}Cu_xO_6$, $Sr_2TbRu_{1-x}Cu_xO_6$ and $Sr_2Ho_{1-y}Tb_yRu_{1-x}Cu_xO_6$.

In the $Ba_2PrRu_{1-x}Cu_xO_6$ series the ruthenium sublattice orders in a Type I magnetic structure with the magnetic moment of ~ 2 μ_B, just like the other ruthenate series. This indicates that the Ru-O-O-Ru interaction, which was determined to be approximately

the same strength in the ruthenates, though slightly dependent on octahedral tilting, is likely to be operating in $Ba_2PrRu_{1-x}Cu_xO_6$. This Ru-O-O-Ru interaction, when acting on its own, leads to a magnetic ordering temperature of only ~ 40 K, even in the relatively distortion-free $Ba_2YRu_{0.90}Cu_{0.10}O_6$ material. So, this intra-species ruthenium interaction on its own cannot explain the high Néel temperature of $Ba_2PrRu_{1-x}Cu_xO_6$.

In the previously discussed ruthenates of general formula, A_2LnRuO_6 , where *Ln* is a rare-earth element, the *Ln*-O-O-*Ln* interaction was always weak enough to be ignored and the Pr-O-O-Pr interaction is no exception. Besides, this Pr-O-O-Pr interaction would only order the praseodymium sublattice, which would lead to two magnetic ordering temperatures being observed, one for each sublattice, contradicting the experimental result of one coincident ordering temperature for both ions.

The remaining alternative is that the Ru-O-Pr interaction is responsible for the ordering of the praseodymium sublattice and also the high magnetic ordering temperature of the $Ba_2PrRu_{1-x}Cu_xO_6$ samples. From the neutron diffraction results, the Ru-O-Pr interaction has been shown to be ferromagnetic, as the two Type I sublattices are parallel to one another. Thus, the inter-species interaction shows variation in its nature because the Ru-O-Ho and Ru-O-Tb interactions are antiferromagnetic. Comparison of the Ho and Tb systems in Chapter 4 showed that the inter-species interaction strength could also vary significantly and as it increased the magnetic ordering temperature of the ruthenate also rose. For Sr_2TbRuO_6, where the Ru-O-Tb interaction is a factor of ~ 0.7 the strength of the Ru-O-O-Ru interaction, the increase was estimated to be from 33 K to 39 K. Clearly, the Ru-O-Pr interaction will have to be much stronger than this to be able to account for the magnetic ordering temperature of 104 K.

It was discussed in Chapter 4 how the introduction of the inter-species interaction, such as Ru-O-Pr, leads to both magnetic sublattices having a coincident ordering temperature. The Ru-O-O-Ru interaction was seen to drive the magnetic ordering in the material, and it was only as the ruthenium sublattice started to order that the Ru-O-*Ln* interaction could order the *Ln* sublattice. This explained successfully the coincident ordering temperatures of the two sublattices. Owing to the asymmetry of the beneficiaries of the magnetic interactions, Ru-O-O-Ru and Ru-O-*Ln*, the level of order present in the ruthenium sublattice could not be overtaken by the *Ln* sublattice, irrespective of the relative strengths of the two interactions. In the limit where the Ru-O-*Ln* interaction is much stronger than the Ru-O-O-Ru interaction, the two

magnetic sublattices would order at the same rate, yielding the same shape of moment with temperature curve, but allowing different magnitudes. This describes the results of the refinements for $Ba_2PrRu_{1-x}Cu_xO_6$ which were exhibited in Figure 5.11. Both the Ru^{5+} and Pr^{3+} magnetic moments order at 104 K and saturate at 70-80 K, though with ~ 1.95(17) μ_B for Ru^{5+} and 1.15(10) μ_B for Pr^{3+}. Hence, there is some basis for the idea that the Ru-O-Pr interaction is much stronger than the Ru-O-O-Ru interaction.

The strength of the Ru-O-Pr interaction cannot be increased without limit however, as the magnetic structure of the material would eventually change. In the case of the Ru-O-Pr *ferromagnetic* interaction being very much stronger than the Ru-O-O-Ru interaction, and completely dominating the magnetic structure, both the Ru^{5+} and Pr^{3+} magnetic moments would align in the same direction giving a *ferromagnetic* structure. Clearly, as an interpenetrating Type I magnetic structure is adopted in Ba_2PrRuO_6, the Ru-O-Pr interaction is not this strong. However, for the Ru-O-Pr interaction to be responsible for the high magnetic ordering temperature of Ba_2PrRuO_6, one must ensure that the strength of the Ru-O-Pr interaction is not inconsistent with the interpenetrating Type I magnetic structure. This detailed analysis has been performed and is discussed in Appendix A.6. In fact, it turns out that the interpenetrating Type I magnetic structure is surprisingly robust to strong inter-species interactions, even when only one intra-species interaction is considered. This is the Ru-O-O-Ru interaction as *Ln*-O-O-*Ln* is negligibly weak. Irrespective of the nature of the Ru-O-*M* interaction, ferromagnetic or antiferromagnetic, the interpenetrating Type I magnetic structure will be adopted provided that the Ru-O-*Ln* interaction is not greater than a factor of 4 stronger than the Ru-O-O-Ru interaction.

The Ru-O-O-Ru interaction is approximately the same strength in all the ruthenates, though it is slightly dependent on the octahedral tilting distortions of the crystal structure. For the least distorted system where only the Ru-O-O-Ru interactions are significant, $Ba_2YRu_{1-x}Cu_xO_6$, the ordering temperature is 39 K and saturates at 35 K. The interpenetrating Type I magnetic structure allows the Ru-O-*Ln* interaction to be four times as strong, so provides an estimate for the maximum magnetic ordering temperature to be ~ 160 K with saturation at 140 K. For the more typical ruthenate, $Sr_2YRu_{0.85}Cu_{0.15}O_6$, which is distorted, the ordering temperature is ~ 33 K and saturation temperature ~ 24 K. This sets the limits for a distorted double perovskite as ~ 130 K for the magnetic ordering temperature and ~ 100 K for the saturation of the moments, if the Ru-O-*Ln* interaction acts alone. The Ru-O-O-Ru interaction will raise

these values slightly, but this increase will be small, as the strongest interaction almost entirely determines the ordering temperature when there is a large difference in the two interaction strengths. For example, in Sr_2HoRuO_6, with the Ru-O-O-Ru interaction is approximately 5 times stronger than the Ru-O-Ho interaction, the ordering temperature was 34 K, whereas this is 33 K in $Sr_2YRu_{0.85}Cu_{0.15}O_6$, where there is negligible Ru-O-Y interaction.

As the magnetic ordering temperatures of the $Ba_2PrRu_{1-x}Cu_xO_6$ samples studied are ~ 105 K, this is below the limit, and so the interpenetrating Type I magnetic structure is preferred. This magnetic ordering temperature is approximately a factor of 3 larger than the typical ordering temperature of the ruthenates, when there is only the Ru-O-O-Ru interaction, as is the saturation temperature of the ruthenium sublattice. So the Ru-O-Pr interaction is a factor of 3 stronger than the Ru-O-O-Ru interaction. As indicated for Sr_2HoRuO_6 above, when there is a large difference in the interaction strengths the ordering temperature is largely determined by the stronger interaction. Thus, the ratio of ordering temperatures and saturation temperatures does give an accurate ratio of the interaction strengths, as the Ru-O-O-Ru interaction will not have raised these temperatures significantly in $Ba_2PrRu_{1-x}Cu_xO_6$. Also, as the magnetic ordering temperature and the saturation temperature are increased by a factor of 3, so will the difference between these two temperatures. This explains why the temperature difference between the onset of ordering and saturation is increased to 25-35 K in $Ba_2PrRu_{0.90}Cu_{0.10}O_6$.

The order of interactions strengths in $Ba_2PrRu_{1-x}Cu_xO_6$ is different to the other ruthenates, as Ru-O-Pr > Ru-O-O-Ru > Pr-O-O-Pr, and this is the first time that an interaction between ruthenium and a 4*f* element has been shown to be stronger than the Ru-O-O-Ru interaction. So, the order of interactions strengths as Ru-O-O-Ru > Ru-O-*Ln* > *Ln*-O-O-*Ln*, is not true in general. This does not contradict the work of Battle *et al* on Sr_2ErRuO_6 [13], where the interaction strength order is Ru-O-O-Ru > Ru-O-Er > Er-O-O-Er, as the study just referred to this one specific case.

Above the magnetic ordering temperature of ~ 105 K both the Ru^{5+} and Pr^{3+} moments are randomly orientated. As the temperature is lowered below ~ 105 K, the Ru-O-Pr interaction begins to order neighbouring Ru^{5+} and Pr^{3+} magnetic moments parallel to each other. However, as the Ru-O-Pr interaction is not the only interaction present, the Ru-O-O-Ru interaction modifies the magnetic structure which is energetically

favoured. Instead of the ferromagnetic structure, the interpenetrating Type I antiferromagnetic structure is preferred. Thus, although the Ru-O-Pr interaction is ferromagnetic, it has led to the development of an antiferromagnetic structure and enhanced its ordering temperature dramatically. By necessity, as the Ru-O-Pr is the primary driving force of the magnetic order at high temperatures, the ruthenium and praseodymium sublattices order at approximately the same rate. (The temperature resolution at high temperatures was not sufficient to observe the ruthenium sublattice to order fully at a slightly higher temperature due to the extra assistance of the Ru-O-O-Ru interaction, though this difference would have been small anyway.) The Ru^{5+} and Pr^{3+} magnetic moments progressively order, primarily due to the Ru-O-Pr interaction, until the moments saturate at 70-80 K. In summary, the Ru-O-Pr interaction drives the magnetic ordering, while the Ru-O-O-Ru interaction modifies the magnetic structure which is adopted. The scheme developed here explains for the first time the anomalously high magnetic ordering temperature in Ba_2PrRuO_6. Of course, the scheme can be extended and for Ba_2NdRuO_6 and its Néel temperature of 57 K can be explained similarly, with a Ru-O-Nd interaction approximately 1.5 times the strength of the Ru-O-O-Ru interaction. As many of the rare-earth ruthenium double perovskites have ordering temperatures of 40-50 K [5, 13, 14, 16-21, 23], the Ru-O-O-Ru and Ru-O-*Ln* interactions in these cases will be approximately equal. It is also noted that for A_2LnRuO_6 where A = Sr or Ba, the barium analogue has the higher ordering temperature [23]. From the work in this thesis (Chapter 3) this is believed to be due to the reduced tilting of the oxygen octahedra as the larger Ba allows them more space, which results in more linear Ru-O-*Ln* bonds and thus strengthening the magnetic interactions.

Thus, we have seen with just the few series studied a great variety of magnetic interactions involving the Ru^{5+} ion. Its interaction with other Ru^{5+} ions via Ru-O-O-Ru superexchange is approximately constant for all the ruthenates studied, though varies slightly depending on crystallographic distortions. Its interactions with 4*f* rare-earths, Ru-O-*Ln*, can vary in nature as they are antiferromagnetic for Ho^{3+} and Tb^{3+}, but ferromagnetic for Pr^{3+}. The interaction can vary enormously in magnitude, with Ru-O-Ho, Ru-O-Tb and Ru-O-Pr having interaction strengths of ~ 0.2, ~ 0.7 and ~ 3 times the strength of the Ru-O-O-Ru interaction. This trend across the rare-earth series should be expected because as the extent of the 4*f* orbitals increase (Pr > Tb > Ho) the overlap and magnetic interactions will increase too. The Ru-O-Pr

interaction is also stronger due to its more linear bond of 167-173°, compared to the others of 156-158°. Thus we have seen that the magnetic interactions of the Ru^{5+} ion with other species, particular 4*f* rare-earths, are varied and extremely interesting.

5.4 Conclusions

From neutron powder diffraction experiments, Ba_2PrRuO_6 and $Ba_2PrRu_{0.90}Cu_{0.10}O_6$ have been shown to both adopt the 2116 structure of a double perovskite. The crystal structures did not vary greatly with temperature or copper doping. Although there were small amounts of impurities present, these are not superconducting, and should superconductivity be confirmed in the materials it could be unambiguously attributed to the $Ba_2PrRu_{1-x}Cu_xO_6$ phase.

Magnetic measurements confirmed the Néel temperatures to be 107 ± 5 K for Ba_2PrRuO_6 and 103 ± 3 K for $Ba_2PrRu_{0.90}Cu_{0.10}O_6$. The magnetic ordering temperature for the copper doped sample was confirmed by neutron powder diffraction as 104 ± 6 K, in agreement with the above value. These ordering temperatures are higher than the ordering temperatures reported for any other ruthenate double perovskites and this was explained by the strength of the Ru-O-Pr interaction. Although the Ru-O-Pr interaction is ferromagnetic, the $Ba_2PrRu_{1-x}Cu_xO_6$ series still adopts an interpenetrating Type I arrangement of the ruthenium and praseodymium sublattices. This can be explained as although the Ru-O-Pr interaction is a factor of ~ 3 stronger than the Ru-O-O-Ru interaction, and is the driving force for long-range magnetic order, the Ru-O-O-Ru modifies the energy balance slightly so that the interpenetrating Type I magnetic structure is preferred. This hypothesis can also be applied to other ruthenate double perovskites with high magnetic ordering temperatures.

Ba_2PrRuO_6 adopts a magnetic structure with each sublattice of Ru^{5+} and Pr^{3+} ions arranged in a Type I antiferromagnetic arrangement, with moments of 1.82(15) μ_B and 1.14(11) μ_B at 5 K respectively. The two sublattices are parallel to each other, indicating a ferromagnetic Ru-O-Pr interaction, with the magnetic moments orientated in the *c*-direction. In $Ba_2PrRu_{0.90}Cu_{0.10}O_6$ the magnetic structure is very similar, with a small *ab* component of ~ 0.6 μ_B being introduced by the copper doping, though it cannot be unambiguously assigned to any particular magnetic ion. The *z*-components of magnetic moments at 5 K are 1.98(13) μ_B and 1.14(7) μ_B for Ru^{5+} and

Pr^{3+} respectively. Thus there is some evidence that the small increase in magnetic moment with copper doping is borne by the Ru^{5+} ion, but owing to the uncertainty of the allocation of the *ab* component, an increase in the Pr^{3+} moment cannot be ruled out conclusively.

The $Ba_2PrRu_{1-x}O_6$ series potentially can provide tremendous support for the argument of superconductivity in the mixed ruthenium-copper double perovskites. But, also it has provided a wonderful opportunity to examine the interactions between the Ru^{5+} and Pr^{3+} ions, which has also tested the previous framework used to explain the magnetic ordering in the $Sr_2YRu_{1-x}Cu_xO_6$, $Ba_2YRu_{1-x}Cu_xO_6$, $Sr_2HoRu_{1-x}Cu_xO_6$, $Sr_2TbRu_{1-x}Cu_xO_6$ and mixed $Sr_2Ho_{1-y}Tb_yRu_{1-x}Cu_xO_6$ systems.

5.5 References

1 C.H. Booth, F. Bridges, J.B. Boyce, T. Claeson, Z.X. Zhao and P. Cervantes, *Physical Review B* **49,** 3432 (1994).

2 M. Luszczek, W. Sadowski, T. Klimczuk, J. Olchowik, B. Susla and R. Czajka, *Physica C* **322,** 57 (1999).

3 M.K. Wu, B.H. Mok, M.J. Wang, D.C. Yuan, S.M. Rao, P.D. Hatton and N.G. Parkinson, *Journal of Low Temperature Physics* **131,** 1053 (2003).

4 A.C. Larson and R.B. Von Dreele, *Los Alamos National Laboratory Report* **LAUR 86-748,** 1 (1990).

5 Y. Izumiyama, Y. Doi, M. Wakeshima, Y. Hinatsu, Y. Shimojo and Y. Morii, *Journal of Physics-Condensed Matter* **13,** 1303 (2001).

6 http://www.ill.fr/dif/ccsl/ffacts/ffactnode7.html

7 R. Greatrex, N.N. Greenwood, M. Lal and I. Fernandez, *Journal of Solid State Chemistry* **30,** 137 (1979).

8 I. Fernandez, R. Greatrex and N.N. Greenwood, *Journal of Solid State Chemistry* **32,** 97 (1980).

9 P.D. Battle, J.B. Goodenough and R. Price, *Journal of Solid State Chemistry* **46,** 234 (1983).

10 P.D. Battle and W.J. Macklin, *Journal of Solid State Chemistry* **52,** 138 (1984).

11 P.D. Battle and C.W. Jones, *Journal of Solid State Chemistry* **78,** 108 (1989).

12 P.D. Battle, T.C. Gibb, C.W. Jones and F. Studer, *Journal of Solid State Chemistry* **78,** 281 (1989).

13 P.D. Battle, C.W. Jones and F. Studer, *Journal of Solid State Chemistry* **90,** 302 (1991).

14 Y. Doi and Y. Hinatsu, *Journal of Physics-Condensed Matter* **11,** 4813 (1999).

15 K.P. Hong, Y.H. Choi, Y.U. Kwon, D.Y. Jung, J.S. Lee, H.S. Shim and C.H. Lee, *Journal of Solid State Chemistry* **150,** 383 (2000).

16 Y. Doi, Y. Hinatsu, K. Oikawa, Y. Shimojo and Y. Morii, *Journal of Materials Chemistry* **10,** 797 (2000).

17 Y. Doi, Y. Hinatsu, K. Oikawa, Y. Shimojo and Y. Morii, *Journal of Materials Chemistry* **10,** 1731 (2000).

18 Y. Izumiyama, Y. Doi, M. Wakeshima, Y. Hinatsu, K. Oikawa, Y. Shimojo and Y. Morii, *Journal of Materials Chemistry* **10,** 2364 (2000).

19 Y. Doi, Y. Hinatsu, K. Oikawa, Y. Shimojo and Y. Morii, *Journal of Alloys and Compounds* **323,** 455 (2001).

20 Y. Izumiyama, Y. Doi, M. Wakeshima, Y. Hinatsu, A. Nakamura and Y. Ishii, *Journal of Solid State Chemistry* **169,** 125 (2002).

21 T.P. Papageorgiou, T. Herrmannsdorfer, R. Dinnebier, T. Mai, T. Ernst, M. Wunschel and H.F. Braun, *Physica C* **377,** 383 (2002).

22 N.G. Parkinson, P.D. Hatton, J.A.K. Howard, C. Ritter, F.Z. Chien and M.K. Wu, *Journal of Materials Chemistry* **13,** 1468 (2003).

23 Y. Doi, Y. Hinatsu, A. Nakamura, Y. Ishii and Y. Morii, *Journal of Materials Chemistry* **13,** 1758 (2003).

6 Anomalous Scattering Measurements

6.1 Introduction

The ordering of the *B* cations in the $A_2B'B''O_6$ systems is important due to their effect on the magnetic structure. For a long-range magnetic structure to develop in a material there must be a high degree of ordering of the *B* cations as was discussed extensively in Chapter 1. In the systems examined here, there may be two or three *B* cations depending on whether copper has been added as a dopant. In the parent compounds, those with *no* copper doping for instance Sr_2TbRuO_6, an ordered *B* arrangement of cations has all the Tb on the 2*c* site, and all the Ru on the 2*d* site as in Figure 6.1. From previous discussions one would expect the large Tb^{3+} and small Ru^{5+} ions to occupy different *B* sites and allow a magnetic structure to develop.

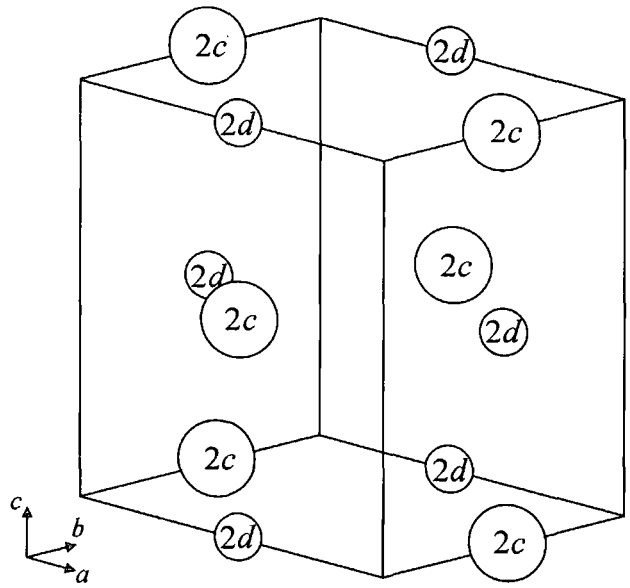

Figure 6.1 Unit cell of Sr_2TbRuO_6, which has an ordered 1:1 arrangement of *B* cations with all the Tb (large circles) on the 2*c* site and all the Ru on the 2*d* site (small circles). Only the *B* cations are shown for clarity.

In the mixed systems, such as $Sr_2TbRu_{0.90}Cu_{0.10}O_6$, the ordered arrangement is defined as having all the Tb on the 2*c* site while all the Ru and Cu share the 2*d* site. Here there is less certainty, although the Tb^{3+} and Ru^{5+} will once again occupy principally different sites, the addition of copper probably in the +2 or +3 state, leads to some ambiguity. The location of the 10 % copper will affect the magnetic interactions within any sublattice into which it is imbedded. Although unlikely to prohibit magnetic structure development, it can lead to modifications of magnetic structure

development. This was observed in both the magnetic moment magnitude and ordering temperature of the materials varying with copper doping content.

The location of the copper is not just a concern for the magnetic structure as copper doping induces superconductivity in the system. The location of the copper could be critical for a superconducting theory which has to be developed to explain the properties of these materials. Alternatively the copper may just introduce holes into the structure and be of a reasonable size to dope efficiently into the ruthenate material. In this case superconductivity could be observed in a range of 2116 mixed ruthenium-copper samples with the copper location varying extensively from material to material.

This chapter will report an attempt to determine the *B* cation ordering in the materials in order to clarify the effect on both the magnetic structure and any restrictions this imposes on any superconducting theory for the materials.

6.2 Which peaks determine the ordering of the B cations?

For the 1:1 ordered double perovskite $A_2B'B''O_6$, the *B'* ions occupy the 2*c* site and the *B''* ions the 2*d* site. In a disordered material a percentage of *B'* and *B''* ions exchange site location and this defines the level of disorder. It is the aim of this chapter to determine this disorder for the systems under study. In order to do this it is important to know which peaks in the diffraction pattern help determine this disorder level most easily, to aid both experimental planning and data analysis.

The *B* cations occupy crystallographic sites which are very similar, and so all contribute to the same reflections together. In Appendix A.1 there is a proof which shows that the *B* cations contribute in two ways to the structure factor F_{hkl}. There are reflections which involve the summation of the scattering factors of the *B* cations on the 2*c* and 2*d* sites. There are also reflections which involve the difference of the scattering powers on the 2*c* and 2*d* sites. These reflections conditions are summarised in Table 6.1 and in practice, due to the similarity of the lattice parameters usually *many* reflections of the *same* type contribute to *one* peak in the diffraction pattern.

Type of Reflection	h and k	l
Summation	$h + k$ = even	l = even
Difference	$h + k$ = odd	l = odd

Table 6.1 Reflection conditions for the contribution of the *B* cations.

The intensity of a summation peak, I_{sum}, is given by $I_{sum} = A^2(\Sigma f_{2c} + \Sigma f_{2d})^2$ where A is a constant of proportionality, and Σf_{2c} and Σf_{2d} are the total scattering factors on the $2c$ and $2d$ sites respectively. The intensity of a difference peak, I_{ord}, is given by $I_{ord} = A^2(\Sigma f_{2c} - \Sigma f_{2d})^2$. The summation peaks determine whether the sites are fully occupied while the difference peaks indicate the level of disorder in the material. Exchange of *B* cations between the $2c$ and $2d$ sites will not change the total scattering factor, hence the summation peaks will remain unchanged. However the balance of scattering factors on the $2c$ and $2d$ sites will change and this will be reflected in modified intensities of the difference peaks. These peaks are necessarily among the smaller peaks in the diffraction pattern as their intensity is related to the difference of the scattering factors of the two sites. Hence determining the level of disorder in the material involves gauging correctly the level of intensity of some of the weakest peaks.

6.3 Strategy

6.3.1 Why can't the problem be solved by neutron diffraction?

The reason the neutron diffraction patterns could not be of use in determining the disorder of the *B* cations in the materials is twofold. Firstly, neutron sources have a relatively low incident beam flux (certainly when compared with synchrotron X-ray facilities) and hence determining small structural features from weak diffraction peaks will subject the result to greater error due to reduced counting statistics. Secondly, the neutron scattering lengths [1] of the elements on the *B* sites are remarkably similar as shown in Table 6.2. Thus the intensities of the neutron diffraction patterns are relatively similar whatever the *B* cation compositions of the $2c$ and $2d$ sites, given this choice of elements. This is especially true of the difference peaks which will be very small and therefore could not be used to determine this level of *B* ordering accurately.

Element	Scattering Length / fm
Ru	7.21 (7)
Cu	7.718(4)
Y	7.75(2)
Tb	7.38(3)
Ho	8.08(5)

Table 6.2 Table of neutron scattering lengths of the *B* cations in the systems studied.

Thus neutron powder diffraction patterns are insensitive to the composition of the 2*c* and 2*d* sites. So the diffraction profile is largely left unchanged by the choice of refining the crystal model as fully ordered structures (rather than a disordered variant) in the previous chapters.

6.3.2 The case for X-ray diffraction

The similarity of neutron scattering lengths was the most important factor in the failure of the neutron diffraction patterns to be used to determine the precise composition between the *B* sites. However the X-ray scattering factor is directly related to the number of electrons of the atom and is shown explicitly for the elements under study in Table 6.3.

Element	Scattering Factor $(\sin\theta)/\lambda = 0$
Ru	44
Cu	29
Y	39
Tb	65
Ho	67

Table 6.3 X-ray scattering factors for the elements which occupy the *B* sites.

There is a far greater variation between the different scattering powers of these particular elements for X-ray rather than neutron scattering. The difference peaks with intensity, $I_{ord} = A^2(\Sigma f_{2c} - \Sigma f_{2d})^2$, will have increased intensity due to the greater difference of the scattering factors of the contributing atoms. (Though the compositions on each site could lead to a balance of scattering power on each site,

most easily visualised by half the atoms of each type on each *B* site, in practice they do not balance and large difference peak intensities are observed.)

In addition to the large peak intensities of the difference peaks expected, the large variation in scattering power of the relevant elements will lead to these peaks being sensitive to their composition. For instance, in the case of Sr_2TbRuO_6 with full ordering of the *B'* and *B"* ions, there is 100 % Tb on the 2*c* site and 100 % Ru on the 2*d* site. Hence there is a large difference in the scattering powers on the two sites leading to a large peak intensity. Here $I = A^2[(65 \times 1.00)-(44 \times 1.00)]^2 = 441A^2$, but for a 5 % disorder $I = A^2[(65 \times 0.95 + 44 \times 0.05)-(44 \times 0.95 + 65 \times 0.05)]^2 = 357.21A^2$, a decrease to just 81 % of the former peak intensity. Clearly the large difference in scattering powers between the *B* cations is not only beneficial for the peak intensity, but also for its sensitivity, which will be useful when determining the precise atomic distribution amongst the *B* sites, particularly when the differences are rather small.

6.3.3 How many X-ray diffraction patterns will be required?

For a double perovskite with only two *B* cations, $A_2B'B''O_6$, assuming that there is full occupancy of the two *B* sites there is only one unknown quantity, the amount of disordered *B'* (and identically the amount of disordered *B"*), and so only one diffraction pattern is required. This can be illustrated with the occupancies of the 2*c* and 2*d* sites using the example of Sr_2TbRuO_6.

For the 100 % ordered structure, the occupancies of each site are: -

	Site 2*c*	Site 2*d*
Tb	1	0
Ru	0	1
Total	1	1

For a disordered structure, the occupancies of each site are: -

	Site 2*c*	Site 2*d*
Tb	$1 - \Delta w$	Δw
Ru	Δw	$1 - \Delta w$
Total	1	1

One can clearly see that there is only one parameter in this problem, namely Δw, which is the disorder of either of the two ions, and due to full site occupancies is the same in each case. This can be modelled as the free parameter to give the intensity of the ordering peaks, where the intensity of the ordering peaks will be given by $I_{ord} = f(\Delta w)$, and hence only one diffraction pattern is required.

For a mixed ruthenium-copper system there are three B cations spread over two crystallographic sites, namely a rare earth, ruthenium and copper. The number of diffraction patterns required will be illustrated with the case of $Sr_2TbRu_{1-x}Cu_xO_6$. The occupancy of Tb on site 2*c* is 1, though for reasons that will become clear this will be expressed in two parts u and v, with $u + v = 1$.

For the 100 % ordered structure, the occupancies of each site are: -

	Site 2*c*	Site 2*d*
Tb	u	0
Ru	0	$(1-x)$
Tb	v	0
Ru	0	x
Total	$u + v = 1$	1

For a disordered structure, the occupancies of each site are: -

	Site 2*c*	Site 2*d*
Tb	$u - \Delta u$	$0 + \Delta u$
Ru	$0 + \Delta u$	$(1 - x) - \Delta u$
Tb	$v - \Delta v$	$0 + \Delta v$
Ru	$0 + \Delta v$	$x - \Delta v$
Total	$u + v = 1$	1

In this case the disordered structure is defined by the disorder of the Ru, Δu, and the Cu disorder which is Δv. The Tb disorder (which is ***not*** an ***independent*** parameter) is given as the sum $\Delta u + \Delta v$. As there are now two unknown parameters, Δu and Δv, which determine the intensity of the ordering peak, one diffraction pattern will not provide enough information to determine these quantities. However a second

diffraction pattern with different scattering factors would provide a second intensity level to be modelled (using the same crystal structure) and thus the problem can be solved, as there are two unknown parameters and two known intensity levels, hence two equations. Hence the intensity levels of the ordering peaks in the two diffraction patterns, I_1 and I_2, which are given by $I_1 = f(\Delta u, \Delta v)$ and $I_2 = g(\Delta u, \Delta v)$ allow the disorder levels Δu and Δv to be determined uniquely. Therefore two X-ray diffraction patterns are required, each with a different set of scattering factors of the *B* elements, so that two radically different diffraction intensities of the ordering peaks, I_1 and I_2 can be obtained.

Clearly the problem can be extended and in general, *N* types of *B* cations require *(N-1)* diffraction patterns with different scattering factors for each.

6.3.4 The need for a synchrotron source

For the parent compounds (e.g. Sr_2TbRuO_6), which only have two types of *B* cation (Tb and Ru) only one X-ray diffraction pattern is required. As such the experiment can be performed using a laboratory based X-ray diffractometer provided the elements have reasonably different scattering factors and the intensities are sufficient to allow *accurate* ordering level refinement.

The situation is more complicated for mixed ruthenium-copper systems as two different sets of scattering factors must be provided. Normally these two patterns could be provided by an X-ray and a neutron diffraction pattern used in combination to determine the ordering in a mixed system. Unfortunately in these systems, all the neutron scattering lengths are similar for the *B* cations under study, hence the neutron diffraction pattern provides little additional information on the ordering. Thus, although standard X-ray diffraction can provide one pattern, this is insufficient to solve the ordering problem.

However anomalous X-ray diffraction experiments can be used to provide patterns utilising different scattering factors, thus enabling the problem to be solved. In an anomalous diffraction experiment the incident energy is selected such that it is close to an absorption edge of an element in the material. This radiation can be absorbed by the element and an electron is promoted to a higher energy level. In some of the atoms the electron will return to its initial state by the reverse process with the emission of the photon with the same energy as the incident energy. This emission may be at any angle with respect to the incident beam and can lead to a count on the diffraction

pattern. However the energy may be permanently absorbed or the electron may relax back by a succession of transitions, releasing photons of different and lesser energy as it does so. As this energy will be of a different wavelength to the incident wavelength this would not affect any diffraction pattern in a coherent way. Clearly as some of the incident radiation is lost to other processes when scattering from the element of the absorption edge, this means its effective scattering factor is reduced. Hence, the use of anomalous scattering with the incident energy tuned to the wavelength of one of the elements provides a different set of scattering factors. This can be used as a second diffraction pattern in order to determine the *B* cation ordering in the mixed systems.
The incident energy has to be close to the absorption edge of one of the *B* cation elements for a different scattering factor to result. This requires a source of X-rays where the incident energy, and hence wavelength, can be tuned to such an edge. This clearly requires the use of a synchrotron facility where the incident energy be tuned. Also much higher intensities are available which will be particularly important for this problem as the weakest peaks in the diffraction pattern are being studied because their intensity level ultimately enables the extent of the disorder to be calculated. Ideally the edges of all the *B* cations should be attainable so that more diffraction patterns can be collected with more different sets of scattering factors, allowing confirmation of the result.

6.4 Non-anomalous Data Collections at the ESRF

The greatest interest in the problem was to determine the location of the copper atoms in the crystal structure. It was expected that were there to be any disorder in the samples, this disorder would be greatest and hence easiest to detect in the highest copper doped samples available. Thus, the samples $Sr_2YRu_{0.85}Cu_{0.15}O_6$, $Sr_2HoRu_{0.85}Cu_{0.15}O_6$, $Sr_2TbRu_{0.90}Cu_{0.10}O_6$ and $Sr_2Ho_{0.8}Tb_{0.2}Ru_{0.90}Cu_{0.10}O_6$ were chosen to be examined at the ESRF, Grenoble, France on station BM1B. Initial diffraction patterns were collected at a non-anomalous wavelength (well away from the edges of any of the elements in the material) to determine the approximate level of disorder in the sample. Of course, measuring only one diffraction pattern for each sample would not be able to determine the exact composition or nature of the disorder (whether it was 8 % ruthenium disorder, 8 % copper disorder, or anywhere in between such as 5 % ruthenium and 3 % copper disorder.) But an indication would be given as to which system would be the best to examine by anomalous diffraction.

A description of the diffractometer BM1B at the ESRF is given in Chapter 2 and only those points which are supplementary to that discussion will be mentioned here. Approximately 0.15 g of material was loaded into 0.05 cm capillary tubes and a wavelength of ~ 0.5 Å was used to study each material. Diffraction patterns were collected from 2.524 to 75.484° in 2θ with a resolution of 0.004° with the data collection typically taking half a day. This yielded full diffraction patterns of both high resolution and high intensity. Since a large angular range was measured with quite a short wavelength (to minimise absorption), the crystal structure could be determined very accurately as the data extended to $\sin\theta/\lambda \sim 1.22$ Å^{-1}. The experiments were performed at room temperature and were all conducted by Dr. Philip Pattison, the instrument scientist at BM1B.

6.4.1 $Sr_2TbRu_{0.90}Cu_{0.10}O_6$

A diffraction pattern of $Sr_2TbRu_{0.90}Cu_{0.10}O_6$ was collected and the structure was refined in space group $P2_1/n$ which allows ordering of the *B* cations in a 1:1 arrangement. Initially 100 % ordering of the *B* cations was assumed with Tb on the 2*c* site and Ru and Cu on the 2*d* site. An accurate crystal structure was refined without bias from the degree of ordering that was assumed because the ordering peaks were excluded from the refinement at this stage. The full diffraction pattern is shown in Figure 6.2 and the crystal structure refined with the ordering peaks excluded is given in Table 6.4. The large difference in the magnitude of the intensities between the sum (e.g. ~ 9.9°, 14.0°, 17.2°) and difference peaks (some are arrowed) is clear to see, hence the strongest ordering peaks are also shown enlarged. The first of these peaks is composed of the (0 1 1), (1 0 -1) and (1 0 1) reflections and the second of the (1 2 –1), (1 0 –3), (1 2 1), (2 1 –1), (0 1 3), (2 1 1) and (1 0 3), obeying the difference peak rule of $(h + k)$ and l both odd, as shown in Table 6.1.

The refinement profile in general is quite good indicating that the crystal structure is well described by the model, which is reasonably similar to that used for the neutron diffraction. The oxygen atom fractional coordinates have a much larger error associated with them than the strontium atom due to the X-ray scattering factor being much smaller for oxygen.

However as can been seen from the magnified ordering peaks (Figure 6.2), the intensities of these peaks are grossly overestimated and contribute significantly to the

residual *R*-factors. This is not surprising as the ordering peaks were excluded in the refinement of the crystal structure although are included in the plot.

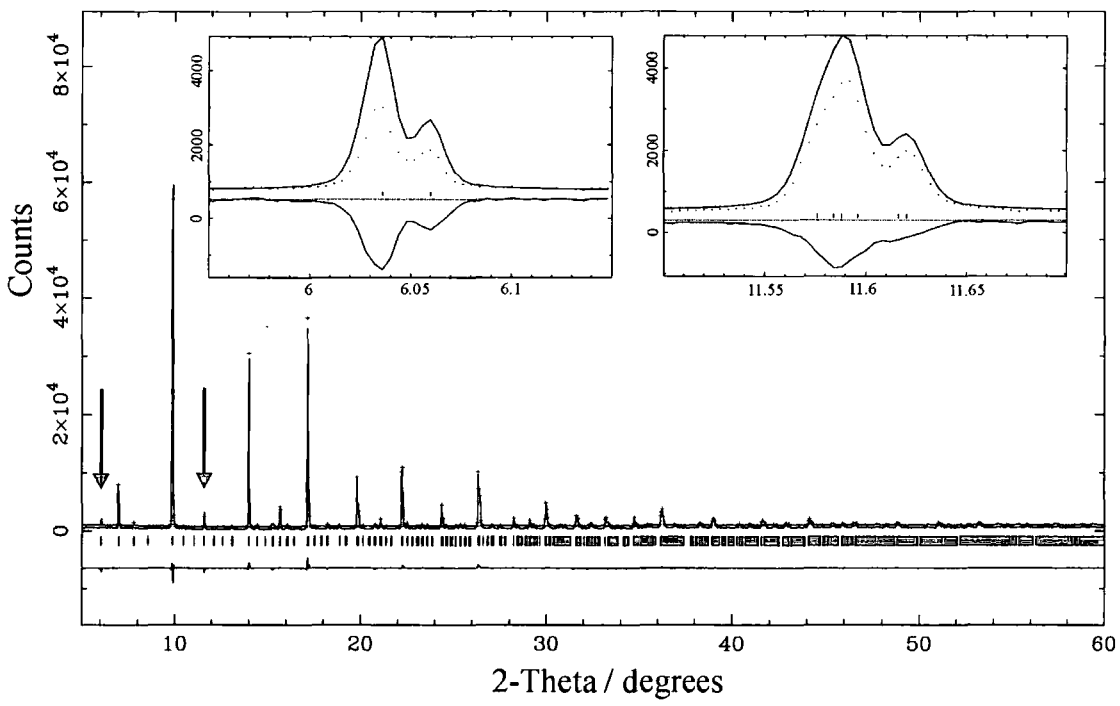

Figure 6.2 The diffraction pattern of $Sr_2TbRu_{0.90}Cu_{0.10}O_6$ measured at room temperature at BM1B of the ESRF. The data points are indicated by crosses, the diffraction profile and difference curve by lines. Tick marks indicate the calculated reflection positions. 100 % ordering of *B* cations was assumed and the two principal ordering peaks are indicated by arrows and are shown enlarged in the two insets.

$Sr_2TbRu_{0.90}Cu_{0.10}O_6$		$P2_1/n$			Room temperature	
a / Å		*b* / Å	*c* / Å	*β* / °	Volume / Å^3	
5.79773(4)		5.81657(4)	8.20683(5)	90.245(1)	276.756(2)	
Atom	Site	*x*	*y*	*z*	Occ	B_{iso}/Å^2
Sr	4*e*	0.0021(4)	0.0301(1)	0.7518(4)	1.000(0)	2.23(2)
Tb	2*c*	0	½	0	1.000(0)	1.61(1)
Ru	2*d*	½	0	0	0.900(0)	1.61(1)
Cu	2*d*	½	0	0	0.100(0)	1.61(1)
O1	4*e*	0.2761(20)	0.2955(18)	0.5312(15)	1.000(0)	1.98(19)
O2	4*e*	0.2066(21)	-0.2198(20)	0.5348(14)	1.000(0)	2.29(17)
O3	4*e*	-0.0795(20)	0.4820(9)	0.7400(13)	1.000(0)	2.32(17)

R_p = 3.59 %, R_{wp} = 4.99 %, R_{exp} = 3.23 %, R_{F^2} = 11.21 %

Table 6.4 The lattice parameters and atomic coordinates of $Sr_2TbRu_{0.90}Cu_{0.10}O_6$ as refined from the BM1B data assuming a 100 % ordering of the *B* cations.

An additional refinement of the crystal structure was performed including the ordering peaks and this resulted in changes of atomic coordinates by ~ 10σ. However there was only a small improvement in the *R*-factor and the profile was very similar to that shown in Figure 6.2, even at the ordering peaks. This is because the strontium and oxygen displacements only contribute ~ 10-20 % of the peak intensity of the ordering peaks. So even with the relatively large changes in their atomic coordinates of ~ 10σ the ordering peaks were still grossly overestimated, hence slight adjustments of the crystal structure cannot correct for this. As the change in the coordinates is trying to compensate falsely for the deficiency in the ordering level, these new coordinates are likely to give a less accurate crystal structure.

The major problem with the diffraction profile is the gross overestimation of intensities for the ordering peaks due to the assumption of 100 % *B* cation ordering. This is because the scattering factor of Tb is greater than that of Ru and Cu and so the difference in scattering factors on the 2*c* and 2*d* sites is maximised in the 100 % ordered arrangement. Therefore the actual *B* cation ordering level must be somewhat less than 100 %, if it is in fact ordered at all.

To determine whether there was any ordering of the *B* cations the data were refined with the same model structure as listed in Table 6.4 (above) except no ordering of the *B* cations was assumed. This was achieved by placing half of the Tb, Ru and Cu on the 2*c* and half on the 2*d* site. In this case, any ion had an equal chance of being on either site so that there was a random arrangement of *B* cations as discussed in Chapter 1. The resultant diffraction profile (Figure 6.3) is broadly similar, but the most significant changes take place at the ordering peaks, of which the two principal peaks are highlighted. There the intensity is greatly reduced and the small residual intensity that remains is due to the displacement of the strontium and oxygen atoms away from ideal perovskite positions, resulting in the distortion of the oxygen octahedra, that is observed in all these compounds. This anion contribution is about 10-20 % of the peak intensity as mentioned previously, and changes of these atomic coordinates result in changes on a scale smaller than this.

In some papers [2] conclusions have been drawn concerning *B* cation ordering in double perovskites based upon the observation of intensity at the ordering peak positions. Figure 6.3 illustrates that the observation of a small intensity at the ordering peak positions does not in all cases imply ordering of the *B* cations, it could simply be due to the anion displacements.

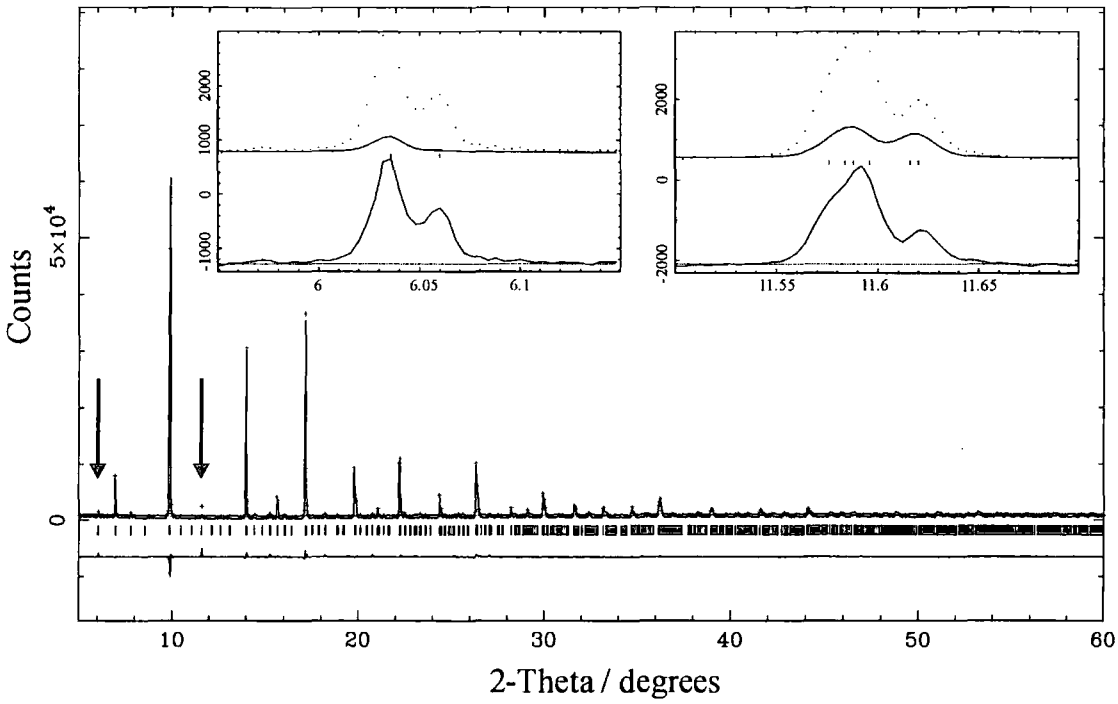

Figure 6.3 The diffraction pattern of $Sr_2TbRu_{0.90}Cu_{0.10}O_6$. The model structure was refined with a random arrangement of *B* cations. The change in the diffraction profile is most evident in the principal ordering peaks highlighted. The *R*-factors are R_p = 4.01 %, R_{wp} = 6.66 % and R_{exp} = 3.23 %.

Clearly in this case, the diffraction intensity of these peaks is severely underestimated and this indicates that there is *B* cation ordering to a certain extent. Comparison of both the diffraction profiles and the *R*-factors for the 100 % ordered and completely disordered cation arrangements, indicates that the ordered system is the better of the two. This simple analysis suggests that the actual arrangement, although not fully ordered is likely to be highly ordered.

With the fully ordered *B* cation arrangement, the ordering peaks were overestimated as shown in Figure 6.2. This is because the scattering factor of Tb is greater than that of Ru and Cu and so the difference in scattering factors on the 2*c* and 2*d* sites is maximised in the 100 % ordered arrangement. Partial exchange of Tb from the 2*c* to the 2*d* site and either Ru (or Cu) in the reverse direction would reduce the difference in scattering factors between the two sites, thereby reducing the ordering peak intensities. Any diffraction peaks involving the sum of scattering factors on both the 2*c* and 2*d* sites remain unaffected as the total scattering factor is unchanged.

With the introduction of the ordering peaks into the refinement, the partial exchange of Tb and Ru between the 2*c* and 2*d* sites was allowed and this result is illustrated in Figure 6.4. The crystal structure (Table 6.5) is virtually unchanged from the refinement with 100 % ordering of the *B* cations, the atomic coordinates of strontium and oxygen only changing by ~ 3σ. This indicated that the ordering level is largely independent of the rest of the crystal structure. The refined diffraction profile models very well the experimental data and there is no major discrepancy between the two, with the *R*-factors significantly improved. The degree of disorder involves an 11.3 ± 0.2 % exchange of Ru and Tb between the two sites so the material is still a highly ordered system. As can be evidenced from the most intense ordering peaks, this is sufficient to model very well the observed diffraction intensity.

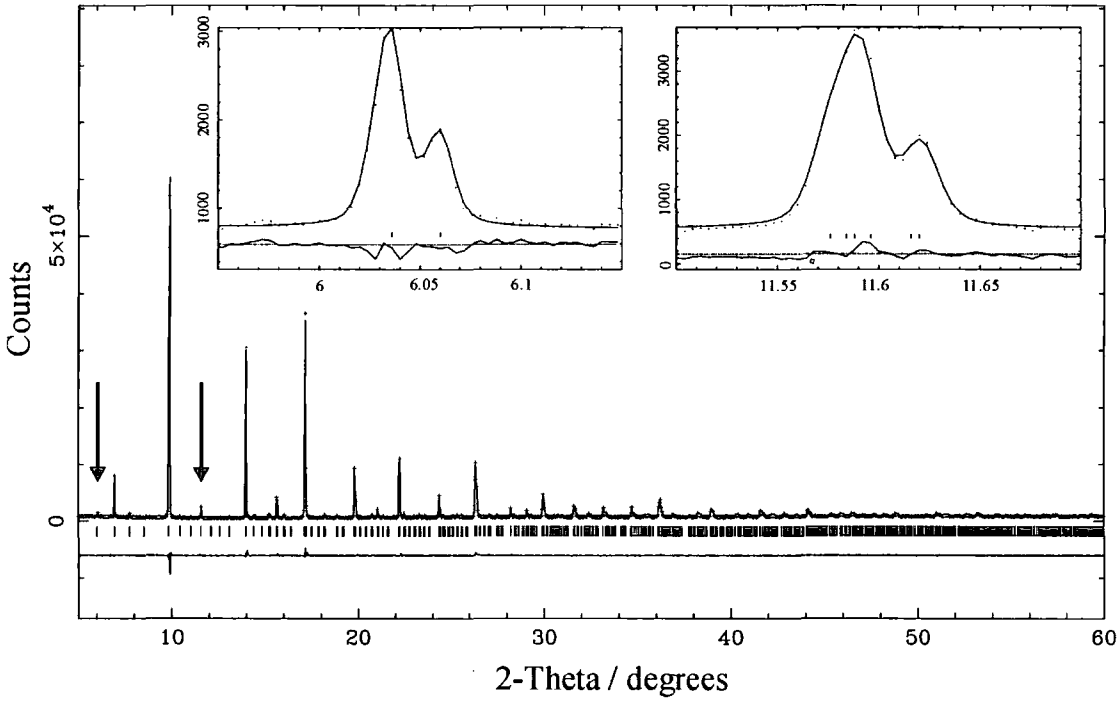

Figure 6.4 The diffraction pattern of $Sr_2TbRu_{0.90}Cu_{0.10}O_6$. The refinement allowed partial exchange of Tb with Ru between the 2*c* and 2*d* sites. The most intense ordering peaks are shown explicitly in the insets.

$Sr_2TbRu_{0.90}Cu_{0.10}O_6$		$P2_1/n$			Room temperature	
a / Å		b / Å	c / Å	β / °	Volume / Å^3	
5.79769(4)		5.81659(4)	8.20683(5)	90.245(1)	276.755(2)	
Atom	Site	x	y	z	Occ	B_{iso}/Å^2
Sr	4*e*	0.0049(3)	0.0295(1)	0.7497(3)	1.000(0)	2.23
Tb	2*c*	0	½	0	0.887(2)	1.61
Ru	2*c*	0	½	0	0.113(2)	1.61
Tb	2*d*	½	0	0	0.113(2)	1.61
Ru	2*d*	½	0	0	0.787(2)	1.61
Cu	2*d*	½	0	0	0.100(0)	1.61
O1	4*e*	0.2688(14)	0.2985(14)	0.5361(12)	1.000(0)	1.98
O2	4*e*	0.2005(15)	-0.2281(14)	0.5370(10)	1.000(0)	2.29
O3	4*e*	-0.0761(14)	0.4823(9)	0.7340(9)	1.000(0)	2.32

R_p = 3.51 %, R_{wp} = 4.90 %, R_{exp} = 3.23 %, R_{F^2} = 9.47 %

Table 6.5 Lattice parameters and atomic coordinates of $Sr_2TbRu_{0.90}Cu_{0.10}O_6$ as refined from the data of Figure 6.4. Partial exchange of Tb with Ru between the 2*c* and 2*d* sites was refined to be 11.3 ± 0.2 %.

The quality of the refinement can be indicated further from close inspection of each part of the diffraction pattern, particularly at high 2θ, where due to the form factor, the intensity level is on a smaller scale and so is not adequately clear in Figure 6.4. Each 10° segment of the diffraction pattern is shown from 5-55° in Figure 6.5 through to Figure 6.9. Every diffraction peak is well matched with no significant discrepancy, thus indicating the high quality of the data collected at BM1B and the model structure used in refinement. The proximity of the R values, R_{wp} = 4.90 % and R_{exp} = 3.23 % confirms this. The quality of the profile does not degrade with increasing 2θ, the counting statistics simply become worse as the form and temperature factors reduce the intensities of the peaks. No unindexed peaks are present and this means that there is *no crystalline impurity phase* measurable (above ~ 0.1 %), even though one of the highest intensity X-ray sources has been employed. Thus, there is no ambiguity with the $Sr_2TbRu_{0.90}Cu_{0.10}O_6$ sample, any superconductivity observed in this sample is due to a 2116 ruthenate phase, provided there is no amorphous impurity either.

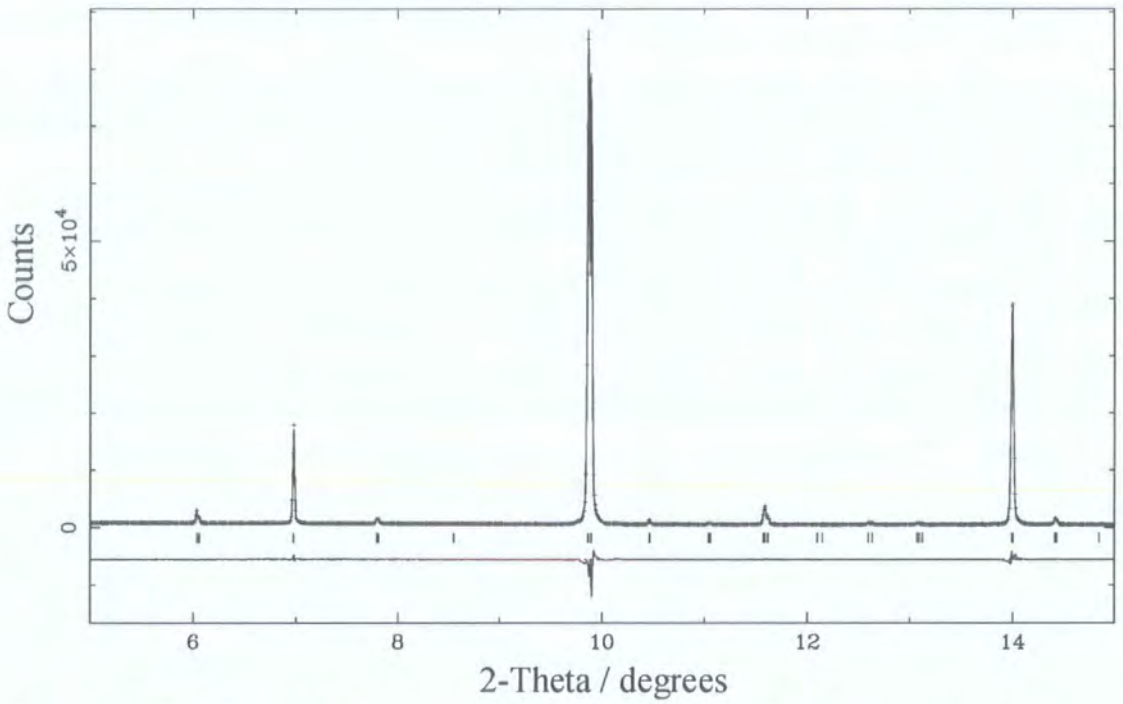

Figure 6.5 The 5-15° angular range of the diffraction pattern of $Sr_2TbRu_{0.90}Cu_{0.10}O_6$. The model structure was refined with partial *B* cation disorder.

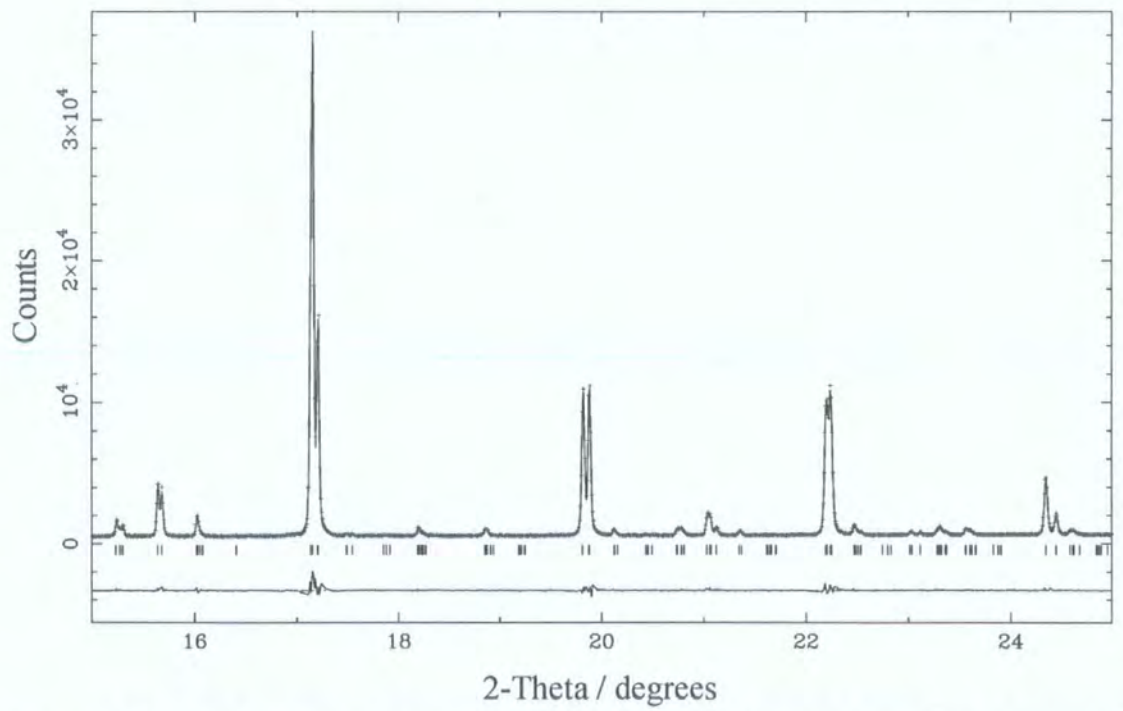

Figure 6.6 The diffraction pattern (15-25°) of $Sr_2TbRu_{0.90}Cu_{0.10}O_6$. The model structure was refined with partial *B* cation disorder.

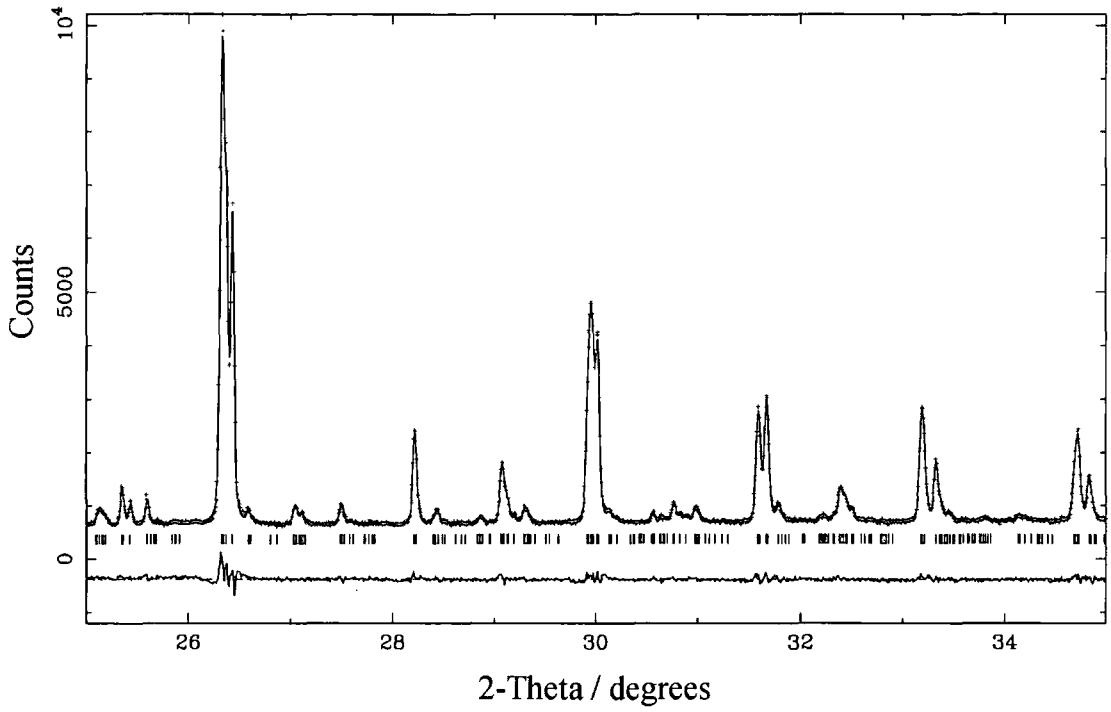

Figure 6.7 The diffraction pattern (25-35°) of $Sr_2TbRu_{0.90}Cu_{0.10}O_6$. The model structure was refined with partial *B* cation disorder.

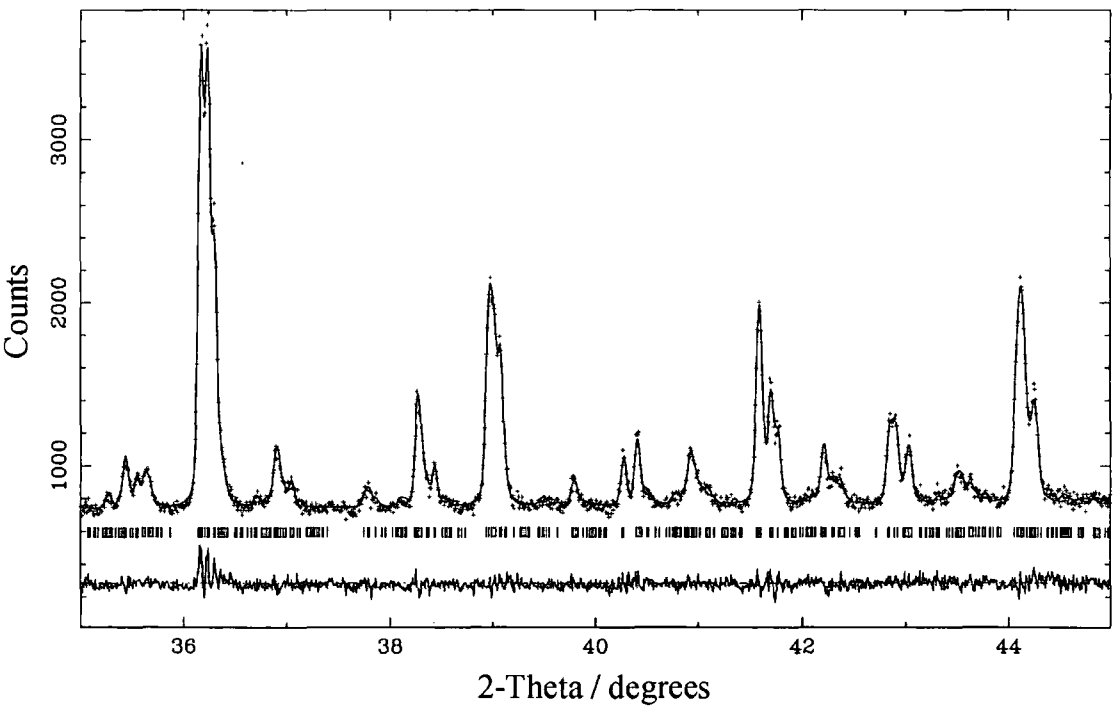

Figure 6.8 The diffraction pattern (35-45°) of $Sr_2TbRu_{0.90}Cu_{0.10}O_6$. The model structure was refined with partial *B* cation disorder.

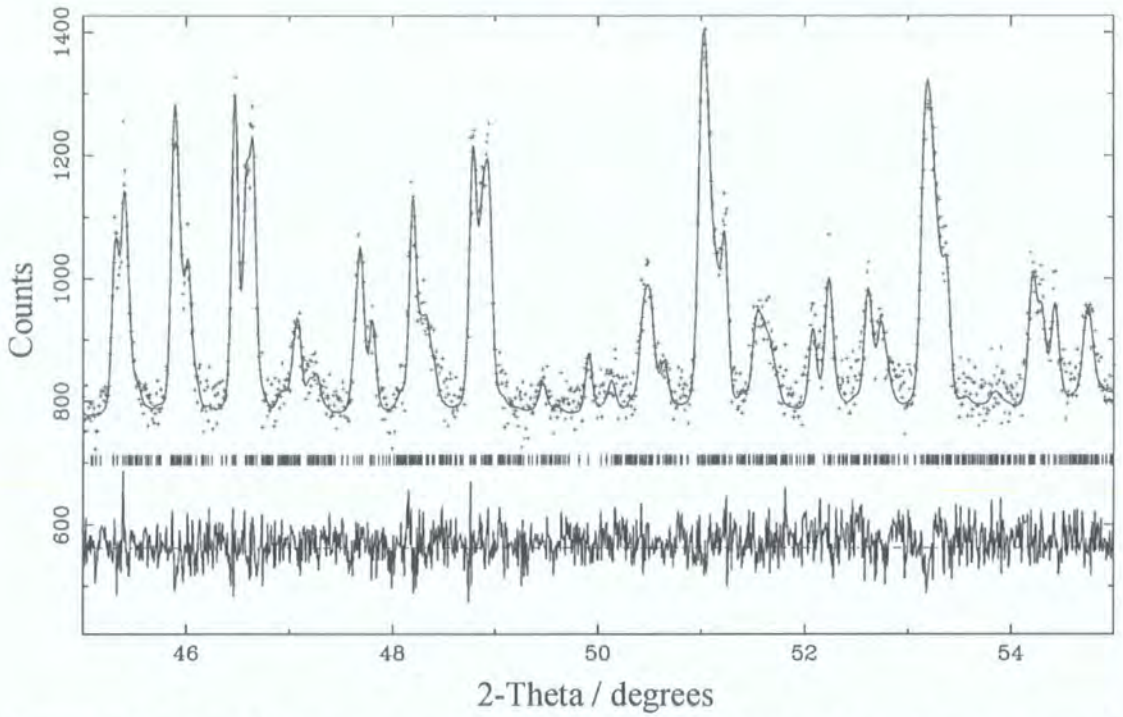

Figure 6.9 The diffraction pattern (45-55°) of $Sr_2TbRu_{0.90}Cu_{0.10}O_6$. The model structure was refined with partial *B* cation disorder.

Refinements were also undertaken for a partial exchange of Tb with Cu instead of Ru with the result that the disorder in this case was 7.4 ± 0.1 %. The refined diffraction profile and atomic positions were virtually identical to those already shown in Figure 6.4 and Table 6.5. The atomic coordinates of strontium and oxygen agreed as they were within one σ of each other. The diffraction profile was also identical because the scattering factors on the 2*c* and 2*d* sites were the same in both the Ru and Cu exchange cases.

The refinements have yielded two indistinguishable answers for the disorder level of the *B* cations, either an exchange of Ru of 11.3 ± 0.2 %, or Cu of 7.4 ± 0.1 %. A larger exchange of Ru than Cu was required as its scattering factor is closer to that of Tb and so a greater exchange was needed to have the same effect on the total scattering factor of each site. However, the disorder could be also represented by a mixture of Ru and Cu exchange with Tb, provided the total scattering factor on each site remained the same as in the cases shown in Figure 6.10. The two data points discussed above are the end points on the line, the remaining data points are the results of additional refinements and hence the line connecting them represents all the other possible solutions. As stated earlier a second diffraction pattern will be required to determine where the solution lies on the line. The gradient of the line simply

reflects the rate of change of scattering factor of each site when Cu and Ru are partially exchanged for Tb. As shown in the Appendix A.5 the gradient of the line is given by

$$m = -\frac{\Delta u(\Delta v = 0)}{\Delta v(\Delta u = 0)} = -\frac{Cu(\lambda) - Tb(\lambda)}{Ru(\lambda) - Tb(\lambda)}$$

where $\Delta u(\Delta v = 0)$ and $\Delta v(\Delta u = 0)$ are the amount of disorder of Ru and Cu respectively at the axes intercepts, whereas Cu(λ), Ru(λ) and Tb(λ) are the scattering factors of the elements at the wavelength used. The scattering factor at $\sin\theta/\lambda = 0.20$, the approximate location of the most intense ordering peak, is used with any anomalous scattering factor included. This yields a predicted gradient of this line to be $m_{pred} = -1.54 \pm 0.08$ (full details are given in Appendix A.5), while from the graph the experimentally determined value, $m_{exp} = -1.53 \pm 0.03$. The agreement of the two indicates just how similar the diffraction profiles and *R*-factors will be anywhere along the line on the Ru-Cu disorder plot. Additionally it shows that refining the two end values and connecting them with a line is sufficient to determine the disorder plot for any diffraction pattern.

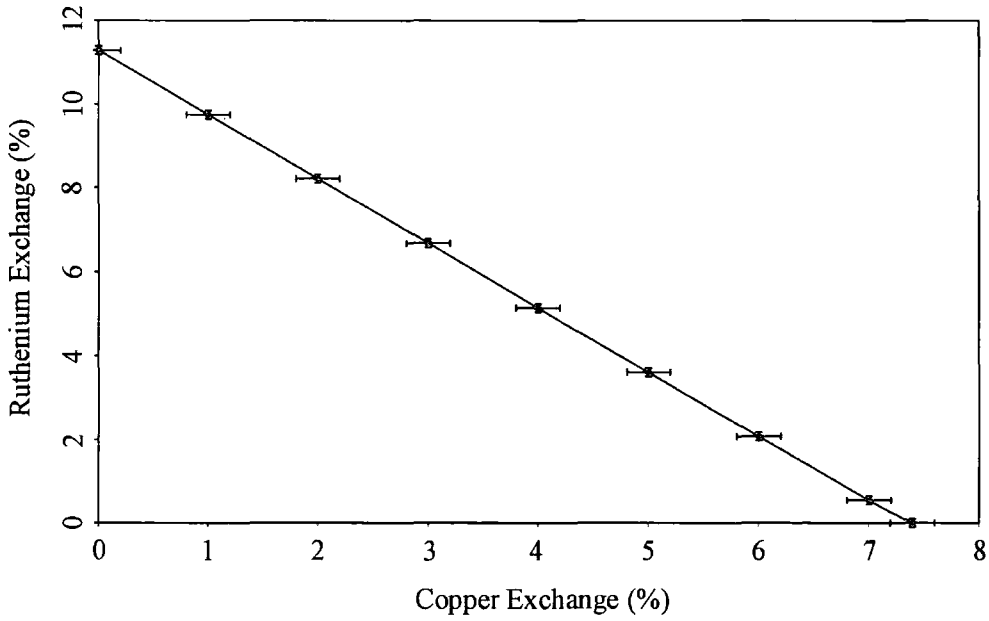

Figure 6.10 The disorder diagram of $Sr_2TbRu_{0.90}Cu_{0.10}O_6$ showing the allowed solutions of *B* cation disorder which yield identical diffraction profiles.

The disorder in the system is therefore ~ 10 % and so the material is still highly ordered. However the precise composition of the disorder is not yet known and would require more diffraction patterns to be measured in order to clarify its nature.

6.4.2 $Sr_2YRu_{0.85}Cu_{0.15}O_6$

A full diffraction pattern was collected on $Sr_2YRu_{0.85}Cu_{0.15}O_6$ as it was believed that the larger copper concentration in the material may lead to a larger, and hence easier to detect, disorder. The high intensity and quality of the diffraction pattern obtainable on BM1B was able to highlight some small unindexed peaks, which were not so clear in the neutron diffraction results. The diffraction pattern shown in Figure 6.11 has these small impurity peaks removed and was refined allowing *B* cation disorder, in this case Cu with Y. The atomic coordinates and lattice parameters are detailed in Table 6.6. The crystal structure is similar to that measured by neutrons at lower temperatures, though greater uncertainty is noted in the oxygen positions with the synchrotron X-ray data, due to its relative reduced scattering power. The lattice parameters at 300 K indicate that the lattice continues to expand between 100 K and 300 K at a rate of ~2.5 times that observed below 100 K, where the volume expansivity was $\alpha = 1.1(3) \times 10^{-5}\ K^{-1}$.

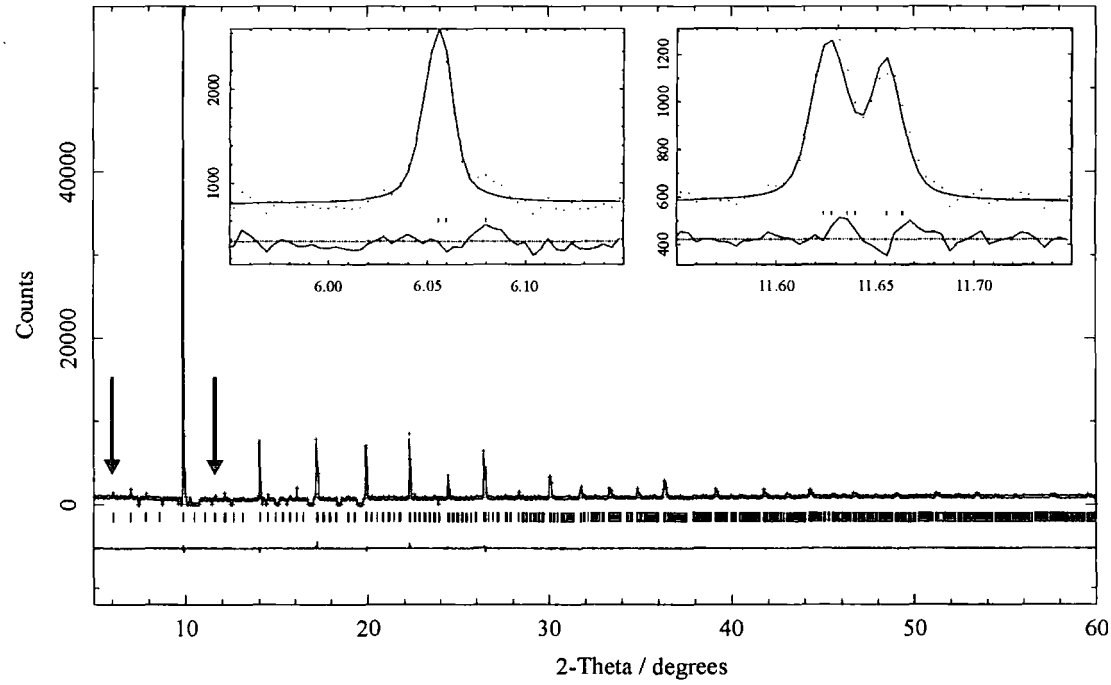

Figure 6.11 The diffraction pattern of $Sr_2YRu_{0.85}Cu_{0.15}O_6$ measured at room temperature. The data points are indicated as crosses and the lines as the calculated profile and difference curve. The tick marks indicate the positions of the calculated reflections. Here *B* cation exchange has been refined.

$Sr_2YRu_{0.85}Cu_{0.15}O_6$		$P2_1/n$			Room temperature	
a / Å		b / Å	c / Å	β / °	Volume / Å^3	
5.77596(2)		5.78744(2)	8.17145(3)	90.249(1)	273.153(1)	
Atom	Site	x	y	z	Occ	B_{iso}/Å^2
Sr	4*e*	0.0083(4)	0.0264(1)	0.7508(3)	1.000(0)	1.77(1)
Y	2*c*	0	½	0	0.863(11)	1.34(1)
Cu	2*c*	0	½	0	0.137(11)	1.34(1)
Ru	2*d*	½	0	0	0.850(0)	1.34(1)
Cu	2*d*	½	0	0	0.013(11)	1.34(1)
Y	2*d*	½	0	0	0.137(11)	1.34(1)
O1	4*e*	0.2898(22)	0.2692(21)	0.9652(16)	1.000(0)	1.95(13)
O2	4*e*	0.2832(21)	0.3069(21)	0.5366(15)	1.000(0)	1.46(12)
O3	4*e*	0.9400(17)	0.4858(11)	0.7443(14)	1.000(0)	1.38(12)

R_p = 2.58 %, R_{wp} = 3.54 %, R_{exp} = 3.21 %, R_{F^2} = 8.35 %

Table 6.6 The crystal structure of $Sr_2YRu_{0.85}Cu_{0.15}O_6$ as refined from the data at room temperature.

With the small impurity peaks removed, the general agreement between the observed and model profile is good with R_p = 2.58 %, R_{wp} = 3.54 % and R_{exp} = 3.21 %. Refinements with 100 % and a random *B* cation arrangement also led to similar *R*-factors of R_p = 2.60 %, R_{wp} = 3.58 % and R_{exp} = 3.20 % and R_p = 2.61 %, R_{wp} = 3.66 % and R_{exp} = 3.20 % respectively, due to the small intensities of the ordering peaks. Figure 6.12 shows the ordering peaks for both refinements and it is noted that the random arrangement leads to low peak intensity for the same reason as in the diffraction profile of $Sr_2TbRu_{0.90}Cu_{0.10}O_6$. The difference peak for the 100 % ordered model is noticeably less than the for the disordered model profile presented in Figure 6.11.

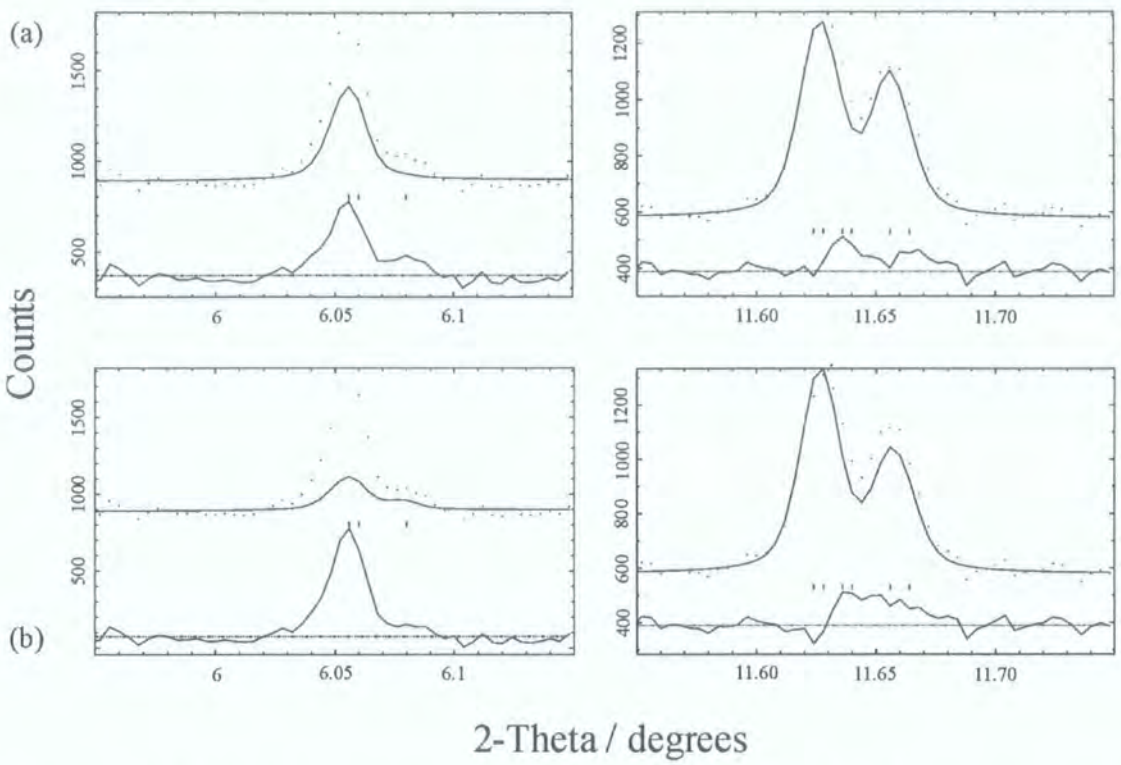

Figure 6.12 The ordering peak intensities for both (a) 100 % ordered and (b) random ordering of *B* cations.

The reason is that the 100 % ordered model does not give the maximal difference in scattering factors on the two sites as Y (39 electrons) on the 2*c* site is lighter than the Ru (44 electrons), but heavier than Cu (29 electrons), the ions on the 2*d* site. This difference can only be increased by exchange of the lighter Cu with Y, and not with the heavier Ru. The similarity of the scattering factors of the *B* cations manifests itself as small ordering peaks and so small changes in *R*-factors for disorder refinements as noted above. The refinements suggest that ~ 13 % of copper is on the 2*c* site, with any additional copper (at most 2 % as the total amount is 15 %) being compensated by a small amount of ruthenium exchange too. Therefore with this system there is no need to perform anomalous measurements, as the disorder is known to within ~ 2 %, as the rest of the solutions are unphysical. The larger peak intensities and ordering sensitivities observed in the $Sr_2TbRu_{0.90}Cu_{0.10}O_6$ system make this a better sample for further study.

The diffraction pattern of $Sr_2YRu_{0.85}Cu_{0.15}O_6$ did contain peaks which could not be indexed to the main phase, with intensities ~ 2 % of the largest peaks in the pattern. Inclusion of the impurity peaks did not significantly affect the crystal structure of the main phase and hence its exclusion from the above discussion. An extensive search of

the Inorganic Crystal Structure Database (ICSD) [3] and PCPDFWIN [4] by JCPDS-ICDD (International Centre for Diffraction Data) was undertaken with specific emphasis on oxides containing the title elements. The majority of these peaks throughout the entire pattern were indexed to the single impurity oxide, SrY_2O_4, which was 3.8 ± 0.2 % by weight of the total sample. This had no effect on the refinement of the major phase but did reduce the residual *R*-factors from R_p = 3.18 %, R_{wp} = 5.80 % and R_{exp} = 3.22 % to R_p = 2.88 %, R_{wp} = 4.88 % and R_{exp} = 3.22 % when all the peaks were included, a significant improvement.

The remaining regions of intensity mismatch were for $2\theta \sim 10.43°$, 10.60°, 10.74°, 12.50°, 15.00° and 18.43° and all of the features were broader than peaks attributed to the first two phases. Assignment of these peaks was more difficult as most of the oxides of Sr, Y, Ru and Cu have their largest diffraction peak at ~ 10.5° in this pattern and few of the other peaks would be visible for a small level of impurity. However the peak at 10.60° and the 12.50°, 15.00° and 18.43° features *could* be modelled by an YSCO-like ($YSr_2Cu_3O_{7-\delta}$) impurity. This requires the space group *P4/mmm* with a unit cell of a = 3.8348(2) Å and c = 11.433(2) Å, but with a precise composition which is unknown.

There are many subtle variations in the composition of YSCO which are possible with the elements known to be present, or a small contaminant, which would be able to give the required unit cell and which would also superconduct. The actual crystal structure chosen was $YSr_2Cu_2FeO_{6.536}$ [5] as the unit cell was within 0.01Å of the required cell and the scattering factor of Fe is similar to Cu, an element already present. The breadth of the diffraction peaks indicates the regions of YSCO are small and allows an estimate of the crystallite size to be made. The instrumental broadening effects are negligible as the main phase has much sharper diffraction peaks and thus crystallite size is estimated using the Scherrer equation to be ~ 190 ± 50 Å from the one well defined peak at 10.60° as shown in Figure 6.13.

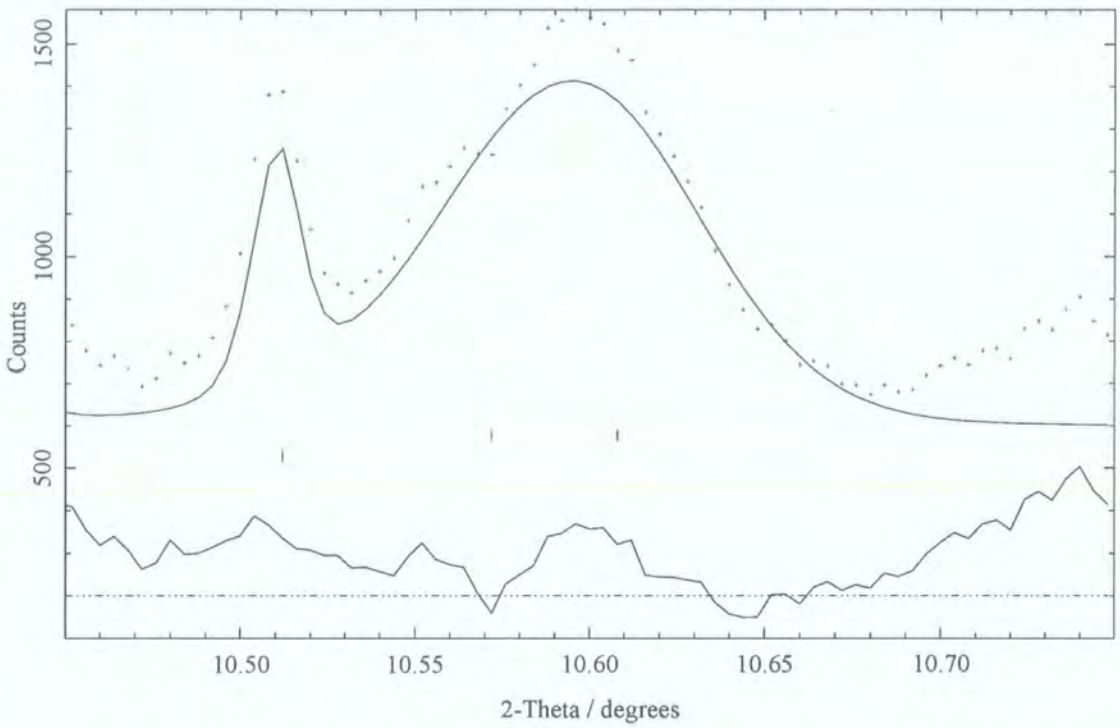

Figure 6.13 The diffraction intensity in the pattern of $Sr_2YRu_{0.85}Cu_{0.15}O_6$ could be replicated by an YSCO-like impurity. The peak at 10.52° is indexed by the main phase and the 10.60° peak is indexed by two YSCO reflections. Part of the intensity of the peak at 10.60° is given by a further impurity which is not yet included. It is omitted from this figure to allow an estimate of the peak width to be made.

The *possible* presence of an YSCO-like phase is an obvious concern when a novel superconducting system is discovered. As the precise composition is not known, although it can't be proved that the YSCO-like phase does superconduct, the case in which it does will be discussed. However, in such case the 3.4 ± 1 % of the sample by weight which is YSCO-like is unlikely to be able to explain all the superconductivity reported in the system. Bulk measurements have reported that more than 8 % of the sample is superconducting [6], so clearly there must be a contribution from the rest of the sample, most probably the main phase, $Sr_2YRu_{0.85}Cu_{0.15}O_6$. Additionally, for the observation of zero resistance a percolative pathway through the material of zero resistance must exist, which is highly unlikely were the ~ 3.4 % of YSCO to be the sole contributor. This too supports the notion that the main phase, $Sr_2YRu_{0.85}Cu_{0.15}O_6$, must contribute significantly to the reported superconductivity in the system. Powder diffraction would not be able to yield information on the composition of a filamentary route supporting a supercurrent. However to be solely responsible it would have to extend throughout the material, or else connect to islands of superconducting material

together. With only ~ 3.4 % YSCO it is unlikely that there would just be YSCO islands responsible. The existence of superconducting Sr_2RuO_4 [7] gives support to a superconducting ruthenate phase, while $Sr_2TbRu_{0.90}Cu_{0.10}O_6$, which has no YSCO-like impurities, suggests that this is possible in a 2116 ruthenate also. Therefore the presence of a small amount of an YSCO-like phase does not rule out the possibility of superconductivity in the $Sr_2YRu_{1-x}Cu_xO_6$ system.

The remaining two peaks could not be indexed by a single phase, though they could with two separate impurities. The 10.74° peak was modelled by ~1.5 % by weight of $SrCuO_{2.5}$ and this aided the 10.60° peak by also increasing its intensity. The perovskite $SrRuO_3$ was able to model the 10.43° peak with only 0.7 % of the total sample by weight. Formation of a single perovskite as an impurity is always likely when fabricating double perovskites due to their obviously very similar lattice parameters and constituents. However, *extreme caution* must be taken with assigning the last of the diffraction intensity to these two phases as essentially only one peak was used for each. Although they were the only materials which could match the peaks well, without adding unwanted intensity elsewhere in the pattern, the peaks were quite broad. The breadth of the peaks indicates a small crystallite size or a strained region, which can be envisaged as a variation in the lattice parameter within the region. It is possible that a different oxide is actually present and its lattice has tried to match that of the main phase and has resulted in the strained and broadened peaks.

The region around 10° is rich in the peaks from all the phases and Figure 6.14 highlights this section of the diffraction pattern with all five phases contributing. The sole unindexed peak in the pattern at 10.27° is also included, though no attempt was made to determine its origin as it would represent ~ 0.1 % of the sample. The largest peak in Figure 6.14 is due to the main phase and its peak intensity some 50 times greater than these impurity peaks, which are themselves the largest and most significant impurity peaks in the pattern.

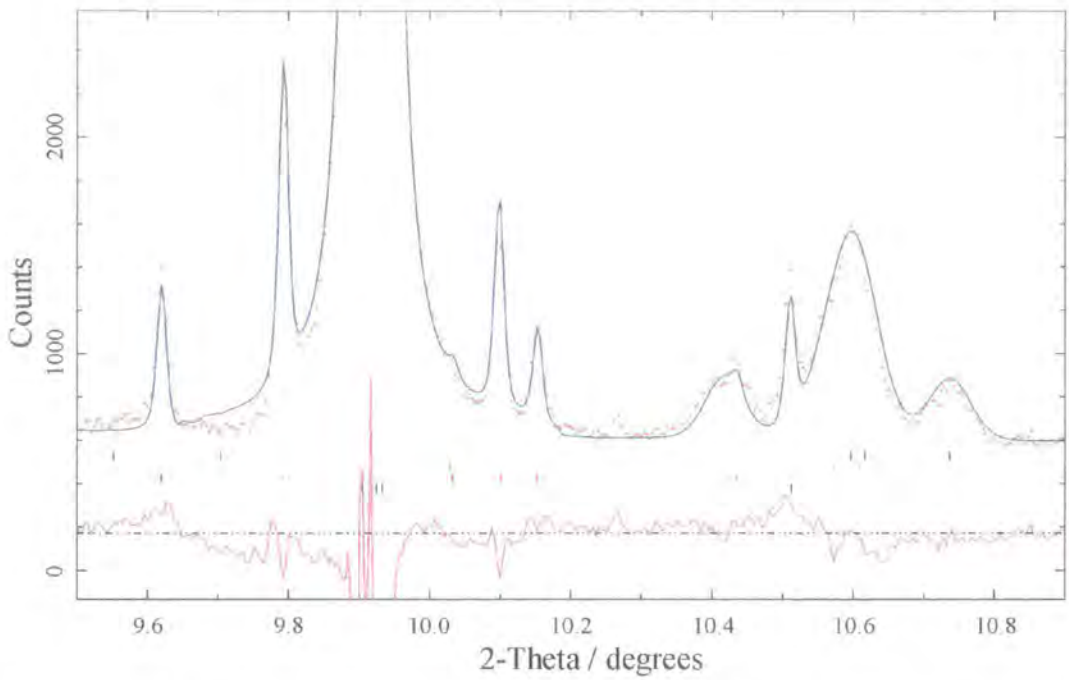

Figure 6.14 The diffraction pattern of $Sr_2YRu_{0.85}Cu_{0.15}O_6$ highlighting the impurity rich region of the profile. The lowest series of tick marks indexes the main phase of $Sr_2YRu_{0.85}Cu_{0.15}O_6$ (black), then progressing upwards, SrY_2O_4 (red), YSCO (green), $SrCuO_{2.5}$ (blue) and $SrRuO_3$ (light blue). SrY_2O_4 provides the intensity of the four peaks surrounding the largest peak at 9.9°, YSCO the peak at 10.60°, $SrCuO_{2.5}$ the peak at 10.74° and a little of 10.60°, while $SrRuO_3$ only contributes significantly at 10.43°.

The effect of the impurities would have a significant effect on the composition of the material, however as they are not precisely known it is difficult to quantify. The largest change in composition would be to the copper concentration due to the YSCO-like impurity, were it to be $YSr_2Cu_3O_{7-\delta}$. The copper concentration would be severely depleted in the main phase and would become $Sr_{2.12}YRu_{0.965}Cu_{0.037}O_6$, were all the other impurities correctly assigned. However the copper depletion is unlikely to be close to that degree of severity for two reasons. Firstly, the YSCO-like phase does not have a precisely known composition as there are very few peaks and only one of which is well defined. Therefore structural refinement of this phase is not possible to confirm the copper level. It is unlikely that with copper at such a premium in the samples for it all to be taken into an YSCO-like phase. Secondly, there is evidence from the neutron diffraction that the lattice parameter increases with copper doping and thus more copper is progressively included into the main phase as it replaces the smaller ruthenium.

The other impurities, SrY_2O_4 and the more doubtful $SrCuO_{2.5}$ and $SrRuO_3$ have a much smaller impact on the composition and the crystal structure. Furthermore any

amorphous impurity phases, which would not appear as sharp diffraction peaks, would also be impossible to identify and quantify accurately. Thus, the composition of the main phase was refined as $Sr_2YRu_{0.85}Cu_{0.15}O_6$ because an alternative precise composition could not be attained. All the potential compositions are best considered as deviations from the perfect stoichiometry of $Sr_2YRu_{0.85}Cu_{0.15}O_6$. Clearly the presence of impurities has an effect on the composition, which would have a devastating effect on *B* cation order analysis. Hence the prior conclusion that ~ 13 % of the copper is disordered cannot be validated. This further reinforces the opinion that the $Sr_2TbRu_{0.90}Cu_{0.10}O_6$ sample is a good one to study as there are no crystalline impurities in this material. The neutron diffraction data and resulting crystal structure refinements are less affected by this problem due to the scattering factors of the *B* cations being so similar.

6.4.3 $Sr_2HoRu_{0.85}Cu_{0.15}O_6$

A high copper concentration was available for the Ho series, which unlike the Y analogue should give large difference peaks in the pattern as Ho is even heavier than Tb. A full diffraction pattern was collected for $Sr_2HoRu_{0.85}Cu_{0.15}O_6$ and refined with the small impurity peaks removed as had been necessary for $Sr_2YRu_{0.85}Cu_{0.15}O_6$. Figure 6.15 shows the diffraction profile for $Sr_2HoRu_{0.85}Cu_{0.15}O_6$ refined with partial exchange of Ru with Ho between the two *B* cation sites.

With the impurity peaks excluded from the refinement, the crystal structure was refined to the values given in Table 6.7 with R_p = 2.55 %, R_{wp} = 3.64 %, and R_{exp} = 2.99 %. These *R*-factors are more in keeping with the those obtained from refinement of the $Sr_2TbRu_{0.90}Cu_{0.10}O_6$ diffraction pattern and indicate the quality of the data and model are of similar standard were there to have been no impurity phase. This crystal structure compares very well with the structure determined by low temperature neutron diffraction used in Chapter 4. The diffraction profile was identical for Ho exchange with Ru of 4.4 ± 0.1 %, or for a Cu exchange of 3.0 ± 0.1 %. These exchanges produce a disorder gradient of m_{exp} = -1.48 ± 0.06 and the predicted gradient, m_{pred} = -1.48 ± 0.08 is in agreement. The Ho system therefore appears to be highly ordered, but it also indicates that it will be easier to study the disorder in the Tb system where the disorder is greater.

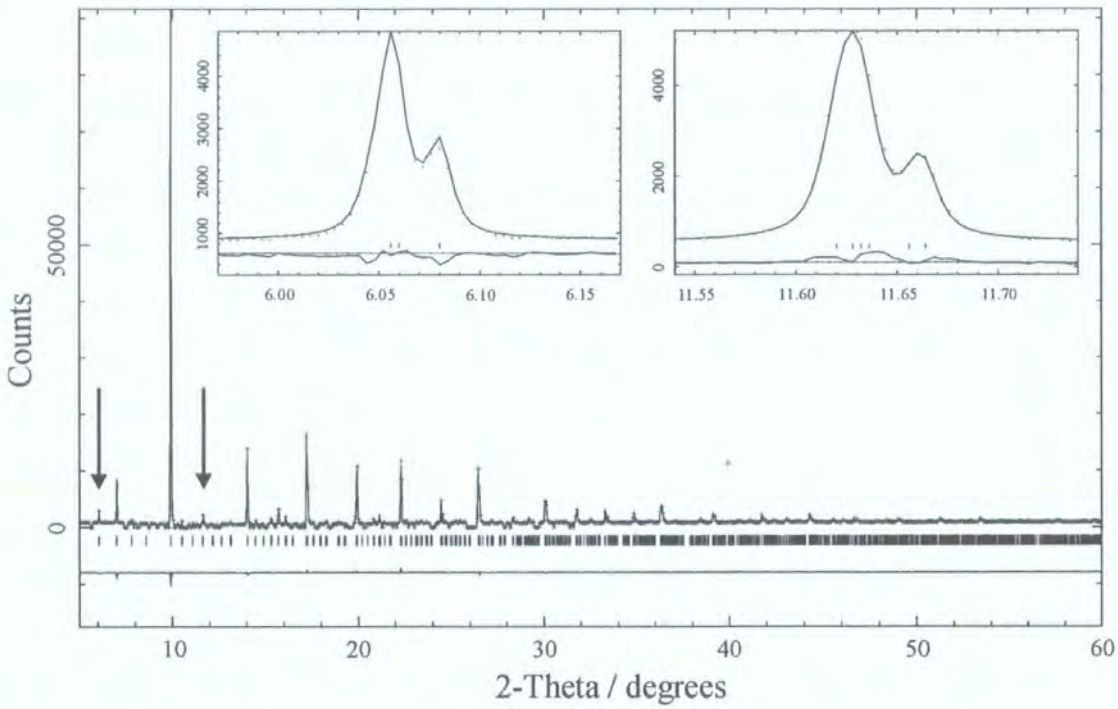

Figure 6.15 The diffraction profile of $Sr_2HoRu_{0.85}Cu_{0.15}O_6$, with impurity peaks excluded, refined with a partial exchange of the *B* cations.

$Sr_2HoRu_{0.85}Cu_{0.15}O_6$		$P2_1/n$			Room temperature	
a / Å		*b* / Å	*c* / Å	*β* / °	Volume / Å^3	
5.77500(2)		5.78884(2)	8.17242(3)	90.256(1)	273.206(1)	
Atom	Site	*x*	*y*	*z*	Occ	B_{iso}/Å^2
Sr	4*e*	0.0050(2)	0.0280(1)	0.7493(2)	1.000(0)	2.24(7)
Ho	2*c*	0	½	0	0.956(1)	1.79(1)
Ru	2*c*	0	½	0	0.044(1)	1.79(1)
Ho	2*d*	½	0	0	0.044(1)	1.79(1)
Ru	2*d*	½	0	0	0.806(0)	1.79(1)
Cu	2*d*	½	0	0	0.150(0)	1.79(1)
O1	4*e*	0.2992(11)	0.2634(11)	0.9642(8)	1.000(0)	1.80(10)
O2	4*e*	0.2701(11)	0.3080(11)	0.5280(9)	1.000(0)	1.74(11)
O3	4*e*	0.9272(10)	0.4867(7)	0.7364(6)	1.000(0)	1.65(10)

$R_p = 2.55$ %, $R_{wp} = 3.64$ %, $R_{exp} = 2.99$ %, $R_{F^2} = 5.48$ %

Table 6.7 The atomic coordinates and lattice parameters of $Sr_2HoRu_{0.85}Cu_{0.15}O_6$ refined allowing exchange of Ho and Ru between the 2*c* and 2*d* sites.

Again the high quality of the diffraction data was able to highlight impurity peaks, the largest of which were ~ 5 % of the size of the main phase. Their position in the diffraction pattern and form was very similar to the impurities present in the $Sr_2YRu_{0.85}Cu_{0.15}O_6$ sample. The majority of the peaks were easily refined as a

5.4 ± 0.3 % by weight impurity of $SrHo_2O_4$, analogous to SrY_2O_4. The other impurity peaks which were the same in each pattern were ascribed to a ~ 3.3 %YSCO-like phase, ~ 0.6 % $SrCuO_{2.5}$ and ~ 0.8 % $SrRuO_3$, similar to before. These can't be identified with certainty as they were determined by fewer peaks. Again the composition of the YSCO-like phase is unknown and as yttrium should not be present in the samples, it would have to be a contaminant or have Ho in place of Y. Therefore it is unknown whether this YSCO-like phase would be superconducting or whether it is actually another impurity of unknown nature. Thus, while it can't be confirmed whether any YSCO-like impurity phase is present in $Sr_2HoRu_{0.85}Cu_{0.15}O_6$, or whether it would be superconducting or not, the possibility exists that it may. The pattern of $Sr_2HoRu_{0.85}Cu_{0.15}O_6$ did contain an extra set of impurity peaks (most obviously the peak at $2\theta \sim 11°$) compared to $Sr_2YRu_{0.85}Cu_{0.15}O_6$ and these were easily indexed by ~ 1.6 % by weight of sample of $SrCuO_2$. The impurity rich region is again around $2\theta \sim 10°$ and is shown in Figure 6.16.

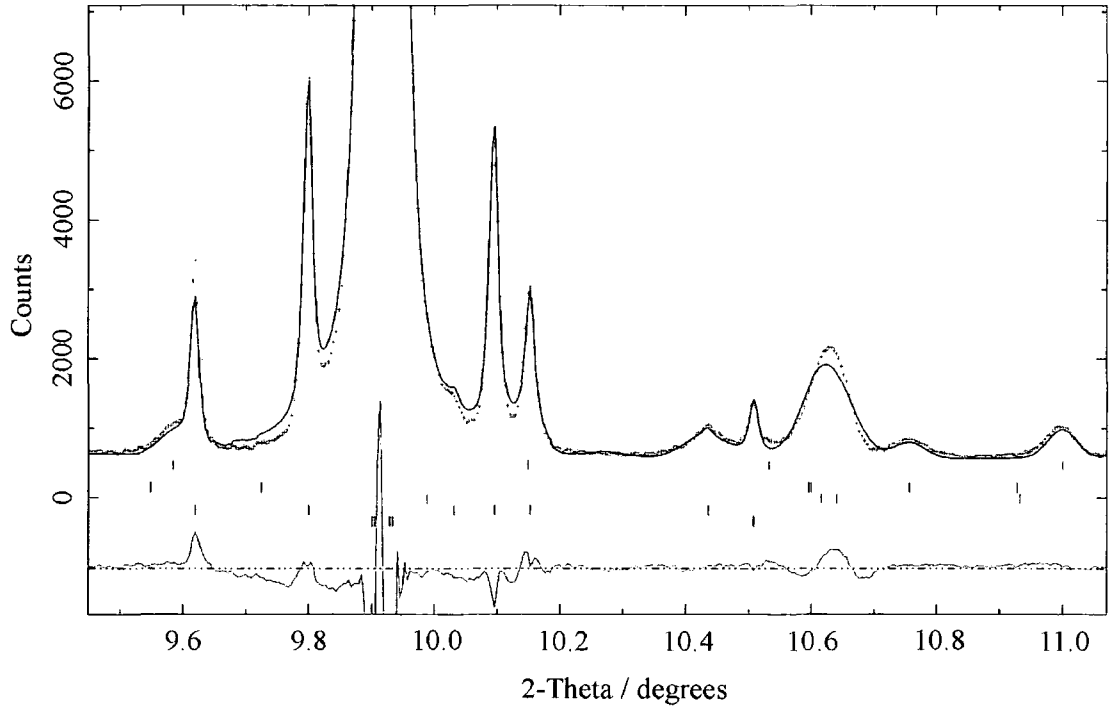

Figure 6.16 The diffraction pattern of $Sr_2HoRu_{0.85}Cu_{0.15}O_6$ highlighting the impurity rich region of the profile. The lowest series of tick marks indexes the main phase of $Sr_2HoRu_{0.85}Cu_{0.15}O_6$ (black), then progressing upwards, SrY_2O_4 (red), YSCO (green), $SrCuO_{2.5}$ (blue), $SrRuO_3$ (light blue) and $SrCuO_2$ (purple), which was not present in $Sr_2YRu_{0.85}Cu_{0.15}O_6$ pattern, evidenced here at $2\theta \sim 9.59°$ and 11.00°.

As the diffraction pattern of $Sr_2HoRu_{0.85}Cu_{0.15}O_6$ includes some small impurity phases of composition and quantity which is not precisely known, then the amount of

material left on the *B* sites is unknown. Clearly the introduction of these extra variables into the problem will prohibit a unique solution to the ordering in $Sr_2HoRu_{0.85}Cu_{0.15}O_6$, and hence this system was not chosen for further study. However, the only crystalline impurity which alters significantly the stoichiometry (more than 2%) away from $Sr_2HoRu_{0.85}Cu_{0.15}O_6$, is the YSCO-like phase if it contains 3 copper atoms per formula unit (i.e. $YSr_2Cu_3O_{7-\delta}$). As the composition of this phase is completely open to speculation, the refinements of the diffraction patterns of $Sr_2HoRu_{0.85}Cu_{0.15}O_6$ have been refined assuming the stoichiometry of this phase remains.

6.4.4 $Sr_2Ho_{0.8}Tb_{0.2}Ru_{0.90}Cu_{0.10}O_6$

A trial investigation was carried out on the title material to determine whether the disorder would be any different were extra variation allowed from the use of two rare-earth elements in the composition. The crystal structure of $Sr_2Ho_{0.80}Tb_{0.20}Ru_{0.90}Cu_{0.10}O_6$ was refined using the diffraction data shown in Figure 6.17, again with the removal of any small impurity peaks.

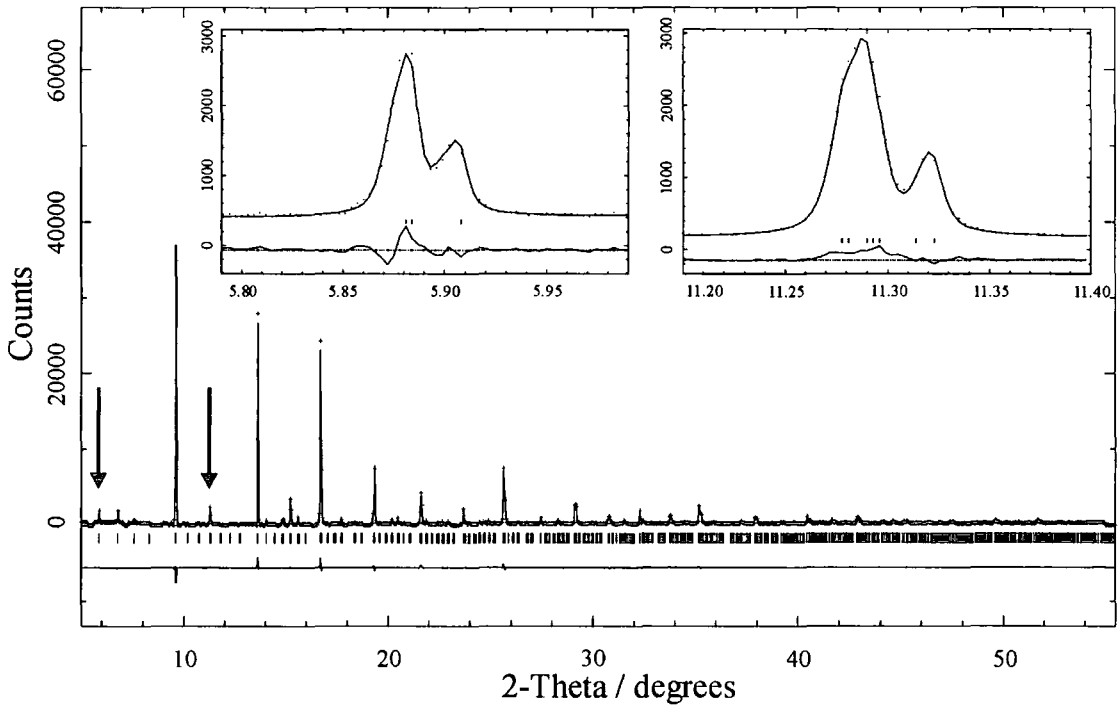

Figure 6.17 The diffraction pattern of $Sr_2Ho_{0.80}Tb_{0.20}Ru_{0.90}Cu_{0.10}O_6$ with all impurity peaks removed and the model structure refined allowing for *B* cation disorder.

The results of the refinement of the crystal structure are shown in Table 6.8 with exchange of Ho with Ru. This is very similar to the crystal structure which was used

to successfully analyse the neutron data in Chapter 4. Again the proposed exchanges of *B* cations were small whether Ru (~ 4.0 ± 0.2 %) or Cu (~ 2.7 ± 0.1 %) were exchanged with Ho. (As Ho and Tb have similar atomic numbers there was very little difference from these figures for Tb exchanges.) However once again the impurity peaks were present in the diffraction pattern and very similar to those observed in the $Sr_2YRu_{0.85}Cu_{0.15}O_6$ and $Sr_2HoRu_{0.85}Cu_{0.15}O_6$ data sets. They could be refined as ~ 3.0 ± 0.3 % $SrHo_2O_4$, ~ 0.7 % $SrCuO_{2.5}$ and ~ 0.8 % $SrRuO_3$, and ~ 1.2 % of a potentially YSCO-like phase by weight. Only the $SrHo_2O_4$ impurity is certainly present with known composition and so the effect of the others on the main phase of the sample is undeterminable. Taking the impurities to be as above would change the composition of the main phase to $Sr_2Ho_{0.770}Tb_{0.210}Ru_{0.924}Cu_{0.049}O_6$, mainly a reduction in copper content due to the YSCO-like feature. Once again this has assumed that there is no significant amorphous impurity and that the volatility is low so all of the starting material forms the final compound. Thus, although the ordering problem can't be solved with this degree of uncertainty, this worst case scenario (except copper) is not too far from stoichiometry and so the main phase was refined as stoichiometric $Sr_2Ho_{0.80}Tb_{0.20}Ru_{0.90}Cu_{0.10}O_6$, here and from the neutron data.

$Sr_2Ho_{0.80}Tb_{0.20}Ru_{0.90}Cu_{0.10}O_6$		$P2_1/n$		Room temperature		
a / Å		*b* / Å	*c* / Å	*β* / °	Volume / Å^3	
5.77789(2)		5.79353(2)	8.17681(3)	90.263(1)	273.710(1)	
Atom	Site	*x*	*y*	*z*	Occ	B_{iso}/Å^2
Sr	4*e*	0.0044(2)	0.0284(1)	0.7501(2)	1.000(0)	1.88(1)
Tb	2*c*	0	½	0	0.200(0)	1.40(1)
Ho	2*c*	0	½	0	0.760(2)	1.40(1)
Ru	2*c*	0	½	0	0.040(2)	1.40(1)
Ho	2*d*	½	0	0	0.040(2)	1.40(1)
Ru	2*d*	½	0	0	0.860(0)	1.40(1)
Cu	2*d*	½	0	0	0.100(0)	1.40(1)
O1	4*e*	0.2691(11)	0.3022(11)	0.5341(9)	1.000(0)	1.61(10)
O2	4*e*	0.1977(10)	-0.2327(11)	0.5343(8)	1.000(0)	1.49(10)
O3	4*e*	-0.0711(11)	0.4863(8)	0.7395(7)	1.000(0)	1.68(11)

R_p = 5.24 %, R_{wp} = 6.91 %, R_{exp} = 4.85 %, R_{F^2} = 19.61 %

Table 6.8 Lattice parameters and atomic coordinates refined from the data for $Sr_2Ho_{0.80}Tb_{0.20}Ru_{0.90}Cu_{0.10}O_6$ with *B* cation disorder and impurity peaks excluded.

6.4.5 Summary

The best sample for examining the disorder of the *B* cations is clearly $Sr_2TbRu_{0.90}Cu_{0.10}O_6$. This is due to two major factors. Firstly the disorder is the largest in this material and so with the use of anomalous diffraction there will be the greatest difference between the two end members of the disorder (i.e. 11.3 % Ru exchange or 7.4 % Cu exchange.) The second is that as there were no crystalline impurities their composition is known precisely, 1 part Tb, 0.9 parts Ru and 0.1 parts Cu. Thus, the disorder is most likely to manifest as an exchange of *B* cations between the two sites, rather than a vacancies or interstitals. These are far more likely when the composition is removed from stoichiometry, which could arise from an amorphous component or volatility of the starting materials.

Ascertaining disorder levels in the compounds with impurities is not possible as the precise composition of the main phase is not known well enough and so fine-tuning of scattering powers on crystallographic sites becomes irrelevant.

6.5 Anomalous Data Collections

6.5.1 The Choice of Absorption Edge

As the best system to study, $Sr_2TbRu_{0.90}Cu_{0.10}O_6$ offers the choice of three elements on the *B* sites, namely Tb, Ru and Cu. For each element the energies of their edges and wavelengths were examined for suitability for diffraction experimentation. For copper, the *K*-edge at 8979 eV (λ = 1.381 Å) is the only edge suitable for crystallographic purposes as the next nearest edge, the L_I is at 1096 eV. This corresponds to a wavelength of 11.31 Å, which is so large that no diffraction peaks would remain in the pattern. With ruthenium, again the *K*-edge is the only practical edge to use with an energy of 22117 eV and wavelength of 0.5606 Å. The L_I edge has a wavelength of 3.846 Å, which is accessible at synchrotron sources, but the absorption is much too high. For a heavy element such as terbium the *K*-edge is very high (55618 eV) and can't be accessed easily on current powder diffraction beamlines at synchrotron sources. The three *L* edges however fall in the wavelength range 1.3198 – 1.5362 Å and the L_{III} edge induces the greatest change in scattering factor of terbium and so was selected. The *M* edges of terbium correspond to longer wavelengths and these too would suffer too greatly from absorption effects and few diffraction peaks in the pattern.

The scattering factors of the elements occupying the *B* sites were calculated using the Brennan-Cowan tables [8] in XOP [9], for the energies of the selected edges and for the energy of the previously collected pattern. The results are shown in Table 6.9 and indicate that the scattering factor of an element generally remains constant unless the energy corresponds to the edge of that element. The partial reduction of the copper and terbium scattering factors at each other's edges is due to the Tb L_I edge at 8708 eV being quite close to the Cu *K*-edge.

Energy	Total Scattering Factor ($Å^{-1}$)		
	Cu	Ru	Tb
λ = 0.50060 Å 24832 eV	29.30	42.87	66.62
Cu (*K*-edge) 8979 eV	24.82	43.96	59.38
Ru (*K*-edge) 22117 eV	29.33	36.01	64.71
Tb (L_{III}-edge) 7514 eV	27.43	44.12	51.53

Table 6.9 The total scattering factor ($f = f_0 + f'$) of the elements at each of the edges and for the energy of the earlier diffraction experiment.

The scattering powers at the edges are ~ 84 % for Cu and Ru and ~ 77 % for Tb of their former values, which should have quite significant changes on the diffraction intensities. Diffraction patterns studying $Sr_2TbRu_{0.90}Cu_{0.10}O_6$ were collected at these three edges to determine the ordering level in the material.

The energy spread of the edges required the use of more than one instrument as no one would be appropriate for the entire energy range. The high resolution powder diffractometer, BM1B, is ideally suited to working at the Ru *K*-edge as this is the region where the flux is at its highest. Station 2.3 at the Synchrotron Radiation Source (SRS), Daresbury, is unable to reach 22117 eV, but can access the lower energy edges easily. The flux at 2.3 is optimised around 1 Å (12398 eV) and so it better matched to the lower energy edges of Tb and Cu.

6.5.2 Experiments at the Terbium Edge

The experiments at the terbium edge were conducted at station 2.3 at the SRS using $Sr_2TbRu_{0.90}Cu_{0.10}O_6$. In order to enable easy analysis and fair comparison of results a non-anomalous wavelength of 1 Å was selected in order to have measured a standard diffraction pattern. The angular range from 10° to 50° was recorded with a step size of 0.01° with a count time of 1 second per data point. As the flux at the SRS is much lower than the ESRF, flat plate geometry was used for the experiments as more material could be measured, allowing respectable intensities to be obtained. Preferred orientation was unlikely to be a problem in these perovskite systems and this could be checked by comparison of the results of the non-anomalous experiments performed at each source. The crystal structure was taken to be the same as previously refined and given in Table 6.5, except that the disorder was allowed to refine. The resultant diffraction profile is shown in Figure 6.18 with R_p = 7.09 %, R_{wp} = 8.90 % and R_{exp} = 7.15 %. The quality of the data is not as good as those patterns collected at BM1B as would be expected when comparing a second with a third generation synchrotron source.

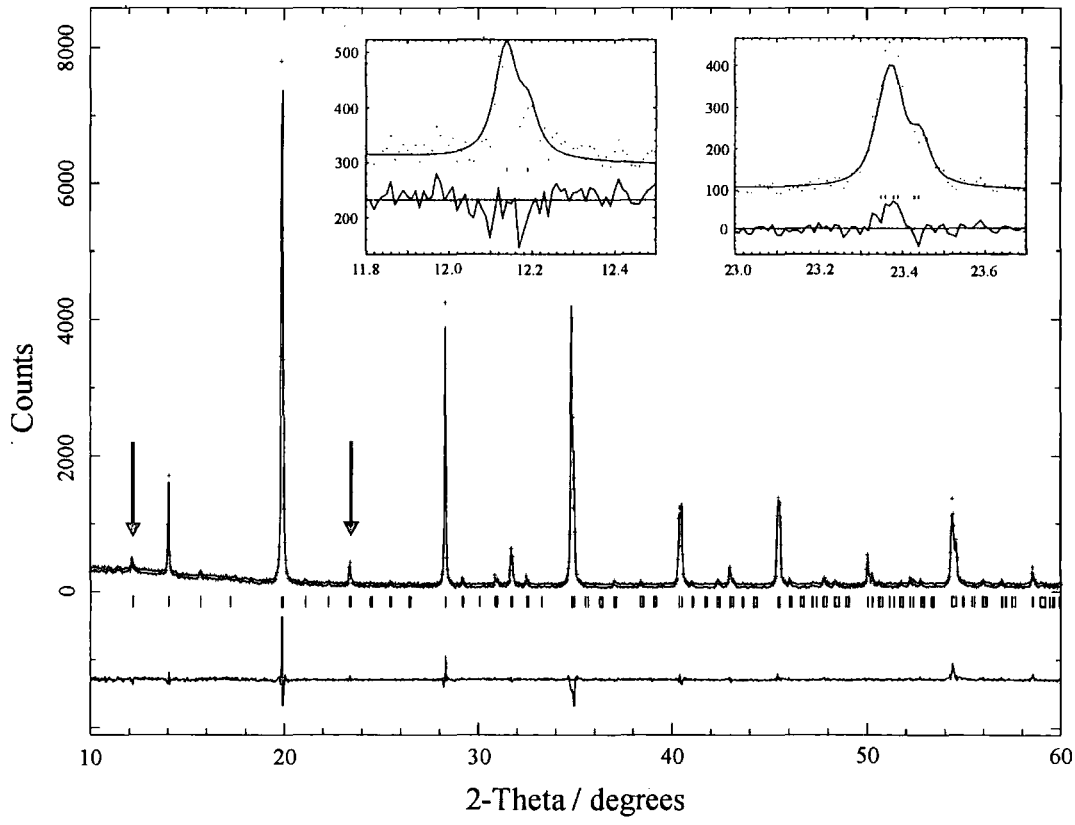

Figure 6.18 Diffraction pattern of $Sr_2TbRu_{0.90}Cu_{0.10}O_6$ measured at station 2.3 with a wavelength of 1 Å using the same crystal structure as previously refined at BM1B, but with a Ru exchange of 12.0 ± 0.4 % or Cu exchange of 7.8 ± 0.3 %.

The crystal structure did model the diffraction pattern well and the refined exchanges of 12.0 ± 0.4 % for Ru or 7.8 ± 0.3 % for Cu compare well with those determined at BM1B of 11.3 ± 0.2 % for Ru or 7.4 ± 0.1 % for Cu. As these disorder levels are chiefly determined by small angle peaks, the proximity of these values indicates that preferred orientation is not a problem and the use of flat plate geometry is acceptable.

Before anomalous diffraction patterns could be collected, the location of the edge had to be determined precisely as it differs from its theoretical value, typically by a few eV. It depends not only on the ionic state of the ion, but also its chemical environment [10] and so must be determined for each compound studied. For this reason the detector was positioned at 27.3°, a location where there would be no Bragg peaks, and an energy scan performed around the theoretical value for the Tb L_{III}-edge of 7514 eV. The energy scan of Figure 6.19 shows the inflexion point to be at 7516 ± 1 eV, which defines the absorption edge value. Thus, all experimental values required a shift of 2 eV for comparison with the theoretical values, this demonstrates that the terbium ions are not greatly affected by their local environment.

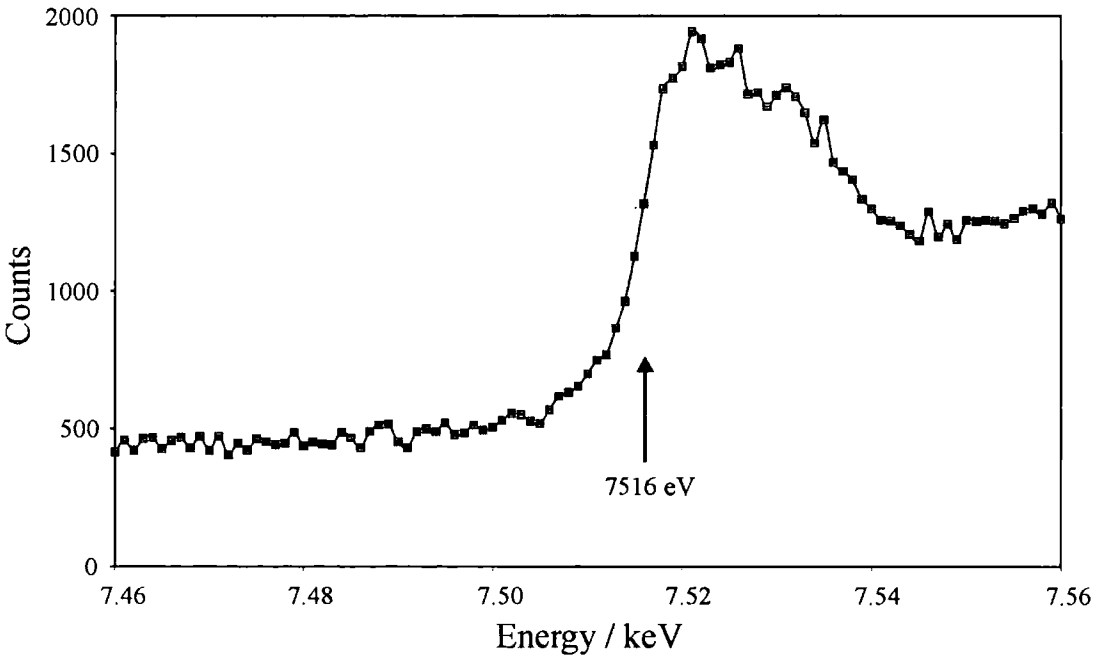

Figure 6.19 Energy scan around the Tb L_{III}-edge in the $Sr_2TbRu_{0.90}Cu_{0.10}O_6$ sample measured at 2θ = 27.3°. The inflexion point, which defines the edge energy, is highlighted with an arrow at 7516 eV.

Two diffraction patterns were collected, one at an energy of 7470 eV, below the edge and the other at 7514 eV, on the edge. The patterns were collected from 10° to 90° with the same resolution and count time as the non-anomalous measurement to allow direct comparison of results. The scattering factors were calculated using the program fprime from the GSAS suite [11-14] and the previously determined crystal structure was used again. The diffraction pattern collected with an incident energy of 7470 eV is shown in Figure 6.20 and the model structure was refined with 100 % ordering of the *B* cations assumed. The positions of the first two ordering peaks indicated by arrows and are shown enlarged.

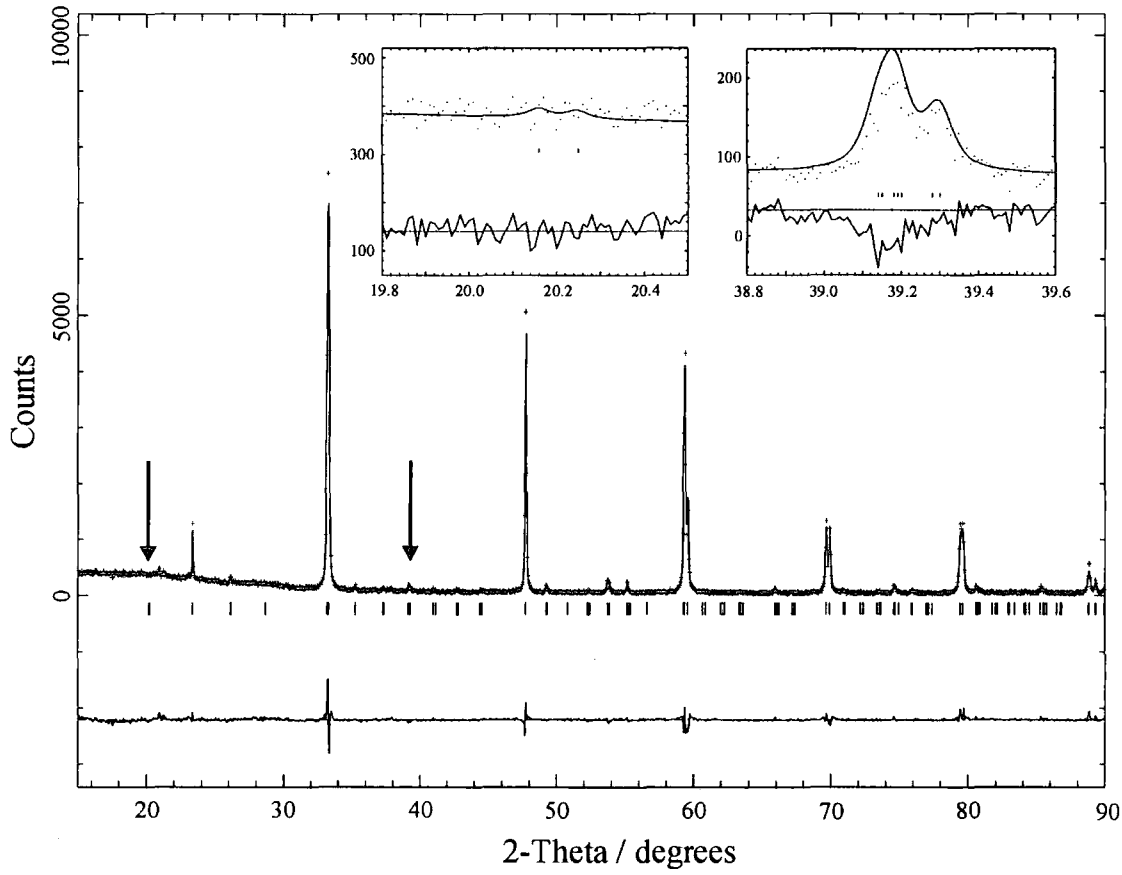

Figure 6.20 Diffraction pattern collected at 7470 eV on the $Sr_2TbRu_{0.90}Cu_{0.10}O_6$ sample refined with a 100 % ordering of *B* cations.

As can be seen the ordering peaks are very small, in fact the first ordering peak is washed out in the background. This led to refinements with 100 % and random ordering of the *B* cations yielding very similar *R*-factors of R_p = 9.36 %, R_{wp} = 12.18 % and R_{exp} = 7.42 % and R_p = 9.30 %, R_{wp} = 12.10 % and R_{exp} = 7.42 % respectively. Therefore ordering analysis was impossible due to the low peak intensities.

The second diffraction pattern measured using an energy (7514 eV,) much closer to the edge energy is displayed in Figure 6.21. Again the structural model was refined with 100 % ordering of the *B* cations. The ordering peaks are slightly larger in this pattern, however once again there is *no* difference between a completely ordered and random *B* cation refinement, with both giving R_p = 5.43 %, R_{wp} = 6.95 % and R_{exp} = 4.54 %. Allowing refinement of the disorder simply lead to unphysical exchanges of ruthenium or copper. The reason is due to the scattering factors used to model the intensity at 7514 eV are 44.143 electrons for terbium and 43.943 electrons for ruthenium, hence once again the refinement is blind to the cation distribution.

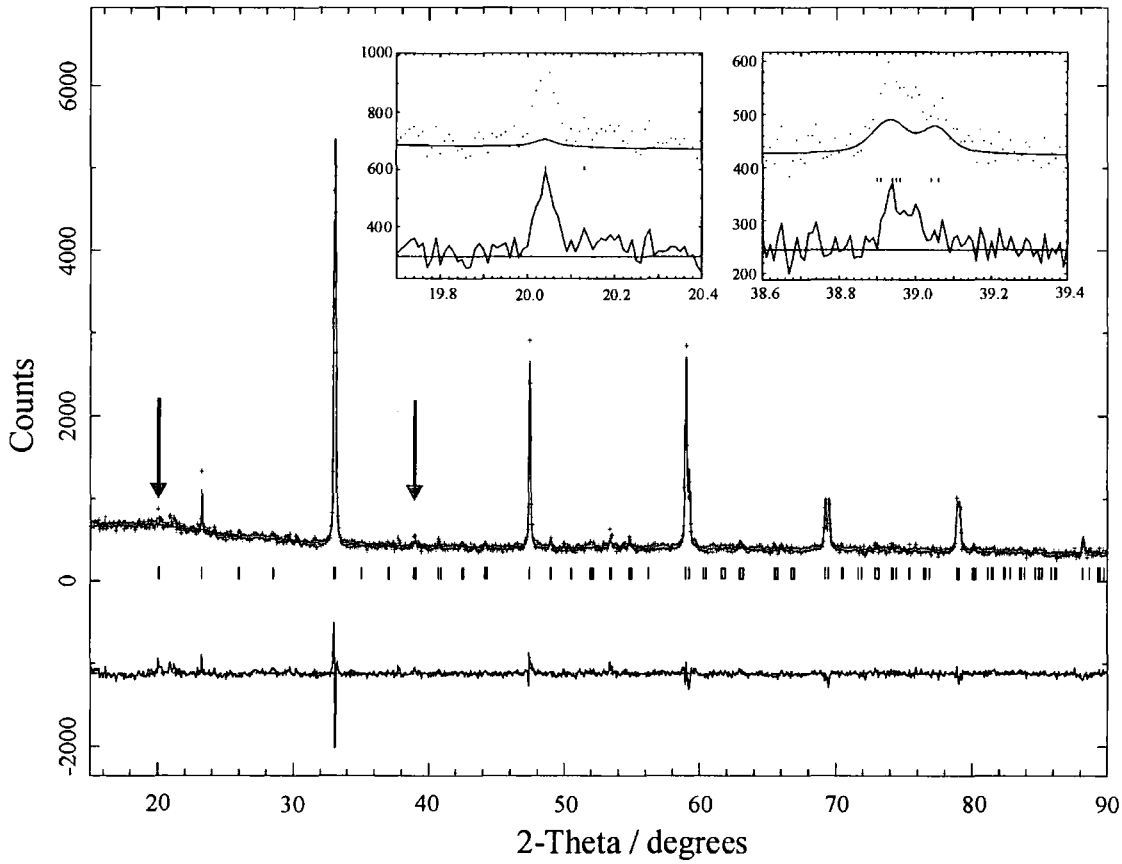

Figure 6.21 Diffraction pattern of $Sr_2TbRu_{0.90}Cu_{0.10}O_6$ measured with an energy of 7514 eV. The model structure was refined with a 100 % ordering of *B* cations.

Clearly as there is significant ordering peak intensity, the scattering factor used to model the profile was not correct. Closer inspection of the scattering factor of terbium at the L_{III}-edge shows that over 1 eV it varies by over 22 electrons. So when measuring a diffraction pattern very close to the edge there will be massive uncertainty in the scattering factor. The scattering factor could be refined as well as the fractional occupancies of the *B* sites as the peaks involving the sum of the scattering factors will allow this to be fixed, while the ordering peaks will determine

the occupancy. However, in this case though the peak intensities were much improved, the scattering factor only changed by ~ 3 electrons and the exchanges still remained unphysical.

Therefore none of the refinements undertaken near the terbium edge were able to lead to a solution of the ordering problem. This was due to the scattering factors of terbium and ruthenium being brought too close together resulting in small peak intensities, poor peak sensitivity and large uncertainty in the scattering factor.

6.5.3 Experiments at the Copper Edge

Owing to the low copper concentration in the sample the location of the copper edge was determined by moving the detector to $2\theta = 27.5°$, the position of a Bragg peak when the incident energy is 8979 eV, that of the *K*-edge. An energy scan was performed around 8979 eV, the slight change in energy through the scan being compensated for by the corresponding change in angle 2θ, so that the detector was fixed on the Bragg peak. Figure 6.22 shows the intensity decreasing as the energy of the incident radiation moves through the absorption edge, with the edge energy determined to be 8952 ± 1 eV.

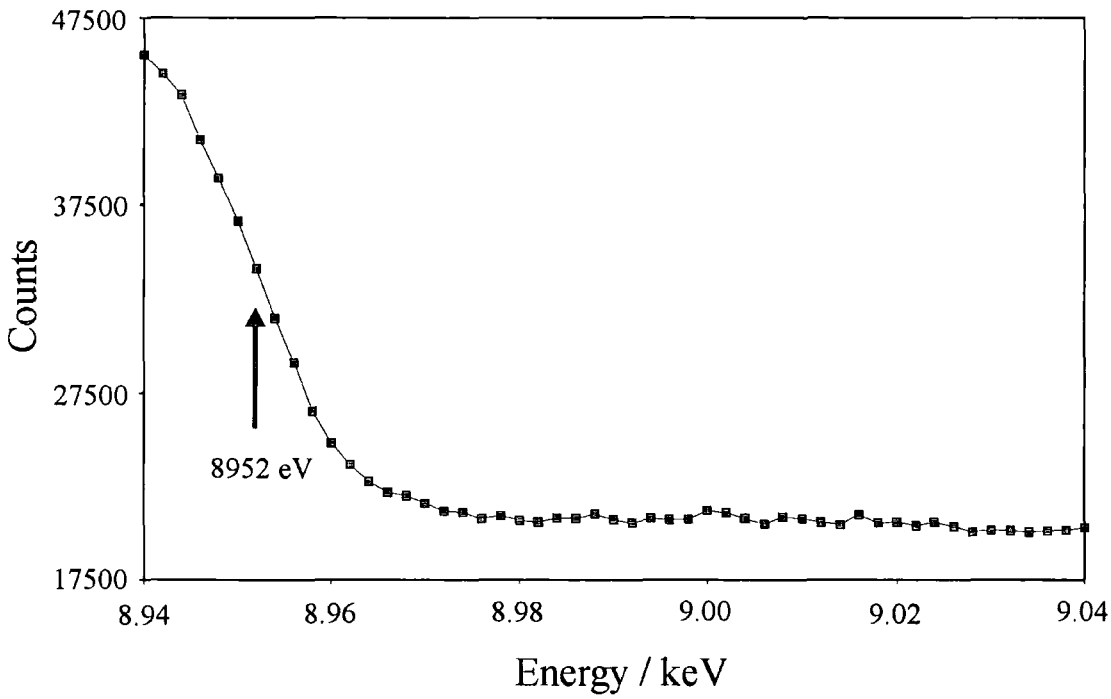

Figure 6.22 Energy scan of $Sr_2TbRu_{0.90}Cu_{0.10}O_6$ to determine the location of the copper edge with the detector fixed on the Bragg peak at 2θ ~ 27.5°. The inflexion point (arrowed) occurs at 8952 eV.

A diffraction pattern in the 2θ range 10° to 100° was collected utilising an incident energy of 8960 eV, 8 eV above the edge. The scattering factors of the elements were calculated using the energy 8987 eV, 8 eV above the edge, as this far away from the edge the scattering factor of copper only varies by 0.3 electrons per eV. This avoids the problem observed at the terbium edge with the scattering factor being excessively sensitive to slight changes in the incident energy very close to the edge.

The diffraction pattern (Figure 6.23) was refined with the same crystal structure as for all the anomalous data sets, but with amount of exchange of cations from the 2*c* and 2*d* sites as a free parameter. For ruthenium the required exchange with terbium is 16.3 ± 0.9 % and for copper it is 8.8 ± 0.5 %. The *R*-factors are acceptable with R_p = 6.31 %, R_{wp} = 8.00 % and R_{exp} = 5.32 % and the relatively large ordering peaks are modelled reasonably well.

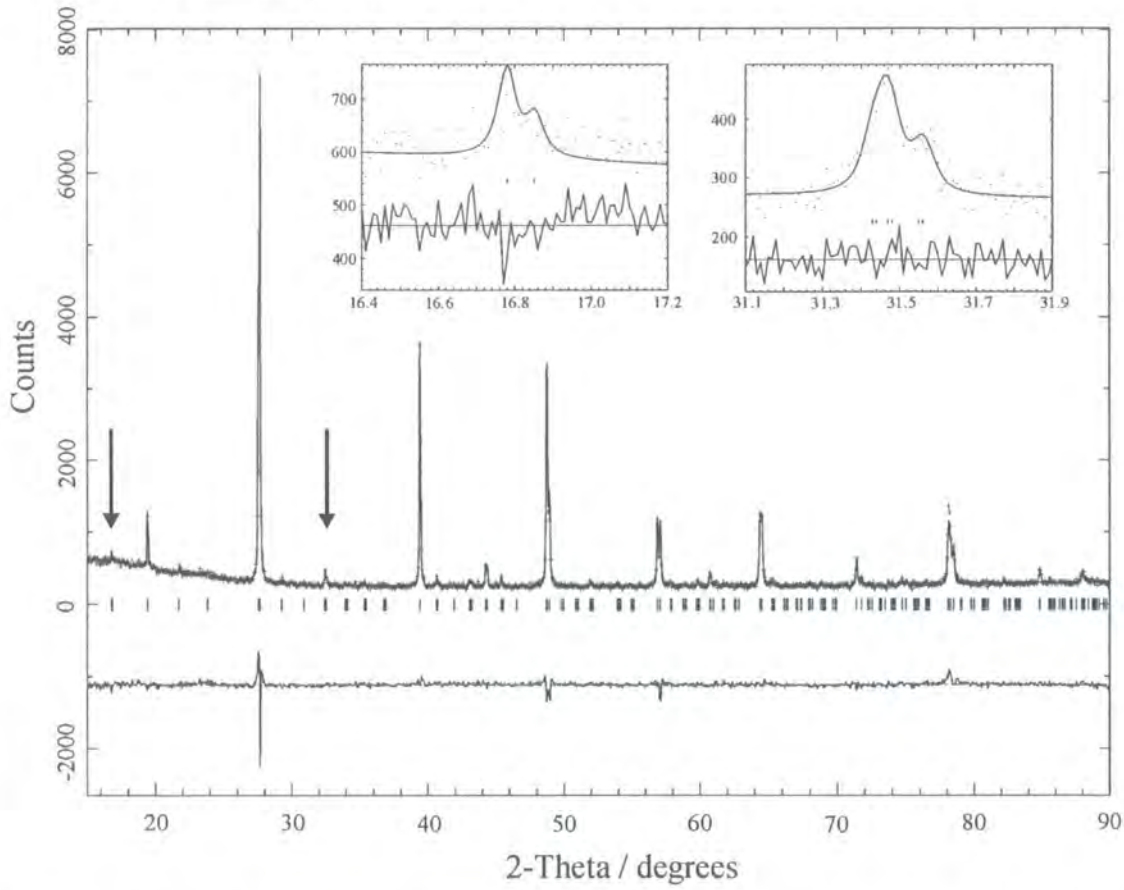

Figure 6.23 The diffraction pattern of $Sr_2TbRu_{0.90}Cu_{0.10}O_6$ measured with an incident energy 8960 eV with the refined exchange of Tb with Ru of 16.3 ± 0.9 %. The two principal ordering peaks are again highlighted.

The successful refinement of a second diffraction pattern that utilises a different set of scattering powers should allow a unique solution to the disorder of the *B* cations to be determined. The results of the two non-anomalous refinements and this Cu *K*-edge refinement were compiled and compared on a disorder plot shown in Figure 6.24.

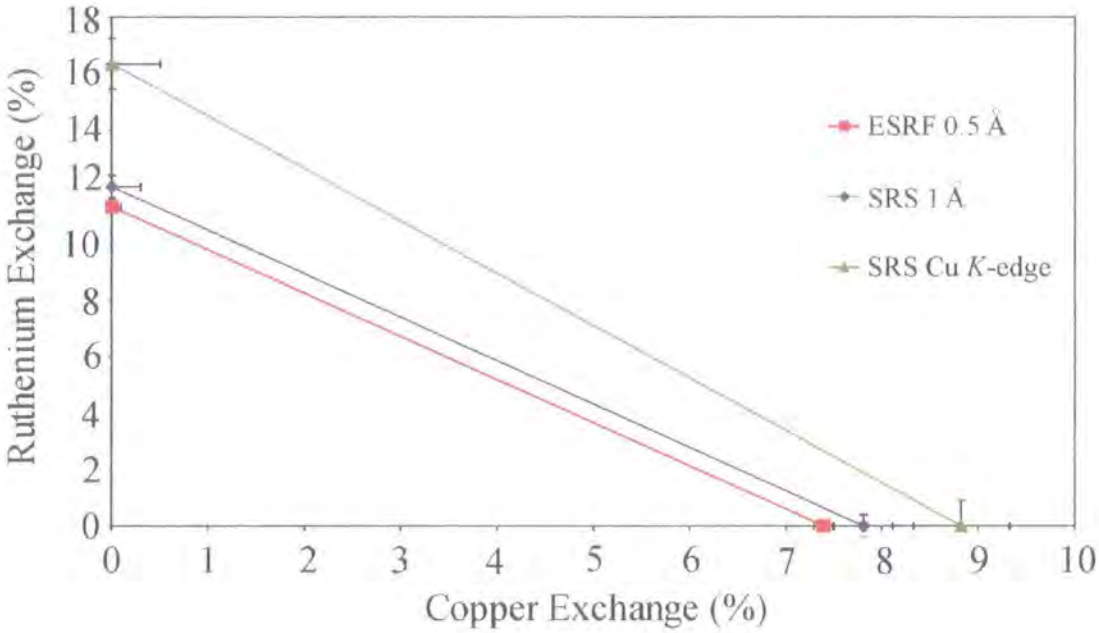

Figure 6.24 Disorder plot for *B* cations in $Sr_2TbRu_{0.90}Cu_{0.10}O_6$ resulting from having utilised the two non-anomalous data sets collected at the ESRF and SRS, as well as the Cu *K*-edge data.

The results of the two non-anomalous experiments yield gradients which are very similar as the scattering factors away from any edge do not vary significantly. The disorder line resulting from refinement of data obtained using the Cu *K*-edge wavelength has a noticeably different gradient for this reason. The agreement between the two non-anomalous results is quite good and the remaining line on the disorder plot should intersect them indicating the actual disorder in the system. The results suggest that the disorder is likely to manifest itself primarily as a copper exchange with terbium, as the lines almost intersect near the Cu-axis. However the result is not entirely convincing due to the larger errors present with the refinement of the copper edge data, which would manifest in a change of the position of this line in the disorder plot. Also the gradient of the Cu edge line in the disorder plot is $m_{expt} = -1.85 \pm 0.15$ whereas theory suggests $m_{pred} = -2.19 \pm 0.11$, which may indicate a slight problem with the refinement, which will be discussed in section 6.5.4. However were the theoretical gradient adopted, this would tend to increase the intercept on the Ru axis

and/or decrease the intercept on the Cu axis, either way making the Cu disorder only scenario even more likely. The inclusion of the copper edge work thus tends to indicate that copper disorder is more likely, though does not prove this conclusively.

6.5.4 Experiments at the Ruthenium Edge

The experiments at the ruthenium edge were all performed by Dr. Philip Pattison, the instrument scientist on BM1B. To determine the location of the edge an AMPTEK X-ray detector was set at 30 cm from the $Sr_2TbRu_{0.90}Cu_{0.10}O_6$ sample reported on above. A fluorescence scan was made concentrating on the Ru *K*-edge and this is shown in Figure 6.25. The inflexion point defines the edge energy and was 22130 eV in $Sr_2TbRu_{0.90}Cu_{0.10}O_6$. So a shift of -13 eV had to applied to all experimental energies in order to use theoretically calculated values as they place the edge at 22117 eV.

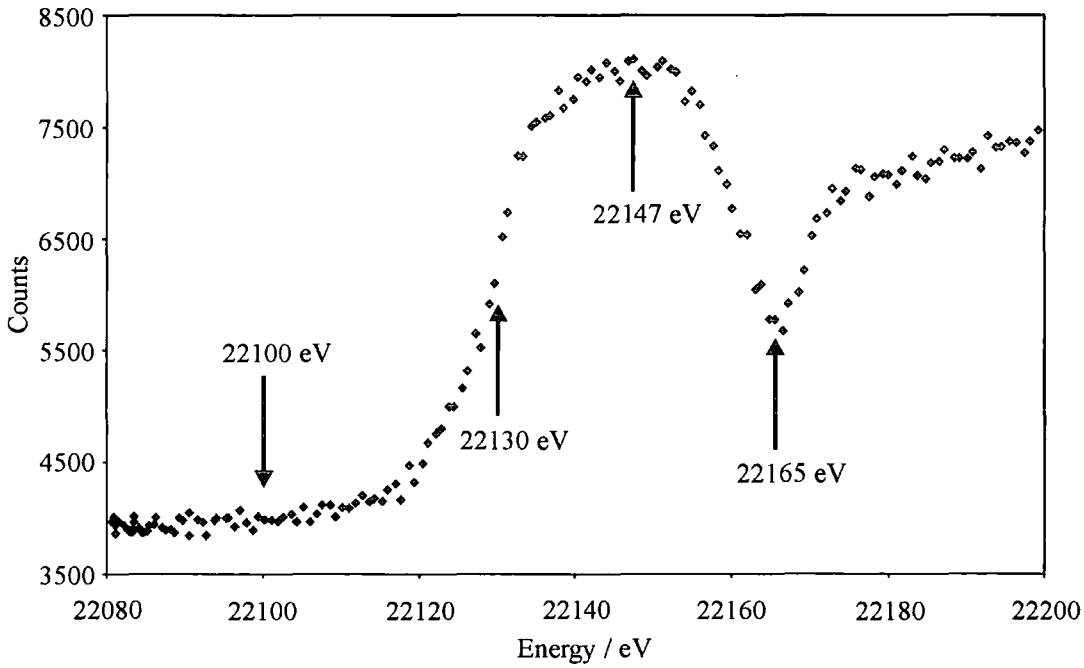

Figure 6.25 Fluorescence scan of the Ru *K*-edge with arrows indicating the energies selected for diffraction patterns to be measured. Another diffraction pattern was collected at 22050 eV which is not shown on this scale as it was deliberately chosen well below the edge.

Data were measured at five different energies in the available beamtime, focussing on just the low angle section of the diffraction pattern, typically between 2° and 22° (2θ). At the wavelengths around the ruthenium edge this angular range includes the largest and most important ordering peaks so little is lost from adoption of only this narrow region. The previous full pattern refinement of $Sr_2TbRu_{0.90}Cu_{0.10}O_6$ had already

determined the crystal structure and this was used for these ordering refinements. As shown earlier the crystal structure does not change significantly for these small changes in *B* cation ordering. The energies selected were 22050, 22100, 22130, 22147 and 22165 eV (some of which are shown in Figure 6.25) so that a range of ruthenium scattering factors would be utilised and the results could be compared for consistency. All the patterns were collected with the same step size of 0.004° and for the same count time, so they are directly comparable for the angular region over which they coincide. Figure 6.26 shows three of the five diffraction patterns and the effect of this range of scattering factors of ruthenium was very evident from the different intensities of the peaks in each pattern. The peak at $2\theta \sim 6.8°$ is an ordering peak and its intensity varies as one would predict. As the energy is increased through the edge, the ruthenium scattering factor will first fall, reach a minimum at the edge energy, then begin to rise again. From the previous work the system is known to be largely ordered, terbium occupies the other site and is heavier than ruthenium. Thus as the ruthenium scattering factor falls, then rises as the energy increases through the edge, the intensity of the ordering peaks which is related to the difference in the scattering powers on the 2*c* and 2*d* sites will rise, then fall as observed in Figure 6.26. The small shift in the positions of the peaks is simply due to the slightly different wavelength of each diffraction pattern.

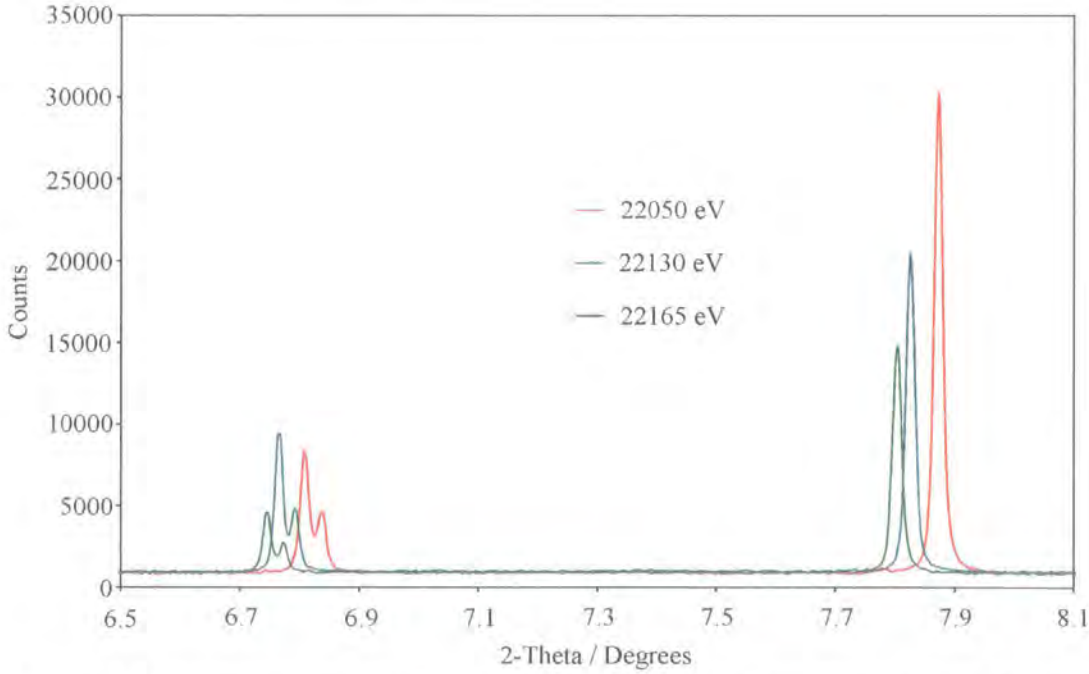

Figure 6.26 Comparison of the same section of the diffraction pattern for three different energies, one below the edge (22050 eV), one at the edge (22130 eV) and one above the edge (22165 eV).

The second peak at $2\theta \sim 7.8°$ is the combination of the (110) and (002) reflections which both involve the sum of the *B* atom scattering powers. From considering just the change in scattering factor of ruthenium through the edge the intensity should fall, then rise, opposite to the effect of the difference peak at $2\theta \sim 6.8°$. Here the intensity just decreases, so the energy dependence is different from what would be expected and this is due to an additional effect.

To determine the source of the problem, the intensities of all the peaks in the two diffraction patterns measured at 22100 eV and 22147 eV, above and below the Ru edge, were compared. Direct comparison was allowed as the same step resolution and counting time were used to collect each pattern between 2° and 22°. Every peak in the 22100 eV pattern which was larger than its equivalent in the 22147 eV pattern was composed only of reflections where $h + k + l = 2n$, where n is any integer, i.e. an even number. Clearly this special reflection condition is related to the anomalous nature of the diffraction experiment as it varies through the edge.

The ruthenium atoms only make a sizeable contribution to the diffraction intensity when $h + k + l$ is even, as proved in Appendix A.2, and these peaks are larger below the edge. Therefore the cause of the reduction in intensity of the $h + k + l = 2n$ peaks as the energy goes through the absorption edge is due to the increased absorption of the ruthenium in the sample. The absorption of a single species in material is determined by f'', the imaginary component of the scattering factor. Its value is also calculated by the program fprime, and typically at the absorption edge this rises by approximately 3-4 electrons.

The scattering factors of the elements were calculated using the program fprime from the GSAS suite for each diffraction pattern. The crystal structure which was previously determined from the non-anomalous data collection was used, but the disorder of the *B* cations allowed to refine. Each of the five patterns were refined separately and the profile of the 22100 eV refinement is shown in Figure 6.27 with R_p = 5.49 %, R_{wp} = 7.81 %, and R_{exp} = 3.15 %. There are four peaks in the pattern which are sensitive to the ordering of the *B* cations. These match only approximately, with the two most intense peaks again highlighted, in Figure 6.27.

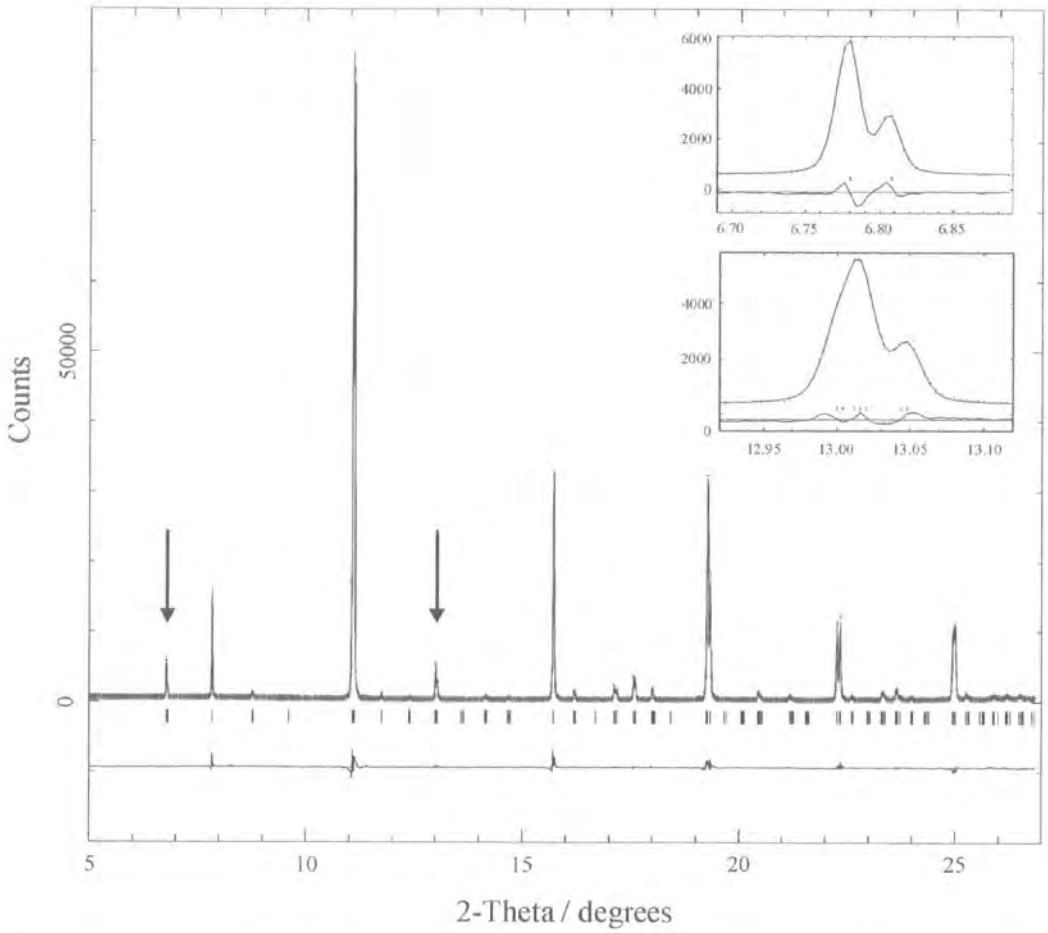

Figure 6.27 Diffraction pattern measured of the $Sr_2TbRu_{0.90}Cu_{0.10}O_6$ sample with energy 22100 eV. The two most important ordering peaks are highlighted.

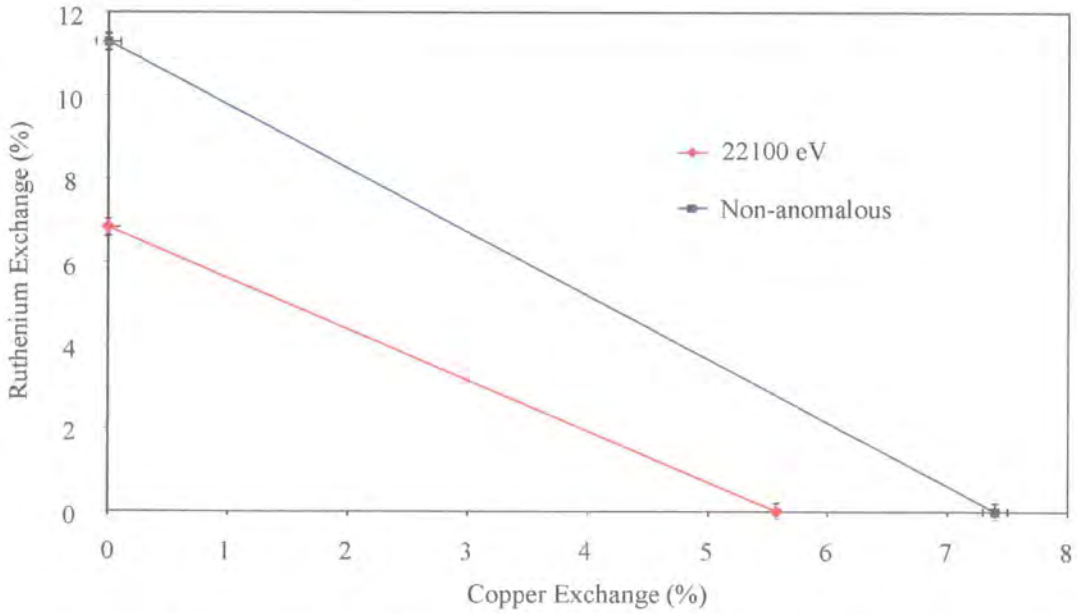

Figure 6.28 Disorder plot for the $Sr_2TbRu_{0.90}Cu_{0.10}O_6$ comparing the results of the refinements of the 22100 eV data and the non-anomalous measurements at the ESRF.

The refined disorder from the 22100 eV data is a line with a smaller gradient than the non-anomalous disorder in the disorder plot of Figure 6.28. This is expected as the scattering factor of ruthenium has been reduced and m_{pred} = -1.29 ± 0.06 compares well with m_{expt} = -1.23 ± 0.04. However the two lines were expected to cross and the point of intersection on the diagram would be the solution to the problem. The disorder of Ru and Cu with Tb would then be able to accurately replicate the diffraction intensity in both patterns. The proximity of the predicted and observed disorder gradients indicates that the problem lies not with the gradients of the lines on the disorder plot, but their position and hence its error. The most likely source of this error was the failure to incorporate the observed additional absorption of ruthenium at the Ru *K*-edge. Attempts were made to change the absorption of ruthenium to match physical reality by refining its *f''* parameter. However this did not lead to a significant change in the refined disorder of the *B* cations, but did give negative and unphysical values of *f''*, so these refinements are not shown here.

The refinements of the other four diffraction patterns all gave results with slightly better *R*-factors than the 22100 eV data refinement, however the ordering peaks were no better calculated. The results are shown in Figure 6.29 and the scatter of results indicates that the problem of absorption has had a severe effect.

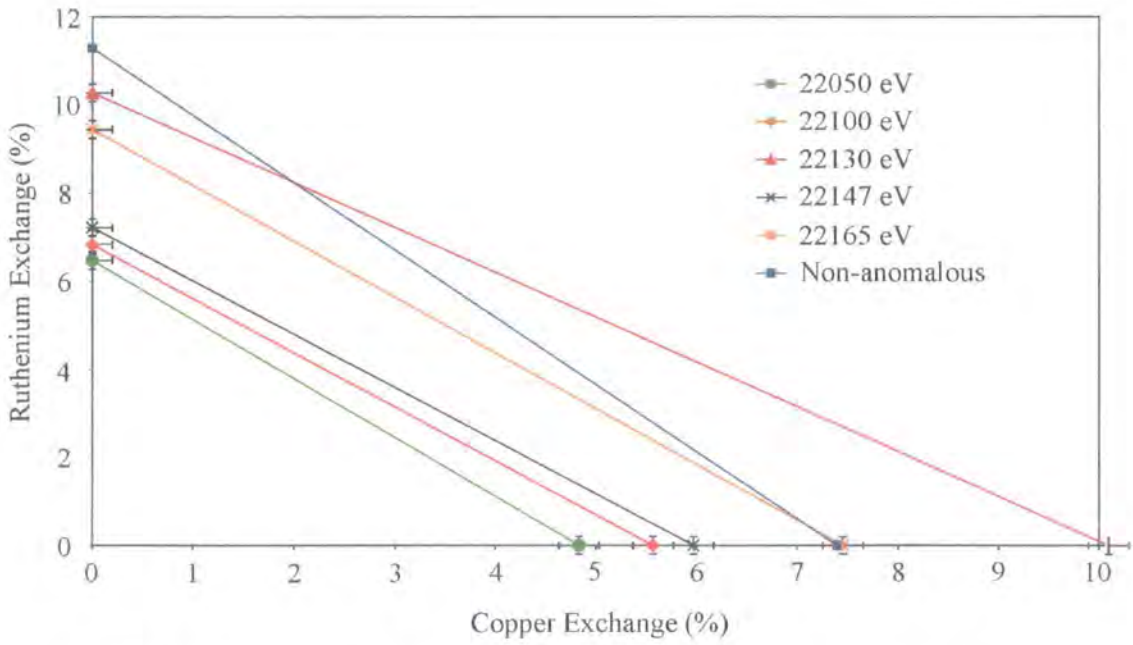

Figure 6.29 Compilation of the disorder results calculated from all the ruthenium edge patterns and non-anomalous patterns undertaken at the ESRF.

The disorder as determined from the 22130 eV diffraction pattern is the furthest out simply due to uncertainty in the scattering factor very close to the edge. Within the experimental uncertainty of the instrument, ~ 1 eV, the change in the scattering factor varies sufficiently (~ 1.8 electrons) to shift the disorder line so that it intersects the non-anomalous line, while a further 1 eV change (~ 0.7 electrons) induces intersection with the 22100 eV and 22147 eV lines. Clearly this degree of sensitivity to the energy very close to the edge precludes useful extraction of results from the 22130 eV pattern. The remaining ruthenium edge patterns have broadly similar gradients to each other, but significantly different to the non-anomalous line. This indicates that it is best to perform anomalous diffraction measurements, not exactly on the edge, but 20 – 50 eV away where the anomalous effects are still important, but the scattering factor can be defined to 0.1 – 0.05 electrons respectively. However, due to the failure to incorporate correctly the extra absorption of ruthenium into the model none of the refinements at the ruthenium edge can be trusted. Although the experiments at the ruthenium edge have not contributed anything positive concerning the disorder in these perovskite systems, they have indicated that the best energy relative to the edge to conduct experiments is 20 – 50 eV below the edge. This could be useful for future experiments, should the extra absorption of the anomalous species be accounted for accurately.

6.5.5 Summary of anomalous diffraction results

The anomalous diffraction experiments were not able to determine convincingly the nature of the *B* cation disorder in $Sr_2TbRu_{0.90}Cu_{0.10}O_6$. Experiments at the terbium edge reduced the scattering factor close to that of ruthenium and so differentiating between the two was not possible with good precision. Experiments at the ruthenium edge suffered overly from the increased absorption of ruthenium, and so accurate refinement of the cation disorder could not be obtained due to poorly replicated intensities. Only the experiments at the Cu *K*-edge produced results which may possibly aid solution of the problem.

The results at the copper edge in combination with the non-anomalous results suggested that the disorder was due to ~ 7-8 % copper exchange with terbium. However, the experiments at the ruthenium edge showed that absorption was a major problem so this effect must also be considered for the experiments undertaken at the copper edge. The change in scattering factor helps to determine the amount exchanged

and the scattering factor was well defined and about the same relative magnitude changes at both the copper and ruthenium edges. The extra absorption of the anomalous species was not well defined in either case, however while this had a large effect on the refinement of the ruthenium edge data, as there is nine times less copper, the effect on the copper data was approximately an order of magnitude less. Additionally, as it appears the copper is spread over the 2*c* and 2*d* sites and it is a factor of 9 less abundant, therefore the reflection condition will not be as severe and so the absorption effect will be much reduced. The validity of these statements can be confirmed by considering the *R*-factors determined from refinements of the same $(\sin\theta)/\lambda$ range of 0.095 Å to 0.413 Å. The refinements of the BM1B data degrade quite severely from the non-anomalous *R*-factors of R_p = 3.67 %, R_{wp} = 5.42 %, and R_{exp} = 2.89 % to the ruthenium edge result of R_p = 5.18 %, R_{wp} = 7.68 %, and R_{exp} = 3.10 %. The quality of the refinement of the copper edge data does not decrease so markedly as evidenced by the *R*-factors derived from the SRS data at the non-anomalous energy of R_p = 6.89 %, R_{wp} = 8.65 %, and R_{exp} = 6.91 % and at the copper edge of R_p = 5.92 %, R_{wp} = 7.56 %, and R_{exp} = 5.21 %. For these reasons the refinement of the copper edge data does have some value, though it is hard to justify the result as more than a suggested disorder, rather than a definitive proof.

6.6 Non-anomalous Data Collection of Sr_2TbRuO_6

A diffraction pattern was collected at room temperature at station 2.3 of the SRS on Sr_2TbRuO_6, the parent compound of the $Sr_2TbRu_{1-x}Cu_xO_6$ series. The data were collected with a count time of 1 second and step size of 0.01°, as for the $Sr_2TbRu_{0.90}Cu_{0.10}O_6$ measurements. As there is no copper present in the sample, there is no utility in studying the compound at one of the edges, and the disorder can only manifest between Tb and Ru on the *B* sites. The crystal structure of Sr_2TbRuO_6 was refined with 100 % ordering of the *B* cations and is shown in Figure 6.30. As there are no unindexed peaks in the pattern there is no crystalline impurity present. Therefore the sample is more likely to be stoichiometric and any disorder is far more likely to manifest as an exchange rather than a vacancy.

The diffraction profile is well matched with 100 % ordering of the *B* cations and the ordering peaks are particularly well determined. The details of the crystal structure are listed in Table 6.10 and the *R*-factors are good with R_p = 5.96 %, R_{wp} = 7.64 %, and R_{exp} = 5.05 %. The structure agrees with the structure used for the neutron diffraction,

considering the oxygen positions will be less well defined using a second generation synchrotron source than the latest neutron facility.

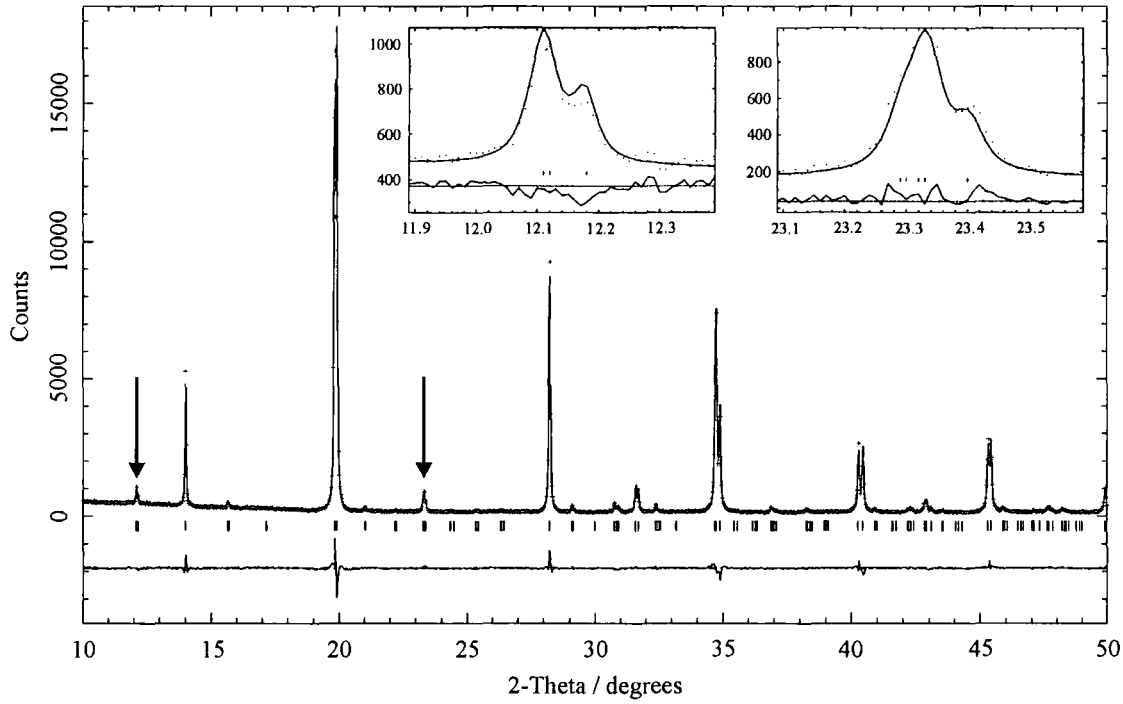

Figure 6.30 The diffraction pattern of Sr_2TbRuO_6 refined with 100 % ordering of the *B* cations. The ordering peaks have intensities which this level of order determines very well. There were no unindexed peaks in the pattern, hence no impurity phase.

Sr_2TbRuO_6		$P2_1/n$			Room temperature	
a / Å		b / Å	c / Å	β / °	Volume / Å^3	
5.79683(14)		5.82394(13)	8.21488(23)	90.303(2)	277.334(3)	
Atom	Site	x	y	z	Occ	B_{iso}/Å^2
Sr	4*e*	0.0040(10)	0.0298(3)	0.7499(9)	1.000(0)	1.96(4)
Tb	2*c*	0	½	0	1.000(0)	1.41(3)
Ru	2*d*	½	0	0	1.000(0)	1.41(3)
O1	4*e*	0.2604(40)	0.3272(38)	0.5335(33)	1.000(0)	2.31(57)
O2	4*e*	0.1930(42)	-0.2502(42)	0.5149(29)	1.000(0)	2.67(76)
O3	4*e*	-0.0484(45)	0.4877(22)	0.7414(32)	1.000(0)	2.43(63)

R_p = 5.96 %, R_{wp} = 7.64 %, R_{exp} = 5.05 %, R_{F^2} = 4.47 %

Table 6.10 The lattice parameters and atomic coordinates of Sr_2TbRuO_6 refined from room temperature data taken at station 2.3 of the SRS. The 100 % ordering of the *B* cations was assumed.

As the ordering peaks are well determined with 100 % ordering of the *B* cations, this leaves two distinct possibilities, either the system is in fact, highly ordered, or the refinements are insensitive to ordering of the *B* cations in this case.

To test these different options, the ordering level was set to the random arrangement of *B* cations, which involves placing 50 % of both Tb and Ru on each *B* site. The refined diffraction pattern is shown in Figure 6.31 and although the general pattern is described nicely, the ordering peaks are far from ideal, which results in the increased *R*-factors of R_p = 6.81 %, R_{wp} = 9.08 %, and R_{exp} = 5.05 %. Hence, the crystal structure is definitely not a random arrangement of *B* cations and the refinements of *B* cation disorder are likely to be sensitive.

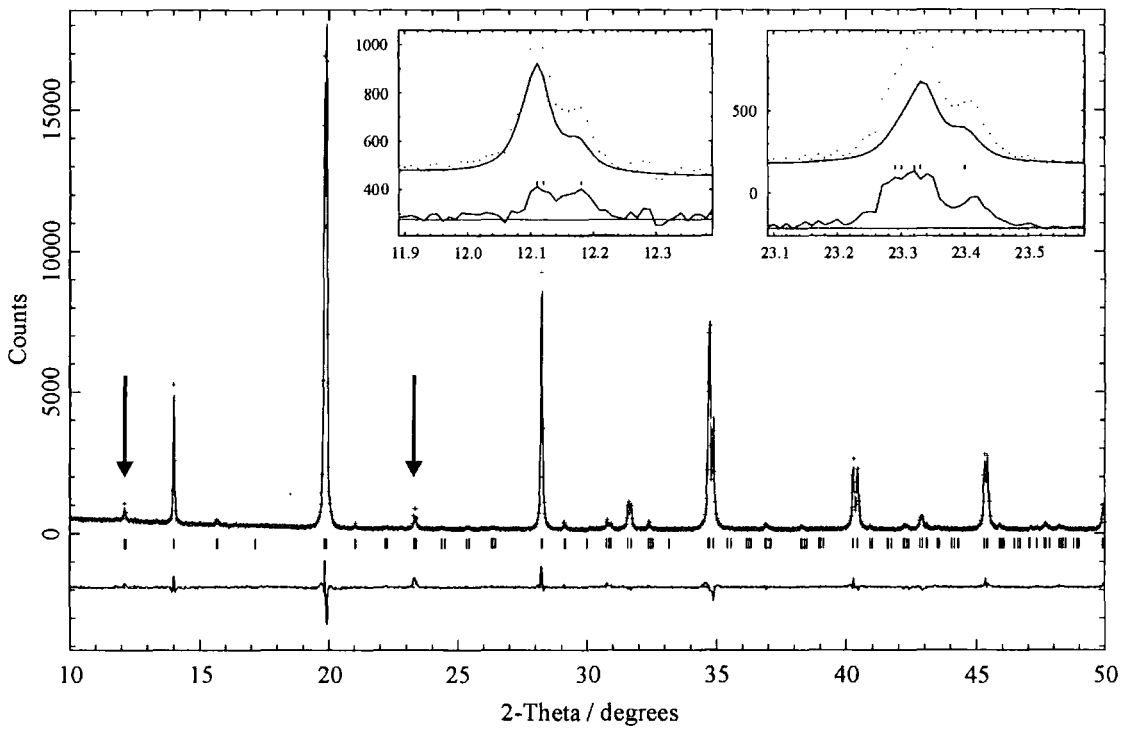

Figure 6.31 The same diffraction pattern of Sr_2TbRuO_6 but now refined with a random arrangement of *B* cations on the 2*c* and 2*d* sites. The ordering peaks, the two most intense of which are highlighted, have intensities much different from those calculated from this random arrangement of *B* cations.

Finally, the crystal structure of Sr_2TbRuO_6 was refined allowing for exchange of Tb and Ru between the 2*c* and 2*d* sites and is shown in Figure 6.32. The model structure is able to replicate the diffraction profile well, but the ordering peaks are not as well matched in Figure 6.32 as they are when 100 % ordering is assumed. Thus, this refined exchange of Tb and Ru between the two sites of 1.8 ± 0.2 % and leads to a worse result. Owing to this, the disorder of the *B* cations must be less than this value, and probably no more than 1 %, judging from the deterioration of the ordering peaks.

Therefore the crystal structure of Sr_2TbRuO_6 is as given in Table 6.10 with a 1:1 ordered arrangement, with disorder of the *B* cations no more than 1 %.

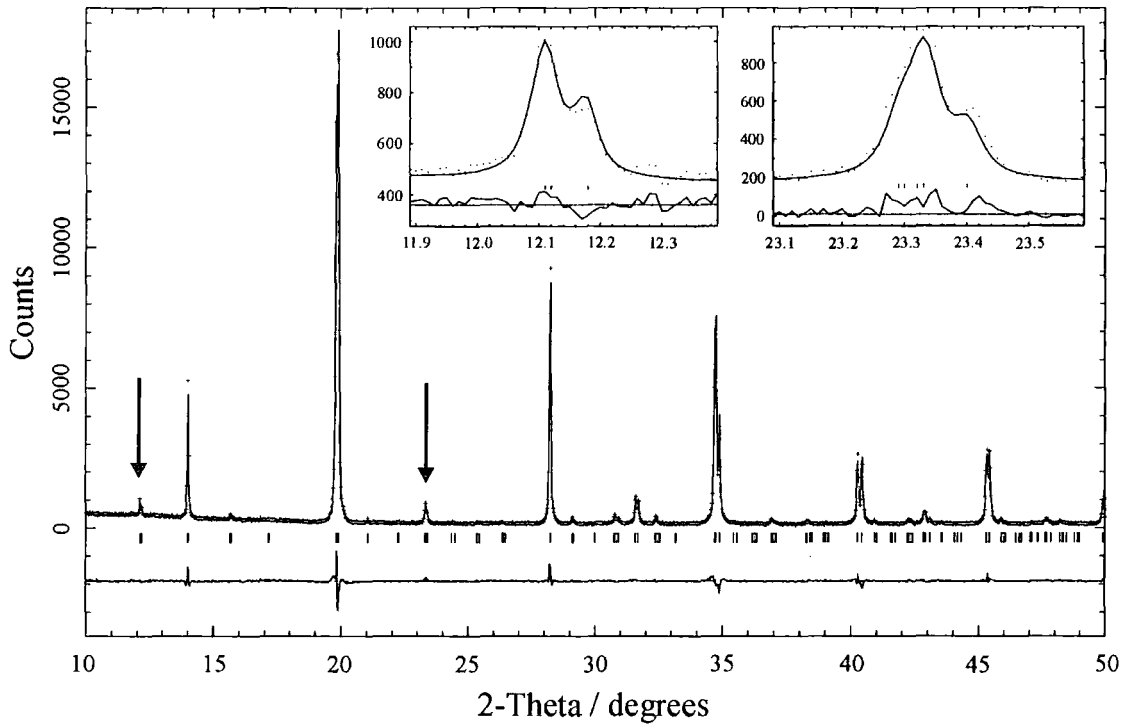

Figure 6.32 The diffraction pattern of Sr_2TbRuO_6 refined allowing for exchange of the only *B* cations, Tb and Ru between the 2*c* and 2*d* sites.

6.6.1 Implications for Ordering in $Sr_2TbRu_{0.90}Cu_{0.10}O_6$

As Sr_2TbRuO_6 has been determined to have a fully ordered *B* cation structure this will have implications for the ordering in $Sr_2TbRu_{0.90}Cu_{0.10}O_6$. From the difference in charge and size [15] of the Tb^{3+} and Ru^{5+} ions (Table 6.11) an ordered 1:1 arrangement was expected [16] in Sr_2TbRuO_6. With the introduction of 10 % copper into the sample, the disorder level as determined from non-anomalous data increased to ~ 7-8 %. As no ruthenium was disordered in Sr_2TbRuO_6, in this sample it is most likely to be copper. The charge and size of the Cu^{2+} or Cu^{3+} ion is also more similar to Tb^{3+} than the Ru^{5+} ion is, further supporting a copper rather than ruthenium exchange. Thus, given that there is disorder in $Sr_2TbRu_{0.90}Cu_{0.10}O_6$, this is probably due to a 7-8 % exchange of copper with terbium between the 2*c* and 2*d* sites. This result is also consistent with the results of the refinements of the data obtained at the copper edge. As charge is the dominant consideration it is expected that $Sr_2TbRu_{0.90}Cu_{0.10}O_6$ would be fully ordered if the Cu was just in the +3 state and 10 % disordered were it to be +2. Thus the 7-8 % copper on the 2*c* site may indicate crudely that ~ 70-80 % of the copper is Cu^{2+} and 20-30 % Cu^{3+}.

Ion	Ionic Radius / Å
Cu^{2+}/Cu^{3+}	0.62 / 0.60
Tb^{3+}	0.92
Ru^{5+}	0.52

Table 6.11 The size and charge of the *B* cations present in $Sr_2TbRu_{0.90}Cu_{0.10}O_6$.

6.7 Conclusions

High intensity and high-resolution powder diffraction measurements have determined that potentially superconducting impurities are contained in the compounds $Sr_2YRu_{0.85}Cu_{0.15}O_6$, $Sr_2HoRu_{0.85}Cu_{0.15}O_6$ and $Sr_2Ho_{0.80}Tb_{0.20}Ru_{0.90}Cu_{0.10}O_6$. These impurities are at such a level that they are highly unlikely to be able to account for the bulk superconductivity observed in the samples. However, imprecise knowledge of the precise composition of these samples prevented accurate determination of the *B* cation ordering. No crystalline impurities were detected in the $Sr_2TbRu_{1-x}Cu_xO_6$ series and hence any superconductivity in $Sr_2TbRu_{0.90}Cu_{0.10}O_6$ is due to this ruthenate phase. Non-anomalous refinement of the data on $Sr_2TbRu_{0.90}Cu_{0.10}O_6$ determined the disorder to be an exchange of the *B* cations of 7-11 % depending on its nature.

Anomalous diffraction measurements were undertaken at the most suitable edge for each of the *B* cation elements in $Sr_2TbRu_{0.90}Cu_{0.10}O_6$. The scattering factor of terbium at its L_{III}-edge was reduced to the extent that it was indistinguishable from ruthenium and so these results were not able to add anything. The experiments at the ruthenium edge could not be refined adequately due to the increased absorption of the ruthenium in the sample badly distorting the diffraction intensities of the $h + k + l = 2n$ peaks. The diffraction pattern collected at the copper edge was more useful as the absorption problem was much smaller and suggested the disorder was an exchange of 7-8 % of Tb with Cu.

Further non-anomalous data collections on the parent compound Sr_2TbRuO_6 confirmed that this material was fully ordered and supported the argument that the disorder present in $Sr_2TbRu_{0.90}Cu_{0.10}O_6$ was due to an exchange of 7-8 % of Tb with Cu. This can be represented explicitly as $Sr_2(Tb_{0.93}Cu_{0.07})(Ru_{0.90}Tb_{0.07}Cu_{0.03})O_6$ and it is possible that the other 2116 systems reported here behave similarly.

At first glance, the possibility of ~ 70 % percent of the copper in the sample being located on the other *B* site could be a cause for concern, however further inspection shows that this is not necessarily so. The existence of Sr_2RuO_4 shows that RuO planes can superconduct [7] under the right conditions. However in the double perovskites there are no single ion oxide sheets except in the layered structures [17-19]. In the 1:1 ordered structures such as Sr_2TbRuO_6 there are only mixed ruthenium-terbium oxide layers as illustrated in Figure 6.33. If the copper is just responsible for doping holes into the structure which allows the superconductivity, then it does not matter which of the two sites, 2*c* or 2*d*, it is doped onto, as both are in the same plane.

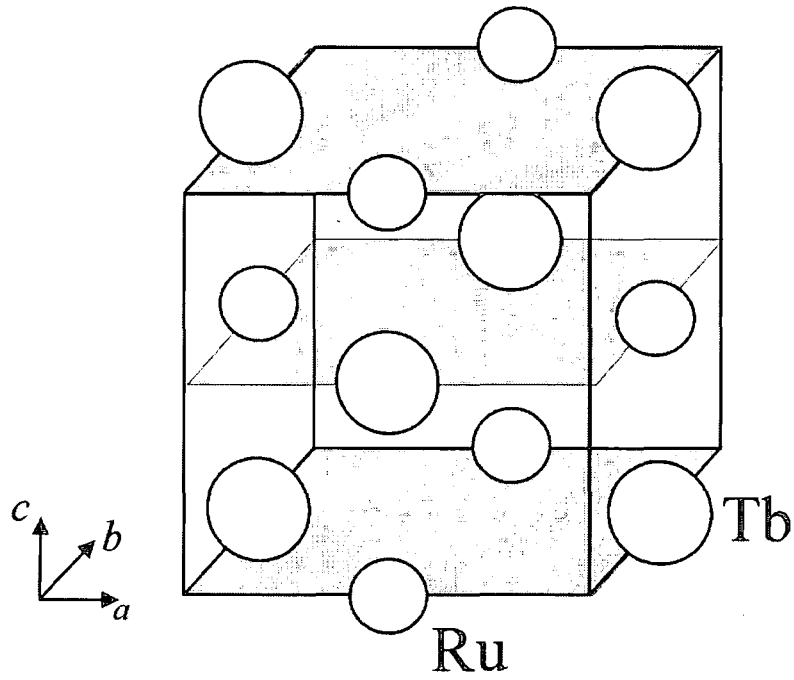

Figure 6.33 The (002) planes in Sr_2TbRuO_6 with the oxygen atoms omitted for clarity. Each (002) plane is a mixed ruthenium-terbium oxide layer with both ruthenium (small circles) and terbium (large circles) present.

The exchange of Tb and Cu between the 2*c* and 2*d* sites will affect the magnetic moment values of the Tb^{3+} and Ru^{5+} ions. The magnetic intensity, which is generated from the 2*c* and 2*d* sites, must remain the same as the previous refinements (Chapter 4), which assumed 100 % ordering of the ions. With a 7.5 % exchange the magnetic moment values of Tb^{3+} and Ru^{5+} determined at 2 K change from 1.93(10) μ_B and 4.17(10) μ_B to 1.51(10) μ_B and 4.55(10) μ_B. Clearly, the location of the copper has an effect on the size of the refined magnetic moment. These changes can't account for all of the trends of magnetic moment with copper doping observed in the $Sr_2TbRu_{1-x}Cu_xO_6$ and $Sr_2HoRu_{1-x}Cu_xO_6$, particularly as they are opposite in nature in

the two series. The presence of copper within a host magnetic lattice will also affect the magnetic interactions within that lattice and this will vary from host ion to ion. The magnetic moment decrease with copper doping in $Sr_2TbRu_{1-x}Cu_xO_6$ and the increase in $Sr_2HoRu_{1-x}Cu_xO_6$ are more likely due to the opposite nature of the copper-rare-earth magnetic interaction. Clearly the slew of interactions in such a mixed system will be complicated and completely impossible to deduce for those systems where the precise ordering is not known.

6.8 References

1 A.J.C. Wilson, ed. *International Tables for Crystallography, Volume C, Mathematical, Physical and Chemical Tables.* Vol. C, Kluwer Academic Press: London. 883 (1992).

2 S.H. Kim and P.D. Battle, *Journal of Solid State Chemistry* **114,** 174 (1995).

3 FIZ-Karlsruhe, *Inorganic Crystal Structure Database* (ICSD) (1997).

4 JCPDS-ICDD (International Centre for Diffraction Data), *PCPDFWIN* (1995).

5 M. Pissas, G. Kallias, A. Simopoulos, D. Niarchos and R. Sonntag, *Physica B* **253,** 1 (1998).

6 M.K. Wu, D.Y. Chen, F.Z. Chien, S.R. Sheen, D.C. Ling, C.Y. Tai, G.Y. Tseng, D.H. Chen and F.C. Zhang, *Zeitschrift Fur Physik B-Condensed Matter* **102,** 37 (1997).

7 Y. Maeno, H. Hashimoto, K. Yoshida, S. Nishi Zaki, T. Fujita, J.G. Bednorz and F. Lichtenberg, *Nature* **372,** 532 (1994).

8 S. Brennan and P.L. Cowan, *Review of Scientific Instruments* **63,** 850 (1992).

9 M. Sanchez del Rio and R.J. Dejus, *X-ray Orientated Program (XOP)* (2000).

10 F. Bernard, J. Lorimier, V. Nivoix, N. Millot, P. Perriat, B. Gillot, J.F. Berar and J.C. Niepce, *Journal of Solid State Chemistry* **141,** 105 (1998).

11 A.C. Larson and R.B. Von Dreele, *Los Alamos National Laboratory Report* **LAUR 86-748,** 1 (1990).

12 D.T. Cromer and D.A. Liberman, *Acta Crystallographica Section A* **37,** 267 (1981).

13 D.T. Cromer, *Journal of Applied Crystallography* **16,** 437 (1983).

14 L. Kissel and R.H. Pratt, *Acta Crystallographica Section A* **46,** 170 (1990).

15 http://barns.ill.fr/dif/icsd/elementr.html

16 M.T. Anderson, K.B. Greenwood, G.A. Taylor and K.R. Poeppelmeier, *Progress in Solid State Chemistry* **22,** 197 (1993).

17 M.T. Anderson and K.R. Poeppelmeier, *Chemistry of Materials* **3,** 476 (1991).

18 M.T. Anderson, K.R. Poeppelmeier, S.A. Gramsch and J.K. Burdett, *Journal of Solid State Chemistry* **102,** 164 (1993).

19 M. Azuma, S. Kaimori and M. Takano, *Chemistry of Materials* **10,** 3124 (1998).

7 Copper Doping in the Ruthenate Systems

7.1 Introduction

In the mixed ruthenium-copper systems studied, $A_2M\mathrm{Ru}_{1-x}\mathrm{Cu}_x\mathrm{O}_6$, the role of the copper dopant is crucial to the electronic properties of the material, with superconductivity induced typically for doping levels between 5 and 15 %. At higher doping levels, impurity phases begin to develop. A parallel study which attempted to synthesise $\mathrm{Sr}_2\mathrm{YRu}_{1-x}\mathrm{Cu}_x\mathrm{O}_6$ with x = 0.80 failed [1], as not surprisingly a large impurity phase of $\mathrm{YSr}_2\mathrm{Cu}_3\mathrm{O}_{7-\delta}$ formed, which was able to account for its superconducting nature.

The effect of the copper on the magnetic properties of the material will also be significant, irrespective of whether the copper is itself magnetic. Figure 7.1 shows the crystal structure of a parent ruthenate, $A_2M\mathrm{RuO}_6$, with the M cations on the 2*c* site and the Ru cations on the 2*d* site. With doping, the site on which the copper resides, 2*c* or 2*d*, will affect the combination of the magnetic interactions of the host ion in that sublattice. If the copper resides on the 2*c* site, then there will be fewer *M*-O-O-*M* interactions present, with *M*-O-O-Cu and Cu-O-O-Cu interactions in their place. However, if copper is situated on the 2*d* site then the ruthenium sublattice will not only have Ru-O-O-Ru interactions, but also Ru-O-O-Cu and some Cu-O-O-Cu magnetic interactions too. In either case, the inter-species interactions between the two sublattices will be affected also, leading to fewer Ru-O-*M* interactions and more Ru-O-Cu and *M*-O-Cu interactions, depending on the proportion of copper on the 2*c* and 2*d* sites.

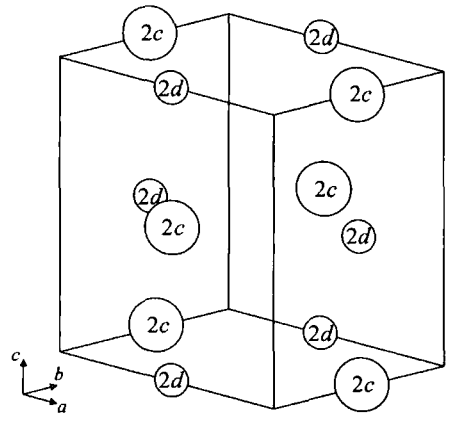

Figure 7.1 The unit cell of a parent (x = 0) ruthenate, $A_2M\mathrm{RuO}_6$. There is an ordered 1:1 arrangement of the *B* cations (*M* and Ru), with the *M* cations on the 2*c* site and the Ru cations on the 2*d* site.

When the copper is non-magnetic, the effect of doping on the 2*c* site will be less than had it been on the 2*d* site, as the *M* sublattice does not order via *M*-O-O-*M* interactions anyway. The Ru-O-*M* interactions will also be reduced in number and weaken the inter-species coupling between the sublattices. For the Ho, Tb and Pr systems this would lead to lower magnetic ordering temperatures of the copper doped materials, though the effect in $Sr_2HoRu_{1-x}Cu_xO_6$ would be smaller than that of $Ba_2PrRu_{1-x}Cu_xO_6$.

A non-magnetic copper situated on the 2*d* site, which is normally host to ruthenium, would have a larger effect. As well as reducing the inter-species interactions, the reduced number of Ru-O-O-Ru interactions will lower the magnetic ordering temperature of the material, particularly in the $Sr_2YRu_{1-x}Cu_xO_6$, $Ba_2YRu_{1-x}Cu_xO_6$ and $Sr_2HoRu_{1-x}Cu_xO_6$ systems where the Ru-O-*M* interaction is weak.

However, if the copper were magnetic then the interactions listed above would operate, though as the dopant is only at the 5-15 % level it is unlikely to affect the ordering type of the material. These additional *M*-O-O-Cu, Cu-O-O-Cu, *M*-O-Cu, Ru-O-Cu and Ru-O-O-Cu interactions, depending on the copper's location, may not all be significant in the temperature range studied and could vary enormously in strength. Neither do they have to be mutually supportive of the existing magnetic interactions, or of each other, though their effect cannot be too dramatic, as the magnetic structure and Néel temperature does not change greatly with copper doping. However, if the interactions are mutually cooperative then the copper is more likely to order magnetically. Irrespective of whether these interactions are mutually cooperative with the existing interactions or not, they can influence the magnetic ordering temperature and refined magnetic moment.

The refined magnetic moments on the *B* sites can be separated into the two components, the 2*c* site contribution and the 2*d* site contribution. This process was first described for Sr_2HoRuO_6 in this thesis, and is perfectly valid when the copper is not magnetic for the whole series of $Sr_2HoRu_{1-x}Cu_xO_6$. However, with copper magnetically ordered, there is not sufficient information from sum and difference peaks to determine uniquely the magnetic moment of the three species, unless further assumptions are made. For instance, having refined the magnetic moments of Ru^{5+} and Ho^{3+} for Sr_2HoRuO_6, these could then be *assumed* constant for the rest of the series of $Sr_2HoRu_{1-x}Cu_xO_6$, and the remaining magnetic moment attributed to the copper.

As discussed above, the location of the copper in the structure is important for the magnetic properties, as it determines which of the above interactions are present, and will modify the refined magnetic structure. This explains the great effort that was invested using anomalous X-ray scattering (Chapter 6) to try to determine the location of the copper, though this was without complete success.

Clearly the role and behaviour of the dopant is complicated in these mixed ruthenium-copper systems. However, it is the aim of this chapter to discuss some of the possibilities for the role of the copper in the ruthenates, both for the magnetic and electrical properties. The results from Chapters 3 to 6 will be called upon to support and suppress some of the possible behaviours of copper in these intriguing materials. The first section will add some of the reasoning behind the refinement of these magnetic structures with the copper non-magnetic. The second section will suggest an alternative, with the copper ordered magnetically and detail how the existing results would be modified slightly. The third section will give a brief account of the consequences of copper not being successfully doped into the main phase. The chapter then closes with some of the implications of this work for the superconductivity in the mixed ruthenium-copper materials.

7.2 Non-magnetic Copper

The crystal structures were refined in Chapters 3 to 5 using powder neutron diffraction patterns and assuming a 1:1 ordering of the Ru:*M* cations. This is justified based on the charges and sizes of the ions and the evidence of a long-range magnetic structure [2]. With the introduction of the copper, probably as Cu^{3+}, this 1:1 ordering of Ru(Cu):*M* should continue, as the M^{3+} ions are appreciably larger. The formation of long-range magnetic order supports this view, as it usually only survives in crystallographically ordered materials. The refined magnetic moments of the 2*c* and 2*d* sites confirm this, the most clear example being Sr_2HoRuO_6 where these refined moments of ~ 8 μ_B and ~ 2 μ_B on the sites can be attributed to Ho^{3+} and Ru^{5+} ions, without fear of much site mixing of the species.

The trends with copper doping for each $A_2MRu_{1-x}Cu_xO_6$ have been reported in Chapters 3 to 5, and will not be repeated here in detail. The refined magnetic moment of Ru^{5+} increases with copper doping in $Sr_2YRu_{1-x}Cu_xO_6$, $Sr_2HoRu_{1-x}Cu_xO_6$ and $Ba_2PrRu_{1-x}Cu_xO_6$, whereas it remains constant for $Sr_2TbRu_{1-x}Cu_xO_6$. The copper is believed to induce superconductivity in the materials also and it is possible that its

electronic effect extends to increasing the moment of the Ru^{5+} ions. As the magnetic moment of Ru^{5+} is 1.8-2.5 μ_B, while the spin-only value predicts 3.87 μ_B, it is possible that the copper dopant reduces this deficit from electronic or covalent effects, though no precise mechanism is proposed. Owing to the small moment size of the Pr^{3+} magnetic moment and the ambiguity of the *ab* component assignment, this effect of copper doping on this ion is unclear. However, the refined magnetic moment increased for the Ho^{3+} in the $Sr_2HoRu_{1-x}Cu_xO_6$ series and decreased for Tb^{3+} in $Sr_2TbRu_{1-x}Cu_xO_6$. Again, this system is not really determined well enough to discuss in detail, though it is possible that a similar mechanism to that which increases the Ru^{5+} moment operates for the Ho^{3+} moment too. The $Sr_2TbRu_{1-x}Cu_xO_6$ system is different to the others in both regards as the Ru^{5+} magnetic moment remains constant and the Tb^{3+} moment decreases. This could be because the dopant copper could be predominantly on the 2*c* site (Chapter 6), which is host to the Tb^{3+} ions.

Consider this situation where the copper is on the 2*c* site and this displaces 10 % of the terbium to the 2*d* site, which could be responsible for the unit cell volume decrease in $Sr_2TbRu_{0.90}Cu_{0.10}O_6$ from Sr_2TbRuO_6. (i.e. The 2*c* site has 90 % terbium and 10 % copper, whereas the 2*d* site has 90 % ruthenium and 10 % terbium.) In Sr_2TbRuO_6 the Tb^{3+} ions order magnetically due to the Ru-O-Tb interaction, rather than a direct Tb-O-O-Tb interaction. For $Sr_2TbRu_{0.90}Cu_{0.10}O_6$, as 10 % of the Tb^{3+} ions are now on the 2*d* site, where the host ion is Ru^{5+}, the interactions are different. One of the interactions affecting those Tb^{3+} ions which are on the predominantly ruthenium sublattice is the Ru-O-O-Tb interaction, which should be weaker than the Ru-O-Tb interaction. Although Tb-O-Tb interactions are also present, these are known to be weak, as the low Néel temperature of Tb_2O_3 is only 2.4 K [3, 4]. Therefore the Tb^{3+} ions are not going to order as well on the 2*d* site, so to a first approximation its ordered magnetic moment will be neglected. Thus, the magnetic intensity attributable to the 2*d* site is entirely due to the Ru^{5+} ions, which have not changed in number, so the moment is the same. The magnetic intensity attributable to the 2*c* site is now due to 90 % of Tb^{3+}, rather than the full occupancy and so the refined magnetic moment must increase by the inverse of this factor, in order that the calculated profile remain the same as before to continue to match the observed pattern. The previously refinements of the Tb^{3+} magnetic moment in $Sr_2TbRu_{0.90}Cu_{0.10}O_6$ (Chapter 4) are thus modified by the factor of (1/0.90) to account for the change in the distribution of the *B* cations. These new results, which show the

effect of the copper on the 2*d* site are shown in Figure 7.2, where only the Tb^{3+} magnetic moment has been changed from the previous results.

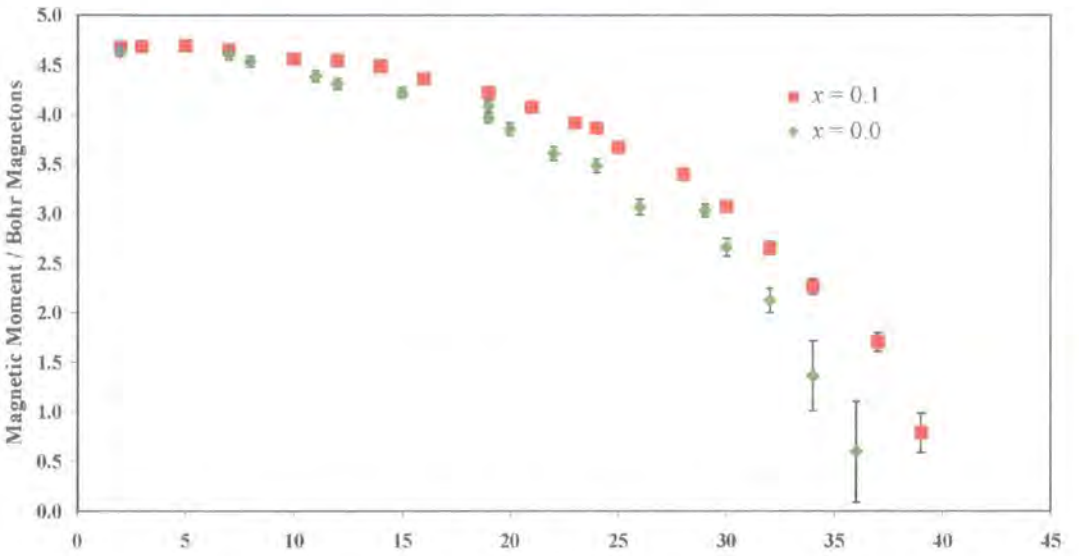

Figure 7.2 The refined magnetic moments of Tb^{3+} ions in $Sr_2TbRu_{1-x}Cu_xO_6$ as obtained from D1B data. The magnetic moment of Tb^{3+} in $Sr_2TbRu_{0.90}Cu_{0.10}O_6$ has been scaled by 1/0.90 in order to account for the trial situation of the copper in the Tb^{3+} host sublattice.

As can be seen from Figure 7.2, both the refined magnetic moments of Ru^{5+} and Tb^{3+} are the same for both members, $x = 0$ and 0.10, of the $Sr_2TbRu_{1-x}Cu_xO_6$ series. The only difference is the lower ordering temperature of the 10 % copper doped sample which is due to a weakening of the magnetic structure, most probably due to the fewer Ru-O-Tb interactions which are known to raise the Néel temperature. In this scenario, the copper has been doped on to the "wrong site," but has led to no real change in the magnetic behaviour of the Ru^{5+} or Tb^{3+} ions with copper doping. This implies that from the parent compound, Sr_2TbRuO_6, to the doped compound, $Sr_2TbRu_{0.90}Cu_{0.10}O_6$, the addition of a 10 % magnetically inactive ion to each site has no change on the magnetic behaviour of the remaining Ru^{5+} and Tb^{3+} ions. Whether this interpretation of the data is preferred, rather than the magnetic moment of Tb^{3+} decreasing with copper doping is open to debate.

The observation of magnetic ordering of copper in $Sr_2YRu_{1-x}Cu_xO_6$ at temperatures higher than the ordering temperature of ruthenium [5], in fact up to 85 K, has been dismissed. This is because the calculated magnetic intensity was completely within their background noise, and the experimental data showed no peak. In Chapter 3 this

is discussed extensively and shown that the magnetic moments would have to be very large ~ 5 μ_B to be observed if the only magnetic ion is copper, as the sensitivity of powder diffraction is typically low. This is far larger than the spin-only value for Cu^{2+} of 1.73 μ_B, or even the 2.83 μ_B for Cu^{3+}, and so this moment cannot be measured from such a small fraction. However, copper ordering below the Néel temperature cannot and has not been dismissed so readily and will be discussed in the next section. Here, any refined magnetic moment of the copper is determined by the resolution, not the sensitivity.

7.3 Magnetic Copper

This section examines the possibility of the copper magnetically ordering in the ruthenates $A_2MRu_{1-x}Cu_xO_6$, and exhibiting similar behaviour to the Ru and *M* cations. As detailed in Section 7.1, the neutron diffraction patterns are unable to separate out three separate magnetic moments, and only the magnetic moment per 2*c* and 2*d* site can be calculated. The anomalous X-ray measurements were not able to determine the copper distribution between the 2*c* and the 2*d* sites owing to small impurity phases in many of the systems. The neutron scattering lengths of the Ru, Cu and *M* cations are all similar so the diffraction pattern intensity is insensitive to the precise distribution of cations among the 2*c* and 2*d* sites. However, the magnetic intensity of the neutron diffraction patterns depends quite markedly on the *B* cations. Thus, the refined magnetic moments from Chapters 3 to 5 could give information about the *B* cation distribution, and allow this to be modified slightly based on the copper ions ordering magnetically also, giving a further plausible interpretation of the data.

An increase was noted in the refined magnetic moment of the Ru^{5+} as the copper doping level was increased in $Sr_2YRu_{1-x}Cu_xO_6$, which is magnetically the simplest of the mixed ruthenium-copper systems. In Section 7.2 this was explained purely by an increase in the magnetic moment of the Ru^{5+} ions. However, the possibility that the copper becomes magnetically ordered too will be considered. As the refinements proceeded well with all the magnetic ions on the 2*d* site, it will continue to be assumed that both ions, Ru^{5+} and Cu^{3+} are on the 2*d* site.

The magnetic intensity in the pattern is matched by the calculated magnetic intensity, which is formed from the magnetic moment of each site. No further separation of the magnetic moment into two contributions from the same crystallographic site can be made. Thus, there are three approaches. The assumption that the copper does not

magnetically order has been investigated (Section 7.2), that the Ru^{5+} magnetic moment is constant throughout the series and the remaining magnetic moment required to calculate the magnetic intensity has a copper origin. Alternatively the magnetic moment per 2*d* site, per Ru/Cu ion, can be calculated, and these last two approaches will now be discussed.

First, the calculation where the magnetic moment of copper is assumed equal to that of ruthenium will be considered. There is no need to refine the results again as the magnetic moment on the fraction (1-x) of Ru^{5+} ions now needs to be distributed over the Ru/Cu ions, where the occupancy is unity. Thus the magnetic refinements from Chapter 3 are scaled by the factor of (1-x) to account for the increased number of magnetic ions in the calculation. The only further approximation of this approach, rather than a full refinement, is that the magnetic form factor of copper is assumed to be that of ruthenium, though as the proportion x is small, this is acceptable. The results of the calculation are shown in Figure 7.3 and it can be seen that there is little variation of the magnetic moment of Ru/Cu with increased copper doping. This could imply that the magnetic behaviour and interactions of copper are similar to that of ruthenium. It is noted that the spin-only value for the magnetic moment of Cu^{2+} is 1.73 μ_B and for Cu^{3+} is 2.83 μ_B, and as the value for Cu^{2+} is exceeded, it is more likely that the copper is in the 3+ state, if magnetic. This is consistent with the charge and size analysis, as Cu^{3+} would be expected to be doped on the 2*d* site, where the host ion is Ru^{5+}, whereas any Cu^{2+} would be preferred on the 2*c*, where Y^{3+} is the host. However, the average magnetic moment per Ru/Cu ion was always going to be close to the previously refined magnetic moment of the Ru^{5+} ion simply because the copper fraction of x is small, between 0.05 and 0.15.

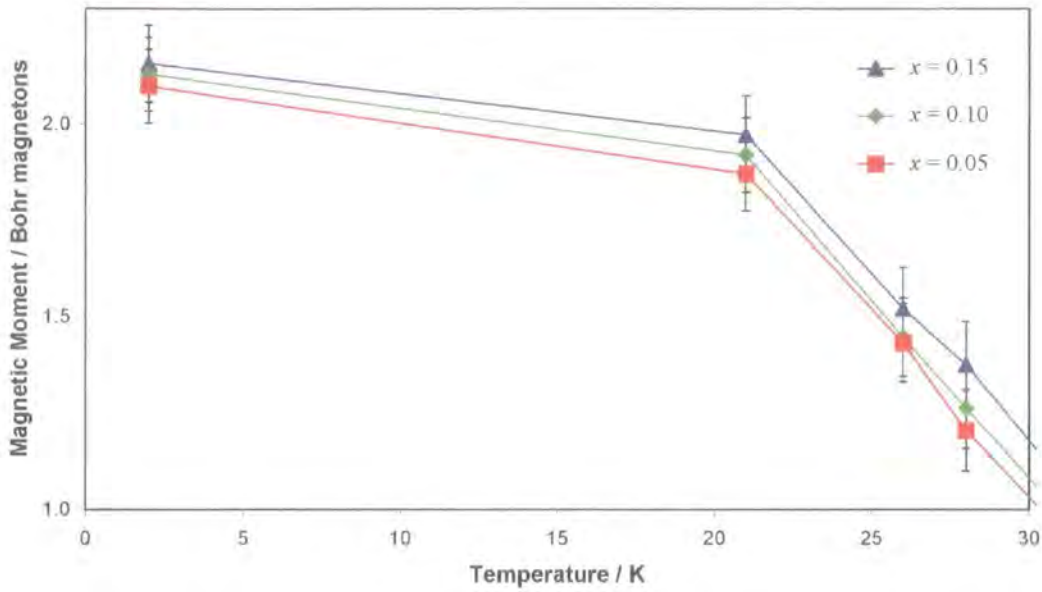

Figure 7.3 The calculated magnetic moment per Ru/Cu ion for the $Sr_2YRu_{1-x}Cu_xO_6$ series with temperature, based on the refinements of $Sr_2YRu_{1-x}Cu_xO_6$ performed in Chapter 3.

The alternative assumption is that the Ru^{5+} magnetic moment is constant throughout the $Sr_2YRu_{1-x}Cu_xO_6$ series, based on the Sr_2YRuO_6 extrapolated values, with the copper accounting for the rest of the magnetic moment on the 2*d* site. Performing this calculation it is found that required magnetic of copper is constant with temperature up to 28 K, the highest temperature that magnetic ordering was observed. The magnetic moment was ~ 2.4 μ_B for $Sr_2YRu_{0.95}Cu_{0.05}O_6$ and increased by 0.2 μ_B for each extra 0.05 increment in *x*. This moment size is commensurate with the Cu^{3+} ion, though the increase in moment size with increased doping needs to be explained, just as it would if the Ru^{5+} moment had increased.

For the $Sr_2HoRu_{1-x}Cu_xO_6$ series both the magnetic moment of the Ru^{5+} and Ho^{3+} increased as the copper doping increased. Again, appealing for a magnetically ordered copper in the ruthenium host sublattice, similar to above, yields the results of Figure 7.4 for the average moment per Ru/Cu ion. Again the tendency is for the difference in the average moment in the materials to merge.

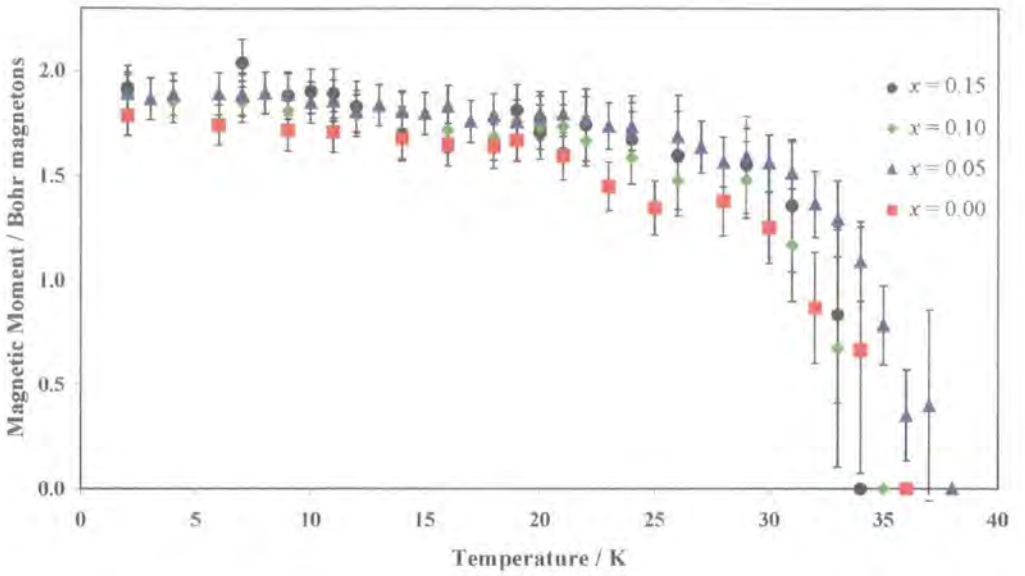

Figure 7.4 The calculated magnetic moment per Ru/Cu ion for the $Sr_2HoRu_{1-x}Cu_xO_6$ series with temperature, based on the refinements of $Sr_2HoRu_{1-x}Cu_xO_6$ performed in Chapter 4.

Calculations which assumed that the magnetic moment of Ru^{5+} was constant based upon the refined values for Sr_2HoRuO_6 gave magnetic moments for copper of ~ 0.5 μ_B for the whole temperature range for $Sr_2HoRu_{1-x}Cu_xO_6$, when x = 0.10 and 0.15. This result serves to show that if the copper is magnetically ordered within these mixed ruthenium-copper perovskites, then as it is such a small fraction, when independently determined the results will be highly variable between the series and members. This suggests that if the copper is treated as magnetic then the most sensible treatment is calculating the average moment per Ru/Cu ion, or *M*/Cu ion, depending on the dopant's location.

The Ho^{3+} magnetic moment increases with copper doping and the 2*c* site is occupied by 100 % of holmium. Ruthenium or copper substitution on to the 2*c* site would only reduce the magnetic moment as these moments will be less than the ~ 8 μ_B of the Ho^{3+} ion. Thus, the increase in magnetic moment of the Ho^{3+} with copper doping suggests that the dopant can increase the magnetic moment size of the magnetic ions in the material, without recourse to magnetically ordered copper.

In Section 7.2 the situation was discussed that the copper may not reside on the 2*d* with ruthenium, but on the 2*c* site with terbium. This section now examines the possibility of the copper magnetically ordering on this site. Clearly, the magnetic moment of copper will not be as large as that of terbium, so it is safer to calculate the

moment per Ru/Cu ion. This implies that the copper orders due to the Ru-O-Cu interaction between the two sublattices. The magnetic moment on the 2*d* site is still calculated from the 90 % ruthenium occupancy and so does not change, and thus determines the assumed size of the copper moment. The magnetic moment required for the Tb^{3+} ion will either decrease or increase dependant on whether the magnetic moment of copper is in the same or opposite direction to the terbium sublattice. This will yield a modification of the magnetic moment of Tb^{3+} ion to the values shown in Figure 7.5

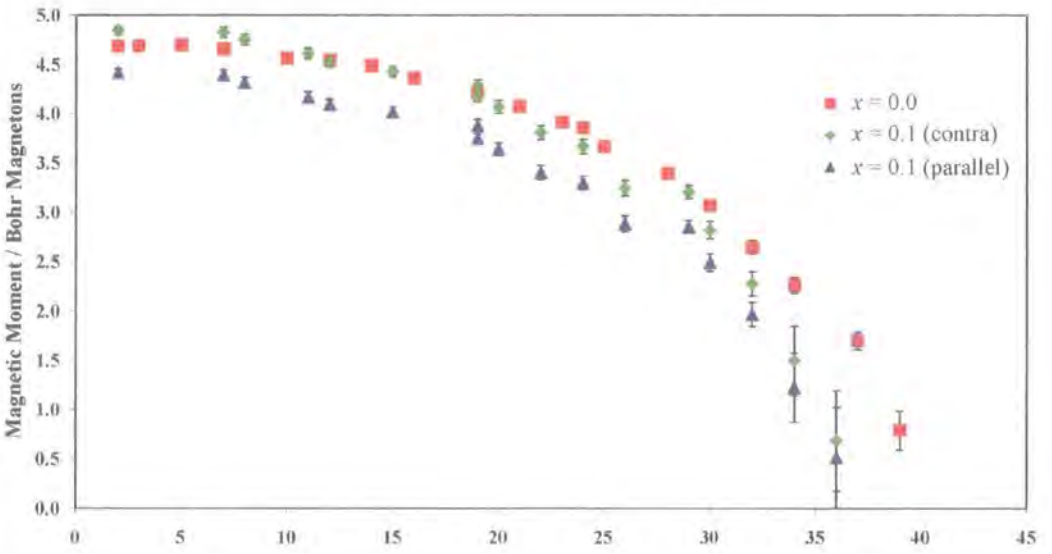

Figure 7.5 The calculated magnetic moment of Tb^{3+} in the $Sr_2TbRu_{1-x}Cu_xO_6$ series when the copper is assumed to be magnetically ordered within the Tb^{3+} sublattice, both in the same and opposite directions to the host sublattice.

The calculated values show that if the copper is oppositely directed to the host terbium sublattice then results similar to those displayed in Figure 7.2 are obtained. Therefore, the magnetic moments of both the Ru^{5+} and Tb^{3+} ions could be constant for the series, if the copper is magnetically ordered on the 2*d* site, or non-magnetically ordered on the 2*d* site. Hence, once again there is no compelling evidence to assume that the copper is magnetically ordered.

For the $Ba_2PrRu_{1-x}Cu_xO_6$ system there are very few results to compare for the $x = 0$ and $x = 0.10$ samples. By attributing a magnetic moment to the 10 % of copper in $Ba_2PrRu_{0.90}Cu_{0.10}O_6$ the moment is reduced from 1.98(15) μ_B to 1.78(15) μ_B per Ru/Cu ion, which is closer to the value of 1.66(16) for Ba_2PrRuO_6. However, with so few values for comparison and the unattributed *ab* component in $Ba_2PrRu_{0.90}Cu_{0.10}O_6$, to analyse this further would be to over-interpret the data.

In the previous studies of mixed ruthenium-copper perovskite systems, $SrLaCuRuO_6$ or La_2CuRuO_6 [6-8], there has been no evidence of long-range magnetic order. In both these systems the copper is believed to be in +2 state, whereas the ruthenium is thought to be present as Ru^{5+} and Ru^{4+} respectively. Restricting the discussion to the former compound, $SrLaCuRuO_6$, it is believed that the random ordering of the *B* cations leads to competing Ru-O-Ru antiferromagnetic, Ru-O-Cu ferromagnetic and Cu-O-Cu antiferromagnetic interactions. The last two interactions change character if the bond deviates more than 10° from linearity and as the average Ru/Cu-O-Ru/Cu bond angles are 160.6° and 158.2° this will occur. However, as the *B* cations are randomly ordered there will be large variations of these bond angles depending on the local crystal structure, so the interactions can change throughout the material also. Therefore, it is no surprise that $SrLaCuRuO_6$ forms a spin-glass. In the brief analysis in this thesis, where the copper has been assumed to magnetic, the magnetic moment size has indicated that the Cu^{3+} ion is the most likely species to be present. Thus, these results from the literature are of only limited usage.

Refining the data with magnetically ordered copper does not greatly aid any of the explanations of the properties of the materials. For $Sr_2HoRu_{1-x}Cu_xO_6$, the increase in the Ho^{3+} magnetic moment with increased copper doping is present whether copper is magnetically ordered or not. Whatever the mechanism for this increase, it could also then be used to explain the similar trend of the Ru^{5+} ion in $Sr_2YRu_{1-x}Cu_xO_6$, $Sr_2HoRu_{1-x}Cu_xO_6$, and if necessary for $Ba_2PrRu_{1-x}Cu_xO_6$. For the $Sr_2TbRu_{1-x}Cu_xO_6$ system the decrease of Tb^{3+} moment with increased copper doping can arise from copper imbedded within the terbium sublattice, whether the dopant is magnetically ordered or not.

In fact, owing to the uncertainty of the amount of copper inclusion, as some is locked into impurities, the uncertainty of the location of the copper on the 2*c* or 2*d* site and its small fraction, it is very difficult to conclude anything of the magnetic behaviour of the copper. This brief discussion of the possibility of magnetically ordered copper in the mixed ruthenium-copper oxides only serves to illustrate this point. This explains why the neutron powder diffraction patterns presented in Chapter 3 to 5 were refined without recourse to a magnetically ordered copper ion, as to do so would require assumptions as to the moment size, and therefore would over-interpret the data.

7.4 Copper not included in the main 2116 phase

For some of the mixed ruthenium-copper series, the refined magnetic moment increased in inverse proportion to the amount of the magnetic ion in the sample. This section examines the consequences of the copper not being included in the 2116 main phase, which can explain some, though not all of the results.

There was evidence from the synchrotron measurements at the ESRF from BM1B that $YSr_2Cu_3O_{7-\delta}$ or similar materials (YSCO-like) had formed in some of the systems, namely $Sr_2YRu_{1-x}Cu_xO_6$ and $Sr_2HoRu_{1-x}Cu_xO_6$. Owing to the small size of the impurity phases the precise composition of the materials could not be confirmed, though it could deplete the main 2116 phase of a substantial fraction of its copper. With this depletion, the stoichiometry of the sample of $Sr_2YRu_{0.85}Cu_{0.15}O_6$ would actually be $Sr_{2.12}YRu_{0.97}Cu_{0.04}O_6$ (Section 6.4.2), very close to the parent compound composition of Sr_2YRuO_6. If the same were true for the other members of the $Sr_2YRu_{1-x}Cu_xO_6$ series, then all the samples would in fact be only subtle variations of the parent compound. In this case, the refinements of the neutron diffraction data should have proceeded with almost 100 % of Y on the 2*c* site and ~ 100 % of Ru on the 2*d* site. As the proportion of ruthenium has increased (at the expense of copper) then the refined magnetic moment of Ru^{5+} would decrease also by this factor, yielding a similar result to that of Section 7.3. Thus, the idea that copper is not present in the main phase can explain some of the data obtained on the $Sr_2YRu_{1-x}Cu_xO_6$ series.

Likewise, the $Sr_2HoRu_{0.85}Cu_{0.15}O_6$ study using BM1B also indicates some impurity content. Assuming these impurity levels and compositions to be exact, the stoichiometry of the sample is $Sr_{2.04}HoRu_{0.95}O_6$, which is far closer to the parent compound again. As the refined magnetic moments in $Sr_2HoRu_{1-x}Cu_xO_6$ increase with increasing x values, these too can be explained using the same idea as for $Sr_2YRu_{1-x}Cu_xO_6$ above. The impurities, in particular the potential 123 YSCO-like phase, reduce the copper content significantly while the other constituents remain broadly unchanged. Thus, the proportion of magnetic ions is increased and the refined magnetic moment must decrease by this amount, yielding similar results to Section 7.3.

The notion that copper is largely not present in the main phase and that the samples are very similar to the parent compounds, while the superconductivity is attributed to an impurity phase, is the most negative viewpoint. The arguments against this

proposal are that the unit cell volume increases in all the materials studied, as the copper replaces the smaller ruthenium in the main phase of the sample. The one series where this trend is reversed is $Sr_2TbRu_{1-x}Cu_xO_6$, where no impurities are observed in these samples, so that the copper is in the main phase here also. In the $Ba_2PrRu_{0.90}Cu_{0.10}O_6$ sample, no impurities are observed either, albeit from neutron data. More importantly, the magnetic structure changed subtly with the magnetic moments developing an *ab* component, which was not present in the copper-free samples. For these reasons, there is enough evidence to suggest that the copper is present in the 2116 phase of the samples.

7.5 Implications

Provided the copper is doped successfully into the 2116 phase, its location on the 2*c* or 2*d* site is irrelevant as far as the superconductivity is concerned, if the purpose of the copper is simply to dope holes into the structure and the magnetic properties of the material are unimportant. This is because both the 2*c* and 2*d* sites are present in every mixed ruthenium-copper plane, as discussed in Chapter 6, and so a superconducting path through the material is present for either site. However, if the magnetic properties of the material are important then its situation on the 2*c* and 2*d* sites is important due to the different interactions, and their numbers, which are present dependent on site occupation of copper, irrespective of whether the copper is magnetic or not.

Initially, it was believed that there may be a very close relation between the superconducting and the magnetic properties of the materials, as the two transition temperatures are close, approximately 30-40 K for the $Sr_2YRu_{1-x}Cu_xO_6$ and $Ba_2YRu_{1-x}Cu_xO_6$ systems. The recent synthesis of the $Ba_2PrRu_{1-x}Cu_xO_6$ system throws doubt over this link however. Its magnetic ordering temperature is ~ 105 K, whereas its superconducting transition temperature is currently reported as 10 K [9], though this may increase as the sample preparation conditions are perfected. However, it is unlikely to reach 105 K, and so there will be a rather large gap between the two transition temperatures, which would suggest no obvious link. On the other hand, the ruthenium is believed to be responsible for the superconductivity [10-17] and the Ru-O-O-Ru interaction is thought to be approximately the same strength in all of the materials, so this may be the important parameter. Hence, the link between the observed superconductivity and a magnetic mechanism cannot be ruled out completely. If the $Ba_2PrRu_{1-x}Cu_xO_6$ is subsequently shown to be not superconducting,

then it needs to be explained why this mixed ruthenium-copper material is not, though it may be related to the high Néel temperature. However, a non-superconducting result would be detrimental for arguments supporting superconductivity in the $Sr_2YRu_{1-x}Cu_xO_6$ and $Ba_2YRu_{1-x}Cu_xO_6$ systems, where there remain superconducting impurity issues.

If there is a link between the magnetism and the superconductivity in the materials, then the role and location of the copper will take on a special significance if it too is magnetic. This is due to all the copper interactions, which were discussed in Section 7.1, and the important effect that they will have. The situation where copper is magnetic is discussed in Section 7.3, where the copper behaves similarly to the ruthenium in terms of moment size and interaction strengths, particularly the Ru-O-O-Ru and Ru-O-O-Cu (Cu-O-O-Cu) interactions. This could explain why copper doping induces superconductivity in these ruthenate materials. It is not that the copper allows a 123 type superconducting impurity to form. Rather, the copper easily replaces ruthenium in the crystal structure, has those magnetic properties which are important in these systems similar to ruthenium, and dopes the necessary holes into the material for superconductivity. Clearly, there will not be many elements capable of filling such a role and this could explain the many failures of Wu to synthesise a superconducting ruthenate material, doped with an element other than copper. Obviously, it would be preferred that copper was not the dopant element, as the suspicions of 123 type superconductor impurities will linger as long as copper is used. However, these findings suggest a new avenue of research in the hunt for an alternative dopant.

Although the copper is believed to be doped into the main 2116 phase, the impurities in some of the mixed ruthenium-copper oxides are a cause for concern. Clearly, further work is required, especially for the $Sr_2YRu_{1-x}Cu_xO_6$ and $Sr_2HoRu_{1-x}Cu_xO_6$ series to improve the sample preparation in order to eliminate the impurity content. Although this is not firmly linked to a superconducting YSCO-like superconductor, in order to be convinced of superconductivity in the mixed ruthenium-copper phases the samples should be of higher quality. The $Sr_2TbRu_{1-x}Cu_xO_6$ series, which is shown to be impurity free from synchrotron X-ray data, needs to have its superconducting status confirmed. Additionally, members of the $Ba_2PrRu_{1-x}Cu_xO_6$ series are shown to have no impurities, albeit from neutron data. Even if 123 type impurities are present

in this material they would not be superconducting, so convincing evidence for superconductivity is required for these samples also.

7.6 Conclusions

The doping of copper is believed to induce superconductivity in these ruthenate materials. Increasing the doping level in the $Sr_2YRu_{1-x}Cu_xO_6$, $Sr_2HoRu_{1-x}Cu_xO_6$ and $Ba_2PrRu_{1-x}Cu_xO_6$ systems leads to an increase of the Ru^{5+} (and Ho^{3+}) magnetic moment, probably due to electronic effects induced by the copper. The decrease of the Tb^{3+} magnetic moment with increased copper concentration in $Sr_2TbRu_{1-x}Cu_xO_6$ can be explained by a similar phenomenon, or copper doping into the terbium, rather than ruthenium sublattice. This second explanation would be favoured by the Cu^{2+} ion, rather than the Cu^{3+} species.

If the copper is assumed to order magnetically, then other assumptions have to be introduced and only the magnetic moment per Ru/Cu ion can be calculated, which is generally constant for a series of $A_2MRu_{1-x}Cu_xO_6$. Its similar magnetic behaviour to ruthenium may explain why it can successfully dope holes into the structure, which are required for superconductivity, and also be accommodated in the host sublattice. These properties may be unique to copper and explain the failure to produce superconducting samples with other dopants. Other than this possible explanation, the introduction of the magnetically ordered copper does not greatly aid any explanation of these materials' properties and so the analysis here serves to justify the approach adopted in Chapters 3 to 5. Certainly any serious discussion of the role of copper is hindered by impurity phases, which may contain copper, uncertainty over the copper site and magnetic moment size. Clearly, the first way to address these problems is to synthesise single-crystal single-phase material of the 2116 compounds.

7.7 References

1 T. Motohashi, A. Yoshikawa, J. Shimoyama and K. Kishio, *Physica C* **282,** 515 (1997).

2 M.T. Anderson, K.B. Greenwood, G.A. Taylor and K.R. Poeppelmeier, *Progress in Solid State Chemistry* **22,** 197 (1993).

3 B.C. Gerstein, F.J. Jelinek and F.H. Spedding, *Physical Review Letters* **8,** 425 (1962).

4 R.W. Hill, *Journal of Physics C-Solid State Physics* **19,** 673 (1986).

5 H.A. Blackstead, J.D. Dow, D.R. Harshman, W.B. Yelon, M.X. Chen, M.K. Wu, D.Y. Chen, F.Z. Chien and D.B. Pulling, *Physical Review B* **63 21,** 4412 (2001).

6 M.P. Attfield, P.D. Battle, S.K. Bollen, S.H. Kim, A.V. Powell and M. Workman, *Journal of Solid State Chemistry* **96,** 344 (1992).

7 S.H. Kim and P.D. Battle, *Journal of Magnetism and Magnetic Materials* **123,** 273 (1993).

8 P.D. Battle, J.R. Frost and S.H. Kim, *Journal of Materials Chemistry* **5,** 1003 (1995).

9 M.K. Wu, B.H. Mok, M.J. Wang, D.C. Yuan, S.M. Rao, P.D. Hatton and N.G. Parkinson, *Journal of Low Temperature Physics* **131,** 1053 (2003).

10 D.Y. Chen, F.Z. Chien, D.C. Ling, J.L. Tseng, S.R. Sheen, M.J. Wang and M.K. Wu, *Physica C* **282,** 73 (1997).

11 M.K. Wu, D.Y. Chen, F.Z. Chien, S.R. Sheen, D.C. Ling, C.Y. Tai, G.Y. Tseng, D.H. Chen and F.C. Zhang, *Zeitschrift Fur Physik B-Condensed Matter* **102,** 37 (1997).

12 H.C. Ren and M.K. Wu, *Physical Review B* **58,** 15440 (1998).

13 M.K. Wu, D.Y. Chen, F.Z. Chien, D.C. Ling, Y.Y. Chen and H.C. Ren, *International Journal of Modern Physics B* **13,** 3585 (1999).

14 M.K. Wu, D.Y. Chen, D.C. Ling and F.Z. Chien, *Physica B* **284,** 477 (2000).

15 D.Y. Chen, M.K. Wu, N.G. Parkinson, C.H. Du, P.D. Hatton, F.Z. Chien and C. Ritter, *Physica C* **341,** 2157 (2000).

16 S.M. Rao, J.K. Srivastava, H.Y. Tang, D.C. Ling, C.C. Chung, J.L. Yang, S.R. Sheen and M.K. Wu, *Journal of Crystal Growth* **235,** 271 (2002).

17 N.G. Parkinson, P.D. Hatton, J.A.K. Howard, C. Ritter, F.Z. Chien and M.K. Wu, *Journal of Materials Chemistry* **13,** 1468 (2003).

8 Conclusions

This thesis reports both the crystal and magnetic structures of a class of mixed ruthenium-copper oxides, $A_2M\mathrm{Ru}_{1-x}\mathrm{Cu}_x\mathrm{O}_6$ with $x = 0$ to 0.15, which have been reported to be superconducting. From variable temperature neutron powder diffraction experiments, not only has the magnetic structure development been elucidated, but also important information concerning the magnetic interactions discovered. For the first time, the relative strengths of the predominant magnetic interactions in these materials have been determined.

The crystal structure of the $\mathrm{Sr}_2\mathrm{YRu}_{1-x}\mathrm{Cu}_x\mathrm{O}_6$ series is a distorted double perovskite, with the distortion manifesting itself in the tilting, rather than irregularity, of the oxygen octahedra that surround the *B* cations. The Ru(Cu):Y cations are in an ordered arrangement, which is necessary for the development of a long-range magnetic structure that is duly observed below ~ 30 K. The Ru^{5+} magnetic ions adopt a Type I antiferromagnetic structure which is ordered due to the super-exchange interaction via the Ru-O-O-Ru pathway. The magnetic moment increases with copper doping, by approximately 0.3 μ_B from 2.2 (1) μ_B for $x = 0.05$ to 2.5(1) μ_B for $x = 0.15$, and is directed in the *ab* plane. However, in order to determine the magnetic moment size it was necessary to calculate a practical magnetic form factor for the Ru^{5+} ion, rather than use the isoelectronic Zr^{+} factor, which consistently over-estimates moment sizes and thereby explains some discrepancies in the literature.

The magnetic structure of $\mathrm{Ba}_2\mathrm{YRu}_{0.90}\mathrm{Cu}_{0.10}\mathrm{O}_6$ is similar to that of $\mathrm{Sr}_2\mathrm{YRu}_{1-x}\mathrm{Cu}_x\mathrm{O}_6$, a Type I antiferromagnet, with a similar moment size. However, the material was determined to be crystallographically cubic, with regular oxygen octahedra. This is believed to be responsible for the higher magnetic ordering temperature reported in this compound compared with its strontium analogue. The neutron diffraction data showed no evidence of a canted magnetic moment, so setting a maximum limit of ~ 0.8 μ_B for any ferromagnetic component, which is required by Wu's double-exchange theory.

The introduction of a second magnetic ion into the double perovskite structure was expected to have significant implications for the superconductivity. The double perovskite structure of $\mathrm{Sr}_2\mathrm{HoRu}_{1-x}\mathrm{Cu}_x\mathrm{O}_6$ is shown to be largely independent of copper doping and temperature. The magnetic structure is composed of two sublattices, one

of Ru^{5+} ions and the other of Ho^{3+} ions, each of which adopts an antiferromagnetic Type I arrangement with the moments predominantly in the *c*-direction. While the magnetic moment at 2 K of the Ru^{5+} ions is ~ 2 μ_B, the magnetic moment of the Ho^{3+} ions is ~ 8 μ_B, and both these values apparently increased slightly with increased copper doping. The $Sr_2TbRu_{1-x}Cu_xO_6$ series was refined with a very similar magnetic structure, though with a slightly greater deviation of the magnetic moments from the *c*-direction. Although the saturated magnetic moment of the Ru^{5+} ion remains constant (~ 1.9 μ_B) through the series, the Tb^{3+} moment decreases with additional copper doping from ~ 4.7 μ_B for x = 0.0 to ~ 4.2 μ_B for x = 0.10. This may suggest an electronic effect of the copper, or that the dopant imbeds in the terbium, rather than ruthenium sublattice.

These systems formed the basis for the development of a semi-quantitative theory for the magnetic ordering observed in the ruthenate double perovskites, A_2LnRuO_6 where *Ln* is a rare-earth element. The Ru-O-O-Ru interaction is approximately constant, though dependent on the tilting of the oxygen octahedra, and is responsible for the antiferromagnetic ordering of the ruthenium sublattice with a Néel temperature of 30 - 40 K. The *Ln* sublattice is not ordered by a direct *Ln*-O-O-*Ln* interaction, since the study of the $Sr_2Ho_{1-y}Tb_yRu_{1-x}Cu_xO_6$ system determined this interaction to be weak, as long-range magnetic order is observed, rather than a spin-glass. The *Ln* sublattice is ordered by the Ru-O-*Ln* interaction, and can therefore only order if the ruthenium sublattice is ordered, which explains the coincident magnetic ordering temperatures of the two sublattices. This Ru-O-*Ln* interaction depends on the bond angle and is shown to have varying strengths and natures dependent on the rare-earth element, which was determined from close inspection of variable temperature neutron data. The saturation temperatures of the sublattices determine the Ru-O-Ho and Ru-O-Tb antiferromagnetic interactions to be ~ 0.2 and ~ 0.7 times as strong as the Ru-O-O-Ru interaction, leading to progressively higher Néel temperatures.

The study of $Ba_2PrRu_{1-x}Cu_xO_6$ provides striking confirmation of the importance of the Ru-O-*Ln* interaction, in this case, the Ru-O-Pr magnetic interaction. The high Néel temperature of ~105 K for members of this series is explained by a ferromagnetic Ru-O-Pr interaction which is ~3 times stronger than the Ru-O-O-Ru interaction. The Type I interpenetrating structure is still adopted, because although the ferromagnetic Ru-O-Pr interaction drives the magnetic ordering, the antiferromagnetic Ru-O-O-Ru interaction subtly alters the magnetic moments into this arrangement. The ordering of

the two sublattices occurs at the same rate, as predicted when the Ru-O-*Ln* interaction is much stronger than the Ru-O-O-Ru interaction. With 10 % copper doping, the saturated magnetic moments in the *c*-direction are 1.95(10) μ_B and 1.15(10) μ_B for the Ru^{5+} and Pr^{3+} ions respectively, while the additional 0.65 μ_B component in the *ab* plane could not be assigned to a particular ion.

As $PrBa_2Cu_3O_{7-\delta}$ is difficult to produce in the superconducting form, then impurities of it in $Ba_2PrRu_{1-x}Cu_xO_6$ would not be expected to be superconducting. Therefore, if superconductivity is confirmed in the $Ba_2PrRu_{1-x}Cu_xO_6$ system, then superconductivity in the mixed ruthenium-copper oxides will have been demonstrated.

X-ray synchrotron measurements determined that impurities are present in both the $Sr_2YRu_{1-x}Cu_xO_6$ and $Sr_2HoRu_{1-x}Cu_xO_6$ series, and could be related to a superconducting 123 material, such as $YSr_2Cu_3O_{7-\delta}$. However, the $Sr_2TbRu_{1-x}Cu_xO_6$ series was shown to be free of crystalline impurities and anomalous X-ray diffraction measurements were performed to try to determine the location of the dopant copper in these materials. The results suggested that in this system the copper might dope into the terbium, rather than ruthenium sublattice, though absorption problems limited analysis.

The introduction of copper into these ruthenate materials induces superconductivity and this is probably due to the doping of holes into the structure. This is achieved without altering the magnetic behaviour of the ruthenate materials markedly and may explain the success of copper as dopant.

The superconductivity in these mixed ruthenium-copper oxides, such as $Sr_2YRu_{1-x}Cu_xO_6$, is controversial because of the possible presence of 123 impurities, related to $YSr_2Cu_3O_{7-\delta}$, which could account for the superconductivity. This problem is being addressed with the synthesis of the $Ba_2PrRu_{1-x}Cu_xO_6$ system and also attempts to grow single crystals of these materials by Wu. Currently, only small crystals of $Sr_2YRu_{1-x}Cu_xO_6$, $Ba_2YRu_{1-x}Cu_xO_6$ and $Ba_2PrRu_{1-x}Cu_xO_6$ are available, though the crystals need to increase further in size. Future electrical and magnetic measurements of the single crystals will hopefully be able to conclude decisively whether the materials are superconducting. This would allow single crystal neutron diffraction experiments, which can determine the magnetic structure much more accurately, to be undertaken and advance the understanding of these intriguing materials.

A. Appendix – Derivations

A.1 Contribution of B Cations to the Diffraction Pattern

In the $A_2B'B''O_6$ double perovskites the B cations occupy the $2c$ and $2d$ sites in the system as shown in Figure A.1. The average scattering factor on the $2c$ site is denoted f_{2c} and likewise for the $2d$ site f_{2d}. For a fully general coordinate system if one $2c$ site is at (x, y, z) then the other is at $(x+ ½, y + ½, z + ½)$. The $2d$ sites are thus $(x+ ½, y + ½, z)$ and $(x, y, z + ½)$.

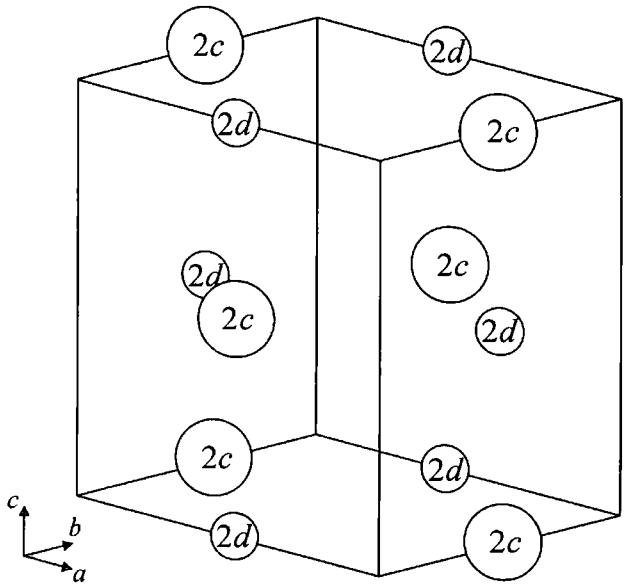

Figure A.1 Unit cell of a double perovskite displaying only the *B* cations on the 2*c* and 2*d* sites.

The structure factor, F_{hkl}, which when squared is proportional to the diffracted intensity.

$$F_{hkl} = \sum_{1}^{N} f_j \, e^{2\pi i (hx_j + ky_j + lz_j)} \qquad \text{A.1}$$

Consider the structure factor for the B cations only.

$$F_{hkl} = \sum_{1}^{N/4} \Big\{ f_{2c} e^{2\pi i (hx + ky + lz)} + f_{2c} e^{2\pi i (h(x + 1/2) + k(y + 1/2) + l(z + 1/2))} + f_{2d} e^{2\pi i (h(x + 1/2) + k(y + 1/2) + lz)} + f_{2d} e^{2\pi i (hx + ky + l(z + 1/2))} \Big\} \qquad \text{A.2}$$

$$= \sum_{1}^{N/4} e^{2\pi i(hx + ky + lz)} \left\{ f_{2c} + f_{2c} e^{\pi i(h + k + l)} + f_{2d} e^{\pi i(h + k)} + f_{2d} e^{\pi i l} \right\} \quad \text{A.3}$$

So,

$$F_{hkl} = \sum_{1}^{N/4} e^{2\pi i(hx + ky + lz)} \left\{ f_{2c} \left(1 + (-1)^{(h + k + l)}\right) + f_{2d} \left((-1)^{(h + k)} + (-1)^{l}\right) \right\} \quad \text{A.4}$$

Consider the section in the parentheses {} only, for all the possible combinations of h, k, l in Table A.1.

Index			f_{2c}	f_{2d}	Total
h	k	l			
e	e	e	2	2	$2(f_{2c} + f_{2d})$
e	e	o	0	0	0
e	o	e	0	0	0
o	e	e	0	0	0
e	o	o	2	-2	$2(f_{2c} - f_{2d})$
o	e	o	2	-2	$2(f_{2c} - f_{2d})$
o	o	e	2	2	$2(f_{2c} + f_{2d})$
o	o	o	0	0	0

Table A.1 The different combinations of h, k, l for the B cation reflections. In the index columns e represents an even number and o and odd number. The columns f_{2c} and f_{2d} represent the factor for this enclosed within the parentheses. The total shows clearly which h, k, l involve the sum and difference of the scattering factors on the two sites.

Table A.1 shows clearly that $F_{hkl} = 0$ when the sum $h + k + l$ is odd, and $F_{hkl} \neq 0$ when the sum $h + k + l$ is even. Additionally, when l is even, the sum of $h + k$ must also be even to generate a strong reflection from the sum of the scattering factors on the two sites. When l is odd, the sum of $h + k$ must be odd to generate a reflection from the difference of the scattering factors on the two sites. The B cations do not contribute any intensity to any other reflection h, k, l. As the intensity is proportional to the square of the structure factor we may represent the intensity of a sum peak, I_{sum}, where $I_{sum} = A^2(\Sigma f_{2c} + \Sigma f_{2d})^2$ where A^2 is the constant of proportionality and Σf_{2c} and Σf_{2d} the total scattering factor on the $2c$ and $2d$ sites respectively. Likewise the intensity of a difference peak, I_{ord}, which determines the ordering can be represented as $I_{ord} = A^2(\Sigma f_{2c} - \Sigma f_{2d})^2$.

A.2 Contribution of B' Cations to the Diffraction Pattern

For the $A_2B'B''O_6$ double perovskites the contribution of just one of the B cations to the diffraction pattern is considered. Figure A.2 shows the unit cell with just the B' ions displayed and it can be seen that there are only two positions in the unit cell for a $2d$ site, namely (½, 0, 0) and (0, ½, ½).

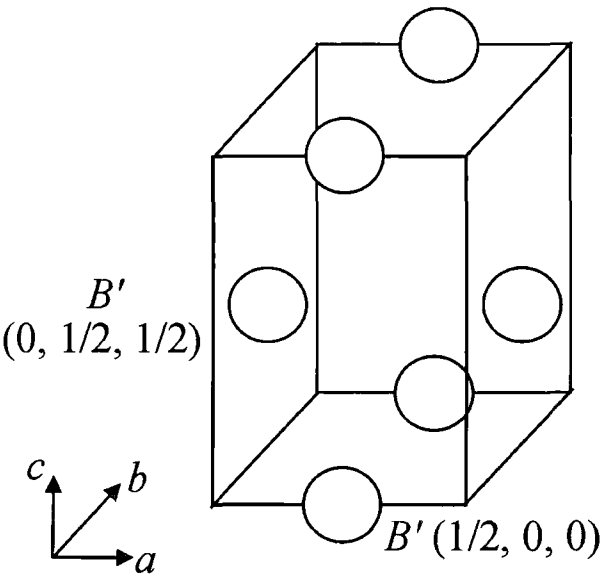

Figure A.2 The unit cell of a double perovskite with only one type of *B* cation, *B'* displayed explicitly.

Consider the structure factor, F_{hkl}, which when squared is proportional to the diffracted intensity.

$$F_{hkl} = \sum_{1}^{N} f_j e^{2\pi i (hx_j + ky_j + lz_j)} \qquad \text{A.5}$$

Considering just the contributions from the B' cations and noting that for every B' cation at (x, y, z) there is another at $(x+ ½, y + ½, z + ½)$ in a fully generalised coordinate system.

$$F_{hkl} = \sum_{1}^{N/2} \left\{ f_{2c} e^{2\pi i (hx + ky + lz)} + f_{2c} e^{2\pi i (h(x + 1/2) + k(y + 1/2) + l(z + 1/2))} \right\} \qquad \text{A.6}$$

$$= \sum_{1}^{N/2} f_{2c} e^{2\pi i (hx + ky + lz)} \left(1 + e^{\pi i (h + k + l)}\right) \qquad \text{A.7}$$

So,

$$F_{hkl} = \sum_{1}^{N/2} f_{2c} e^{2\pi i (hx + ky + lz)} \left(1 + (-1)^{(h + k + l)}\right) \qquad \text{A.8}$$

If $h + k + l$ is odd, then $F_{hkl} = 0$ and the B' cations do not contribute to the diffraction intensity. However if $h + k + l$ is even, then $F_{hkl} \neq 0$ and the B' cations do make a contribution to the diffraction pattern. (This agrees with the earlier subset findings that sum peaks must have $(h + k)$ and l both even, while difference peaks must have them both odd. In either case the sum $h + k + l$ is even.)

Non-anomalous measurements have been used to determine that the systems all are highly ordered, so to very good first approximation the ruthenium atoms can be considered only to occupy one B site. Thus, the ruthenium in the sample makes a sizeable contribution to the diffraction pattern only when $h + k + l$ is even.

A.3 Reflections Conditions of the One Magnetic Ion Systems

Consider only the double perovskite systems $A_2B'B''O_6$ where one of the B cations is magnetic. There are different reflection conditions depending on whether the interaction between the two magnetic ions in the magnetic unit cell is ferromagnetic or antiferromagnetic. It is possible that both may be present simultaneously, giving rise to a canted magnetic state. Figure A.3 shows the magnetic unit cell with just the magnetic B' cation displayed and the two independent sites in the unit cell at (½, 0, 0) and (0, ½, ½), which in a fully generalised coordinate system are at (x, y, z) and $(x+ ½, y + ½, z + ½)$. For clarity, these two sites will be labelled Ru1 and Ru2 respectively.

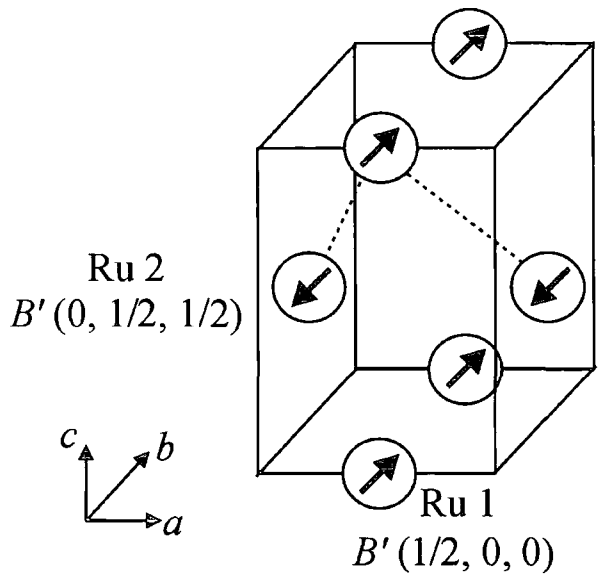

Figure A.3 The magnetic unit cell of a double perovskite with only one magnetic *B* cation, *B'* displayed explicitly. The two sites of the *B'* cation are labelled Ru1 and Ru2 respectively. In this example the magnetic moments on the two sites are coupled antiferromagnetically as indicated by the dotted lines.

Consider the magnetic structure factor, FM_{hkl}, which when squared is proportional to the magnetic diffracted intensity, for both cases of a ferromagnetic and an antiferromagnetic coupling between the two sites.

$$FM_{hkl} = \sum_{1}^{N} q_j \, b_{mj} \, e^{2\pi i \, (hx_j + ky_j + lz_j)} \qquad \text{A.9}$$

Here $q = \kappa(\kappa.\sigma) - \sigma$, the factor b_m is the magnetic scattering amplitude and κ is the unit scattering vector, whereas σ is the unit magnetic moment vector. In particular, note that $q = 0$ when κ and σ are parallel. i.e. The magnetic structure factor is zero, hence there will be no magnetic intensity when the magnetic moment and the scattering vector are parallel, irrespective of the magnetic structure adopted. Alternatively expressed, a scattering vector will only examine a perpendicular component of the magnetic moment.

The magnetic structure factor for this system is thus,

$$FM_{hkl} = \sum_{1}^{N/2} \left\{ q_{Ru1} \, b_{mRu1} \, e^{2\pi i \, (hx + ky + lz)} + q_{Ru2} \, b_{mRu2} \, e^{2\pi i \, (h(x + 1/2) + k(y + 1/2) + l(z + 1/2))} \right\} \qquad \text{A.10}$$

which simplifies to Equation A.11,

$$= \sum_{1}^{N/2} e^{2\pi i \, (hx + ky + lz)} \left\{ q_{Ru1} \, b_{mRu1} + q_{Ru2} \, b_{mRu2} \, e^{\pi i \, (h + k + l)} \right\} \qquad \text{A.11}$$

and finally to Equation A.12.

$$FM_{hkl} = \sum_{1}^{N/2} e^{2\pi i \, (hx + ky + lz)} \left\{ q_{Ru1} \, b_{mRu1} + q_{Ru2} \, b_{mRu2} \, (-1)^{(h + k + l)} \right\} \qquad \text{A.12}$$

There are two cases, ferromagnetic coupling and antiferromagnetic coupling between the two ions Ru1 and Ru2.

A.3.1 Ferromagnetic Interaction

When the ions on the two sites are coupled ferromagnetically the moments have the same magnitude and point in the same direction. i.e. $q_{\mathrm{Ru1}}\, b_{\mathrm{mRu1}} = q_{\mathrm{Ru2}}\, b_{\mathrm{mRu2}}$. Therefore Equation A.12 reduces to Equation A.13.

$$FM_{\mathrm{hkl}} = \sum_{1}^{N/2} q_{\mathrm{Ru1}}\, b_{\mathrm{mRu1}}\, e^{2\pi i\,(hx + ky + lz)} \left\{1 + (-1)^{(h+k+l)}\right\} \qquad \text{A.13}$$

As the moments are now collinear (i.e. moments point along same straight line) the magnitude of the vector sum is simply the sum of magnitudes of the component vectors, yielding Equation A.14.

$$FM_{\mathrm{hkl}} = \sum_{1}^{N/2} q_{\mathrm{Ru1}}\, b_{\mathrm{mRu1}}\, e^{2\pi i\,(hx + ky + lz)} \left\{1 + (-1)^{(h+k+l)}\right\} \qquad \text{A.14}$$

Therefore if $h + k + l$ is <u>odd</u>, then $FM_{\mathrm{hkl}} = 0$ and there is no magnetic intensity contribution to the diffraction pattern. However when $h + k + l$ is <u>even</u>, then $FM_{\mathrm{hkl}} \neq 0$, there is ferromagnetic intensity in the diffraction pattern. This reflection condition is the *same* as that for the crystal structure and hence confirms the ferromagnetic peaks will add intensity to existing crystal structure peaks. However the magnetic structure factor is *different* in the respect of the prefactor q_{Ru1}. This modifies the magnetic intensity, dependant on the relative orientations of the magnetic moment and the scattering vector, and can reduce it even to zero, as discussed above.

A.3.2 Antiferromagnetic Interaction

In the case of the two ions on the sites being coupled antiferromagnetically, the moments are equal in magnitude but opposite in direction, so that $q_{\mathrm{Ru1}}\, b_{\mathrm{mRu1}} = -\, q_{\mathrm{Ru2}}\, b_{\mathrm{mRu2}}$.

Therefore Equation A.12 becomes Equation A.15 as the moments are collinear.

$$FM_{\mathrm{hkl}} = \sum_{1}^{N/2} q_{\mathrm{Ru1}}\, b_{\mathrm{mRu1}}\, e^{2\pi i\,(hx + ky + lz)} \left\{1 - (-1)^{(h+k+l)}\right\} \qquad \text{A.15}$$

Therefore if $h + k + l$ is <u>even</u>, then $FM_{\mathrm{hkl}} = 0$, and there is no magnetic intensity contribution to the diffraction pattern. However when $h + k + l$ is <u>odd</u>, then $FM_{\mathrm{hkl}} \neq 0$ and there is antiferromagnetic intensity in the diffraction pattern. This reflection condition is the *opposite* to that for the crystal structure *when only one B cation is considered.* Thus, the antiferromagnetic intensity will appear in the diffraction pattern at different locations to the crystal structure peaks, and is often the first indicator of an

antiferromagnetic structure. However note, antiferromagnetic peaks may coincide with existing crystal structure peaks, as there are usually more atoms in the material, which may have different reflection conditions. Note again, the prefactor q_{Ru1} modifies the magnitude of the magnetic reflection due to the direction of the magnetic moment.

Hence, the location of the magnetic peaks in the diffraction pattern determines whether the magnetic structure is ferromagnetic or antiferromagnetic. In a canted magnetic structure there will be contributions to each reflection and the relative proportions will give the degree of canting.

A.4 Reflections Conditions of the Two Magnetic Ion Systems

Consider only the double perovskites of general formula $A_2B'B''O_6$. When both B cations are magnetic there are different reflection conditions, dependant on the particular magnetic structure adopted. Consider the magnetic unit cell in Figure A.4, where the B' cations reside on the $2c$ sites and the B'' ions on the $2d$ sites. For a fully general coordinate system, if one of the $2c$ sites is at (x, y, z) then the other is at $(x+ ½, y + ½, z + ½)$. The $2d$ sites are thus $(x+ ½, y + ½, z)$ and $(x, y, z + ½)$. For clarity of notation these sites are labelled Ho1, Ho2, Ru1 and Ru2 respectively, as shown in Figure A.4.

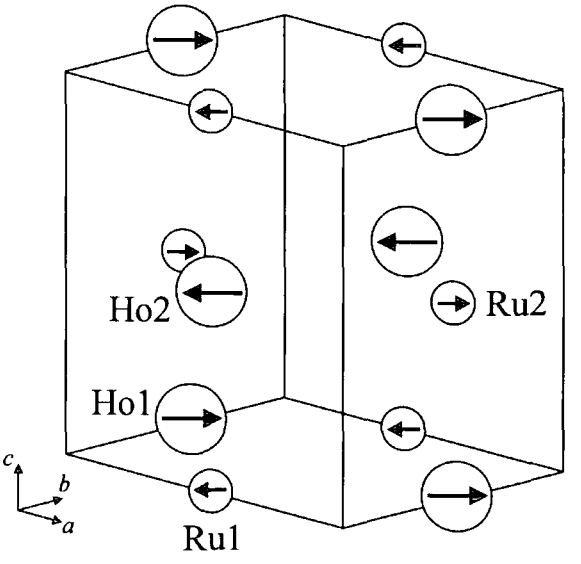

Figure A.4 The positions of the *B* cations in relation to the unit cell, with the independent magnetic sites explicitly labelled Ho1, Ho2, Ru1 and Ru2. In this particular case, the magnetic moments are arranged in two interpenetrating Type I sublattices.

The magnetic structure factor, which when squared is proportional to the magnetic diffracted intensity, is given by Equation A.16,

$$\boldsymbol{FM}_{hkl} = \sum_{1}^{N} \boldsymbol{q}_j \, b_{mj} \, e^{2\pi i (hx_j + ky_j + lz_j)} \qquad \text{A.16}$$

where $\boldsymbol{q} = \boldsymbol{\kappa}(\boldsymbol{\kappa}.\boldsymbol{\sigma}) - \boldsymbol{\sigma}$, the factor b_m is the magnetic scattering amplitude and $\boldsymbol{\kappa}$ is the unit scattering vector, whereas $\boldsymbol{\sigma}$ is the unit magnetic moment vector. For the crystal structure in Figure A.4 the magnetic scattering factor becomes,

$$\begin{aligned} \boldsymbol{FM}_{hkl} = \sum_{1}^{N/4} \Big\{ & \boldsymbol{q}_{Ho1} b_{mHo1} e^{2\pi i (hx + ky + lz)} \\ & + \boldsymbol{q}_{Ho2} b_{mHo2} e^{2\pi i (h(x + 1/2) + k(y + 1/2) + l(z + 1/2))} \\ & + \boldsymbol{q}_{Ru1} b_{mRu1} e^{2\pi i (h(x + 1/2) + k(y + 1/2) + lz)} \\ & + \boldsymbol{q}_{Ru2} b_{mRu2} e^{2\pi i (hx + ky + l(z + 1/2))} \Big\} \end{aligned} \qquad \text{A.17}$$

where the common factor is taken out of the parentheses to yield Equation A.18.

$$\begin{aligned} = \sum_{1}^{N/4} e^{2\pi i (hx + ky + lz)} \Big\{ & \boldsymbol{q}_{Ho1} b_{mHo1} + \boldsymbol{q}_{Ho2} b_{mHo2} e^{\pi i (h + k + l)} \\ & + \boldsymbol{q}_{Ru1} b_{mRu1} e^{\pi i (h + k)} + \boldsymbol{q}_{Ru2} b_{mRu2} e^{\pi i l} \Big\} \end{aligned} \qquad \text{A.18}$$

Equation A.18 is written more succinctly as Equation A.19.

$$\begin{aligned} \boldsymbol{FM}_{hkl} = \sum_{1}^{N/4} e^{2\pi i (hx + ky + lz)} \Big\{ & \boldsymbol{q}_{Ho1} b_{mHo1} + \boldsymbol{q}_{Ho2} b_{mHo2} (-1)^{(h + k + l)} \\ & + \boldsymbol{q}_{Ru1} b_{mRu1} (-1)^{(h + k)} + \boldsymbol{q}_{Ru2} b_{mRu2} (-1)^{l} \Big\} \end{aligned} \qquad \text{A.19}$$

There are four cases of magnetic ordering depending on the *apparent* intra-species interaction. The Ho and Ru couplings can be both ferromagnetic, both antiferromagnetic, or one of either.

A.4.1 Both Ferromagnetic

In this case, the moments on Ho1 and Ho2 will be in the same direction and equal in magnitude. i.e. $q_{\mathrm{Ho1}}\, b_{\mathrm{mHo1}} = q_{\mathrm{Ho2}}\, b_{\mathrm{mHo2}}$. Likewise for Ru1 and Ru2, so that $q_{\mathrm{Ru1}}\, b_{\mathrm{mRu1}} = q_{\mathrm{Ru2}}\, b_{\mathrm{mRu2}}$. Therefore Equation A.19 becomes,

$$FM_{\mathrm{hkl}} = \sum_{1}^{N/4} e^{2\pi i\,(hx + ky + lz)} \left\{ q_{\mathrm{Ho1}}\, b_{\mathrm{mHo1}} \left(1 + (-1)^{(h+k+l)}\right) + q_{\mathrm{Ru1}}\, b_{\mathrm{mRu1}} \left((-1)^{(h+k)} + (-1)^{l}\right) \right\} \qquad \text{A.20}$$

and this allows the construction of Table A.2 from the factors in the parentheses, {}.

Index			$q_{\mathrm{Ho1}}b_{\mathrm{mHo1}}$	$q_{\mathrm{Ru1}}b_{\mathrm{mRu1}}$	Total
h	k	l			
e	e	e	2	2	$2(q_{\mathrm{Ho1}}b_{\mathrm{mHo1}} + q_{\mathrm{Ru1}}b_{\mathrm{mRu1}})$
e	e	o	0	0	0
e	o	e	0	0	0
o	e	e	0	0	0
e	o	o	2	-2	$2(q_{\mathrm{Ho1}}b_{\mathrm{mHo1}} - q_{\mathrm{Ru1}}b_{\mathrm{mRu1}})$
o	e	o	2	-2	$2(q_{\mathrm{Ho1}}b_{\mathrm{mHo1}} - q_{\mathrm{Ru1}}b_{\mathrm{mRu1}})$
o	o	e	2	2	$2(q_{\mathrm{Ho1}}b_{\mathrm{mHo1}} + q_{\mathrm{Ru1}}b_{\mathrm{mRu1}})$
o	o	o	0	0	0

Table A.2 The table of reflection conditions for the two magnetic ion system when both intra-species coupling are ferromagnetic. The letter e denotes an even number and o an odd number.

From Table A.2 it is clear that $\boldsymbol{FM}_{\mathrm{hkl}} = \mathbf{0}$ when $h + k + l$ is odd, and provided the scattering vector is *perpendicular* to a net magnetic moment vector then $\boldsymbol{FM}_{\mathrm{hkl}} \neq \mathbf{0}$ when $h + k + l$ is even. Consider the two special cases where $q_{\mathrm{Ho1}} = q_{\mathrm{Ru1}}$ and $q_{\mathrm{Ho1}} = -\,q_{\mathrm{Ru1}}$. As $\boldsymbol{q} = \boldsymbol{\kappa}(\boldsymbol{\kappa}.\boldsymbol{\sigma}) - \boldsymbol{\sigma}$, these correspond to the cases where the two magnetic moments on the sublattices are parallel and anti-parallel to each other as shown in Figure A.5.

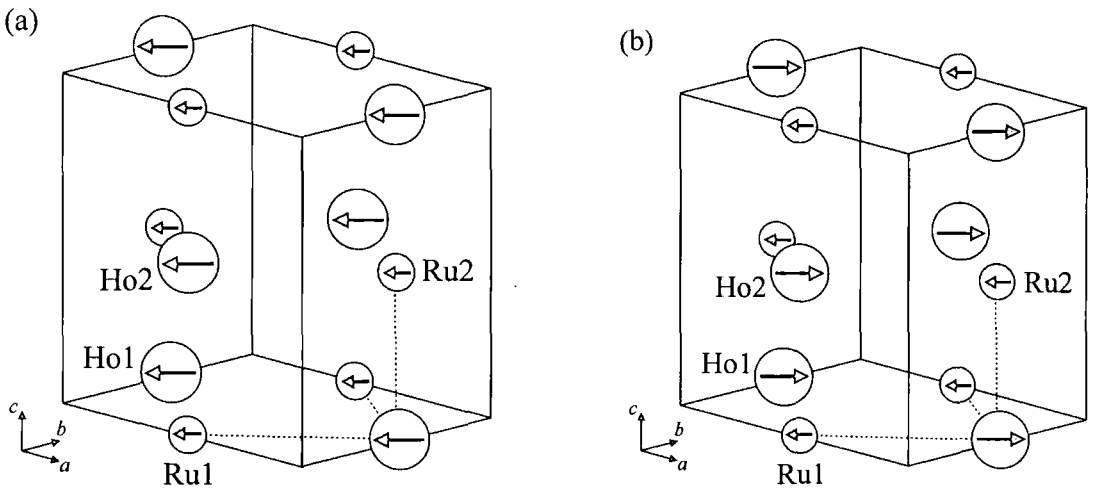

Figure A.5 Each sublattice is coupled ferromagnetically, and the two sublattices couple to each other (a) ferromagnetically and (b) ferrimagnetically. These interactions are shown by the dotted lines and the nature of the interaction is most easily seen in the *ab* plane. The absolute directions of the moments are arbitrarily shown, but the relative orientations of the moments with respect to one another are not arbitrary.

The moments are collinear so Equation A.20 can simplify greatly as the magnitude of the vector sum is equal to the sum of the magnitudes of the component vectors. Therefore, for the case of $q_{\mathrm{Ho1}} = q_{\mathrm{Ru1}}$ one obtains,

$$FM_{\mathrm{hkl}} = \sum_{1}^{N/4} q_{\mathrm{Ho1}}\, e^{2\pi i\,(hx + ky + lz)} \left\{ b_{\mathrm{mHo1}} \left(1 + (-1)^{(h+k+l)}\right) + b_{\mathrm{mRu1}} \left((-1)^{(h+k)} + (-1)^{l}\right) \right\} \quad \text{A.21}$$

and for the case of $q_{\mathrm{Ho1}} = -q_{\mathrm{Ru1}}$ one obtains Equation A.22

$$FM_{\mathrm{hkl}} = \sum_{1}^{N/4} q_{\mathrm{Ho1}}\, e^{2\pi i\,(hx + ky + lz)} \left\{ b_{\mathrm{mHo1}} \left(1 + (-1)^{(h+k+l)}\right) - b_{\mathrm{mRu1}} \left((-1)^{(h+k)} + (-1)^{l}\right) \right\} \quad \text{A.22}$$

With the extra conditions of $q_{\mathrm{Ho1}} = q_{\mathrm{Ru1}}$ and $q_{\mathrm{Ho1}} = -q_{\mathrm{Ru1}}$, Table A.2 can be simplified to Table A.3 as q_{Ho1} has been taken out of the parentheses in Equation A.21 and Equation A.22.

Index			Lattices Parallel Ferromagnetic	Lattices Anti-Parallel Ferrimagnetic
h	k	l		
e	e	e	$2(b_{mHo1} + b_{mRu1})$	$2(b_{mHo1} - b_{mRu1})$
e	e	o	0	0
e	o	e	0	0
o	e	e	0	0
e	o	o	$2(b_{mHo1} - b_{mRu1})$	$2(b_{mHo1} + b_{mRu1})$
o	e	o	$2(b_{mHo1} - b_{mRu1})$	$2(b_{mHo1} + b_{mRu1})$
o	o	e	$2(b_{mHo1} + b_{mRu1})$	$2(b_{mHo1} - b_{mRu1})$
o	o	o	0	0

Table A.3 The simplified table of reflection conditions for both the ferromagnetic and ferrimagnetic case.

The reflection conditions for the magnetic intensity still hold, i.e. $FM_{hkl} = 0$ if $h + k + l$ is odd, and $FM_{hkl} \neq 0$ if $h + k + l$ is even. However, now it is much more clear which peaks are formed from the summation of the two magnetic moments on the two sublattices, and which on the difference, depends on the relative orientation of the two sublattices as summarised in Table A.4. This table is able to assist magnetic moment determination of the two species, from consideration of the relative intensities of the sum and difference peaks.

Type of Reflection	Lattices Parallel Ferromagnetic		Lattices Anti-Parallel Ferrimagnetic	
	$(h + k)$	l	$(h + k)$	l
Sum	even	even	odd	odd
Difference	odd	odd	even	even

Table A.4 The reflection conditions for strong peaks and for weak peaks depend on the relative orientations of the moments on each sublattice.

For moments on sublattices which are orientated at some intermediate angle with respect to one another, there are two equivalent approaches. The parallel and perpendicular components can be considered separately using Table A.4, or the full Table A.3 can be used with the total magnetic moments.

It is important to note, *inter-species* coupling does not generate any magnetic intensity in different locations in the diffraction pattern. However, it does influence the relative magnitudes of the existing magnetic reflections (derived from *intra-species* coupling.)

A.4.2 Both Antiferromagnetic

In this case, the moments on Ho1 and Ho2 will be opposite in direction but equal in magnitude. i.e. $q_{\mathrm{Ho1}}\, b_{\mathrm{mHo1}} = -\, q_{\mathrm{Ho2}}\, b_{\mathrm{mHo2}}$. Likewise for Ru1 and Ru2, so that $q_{\mathrm{Ru1}}\, b_{\mathrm{mRu1}} = -\, q_{\mathrm{Ru2}}\, b_{\mathrm{mRu2}}$. Therefore Equation A.19 becomes,

$$FM_{\mathrm{hkl}} = \sum_{1}^{N/4} e^{2\pi i\,(hx + ky + lz)} \left\{ q_{\mathrm{Ho1}}\, b_{\mathrm{mHo1}} \left(1 - (-1)^{(h+k+l)}\right) + q_{\mathrm{Ru1}}\, b_{\mathrm{mRu1}} \left((-1)^{(h+k)} - (-1)^{l}\right)\right\} \qquad \text{A.23}$$

The reflection conditions are examined in Table A.5 from consideration of the information within the parentheses.

Index			$q_{\mathrm{Ho1}}b_{\mathrm{mHo1}}$	$q_{\mathrm{Ru1}}b_{\mathrm{mRu1}}$	Total
h	k	l			
e	e	e	0	0	0
e	e	o	2	2	$2(q_{\mathrm{Ho1}}b_{\mathrm{mHo1}} + q_{\mathrm{Ru1}}b_{\mathrm{mRu1}})$
e	o	e	2	-2	$2(q_{\mathrm{Ho1}}b_{\mathrm{mHo1}} - q_{\mathrm{Ru1}}b_{\mathrm{mRu1}})$
o	e	e	2	-2	$2(q_{\mathrm{Ho1}}b_{\mathrm{mHo1}} - q_{\mathrm{Ru1}}b_{\mathrm{mRu1}})$
e	o	o	0	0	0
o	e	o	0	0	0
o	o	e	0	0	0
o	o	o	2	2	$2(q_{\mathrm{Ho1}}b_{\mathrm{mHo1}} + q_{\mathrm{Ru1}}b_{\mathrm{mRu1}})$

Table A.5 Table of reflection conditions for the case when both inter-species couplings appear antiferromagnetic.

The reflection conditions are $\boldsymbol{FM}_{\mathrm{hkl}} = \mathbf{0}$ when $h + k + l$ is even, and provided the scattering vector is perpendicular to a net magnetic moment, then $\boldsymbol{FM}_{\mathrm{hkl}} \neq \mathbf{0}$ when $h + k + l$ is odd. These are the same reflection conditions as the case of an antiferromagnetic single ion system, though the intensities are clearly different, based on various combinations of the two moments of the species. Again, we consider the cases where the moments in the two sublattices are collinear, so set $q_{\mathrm{Ho1}} = q_{\mathrm{Ru1}}$ which yields Equation A.24 and indicates a ferromagnetic *inter-species* interaction.

$$FM_{\mathrm{hkl}} = \sum_{1}^{N/4} q_{\mathrm{Ho1}}\, e^{2\pi i\,(hx + ky + lz)} \left\{ b_{\mathrm{mHo1}} \left(1 - (-1)^{(h+k+l)}\right) + b_{\mathrm{mRu1}} \left((-1)^{(h+k)} - (-1)^{l}\right)\right\} \qquad \text{A.24}$$

In the case where $q_{Ho1} = -q_{Ru1}$ then Equation A.23 generates Equation A.25 for the antiferromagnetic *inter-species* interaction.

$$FM_{hkl} = \sum_{1}^{N/4} q_{Ho1}\, e^{2\pi i (hx + ky + lz)} \left\{ b_{mHo1} \left(1 - (-1)^{(h+k+l)}\right) - b_{mRu1} \left((-1)^{(h+k)} - (-1)^{l}\right)\right\} \quad \text{A.25}$$

These cases have the two sublattice moments parallel or anti-parallel with respect to one another, as Figure A.6 shows. Unlike the ferromagnetic *intra-species* case detailed in Section A.4.1 where all the *inter-species* couplings could be satisfied, for the antiferromagnetic *intra-species* case, it is only possible for 4 out of 6 *inter-species* couplings to be satisfied.

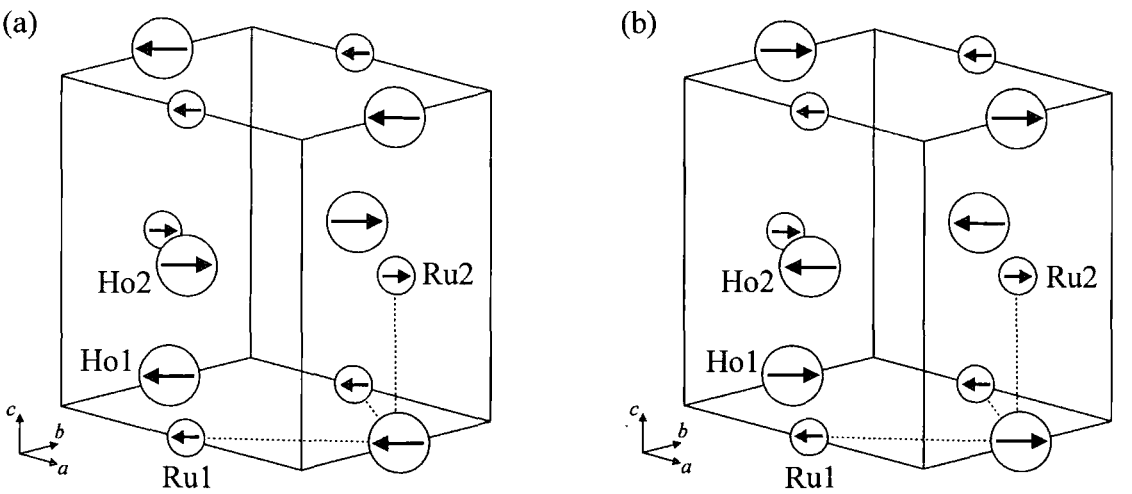

Figure A.6 Each sublattice is coupled antiferromagnetically in a Type I structure. However, the two sublattices couple (a) ferromagnetically and (b) ferrimagnetically. This is most easily seen from the directions of the moments in the *ab* plane as indicated by the dotted lines. It is not possible for all the inter-species couplings to be of the same kind, the maximum is 4 out 6, as indicated by the dotted lines out of the *ab* plane. The absolute directions of the moments are arbitrarily shown, but the relative orientations of the moments with respect to one another are not.

Both of these arrangements have been observed and the reflection conditions are determined explicitly for the two cases where $q_{Ho1} = q_{Ru1}$ (ferromagnetic) and $q_{Ho1} = -q_{Ru1}$ (ferrimagnetic) in Table A.6, from the parentheses of Equation A.24 and Equation A.25.

Index			Lattices Parallel Ferromagnetic	Lattices Anti-Parallel Ferrimagnetic
h	k	l		
e	e	e	0	0
e	e	o	$2(b_{mHo1} + b_{mRu1})$	$2(b_{mHo1} - b_{mRu1})$
e	o	e	$2(b_{mHo1} - b_{mRu1})$	$2(b_{mHo1} + b_{mRu1})$
o	e	e	$2(b_{mHo1} - b_{mRu1})$	$2(b_{mHo1} + b_{mRu1})$
e	o	o	0	0
o	e	o	0	0
o	o	e	0	0
o	o	o	$2(b_{mHo1} + b_{mRu1})$	$2(b_{mHo1} - b_{mRu1})$

Table A.6 Reflection conditions for two interpenetrating Type I lattices for the case of ferromagnetic and ferrimagnetic coupling between the two species.

These results confirm that $FM_{hkl} = 0$ if $h + k + l$ is even and that $FM_{hkl} \neq 0$ if $h + k + l$ is odd. Further the size of the magnetic moment of each species can be determined from consideration of Table A.7 and the diffraction pattern.

Type of Reflection	Lattices Parallel Ferromagnetic		Lattices Anti-Parallel Ferrimagnetic	
	$(h + k)$	l	$(h + k)$	l
Sum	even	odd	odd	even
Difference	odd	even	even	odd

Table A.7 The magnitude of the reflections is governed also by the intra-species coupling, as indicated from the sum and difference peaks.

This confirms the previous findings, but now for the case where both intra-species couplings are antiferromagnetic. Note, that while the intra-species couplings determine the location of the reflection intensity, it is the inter-species couplings which govern the relative magnitude of the magnetic peaks. The intra-species couplings affect the magnitude of the magnetic intensity from the size of the ordered moment.

A.4.3 One Ferromagnetic, One Antiferromagnetic

As the situation is perfectly symmetric with regards to magnetic diffraction, just one of the two combinations will be dealt with explicitly, a ferromagnetic coupling between the Ho1 and Ho2 ions, but an antiferromagnetic coupling between the Ru1 and Ru2 ions. In this case, $q_{Ho1}\, b_{mHo1} = q_{Ho2}\, b_{mHo2}$ and $q_{Ru1}\, b_{mRu1} = -\, q_{Ru2}\, b_{mRu2}$, so that Equation A.19 generates Equation A.26.

$$FM_{hkl} = \sum_{1}^{N/4} e^{2\pi i\,(hx + ky + lz)} \left\{ q_{Ho1}\, b_{mHo1} \left(1 + (-1)^{(h+k+l)}\right) + q_{Ru1}\, b_{mRu1} \left((-1)^{(h+k)} - (-1)^{l}\right) \right\} \quad \text{A.21}$$

The reflection conditions are examined in Table A.8 from consideration of the information within the parentheses.

Index			$q_{Ho1}b_{mHo1}$	$q_{Ru1}b_{mRu1}$	Total
h	*k*	*l*			
e	e	e	2	0	$2q_{Ho1}b_{mHo1}$
e	e	o	0	2	$2q_{Ru1}b_{mRu1}$
e	o	e	0	-2	$-2q_{Ru1}b_{mRu1}$
o	e	e	0	-2	$-2q_{Ru1}b_{mRu1}$
e	o	o	2	0	$2q_{Ho1}b_{mHo1}$
o	e	o	2	0	$2q_{Ho1}b_{mHo1}$
o	o	e	2	0	$2q_{Ho1}b_{mHo1}$
o	o	o	0	2	$2q_{Ru1}b_{mRu1}$

Table A.8 The reflection conditions when one sublattice has ferromagnetic couplings, the other antiferromagnetic.

The ferromagnetic intensity only displays itself for reflections where $h + k + l$ is even, and the antiferromagnetic intensity where $h + k + l$ is odd. The result is the obvious one, with the reflection conditions of each ion obeying the reflection conditions that would be observed by considering both a ferromagnetic one magnetic ion system, and an antiferromagnetic one magnetic ion system. From the relative proportions of the ferromagnetic and antiferromagnetic intensities the magnetic moments on each ion species can be determined. Owing to the mixture of ferromagnetic and antiferromagnetic intra-species couplings, there are equal numbers of both ferromagnetic and ferrimagnetic inter-species couplings as illustrated in Figure A.7.

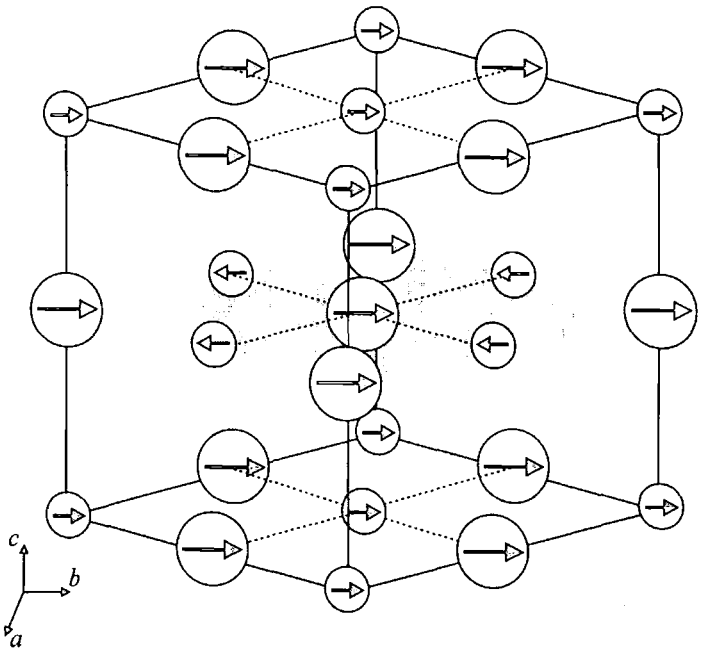

Figure A.7 With one species having ferromagnetic couplings, the other species antiferromagnetic couplings, there are equal numbers of ferromagnetic and ferrimagnetic inter-species couplings. These are shown as the dotted lines in the *ab* plane for an expanded cell, though the out of plane interactions are also equally distributed. The absolute directions of the moments are arbitrarily shown, but the relative orientations of the moments with respect to one another are not.

A.4.4 Summary of Two Magnetic Ion Findings for $A_2B'B''O_6$

The reflection conditions of FM_{hkl} are determined *solely* by the intra-species coupling. i.e. The location of the magnetic diffraction intensity determines whether the sublattices are ferromagnetic or antiferromagnetic. The magnitude of the magnetic intensity is related to the size of the ordered magnetic moment. However, the relative strengths of the magnetic peaks determine whether the sublattices are parallel or anti-parallel. i.e. whether the inter-species coupling is ferromagnetic or antiferromagnetic. But note that a given magnetic reflection can only determine the magnetic component perpendicular to that scattering vector.

In practice, the moments on the two sublattices are assumed to be collinear, as this gives well calculated diffraction patterns, however non-collinear structures may be possible.

A.5 Type I Magnetic Structure in $A_2B'RuO_6$

The magnetic unit cell is shown for $A_2B'RuO_6$ in Figure A.8, with the Ru ions on the two independent sites at (½, 0, 0) and (0, ½, ½), which are labelled Ru1 and Ru2 respectively. When Ru is the only magnetic ion, the Ru-O-O-Ru antiferromagnetic interaction is the dominant one and Ru1 and Ru2 couple antiferromagnetically. Owing to the crystal structure, it is not possible for all the nearest-neighbour Ru ions to couple antiferromagnetically, and in fact, only 8 out of the 12 may do so. This is shown most clearly if we expand our picture to include more of the Ru neighbours, as shown in Figure A.9. By regarding the central Ru ion, the four nearest-neighbours in the plane couple ferromagnetically, but the 4 in each adjacent plane couple antiferromagnetically.

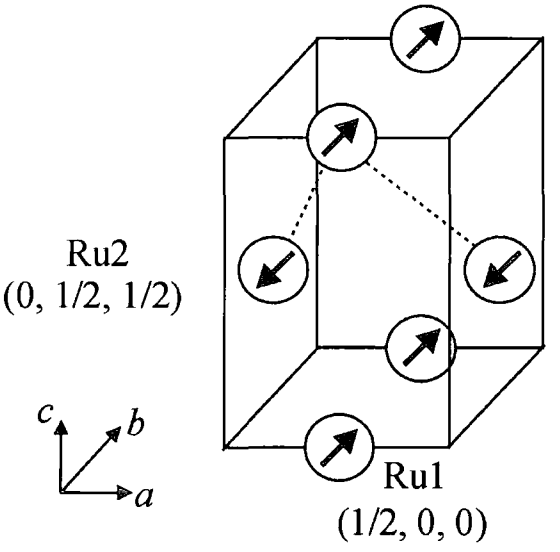

Figure A.8 The magnetic unit cell of $A_2B'RuO_6$ where the two independent Ru ions are labelled Ru1 and Ru2, with the antiferromagnetic interaction between them shown as the dotted line.

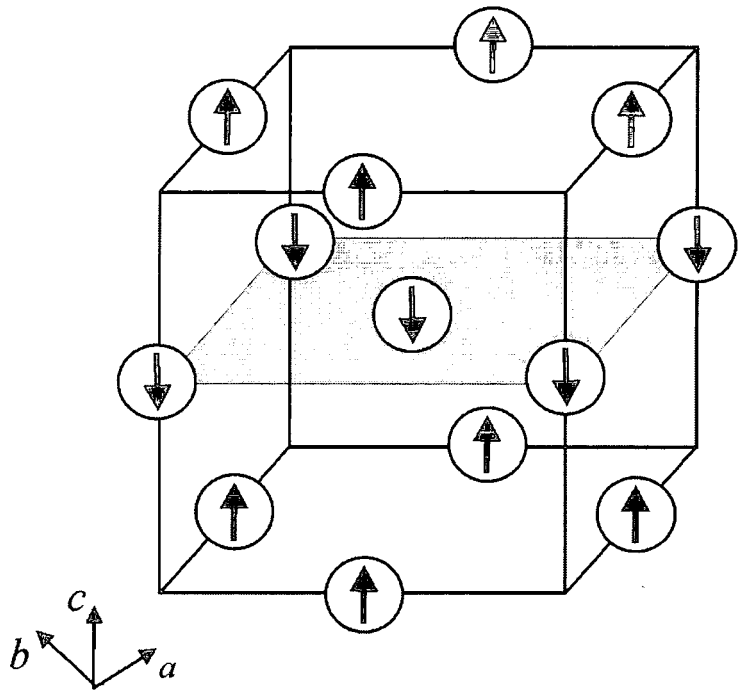

Figure A.9 It is not possible for all the nearest-neighbour Ru ions to be coupled antiferromagnetically. This expanded picture shows more clearly that 8 are antiferromagnetically coupled in the two adjacent (002) planes and 4 ferromagnetically coupled in the same plane. The Ru1 ions are all in the top and bottom (002) planes shown, while the Ru2 ions all reside in the middle (grey) (002) plane.

A.6 Stability of the Type I Magnetic Structure in A_2MRuO_6

The double perovskites of the form A_2RuMO_6, with both the Ru and M ions magnetic, typically adopt a magnetic structure in which the two sublattices each order in a Type I structure as shown in Figure A.10. The Ru-O-O-Ru antiferromagnetic interaction is responsible for the Ru sublattice adopting the Type I magnetic structure where 8 out of 12 interactions are satisfied (Section A.5). The M-O-O-M interaction is usually weak, and so is not responsible for the M sublattice adopting this structure. The Type I magnetic structure is adopted in the M sublattice because the Ru-O-M interaction (shown as the dotted lines in Figure A.10) orders the M sublattice in a structure compatible with its own Type I sublattice. The cases of the Ru-O-M interaction being of ferromagnetic and antiferromagnetic nature are shown in Figure A.10. It can be seen from the interactions (dotted lines) that 4 out of 6 *inter-species* couplings are satisfied when both sublattices adopt a Type I magnetic structure.

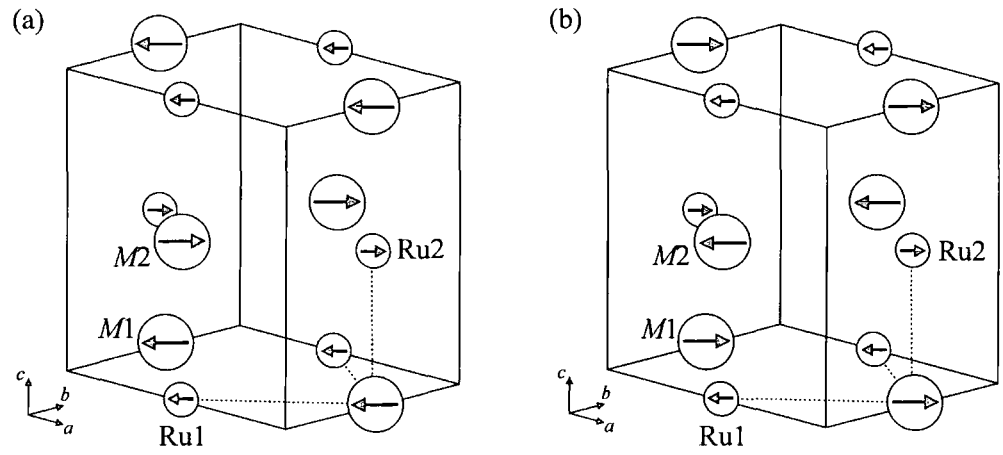

Figure A.10 The magnetic structure of A_2MRuO_6 where each sublattice orders with a Type I antiferromagnetic structure. The inter-species interaction (shown as dotted lines) is (a) ferromagnetic or (b) antiferromagnetic, though both lead to adoption of a Type I magnetic structure in the *M* sublattice. The two different sites for the magnetic ions of each species are labelled 1 and 2.

However, if the Ru-O-*M* interaction were much stronger than the Ru-O-O-Ru interaction, then the preference would be for the magnetic structure shown in Figure A.11, as all the Ru-O-*M* interactions, but none of the Ru-O-O-Ru antiferromagnetic interactions, would be satisfied. When the Ru-O-*M* interaction is ferromagnetic, the structure is the obvious ferromagnetic one, however, when the interaction is ferrimagnetic, the magnetic structure is ferrimagnetic, and would be classed as a Type G magnetic structure if all the ions were of the same species.

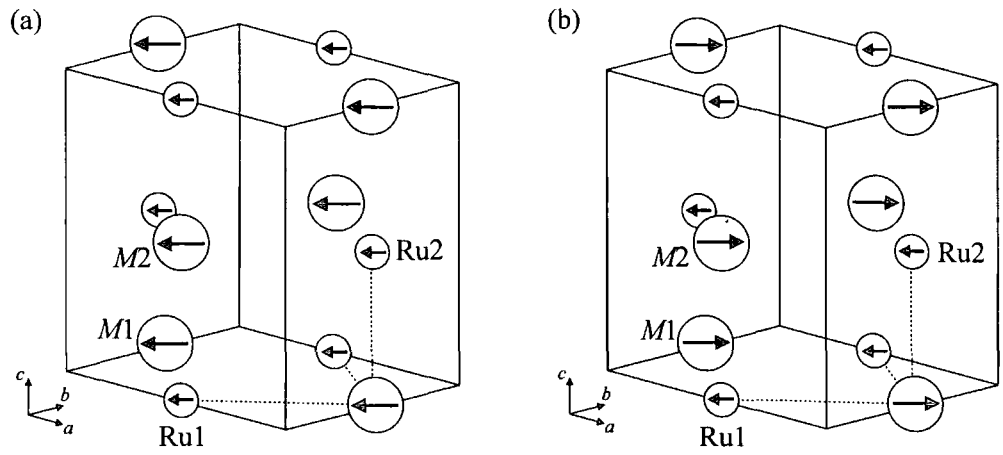

Figure A.11 The magnetic structure adopted when the Ru-O-*M* interaction is much the strongest in the material and is (a) ferromagnetic and (b) antiferromagnetic. From the dotted lines indicating the inter-species interactions, all 6 are satisfied in both cases. However, all the Ru ions are now coupled ferromagnetically (in both cases) and so none of the 12 Ru-O-O-Ru antiferromagnetic interactions is satisfied. The two different sites for the magnetic ions of each species are labelled 1 and 2.

Table A.9 summarises the number of each type of interaction which are satisfied, depending on the magnetic structure adopted.

Magnetic Structure	Ru-O-*M*		Ru-O-O-Ru	
	Satisfied	Unsatisfied	Satisfied	Unsatisfied
Interpenetrating Ferromagnetic Type I (Figure A.10a)	4	2	8	4
Interpenetrating Ferrimagnetic Type I (Figure A.10b)	4	2	8	4
Ferromagnetic (Figure A.11a)	6	0	0	12
Ferrimagnetic "Type G" (Figure A.11b)	6	0	0	12

Table A.9 The type and number of magnetic interactions which are satisfied depending on which magnetic structure is adopted.

As the number of Ru-O-*M* and Ru-O-O-Ru interactions which are satisfied is the same, irrespective of whether the Ru-O-*M* interaction is ferromagnetic or antiferromagnetic, the two may be grouped as one for further discussion. It is clear from Table A.9 that the advantage of the ferromagnetic or ferrimagnetic "Type G" structure is that 2 more Ru-O-*M* interactions are satisfied than in the interpenetrating Type I structure. However, this is at the price that 8 fewer Ru-O-O-Ru antiferromagnetic interactions are satisfied, as these are all now coupled ferromagnetically. Thus, the ferromagnetic or ferrimagnetic "Type G" structure will only be adopted by a material if the Ru-O-*M* interaction is at least 4 times stronger than the Ru-O-O-Ru interaction. If the Ru-O-*M* interaction is weaker than this, though it still can be stronger than the Ru-O-O-Ru interaction, the interpenetrating Type I magnetic structure will be preferred. This analysis indicates that the interpenetrating Type I magnetic structure is surprisingly robust from even quite strong Ru-O-*M* interactions.

A.7 Disorder Plot Gradient for Exchanges of B cations

In a mixed ruthenium-copper system, such as $Sr_2TbRu_{0.90}Cu_{0.10}O_6$, the intensity of an ordering peak, when a partial exchange of cations between the 2*c* and 2*d* sites is allowed, can be calculated in three ways. Namely, Tb exchanging only with Ru, Tb exchanging only with Cu, or Tb exchanging with an amount of Ru and an amount of Cu. This section investigates the link the between these, using the example of $Sr_2TbRu_{1-x}Cu_xO_6$ simply to avoid excessive notation of B_1, B_2 and B_3 for the elements. The occupancies of the two *B* sites in the 100 % ordered structure are: -

	Site 2*c*	Site 2*d*
Tb	1	0
Ru	0	$(1 - x)$
Cu	0	x
Total	1	1

where x is the amount of Cu in the sample, typically $x = 0$ to 0.15. The scattering factors of the elements at a given wavelength λ are Tb(λ), Ru(λ) and Cu(λ) and thus the equations remain valid for anomalous scattering analysis.

Each ordering peak has a contribution from the crystal structure which is small and approximately constant. Thus to have a good match between the observed data and the model profile, the ordering contribution to the intensity needs to be $I_{ord} = A^2(\Sigma f_{2c} - \Sigma f_{2d})^2$. Here A is simply a scaling constant between the scattering factors and the observed intensity. Σf_{2c} and Σf_{2d} are the total scattering factors on the 2*c* and 2*d* sites respectively.

Consider the case of Tb exchange with Ru only. The *B* cation distribution then becomes:

	Site 2*c*	Site 2*d*
Tb	$1 - \Delta u$	$0 + \Delta u$
Ru	$0 + \Delta u$	$(1 - x) - \Delta u$
Cu	0	x
Total	1	1

Consider the case of Tb exchange with Cu only. The *B* cation distribution then becomes:

	Site 2*c*	Site 2*d*
Tb	$1 - \Delta v$	$0 + \Delta v$
Ru	0	$(1 - x)$
Cu	$0 + \Delta v$	$x - \Delta v$
Total	1	1

As the two scenarios will be able to describe the diffraction pattern equally well, the intensity $I_{Ru} = I_{Cu}$, so $A^2(\Sigma f_{2c} - \Sigma f_{2d})^2_{Ru} = A^2(\Sigma f_{2c} - \Sigma f_{2d})^2_{Cu}$, where I_{Ru} is the intensity of the ordering peak in the Ru exchanged pattern, and I_{Cu} likewise for Cu. A solution exists when $(\Sigma f_{2c} - \Sigma f_{2d})_{Ru} = (\Sigma f_{2c} - \Sigma f_{2d})_{Cu}$. Following this through explicitly :-

$$[(1 - \Delta u)\mathrm{Tb}(\lambda) + \Delta u\mathrm{Ru}(\lambda) + 0 \times \mathrm{Cu}(\lambda)] - [\Delta u\mathrm{Tb}(\lambda) + (1 - x - \Delta u)\mathrm{Ru}(\lambda) + x\mathrm{Cu}(\lambda)]$$
$$= [(1 - \Delta v)\mathrm{Tb}(\lambda) + 0 \times \mathrm{Ru}(\lambda) + \Delta v\mathrm{Cu}(\lambda)] - [\Delta v\mathrm{Tb}(\lambda) + (1 - x)\mathrm{Ru}(\lambda) + (x - \Delta v)\mathrm{Cu}(\lambda)]$$

Cancelling on both sides to obtain: -

$$-2\Delta u\mathrm{Tb}(\lambda) + 2\Delta u\mathrm{Ru}(\lambda) = -2\Delta v\mathrm{Tb}(\lambda) + 2\Delta v\mathrm{Cu}(\lambda)$$

$$2\Delta u[\mathrm{Ru}(\lambda) - \mathrm{Tb}(\lambda)] = 2\Delta v[\mathrm{Cu}(\lambda) - \mathrm{Tb}(\lambda)]$$

So that,

$$\frac{\Delta u}{\Delta v} = \frac{\mathrm{Cu}(\lambda) - \mathrm{Tb}(\lambda)}{\mathrm{Ru}(\lambda) - \mathrm{Tb}(\lambda)}$$

and we can define *m* as :-

$$m = -\frac{\Delta u(\Delta v = 0)}{\Delta v(\Delta u = 0)} = -\frac{\mathrm{Cu}(\lambda) - \mathrm{Tb}(\lambda)}{\mathrm{Ru}(\lambda) - \mathrm{Tb}(\lambda)}$$

where *m* is the exchange gradient of the disorder plot. The quantity $\Delta u(\Delta v = 0)$ is the ruthenium disorder when there is no copper disorder, and likewise, $\Delta v(\Delta u = 0)$ is the copper disorder when there is no ruthenium disorder. i.e. They define the intercepts on the axes, the negative sign indicating the gradient is negative.

A.7.1 Example Calculation of Disorder Plot Gradient

For $Sr_2TbRu_{0.90}Cu_{0.10}O_6$, the experimental determined value of the exchange gradient is m_{exp}, where $m_{exp} = -1.53 \pm 0.03$ as the two end points in the series were for a Ru exchange of 11.288 ± 0.2 %, and a Cu exchange of 7.395 ± 0.1 %.

The scattering factors, Cu(λ), Ru(λ) and Tb(λ) at $\sin\theta/\lambda = 0$ Å^{-1} and $\sin\theta/\lambda = 0.20$ Å^{-1} (location of the most intense ordering peak as $\sin(11.6°/2)/0.5006$ Å^{-1} = 0.202 Å^{-1}) were taken from the *International Tables of Crystallography*, Volume C.

Element	Scattering Factor $(\sin\theta)/\lambda = 0$	Scattering Factor $(\sin\theta)/\lambda = 0.20$
Cu	29	23.540
Ru	44	35.088
Tb	65	53.985

Table A.10 The scattering factors of the *B* cations at different points in the diffraction pattern.

Although not very close to an edge in this case, for consistency the small anomalous scattering factor, $\Delta f'$, was applied and scaled by the same factor that the as the scattering factor above. The program fprime in the GSAS suite was used to calculate anomalous scattering factors, as this output was most appropriate for use in GSAS refinement. The anomalous scattering factor was scaled and the results noted in Table A.11.

Element	$\Delta f'$ $(\sin\theta)/\lambda = 0$	$\Delta f'$ $(\sin\theta)/\lambda = 0.20$
Cu	0.241	0.196
Ru	-1.326	-1.056
Tb	-0.907	-0.753

Table A.11 The anomalous scattering factor of the *B* cations as determined by GSAS for the wavelength λ = 0.5006 Å.

Thus the predicted exchange gradient representing Ru-Cu disorder is given by

$$m_{pred} = -\frac{(23.540 + 0.196) - (53.985 - 0.753)}{(35.088 - 1.056) - (53.985 - 0.753)}$$

$$m_{pred} = -1.54 \pm 0.08$$

as the combined error from all the sources is approximately 5 %. Each scattering factor can vary by ~ 0.5 to 1.5 as the incremental steps in the tables are 0.01 Å^{-1}. Also the calculation does not average the contributions from all of the pattern, but focuses on the most important peak to give an indication.

B. Appendix – Crystal and Magnetic Structures

All refinements used the GSAS Rietveld refinement suite.

B.1 Neutron Diffraction Refinements of $Sr_2YRu_{1-x}Cu_xO_6$

B.1.1 D2B Refinements

B.1.1.1 $Sr_2YRu_{0.95}Cu_{0.05}O_6$

$Sr_2YRu_{0.95}Cu_{0.05}O_6$		$P2_1/n$			2 K		
a / Å		b / Å	c / Å	β / °	Volume / Å^3		
5.75943(2)		5.77851(2)	8.14790(5)	90.327(1)	271.165(3)		
Atom	Site	x	y	z	Occ	B_{iso}/Å^2	μ/μ_B
Sr	4*e*	0.0070(5)	0.0308(2)	0.7491(3)	1.000	0.10(2)	
Y	2*c*	0	½	0	1.000	0.18(4)	
Ru	2*d*	½	0	0	0.950	0.04(4)	2.21(10)
Cu	2*d*	½	0	0	0.050	0.04(4)	
O1	4*e*	0.3020(4)	0.2700(4)	0.9625(3)	1.000	0.25(4)	
O2	4*e*	0.2674(4)	0.2983(4)	0.5362(4)	1.000	0.23(4)	
O3	4*e*	0.9308(4)	0.4848(4)	0.7340(3)	1.000	0.26(3)	

R_p = 4.76 %, R_{wp} = 6.63 %, R_{exp} = 6.89 %, R_{F^2} = 4.37 %

$Sr_2YRu_{0.95}Cu_{0.05}O_6$		$P2_1/n$			21 K		
a / Å		b / Å	c / Å	β / °	Volume / Å^3		
5.75944(2)		5.77853(2)	8.14794(5)	90.327(1)	271.168(3)		
Atom	Site	x	y	z	Occ	B_{iso}/Å^2	μ/μ_B
Sr	4*e*	0.0070(5)	0.0309(2)	0.7492(4)	1.000	0.09(2)	
Y	2*c*	0	½	0	1.000	0.23(4)	
Ru	2*d*	½	0	0	0.950	0.02(4)	1.97(10)
Cu	2*d*	½	0	0	0.050	0.02(4)	
O1	4*e*	0.3017(4)	0.2702(4)	0.9626(3)	1.000	0.23(4)	
O2	4*e*	0.2670(4)	0.2981(4)	0.5365(4)	1.000	0.24(4)	
O3	4*e*	0.9300(4)	0.4839(4)	0.7342(3)	1.000	0.24(3)	

R_p = 4.67 %, R_{wp} = 6.51 %, R_{exp} = 9.76 %, R_{F^2} = 4.32 %

$Sr_2YRu_{0.95}Cu_{0.05}O_6$		$P2_1/n$			26 K		
a / Å		b / Å	c / Å	β / °	Volume / Å^3		
5.75945(2)		5.77853(2)	8.14795(5)	90.327(1)	271.168(3)		
Atom	Site	x	y	z	Occ	B_{iso}/Å^2	μ/μ_B
Sr	4*e*	0.0072(4)	0.0310(2)	0.7494(4)	1.000	0.10(2)	
Y	2*c*	0	½	0	1.000	0.24(4)	
Ru	2*d*	½	0	0	0.950	0.05(4)	1.51(10)
Cu	2*d*	½	0	0	0.050	0.05(4)	
O1	4*e*	0.3018(4)	0.2702(4)	0.9627(3)	1.000	0.27(4)	
O2	4*e*	0.2670(4)	0.2983(4)	0.5367(4)	1.000	0.27(4)	
O3	4*e*	0.9307(4)	0.4845(4)	0.7344(3)	1.000	0.26(3)	

R_p = 4.67 %, R_{wp} = 6.48 %, R_{exp} = 9.78 %, R_{F^2} = 4.14 %

$Sr_2YRu_{0.95}Cu_{0.05}O_6$		$P2_1/n$			28 K		
a / Å		b / Å	c / Å	β / °	Volume / Å^3		
5.75948(2)		5.77856(2)	8.14804(5)	90.327(1)	271.175(3)		
Atom	Site	x	y	z	Occ	B_{iso}/Å^2	μ/μ_B
Sr	4*e*	0.0074(4)	0.0310(2)	0.7494(4)	1.000	0.08(2)	
Y	2*c*	0	½	0	1.000	0.22(4)	
Ru	2*d*	½	0	0	0.950	0.07(4)	1.27(10)
Cu	2*d*	½	0	0	0.050	0.07(4)	
O1	4*e*	0.3018(4)	0.2702(4)	0.9629(3)	1.000	0.25(4)	
O2	4*e*	0.2675(4)	0.2984(4)	0.5365(4)	1.000	0.26(4)	
O3	4*e*	0.9305(4)	0.4847(4)	0.7342(3)	1.000	0.22(3)	

R_p = 4.69 %, R_{wp} = 6.47 %, R_{exp} = 9.77 %, R_{F^2} = 4.07 %

$Sr_2YRu_{0.95}Cu_{0.05}O_6$		$P2_1/n$			42 K		
a / Å		b / Å	c / Å	β / °	Volume / Å^3		
5.75955(2)		5.77864(2)	8.14825(5)	90.326(1)	271.189(3)		
Atom	Site	x	y	z	Occ	B_{iso}/Å^2	μ/μ_B
Sr	4*e*	0.0074(5)	0.0308(2)	0.7493(4)	1.000	0.09(2)	
Y	2*c*	0	½	0	1.000	0.18(4)	
Ru	2*d*	½	0	0	0.950	0.06(4)	
Cu	2*d*	½	0	0	0.050	0.06(4)	
O1	4*e*	0.3018(4)	0.2700(4)	0.9626(3)	1.000	0.20(4)	
O2	4*e*	0.2672(4)	0.2984(4)	0.5359(4)	1.000	0.26(5)	
O3	4*e*	0.9305(4)	0.4846(4)	0.7342(3)	1.000	0.24(3)	

R_p = 4.82 %, R_{wp} = 6.64 %, R_{exp} = 9.76 %, R_{F^2} = 4.20 %

B.1.1.2 $Sr_2YRu_{0.90}Cu_{0.10}O_6$

$Sr_2YRu_{0.90}Cu_{0.10}O_6$		$P2_1/n$			2 K		
a / Å		b / Å	c / Å	β / °	Volume / Å^3		
5.75954(2)		5.77863(2)	8.14824(5)	90.326(1)	271.188(4)		
Atom	Site	x	y	z	Occ	B_{iso}/Å^2	μ/μ_B
Sr	4*e*	0.0081(5)	0.0307(2)	0.7491(4)	1.000	0.08(2)	
Y	2*c*	0	½	0	1.000	0.22(4)	
Ru	2*d*	½	0	0	0.900	0.07(4)	2.37(10)
Cu	2*d*	½	0	0	0.100	0.07(4)	
O1	4*e*	0.3025(4)	0.2706(4)	0.9619(3)	1.000	0.22(4)	
O2	4*e*	0.2670(4)	0.2982(4)	0.5358(4)	1.000	0.33(5)	
O3	4*e*	0.9302(4)	0.4842(4)	0.7339(3)	1.000	0.23(3)	

R_p = 4.64 %, R_{wp} = 6.37 %, R_{exp} = 9.94 %, R_{F^2} = 4.88 %

$Sr_2YRu_{0.90}Cu_{0.10}O_6$		$P2_1/n$			21 K		
a / Å		b / Å	c / Å	β / °	Volume / Å^3		
5.75954(2)		5.77862(2)	8.14822(5)	90.326(1)	271.186(4)		
Atom	Site	x	y	z	Occ	B_{iso}/Å^2	μ/μ_B
Sr	4*e*	0.0080(4)	0.0307(2)	0.7495(4)	1.000	0.10(2)	
Y	2*c*	0	½	0	1.000	0.22(4)	
Ru	2*d*	½	0	0	0.900	0.04(4)	2.13(10)
Cu	2*d*	½	0	0	0.100	0.04(4)	
O1	4*e*	0.3023(4)	0.2699(4)	0.9621(3)	1.000	0.19(4)	
O2	4*e*	0.2669(4)	0.2980(4)	0.5368(4)	1.000	0.29(4)	
O3	4*e*	0.9305(4)	0.4842(4)	0.7339(3)	1.000	0.26(3)	

R_p = 4.58 %, R_{wp} = 6.36 %, R_{exp} = 9.94 %, R_{F^2} = 4.79 %

$Sr_2YRu_{0.90}Cu_{0.10}O_6$		$P2_1/n$			26 K		
a / Å		b / Å	c / Å	β / °	Volume / Å^3		
5.75953(2)		5.77862(2)	8.14820(5)	90.326(1)	271.185(4)		
Atom	Site	x	y	z	Occ	B_{iso}/Å^2	μ/μ_B
Sr	4*e*	0.0070(5)	0.0311(2)	0.7490(4)	1.000	0.10(2)	
Y	2*c*	0	½	0	1.000	0.25(4)	
Ru	2*d*	½	0	0	0.900	0.07(4)	1.61(10)
Cu	2*d*	½	0	0	0.100	0.07(4)	
O1	4*e*	0.3023(5)	0.2700(5)	0.9623(3)	1.000	0.31(4)	
O2	4*e*	0.2671(4)	0.2982(5)	0.5363(4)	1.000	0.33(5)	
O3	4*e*	0.9300(4)	0.4846(4)	0.7338(3)	1.000	0.22(3)	

R_p = 4.89 %, R_{wp} = 6.56 %, R_{exp} = 9.93 %, R_{F^2} = 5.44 %

$Sr_2YRu_{0.90}Cu_{0.10}O_6$		$P2_1/n$			28 K		
a / Å		b / Å	c / Å	β / °	Volume / Å^3		
5.75956(2)		5.77864(2)	8.14828(5)	90.326(1)	271.190(4)		
Atom	Site	x	y	z	Occ	B_{iso}/Å^2	μ/μ_B
Sr	4*e*	0.0074(5)	0.0309(2)	0.7492(4)	1.000	0.10(2)	
Y	2*c*	0	½	0	1.000	0.21(4)	
Ru	2*d*	½	0	0	0.900	0.05(4)	1.40(10)
Cu	2*d*	½	0	0	0.100	0.05(4)	
O1	4*e*	0.3020(4)	0.2700(4)	0.9623(3)	1.000	0.23(4)	
O2	4*e*	0.2669(4)	0.2982(5)	0.5363(4)	1.000	0.30(5)	
O3	4*e*	0.9299(4)	0.4845(4)	0.7336(3)	1.000	0.23(3)	

R_p = 4.80 %, R_{wp} = 6.47 %, R_{exp} = 9.92 %, R_{F^2} = 4.93 %

$Sr_2YRu_{0.90}Cu_{0.10}O_6$		$P2_1/n$			42 K		
a / Å		b / Å	c / Å	β / °	Volume / Å^3		
5.75962(2)		5.77870(2)	8.14845(5)	90.325(1)	271.202(4)		
Atom	Site	x	y	z	Occ	B_{iso}/Å^2	μ/μ_B
Sr	4*e*	0.0075(5)	0.0311(2)	0.7491(4)	1.000	0.09(2)	
Y	2*c*	0	½	0	1.000	0.26(4)	
Ru	2*d*	½	0	0	0.900	0.04(4)	
Cu	2*d*	½	0	0	0.100	0.04(4)	
O1	4*e*	0.3015(4)	0.2701(4)	0.9623(3)	1.000	0.26(4)	
O2	4*e*	0.2669(4)	0.2983(5)	0.5363(4)	1.000	0.35(5)	
O3	4*e*	0.9301(4)	0.4840(4)	0.7341(3)	1.000	0.22(3)	

R_p = 4.79 %, R_{wp} = 6.49 %, R_{exp} = 9.94 %, R_{F^2} = 4.77 %

B.1.1.3 $Sr_2YRu_{0.85}Cu_{0.15}O_6$

$Sr_2YRu_{0.85}Cu_{0.15}O_6$		$P2_1/n$			2 K		
a / Å		b / Å	c / Å	β / °	Volume / Å^3		
5.75961(2)		5.77870(2)	8.14843(6)	90.325(1)	271.200(4)		
Atom	Site	x	y	z	Occ	B_{iso}/Å^2	μ/μ_B
Sr	4*e*	0.0077(6)	0.0302(3)	0.7493(5)	1.000	0.24(3)	
Y	2*c*	0	½	0	1.000	0.43(5)	
Ru	2*d*	½	0	0	0.850	0.05(5)	2.54(10)
Cu	2*d*	½	0	0	0.150	0.05(5)	
O1	4*e*	0.3020(5)	0.2709(5)	0.9620(4)	1.000	0.34(5)	
O2	4*e*	0.2662(5)	0.2983(5)	0.5370(4)	1.000	0.41(5)	
O3	4*e*	0.9309(5)	0.4843(5)	0.7345(3)	1.000	0.36(4)	

R_p = 5.06 %, R_{wp} = 7.04 %, R_{exp} = 9.79 %, R_{F^2} = 6.39 %

$Sr_2YRu_{0.85}Cu_{0.15}O_6$		$P2_1/n$			21 K		
a / Å		b / Å	c / Å	β / °	Volume / Å^3		
5.75964(2)		5.77873(2)	8.14851(6)	90.325(1)	271.205(4)		
Atom	Site	x	y	z	Occ	B_{iso}/Å^2	μ/μ_B
Sr	4*e*	0.0077(6)	0.0302(3)	0.7493(5)	1.000	0.22(3)	
Y	2*c*	0	½	0	1.000	0.42(5)	
Ru	2*d*	½	0	0	0.850	0.07(5)	2.32(10)
Cu	2*d*	½	0	0	0.150	0.07(5)	
O1	4*e*	0.3015(5)	0.2708(5)	0.9624(4)	1.000	0.34(5)	
O2	4*e*	0.2669(5)	0.2983(5)	0.5364(4)	1.000	0.41(6)	
O3	4*e*	0.9308(5)	0.4843(5)	0.7342(3)	1.000	0.36(4)	

R_p = 5.10 %, R_{wp} = 7.06 %, R_{exp} = 9.80 %, R_{F^2} = 6.18 %

$Sr_2YRu_{0.85}Cu_{0.15}O_6$		$P2_1/n$			26 K		
a / Å		b / Å	c / Å	β / °	Volume / Å^3		
5.75967(2)		5.77876(2)	8.14859(6)	90.324(1)	271.211(4)		
Atom	Site	x	y	z	Occ	B_{iso}/Å^2	μ/μ_B
Sr	4*e*	0.0074(6)	0.0308(3)	0.7493(4)	1.000	0.25(2)	
Y	2*c*	0	½	0	1.000	0.46(5)	
Ru	2*d*	½	0	0	0.850	0.06(5)	1.79(11)
Cu	2*d*	½	0	0	0.150	0.06(5)	
O1	4*e*	0.3014(5)	0.2710(5)	0.9621(4)	1.000	0.38(5)	
O2	4*e*	0.2666(5)	0.2985(5)	0.5364(4)	1.000	0.47(6)	
O3	4*e*	0.9304(5)	0.4847(4)	0.7346(3)	1.000	0.35(4)	

R_p = 5.07 %, R_{wp} = 6.95 %, R_{exp} = 9.79 %, R_{F^2} = 5.89 %

$Sr_2YRu_{0.85}Cu_{0.15}O_6$		$P2_1/n$			28 K		
a / Å		b / Å	c / Å	β / °	Volume / Å^3		
5.75964(2)		5.77873(2)	8.14851(6)	90.325(1)	271.206(4)		
Atom	Site	x	y	z	Occ	B_{iso}/Å^2	μ/μ_B
Sr	4*e*	0.0070(6)	0.0303(3)	0.7493(5)	1.000	0.25(2)	
Y	2*c*	0	½	0	1.000	0.42(5)	
Ru	2*d*	½	0	0	0.850	0.10(5)	1.62(11)
Cu	2*d*	½	0	0	0.150	0.10(5)	
O1	4*e*	0.3017(5)	0.2706(5)	0.9622(4)	1.000	0.36(5)	
O2	4*e*	0.2667(5)	0.2985(5)	0.5367(4)	1.000	0.42(6)	
O3	4*e*	0.9311(5)	0.4840(4)	0.7344(3)	1.000	0.35(4)	

R_p = 5.10 %, R_{wp} = 7.02 %, R_{exp} = 9.79 %, R_{F^2} = 6.18 %

$Sr_2YRu_{0.85}Cu_{0.15}O_6$		$P2_1/n$			42 K		
a / Å		b / Å	c / Å	β / °	Volume / Å^3		
5.75972(2)		5.77881(2)	8.14873(6)	90.323(1)	271.220(4)		
Atom	Site	x	y	z	Occ	B_{iso}/Å^2	μ/μ_B
Sr	4*e*	0.0079(6)	0.0304(3)	0.7494(4)	1.000	0.24(2)	
Y	2*c*	0	½	0	1.000	0.41(5)	
Ru	2*d*	½	0	0	0.850	0.10(5)	
Cu	2*d*	½	0	0	0.150	0.10(5)	
O1	4*e*	0.3013(5)	0.2705(5)	0.9620(4)	1.000	0.33(5)	
O2	4*e*	0.2669(5)	0.2985(5)	0.5367(4)	1.000	0.49(6)	
O3	4*e*	0.9306(5)	0.4845(4)	0.7346(3)	1.000	0.37(4)	

R_p = 5.02 %, R_{wp} = 6.89 %, R_{exp} = 9.80 %, R_{F^2} = 5.75 %

B.1.2 OSIRIS refinements

B.1.2.1 $Sr_2YRu_{0.90}Cu_{0.10}O_6$

$Sr_2YRu_{0.90}Cu_{0.10}O_6$		$P2_1/n$			2 K		
a / Å		b / Å	c / Å	β / °	Volume / Å^3		
5.75954(16)		5.77863(16)	8.14824(16)	90.326(2)	271.188(4)		
5.75954(16)		**5.77863(16)**	**8.14824(16)**	**90.326(2)**	**271.188(4)**		
Atom	Site	x	y	z	Occ	B_{iso}/Å^2	μ/μ_B
Sr	4*e*	0.0102(7)	0.0281(4)	0.7436(6)	1.000	0.08	
		0.0102(7)	**0.0279(4)**	**0.7437(5)**		**0.08**	
Y	2*c*	0	½	0	1.000	0.22	
						0.22	
Ru	2*d*	½	0	0	0.900	0.07	2.12(10)
						0.07	**2.34(10)**
Cu	2*d*	½	0	0	0.100	0.07	
						0.07	
O1	4*e*	0.3111(8)	0.2717(9)	0.9573(4)	1.000	0.22	
		0.3111(7)	**0.2719(9)**	**0.9575(4)**		**0.22**	
O2	4*e*	0.2676(7)	0.2927(7)	0.5325(6)	1.000	0.33	
		0.2673(7)	**0.2923(7)**	**0.5329(6)**		**0.33**	
O3	4*e*	0.9304(6)	0.4904(9)	0.7324(4)	1.000	0.23	
		0.9305(6)	**0.4902(8)**	**0.7324(4)**		**0.23**	

ZERO = -2.80(1.75)	DIFC = 17450.97(1.62)	DIFA = -10.24(0.37)	
ZERO = -1.59(1.67)	**DIFC = 17449.79(1.55)**	**DIFA = -9.94(0.36)**	**Crystal**
ZERO = -1.59(1.67)	**DIFC = 17449.79(1.55)**	**DIFA = -4.44(0.44)**	**Magnetic**

R_p = 6.76 %, R_{wp} = 6.58 %, R_{exp} = 2.13 %, R_{F^2} = 14.57 %
R_p = 5.93 %, R_{wp} = 6.20 %, R_{exp} = 2.13 %, R_{F^2} = 14.55 %

$Sr_2YRu_{0.90}Cu_{0.10}O_6$		$P2_1/n$			60 K	
a / Å		b / Å	c / Å	β / °	Volume / Å^3	
5.76056(16)		5.77898(16)	8.14772(16)	90.307(2)	271.235(4)	
Atom	Site	x	y	z	Occ	B_{iso}/Å^2
Sr	4*e*	0.0107(7)	0.0286(7)	0.7441(6)	1.000	0.08
Y	2*c*	0	½	0	1.000	0.24
Ru	2*d*	½	0	0	0.900	0.08
Cu	2*d*	½	0	0	0.100	0.08
O1	4*e*	0.3104(7)	0.2714(9)	0.9571(4)	1.000	0.25
O2	4*e*	0.2672(7)	0.2923(7)	0.5318(6)	1.000	0.36
O3	4*e*	0.9302(5)	0.4894(8)	0.7316(4)	1.000	0.25

R_p = 5.69 %, R_{wp} = 5.75 %, R_{exp} = 1.99 %, R_{F^2} = 12.53 %

B.1.2.2 $Sr_2YRu_{0.85}Cu_{0.15}O_6$

$Sr_2YRu_{0.85}Cu_{0.10}O_6$		$P2_1/n$			35 K	
a / Å		b / Å	c / Å	β / °	Volume / Å^3	
5.75968(16)		5.77878(16)	8.14865(16)	90.324(2)	271.203(4)	
Atom	Site	x	y	z	Occ	B_{iso}/Å^2
Sr	4*e*	0.0102(8)	0.0280(5)	0.7453(6)	1.000	0.08
Y	2*c*	0	½	0	1.000	0.22
Ru	2*d*	½	0	0	0.850	0.07
Cu	2*d*	½	0	0	0.150	0.07
O1	4*e*	0.3100(9)	0.2709(10)	0.9594(5)	1.000	0.25
O2	4*e*	0.2663(8)	0.2963(8)	0.5321(7)	1.000	0.26
O3	4*e*	0.9264(7)	0.4887(9)	0.7341(4)	1.000	0.22

R_p = 14.45 %, R_{wp} = 10.06 %, R_{exp} = 1.18 %, R_{F^2} = 15.00 %

B.1.3 D1B Refinements

B.1.3.1 $Sr_2YRu_{0.85}Cu_{0.15}O_6$

The crystal structure (atomic and thermal parameters) used for the refinements was the D2B 2 K structure of $Sr_2YRu_{0.85}Cu_{0.15}O_6$.

Temperature	Lattice Parameters				
/ K	a / Å	b / Å	c / Å	β / °	Volume / Å^3
2	5.75930(11)	5.77839(11)	8.14756(31)	90.329(2)	271.142(21)
3	5.75875(11)	5.77782(11)	8.14597(32)	90.337(2)	271.036(21)
6	5.75900(11)	5.77808(12)	8.14669(32)	90.333(2)	271.084(22)
8	5.75946(12)	5.77855(12)	8.14800(33)	90.327(2)	271.172(22)
11	5.75942(12)	5.77851(12)	8.14789(33)	90.328(2)	271.165(22)
14	5.75944(11)	5.77853(11)	8.14795(32)	90.327(2)	271.168(20)
17	5.75941(11)	5.77849(11)	8.14786(31)	90.328(2)	271.162(21)
20	5.75943(11)	5.77852(12)	8.14792(32)	90.327(2)	271.167(21)
22	5.75942(11)	5.77851(11)	8.14790(32)	90.327(2)	271.165(21)
24	5.75945(11)	5.77854(12)	8.14797(32)	90.327(2)	271.170(22)
27	5.75944(11)	5.77853(11)	8.14794(32)	90.327(2)	271.168(21)
29	5.75941(11)	5.77850(11)	8.14786(32)	90.328(2)	271.162(21)
31	5.75944(11)	5.77853(12)	8.14794(32)	90.327(2)	271.168(22)
33	5.75939(12)	5.77848(12)	8.14780(33)	90.328(2)	271.158(22)
35	5.75942(12)	5.77850(12)	8.14787(33)	90.328(2)	271.164(22)
37	5.75942(12)	5.77850(12)	8.14787(35)	90.328(2)	271.163(23)
39	5.75950(11)	5.77858(11)	8.14810(32)	90.326(2)	271.178(21)
40	5.75943(12)	5.77851(12)	8.14789(34)	90.328(2)	271.165(23)
42	5.75948(12)	5.77856(12)	8.14803(33)	90.327(2)	271.174(22)
44	5.75952(11)	5.77861(12)	8.14816(32)	90.326(2)	271.183(22)
44	5.75945(12)	5.77854(12)	8.14797(33)	90.327(2)	271.170(22)
47	5.75952(12)	5.77861(12)	8.14816(33)	90.326(2)	271.183(22)
49	5.75951(12)	5.77860(12)	8.14812(34)	90.326(2)	271.181(22)
52	5.75919(13)	5.77827(13)	8.14722(36)	90.331(2)	271.120(24)
50	5.75961(13)	5.77870(13)	8.14840(36)	90.325(2)	271.199(24)
51	5.75960(11)	5.77869(11)	8.14838(32)	90.325(2)	271.198(21)
59	5.75944(11)	5.77853(11)	8.14794(32)	90.327(2)	271.168(21)
67	5.75947(11)	5.77856(11)	8.14803(32)	90.327(2)	271.174(21)
75	5.75957(11)	5.77866(11)	8.14830(31)	90.325(2)	271.192(21)
83	5.75970(11)	5.77879(11)	8.14868(32)	90.324(2)	271.217(21)
91	5.75984(11)	5.77894(11)	8.14908(31)	90.322(2)	271.244(21)
99	5.75998(11)	5.77908(11)	8.14947(31)	90.320(2)	271.270(21)
107	5.76013(11)	5.77923(11)	8.14989(32)	90.317(2)	271.298(21)
115	5.76033(11)	5.77943(11)	8.15046(32)	90.315(2)	271.336(21)
123	5.76048(11)	5.77958(12)	8.15090(32)	90.313(2)	271.365(22)
131	5.76067(12)	5.77978(12)	8.15144(33)	90.310(2)	271.402(22)
139	5.76087(12)	5.77998(12)	8.15201(33)	90.307(2)	271.440(22)
147	5.76105(12)	5.78017(12)	8.15253(33)	90.304(2)	271.474(22)
150	5.76110(11)	5.78021(12)	8.15265(32)	90.304(2)	271.483(22)

Temperature / K	Magnetic Moment in a-b plane / μ_B	R_p / %	R_{wp} / %	R_{exp} / %	R_{F^2} / %
2	2.43(10)	3.23	4.52	0.95	10.59
3	2.45(10)	3.47	4.71	1.27	10.20
6	2.40(10)	3.54	4.73	1.27	10.70
8	2.43(10)	3.52	4.79	1.27	10.55
11	2.44(10)	3.49	4.79	1.27	10.66
14	2.41(10)	3.42	4.66	1.27	26.83
17	2.40(10)	3.35	4.55	1.27	9.01
20	2.35(10)	3.40	4.68	1.27	10.78
22	2.35(10)	3.39	4.67	1.27	18.45
24	2.26(11)	3.48	4.74	1.27	10.46
27	2.09(11)	3.43	4.63	1.27	10.55
29	1.89(11)	3.43	4.64	1.27	10.44
31	1.70(11)	3.55	4.72	1.27	21.98
33	1.31(13)	3.64	4.82	1.27	13.13
35	0	3.66	4.83	1.27	7.98
37	0	3.91	5.06	1.27	9.87
39	0	3.52	4.62	1.28	9.88
40	0	3.86	4.95	1.27	14.23
42	0	3.70	4.80	1.27	9.63
44	0	3.57	4.72	1.28	9.93
44	0	3.68	4.86	1.27	17.75
47	0	3.69	4.84	1.27	14.49
49	0	3.75	4.91	1.27	8.33
52	0	3.88	5.40	0.96	10.92
50	0	3.18	3.18	0.62	11.54
51	0	2.70	3.85	0.85	10.27
59	0	2.86	3.95	0.86	10.52
67	0	2.74	3.91	0.86	10.33
75	0	2.73	3.88	0.86	10.44
83	0	2.76	3.92	0.86	10.49
91	0	2.69	3.88	0.86	10.37
99	0	2.73	3.89	0.86	10.34
107	0	2.73	3.92	0.86	10.44
115	0	2.73	3.92	0.86	8.18
123	0	2.84	4.03	0.90	13.92
131	0	2.94	4.10	0.86	14.27
139	0	3.00	4.13	0.87	10.91
147	0	2.91	4.10	0.86	11.86
150	0	2.85	4.03	0.86	12.42

B.2 Neutron Diffraction Refinements of $Ba_2YRu_{1-x}Cu_xO_6$

B.2.1 D2B Refinements

B.2.1.1 $Ba_2YRu_{0.90}Cu_{0.10}O_6$

$Ba_2YRu_{0.90}Cu_{0.10}O_6$		*Fm3m*			200 K and **2 K**		
a / Å		Volume / Å^3					
8.32365(6)		576.689(13)					
8.31696(4)		**575.298(8)**					
Atom	Site	*x*	*y*	*z*	Occ	B_{iso}/Å^2	μ/μ_B
Ba	8*c*	¼	¼	¼	1.000	0.18(10)	
						0.14(6)	
Y	4*c*	0	0	0	1.000	0.04(15)	
						0.13(5)	
Ru	4*b*	½	0	0	0.900	0.13(16)	
						0.13(5)	**2.43(19)**
Cu	4*b*	½	0	0	0.100	0.13(16)	
						0.13(5)	
O	24*e*	0.2654(4)	0	0	1.000	0.11(7)	
		0.2653(3)				**0.17(4)**	

R_p = 16.04 %, R_{wp} = 20.99 %, R_{exp} = 17.61 %, R_{F^2} = 7.98 %
R_p = 11.57 %, R_{wp} = 14.60 %, R_{exp} = 11.18 %, R_{F^2} = 32.21 %

B.2.2 D1B Refinements

B.2.2.1 $Ba_2YRu_{0.90}Cu_{0.10}O_6$

The crystal structure (atomic and thermal parameters) used for the refinements was the D2B 2 K structure of $Ba_2YRu_{0.90}Cu_{0.10}O_6$.

Temperature / K	Lattice Parameter a / Å	Magnetic Moment / μ_B	R_p / %	R_{wp} / %	R_{exp} / %	R_{F^2} / %
2	8.31750(2)	2.41(10)	2.20	3.34	0.90	5.05
2	8.31721(2)	2.43(11)	2.48	3.54	1.11	5.20
3	8.31677(2)	2.42(11)	2.50	3.60	1.12	5.72
6	8.31770(2)	2.43(11)	2.51	3.55	1.12	5.43
10	8.31757(2)	2.41(11)	2.45	3.57	1.12	4.85
13	8.31762(2)	2.44(11)	2.38	3.46	1.12	4.99
16	8.31758(2)	2.38(11)	2.42	3.50	1.12	5.26
19	8.31760(2)	2.44(11)	2.41	3.47	1.11	5.04
22	8.31775(2)	2.35(11)	2.40	3.51	1.12	5.05
25	8.31765(2)	2.39(11)	2.47	3.59	1.12	5.23
28	8.31784(2)	2.35(11)	2.42	3.53	1.12	4.81
30	8.31765(2)	2.30(11)	2.48	3.51	1.12	4.85
32	8.31771(2)	2.26(11)	2.37	3.48	1.11	4.68
35	8.31782(2)	2.20(11)	2.37	3.43	1.11	4.83
37	8.31778(2)	2.04(11)	2.40	3.50	1.12	3.89
39	8.31711(2)	1.28(13)	2.51	3.48	1.12	3.17
41	8.31711(2)	0	2.64	3.65	1.12	1.48
43	8.31724(2)	0	2.57	3.59	1.12	1.43
44	8.31732(2)	0	2.60	3.60	1.12	1.45
46	8.31719(2)	0	2.60	3.52	1.12	1.34
49	8.31736(2)	0	2.44	3.54	1.11	1.39
50	8.31730(2)	0	2.17	3.27	0.89	1.48
50	8.31727(2)	0	2.40	3.47	1.11	1.42
54	8.31745(2)	0	2.34	3.45	1.11	1.55
61	8.31755(2)	0	2.23	3.36	1.11	1.64
69	8.31782(2)	0	2.30	3.29	1.11	1.37
76	8.31815(2)	0	2.23	3.26	1.11	1.36
84	8.31845(2)	0	2.41	3.43	1.11	1.22
92	8.31868(2)	0	2.31	3.38	1.11	1.55
100	8.31879(2)	0	2.08	3.20	0.89	1.44

B.3 Neutron Diffraction Refinements of $Sr_2HoRu_{1-x}Cu_xO_6$

B.3.1 HRPD Refinements

B.3.1.1 Sr_2HoRuO_6

Sr_2HoRuO_6		$P2_1/n$			2 K		
a / Å		b / Å	c / Å	β / °	Volume / Å^3		
5.75773(4)		5.77679(4)	8.14285(11)	90.344(1)	270.836(8)		
Atom	Site	x	y	z	Occ	B_{iso}/Å^2	μ/μ_B
Sr	4*e*	-0.0057(17)	0.0340(7)	0.7550(11)	1.000	0.27	
Ho	2*c*	0	½	0	1.000	0.19	8.16(5)
Ru	2*d*	½	0	0	1.000	0.43	1.66(10)
O1	4*e*	0.2888(14)	0.2842(15)	0.9624(9)	1.000	0.34	
O2	4*e*	0.2624(13)	0.3017(15)	0.5395(11)	1.000	0.47	
O3	4*e*	0.9324(14)	0.4731(11)	0.7271(8)	1.000	0.24	

R_p = 9.18 %, R_{wp} = 10.91 %, R_{exp} = 5.99 %, R_{F^2} = 6.36 %

Sr_2HoRuO_6		$P2_1/n$			20 K		
a / Å		b / Å	c / Å	β / °	Volume / Å^3		
5.75742(4)		5.77647(4)	8.14197(12)	90.348(1)	270.778(8)		
Atom	Site	x	y	z	Occ	B_{iso}/Å^2	μ/μ_B
Sr	4*e*	0.0044(14)	0.0311(7)	0.7537(11)	1.000	0.29	
Ho	2*c*	0	½	0	1.000	0.20	4.03(7)
Ru	2*d*	½	0	0	1.000	0.41	1.50(10)
O1	4*e*	0.2980(15)	0.2789(14)	0.9624(9)	1.000	0.38	
O2	4*e*	0.2646(12)	0.2968(14)	0.5400(11)	1.000	0.45	
O3	4*e*	0.9317(14)	0.4792(11)	0.7304(8)	1.000	0.25	

R_p = 6.11 %, R_{wp} = 7.24 %, R_{exp} = 5.10 %, R_{F^2} = 7.49 %

Sr_2HoRuO_6		$P2_1/n$			50 K		
a / Å		b / Å	c / Å	β / °	Volume / Å^3		
5.75735(5)		5.77640(5)	8.14202(14)	90.356(1)	270.772(9)		
Atom	Site	x	y	z	Occ	B_{iso}/Å^2	μ/μ_B
Sr	4*e*	0.0075(16)	0.0306(7)	0.7552(11)	1.000	0.30	
Ho	2*c*	0	½	0	1.000	0.20	
Ru	2*d*	½	0	0	1.000	0.38	
O1	4*e*	0.3015(15)	0.2776(14)	0.9605(9)	1.000	0.35	
O2	4*e*	0.2667(12)	0.2935(14)	0.5403(11)	1.000	0.42	
O3	4*e*	0.9329(14)	0.4809(11)	0.7304(8)	1.000	0.27	

R_p = 10.59 %, R_{wp} = 12.70 %, R_{exp} = 7.84 %, R_{F^2} = 7.75 %

B.3.1.2 $Sr_2HoRu_{0.95}Cu_{0.05}O_6$

$Sr_2HoRu_{0.95}Cu_{0.05}O_6$		$P2_1/n$			2 K		
a / Å		b / Å	c / Å	β / °	Volume / Å^3		
5.75806(3)		5.77712(3)	8.14401(8)	90.346(1)	270.906(5)		
Atom	Site	x	y	z	Occ	B_{iso}/Å^2	μ/μ_B
Sr	4*e*	-0.0095(15)	0.0359(6)	0.7520(10)	1.000	0.27(4)	
Ho	2*c*	0	½	0	1.000	0.19(4)	9.16(4)
Ru	2*d*	½	0	0	0.950	0.43(9)	1.86(10)
Cu	2*d*	½	0	0	0.050	0.43(9)	
O1	4*e*	0.2908(12)	0.2800(12)	0.9630(8)	1.000	0.34(14)	
O2	4*e*	0.2648(10)	0.3027(12)	0.5379(9)	1.000	0.47(17)	
O3	4*e*	0.9282(11)	0.4740(10)	0.7279(6)	1.000	0.24(10)	

R_p = 7.00 %, R_{wp} = 7.48 %, R_{exp} = 2.86 %, R_{F^2} = 6.04 %

$Sr_2HoRu_{0.95}Cu_{0.05}O_6$		$P2_1/n$			20 K		
a / Å		b / Å	c / Å	β / °	Volume / Å^3		
5.75767(3)		5.77672(3)	8.14291(8)	90.352(1)	270.832(5)		
Atom	Site	x	y	z	Occ	B_{iso}/Å^2	μ/μ_B
Sr	4*e*	0.0051(9)	0.0326(4)	0.7510(7)	1.000	0.29(3)	
Ho	2*c*	0	½	0	1.000	0.20(7)	4.53(4)
Ru	2*d*	½	0	0	0.950	0.41(9)	1.66(10)
Cu	2*d*	½	0	0	0.050	0.41(9)	
O1	4*e*	0.2989(9)	0.2752(9)	0.9625(6)	1.000	0.38(11)	
O2	4*e*	0.2666(8)	0.2968(9)	0.5365(7)	1.000	0.45(13)	
O3	4*e*	0.9258(8)	0.4789(7)	0.7300(5)	1.000	0.25(8)	

R_p = 7.41 %, R_{wp} = 5.96 %, R_{exp} = 4.58 %, R_{F^2} = 6.05 %

$Sr_2HoRu_{0.95}Cu_{0.05}O_6$		$P2_1/n$			50 K		
a / Å		b / Å	c / Å	β / °	Volume / Å^3		
5.75784(3)		5.77689(3)	8.14340(7)	90.350(1)	270.864(5)		
Atom	Site	x	y	z	Occ	B_{iso}/Å^2	μ/μ_B
Sr	4*e*	0.0067(8)	0.0313(4)	0.7507(6)	1.000	0.30(3)	
Ho	2*c*	0	½	0	1.000	0.20(9)	
Ru	2*d*	½	0	0	0.950	0.38(10)	
Cu	2*d*	½	0	0	0.050	0.38(10)	
O1	4*e*	0.3013(8)	0.2732(8)	0.9620(5)	1.000	0.42(10)	
O2	4*e*	0.2676(7)	0.2969(8)	0.5357(6)	1.000	0.27(12)	
O3	4*e*	0.9258(8)	0.4814(7)	0.7311(5)	1.000	0.38(7)	

R_p = 5.86 %, R_{wp} = 7.12 %, R_{exp} = 4.60 %, R_{F^2} = 5.01 %

B.3.2 D1B Refinements

B.3.2.1 Sr_2HoRuO_6

The crystal structure (atomic and thermal parameters) used for the refinements was the HRPD 20 K structure of Sr_2HoRuO_6.

Temperature	Lattice Parameters				
/ K	a / Å	b / Å	c / Å	β / °	Volume / Å^3
2	5.75715(10)	5.77619(10)	8.14118(29)	90.352(1)	270.725(19)
6	5.75667(11)	5.77571(11)	8.13983(30)	90.359(1)	270.635(20)
9	5.75698(11)	5.77602(12)	8.14070(32)	90.355(2)	270.693(22)
11	5.75689(11)	5.77593(11)	8.14045(31)	90.356(2)	270.676(21)
14	5.75675(11)	5.77579(12)	8.14006(32)	90.358(2)	270.649(22)
16	5.75657(11)	5.77560(11)	8.13954(31)	90.360(2)	270.615(21)
18	5.75657(12)	5.77561(12)	8.13955(33)	90.360(2)	270.616(22)
19	5.75686(11)	5.77590(10)	8.14037(28)	90.356(1)	270.670(18)
21	5.75651(12)	5.77555(12)	8.13940(34)	90.361(2)	270.605(23)
23	5.75653(12)	5.77556(12)	8.13944(34)	90.361(2)	270.608(22)
25	5.75653(12)	5.77557(12)	8.13946(35)	90.361(2)	270.609(23)
28	5.75666(12)	5.77569(12)	8.13981(34)	90.359(2)	270.633(23)
30	5.75659(11)	5.77562(11)	8.13961(30)	90.360(1)	270.619(20)
32	5.75672(12)	5.77576(13)	8.14000(35)	90.358(2)	270.645(24)
34	5.75663(13)	5.77566(13)	8.13974(36)	90.359(2)	270.628(24)
36	5.75674(13)	5.77577(14)	8.14004(38)	90.358(2)	270.648(25)
38	5.75694(13)	5.77598(13)	8.14061(36)	90.355(2)	270.686(24)
41	5.75691(13)	5.77596(13)	8.14055(36)	90.355(2)	270.682(24)
43	5.75673(13)	5.77577(13)	8.14004(36)	90.358(2)	270.648(24)
45	5.75678(12)	5.77582(12)	8.14017(34)	90.357(2)	270.656(23)

Temperature / K	Magnetic Moment / μ_B Ru^{5+} z	xy	Ho^{3+} z	total	R_p / %	R_{wp} / %	R_{exp} / %	R_{F^2} / %
2	1.79(9)	0.97(12)	7.87(4)	7.93(4)	2.06	3.06	0.87	3.75
6	1.74(10)	0.99(13)	7.53(4)	7.59(4)	2.20	3.11	1.29	3.87
9	1.72(10)	1.00(13)	6.68(5)	6.76(4)	2.37	3.24	1.82	3.99
11	1.71(10)	0	5.93(4)	5.93(4)	2.25	3.08	1.82	3.62
14	1.68(10)	0	5.22(5)	5.22(5)	2.24	3.08	1.85	3.63
16	1.65(10)	0	4.57(5)	4.57(5)	2.20	2.98	1.82	4.18
18	1.64(11)	0	4.03(6)	4.03(6)	2.21	3.13	1.82	4.06
19	1.67(10)	0	4.05(5)	4.05(5)	1.72	2.57	1.05	3.31
21	1.59(11)	0	3.50(7)	3.50(7)	2.26	3.16	1.82	4.60
23	1.45(12)	0	3.12(7)	3.12(7)	2.24	3.12	1.84	4.57
25	1.35(13)	0	2.69(9)	2.69(9)	2.25	3.17	1.83	4.01
28	1.38(17)	0	2.09(13)	2.09(13)	2.17	3.10	1.83	3.19
30	1.25(17)	0	1.84(13)	1.84(13)	1.72	2.72	0.82	3.70
32	0.87(27)	0	1.20(23)	1.20(23)	2.28	3.20	1.83	3.82
34	0.66(59)	0	0.67(53)	0.67(53)	2.27	3.27	1.85	4.26
36	0	0	0	0	2.43	3.45	1.83	3.23
38	0	0	0	0	2.30	3.31	1.83	3.47
41	0	0	0	0	2.33	3.26	1.84	3.79
43	0	0	0	0	2.39	3.28	1.83	2.80
45	0	0	0	0	2.09	3.09	1.30	3.72

B.3.2.2 $Sr_2HoRu_{0.95}Cu_{0.05}O_6$

The crystal structure (atomic and thermal parameters) used for the refinements was the HRPD 20 K structure of $Sr_2HoRu_{0.95}Cu_{0.05}O_6$.

Temperature / K	Lattice Parameters a / Å	b / Å	c / Å	β / °	Volume / $Å^3$
2	5.75766(11)	5.77670(12)	8.14287(32)	90.352(2)	270.829(21)
2	5.75746(13)	5.77651(13)	8.14232(36)	90.355(2)	270.793(24)
3	5.75703(13)	5.77607(13)	8.14110(36)	90.361(2)	270.710(24)
4	5.75777(13)	5.77682(13)	8.14320(36)	90.351(2)	270.851(24)
6	5.75814(12)	5.77720(12)	8.14426(35)	90.345(2)	270.922(23)
7	5.75806(12)	5.77712(12)	8.14401(34)	90.347(2)	270.905(23)
7	5.75807(12)	5.77712(13)	8.14403(35)	90.347(2)	270.907(23)
8	5.75786(12)	5.77691(13)	8.14344(35)	90.349(2)	270.867(24)
9	5.75796(13)	5.77701(13)	8.14373(36)	90.348(2)	270.886(24)
10	5.75783(12)	5.77688(12)	8.14337(34)	90.350(2)	270.862(23)
11	5.75777(12)	5.77682(12)	8.14318(34)	90.350(2)	270.850(23)
12	5.75782(13)	5.77687(13)	8.14333(36)	90.350(2)	270.860(24)
13	5.75783(12)	5.77688(12)	8.14337(34)	90.349(2)	270.862(23)
14	5.75769(12)	5.77673(12)	8.14296(34)	90.352(2)	270.835(23)
15	5.75771(12)	5.77675(13)	8.14301(35)	90.351(2)	270.838(23)
16	5.75771(13)	5.77675(13)	8.14302(36)	90.351(2)	270.839(24)
17	5.75757(12)	5.77662(13)	8.14263(35)	90.353(2)	270.813(23)
18	5.75757(13)	5.77662(14)	8.14263(38)	90.353(2)	270.813(25)

19	5.75760 (13)	5.77664 (13)	8.14269 (37)	90.353 (2)	270.818 (25)
20	5.75763 (13)	5.77668 (12)	8.14279 (38)	90.352 (2)	270.824 (25)
20	5.75768 (13)	5.77673 (14)	8.14292 (38)	90.352 (2)	270.833 (25)
21	5.75770 (13)	5.77675 (14)	8.14298 (38)	90.351 (2)	270.837 (26)
22	5.75769 (13)	5.77674 (14)	8.14295 (38)	90.352 (2)	270.835 (25)
23	5.75763 (14)	5.77668 (14)	8.14279 (39)	90.352 (2)	270.824 (26)
24	5.75763 (11)	5.77668 (12)	8.14280 (32)	90.352 (2)	270.824 (21)
24	5.75770 (13)	5.77675 (13)	8.14298 (38)	90.351 (2)	270.837 (25)
26	5.75765 (14)	5.77669 (14)	8.14283 (40)	90.352 (2)	270.827 (27)
27	5.75758 (14)	5.77662 (14)	8.14264 (40)	90.353 (2)	270.814 (27)
28	5.75752 (13)	5.77656 (13)	8.14247 (36)	90.354 (2)	270.803 (24)
29	5.75766 (14)	5.77670 (14)	8.14287 (38)	90.352 (2)	270.829 (26)
30	5.75765 (13)	5.77670 (13)	8.14285 (37)	90.352 (2)	270.828 (25)
31	5.75770 (14)	5.77675 (14)	8.14299 (39)	90.351 (2)	270.837 (26)
32	5.75763 (14)	5.77668 (14)	8.14279 (39)	90.352 (2)	270.824 (26)
33	5.75772 (14)	5.77677 (15)	8.14305 (41)	90.351 (2)	270.841 (27)
34	5.75786 (14)	5.77692 (15)	8.14347 (41)	90.349 (2)	270.869 (27)
35	5.75763 (14)	5.77668 (14)	8.14281 (40)	90.352 (2)	270.825 (26)
36	5.75777 (14)	5.77682 (14)	8.14321 (40)	90.350 (2)	270.851 (27)
37	5.75772 (14)	5.77677 (15)	8.14307 (41)	90.350 (2)	270.842 (27)
38	5.75785 (14)	5.77690 (15)	8.14342 (41)	90.349 (2)	270.866 (27)
39	5.75784 (14)	5.77690 (14)	8.14342 (40)	90.349 (2)	270.866 (27)
40	5.75766 (14)	5.77671 (14)	8.14290 (38)	90.351 (2)	270.830 (26)
41	5.75788 (14)	5.77694 (14)	8.14353 (39)	90.348 (2)	270.872 (26)
42	5.75779 (14)	5.77685 (15)	8.14329 (40)	90.349 (2)	270.856 (27)
43	5.75777 (14)	5.77683 (14)	8.14323 (40)	90.350 (2)	270.852 (27)
44	5.75773 (14)	5.77679 (14)	8.14310 (39)	90.350 (2)	270.844 (26)
44	5.75778 (14)	5.77684 (14)	8.14325 (39)	90.349 (2)	270.854 (26)
45	5.75802 (14)	5.77709 (14)	8.14395 (40)	90.346 (2)	270.900 (27)
46	5.75782 (13)	5.77688 (14)	8.14337 (38)	90.349 (2)	270.861 (25)
47	5.75791 (13)	5.77698 (14)	8.14364 (38)	90.347 (2)	270.880 (25)
49	5.75779 (13)	5.77685 (13)	8.14328 (38)	90.349 (2)	270.856 (25)
49	5.75778 (14)	5.77684 (15)	8.14326 (41)	90.349 (2)	270.854 (27)
50	5.75786 (12)	5.77692 (12)	8.14349 (34)	90.348 (2)	270.869 (23)

Temperature / K	Magnetic Moment / μ_B				R_p / %	R_{wp} / %	R_{exp} / %	R_{F^2} / %
	Ru^{5+}		Ho^{3+}					
	z	xy	z	total				
2	1.99 (10)	1.20 (15)	8.94 (5)	9.02 (5)	1.91	2.76	0.79	11.43
2	1.99 (10)	1.25 (16)	8.99 (6)	9.07 (6)	2.19	3.02	1.39	10.08
3	1.97 (10)	1.11 (17)	9.01 (6)	9.08 (6)	2.24	3.03	1.39	6.28
4	1.99 (10)	1.26 (16)	8.78 (6)	8.87 (6)	2.20	2.98	1.39	26.99
6	1.99 (10)	1.21 (16)	8.98 (6)	9.07 (6)	2.21	3.00	1.39	21.47
7	1.98 (10)	1.32 (15)	8.91 (6)	9.00 (6)	2.26	3.07	1.41	48.68
7	1.99 (10)	1.14 (16)	8.80 (6)	8.88 (6)	2.18	2.97	1.39	11.48
8	2.00 (10)	1.21 (16)	8.74 (6)	8.82 (6)	2.20	2.97	1.39	6.32
9	1.99 (10)	1.16 (17)	8.53 (6)	8.61 (6)	2.20	3.03	1.39	13.75
10	1.95 (10)	0	8.37 (5)	8.37 (5)	1.99	2.80	1.39	6.32
11	1.96 (10)	0	8.12 (5)	8.12 (5)	2.01	2.75	1.39	22.60

12	1.90(10)	0	7.95(5)	7.95(5)	2.16	2.88	1.39	7.73
13	1.93(10)	0	7.62(5)	7.62(5)	1.88	2.68	1.39	15.18
14	1.90(10)	0	7.35(5)	7.35(5)	1.88	2.64	1.39	6.43
15	1.89(10)	0	7.08(5)	7.08(5)	1.93	2.68	1.40	7.42
16	1.93(10)	0	6.72(5)	6.72(5)	1.93	2.75	1.40	22.41
17	1.85(10)	0	6.47(5)	6.47(5)	1.87	2.60	1.40	26.87
18	1.88(10)	0	6.14(5)	6.14(5)	2.00	2.80	1.40	17.79
19	1.85(10)	0	5.88(5)	5.88(5)	1.88	2.73	1.39	39.99
20	1.87(11)	0	5.61(5)	5.61(5)	1.87	2.74	1.40	8.62
20	1.89(11)	0	5.44(6)	5.44(6)	1.84	2.72	1.40	20.60
21	1.89(11)	0	5.18(6)	5.18(6)	1.86	2.73	1.40	44.12
22	1.86(11)	0	4.99(6)	4.99(6)	1.81	2.68	1.40	28.00
23	1.83(11)	0	4.79(6)	4.79(6)	1.91	2.74	1.40	9.03
24	1.79(10)	0	4.65(5)	4.65(5)	1.40	2.27	0.60	22.60
24	1.83(11)	0	4.39(6)	4.39(6)	1.82	2.63	1.40	31.63
26	1.78(12)	0	4.08(7)	4.08(7)	1.94	2.80	1.40	9.47
27	1.72(12)	0	3.82(8)	3.82(8)	1.94	2.78	1.40	25.40
28	1.65(12)	0	3.63(7)	3.63(7)	1.78	2.51	1.40	18.40
29	1.68(13)	0	3.28(8)	3.28(9)	1.81	2.64	1.40	23.14
30	1.64(14)	0	3.04(9)	3.04(9)	1.85	2.58	1.42	23.95
31	1.59(15)	0	2.82(10)	2.82(11)	1.83	2.64	1.40	26.88
32	1.43(16)	0	2.59(11)	2.59(11)	1.82	2.65	1.40	41.58
33	1.36(18)	0	2.29(14)	2.29(14)	1.86	2.76	1.40	45.60
34	1.15(19)	0	2.08(15)	2.08(15)	1.92	2.76	1.40	31.59
35	0.82(19)	0	1.77(14)	1.77(14)	1.91	2.72	1.42	32.24
36	0.37(22)	0	1.29(17)	1.29(17)	1.88	2.75	1.42	56.38
37	0.42(46)	0	0.71(39)	0.71(39)	1.96	2.76	1.40	40.68
38	0	0	0	0	1.89	2.77	1.40	56.40
39	0	0	0	0	1.89	2.77	1.42	56.39
40	0	0	0	0	1.79	2.61	1.41	22.57
41	0	0	0	0	1.84	2.69	1.42	9.29
42	0	0	0	0	1.94	2.77	1.42	16.80
43	0	0	0	0	1.84	2.72	1.41	10.86
44	0	0	0	0	1.83	2.67	1.40	30.68
44	0	0	0	0	1.84	2.66	1.42	25.82
45	0	0	0	0	1.79	2.71	1.40	33.88
46	0	0	0	0	1.75	2.57	1.40	21.04
47	0	0	0	0	1.79	2.59	1.41	28.87
49	0	0	0	0	1.76	2.56	1.41	34.22
49	0	0	0	0	1.91	2.78	1.40	32.38
50	0	0	0	0	1.31	2.32	0.61	21.77

B.3.2.3 $Sr_2HoRu_{0.90}Cu_{0.10}O_6$

The crystal structure (atomic and thermal parameters) used for the refinements was the HRPD 20 K structure of $Sr_2HoRu_{0.95}Cu_{0.05}O_6$.

Temperature	Lattice Parameters				
/ K	a / Å	b / Å	c / Å	β / °	Volume / Å^3
2	5.75936 (11)	5.77844 (11)	8.14772 (31)	90.328 (2)	271.153 (20)
4	5.75940 (12)	5.77848 (12)	8.14784 (34)	90.328 (2)	271.160 (23)
7	5.75921 (12)	5.77828 (12)	8.14728 (34)	90.330 (2)	271.123 (22)
9	5.75908 (12)	5.77815 (12)	8.14690 (33)	90.332 (2)	271.098 (22)
12	5.75895 (12)	5.77802 (12)	8.14656 (33)	90.334 (2)	271.075 (22)
14	5.75873 (12)	5.77780 (12)	8.14595 (34)	90.337 (2)	271.034 (22)
16	5.75891 (12)	5.77798 (12)	8.14646 (34)	90.334 (2)	271.068 (23)
18	5.75887 (13)	5.77794 (13)	8.14634 (36)	90.335 (2)	271.060 (24)
19	5.75892 (11)	5.77799 (12)	8.14646 (32)	90.334 (2)	271.068 (22)
20	5.75894 (11)	5.77801 (11)	8.14652 (32)	90.334 (2)	271.072 (21)
21	5.75891 (11)	5.77798 (11)	8.14646 (35)	90.334 (1)	271.068 (20)
22	5.75888 (13)	5.77795 (13)	8.14636 (36)	90.335 (2)	271.062 (24)
24	5.75895 (13)	5.77802 (13)	8.14655 (36)	90.334 (2)	271.074 (24)
26	5.75898 (12)	5.77805 (12)	8.14663 (34)	90.333 (2)	271.080 (23)
29	5.75897 (12)	5.77804 (12)	8.14662 (34)	90.333 (2)	271.079 (23)
31	5.75901 (14)	5.77808 (14)	8.14673 (39)	90.333 (2)	271.086 (25)
33	5.75900 (13)	5.77807 (13)	8.14670 (37)	90.333 (2)	271.084 (25)
35	5.75902 (13)	5.77809 (13)	8.14675 (36)	90.333 (2)	271.088 (24)
38	5.75893 (12)	5.77800 (13)	8.14652 (36)	90.333 (2)	271.072 (24)
40	5.75914 (13)	5.77821 (13)	8.14710 (37)	90.331 (2)	271.111 (25)
43	5.75902 (13)	5.77809 (14)	8.14677 (38)	90.332 (2)	271.088 (26)
45	5.75910 (13)	5.77816 (13)	8.14698 (37)	90.331 (2)	271.103 (24)
47	5.75921 (13)	5.77828 (13)	8.14731 (37)	90.329 (2)	271.125 (25)
50	5.75913 (11)	5.77820 (11)	8.14708 (31)	90.330 (2)	271.109 (21)

Temperature / K	Magnetic Moment / μ_B				R_p / %	R_{wp} / %	R_{exp} / %	R_{F^2} / %
	Ru^{5+}		Ho^{3+}					
	z	*xy*	*z*	total				
2	2.09(10)	1.25(12)	8.73(5)	8.82(5)	2.36	3.16	1.00	3.73
4	2.06(10)	1.28(14)	8.61(5)	8.71(5)	2.63	3.51	1.74	3.50
7	2.06(10)	1.04(15)	8.26(5)	8.32(5)	2.64	3.35	1.74	3.72
9	2.01(10)	1.05(15)	7.63(5)	7.70(5)	2.42	3.19	1.74	4.19
12	1.99(10)	0.92(16)	6.72(5)	6.78(5)	2.44	3.07	1.74	4.30
14	1.99(10)	0	5.85(5)	5.85(5)	2.37	3.06	1.74	4.59
16	1.91(10)	0	5.16(5)	5.16(5)	2.36	3.04	1.74	4.42
18	1.87(11)	0	4.58(5)	4.58(5)	2.49	3.19	1.76	5.30
19	1.95(11)	0	4.46(5)	4.46(5)	2.07	2.82	1.74	3.44
20	1.93(11)	0	4.34(5)	4.34(5)	2.02	2.75	1.23	4.67
21	1.93(10)	0	4.51(5)	4.51(5)	1.96	2.61	1.01	3.98
22	1.85(12)	0	3.74(7)	3.74(7)	2.32	3.04	1.74	4.41
24	1.76(13)	0	3.22(8)	3.22(8)	2.33	3.05	1.74	4.08
26	1.64(14)	0	2.78(9)	2.78(9)	2.17	2.89	1.75	3.81
29	1.64(18)	0	2.15(13)	2.15(13)	2.20	2.94	1.77	4.28
31	1.30(27)	0	1.61(21)	1.61(21)	2.38	3.19	1.74	5.10
33	0.75(57)	0	0.76(46)	0.76(46)	2.20	2.90	1.75	4.70
35	0	0	0	0	2.22	2.98	1.75	3.54
38	0	0	0	0	2.25	2.96	1.75	4.34
40	0	0	0	0	2.34	3.14	1.75	3.09
43	0	0	0	0	2.35	3.20	1.75	4.33
45	0	0	0	0	2.26	3.06	1.75	3.44
47	0	0	0	0	2.35	3.06	1.75	3.72
50	0	0	0	0	1.81	2.58	0.78	3.59

B.3.2.4 $Sr_2HoRu_{0.85}Cu_{0.15}O_6$

The crystal structure (atomic and thermal parameters) used for the refinements was the HRPD 20 K structure of $Sr_2HoRu_{0.95}Cu_{0.05}O_6$.

Temperature	Lattice Parameters				
/ K	a / Å	b / Å	c / Å	β / °	Volume / Å^3
2	5.76282 (14)	5.78196 (14)	8.15756 (40)	90.280 (2)	271.810 (27)
2	5.76301 (17)	5.78214 (17)	8.15808 (48)	90.277 (2)	271.845 (32)
7	5.76277 (17)	5.78191 (17)	8.15742 (48)	90.280 (2)	271.800 (32)
9	5.76253 (17)	5.78166 (17)	8.15673 (49)	90.284 (2)	271.755 (32)
10	5.76263 (14)	5.78176 (14)	8.15702 (40)	90.282 (2)	271.774 (26)
11	5.76258 (17)	5.78171 (18)	8.15688 (49)	90.283 (2)	271.764 (33)
12	5.76237 (18)	5.78150 (18)	8.15628 (51)	90.286 (3)	271.724 (34)
14	5.76235 (19)	5.78148 (19)	8.15623 (53)	90.286 (3)	271.720 (36)
19	5.76237 (14)	5.78150 (15)	8.15628 (41)	90.286 (2)	271.724 (27)
20	5.76238 (16)	5.78151 (16)	8.15631 (44)	90.285 (2)	271.726 (29)
22	5.76245 (19)	5.78158 (19)	8.15651 (54)	90.284 (3)	271.739 (36)
24	5.76237 (19)	5.78150 (19)	8.15630 (55)	90.285 (3)	271.725 (36)
26	5.76198 (19)	5.78110 (20)	8.15518 (55)	90.291 (3)	271.651 (37)
29	5.76234 (15)	5.78146 (15)	8.15619 (41)	90.286 (2)	271.718 (28)
31	5.76233 (18)	5.78145 (18)	8.15617 (52)	90.286 (3)	271.716 (35)
33	5.76233 (18)	5.78145 (19)	8.15615 (52)	90.286 (3)	271.716 (35)
34	5.76249 (19)	5.78162 (19)	8.15662 (53)	90.283 (3)	271.747 (35)
36	5.76224 (18)	5.78137 (18)	8.15591 (51)	90.287 (3)	271.700 (34)
38	5.76245 (19)	5.78158 (19)	8.15651 (55)	90.284 (3)	271.739 (36)
39	5.76250 (14)	5.78163 (15)	8.15665 (41)	90.283 (2)	271.749 (27)
42	5.76241 (20)	5.78155 (20)	8.15642 (56)	90.284 (3)	271.733 (37)
45	5.76211 (19)	5.78124 (19)	8.15555 (54)	90.288 (3)	271.676 (36)
49	5.76248 (15)	5.78162 (15)	8.15662 (42)	90.283 (2)	271.747 (28)

Temperature / K	Magnetic Moment / μ_B				R_p / %	R_{wp} / %	R_{exp} / %	R_{F^2} / %
	Ru^{5+}		Ho^{3+}					
	z	*xy*	*z*	total				
2	2.26(11)	1.28(18)	8.88(6)	8.97(6)	1.96	2.77	0.70	4.59
2	2.25(11)	1.26(22)	8.82(8)	8.91(7)	2.51	3.31	1.92	4.97
7	2.40(11)	1.22(23)	8.56(7)	8.65(7)	2.44	3.25	1.92	4.58
9	2.22(11)	0.87(29)	8.06(7)	8.11(7)	2.40	3.17	1.92	5.57
10	2.24(11)	0.96(22)	7.99(6)	8.05(6)	1.84	2.59	0.66	4.70
11	2.23(12)	0.84(29)	7.09(7)	7.14(7)	2.34	3.07	1.91	5.84
12	2.15(12)	0	6.33(7)	6.33(7)	2.32	3.09	1.92	5.47
14	2.00(13)	0	5.42(8)	5.42(8)	2.38	3.16	1.92	6.58
19	2.13(12)	0	4.63(7)	4.63(7)	1.65	2.38	0.56	5.41
20	2.01(13)	0	4.44(7)	4.44(7)	1.83	2.58	1.36	5.69
22	2.05(17)	0	3.60(12)	3.60(12)	2.38	3.07	1.92	7.58
24	1.97(21)	0	3.04(15)	3.04(15)	2.40	3.11	1.92	7.37
26	1.88(28)	0	2.43(21)	2.43(21)	2.45	3.10	1.92	6.84
29	1.83(23)	0	2.34(17)	2.34(17)	1.61	2.33	0.57	5.97
31	1.60(31)	0	2.02(24)	2.02(24)	2.24	2.90	1.92	7.67
33	0.98(42)	0	1.30(32)	1.30(32)	2.25	2.93	1.92	6.27
34	0	0	0	0	2.24	2.98	1.93	5.26
36	0	0	0	0	2.19	2.89	1.93	6.07
38	0	0	0	0	2.29	3.02	1.93	6.49
39	0	0	0	0	1.55	2.32	0.57	4.37
42	0	0	0	0	2.36	3.11	1.93	6.01
45	0	0	0	0	2.33	3.05	1.93	5.27
49	0	0	0	0	1.66	2.37	0.79	4.90

B.4 Neutron Diffraction Refinements of $Sr_2TbRu_{1-x}Cu_xO_6$

B.4.1 D1B Refinements

B.4.1.1 Sr_2TbRuO_6

The crystal structure (atomic and thermal parameters) used for the refinements was the HRPD 20 K structure of Sr_2HoRuO_6.

Temperature	Lattice Parameters				
/ K	a / Å	b / Å	c / Å	β / °	Volume / Å^3
2	5.78874 (8)	5.81485 (9)	8.20043 (24)	90.403 (1)	276.025 (16)
3	5.78880 (10)	5.81492 (10)	8.20063 (28)	90.402 (1)	276.038 (19)
5	5.78871 (10)	5.81483 (10)	8.20036 (27)	90.403 (1)	276.020 (18)
7	5.78884 (10)	5.81495 (10)	8.20071 (27)	90.401 (1)	276.044 (18)
10	5.78883 (9)	5.81495 (10)	8.20069 (27)	90.401 (1)	276.043 (18)
12	5.78852 (11)	5.81463 (10)	8.19983 (27)	90.406 (1)	275.984 (18)
14	5.78872 (8)	5.81484 (8)	8.20041 (23)	90.403 (1)	276.023 (16)
14	5.78852 (9)	5.81463 (10)	8.19981 (27)	90.406 (1)	275.983 (18)
16	5.78838 (9)	5.81448 (10)	8.19940 (27)	90.407 (1)	275.955 (18)
19	5.78851 (10)	5.81462 (10)	8.19977 (28)	90.406 (1)	275.980 (19)
21	5.78847 (10)	5.81458 (10)	8.19966 (28)	90.406 (1)	275.973 (19)
23	5.78841 (10)	5.81452 (10)	8.19950 (28)	90.407 (1)	275.962 (19)
24	5.78872 (8)	5.81483 (8)	8.20035 (23)	90.403 (1)	276.020 (15)
25	5.78837 (9)	5.81448 (9)	8.19940 (26)	90.407 (1)	275.955 (17)
28	5.78834 (9)	5.81445 (9)	8.19937 (25)	90.407 (1)	275.951 (17)
30	5.78845 (9)	5.81457 (9)	8.19968 (25)	90.406 (1)	275.973 (17)
32	5.78849 (9)	5.81461 (9)	8.19980 (26)	90.405 (1)	275.980 (18)
34	5.78875 (8)	5.81487 (8)	8.20052 (23)	90.401 (1)	276.029 (15)
34	5.78856 (10)	5.81468 (10)	8.19997 (28)	90.403 (1)	275.993 (19)
37	5.78836 (9)	5.81448 (9)	8.19942 (26)	90.406 (1)	275.955 (18)
39	5.78853 (10)	5.81465 (10)	8.19988 (27)	90.404 (1)	275.987 (18)
41	5.78850 (9)	5.81461 (10)	8.19979 (27)	90.404 (1)	275.980 (18)
44	5.78858 (9)	5.81470 (10)	8.20004 (27)	90.403 (1)	275.997 (18)
46	5.78857 (9)	5.81469 (9)	8.20000 (26)	90.403 (1)	275.994 (18)
49	5.78888 (8)	5.81501 (8)	8.20088 (22)	90.399 (1)	276.054 (15)
49	5.78856 (9)	5.81468 (9)	8.19997 (25)	90.403 (1)	275.993 (17)
51	5.78862 (10)	5.81475 (10)	8.20016 (28)	90.402 (1)	276.006 (19)
53	5.78858 (9)	5.81470 (9)	8.20003 (25)	90.403 (1)	275.996 (17)
55	5.78857 (10)	5.81468 (10)	8.19999 (27)	90.403 (1)	275.994 (18)
57	5.78873 (9)	5.81485 (9)	8.20046 (26)	90.401 (1)	276.025 (18)

Temperature / K	Magnetic Moment / μ_B Ru^{5+} z	xy	Tb^{3+} z	total	R_p / %	R_{wp} / %	R_{exp} / %	R_{F^2} / %
2	1.91(10)	1.17(8)	4.54(4)	4.68(4)	1.86	2.63	0.76	4.28
3	1.90(10)	1.16(10)	4.54(5)	4.69(4)	2.32	3.04	1.61	4.43
5	1.85(10)	1.10(10)	4.57(5)	4.70(4)	2.33	3.01	1.61	3.55
7	1.90(10)	1.05(10)	4.53(5)	4.65(4)	2.26	3.00	1.61	4.49
10	1.86(10)	1.17(9)	4.41(5)	4.56(4)	2.23	2.96	1.61	4.53
12	1.85(10)	1.19(9)	4.39(5)	4.55(4)	2.35	3.01	1.62	4.27
14	1.84(10)	1.11(8)	4.35(4)	4.49(4)	1.84	2.57	0.76	4.18
14	1.83(10)	1.16(9)	4.33(5)	4.48(4)	2.22	2.96	1.61	4.83
16	1.84(10)	1.14(9)	4.21(5)	4.36(5)	2.23	2.95	1.61	4.37
19	1.83(10)	1.09(10)	4.08(6)	4.22(5)	2.27	3.06	1.62	4.54
21	1.76(10)	1.11(10)	3.92(6)	4.08(5)	2.28	2.99	1.62	4.59
23	1.77(10)	1.04(10)	3.77(6)	3.91(5)	2.21	2.97	1.61	4.10
24	1.74(10)	0.85(10)	3.76(5)	3.86(4)	1.73	2.47	0.76	4.03
25	1.63(10)	0.75(13)	3.59(5)	3.67(5)	2.16	2.75	1.61	4.13
28	1.60(10)	0	3.40(5)	3.40(5)	1.98	2.63	1.62	3.73
30	1.43(11)	0	3.07(5)	3.07(5)	2.05	2.68	1.62	3.89
32	1.30(11)	0	2.65(7)	2.65(7)	2.10	2.74	1.62	3.74
34	1.27(11)	0	2.51(6)	2.51(6)	1.71	2.39	0.76	3.91
34	1.10(12)	0	2.26(8)	2.26(8)	2.22	2.92	1.62	4.66
37	0.78(13)	0	1.70(9)	1.70(9)	2.04	2.69	1.61	3.80
39	0.34(23)	0	0.79(20)	0.79(20)	2.15	2.82	1.62	4.25
41	0	0	0	0	2.10	2.78	1.61	3.82
44	0	0	0	0	2.07	2.77	1.62	3.62
46	0	0	0	0	2.11	2.73	1.62	3.43
49	0	0	0	0	1.59	2.27	0.76	3.38
49	0	0	0	0	1.98	2.62	1.62	3.22
51	0	0	0	0	2.16	2.85	1.62	4.03
53	0	0	0	0	2.05	2.62	1.62	3.46
55	0	0	0	0	2.12	2.83	1.62	3.56
57	0	0	0	0	2.06	2.73	1.62	3.42

B.4.1.2 $Sr_2TbRu_{0.90}Cu_{0.10}O_6$

The crystal structure (atomic and thermal parameters) used for the refinements was the HRPD 20 K structure of $Sr_2HoRu_{0.95}Cu_{0.05}O_6$.

Temperature	Lattice Parameters				
/ K	a / Å	b / Å	c / Å	β / °	Volume / Å^3
2	5.78489(8)	5.80577(9)	8.18962(24)	90.329(1)	275.050(16)
7	5.78503(11)	5.80591(11)	8.19002(30)	90.327(1)	275.077(20)
8	5.78500(11)	5.80588(11)	8.18993(31)	90.328(1)	275.071(21)
11	5.78495(11)	5.80583(11)	8.18981(30)	90.328(1)	275.062(20)
12	5.78480(11)	5.80568(11)	8.18935(31)	90.330(2)	275.032(21)
15	5.78492(10)	5.80582(10)	8.18972(29)	90.328(1)	275.057(20)
19	5.78499(11)	5.80588(11)	8.18991(32)	90.326(2)	275.069(21)
19	5.78502(9)	5.80591(9)	8.19005(25)	90.325(1)	275.077(17)
20	5.78503(10)	5.80592(11)	8.19008(30)	90.325(1)	275.079(20)
22	5.78500(11)	5.80589(11)	8.18998(32)	90.325(2)	275.073(21)
24	5.78498(11)	5.80587(11)	8.18994(32)	90.325(2)	275.070(21)
26	5.78488(11)	5.80576(11)	8.18963(31)	90.329(2)	275.049(21)
29	5.78489(9)	5.80576(9)	8.18964(25)	90.329(1)	275.050(17)
30	5.78497(10)	5.80584(11)	8.18987(30)	90.327(1)	275.066(20)
32	5.78500(10)	5.80588(10)	8.18997(28)	90.327(1)	275.072(19)
34	5.78501(12)	5.80588(12)	8.18998(34)	90.327(2)	275.073(23)
36	5.78504(11)	5.80592(11)	8.19008(31)	90.326(2)	275.080(21)
38	5.78504(11)	5.80592(12)	8.19009(32)	90.326(2)	275.080(22)
39	5.78500(9)	5.80588(9)	8.18998(25)	90.326(1)	275.073(17)
42	5.78495(11)	5.80583(11)	8.18983(31)	90.327(1)	275.062(21)
44	5.78504(11)	5.80592(11)	8.19009(31)	90.326(2)	275.080(21)
46	5.78497(10)	5.80585(10)	8.18990(29)	90.326(1)	275.067(19)
48	5.78506(11)	5.80594(11)	8.19016(30)	90.325(1)	275.085(20)
50	5.78504(11)	5.80592(11)	8.19009(31)	90.326(2)	275.080(21)
53	5.78509(11)	5.80597(11)	8.19025(31)	90.325(2)	275.090(21)
55	5.78504(11)	5.80592(11)	8.19010(30)	90.325(1)	275.080(20)
57	5.78514(9)	5.80603(10)	8.19039(27)	90.324(1)	275.100(18)

Temperature / K	Magnetic Moment / μ_B				R_p / %	R_{wp} / %	R_{exp} / %	R_{F^2} / %
	Ru^{5+}		Tb^{3+}					
	z	*xy*	*z*	total				
2	1.93(10)	0.82(12)	4.08(5)	4.17(4)	1.59	2.37	0.71	3.25
7	1.96(11)	0.90(14)	4.05(6)	4.15(5)	2.28	3.00	1.99	3.86
8	1.97(11)	0.72(16)	4.02(6)	4.08(5)	2.27	3.03	1.99	3.62
11	2.02(11)	0.95(13)	3.83(6)	3.95(6)	2.18	3.00	1.99	4.58
12	1.96(11)	0.59(19)	3.83(6)	3.88(6)	2.31	3.03	1.99	4.00
15	1.84(11)	0.52(19)	3.76(6)	3.80(5)	2.15	2.86	1.99	3.63
19	1.81(12)	0.95(14)	3.55(7)	3.68(6)	2.32	3.14	1.99	4.05
19	1.92(11)	0.71(13)	3.49(6)	3.56(5)	1.64	2.42	0.81	2.99
20	1.93(12)	0.92(13)	3.35(7)	3.47(6)	2.20	2.91	1.99	3.41
22	1.81(12)	0.60(20	3.19(8)	3.25(7)	2.29	3.11	1.99	3.39
24	1.66(13)	0.67(18)	3.06(8)	3.14(7)	2.24	3.10	1.99	3.79
26	1.63(13)	0	2.76(8)	2.76(8)	2.30	3.03	1.99	4.09
29	1.58(12)	0	2.73(6)	2.73(6)	1.70	2.45	0.81	3.05
30	1.48(14)	0	2.39(9)	2.39(9)	2.19	2.90	1.99	3.15
32	1.40(17)	0	1.91(12)	1.91(12)	2.07	2.75	1.99	3.38
34	1.23(43)	0	1.23(35)	1.23(35)	2.44	3.25	1.99	3.50
36	0.77(63)	0	0.54(51)	0.54(51)	2.20	2.97	1.99	3.28
38	0	0	0	0	2.34	3.09	2.00	3.12
39	0	0	0	0	1.71	2.40	0.82	2.64
42	0	0	0	0	2.22	2.93	2.00	2.71
44	0	0	0	0	2.16	2.93	1.99	2.43
46	0	0	0	0	2.05	2.75	2.00	2.00
48	0	0	0	0	2.23	2.90	2.00	2.69
50	0	0	0	0	2.26	3.01	2.00	2.94
53	0	0	0	0	2.22	3.01	2.00	2.66
55	0	0	0	0	2.18	2.91	2.00	2.34
57	0	0	0	0	1.82	2.56	1.00	2.94

B.5 Neutron Diffraction Refinements of $Sr_2Ho_{1-y}Tb_yRu_{1-x}Cu_xO_6$

B.5.1 D1B Refinements

B.5.1.1 $Sr_2Ho_{0.80}Tb_{0.20}Ru_{0.90}Cu_{0.10}O_6$

The crystal structure (atomic and thermal parameters) used for the refinements was the HRPD 20 K structure of $Sr_2HoRu_{0.95}Cu_{0.05}O_6$.

Temperature	Lattice Parameters				
/ K	a / Å	b / Å	c / Å	β / °	Volume / Å^3
2	5.76451 (10)	5.78368 (10)	8.16237 (27)	90.256 (1)	272.131 (18)
3	5.76429 (11)	5.78345 (12)	8.16173 (33)	90.259 (2)	272.089 (22)
5	5.76430 (11)	5.78346 (11)	8.16176 (31)	90.259 (2)	272.090 (21)
7	5.76431 (11)	5.78347 (11)	8.16179 (32)	90.259 (2)	272.093 (21)
10	5.76431 (12)	5.78347 (12)	8.16179 (33)	90.259 (2)	272.093 (22)
12	5.76439 (11)	5.78356 (11)	8.16202 (31)	90.258 (2)	272.108 (21)
14	5.76409 (11)	5.78325 (12)	8.16118 (32)	90.262 (2)	272.052 (22)
17	5.76431 (12)	5.78348 (12)	8.16181 (35)	90.259 (2)	272.094 (23)
19	5.76408 (12)	5.78324 (12)	8.16114 (33)	90.262 (2)	272.049 (22)
19	5.76420 (10)	5.78336 (10)	8.16148 (29)	90.260 (1)	272.072 (22)
21	5.76403 (15)	5.78319 (15)	8.16103 (43)	90.262 (2)	272.041 (28)
23	5.76417 (11)	5.78333 (11)	8.16142 (31)	90.260 (2)	272.067 (21)
26	5.76415 (11)	5.78331 (11)	8.16137 (32)	90.261 (2)	272.064 (21)
28	5.76424 (11)	5.78340 (12)	8.16162 (33)	90.259 (2)	272.080 (22)
30	5.76418 (11)	5.78334 (12)	8.16147 (33)	90.260 (2)	272.070 (22)
33	5.76420 (12)	5.78336 (12)	8.16152 (34)	90.259 (2)	272.073 (23)
35	5.76422 (11)	5.78339 (11)	8.16160 (32)	90.259 (2)	272.078 (21)
37	5.76440 (12)	5.78357 (12)	8.16209 (34)	90.256 (2)	272.112 (22)
40	5.76423 (12)	5.78339 (12)	8.16161 (34)	90.259 (2)	272.079 (23)
40	5.76428 (10)	5.78344 (10)	8.16175 (28)	90.258 (2)	272.089 (19)
42	5.76436 (11)	5.78353 (11)	8.16199 (30)	90.257 (1)	272.105 (20)
45	5.76451 (12)	5.78368 (12)	8.16242 (34)	90.254 (2)	272.133 (22)
47	5.76434 (12)	5.78350 (12)	8.16192 (35)	90.257 (2)	272.100 (23)
50	5.76435 (12)	5.78351 (12)	8.16195 (33)	90.257 (2)	272.102 (22)
52	5.76442 (12)	5.78358 (12)	8.16216 (34)	90.256 (2)	272.115 (23)
54	5.76450 (12)	5.78366 (12)	8.16237 (33)	90.255 (2)	272.130 (22)
56	5.76438 (11)	5.78354 (11)	8.16205 (31)	90.256 (2)	272.108 (21)
59	5.76436 (12)	5.78352 (12)	8.16198 (34)	90.256 (2)	272.104 (23)

Temperature / K	Magnetic Moment / μ_B				R_p / %	R_{wp} / %	R_{exp} / %	R_{F^2} / %
	Ru^{5+}		Ln^{3+}					
	z	xy	z	total				
2	2.03(10)	0	6.73(4)	6.73(4)	1.86	2.55	0.71	3.62
3	2.06(10)	0	6.65(5)	6.65(5)	2.32	3.06	1.76	3.14
5	2.02(10)	0	6.46(4)	6.46(4)	2.17	2.85	1.76	2.66
7	2.03(10)	0	6.05(5)	6.05(5)	2.26	2.92	1.76	3.15
10	2.03(10)	0	5.62(5)	5.62(5)	2.25	2.95	1.76	3.71
12	2.01(10)	0	5.19(5)	5.19(5)	2.08	2.77	1.76	2.95
14	1.98(11)	0	4.79(5)	4.79(5)	2.14	2.85	1.76	4.36
17	1.98(11)	0	4.43(6)	4.43(6)	2.30	3.02	1.76	3.25
19	1.88(11)	0	4.08(6)	4.08(6)	2.20	2.85	1.76	3.65
19	2.03(11)	0	4.15(5)	4.15(5)	1.84	2.54	1.02	3.75
21	1.86(13)	0	3.73(8)	3.73(8)	2.41	3.62	1.76	5.87
23	1.86(12)	0	3.40(7)	3.40(7)	2.00	2.64	1.76	3.51
26	1.70(13)	0	3.06(7)	3.06(7)	2.01	2.72	1.76	2.71
28	1.63(14)	0	2.62(9)	2.62(9)	2.04	2.73	1.76	3.47
30	1.34(15)	0	2.31(10)	2.31(10)	2.06	2.73	1.76	3.30
33	0.84(15)	0	1.86(10)	1.86(10)	1.98	2.63	1.78	2.77
35	0.56(21)	0	1.20(16)	1.20(16)	2.23	2.90	1.78	3.22
37	0	0	0	0	2.12	2.80	1.77	2.92
40	0	0	0	0	2.15	2.82	1.77	3.00
40	0	0	0	0	1.58	2.30	1.02	2.55
42	0	0	0	0	1.87	2.52	1.77	3.26
45	0	0	0	0	2.09	2.81	1.77	3.14
47	0	0	0	0	2.19	2.88	1.77	3.39
50	0	0	0	0	2.03	2.76	1.77	3.07
52	0	0	0	0	2.16	2.82	1.77	3.38
54	0	0	0	0	2.10	2.77	1.77	2.53
56	0	0	0	0	1.91	2.60	1.77	2.35
59	0	0	0	0	2.07	2.83	1.77	3.00

B.5.1.2 $Sr_2Ho_{0.20}Tb_{0.80}Ru_{0.90}Cu_{0.10}O_6$

The crystal structure (atomic and thermal parameters) used for the refinements was the HRPD 20 K structure of $Sr_2HoRu_{0.95}Cu_{0.05}O_6$.

Temperature	Lattice Parameters				
/ K	a / Å	b / Å	c / Å	β / °	Volume / Å^3
2	5.78311 (13)	5.80394 (13)	5.80394 (37)	90.354 (2)	274.709 (25)
2	5.78294 (15)	5.80378 (15)	5.80378 (42)	90.356 (2)	274.677 (28)
7	5.78316 (16)	5.80400 (16)	5.80400 (44)	90.353 (2)	274.718 (30)
10	5.78306 (13)	5.80389 (13)	5.80389 (36)	90.355 (2)	274.699 (24)
11	5.78322 (15)	5.80406 (16)	5.80406 (43)	90.353 (2)	274.730 (29)
16	5.78296 (15)	5.80380 (16)	5.80380 (44)	90.356 (2)	274.681 (30)
20	5.78302 (13)	5.80387 (13)	5.80387 (36)	90.355 (2)	274.693 (24)
21	5.78308 (15)	5.80392 (16)	5.80392 (43)	90.354 (2)	274.703 (29)
25	5.78311 (15)	5.80395 (15)	5.80395 (42)	90.354 (2)	274.710 (28)
29	5.78305 (13)	5.80389 (13)	5.80389 (37)	90.354 (2)	274.698 (25)
30	5.78317 (15)	5.80402 (16)	5.80402 (44)	90.353 (2)	274.722 (29)
34	5.78302 (15)	5.80387 (16)	5.80387 (44)	90.355 (2)	274.694 (29)
39	5.78314 (13)	5.80399 (13)	5.80399 (36)	90.353 (2)	274.717 (24)
39	5.78294 (15)	5.80379 (16)	5.80379 (44)	90.355 (2)	274.679 (30)
40	5.78314 (13)	5.80399 (13)	5.80399 (36)	90.352 (2)	274.717 (25)
44	5.78302 (15)	5.80386 (16)	5.80386 (44)	90.353 (2)	274.693 (30)
49	5.78301 (16)	5.80386 (16)	5.80386 (45)	90.353 (2)	274.692 (30)
50	5.78306 (13)	5.80391 (13)	5.80391 (36)	90.352 (2)	274.702 (24)
53	5.78290 (15)	5.80373 (15)	5.80373 (43)	90.354 (2)	274.670 (29)
57	5.78297 (16)	5.80382 (16)	5.80382 (45)	90.353 (2)	274.686 (30)
58	5.78299 (13)	5.80383 (13)	5.80383 (36)	90.353 (2)	274.688 (25)
59	5.78300 (15)	5.80384 (15)	5.80384 (42)	90.353 (2)	274.690 (28)

Temperature / K	Magnetic Moment / μ_B				R_p / %	R_{wp} / %	R_{exp} / %	R_{F^2} / %
	Ru^{5+}		Ln^{3+}					
	z	xy	z	total				
2	1.94(12)	0.82(20)	4.54(7)	4.61(6)	1.38	2.28	0.63	4.50
2	1.89(12)	0.78(23)	4.52(8)	4.59(7)	1.84	2.59	1.55	5.87
7	1.94(13)	0.83(24)	4.34(9)	4.42(8)	1.94	2.72	1.55	5.56
10	1.94(12)	0.81(20)	4.31(7)	4.39(6)	1.34	2.21	0.63	4.51
11	1.99(13)	0	4.05(8)	4.05(8)	1.81	2.67	1.55	5.10
16	1.86(14)	0	3.76(9)	3.76(9)	1.82	2.69	1.56	5.60
20	1.90(13)	0	3.64(8)	3.64(8)	1.30	2.19	0.64	4.67
21	1.70(15)	0	3.40(10)	3.40(10)	1.82	2.63	1.56	4.44
25	1.65(17)	0	2.82(12)	2.82(12)	1.77	2.52	1.56	4.36
29	1.64(17)	0	2.60(12)	2.60(12)	1.29	2.19	0.64	4.21
30	1.28(24)	0	1.99(19)	1.99(19)	1.86	2.62	1.56	6.17
34	0.92(150)	0	0.65(124)	0.65(124)	1.77	2.59	1.56	4.62
39	0	0	0	0	1.28	2.15	0.64	4.09
39	0	0	0	0	1.73	2.60	1.56	4.11
40	0	0	0	0	1.29	2.15	0.64	4.05
44	0	0	0	0	1.84	2.60	1.56	4.69
49	0	0	0	0	1.83	2.64	1.56	4.21
50	0	0	0	0	1.25	2.13	0.64	3.83
53	0	0	0	0	1.69	2.53	1.56	4.78
57	0	0	0	0	1.85	2.63	1.56	4.00
58	0	0	0	0	1.28	2.14	0.63	4.08
59	0	0	0	0	1.78	2.44	1.56	3.78

B.6 Neutron Diffraction Refinements of $Ba_2PrRu_{1-x}Cu_xO_6$

B.6.1 D1A Refinements

B.6.1.1 Ba_2PrRuO_6

Ba_2PrRuO_6		$P2_1/n$			5 K		
a / Å		b / Å	c / Å	β / °	Volume / Å^3		
5.95311(9)		5.95807(9)	8.46207(25)	89.828(1)	300.140(18)		
Atom	Site	x	y	z	Occ	B_{iso}/Å^2	μ/μ_B
Ba	4*e*	0.0112(29)	0.0091(48)	0.7517(22)	1.000	0.29(12)	
Pr	2*c*	0	½	0	1.000	0.46(7)	1.14(11)
Ru	2*d*	½	0	0	1.000	0.46(7)	1.82(15)
O1	4*e*	0.2452(44)	0.2941(21)	0.5200(18)	1.000	0.53(6)	
O2	4*e*	0.2443(61)	-0.2741(20)	0.5106(22)	1.000	0.53(6)	
O3	4*e*	-0.0296(23)	0.5046(44)	0.7334(12)	1.000	0.53(6)	

R_p = 6.24 %, R_{wp} = 8.19 %, R_{exp} = 7.45 %, R_{F^2} = 4.16 %

Ba_2PrRuO_6		$P2_1/n$			60 K		
a / Å		b / Å	c / Å	β / °	Volume / Å^3		
5.95348(9)		5.95844(9)	8.46313(26)	89.823(1)	300.215(18)		
Atom	Site	x	y	z	Occ	B_{iso}/Å^2	μ/μ_B
Ba	4*e*	0.0110(30)	0.0089(50)	0.7523(22)	1.000	0.39(12)	
Pr	2*c*	0	½	0	1.000	0.52(7)	1.08(12)
Ru	2*d*	½	0	0	1.000	0.52(7)	1.66(16)
O1	4*e*	0.2461(46)	0.2939(23)	0.5201(19)	1.000	0.59(7)	
O2	4*e*	0.2438(63)	-0.2746(21)	0.5110(23)	1.000	0.59(7)	
O3	4*e*	-0.0279(23)	0.5032(44)	0.7336(12)	1.000	0.59(7)	

R_p = 6.31 %, R_{wp} = 8.25 %, R_{exp} = 7.44 %, R_{F^2} = 4.01 %

Ba_2PrRuO_6		$P2_1/n$			150 K		
a / Å		b / Å	c / Å	β / °	Volume / Å^3		
5.96248(7)		5.96746(7)	8.45401(20)	89.781(1)	300.799(15)		
Atom	Site	x	y	z	Occ	B_{iso}/Å^2	μ/μ_B
Ba	4*e*	0.0037(28)	0.0065(48)	0.7524(26)	1.000	0.62(9)	
Pr	2*c*	0	½	0	1.000	0.52(7)	
Ru	2*d*	½	0	0	1.000	0.52(7)	
O1	4*e*	0.2412(42)	0.2899(23)	0.5178(21)	1.000	0.74(5)	
O2	4*e*	0.2427(57)	-0.2704(24)	0.5089(25)	1.000	0.74(5)	
O3	4*e*	-0.0308(23)	0.5031(44)	0.7303(12)	1.000	0.74(5)	

R_p = 5.32 %, R_{wp} = 7.11 %, R_{exp} = 7.42 %, R_{F^2} = 4.54 %

B.6.1.2 $Ba_2PrRu_{0.90}Cu_{0.10}O_6$

$Ba_2PrRu_{0.90}Cu_{0.10}O_6$		$P2_1/n$			5 K		
a / Å		b / Å	c / Å	β / °	Volume / Å^3		
5.95396(5)		5.95892(5)	8.46448(14)	89.817(1)	300.311(10)		
Atom	Site	x	y	z	Occ	B_{iso}/Å^2	μ/μ_B
Ba	4*e*	0.0102(14)	-0.0009(48)	0.7568(10)	1.000	0.35(6)	
Pr	2*c*	0	½	0	1.000	0.39(6)	1.29(7)
Ru	2*d*	½	0	0	0.900	0.39(6)	1.98(13)
Cu	2*d*	½	0	0	0.100	0.39(6)	
O1	4*e*	0.2491(32)	0.2874(28)	0.5174(16)	1.000	0.68(5)	
O2	4*e*	0.2426(37)	-0.2769(26)	0.5125(18)	1.000	0.68(5)	
O3	4*e*	-0.0348(12)	0.5042(60)	0.7368(7)	1.000	0.68(5)	

R_p = 6.55 %, R_{wp} = 8.66 %, R_{exp} = 7.25 %, R_{F^2} = 6.44 %

$Ba_2PrRu_{0.90}Cu_{0.10}O_6$		$P2_1/n$			50 K		
a / Å		b / Å	c / Å	β / °	Volume / Å^3		
5.95409(5)		5.95905(5)	8.46490(13)	89.815(1)	300.340(9)		
Atom	Site	x	y	z	Occ	B_{iso}/Å^2	μ/μ_B
Ba	4*e*	0.0104(15)	0.0047(42)	0.7560(10)	1.000	0.41(7)	
Pr	2*c*	0	½	0	1.000	0.44(5)	1.29(19)
Ru	2*d*	½	0	0	0.900	0.44(5)	1.71(29)
Cu	2*d*	½	0	0	0.100	0.44(5)	
O1	4*e*	0.2434(25)	0.2871(34)	0.5142(23)	1.000	0.76(4)	
O2	4*e*	0.2533(24)	-0.2794(32)	0.5161(22)	1.000	0.76(4)	
O3	4*e*	-0.0324(11)	0.4991(36)	0.7376(7)	1.000	0.76(4)	

R_p = 6.26 %, R_{wp} = 8.35 %, R_{exp} = 7.24 %, R_{F^2} = 5.71 %

$Ba_2PrRu_{0.90}Cu_{0.10}O_6$		$P2_1/n$			125 K		
a / Å		b / Å	c / Å	β / °	Volume / Å^3		
5.96237(4)		5.96744(4)	8.45395(11)	89.782(1)	300.791(9)		
Atom	Site	x	y	z	Occ	B_{iso}/Å^2	μ/μ_B
Ba	4*e*	0.0031(14)	0.0012(40)	0.7562(10)	1.000	0.60(5)	
Pr	2*c*	0	½	0	1.000	0.51(5)	
Ru	2*d*	½	0	0	0.900	0.51(5)	
Cu	2*d*	½	0	0	0.100	0.51(5)	
O1	4*e*	0.2423(22)	0.2856(15)	0.5176(13)	1.000	0.80(4)	
O2	4*e*	0.2481(25)	-0.2745(15)	0.5101(14)	1.000	0.80(4)	
O3	4*e*	-0.0348(12)	0.5016(35)	0.7344(7)	1.000	0.80(4)	

R_p = 5.33 %, R_{wp} = 7.26 %, R_{exp} = 7.21 %, R_{F^2} = 4.97 %

B.6.2 D1B Refinements

B.6.2.1 $Ba_2PrRu_{0.90}Cu_{0.10}O_6$

The crystal structure (atomic and thermal parameters) used for the refinements was the D1A 50 K structure of $Ba_2PrRu_{0.90}Cu_{0.10}O_6$.

Temperature	Lattice Parameters				
/ K	a / Å	b / Å	c / Å	β / °	Volume / Å^3
2	5.95398(14)	5.95894(14)	8.46636(40)	89.799(2)	300.380(28)
4	5.95414(14)	5.95909(14)	8.46680(41)	89.797(2)	300.411(29)
5	5.95410(14)	5.95906(14)	8.46670(41)	89.797(2)	300.404(29)
7	5.95405(14)	5.95901(14)	8.46656(41)	89.798(2)	300.394(29)
8	5.95405(14)	5.95900(14)	8.46655(41)	89.798(2)	300.393(29)
9	5.95405(14)	5.95901(14)	8.46656(40)	89.798(2)	300.394(28)
10	5.95411(14)	5.95907(14)	8.46673(41)	89.797(2)	300.406(29)
11	5.95402(14)	5.95898(14)	8.46648(41)	89.798(2)	300.388(29)
12	5.95406(14)	5.95902(14)	8.46660(41)	89.798(2)	300.396(29)
13	5.95403(14)	5.95899(14)	8.46652(40)	89.798(2)	300.391(29)
15	5.95405(14)	5.95900(14)	8.46656(40)	89.798(2)	300.393(28)
16	5.95408(14)	5.95903(14)	8.46664(41)	89.797(2)	300.399(29)
17	5.95413(14)	5.95909(14)	8.46680(41)	89.797(2)	300.410(29)
18	5.95417(14)	5.95912(14)	8.46690(41)	89.796(2)	300.418(29)
20	5.95427(14)	5.95922(14)	8.46719(40)	89.795(2)	300.438(28)
21	5.95415(14)	5.95910(14)	8.46684(41)	89.797(2)	300.413(29)
22	5.95427(14)	5.95922(14)	8.46718(41)	89.795(2)	300.438(29)
24	5.95423(14)	5.95919(14)	8.46708(41)	89.795(2)	300.430(29)
25	5.95423(14)	5.95918(14)	8.46706(41)	89.796(2)	300.429(29)
26	5.95427(14)	5.95923(14)	8.46720(41)	89.795(2)	300.439(29)
28	5.95445(14)	5.95940(14)	8.46771(41)	89.792(2)	300.475(29)
29	5.95428(14)	5.95923(14)	8.46721(41)	89.795(2)	300.439(29)
30	5.95422(14)	5.95917(14)	8.46704(41)	89.795(2)	300.427(29)
31	5.95415(14)	5.95911(14)	8.46686(41)	89.796(2)	300.414(29)
33	5.95392(14)	5.95887(14)	8.46619(40)	89.800(2)	300.367(28)
34	5.95386(14)	5.95882(14)	8.46602(40)	89.800(2)	300.356(28)
36	5.95387(14)	5.95882(14)	8.46604(40)	89.800(2)	300.357(28)
37	5.95389(15)	5.95885(15)	8.46611(42)	89.800(2)	300.361(30)
38	5.95387(14)	5.95882(14)	8.46604(41)	89.800(2)	300.357(29)
40	5.95392(15)	5.95887(15)	8.46617(42)	89.800(2)	300.366(30)
41	5.95393(15)	5.95888(15)	8.46620(42)	89.799(2)	300.368(30)
42	5.95390(15)	5.95885(15)	8.46613(42)	89.800(2)	300.363(30)
44	5.95399(15)	5.95894(15)	8.46637(43)	89.799(2)	300.380(30)
45	5.95399(15)	5.95894(15)	8.46638(44)	89.799(2)	300.381(31)
47	5.95401(16)	5.95896(15)	8.46643(44)	89.798(2)	300.385(31)
48	5.95399(16)	5.95894(16)	8.46637(45)	89.799(2)	300.380(32)
50	5.95397(16)	5.95892(16)	8.46633(46)	89.799(2)	300.377(33)
63	5.95413(17)	5.95908(17)	8.46678(48)	89.797(2)	300.409(34)
71	5.95441(17)	5.95936(17)	8.46757(48)	89.793(2)	300.465(34)
79	5.95432(16)	5.95927(16)	8.46731(47)	89.794(2)	300.447(33)
85	5.95451(17)	5.95946(17)	8.46789(49)	89.791(2)	300.487(35)

91	5.95469(18)	5.95964(18)	8.46839(52)	89.789(3)	300.522(37)
98	5.95485(19)	5.95980(19)	8.46884(55)	89.787(3)	300.554(39)
104	5.95510(20)	5.96005(20)	8.46957(56)	89.783(3)	300.605(40)
110	5.95538(22)	5.96033(22)	8.47037(62)	89.779(3)	300.663(44)
117	5.95554(22)	5.96049(22)	8.47083(64)	89.777(3)	300.694(45)
122	5.95552(23)	5.96047(22)	8.47078(65)	89.777(3)	300.691(46)
125	5.95583(23)	5.96078(23)	8.47166(66)	89.773(3)	300.753(47)
127	5.95628(23)	5.96122(23)	8.47294(66)	89.767(3)	300.844(46)
129	5.95639(24)	5.96134(24)	8.47326(68)	89.765(3)	300.866(48)
130	5.95630(23)	5.96125(23)	8.47302(67)	89.766(3)	300.849(47)

Temperature / K	Magnetic Moment / μ_B				R_p / %	R_{wp} / %	R_{exp} / %	R_{F^2} / %
	Ru^{5+}		Pr^{3+}					
	z	xy	z	total				
2	1.97(17)	0.65	1.14(11)	1.32(10)	2.18	3.60	0.76	6.26
4	1.99(17)	0.65	1.14(11)	1.31(10)	2.32	3.68	0.80	6.15
5	1.98(18)	0.65	1.16(12)	1.33(10)	2.32	3.68	0.80	6.06
7	2.00(16)	0.65	1.11(11)	1.29(9)	2.31	3.71	0.80	6.41
8	1.96(18)	0.65	1.18(13)	1.35(11)	2.29	3.70	0.80	6.41
9	1.95(17)	0.65	1.13(11)	1.30(10)	2.26	3.65	0.80	6.45
10	1.94(18)	0.65	1.12(12)	1.29(10)	2.44	3.73	1.00	6.17
11	1.99(16)	0.65	1.12(11)	1.29(10)	2.32	3.72	0.80	6.43
12	1.97(17)	0.65	1.14(12)	1.31(10)	2.32	3.71	0.80	6.50
13	1.92(19)	0.65	1.19(13)	1.35(12)	2.34	3.66	0.80	6.21
15	1.91(19)	0.65	1.19(13)	1.35(12)	2.24	3.60	0.80	6.29
16	1.93(19)	0.65	1.17(13)	1.34(11)	2.36	3.71	0.80	6.44
17	1.95(17)	0.65	1.15(12)	1.32(10)	2.33	3.71	0.80	6.26
18	1.88(20)	0.65	1.17(14)	1.34(12)	2.34	3.68	0.80	6.55
20	1.96(18)	0.65	1.17(12)	1.33(11)	2.31	3.66	0.80	6.38
21	1.92(19)	0.65	1.16(13)	1.33(11)	2.36	3.73	0.80	6.15
22	1.99(17)	0.65	1.14(11)	1.31(10)	2.31	3.68	0.80	6.14
24	1.92(19)	0.65	1.16(13)	1.33(11)	2.32	3.70	0.80	6.49
25	1.90(18)	0.65	1.12(12)	1.30(11)	2.30	3.73	0.80	6.44
26	1.94(17)	0.65	1.12(12)	1.29(10)	2.31	3.72	0.80	6.31
28	1.92(18)	0.65	1.13(12)	1.31(11)	2.29	3.68	0.80	6.36
29	1.94(18)	0.65	1.13(12)	1.31(10)	2.24	3.71	0.80	6.61
30	1.90(19)	0.65	1.16(14)	1.33(12)	2.30	3.73	0.80	6.62
31	1.95(18)	0.65	1.13(12)	1.31(10)	2.31	3.73	0.80	6.37
33	1.95(17)	0.65	1.12(11)	1.29(10)	2.29	3.66	0.80	6.73
34	1.90(19)	0.65	1.14(13)	1.32(11)	2.31	3.66	0.80	6.48
36	1.90(18)	0.65	1.11(12)	1.28(10)	2.28	3.65	0.80	6.57
37	1.88(19)	0.65	1.11(13)	1.28(11)	2.34	3.81	0.80	6.57
38	1.85(19)	0.65	1.10(13)	1.28(11)	2.26	3.68	0.80	6.07
40	1.87(19)	0.65	1.11(13)	1.28(11)	2.38	3.83	0.80	6.63
41	1.88(18)	0.65	1.08(12)	1.26(11)	2.40	3.84	0.80	6.50
42	1.76(22)	0.65	1.12(16)	1.30(14)	2.35	3.83	0.80	6.22
44	1.83(20)	0.65	1.10(14)	1.28(12)	2.36	3.89	0.80	6.80

45	1.76(23)	0.65	1.10(16)	1.27(14)	2.44	3.97	0.80	6.55
47	1.75(22)	0.65	1.09(16)	1.27(14)	2.51	4.01	0.80	6.73
48	1.77(21)	0.65	1.07(15)	1.25(13)	2.56	4.09	0.80	6.63
50	1.75(23)	0.65	1.06(16)	1.25(14)	2.56	4.18	0.79	6.60
63	1.67(27)	0.65	1.10(20)	1.28(17)	3.07	4.38	2.44	6.18
71	1.62(27)	0.65	1.03(20)	1.22(17)	2.91	4.38	1.89	6.10
79	1.70(20)	0.65	0.93(14)	1.14(12)	2.90	4.33	1.89	6.32
85	1.45(31)	0.65	0.92(24)	1.13(19)	3.00	4.55	1.89	6.22
91	1.23(45)	0.65	0.83(34)	1.06(27)	3.13	4.86	1.89	6.26
98	1.08(20)	0.65	0.70(14)	0.95(11)	3.30	5.12	1.89	6.46
104	0.84(30)	0.65	0.69(23)	0.95(17)	3.22	5.24	1.90	5.20
110	0	0	0	0	3.54	5.80	1.90	5.47
117	0	0	0	0	3.57	6.01	1.90	5.34
122	0	0	0	0	3.57	6.06	1.90	5.33
125	0	0	0	0	3.65	6.15	1.91	4.81
127	0	0	0	0	3.37	6.12	1.35	5.52
129	0	0	0	0	3.45	6.36	1.35	5.39
130	0	0	0	0	3.36	6.26	1.35	5.34

B.7 Absorption for Neutrons

The linear attenuation factor, μ, is calculated from the incoherent and absorption neutron cross sections, accounting for both the wavelength and density of the material, using the National Institute of Science and Technology (NIST) website (http://www.ncnr.nist.gov/cgi-bin/neutcalc). The table below shows the μ values for the mixed ruthenium-copper oxides, using a wavelength of 1.8 Å and assuming 60 % packing of the material.

Compound	Linear Attenuation Coefficient μ / cm^{-1}			
	$x = 0.00$	$x = 0.05$	$x = 0.10$	$x = 0.15$
$Sr_2YRu_{1-x}Cu_xO_6$	0.053	0.054	0.054	0.055
$Ba_2YRu_{1-x}Cu_xO_6$	0.048	0.049	0.049	0.050
$Sr_2HoRu_{1-x}Cu_xO_6$	0.529	0.532	0.534	0.536
$Sr_2TbRu_{1-x}Cu_xO_6$	0.212	0.213	0.214	0.216
$Ba_2PrRu_{1-x}Cu_xO_6$	0.112	0.113	0.113	0.114

From these μ values, the absorption coefficient, A, required by GSAS can be calculated via, $A = \mu R/ \lambda$, where R is the radius of the vanadium can in cm, and λ is the wavelength (Å). The form may be slightly unfamiliar due to the inclusion of the wavelength, though this facilitates use of the absorption parameter A, for both constant wavelength and time-of-flight neutron diffraction. (The parameter A is largely independent of wavelength, as absorption decreases linearly with wavelength.) For none of the samples did $\mu R > 30$, and so the absorption here did not prevent refinement.

B.8 X-Ray Diffraction Refinements of $Sr_2TbRu_{0.90}Cu_{0.10}O_6$

B.8.1 ESRF Refinements

B.8.1.1 Non-anomalous Wavelength

The diffraction pattern was measured at BM1B using the wavelength, $\lambda = 0.5006$ Å.

Refined with a fully ordered *B* cation arrangement and ordering peaks excluded. Discussed on pages 153-154.

$Sr_2TbRu_{0.90}Cu_{0.10}O_6$		$P2_1/n$			Room temperature	
a / Å		*b* / Å	*c* / Å	*β* / °	Volume / Å^3	
5.79773(4)		5.81657(4)	8.20683(5)	90.245(1)	276.756(2)	
Atom	Site	*x*	*y*	*z*	Occ	B_{iso}/Å^2
Sr	4*e*	0.0021(4)	0.0301(1)	0.7518(4)	1.000(0)	2.23(2)
Tb	2*c*	0	½	0	1.000(0)	1.61(1)
Ru	2*d*	½	0	0	0.900(0)	1.61(1)
Cu	2*d*	½	0	0	0.100(0)	1.61(1)
O1	4*e*	0.2761(20)	0.2955(18)	0.5312(15)	1.000(0)	1.98(19)
O2	4*e*	0.2066(21)	-0.2198(20)	0.5348(14)	1.000(0)	2.29(17)
O3	4*e*	-0.0795(20)	0.4820(9)	0.7400(13)	1.000(0)	2.32(17)

$R_p = 3.59$ %, $R_{wp} = 4.99$ %, $R_{exp} = 3.23$ %, $R_{F^2} = 11.21$ %

Refined with a fully ordered *B* cation arrangement and ordering peaks included. Discussed on page 155.

$Sr_2TbRu_{0.90}Cu_{0.10}O_6$		$P2_1/n$			Room temperature	
a / Å		*b* / Å	*c* / Å	*β* / °	Volume / Å^3	
5.79771(4)		5.81660(4)	8.20685(5)	90.245(1)	276.757(2)	
Atom	Site	*x*	*y*	*z*	Occ	B_{iso}/Å^2
Sr	4*e*	0.0023(4)	0.0298(1)	0.7506(4)	1.000(0)	2.13(1)
Tb	2*c*	0	½	0	1.000(0)	1.60(1)
Ru	2*d*	½	0	0	0.900(0)	1.60(1)
Cu	2*d*	½	0	0	0.100(0)	1.60(1)
O1	4*e*	0.2770(14)	0.3155(14)	0.5279(12)	1.000(0)	2.02(16)
O2	4*e*	0.1853(16)	-0.2278(16)	0.5248(14)	1.000(0)	2.32(17)
O3	4*e*	-0.0473(13)	0.4839(9)	0.7276(9)	1.000(0)	2.31(16)

$R_p = 3.84$ %, $R_{wp} = 5.47$ %, $R_{exp} = 3.23$ %, $R_{F^2} = 10.18$ %

Refined with partial exchange of Tb and Ru between the 2*c* and 2*d* sites. Discussed on pages 157-161.

$Sr_2TbRu_{0.90}Cu_{0.10}O_6$		$P2_1/n$			Room temperature	
a / Å		*b* / Å	*c* / Å	*β* / °	Volume / Å^3	
5.79769(4)		5.81659(4)	8.20683(5)	90.245(1)	276.755(2)	
Atom	Site	*x*	*y*	*z*	Occ	B_{iso}/Å^2
Sr	4*e*	0.0049(3)	0.0295(1)	0.7497(3)	1.000(0)	2.23
Tb	2*c*	0	½	0	0.887(2)	1.61
Ru	2*c*	0	½	0	0.113(2)	1.61
Tb	2*d*	½	0	0	0.113(2)	1.61
Ru	2*d*	½	0	0	0.787(2)	1.61
Cu	2*d*	½	0	0	0.100(0)	1.61
O1	4*e*	0.2688(14)	0.2985(14)	0.5361(12)	1.000(0)	1.98
O2	4*e*	0.2005(15)	-0.2281(14)	0.5370(10)	1.000(0)	2.29
O3	4*e*	-0.0761(14)	0.4823(9)	0.7340(9)	1.000(0)	2.32

R_p = 3.51 %, R_{wp} = 4.90 %, R_{exp} = 3.23 %, R_{F^2} = 9.47 %

Refined with partial exchange of Tb and Cu between the 2*c* and 2*d* sites. Discussed on page 161.

$Sr_2TbRu_{0.90}Cu_{0.10}O_6$		$P2_1/n$			Room temperature	
a / Å		*b* / Å	*c* / Å	*β* / °	Volume / Å^3	
5.79769(4)		5.81659(4)	8.20683(5)	90.245(1)	276.755(2)	
Atom	Site	*x*	*y*	*z*	Occ	B_{iso}/Å^2
Sr	4*e*	0.0048(3)	0.0295(1)	0.7498(3)	1.000(0)	2.23
Tb	2*c*	0	½	0	0.926(2)	1.61
Cu	2*c*	0	½	0	0.074(2)	1.61
Tb	2*d*	½	0	0	0.074(2)	1.61
Ru	2*d*	½	0	0	0.900(2)	1.61
Cu	2*d*	½	0	0	0.026(0)	1.61
O1	4*e*	0.2694(14)	0.2983(14)	0.5360(12)	1.000(0)	1.98
O2	4*e*	0.2008(15)	-0.2275(14)	0.5369(10)	1.000(0)	2.29
O3	4*e*	-0.0760(14)	0.4822(9)	0.7343(9)	1.000(0)	2.32

R_p = 3.51 %, R_{wp} = 4.90 %, R_{exp} = 3.23 %, R_{F^2} = 9.47 %

As the crystal structure does not change appreciably for small partial exchanges of *B* cations, the lattice parameters, atomic coordinates and thermal parameters, as refined for the partial exchange for Tb and Ru listed above, were used for the following refinements. The Cu exchange was set at 1 % increments, and the remaining Ru and Tb partial transfer was refined. These results are discussed on pages 161-162 with the disorder diagram on the page 162.

Copper (%)	Ruthenium (%)	R_p (%)	R_{wp} (%)	R_{exp} (%)	R_{F^2} (%)
0.0(1)	11.3(2)	4.90	3.51	3.24	9.47
1.0(1)	9.8(2)	4.90	3.51	3.24	9.47
2.0(1)	8.2(2)	4.90	3.51	3.24	9.47
3.0(1)	6.7(2)	4.90	3.51	3.24	9.47
4.0(1)	5.1(2)	4.90	3.51	3.24	9.47
5.0(1)	3.6(2)	4.90	3.51	3.24	9.47
6.0(1)	2.1(2)	4.89	3.51	3.23	9.47
7.0(1)	0.5(2)	4.89	3.51	3.23	9.47
7.4(1)	0.0(2)	4.90	3.51	3.23	9.47

B.8.1.2 Anomalous Wavelengths

The crystal structure model used was determined from the refinement of the non-anomalous data, which was refined with partial exchange of Tb and Ru between the 2*c* and 2*d* sites.

$Sr_2TbRu_{0.90}Cu_{0.10}O_6$		$P2_1/n$			Room temperature	
a / Å		*b* / Å	*c* / Å	*β* / °	Volume / Å^3	
5.79769(4)		5.81659(4)	8.20683(5)	90.245(1)	276.755(2)	
Atom	Site	*x*	*y*	*z*	Occ	B_{iso}/Å^2
Sr	4*e*	0.0049(3)	0.0295(1)	0.7497(3)	1.000(0)	2.23
Tb	2*c*	0	½	0	0.887(2)	1.61
Ru	2*c*	0	½	0	0.113(2)	1.61
Tb	2*d*	½	0	0	0.113(2)	1.61
Ru	2*d*	½	0	0	0.787(2)	1.61
Cu	2*d*	½	0	0	0.100(0)	1.61
O1	4*e*	0.2688(14)	0.2985(14)	0.5361(12)	1.000(0)	1.98
O2	4*e*	0.2005(15)	-0.2281(14)	0.5370(10)	1.000(0)	2.29
O3	4*e*	-0.0761(14)	0.4823(9)	0.7340(9)	1.000(0)	2.32

R_p = 3.51 %, R_{wp} = 4.90 %, R_{exp} = 3.23 %, R_{F^2} = 9.47 %

It is repeated above here for clarity, though the occupancy was refined away from these values as indicated in the table below.

Energy / eV	Partial Transfer of Tb with		R_p	R_{wp}	R_{exp}	R_{F^2}
	Ru / %	Cu / %	/ %	/ %	/ %	/ %
22050	6.5(3)	0	5.48	7.62	2.94	7.48
	0	4.8(2)	5.48	7.62	2.94	7.55
22100	6.8(2)	0	5.49	7.81	3.15	3.70
	0	5.6(1)	5.49	7.81	3.15	3.70
22130	10.3(1)	0	5.26	7.23	2.87	5.01
	0	10.1(1)	5.28	7.25	2.87	5.13
22147	7.2(2)	0	4.67	6.42	2.66	4.39
	0	6.0(2)	4.66	6.41	2.66	4.32
22165	9.4(2)	0	4.73	6.47	2.79	1.46
	0	7.5(2)	4.73	6.47	2.79	1.52

These values were used in the disorder plots on pages 187 and 188, and were discussed in the main text on pages 184-189.

B.8.2 SRS Refinements

For $Sr_2TbRu_{0.90}Cu_{0.10}O_6$, **all** the refinements of the partial transfers of *B* cations between the 2*c* and 2*d* sites used the crystal structure model as refined from the non-anomalous data measured at the ESRF. Of course, the occupancies were refined away from these values, as detailed below.

$Sr_2TbRu_{0.90}Cu_{0.10}O_6$		$P2_1/n$			Room temperature	
a / Å		*b* / Å	*c* / Å	*β* / °	Volume / Å^3	
5.79769(4)		5.81659(4)	8.20683(5)	90.245(1)	276.755(2)	
Atom	Site	*x*	*y*	*z*	Occ	B_{iso}/Å^2
Sr	4*e*	0.0049(3)	0.0295(1)	0.7497(3)	1.000(0)	2.23
Tb	2*c*	0	½	0	0.887(2)	1.61
Ru	2*c*	0	½	0	0.113(2)	1.61
Tb	2*d*	½	0	0	0.113(2)	1.61
Ru	2*d*	½	0	0	0.787(2)	1.61
Cu	2*d*	½	0	0	0.100(0)	1.61
O1	4*e*	0.2688(14)	0.2985(14)	0.5361(12)	1.000(0)	1.98
O2	4*e*	0.2005(15)	-0.2281(14)	0.5370(10)	1.000(0)	2.29
O3	4*e*	-0.0761(14)	0.4823(9)	0.7340(9)	1.000(0)	2.32

R_p = 3.51 %, R_{wp} = 4.90 %, R_{exp} = 3.23 %, R_{F^2} = 9.47 %

The refinements of the partial exchange of the *B* cations between the 2*c* and 2*d* sites for $Sr_2TbRu_{0.90}Cu_{0.10}O_6$ from SRS data are summarised below.

Energy / eV	Partial Transfer of Tb with		R_p / %	R_{wp} / %	R_{exp} / %	R_{F^2} / %
	Ru / %	Cu / %				
12374 (1 Å)	12.0(4)	0	7.09	8.90	7.15	10.25
	0	7.8(3)	7.08	8.90	7.15	10.25
7470 (below Tb edge)	50.4(66)	0	9.30	12.09	7.42	8.06
	0	12.1(17)	9.30	12.09	7.41	8.08
7514 (at Tb edge)	-95.8(80)	0	5.39	6.90	4.54	15.18
	0	31.6(14)	5.35	6.84	4.54	14.38
8960 eV (at Cu edge)	16.3(9)	0	5.33	8.00	6.31	24.23
	0	8.8(5)	5.33	8.00	6.31	24.22

The corresponding discussion of these results is on pages 177–184. Clearly, the refinements at the Tb edge lead to unphysical solutions, as was discussed in the main body of the text. For the Tb edge data (7470 eV), for 100 % and random ordering of the *B* cations, the *R*-factors were R_p = 9.36 %, R_{wp} = 12.18 % and R_{exp} = 7.42 % and R_p = 9.30 %, R_{wp} = 12.10 % and R_{exp} = 7.42 % respectively. (Discussion is on page 179). For the Tb edge data (7514 eV), for 100 % and random ordering of the *B* cations, the *R*-factors were R_p = 5.43 %, R_{wp} = 6.95 % and R_{exp} = 4.54 % for both. (Discussion is on pages 180-181).

B.9 X-Ray Diffraction Refinements of $Sr_2YRu_{0.85}Cu_{0.15}O_6$

B.9.1 ESRF Refinements

The only diffraction pattern of $Sr_2YRu_{0.85}Cu_{0.15}O_6$ was measured at the non-anomalous wavelength of $\lambda = 0.50029$ Å.

Refined with partial exchange of Y and Cu between the 2*c* and 2*d* sites. Discussed on pages 163-165.

$Sr_2YRu_{0.85}Cu_{0.15}O_6$		$P2_1/n$			Room temperature	
a / Å		*b* / Å	*c* / Å	*β* / °	Volume / Å^3	
5.77596(2)		5.78744(2)	8.17145(3)	90.249(1)	273.153(1)	
Atom	Site	*x*	*y*	*z*	Occ	B_{iso}/Å^2
Sr	4*e*	0.0083(4)	0.0264(1)	0.7508(3)	1.000(0)	1.77(1)
Y	2*c*	0	½	0	0.863(11)	1.34(1)
Cu	2*c*	0	½	0	0.137(11)	1.34(1)
Ru	2*d*	½	0	0	0.850(0)	1.34(1)
Cu	2*d*	½	0	0	0.013(11)	1.34(1)
Y	2*d*	½	0	0	0.137(11)	1.34(1)
O1	4*e*	0.2898(22)	0.2692(21)	0.9652(16)	1.000(0)	1.95(13)
O2	4*e*	0.2832(21)	0.3069(21)	0.5366(15)	1.000(0)	1.46(12)
O3	4*e*	0.9400(17)	0.4858(11)	0.7443(14)	1.000(0)	1.38(12)

$R_p = 2.58$ %, $R_{wp} = 3.54$ %, $R_{exp} = 3.21$ %, $R_{F^2} = 8.35$ %

The same crystal structure model was used for refinements of 100 % ordered and a random ordering of the *B* cations, yielding the *R*-factors $R_p = 2.60$ %, $R_{wp} = 3.58$ %, $R_{exp} = 3.20$ % and $R_{F^2} = 8.52$ % and $R_p = 2.61$ %, $R_{wp} = 3.66$ %, $R_{exp} = 3.20$ % and $R_{F^2} = 8.62$ % respectively, as discussed on pages 164-165.

With the inclusion of the impurities, the main phase was not further refined. The impurities are discussed on pages 165-170.

First Phase

$Sr_2YRu_{0.85}Cu_{0.15}O_6$		$P2_1/n$			Room temperature	
a / Å		b / Å	c / Å	β / °	Volume / Å^3	
5.77596		5.78744	8.17145	90.249	273.153	
Atom	Site	x	y	z	Occ	B_{iso}/Å^2
Sr	4*e*	0.0083	0.0264	0.7508	1.000	1.77
Y	2*c*	0	½	0	0.863	1.34
Cu	2*c*	0	½	0	0.137	1.34
Ru	2*d*	½	0	0	0.850	1.34
Cu	2*d*	½	0	0	0.013	1.34
Y	2*d*	½	0	0	0.137	1.34
O1	4*e*	0.2898	0.2692	0.9652	1.000	1.95
O2	4*e*	0.2832	0.3069	0.5366	1.000	1.46
O3	4*e*	0.9400	0.4858	0.7443	1.000	1.38

R_p = 2.76 %, R_{wp} = 3.81 %, R_{exp} = 3.22 %, R_{F^2} = 8.39 %

Phase	Weight of Sample (%)
$Sr_2YRu_{0.85}Cu_{0.15}O_6$	90.6(2)
SrY_2O_4	3.8(2)
$YSr_2Cu_2FeO_{6.536}$	3.4(2)
$SrCuO_{2.5}$	1.5(2)
$SrRuO_3$	0.7(2)

B.10 X-Ray Diffraction Refinements of $Sr_2HoRu_{0.85}Cu_{0.15}O_6$

B.10.1 ESRF Refinements

The diffraction pattern was measured at BM1B using the wavelength, $\lambda = 0.5029$ Å. Refinement with partial exchange of Ho and Ru between the 2*c* and 2*d* sites. Discussed on pages 170-171.

$Sr_2HoRu_{0.85}Cu_{0.15}O_6$		$P2_1/n$			Room temperature	
a / Å		*b* / Å	*c* / Å	*β* / °	Volume / Å^3	
5.77500(2)		5.78884(2)	8.17242(3)	90.256(1)	273.206(1)	
Atom	Site	*x*	*y*	*z*	Occ	B_{iso}/Å^2
Sr	4*e*	0.0050(2)	0.0280(1)	0.7493(2)	1.000(0)	2.24(7)
Ho	2*c*	0	½	0	0.956(1)	1.79(1)
Ru	2*c*	0	½	0	0.044(1)	1.79(1)
Ho	2*d*	½	0	0	0.044(1)	1.79(1)
Ru	2*d*	½	0	0	0.806(0)	1.79(1)
Cu	2*d*	½	0	0	0.150(0)	1.79(1)
O1	4*e*	0.2992(11)	0.2634(11)	0.9642(8)	1.000(0)	1.80(10)
O2	4*e*	0.2701(11)	0.3080(11)	0.5280(9)	1.000(0)	1.74(11)
O3	4*e*	0.9272(10)	0.4867(7)	0.7364(6)	1.000(0)	1.65(10)

$R_p = 2.55$ %, $R_{wp} = 3.64$ %, $R_{exp} = 2.99$ %, $R_{F^2} = 5.48$ %

The same crystal structure was used to model the partial exchange of Ho with Cu, as the structure does not change appreciably. The transfer was a 3.0(1) % Ho exchange with Cu, and yielded $R_p = 2.54$ %, $R_{wp} = 3.63$ %, $R_{exp} = 2.99$ % and $R_{F^2} = 5.47$ %, as discussed on page 170.

This crystal structure was also used when the impurity peaks were included in the diffraction pattern as discussed on pages 171-173.

Phase	Weight of Sample (%)
$Sr_2HoRu_{0.85}Cu_{0.15}O_6$	88.1(2)
$SrHo_2O_4$	5.4(2)
$YSr_2Cu_2FeO_{6.536}$	3.3(2)
$SrCuO_2$	1.7(2)
$SrCuO_{2.5}$	0.6(2)
$SrRuO_3$	0.8(2)

B.11 X-Ray Diffraction Refinement of $Sr_2Ho_{0.8}Tb_{0.2}Ru_{0.9}Cu_{0.1}O_6$

The diffraction pattern was measured at BM1B using the wavelength, $\lambda = 0.48572$ Å. Refinement with partial exchange of Ho and Ru between the 2*c* and 2*d* sites. Discussed on pages 173-174.

$Sr_2Ho_{0.80}Tb_{0.20}Ru_{0.90}Cu_{0.10}O_6$		$P2_1/n$		Room temperature	
a / Å	*b* / Å	*c* / Å	*β* / °	Volume / Å^3	
5.77789(2)	5.79353(2)	8.17681(3)	90.263(1)	273.710(1)	
Atom	Site	*x*	*y*	*z*	Occ	B_{iso}/Å^2
Sr	4*e*	0.0044(2)	0.0284(1)	0.7501(2)	1.000(0)	1.88(1)
Tb	2*c*	0	½	0	0.200(0)	1.40(1)
Ho	2*c*	0	½	0	0.760(2)	1.40(1)
Ru	2*c*	0	½	0	0.040(2)	1.40(1)
Ho	2*d*	½	0	0	0.040(2)	1.40(1)
Ru	2*d*	½	0	0	0.860(0)	1.40(1)
Cu	2*d*	½	0	0	0.100(0)	1.40(1)
O1	4*e*	0.2691(11)	0.3022(11)	0.5341(9)	1.000(0)	1.61(10)
O2	4*e*	0.1977(10)	-0.2327(11)	0.5343(8)	1.000(0)	1.49(10)
O3	4*e*	-0.0711(11)	0.4863(8)	0.7395(7)	1.000(0)	1.68(11)

$R_p = 5.24$ %, $R_{wp} = 6.91$ %, $R_{exp} = 4.85$ %, $R_{F^2} = 19.61$ %

The same crystal structure was used to model the partial exchange of Ho with Cu, as the structure does not change appreciably. The transfer was a 2.7(1) % Ho exchange with Cu, and yielded $R_p = 5.24$ %, $R_{wp} = 6.91$ %, $R_{exp} = 4.85$ % and $R_{F^2} = 19.61$ % as discussed on page 174.

This crystal structure was also used when the impurity peaks were included in the diffraction pattern, as discussed on page 174.

Phase	Weight of Sample (%)
$Sr_2Ho_{0.8}Tb_{0.2}Ru_{0.90}Cu_{0.10}O_6$	94.3(2)
$SrHo_2O_4$	3.0(2)
$YSr_2Cu_2FeO_{6.536}$	1.2(2)
$SrCuO_{2.5}$	0.7(2)
$SrRuO_3$	0.8(2)

B.12 X-Ray Diffraction Refinements of Sr_2TbRuO_6

The diffraction pattern was measured at SRS using the wavelength, $\lambda = 1.002$ Å.

Sr_2TbRuO_6			$P2_1/n$		Room temperature	
a / Å		b / Å	c / Å	β / °	Volume / Å^3	
5.79683(14)		5.82394(13)	8.21488(23)	90.303(2)	277.334(3)	
Atom	Site	x	y	z	Occ	B_{iso}/Å^2
Sr	4*e*	0.0040(10)	0.0298(3)	0.7499(9)	1.000(0)	1.96(4)
Tb	2*c*	0	½	0	1.000(0)	1.41(3)
Ru	2*d*	½	0	0	1.000(0)	1.41(3)
O1	4*e*	0.2604(40)	0.3272(38)	0.5335(33)	1.000(0)	2.31(57)
O2	4*e*	0.1930(42)	-0.2502(42)	0.5149(29)	1.000(0)	2.67(76)
O3	4*e*	-0.0484(45)	0.4877(22)	0.7414(32)	1.000(0)	2.43(63)

$R_p = 5.96$ %, $R_{wp} = 7.64$ %, $R_{exp} = 5.05$ %, $R_{F^2} = 4.47$ %

The refinement allowing partial exchange of Tb and Ru used the same crystal structure, except the transfer between the 2*c* and 2*d* sites was refined as 1.8(2) %, with $R_p = 5.99$ %, $R_{wp} = 7.75$ %, $R_{exp} = 5.06$ % and $R_{F^2} = 5.16$ %. The refinement using this model crystal structure, but a random ordering of the *B* cations yielded the *R*-factors of $R_p = 6.81$ %, $R_{wp} = 9.08$ %, $R_{exp} = 5.05$ % and $R_{F^2} = 6.92$ %.

C. Appendix – Publications, Presentations, Courses, Conferences and Seminars

C.1 Publications

The following papers were published at the time of writing, though more are expected from the research performed during the period of the study.

[1] **N.G. Parkinson**, P.D. Hatton, J.A.K. Howard, C. Ritter, F.Z. Chien and M.K. Wu, "Crystal and magnetic structures of $A_2YRu_{1-x}Cu_xO_6$ with A = Sr, Ba and x =0.05 to 0.15", *Journal of Materials Chemistry*, **13**, 1468 – 1474 (2003).

[2] **N.G. Parkinson**, P.D. Hatton, M.K. Wu and K.H. Andersen, "Structure and magnetism of doped ruthenium oxide superconductors", *The Rutherford Appleton Laboratory ISIS Facility Annual Report 1999-2000 (Science Highlight)*, 54 – 55 (2000).

[3] D.Y. Chen, M.K. Wu, **N.G. Parkinson**, C.H. Du. P.D. Hatton, F.Z. Chien and C. Ritter, "Magnetic ordering in the superconducting mixed ruthenium-copper oxide $Sr_2Y(Ru_{1-x}Cu_x)O_6$", *Physica C*, **341**, 2157 – 2158 (2000).

[4] M.K. Wu, B.H. Mok, M.J. Wang, D.C. Yuan, S.M. Rao, P.D. Hatton, **N.G. Parkinson**, "Magnetic ordering in the mixed ruthenium-copper oxide $Ba_2Pr(Ru_{1-x}Cu_x)O_6$ system", *Journal of Low Temperature Physics*, **131(5-6)**, 1053 - 1057 (2003).

C.2 Presentations

C.2.1 Oral Presentations

The following presentations were given on the work included in this thesis. The presentations were given in the Departments of Chemistry and Physics respectively, and were open to any academic at Durham University or beyond.

3rd July 2002 "Crystal and Magnetic Structures of Intriguing Ruthenates" 20 minutes

5th June 2002 "Crystal and Magnetic Structures of Intriguing Ruthenates" 25 minutes

C.2.2 Poster Presentations

26th April 2002 BCA Spring Meeting, University of Nottingham.

"Crystal and Magnetic Structures of $Sr_2HoRu_{1-x}Cu_xO_6$ & $Sr_2TbRu_{1-x}Cu_xO_6$" [1]

17th December 2001 Third Year Postgraduate Poster Session, University of Durham, Chemistry Department.

"Crystal and Magnetic Structures of the Mixed Ruthenium-Copper Oxides $Sr_2YRu_{1-x}Cu_xO_6$ and $Ba_2YRu_{1-x}Cu_xO_6$" [2]

16th March 2001 HERCULES Poster Presentation Session, Grenoble, France.

"The Crystal and Magnetic Structures of Superconducting $Sr_2HoRu_{1-x}Cu_xO_6$"

21st December 2000 CMMP 2000, University of Bristol.

I presented two posters concurrently at this poster session.

"Crystal and Magnetic Structures of the Mixed Ruthenium-Copper Oxides $Sr_2YRu_{1-x}Cu_xO_6$ and $Ba_2YRu_{1-x}Cu_xO_6$"

"The Crystal and Magnetic Structures of Superconducting $Sr_2HoRu_{1-x}Cu_xO_6$" [3]

4th April 2000 BCA Spring Meeting, Heriot-Watt University, Edinburgh.

"Crystal and Magnetic Structures of a Ru-Based Double Perovskite"

24th February 2000 M^2S-HTSC-VI, 6th International Conference on Materials and Mechanisms of Superconductivity and High-Temperature Superconductors, George R. Brown Convention Center, Houston, Texas, USA.

"Magnetic Ordering in the Superconducting Mixed Ruthenium-Copper Oxide $Sr_2Y(Ru_{1-x}Cu_x)O_6$"

[1] In recognition of the poster presentation I was awarded the Physical Crystallography Group Prize for best poster presentation, as reported in Crystallography News, No. 81, 21, June 2002.

[2] The panel of judges, from both the Department of Chemistry and the sponsors Zeneca, decided to award the poster presentation with joint second place.

[3] The poster presentation was awarded a blue ribbon as one of the best student posters, though unfortunately, due to other commitments I was unable to present it in the Grand Final.

Not since the presentation at the BCA Spring Meeting in 2000 has a poster failed to win a prize.

The BCA poster presentations also involve a 2 minute oral presentation the earlier in the day of the poster session.

C.3 Courses

The following courses were attended during the tuition period of study.

24th-25th March 2002	PCG/ ISIS Rietveld Workshop "Introduction to the Principles and Practice of Rietveld Refinement", University of Nottingham.
4th March – 11th April 2001	HERCULES - Higher European Research Course for Users of Large Experimental Systems, 11th Session, Grenoble & Paris, France.

In the Epiphany term 2000, "Diffraction" by A. Goeta and the "Numerical Methods" by M. Wilson were the courses attended in the Department of Chemistry.
In the Michaelmas term 1999, "X-Ray and Neutron Scattering Techniques" by T. Hase, "Electrical and Magnetic Measurement Techniques" by I. Terry, "Spectroscopy" by D. Halliday, "Nuclear Magnetic Resonance" by R.K. Harris, "Computing Simulation" by S. Clark and "Electron Microscopy" by K. Durose were the courses attended in the Department of Physics.
During the academic year 1999-2000, "A Beginner's Guide to UNIX", "Writing Longer Documents", "Web of Science", "Introduction to Endnote", "Introduction to PowerPoint", "Creating WWW Pages", "Using Styles and Templates" and "Writing Longer Documents" were courses organised by the Information Technology Service and attended.

C.4 Conferences

The following conferences were attended during the tuition period of study. Those indicated by an asterisk denote a poster was presented at the conference, as detailed above.

13th November 2002	BCA CCG Autumn Meeting, King's College, London. "Dealing with Difficult Data"
25th-28th March 2002 *	BCA Spring Meeting, University of Nottingham.
14th November 2001	BCA CCG Meeting, Aston University. "Mesomolecular Crystallography"
19th-21st December 2000 *	CMMP 2000, University of Bristol.
15th November 2000	BCA CCG Meeting, GlaxoSmithKline, Harlow, Essex. "Computational Methods"
3rd-6th April 2000 *	BCA Spring Meeting, Heriot-Watt University.
20th-25th February *	M^2S-HTSC-VI, 6th International Conference on Materials and Mechanisms of Superconductivity and High-Temperature Superconductors, George R. Brown Convention Center, Houston, Texas, USA.
17th November 1999	BCA CCG Autumn Meeting, University of Manchester. "Molecular Geometry using Methods Complementary to Crystallography"
4th November 1999	"Manganite Perovskites - Structure, Dynamics and Properties", Institute of Physics, London.

C.5 Seminars

The following seminars were attended during the tuition period of study. An asterisk denotes that the seminar was held in the Department of Physics, and those without an asterisk were presented in the Department of Chemistry.

Date	Title	Speaker
21st March 2003	Manipulating the electronic structure of semiconducting metal oxides.	P.M. Woodward
23rd January 2003	Optics with Laser-Like Atom Waves	W. Philips * (Nobel Prize)
15th October 2002	Supramolecular Synthesis of Functional Molecules and Materials	M. Zaworotko
10th October 2002	Are Crystal Structures Predictable	J. Dunitz
19th August 2002	Communication between spin cross over centres. Thermal, Pressure and Light Induced Spin Change in Iron(II) Complexes	J.A. Real
13th June 2002	Single-Crystal Neutron Diffraction at the ILL : Science and Facilities	G. McIntyre
8th May 2002	"Covalent" Effects in "Ionic" Materials	P. Madden
13th February 2002	The Demise of the Electron	A. Schofield *
31st January 2002	Some Supramolecular Chemistry of Magnets and Superconductors	P. Day
21st November 2001	Crystallography in the Pharmaceutical Industry	R.C.B. Copley
31st October 2001	Ultrafast magnetism: Reorientation of the Macroscopic Magnetisation and Spin Dynamics	R.J. Hicken *
12th September 2001	X-Ray Diffraction Investigations of Morphology of GaN/Sapphire Heteroepitaxial Structures	V Harutyunyan *
6th June 2001	The Melting Point Alternation of n-alkanes and Derivatives	R. Boese

Date	Title	Speaker
17th May 2001	Consideration of the Spherical Cow : The Realities of Magnetodynamics in an Imperfect World	T. Silva *
9th May 2001	Coherent Matter Waves	K. Burnett *
27th February 2001	Dorothy Hodgkin - A Woman's Life in Science	G. Ferry
14th February 2001	Analysis of Bonding Energy Distributions In Polyatomic Molecules	S. Howard
7th December 2000	A Cambridge Database Study of CH3/CF3 Exchange in Organic Crystals	A. Nangia
1st November 2000	Scanning Kelvin Microprobe in the Characterisation of Material Surfaces	M. Thompson
25th October 2000	Science, Art and Drug Discovery - A Personal Perspective	S.F. Campbell
18th October 2000	The Hydrometallation of Phospha-alkynes	A. Hill
11th October 2000	Recent Developments in OLED Technology : Organolanthanide Phosphors	V. Christou
26th May 2000	Exchange Biased Ferromagnets, Asymmetric magnetisation Reversal	C. Leighton *
17th May 2000	Spin Flip Raman Scattering Studies of II-VI Heterostructures	J. Davies *
10th May 2000	Joining the Dots Optoelectronic Devices Using Colloidal Semiconductor Nanocrystals	N. Greenham *
20th March 2000	Design of Molecules for Two-Photon Absorption and their Application to 3D Polymerisation and Imaging	S.R. Marder
1st March 2000	The Computer Simulation of Interfaces, Fact and Friction	D. Tildesley
9th February 2000	Shape and Selectivity	S.C. Moratti
21st January 2000	The Challenges involved in Protein Glycosylation - synthesis Chains and Selective Attachment to Proteins	S. Flisch

Date	Title	Speaker
19th January 2000	Delving into the Structure of Ferroelectric and Antiferroelectric Liquid Crystals	H. Gleeson *
1st December 1999	Spontaneous Emission Studies of Diode Lasers	P. Blood *
23rd November 1999	"Trace evidence" - A Challenge for the Forensic Scientist	B. Caddy
12th November 1999	The Incredible Shrinking Crystal: Formation of a Three Dimensional DNA Polymer	G. Clark
10th November 1999	Improving Organic LEDs by Molecular, Optical and Device Design	I.D.W. Samuel
9th November 1999	Charge Stripe Physics	P.D. Hatton *
25th October 1999	Unlikely Catalysts for Methylmethacrylate	S. Collins
25th October 1999	Magnetism on Small Scale-Spin Waves	R. Chandrell *
13th October 1999	Towards a Pictorial Glossary of Intermolecular Interactions	M.A. Spackman

The above list only includes the 38 seminars which were attended in Durham during the period of study. In total 197 seminars were attended when the various conferences are included also. Additionally, postgraduate presentations were attended in both departments, as well as talks given in Group Meetings.